

CORONA STABILIZATION AND BREAKDOWN  
IN SF<sub>6</sub> AND SF<sub>6</sub>/N<sub>2</sub> MIXTURES IN  
CONCENTRIC CYLINDRICAL GAPS

Thesis presented for the degree of Doctor  
of Philosophy in Electrical Engineering  
of the University of Strathclyde

Celâl Koraşlı, B.Sc., M.Sc.

September, 1981

In the name of Allah,

the Beneficent, the Merciful

## ABSTRACT

Corona and breakdown characteristics of compressed SF<sub>6</sub> and SF<sub>6</sub>/N<sub>2</sub> mixtures are studied experimentally and theoretically in the pressure range 0-8 bar for a wide range of gap nonuniformities under static and impulse voltages. The dielectric strength of SF<sub>6</sub> is compared with that of SF<sub>6</sub>/N<sub>2</sub> mixtures for the factors important in the design of CGI systems.

A comprehensive literature survey is given in the first chapter. Basic gas discharge mechanisms and associated processes are reviewed. Factors degrading the dielectric strength of the gases, especially those of SF<sub>6</sub>, are delineated and proposed models are discussed. Finally, a systematic review is made of recent findings on corona stabilization and corona discharge phenomena.

The results of series conditioning tests performed in SF<sub>6</sub> and SF<sub>6</sub>/N<sub>2</sub> mixtures for various gas and gap combinations are demonstrated in the third chapter. The conditioning is found to be prolonged both by increasing the electrode surface roughness and N<sub>2</sub> concentration. The mixtures are more polarity dependent with rough electrodes.

The statistical assessment of conditioning results for area effect by applying the Weibull type extreme value distribution is made in the fourth chapter. The Maximum Likelihood Method is adapted for the estimation of the distribution parameters, and a method is described to determine the tolerance bounds on each parameter for a given quantile. The area effect is shown to be more pronounced with increasing N<sub>2</sub> concentration. The slopes of distributions for rough electrodes are found to lie in the range 6-20.

The conditioned breakdown levels of successive breakdown tests is used for the evaluation of the breakdown performance of SF<sub>6</sub> and SF<sub>6</sub>/N<sub>2</sub> mixtures in the fifth chapter. The limiting field strength at which the deviation from the similarity starts is  $\sim 180$  kV/cm for polished electrodes and  $\sim 150$  kV/cm for rough electrodes. Breakdown calculations made with an isolated triangular model of 2  $\mu$ m height, show good agreement with experimental results obtained for polished electrodes. The compressibility factor calculated for mixtures is used in breakdown estimations.

The corona stabilized breakdown characteristics of SF<sub>6</sub> and SF<sub>6</sub>/N<sub>2</sub> mixtures are studied in the sixth chapter. The voltage-pressure characteristics exhibit the same anomaly as is observed in point-plane gaps. The rising part of the curve is dependent upon the radius of the outer electrode and the mixture ratio, and at breakdown the space charge field strength achieves a value in the range 35 - 45 kV/cm. The downcurving part of the curve is rather reproducible. The critical pressure is independent of the mixture ratio.

The seventh chapter deals with corona discharge phenomena in SF<sub>6</sub> and SF<sub>6</sub>/N<sub>2</sub> mixtures. The corona is identified as a streamer corona, although in mixtures over the downcurving part of the characteristic, stepwise streamer/leader discharge activity is observed. The ion mobilities is found to exhibit pressure and field dependence at pressures less than 1 bar.

## CONTENTS

|   | Page |
|---|------|
| 1. INTRODUCTION   | 1    |
| 1.1 General   | 1    |
| 1.2 Electrical Conduction Processes and Breakdown<br>in Gases   | 3    |
| 1.2.1 Current growth in gas discharges  | 3    |
| 1.2.2 Townsend breakdown criterion  | 6    |
| 1.2.3 Paschen's Law   | 7    |
| 1.2.4 Streamer breakdown theory   | 8    |
| 1.2.5 Extension of uniform field theories<br>to nonuniform fields                                     | 12   |
| 1.3 Corona Discharge Phenomena  | 16   |
| 1.3.1 General   | 16   |
| 1.3.2 Positive-point corona   | 17   |
| 1.3.2.1 General aspects   | 17   |
| 1.3.2.2 Discharge characteristics   | 19   |
| 1.3.3 Negative-point corona   | 22   |
| 1.3.3.1 General aspects   | 22   |
| 1.3.3.2 Discharge characteristics   | 23   |
| 1.4 Breakdown Phenomena in Compressed Gases   | 26   |
| 1.4.1 General   | 26   |
| 1.4.2 Failure of Paschen's law  | 27   |
| 1.4.2.1 Field emission  | 28   |
| 1.4.2.2 Positive-ion assisted field emission  | 29   |
| 1.4.2.3 Enhanced $\gamma$ -process  | 30   |
| 1.4.2.4 Effect of microprojections  | 31   |
| 1.4.3 Conditioning  | 32   |
| 1.5 Breakdown Phenomena in Compressed SF <sub>6</sub><br>and SF <sub>6</sub> /N <sub>2</sub> Mixtures | 33   |
| 1.5.1 General   | 33   |
| 1.5.2 Basic ion processes   | 34   |
| 1.5.3 Ionisation coefficients   | 36   |
| 1.5.4 Compressibility   | 39   |
| 1.5.5 Breakdown criteria in SF <sub>6</sub>   | 40   |
| 1.6 Experimental Studies in SF <sub>6</sub>   | 42   |
| 1.6.1 General   | 42   |
| 1.6.2 Breakdown in uniform fields   | 42   |
| 1.6.2.1 Low-pressure breakdown studies  | 42   |
| 1.6.2.2 High-pressure breakdown studies   | 43   |

|       |  |     |
|-------|--|-----|
| 1.6.3 | Quasiuniform-field breakdown   | 59  |
| 1.6.4 | Corona and breakdown in nonuniform fields  | 62  |
| 1.6.5 | Prebreakdown phenomena in SF <sub>6</sub> and SF <sub>6</sub> /N <sub>2</sub> mixtures                   | 68  |
| 1.7   | Voltage-time Characteristics   | 72  |
| 1.8   | Present Work   | 75  |
| 2.    | EXPERIMENTAL APPARATUS AND PROCEDURE   | 77  |
| 2.1   | General  | 77  |
| 2.2   | Experimental Vessel  | 77  |
| 2.2.1 | Pumping and gas filling systems  | 78  |
| 2.2.2 | Pressure measurements  | 79  |
| 2.3   | Electrode Assembly   | 79  |
| 2.4   | High-voltage Supplies and Automatic Control Systems  | 80  |
| 2.4.1 | DC voltage supply and gap voltage measurement  | 80  |
| 2.4.2 | Automatic voltage control and data recording system  | 82  |
| 2.4.3 | Impulse generator and voltage measuring system   | 83  |
| 2.4.4 | Automatic time-lag measuring system  | 84  |
| 2.5   | Ancillary Equipment  | 85  |
| 2.6   | Optical Recording System   | 86  |
| 2.7   | Experimental Procedure   | 87  |
| 3.    | SPARK CONDITIONING CHARACTERISTICS OF SF <sub>6</sub> AND SF <sub>6</sub> /N <sub>2</sub> MIXTURES       | 89  |
| 3.1   | General  | 89  |
| 3.2   | Experimental Arrangement and Procedure   | 91  |
| 3.3   | Preliminary Conditioning Experiments   | 92  |
| 3.3.1 | Importance of applied voltage waveform   | 92  |
| 3.3.2 | Effect of the resetting voltage V <sub>r</sub> and rate of rise of voltage r <sub>v</sub>                | 93  |
| 3.3.3 | Choice of the type of gas mixture  | 94  |
| 3.4   | Initial Spark Conditioning Tests in SF <sub>6</sub> and 40% SF <sub>6</sub> -60% N <sub>2</sub> mixtures | 96  |
| 3.5   | Conditioning in SF <sub>6</sub> and SF <sub>6</sub> /N <sub>2</sub> Mixtures                             | 97  |
| 3.5.1 | Effect of radiation  | 98  |
| 3.5.2 | Effect of the type of mixture  | 98  |
| 3.5.3 | Electrode effects  | 101 |
| 3.5.4 | Polarity effect  | 107 |
| 3.5.5 | Stress conditioning  | 108 |
| 3.6   | Discussion   | 110 |
| 3.7   | Conclusion   | 115 |

|         |   |     |
|---------|---|-----|
| 4.      | STATISTICS OF BREAKDOWN IN SF <sub>6</sub> AND SF <sub>6</sub> /N <sub>2</sub> MIXTURES   | 117 |
| 4.1     | General   | 117 |
| 4.2     | Characteristics of Weak Points  | 118 |
| 4.3     | Distribution Function of Extreme-Valve Breakdown Field Strengths  | 119 |
| 4.3.1   | Weibull extreme-value distribution function for an elementary region  | 119 |
| 4.3.2   | Other statistical models for extreme-valve distributions  | 122 |
| 4.4     | Parameter Estimation for the Weibull Distribution   | 124 |
| 4.4.1   | Estimation of minimum field strength (location parameter E <sub>0</sub> )   | 125 |
| 4.4.2   | Estimating of remaining Weibull parameters  | 126 |
| 4.4.3   | Confidence intervals for the Weibull parameters and tolerance bounds  | 129 |
| 4.4.4   | Estimation of density distribution function d <sub>0</sub>  | 131 |
| 4.5     | Weibull Distribution of Field Strengths in Successive Breakdown Tests in SF <sub>6</sub> and SF <sub>6</sub> /N <sub>2</sub> Mixtures | 132 |
| 4.5.1   | Conditioning effect   | 133 |
| 4.5.2   | Electrode area effect   | 136 |
| 4.5.3   | Electrode roughness effect  | 137 |
| 4.5.4   | Electrode material effect   | 138 |
| 4.5.5   | Effect of polarity and of irradiation   | 139 |
| 4.6     | Discussion  | 140 |
| 4.6.1   | Theoretical considerations  | 140 |
| 4.6.2   | Experimental considerations   | 144 |
| 4.7     | Conclusion  | 145 |
| 5.      | DC AND IMPULSE BREAKDOWN CHARACTERISTICS IN SF <sub>6</sub> AND SF <sub>6</sub> /N <sub>2</sub> MIXTURES                              | 147 |
| 5.1     | General   | 147 |
| 5.2     | Breakdown Field Estimations in Compressed SF <sub>6</sub> /N <sub>2</sub> Mixtures  | 149 |
| 5.2.1   | Swarm coefficients  | 149 |
| 5.2.2   | Compressibility effect  | 150 |
| 5.2.3   | Estimation for smooth electrodes  | 152 |
| 5.2.4   | Estimation for rough electrodes   | 154 |
| 5.2.4.1 | Protrusion models   | 156 |
| 5.2.4.2 | Application of models for estimating the roughness factor in SF <sub>6</sub>  | 158 |

|       |   |     |
|-------|---|-----|
| 5.3   | Breakdown Voltage Measurements in SF <sub>6</sub><br>and SF <sub>6</sub> /N <sub>2</sub> Mixtures | 158 |
| 5.3.1 | Test conditions   | 158 |
| 5.3.2 | DC breakdown characteristics  | 159 |
| 5.3.3 | Impulse breakdown characteristics   | 161 |
| 5.4   | Discussion  | 162 |
| 5.5   | Conclusion  | 166 |
| 6.    | CORONA STABILISATION BREAKDOWN IN SF <sub>6</sub> AND<br>SF <sub>6</sub> /N <sub>2</sub> MIXTURES | 168 |
| 6.1   | General   | 168 |
| 6.2   | Experimental Conditions   | 169 |
| 6.3   | DC Corona and Breakdown Voltage Measurements in SF <sub>6</sub>                                   | 170 |
| 6.3.1 | Repeatability of test result  | 170 |
| 6.3.2 | Effect of irradiation   | 171 |
| 6.3.3 | Effect of gap nonuniformity   | 172 |
| 6.3.4 | Effect of polarity  | 173 |
| 6.4   | DC Corona and Breakdown Voltage Measurements<br>in SF <sub>6</sub> /N <sub>2</sub> Mixtures       | 174 |
| 6.4.1 | Effect of mixture ratio   | 174 |
| 6.4.2 | Effect of gap nonuniformity   | 175 |
| 6.4.3 | Effect of polarity  | 176 |
| 6.5   | Impulse Corona and Breakdown Voltage Measurements<br>in SF <sub>6</sub> /N <sub>2</sub> Mixtures  | 177 |
| 6.5.1 | Effect of mixture ratio   | 177 |
| 6.5.2 | Effect of polarity  | 177 |
| 6.6   | Comparison of DC and Impulse Breakdown<br>Characteristics   | 178 |
| 6.7   | Factors Affecting the Behaviour of Voltage-<br>Pressure Characteristics                           | 178 |
| 6.7.1 | Effect of a small percentage of<br>SF <sub>6</sub> in air and nitrogen                            | 179 |
| 6.7.2 | Effect of conducting discs fixed on<br>the inner electrode  | 180 |
| 6.7.3 | Effect of ion injection   | 181 |
| 6.8   | Discussion  | 182 |
| 6.8.1 | Voltage-pressure characteristics  | 182 |
| 6.8.2 | Factors affecting voltage-pressure<br>characteristics   | 187 |
| 6.8.3 | Comparison of voltage-pressure characteristics<br>of point-plane and coaxial electrode gaps       | 190 |
| 6.9   | Conclusion  | 190 |

|        |  |     |
|--------|--|-----|
| 7.     | CORONA CHARACTERISTICS AND CORONA STABILISATION<br>PROCESS IN SF <sub>6</sub> AND SF <sub>6</sub> /N <sub>2</sub> MIXTURES | 193 |
| 7.1    | Introduction   | 193 |
| 7.2    | Experimental Conditions  | 197 |
| 7.3    | The Role of the Coaxial Electrode<br>Configuration in Corona Studies   | 197 |
| 7.4    | Corona Characteristics in Positive-<br>Inner-Coaxial-Electrode Gaps  | 198 |
| 7.4.1  | SF <sub>6</sub>  | 199 |
| 7.4.2  | SF <sub>6</sub> /N <sub>2</sub> Mixture  | 201 |
| 7.5    | Corona Characteristics in Negative-Inner-<br>Coaxial Electrode Gaps  | 203 |
| 7.5.1  | SF <sub>6</sub>  | 204 |
| 7.5.2  | SF <sub>6</sub> /N <sub>2</sub> Mixture (40% SF <sub>6</sub> /N <sub>2</sub> )   | 205 |
| 7.6    | Current-Voltage Relation in SF <sub>6</sub> and<br>SF <sub>6</sub> /N <sub>2</sub> Mixtures                                | 205 |
| 7.7    | Space-Charge Induced Field Measurements<br>at the Outer Electrode  | 207 |
| 7.7.1  | Probe Characteristics  | 207 |
| 7.7.2  | Field measurements in SF <sub>6</sub>  | 209 |
| 7.8    | Determination of Ion Mobilities in SF <sub>6</sub>   | 209 |
| 7.9    | Estimation of Gap Field Distribution<br>with Space Charge  | 210 |
| 7.9.1  | Comparison of experimental data<br>with estimated results  | 212 |
| 7.10   | Model Approach for the Prediction of<br>Critical Pressure  | 213 |
| 7.11   | Discussion   | 216 |
| 7.11.1 | Positive corona characteristics  | 216 |
| 7.11.2 | Negative corona characteristics  | 222 |
| 7.11.3 | Current-voltage characteristics  | 225 |
| 7.11.4 | Space charge field distribution and<br>ion mobility  | 227 |
| 7.11.5 | Critical pressure estimation   | 229 |
| 7.12   | Conclusion   | 230 |

|     |   |     |
|-----|---|-----|
| 8.  | GENERAL CONCLUSION AND RECOMMENDATIONS FOR<br>THE FUTURE WORK | 233 |
| 8.1 | General   | 233 |
| 8.2 | Conditioning and Electrode Area Effects                       | 233 |
| 8.3 | Breakdown Characteristics                                     | 235 |
| 8.4 | Corona-Stabilised Breakdown and<br>Discharge Phenomena        | 236 |
| 8.5 | Recommendations for the Future Work                           | 237 |

INTRODUCTION

1.1 General

The increasing demand for high-power transmission systems has stimulated new research into improved insulating media. Continuing experimental and theoretical investigations have revealed that compressed sulphur hexafluoride ( $\text{SF}_6$ ) has superior insulating properties to most common dielectrics; in the pressure range from 3 to 5 bar, for instance, the breakdown strength of  $\text{SF}_6$  is three times that of nitrogen ( $\text{N}_2$ ) and is approximately the same as that of oil [1]. Along with this beneficial high dielectric strength,  $\text{SF}_6$  is non-toxic, non-flammable and has favourable chemical and physical properties which include chemical inertness, thermal stability and good thermal conductivity. All these properties make  $\text{SF}_6$  attractive for use in many practical high voltage systems.

Initial applications of compressed  $\text{SF}_6$  took place in electrostatic generators, in the design of heavy X-ray equipment used to examine steel castings and in power transformers - an early design and operation of a 10-MVA transformer insulated with compressed  $\text{SF}_6$  was reported by Camili et al [2].

In addition to its insulating properties,  $\text{SF}_6$  has been shown to possess exceptional arc-quenching ability, which makes it valuable for use in circuit breakers. The initial experimental  $\text{SF}_6$  circuit-breaker was introduced in 1953 [3]; since then it has been successfully used in different types of circuit breakers including single and double pressure and puffer-type switchgear.

Very recently, a similar application of SF<sub>6</sub> in lightning arresters has been reported in Japan [4].

The superior insulating and arc-quenching properties of SF<sub>6</sub> have promoted many developments for the employment of this gas in metal-clad substations, with additional advantages such as much smaller physical size, lower installation cost, protection against contact and contamination, and improved reliability. There are now hundreds of substation bays operating throughout the world at voltages between 50 kV and 500 kV [5,6]. Developments for ehv (750 kV) and uhv (1.3 MV) installation are being planned [7,8].

The use of SF<sub>6</sub> for high-power underground transmission, which has been evolved from substation practice, has facilitated new developments in this field over the last twenty years. Currently available designs seem to be promising for voltages up to 500 kV [9] and new developments for three-phase 362 kV and for 1.2 MV transmission lines are in progress [10]. Recently a flexible-type cable design for 400 kV operation has been reported [11].

To make full use of the properties of compressed SF<sub>6</sub> in high-voltage systems, researches have been extended to identify important practical factors affecting the breakdown characteristics of the gas, such as electrode area, gas purity, surface finish, contamination, etc. Further, in order to search for new alternative gaseous insulants which are relatively cheaper and more effective in overall insulating performance than SF<sub>6</sub>, many experimental studies in mixtures of SF<sub>6</sub> with some common gases have been undertaken in different laboratories over the last few years.

Because of the complex nature of the discharge and breakdown characteristics of gaseous insulants, it is intended in this introductory chapter first to give general theories of

ionisation and breakdown mechanism in uniform and nonuniform fields. Following this, as background information to the study of corona in compressed  $\text{SF}_6$  and  $\text{SF}_6/\text{N}_2$  mixtures, a brief account of corona discharges in atmospheric air together with the principal theories has been included. The introduction continues with an account of the general factors which influence the breakdown characteristics of compressed  $\text{SF}_6$  insulating systems, including electrode surface microstructure, free conducting particles, contamination and area effects, and review of previous work on ionisation and breakdown in  $\text{SF}_6$  and its mixtures. Finally, in the last section, the aims and objectives of the present study are given.

## 1.2 Electrical Conduction Processes and Breakdown in Gases

The electrical conduction through gases in an externally applied uniform field builds up mainly by collision of electrons with neutral atoms or molecules producing, in turn, more charged particles. If the number of charged particles rises sufficiently then a transient discharge may take place leading to a complete breakdown.

In the following sections it is intended to give a brief summary of the theories established on the growth of electrical conduction in gases.

### 1.2.1 Current growth in gas discharges

At moderate pressures in a gas over a wide range of experimental conditions the growth of current that precedes breakdown of a uniform discharge gap has been explained by J.S.Townsend [12] and the theoretical work in this field has been reviewed by many authors [13, 14].

According to the theory, in a uniform electric field electrons released at the cathode of the discharge gap by some external agent, for instance U.V. radiation, move across the gap towards the anode under the action of the field and at the same time ionise the gas molecules by collision. In this way, the ionisation process produces further electrons along with positive ions, the number of charges growing exponentially according to the relation

$$n_-(x) = n_0 \exp(\alpha x) \quad (1.1)$$

where  $n_-(x)$  is the number of electrons at a distance  $x$  from the cathode measured in the direction of the field,  $n_0$  is the number of initial electrons released simultaneously from the cathode and  $\alpha$  is the Townsend's first ionisation coefficient which is the number of ionising collisions made by one electron per centimeter of drift across the gap in the direction of the field. The value of  $\alpha$  depends on the nature of the gas, the gas pressure  $p$  and the electric field strength  $E$ , such that  $\alpha/p$  is a function of  $E/p$  only. This means that each electron leaving the cathode produces an 'avalanche' of  $[\exp(\alpha x) - 1]$  electrons together with  $[\exp(\alpha x) - 1]$  positive-ions in traversing the distance  $x$ .

The current in the gap is due to the movement of electrons and positive ions. In the steady state when the avalanche reaches the anode the circuit current is given by

$$I = I_0 \exp(\alpha d) \quad (1.2)$$

where  $d$  is the gap length and  $I_0$  is the current due to external radiation which would flow if the electrons released at the cathode were to cross the gap without ionising.

At large values of  $d$  and at low pressures, the electron

current  $I$  increases faster with increased voltage than predicted by the exponential law given in equation (1.2). This is ascribed to the production of some 'secondary' electrons as the avalanche proceeds through the discharge gap. There are three main processes producing secondary electrons at the cathode:

- i. Positive-ions produced in the primary avalanche drift in the field and cause electron ejection on striking the cathode.
- ii. Gas molecules raised to higher energy levels during inelastic collisions may emit photons on returning to their ground states. This radiation may fall on the cathode to produce electrons by photo-emission.
- iii. Metastable atoms or molecules may diffuse back on to the cathode and cause emission of electrons on striking it.

In the current growth expression all the secondary mechanisms acting separately or together may be represented by a single coefficient  $\gamma$ , defined as the number of secondary electrons produced per ionizing collision in the gap. This coefficient is found to be a function of the field strength and pressure only, i.e.  $\gamma = g(E/p)$ .

Modifying the equation (1.2) to include the effects of secondary mechanisms leads to

$$I = I_0 \frac{\exp(\alpha d)}{1 - \gamma[\exp(\alpha d) - 1]} \quad (1.3)$$

In electronegative gases - gases which have high ability to capture electrons - it is necessary to include the effects of negative-ion formation, and the expression given in equation

(1.3) must be modified by introducing an attachment coefficient  $n$  (defined as the number of attaching collisions made by one electron drifting one centimeter in the direction of the field) and the expression for the average current build-up can be derived as

$$I = I_0 \frac{\frac{\alpha}{\alpha} \exp(\bar{\alpha}d) - \frac{n}{\alpha}}{1 - \gamma \frac{\alpha}{\alpha} [\exp(\bar{\alpha}d) - 1]} \quad (1.4)$$

where  $\bar{\alpha} (= \alpha - n)$  is the effective ionisation coefficient and is a function of  $(E/p)$ , i.e.  $\bar{\alpha}/p = h(E/p)$ .

### 1.2.2 Townsend breakdown criterion

For a fixed gap length a critical condition arises as the voltage increases and the gap current becomes independent of the cathode current. This transition occurs if the expression  $\gamma [\exp(\alpha d) - 1]$  becomes unity. In this case the gap current given in equation (1.3) tends to infinity and will be limited by the external circuitry. The discharge becomes self-sustaining and requires no more initiating electrons. The critical value of the gap length is known as the sparking distance  $d_s$  and the voltage as the sparking voltage  $V_s$ . This condition is defined as the Townsend breakdown criterion and is expressed quantitatively as

$$\gamma [\exp(\alpha d_s) - 1] = 1 \quad (1.5)$$

This theoretical relationship for a self-sustained discharge had been verified [15] experimentally for many gases at low pressures.

When the Townsend breakdown criterion is satisfied, the probability for the production of successive avalanches increases and the accumulated space charge produced by the rapidly

growing series of avalanches favours the ionisation conditions for the electrons and hence the rapid growth of current.

The condition for a self-sustained discharge in electronegative gases is that the denominator of the equation (1.4) becomes zero, i.e.

$$\gamma \frac{\alpha}{\alpha - \eta} [\exp(\alpha d_s) - 1] = 1 \quad (1.6)$$

As long as  $\alpha > \eta$ , breakdown is always possible, irrespective of the values of  $\alpha$ ,  $\eta$  and  $\gamma$ , provided the gap spacing is sufficiently large. For  $\alpha < \eta$  the equation (1.6) approaches an asymptotic form as  $d$  increases and

$$\alpha = \frac{\eta}{1 + \gamma} \quad (1.7)$$

This relationship theoretically sets a limit for  $(E/p)$  below which no breakdown should be possible, independent of the value of  $d$ . Normally, the value of  $\gamma$  is less than unity. Therefore, the limiting value of  $(E/p)$  for electronegative gases is derived from the relationship,  $\alpha = \eta$ . For a number of electronegative gases this relation has been found [16] to be consistent with experimental results.

### 1.2.3 Paschen's law

The Townsend breakdown criterion provides an explanation for the experimental observations made by Paschen [14], who found that the static breakdown voltage  $V_s$  is a function of the product of the pressure and the gap length,  $pd_s$ . It is important to note that this does not necessarily mean a linear relationship, although it may be linear in some ranges of  $pd_s$ . This similarity principle can be derived from the Townsend's breakdown relationship

given in equation (1.5) as follows: since the ionisation coefficients are functions of the field strength and the gas pressure, i.e.

$$\alpha/p = f(E/p) ; \quad \alpha/p = g(E/p)$$

Substituting for these in equation (1.5) yields

$$g(E_s/p) [\exp(pd_s f(E_s/p) - 1)] = 1$$

Since in a uniform field  $E_s = V_s/d_s$ , therefore

$$g(V_s/pd_s) [\exp(pd_s f(V_s/pd_s) - 1)] = 1$$

In this equation there exists only a particular breakdown voltage  $V_s$  for a given  $pd_s$ , i.e.

$$V_s = F(pd_s)$$

This relationship is obtained for a constant gas temperature.

In order to include the effect of the gas temperature, the gas density  $\rho$  rather than the pressure should be used in the equation.

#### 1.2.4 Streamer breakdown theory

On the basis of measurements made at high values of  $(E/p)$  and at low  $pd$ , the Townsend theory of breakdown has been found to be adequate and accurate in calculating the breakdown voltage in gases. Also, if the effect of attachment is considered, the theory gives convincing results in electronegative gases at low pressure. However, the theory has been found [16, 18] to conflict until some experimental results were obtained at atmospheric pressure and above in air and in other gases. Some of the observations which are inconsistent with a multiavalanche process are: i) very short times ( $\lesssim 1$  electron transit time) measured for the breakdown to materialise when transient overvoltages - above the static breakdown voltage - are applied to uniform field

gaps; ii) values of  $\gamma$  obtained at low pressures and short gap lengths are found to be not applicable at higher pressures and long gap lengths; iii) the impulse breakdown voltages of a positive point-plane gap appears to be independent of the cathode material [14]; iv) at high values of  $pd$ , no appreciable change is found in the formative time of a spark channel with changes in the illumination intensity falling upon the cathode, and v) also at high values of  $pd$ , branched and irregular spark developments are observed. To account for such disagreements a new mechanism for the breakdown process was proposed independently by Raether [16] and Meek [17].

The 'streamer' mechanism is based on the consideration of the development of a single avalanche originating from the cathode into a plasma channel which results in a spark breakdown across the gap. The theory involves ionization by electron collision according to the Townsend  $\alpha$ -mechanism, together with secondary electron production by photoionization, and space-charge field effects caused by the ion species generated during the avalanche growth. Thus, in a field of magnitude which is sufficient to cause breakdown, the appearance of a single electron leads to the build-up of an electron avalanche: an accumulation of positive ions will be left behind as this grows. Due to relatively small drift velocity of the positive ions, charge separation occurs along the axis of the growing avalanche. The dipole space-charge field augments the externally applied field ahead of and behind the avalanche.

Since  $\alpha$  changes rapidly with small variations in  $E$ , such field enhancement can effectively favour the advance of the

avalanche towards anode. When the avalanche has crossed the gap electrons are swept into the anode. In the gas surrounding the primary avalanche photo-electrons are produced by photons emitted from the densely ionized gas at various distances from their origin depending on the absorption coefficient ( $\mu$ ) of the gas. These electrons initiate auxiliary avalanches heading towards the main stem of the primary avalanche, if the space-charge field developed by the main avalanche is of the order of the external field. The greatest multiplication in these auxiliary avalanches will occur along the axis of the main avalanche where the space charge supplements the external field. Positive ions left behind by these avalanches effectively lengthen and intensify the space charge of the main avalanche in the direction of the cathode, and the process develops as a self-propagating streamer. As the streamer proceeds across the gap a conducting filament of highly ionized gas follows [14].

In order to calculate the magnitude of the space charge field, it is assumed that, because of the cumulative nature of the ionization, the space charge may be represented by a sphere of charge at the head of the primary avalanche. The field at the surface of the sphere containing  $\exp(\alpha x)$  electrons, having a radius  $r$  is

$$E_r = \frac{e \exp(\alpha x)}{4\pi \epsilon_0 r^2} \quad (1.8)$$

The value of  $r$  is given by the diffusion expression  $r = (2Dt)^{1/2}$  where  $D$  is the diffusion coefficient and  $t$  is the electron transit time of the electrons traversing from  $x = 0$  to  $x$  with the drift velocity  $v$ .

Substituting the known values for  $D$  and  $v$  for any gas, expression (1.8) becomes

$$E_r = k \frac{\alpha \exp(\alpha x)}{(x/p)^{1/2}} \quad (1.9)$$

here  $k$  is a constant and  $p$  is the gas pressure.

The streamer breakdown criterion proposed by Meek and Loeb [19,20] states that a streamer develops when the radial field  $E_r$  due to positive space-charge at the head of the avalanche attains a value in the order of the external field,  $E$ . Thus

$$k' E (x/p)^{1/2} = \alpha \exp(\alpha x) \quad (1.10)$$

A similar criterion proposed by Raether [16] for the anode directed streamer is as follows. Recalling equation (1.9) and substituting for the avalanche radius

$$r = (3Dt)^{1/2} = \frac{9}{2} \left( \frac{U_e x}{E} \right)^{1/2} \quad (1.11)$$

where  $U$  is the thermal energy of electrons, then the formation of the streamer would be possible if

$$\alpha x_c = 17.7 + \ln x_c \quad (1.12)$$

where  $x_c$  is the distance travelled by the avalanche. In a uniform field transition occurs when the avalanche just crosses the gap so that the avalanche length becomes  $d$ . The breakdown criterion is then

$$\alpha d = 17.7 + \ln d \quad (1.13)$$

At low pressures, in various gases, Raether verified the figure of  $\exp(\alpha d) \sim 10^8$  electrons and the corresponding  $\alpha$ -value of about 20 required for streamer propagation.

Pedersen [19] suggested a semi-empirical concept based on Meek's equation to obtain agreement with experiment, that

may be written as

$$g(x, \rho) = \alpha d + \ln \alpha \quad (1.14)$$

Since  $\alpha$  is constant for a uniform field, the numerical values for  $g(x, \rho)$  for any gap would be found by calculating the left-hand side of equation (1.14) from the breakdown field measurements in a uniform field.

In both streamer breakdown criteria, the calculations were based on space charge formation due to an avalanche initiated by a single electron, i.e.  $n_0 \approx 1$ . A number of experimental observations have been performed [20,21] in different gases with various  $\gamma$ -values to verify the equation (1.13). Even in gases with relatively small values of  $\alpha$  the number of initiatory electrons released simultaneously at the cathode was found to be in excess of  $\sim 10^4$ . Therefore, the number of charged particles in an avalanche can reach a level of space charge field predicted by the breakdown criteria.

Due to the lack of experimental data on some important physical parameters, many different views still exist on the actual spark mechanism. However, it is evident that at low gas pressures the mechanism is influenced by the cathode and at high pressures it is not, unless high prebreakdown currents and accompanying space charge distortion exists. The cloud-chamber experiments done by Raether revealed that, in gaps for which the product  $pd$  is less than 1000 torr cm, the breakdown is due to successive avalanche build-up, while at higher  $pd$ -values the breakdown is due to transition from a single avalanche to a streamer.

### 1.2.5 Extension of uniform field theories to nonuniform fields

In nonuniform fields, since the field is high at the

anode or cathode, or at both, the ionization coefficient becomes dependent on position in the gap. It follows that the argument of  $\exp(\alpha d)$  in the current growth equation (1.2) must be modified by changing  $\alpha d$  to  $\int_0^d \alpha dx$ . In longer gaps the ionization region is small relative to the gap length, and avalanches do not cross the entire gap but are confined to the high-field electrode. Since much of the present work is concerned with coaxial-electrode geometry, this may be taken as an example; for this configuration the discharge current is

$$I(r) = I_0 \left( \int_{r_1}^{r_2} \alpha(r) dr \right) \quad (1.15)$$

Here the limits of integration are not taken to cover all the gap length, but instead from the inner electrode ( $r_1$ ) to the boundary ( $r_c$ ) where the collisional ionization ceases, i.e. where  $\alpha = \eta$ . The position of this boundary in the gap is determined by the gas composition, the gas pressure and the nonuniformity of the field distribution in the gap.

The Townsend current-growth equation for electro-negative gases can be expressed in coaxial-cylinder configuration using the same considerations as in equation (1.4) as

$$I(r) = I_0 \frac{\frac{\alpha(r)}{\bar{\alpha}(r)} \left[ \exp \left( \int_{r_1}^{r_c} \bar{\alpha}(r) dr \right) + \frac{\eta}{\bar{\alpha}} \right]}{1 - \gamma \frac{\alpha(r)}{\bar{\alpha}(r)} \left[ \exp \left( \int_{r_1}^{r_c} \bar{\alpha}(r) dr \right) - 1 \right]} \quad (1.16)$$

and the threshold condition for sustaining current is obtained when

$$\gamma \frac{\alpha(r)}{\bar{\alpha}(r)} \exp \left( \int_{r_1}^{r_c} \bar{\alpha}(r) dr \right) = 1 \quad (1.17)$$

Meek [18,22] derived the discharge threshold condition in nonuniform fields in terms of streamer theory. In this case the number of ion pairs in the front of the advancing avalanche from the high stress electrode is given by

$$N(E_x, p) = \exp \left( \int \bar{\alpha} dx \right) \approx 10^8 \quad (1.18)$$

This is the critical avalanche condition for transformation of a single electron avalanche into a streamer when the space-charge field becomes equal to the applied field  $E$ . Thus

$$\bar{\alpha}_x \exp \left( \int \bar{\alpha} dx \right) = k' E_x \left( \frac{x}{N} \right)^{1/2} \quad (1.19)$$

where  $\bar{\alpha}_x$  is the value of  $\bar{\alpha}$  corresponding to the external field  $E_x$  at the position  $x$  of the avalanche head,  $k'$  is a constant and  $N$  is the gas density. A similar criterion was described by Raether [23].

A semiempirical proposal was suggested by Pedersen [19] to take into account the effects of some dominant physical variables in order to correlate the experimental results with the criterion given in equation (1.19). The modified form of the equation (1.19) is then

$$\bar{\alpha}_x \exp \left( \int \bar{\alpha} dx \right) = G(x, N) \quad (1.20)$$

where  $G(x, N)$  is a function of the critical avalanche length  $x$  and gas density  $N$ .  $G(x, N)$  is deducible from the measurements of breakdown voltage in uniform fields.

In strongly divergent fields the transformation from an avalanche into a streamer defines the onset of corona and not the breakdown of the gap. The streamers are formed around the high-

field electrode but will not travel across the gap unless the gap voltage is sufficiently high.

For a given gap voltage the value of  $E_r$  given in equation (1.9) is higher at the head of the avalanche travelling into the high-voltage electrode than for that travelling away from it. Since for the former case the ionization coefficient  $\alpha_x$  will become higher than the later, the streamer formation which occurs when  $E_r \sim E$  can be started at a slightly lower voltage when the high-voltage electrode is negative than when it is positive, as generally observed in nonattaching and attaching gases [14].

### 1.3 Corona Discharge Phenomena

#### 1.3.1 General

The physical discharge mechanism active in a gaseous medium in the vicinity of asymmetrical electrodes, as the voltage is raised from threshold to sparkbreakdown, is known as 'corona discharge'. It manifests itself with the flow of transient and steady currents, accompanied by audible noise and by various types of luminous phenomena. These processes occur in most of the inhomogeneous gap configurations, for example along transmission lines or in the vicinity of irregularities on a conductor at high voltage.

Although the corona discharge has been utilized in many practical applications such as dust precipitation and electrostatic painting, ozone production, telecopying, etc., it often has undesirable effects in power transmission which are responsible for losses and radio interference as well as for insulation failures in apparatus with gaseous insulation. On such an important phenomenon a considerable amount of work has been carried out to identify some of the physical processes taking place in gases of practical importance.

In the earlier studies prior to 1965, major contribution was made by Loeb and his group [24] working mostly in air with a point-plane electrode configuration. Recently, with improvements in experimental techniques and the employment of computers, there have been significant achievements towards understanding the fundamental microscopic and macroscopic properties of corona. However, there still exist many processes and related physical parameters which are not readily explained. In the following sections the well-established dc corona discharge phenomena in air in point-plane gaps will be reviewed so that, in discussing the corona discharge

modes in compressed SF<sub>6</sub> and SF<sub>6</sub>/N<sub>2</sub> mixtures, additional features due to gas composition and pressure would be readily identified.

### 1.3.2 Positive-point corona

#### 1.3.2.1 General aspects

If the voltage in a nonuniform field gap is raised gradually, starting from a very low voltage, the current achieves a value in the order of  $10^{-13}$  to  $10^{-10}$  A [25]. This current results from the electrons and ions caused by external ionizing agents acting on the gas. This current is the saturation current and does not increase with voltage. In air at atmospheric pressure and at low fields, electrons thus produced are promptly attached to molecules - mainly oxygen - to form negative ions, either of the type O<sub>3</sub><sup>-</sup> or the type O<sub>2</sub><sup>-</sup>, which may be clustered with neutral molecules (H<sub>2</sub>O)<sub>n</sub>. Under the effect of the external field these ions will diffuse to the lower field sites and some of them will recombine with each other. In the region with no external field the density of positive and negative ions are necessarily equal.

As the voltage is increased, there will be a gradual rise in current starting from the threshold voltage, and then a sudden jump will follow at the corona-onset voltage V<sub>o</sub>. The current is unsteady and pulsating in nature, signifying the onset of ionization and the subsequent exponential build-up of charge carriers leading to the self-sustained discharge condition described by the Townsend criterion given in equation (1.17), i.e.

$$\mu = \gamma (M - 1) \quad (1.21)$$

where M is the electron multiplication factor which, in coaxial-cylinder geometry, for example,  $M = \int_{r_1}^{r_c} \bar{\alpha}(r) dr$ .

In air at atmospheric pressure, the corresponding field at onset for coaxial geometry was found [26] to be

$$E_0 = E_b \cdot s \cdot \delta \cdot [1 + k/(\delta \cdot r_1)^{1/2}] \quad (1.22)$$

where  $E_b = 31 \text{ kV cm}^{-1}$  is the breakdown field strength for air (measured at STP in a 1-cm uniform field gap),  $s$  is a factor describing the surface condition of the inner conductor and  $\delta$  is the relative air density.

Increasing the field above  $E_0$  does not lead to immediate breakdown, as in a uniform field, but instead causes the current to rise linearly at first and later parabolically following the relation

$$I = C K V (V - V_0) \quad (1.23)$$

where  $k$  is the ion mobility and  $C$  is a constant determined by the gap geometry. In this equation it is a proved fact that the corona-onset voltage  $V_0$  is maintained across the ionizing region independent of the applied voltage and the excess  $(V - V_0)$  appears as a voltage drop across the low field region. This happens in the following way: An increase in the applied voltage to the gap is followed by an increase in ionization and positive ions in the ionizing region. As these ions drift out of the ionizing region, the field near the cathode increases while that near the anode decreases to the value which existed before the voltage was applied, thus restoring the voltage across the ionizing region to  $V_0$  and replacing the new voltage increment across the space charge. This equation (1.23) was derived [27] for coaxial-cylindrical geometry and can be applied to other geometries also, such as point-plane geometry, by simply modifying the constant  $C$  accordingly. In order to have breakdown, the gap voltage must be increased further (to  $V_b$ ). The voltage range from  $V_0$  to  $V_b$  is known as the corona discharge region and over

this region transitions to different corona modes take place as will be explained in the following section.

### 1.3.2.2 Discharge characteristics

As the voltage across a point-plane gap is raised gradually from corona onset to spark breakdown, different corona regimes take place in the gap depending on the physical and geometrical factors such as humidity, gap separation and radius of curvature of the point electrode.

A. Pre-onset streamers and burst pulses: At threshold, due to the statistical nature of the avalanche process and the sensitivity of the effective ionization coefficient  $\bar{\alpha}$  to field variations, the positive corona is usually unstable. However, a single intense avalanche or a group of converging intense avalanches can yield enough space charge distortion to produce a streamer. This is often called a 'pre-onset' streamer and appears as an extremely faint, slightly branched filamentary discharge. It develops away from the point until the potential energy stored in the space charge is dissipated in the gas by electron collision. The positive space charge produced by the streamer reduces the anode field, so that a new streamer cannot develop until this has cleared from the ionization region. Although streamer formation may be inhibited by space charge effects, an avalanche can lead to a discharge which spreads laterally due to secondaries produced by photoionization, and this gives rise to the so-called 'burst pulse' discharge. The current pulse associated with the burst pulse discharge are smaller in amplitude than for the streamer discharge but are much longer in duration (of the order of 100  $\mu$ sec or longer) and with little reproducibility in successive burst. Once burst pulse activity

starts, the formation of a new pre-onset streamer is determined by the density of the space charge and by the falling current-voltage characteristics of the power supply [24].

At the corona onset, the probability of having either a pre-onset streamer or a burst-pulse corona depends essentially on the mean free path ( $1/\mu_i$ ) of the photons, the size of the Townsend avalanche and the geometric parameters. If ( $1/\mu_i$ ) is much larger than the ionizing zone  $r_c$ , the discharge will spread over the point surface as a burst pulse, but if it is only slightly larger or comparable to  $r_c$  and the avalanche size is sufficient to produce enough photons, then the streamer propagation will be favoured [24]. As the radius of curvature of the point is increased, the interdependence between the pre-onset streamer and burst pulse formation is reduced. At a critical point-curvature the corona appears as burst-pulse corona without pre-onset streamers.

B. Positive-glow corona discharge: As the applied voltage is raised above the corona onset voltage, streamer and burst pulse occurrence becomes more frequent. The streamers grow further into the gap and the burst pulse duration increases. Further increase in the gap voltage yields a condition that the space charge is cleared by the applied field as fast as it accumulates in the gap. This discharge activity grows as an extension of the preceding intermittent regime into a stable and continuous glow discharge without any streamer activity. There has been some controversy concerning the precise mechanism of the positive glow discharge. The most well-known theory of this phenomenon which has been accepted a long time and disputed recently was that proposed by Hermstein [28]. As streamers cease to advance into the gap, the positive ions

produced drift away from the point, while photoelectrically-created electrons are drawn towards it. Some of the electrons, before reaching the point, attach to  $O_2$  molecules to form negative ions. As the cloud of negative ions drifts slowly toward the point, it reduces the field between the positive space-charge and the point, while increasing the field near the point. The enhanced field close to the point confines the Townsend discharge into this region. If the negative-ion regeneration mechanism is not disturbed, the discharge close to the point continues steadily and inhibits the advance of further streamers, unless the applied voltage is increased. This explanation does not appear to agree with the following experimental observations of a number of investigators.

(i) In pure  $N_2$  [29] and in  $N_2$  with a trace quantity of oxygen (0.01%) [30], there is glow corona discharge. This also is found to be true in some rare gases [31].

(ii) In  $N_2/O_2$  mixtures with  $O_2$  concentration greater than about 25% and in some mixtures of  $N_2$  with freon, no glow is observed [29].

(iii) Field probe measurements [30,32] at the anode point reveal that the anode point field is decreased during the corona.

In the light of all this evidence, Buchet and Goldman [36] suggested that the role of negative ions is to provide supplementary electrons to the multiplication zone by detachment. This will increase the avalanche activity and effectively the positive space charge in the drift region. They also showed theoretically that the negative-ion sheath is unlikely to coexist in close proximity to the anode point.

Although this proposal is generally confirmed by the results of different investigators, it is questioned by the observations of Beattie [25] who found no glow in  $N_2$  contaminated with 0.005% oxygen, but spark breakdown instead.

C. Prebreakdown and breakdown streamers: At the onset of this regime the discharge becomes intermittent with the reappearance of streamers superimposed over the glow. The streamer current pulses have generally the same characteristics as those of the pre-onset streamers but occur more frequently and are larger in magnitude. As the voltage is raised streamers become more active, extend more into the gap and result in distortion of the field. The transition to spark breakdown involves activity at the cathode [33] in which electrons are injected into the plasma front of the primary streamer, followed by the development of a very intense secondary streamer [34] from anode to cathode, resulting in a transient thermal arc.

### 1.3.3. Negative-point corona

#### 1.3.3.1 General aspects

As the voltage across a negative point-plane gap is increased, a rapid jump in current from the saturation current signifies the start of the Townsend ionization mechanism around the point electrode. After the onset of ionization, the average current variation with voltage is found [31,35] to be generally compatible with the Townsend corona current relation (equation (1.23)) with the exception that there exists a slight discontinuity at the transition from the pulsative mode near onset to the steady-glow regime. This discontinuity has been related [35] to the value of the series

circuit resistance with respect to the negative differential resistance of the discharge at the transition.

Since initiating electrons are readily available from the cathode surface by field emission, the onset voltage level is generally slightly lower than the positive-point case.

#### 1.3.3.2 Discharge characteristics

Over the voltage range from the corona onset  $V_0$  to the spark breakdown voltage  $V_b$  several corona modes take place.

A. Autostabilization: At the onset voltage, the discharge at first appears in the form of isolated irregular current pulses, that tend to group randomly into chains. Each chain consists of a large pulse followed by irregular small pulses. The simultaneous existence of two types of pulse is due to the action of the negative space charge [36] on the point. As the positive ions produced in an avalanche drift towards the cathode point, there is a short-lived drift towards enhancement of the field near the point. Meanwhile, electrons moving away from the cathode in the lower field region have attached to atoms or molecules, forming a negative space charge which moves slowly towards the anode. This weakens the effect of the positive space charge in the vicinity of cathode and retards the development of successive pulses in the chain.

As the voltage is increased above this unstable discharge regime, the time duration of the chains get larger, the smaller pulses become more regular and more numerous and the chains merge with the disappearance of the large pulses. A new regime of small regular pulses starts.

B. Trichel pulse discharge: The above regular pulsative discharge mode is known as Trichel-pulse corona [37]. The pulse shape and the charge per pulse varies with voltage and, for a

given point, the pulse repetition rate is nearly proportional to current. The gap length has no appreciable effect on the frequency variation with current; this signifies that the Trichel pulse activity is confined to the vicinity of the point. A general description of the Trichel pulse cycle is as follows. After a pulse, positive ions drift into the cathode and as the remaining negative ions in the gap move towards the anode, the field in the ionization region rises again to the geometric field value. At this phase of the phenomenon, it has been observed [38,39] that a non-self-sustained electron current flows up to the start of the next pulse flowing from the cathode. Sigmond and Torsethaugen [39] attributed this current to the Townsend  $\gamma$  - mechanism of diffusing metastables produced in the preceding pulse in addition to the electron current produced by  $\gamma_i$  - mechanism and by emission from the cathode point. While this current is decreasing, as the negative ions drift into the anode, the field in the ionization region rises towards the self-sustainment value, at a rate dependent on the gap voltage. When the Townsend discharge condition is met in the ionization region the current rapidly reaches its Trichel pulse maximum value, and the cycle repeats itself.

The effect of the field distortion on the development of the Trichel pulse has been demonstrated by the experiments of Torsethaugen and Sigmond [39].

Although the repetition period of the Trichel pulses was concluded [37] to be the same as that of the negative ion transit time, it may be shorter [35] than the transit time owing to the simultaneous existence of the several negative ion cloud drifting towards the anode.

One of the important characteristics of Trichel pulses which has been studied extensively by many authors [40-42] is their very short rise time ( $\sim 1.5$  ns) which is nearly independent of the radius of the point, and is dependent on the applied voltage. The effect of the geometric factors can be explained on the basis of existing theories developed for the Trichel pulse formation. For the rapid growth of the current Loeb [40] proposed a model in terms of the successive avalanche development; the increase in the number of avalanches at the onset of a Trichel pulse follows a geometric progression. After each avalanche  $q$  - photoelectrons are produced and initiate  $q$  new avalanches. According to this model, the total rise time will be several times the time of development of a single avalanche. The observed rise times for points with radii smaller than  $r = 0.2$  mm are not consistent with the model which gives values which are much too large.

The theory proposed by Aleksandrov [41] accounts successfully for the observed phenomenon for both sharp and blunt points. According to the suggested model, secondary avalanches set in parallel with the primary ones, as soon as the number of electrons in the developing avalanche  $n$ , exceeds  $n_0$ , the number of electrons in the initial avalanche. The field increase in the ionization zone, due to the rapid accumulation of space charge along the path of the developing avalanche leads to an increase in  $n$ . From their detailed study of spatio-temporal development of luminous phenomena over a Trichel pulse period, Ikuta and Kondo [43] suggested that the rapid growth of pulse current (over  $\sim 50$  ns) overlaps with the propagation of a streamer toward the cathode. This has been corroborated by the experiments of Hosokawa et al [44] who showed that the transition from avalanches to a Trichel pulse occurs when the number of

electrons created in the avalanches gives rise to a critical field for the initiation of a streamer.

### C. Pulseless glow discharge and transition to the transient arc

As the voltage is increased in the Trichel-pulse regime, the frequency of the pulses increases and reaches a certain limiting value ( 0.2 - 2 MHz), after which transition to a pulseless glow discharge occurs. This is marked by an abrupt increase in the continuous current, with some slight variation in the total current, depending on the geometric factors. Visually, the transition is characterised by the appearance of a narrow and bright spike, superimposed on the Trichel pulse glow, which extends into the gap.

The transition to a transient arc from the pulseless steady glow regime occurs at a critical current in the order of 200 to 250  $\mu\text{A}$ , which is more or less independent of the gap geometry. When the current reaches this critical value, the physical factor determining the transition is the anode field [44] which is sufficient to initiate a positive streamer from the plane. Transition to a spark occurs when the anode streamers advance toward the negative streamers, leading to a fully ionized channel. In the development of the discharge to sparking, secondary streamers and a return ionizing wave have also been observed [45].

## 1.4 Breakdown Phenomena in Compressed Gases

### 1.4.1 General

For gas pressures below atmospheric and up to a few atmospheres at normal temperatures, there is reasonable agreement on the breakdown mechanism in most gases and the results are in accordance with Paschen's law. Nevertheless, at high pressures the breakdown

results are not so easily predictable using the low-pressure data and the results under the same conditions are often conflicting and deviate from the Paschen curve with some scatter around the mean. In this section, some of the important breakdown mechanisms causing this peculiar behaviour in compressed gases will be discussed.

#### 1.4.2 Failure of Paschen's Law

At pressures exceeding a few atmospheres, when the field achieves a value of the order  $100\text{--}200 \text{ kVcm}^{-1}$ , the sparking voltage  $V_s$  is no longer in conformity with Paschen's law. At and above this limit  $V_s$  exhibits a marked dependence on the cathode material and state of its surface structure, separation and area of electrodes, conducting particle and dust content of the gas, etc. Further, the breakdown voltage is found to increase gradually with repeated sparkings, eventually reaching to an upper limit which may be less than the Paschen's value; this process is known as spark conditioning. All these unexpected effects lead to difficulties in comparing investigations conducted under the same experimental conditions. For instance, in air, James et al [46] observed that Paschen's deviation occurs in a 0.25 mm gap at 50 bar, whereas in a 0.5 mm gap it appears at 40 bar, while the breakdown stress decreases from  $140 \text{ kVmm}^{-1}$  to  $110 \text{ kVmm}^{-1}$ . Similarly, in nitrogen, at small gap lengths the deviation starts at about 30 bar and  $100 \text{ kVmm}^{-1}$ , and at large gap spacing it occurs at about 18 bar and  $40 \text{ kVmm}^{-1}$  [14].

In spite of the large number of investigations in compressed gases for various parameters, there has been no generally accepted theory or means of predicting the breakdown voltage for any given case. The basic difficulty arises from the complex nature of the phenomena taking place at the electrode surface-gas interface

which are controlled by different physical parameters such as thickness of the oxide layer, nature of inclusions, size of the dust particles and the details of the surface microstructure, etc. Some of the proposals made on the fundamental mechanisms and effects which are governed by the aforementioned parameters will be discussed in the following sections.

#### 1.4.2.1 Field emission

Cold field emission from electrode surfaces has been one of the commonly accepted mechanisms in the high-field, high-pressure breakdown studies and many investigators [65] have related the failure of Paschen's law to this mechanism in one way or another. Although the theoretical limit for the field strength in order for a Fowler-Nordheim type field emission to occur is in the order of  $10^7 \text{Vcm}^{-1}$ , this value is hardly obtainable in practice due to surface asperities, impurities or the existence of oxide or other surface layers of low work function.

Lewis [47] reported surface irregularities of height less than  $10^{-5} \text{mm}$  and calculated a field enhancement factor of two at the tip taking into account the proximity effect of the other asperities. Boulloud [51] observed asperities of  $10^{-3} \text{cm}$  height enhancing the field by a factor between 10 and 30.

Dust or other gasborne particles can be effective sites for field emission when the field is above  $5 \cdot 10^4 \text{Vcm}^{-1}$ . Müller [50] showed that with extensive gas filtering the breakdown results in nitrogen up to 12 bar could be in conformity with Paschen's law. The dielectric properties of impurities can also have important influence in compressed gases; although conducting particles [54,55] and gasborne dust [53,56-58] reduce the breakdown voltage considerably,

nonconducting impurities have no effect [57,59].

In breakdown investigations, oxide layers on electrode surfaces are inevitable, but the physical and dielectric properties of the oxide layer are important in breakdown. As will be explained later, positive ions dwelling on the oxide layer can yield enough field intensification to cause field emission [63,65]. However, Philp and Trump [55] observed no detectable field emission from a homogeneously covered  $10^{-4}$  mm thick oxide layer on copper and nickel electrodes up to  $300 \text{ kVcm}^{-1}$  in a uniform field gap with compressed methane.

#### 1.4.2.2 Positive-ion assisted field emission

In compressed gases, positive ions resulting from the electron multiplication process in the gap may enhance the cathode field, as they reside on an oxide or tarnish layer a considerable time, and this will increase the electron emission current from the cathode surface. In his compressed nitrogen and hydrogen studies, Boulloud [52] suggested that the gradual electron-current increase prior to breakdown may be brought on by the positive-ion space charge built-up near the cathode. The positive-ion space charge was considered [64] to increase ionisation near the cathode in compressed hexane, but it was found this was not the case in nitrogen [65]. Doepken [59] proposed that positive ions approaching the cathode could enhance the field sufficiently to cause field emission. List [48] considered that, if the positive ions were being collected on the layer at a rate faster than the ions were being leaked away, then a point was reached at which a further increase in charge will cause a sudden burst of electrons due to field emission. Müller [50] related this sudden increase in emission current to microdischarges in the

cathode oxide layers induced by positive ions remaining on the cathode from avalanche activity in the gap.

#### 1.4.2.3 Enhanced $\gamma$ - process

In addition to the positive space-charge-enhanced emission process outlined in section 1.4.2.2, some attempts have been made to explain the deviations from Paschen's law on the basis of enhanced secondary emission due to positive ion bombardment of the cathode, which increases markedly as the local cathode field increases to the excess of Fowler-Nordheim field limit  $10^7 \text{ Vcm}^{-1}$ . For example, Cobine and Easton [60] suggested that additional energy imparted to the positive ions as they approach to the cathode asperities increases the  $\gamma$ -process. Also, Theobald [61] showed that the enhanced field at the high-field sites decreases the possibility of back-diffusion of released electrons and this will in turn enhance the  $\gamma$ -process. Further, a gradual positive-ion accumulation on the impurity layer of the cathode surface was suggested [62] to increase the field in the order of  $10^4$  to  $10^5$  and thus effectively increasing  $\gamma$ . The field enhancement owed to the positive ion storage on the oxide layer can cause microdischarges across the layer causing a burst of electrons from the cathode. Again, it effectively increases  $\gamma$ .

Llewellyn Jones and Morgan [63] proposed that the field current increase due to positive-ion field across the cathode layer could be considered as enhancing  $\gamma$  by a factor of the order of  $10^4$  to  $10^5$ .

Moreover, in compressed gases, the ionization coefficient  $\alpha$  will be enhanced locally because of the high fields produced either by space-charge effects or by cathode protrusion; this could be an important reason by itself for the apparent deviation from Paschen's

law. The effect of cathode protrusion is discussed in the following section.

#### 1.4.2.4 Effect of microprojections

At high pressure another significant factor causing deviations from Paschen's law is the microstructure of the electrode surface which produces localized field intensification. At these irregularities collisional ionization may be started by an initiating electron provided that the collision mean free path is small compared to the length of the region of intensified field.

Agapov and Razevig [67] derived a set of analytical expressions to calculate the breakdown voltage in air in terms of collisional processes in a uniform field perturbed by a prolate spheroid of rotation. They obtained good agreement between the estimated and the experimental results for a projection of height 10  $\mu\text{m}$  for several gap separations up to a pressure of 15 bar.

For the same type of protrusion, Avrutskii et al [68] derived a rather simple analytic solution for a self maintained discharge condition in a uniform field gap. Satisfactory agreement was achieved between the calculations and the experimental data for air, nitrogen and hydrogen up to 6 bar for protrusions of height 10 - 100  $\mu\text{m}$ .

Berger [69] proposed a novel mechanism to explain the reasons failure of Paschen's law at high pressures; intensive prebreakdown current from the protrusion tip causes a density reduction, therefore enhancing the ionization in this microscopic region.

The presence of microprojections has an important effect on the reduction of breakdown voltage in  $\text{SF}_6$  - insulated systems, as will be explained later in section 1.6.6.2.

### 1.4.3 Conditioning

It is clear from the above discussions that in compressed gases when the applied field is of the order  $10^5 \text{ Vcm}^{-1}$ , the condition of the electrode surface plays an important role in determining the breakdown voltage  $V_s$ . In any compressed gas insulated gap,  $V_s$  increases gradually with repeated sparkings and reaches an upper limit with some scatter around the mean. This spark conditioning process is mainly due to progressive destruction of high field sites or similar localized sites on the electrode surface such as micro-projections, dust or free conducting particles, tarnish layers, etc. Any electrode configuration conditioned at one pressure requires also to be conditioned [70] when the pressure, and therefore the field, is raised. Thus, conditioning can generally be considered as a field dependent electrode process.

The number of sparks required to condition the electrodes is increased with the electrode area. The presence of dust particles between the electrodes leads to a low  $V_s$  and therefore increases the amount of conditioning required. Exposing the electrodes to atmosphere requires reconditioning when they are used in a subsequent test [71]. The electrode material and the surface preparation have considerable influence on  $V_s$  and on the period for conditioning; a smooth, highly polished surface finish reduces the number of conditioning sparks [65].

Usually, the anode has been considered to exert no influence on the amount of conditioning required, but it has been found to be important in some cases when the anode material sputters on the cathode during conditioning [63].

Although the conditioning effect is quite distinguishable

at high pressures for a.c. and d.c. voltages, it is not noticeable in the impulse case [65].

Conditioning can be affected by exposing the electrodes for a length of time to stresses just below  $V_s$ . This effect, which is known as stress conditioning, may be due to the gradual reduction of high field sites under stress, because the tips melt and become rounded owing to the high discharge-current density.

In any fully spark conditioned electrode system, occasionally erratic breakdown voltages may occur [56]. Although the mechanism responsible for this is not fully understood, it is attributed to the trigation type of microdischarge taking place at one of the electrodes or to the disruption of oxide layers locally by the intense field strength across them causing low breakdown [75], as was explained in section 1.4.2.3.

During conditioning, although each sparking yields a crater, it suppresses the one which triggered the discharge; this can result in an improvement in the surface profile, as long as the energy involved in the discharge, which is determined by circuit components such as current limiting resistor, smoothing capacitors and the gap capacitance, is limited [76].

## 1.5 Breakdown Phenomena in Compressed $SF_6$ and $SF_6/N_2$ Mixtures

### 1.5.1 General

Because of the high cost and because of its sensitivity to electrode roughness and particulate contamination, there is considerable interest in finding alternative gases for use in CGI systems. As yet, there has been found no single or multicomponent gas which possesses better overall properties, but some mixtures of

SF<sub>6</sub> with N<sub>2</sub> have been shown to be promising in that their performance approaches that for SF<sub>6</sub> and they have no serious disadvantages with respect to decomposition products, toxicity, etc.

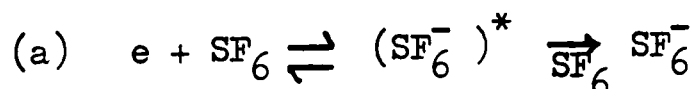
In this section basic knowledge about electron-molecule processes in SF<sub>6</sub> and SF<sub>6</sub>/N<sub>2</sub> mixtures, together with some physical parameters involved in Townsend or the streamer type discharge processes, will be reviewed within the frame of the present work. In addition, the recent uniform and nonuniform field breakdown and prebreakdown investigations in SF<sub>6</sub> and SF<sub>6</sub>/N<sub>2</sub> mixtures, along with the peculiarities causing Paschen's or similar law failures will be revised.

### 1.5.2 Basic ion processes

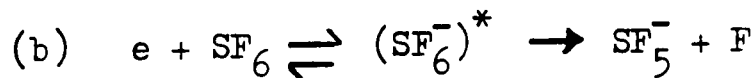
The high dielectric strength of SF<sub>6</sub> is due to its tendency to capture free electrons to form negative ions because of the halogen atoms in the molecular structure of SF<sub>6</sub>.

Negative ion formation processes have been studied spectroscopically at low pressures ( 10<sup>-3</sup> torr) by many investigators. Naidu and Prasad [77] summarized the most likely processes for the formation of negative ions. The ions formed are mainly SF<sub>6</sub><sup>-</sup>, SF<sub>5</sub><sup>-</sup>, F<sup>-</sup> and F<sub>2</sub><sup>-</sup> ions.

SF<sub>6</sub><sup>-</sup> and SF<sub>5</sub><sup>-</sup> ions are produced by resonance capture of low energy electrons (about 0.05 eV) forming first excited ions (SF<sub>6</sub><sup>-</sup>)<sup>\*</sup> which are stabilized either by a collision with a neutral molecule as

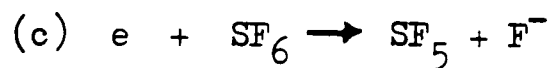


or by a dissociative attachment process of the form



Both SF<sub>6</sub><sup>-</sup> and SF<sub>5</sub><sup>-</sup> are found in large quantities at low electron energies.

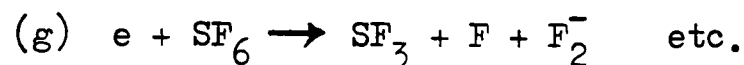
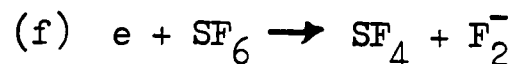
The fluorine ion  $F^-$  may also be produced by dissociative capture for electron energies greater than 4 eV as follows



or for incident electron energies greater than 14 eV

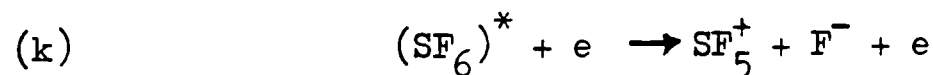
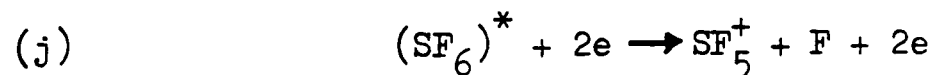
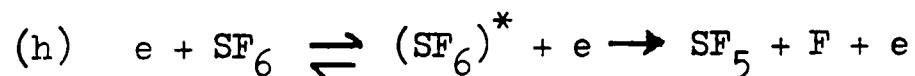


Further dissociative capture may lead to the appearance of  $F_2^-$  ions.



Both processes, resonance and dissociative capture, are effective in prevention of avalanche formation, since the attachment removes electrons before they gain enough energy in the field to promote avalanche growth.

At higher electron energies ( $> 15$  eV), negative-ion formation may also happen [80] by a secondary process in which low energy electrons released by either excitation and ionization processes undergo resonance capture.



Secondary processes given in (h) to (k) do not affect the avalanche formation, because they result in neutral or positive ion or ion pair formation, but the avalanche growth is retarded by the secondary-resonance capture.

In  $SF_6/N_2$  mixtures, apart from the spectral analysis of

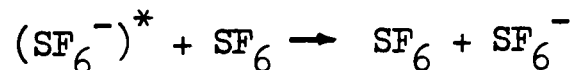
Ermel [79], there is not much known about the molecular and molecule-electron interactions at different electron energy levels. After a prolonged discharge in the mixture of 20% SF<sub>6</sub> - 80% N<sub>2</sub>, Ermel observed that the mass spectrum of the mixture is composed of the known spectra of SF<sub>6</sub> and N<sub>2</sub>. In addition to this at identifiable mass numbers, different from that of SF<sub>6</sub> products, some nitrogen-halogenides such as NF<sub>3</sub> and the radicals NF<sub>2</sub> (from N<sub>2</sub>F<sub>2</sub>) and NF (from NF<sub>3</sub>) exist.

In SF<sub>6</sub>/N<sub>2</sub> mixtures, N<sub>2</sub> molecules sustain energy balance in the gas by de-energizing electrons reaching higher energies (up to 2 to 3 eV) and by returning them to the lower energy range [80] to facilitate the first resonance capture process so that the breakdown may be inhibited.

In order to upgrade the insulation characteristics of SF<sub>6</sub>/N<sub>2</sub> mixtures, further investigation seems to be necessary on the basic collisional processes at different ion and electron energy levels.

### 1.5.3 Ionization coefficients

In investigations at pressures of ~ 0.1 torr, McAfee and Edelson [81], and Fehsenfeld [82] observed that the (SF<sub>6</sub><sup>-</sup>)<sup>\*</sup> ion undergoes collisional stabilization in a three-body process of the type



Fehsenfeld observed that above the pressure .1 torr, the reaction was saturated due to inhibited binary kinetics of the gas, and consequently concluded that the formation of SF<sub>6</sub><sup>-</sup> would exhibit a linear dependence on the gas pressure. McAfee and Edelson measured the relative abundance of SF<sub>6</sub><sup>-</sup> and SF<sub>5</sub><sup>-</sup> ions achieved in a Townsend discharge at 0.5 torr in terms of the energy parameter E/p - the ratio of the electric-field strength to pressure. At values of E/p ≳ 80 V(cm torr)<sup>-1</sup>,

the abundance of  $SF_5^-$  ion was found to be dominating.

These observations indicated that at pressures above 0.1 torr the attachment coefficient  $\eta$  and consequently the net ionization coefficient  $\bar{\alpha}$  is a function of the parameter  $E/p$  only, i.e.  $\bar{\alpha}/p = f(E/p)$ . This has been confirmed by the measurements of several investigators [83-87]. The results of several investigators together with pressure and  $E/p$  range are shown in Figure (1.1). In order to obtain reasonably accurate values of  $\alpha$  and  $\eta$  from the pre-breakdown current measurements, the field variation through the gap should be less than 0.1% and the gap setting accuracy should be within 0.1% [83,88]. Boyd and Crichton [83] gave an upper limit for pressure at 1 bar for this type of experiment. According to Karlson and Pedersen [88] the upper limit for the product  $pd$  of gas pressure and gap length  $d$  was less than a few hundred mmHg.cm; this gives a corresponding pressure of one bar.

It can be easily noted from Figure (1.1) that the relation between  $\bar{\alpha}/p$  and  $E/p$  may well be expressed over the range  $67 \leq E/p \leq 150$  kV (cm bar)<sup>-1</sup> [83] as

$$\frac{\alpha - \eta}{p} = K \left[ \frac{E}{p} - \left(\frac{E}{p}\right)_{lim} \right] \quad (1.24)$$

where  $K = 27.8$  kV<sup>-1</sup> and  $(E/p)_{lim} = 88.4$  kV (cm bar)<sup>-1</sup> is the limiting value of the energy parameter for which  $\alpha = \eta$ , and below which no discharge activity is possible. However under some conditions breakdown has been observed to occur at even lower than  $(E/p)_{lim}$ .

In  $SF_6/N_2$  mixtures there have been a few independent approaches to the estimation of the effective ionization coefficient  $\bar{\alpha}$ . In the simplest one  $\bar{\alpha}$  for the mixture was calculated in terms of the ionization coefficient of the constituent gases on the basis of their

partial pressures [79,91]. The ionization coefficient of  $N_2$  can be approximated by  $\alpha/p = A \exp [-B/(E/p)]$  where  $A = 6.6 \times 10^3 \text{ (bar cm)}^{-1}$  and  $B = 215 \text{ kV cm}^{-1}$  over the range  $30 \leq (E/p) \leq 200 \text{ kV (cm bar)}^{-1}$ , hence the net ionization coefficient of the mixture  $SF_6/N_2$  becomes

$$\frac{\bar{\alpha}_m}{p} = x \left( \frac{\bar{\alpha}}{p} \right)_{SF_6} + (1 - x) \left( \frac{\alpha}{p} \right)_{N_2} \quad (1.25)$$

where  $p$  is the total pressure and  $x = p_{SF_6}/p$ , i.e. the partial pressure of  $SF_6$ . Although this approach has been verified [90] in uniform and nonuniform breakdown experiments, it has limited applicability and also it requires well defined experimental data of ionization coefficients of the component gases.

In the second approach, Brand and Kopainsky [92] proposed a model to estimate  $\bar{\alpha}_m$  by numerically solving the Boltzmann equation for electron energy distribution by making use of the published data for physical parameters of individual gases. Although good agreement is achieved with the experimental uniform-field breakdown results, it requires the measured net ionization coefficient to verify the model.

Two recent measurements of  $\bar{\alpha}_m$  in mixtures have been reported over a limited range of  $E/p$ . Itoh et al [93] measured  $\bar{\alpha}_m$  for  $70 \leq (E/p) \leq 160 \text{ V (cm torr)}^{-1}$ , for the fraction of  $SF_6$  partial pressure between 0.01 and 1. It was found that  $\bar{\alpha}_m/p$  of mixtures can be approximated by a linear function of the partial pressure of  $SF_6$  as given in equation (1.99). Aschwanden [94] measured  $\bar{\alpha}$  using current-pulse techniques for mixtures of  $N_2$  with 10, 20, 40 and 75%  $SF_6$  by volume over the range  $60 \leq (E/p) \leq 170 \text{ V (cm torr)}^{-1}$ . The experimental data was linearized over a narrow range near  $(E/p)_{lim}$  by the equation:

$$\frac{\bar{\alpha}_m}{p} = K C^{0.25} \left[ \frac{E}{p} + \left( \frac{E}{p} \right)_{lim} \cdot C^{0.2} \right] \quad (1.26)$$

where  $K = 28.2 \text{ kV}^{-1}$ ,  $\left( \frac{E}{p} \right)_{lim} = 88.5 \text{ kV (cm bar)}^{-1}$  and  $0.05 < C < 1$ .

Further experimental studies are required in order to predict  $\bar{\alpha}_m$  theoretically as given in equations (1.99) and (1.100).

#### 1.5.4 Compressibility

In the above theoretical models for the estimation of the effective ionization coefficient in  $\text{SF}_6$  and  $\text{SF}_6/\text{N}_2$  mixtures the relevant physical data related to swarm parameters have been obtained from experiments performed at low pressures (up to 400 torr). In  $\text{SF}_6$ , in order to extrapolate the low-pressure data acquired for  $\bar{\alpha}$  to high pressures, Crichton and Tedford [95] proposed to modify  $\bar{\alpha}$  by including the compressibility property of the gas:  $Z(p,T) = p/NKT$ , where  $p$  is the pressure,  $N$  is the number of molecules per unit volume,  $K$  is the Boltzmann constant and  $T$  is the absolute temperature. In a uniform electric-field the equation for  $\bar{\alpha} = f(E, p)$  may be written as  $\bar{\alpha} = f(E, p/Z(p))$  or in general

$$\frac{\bar{\alpha}}{p} = F [Z(p) \cdot E/p] / Z(p) \quad (1.27)$$

under constant temperature conditions. Recently Vibholm and Mollerup [96] developed a general formula to calculate the compressibility factor including variations due to both pressure and temperature in the temperature range  $270 < T < 350 \text{ }^\circ\text{K}$  and the pressure range  $1 < p < 10 \text{ bar}$ .

In mixtures of  $\text{SF}_6$  with  $\text{N}_2$ , as yet there has been no published information on the estimation of the compressibility factor. This is due to unpredictable behaviour of component gases in the

mixture. In spite of this fact, an attempt is made to determine the compressibility factor in section (5.2.2). An approximate method is adapted to calculate the constants in Beattie-Bridgeman equation (cf. Appendix 3) based on linear interpolation between the constants of the constituent gases.

### 1.5.5 Breakdown criteria in SF<sub>6</sub>

For uniform fields, in SF<sub>6</sub>, either multiavalanche Townsend or single-avalanche streamer type current growth to breakdown may be expected to occur when the condition

$$(\alpha - \eta) d = k \quad (1.28)$$

is satisfied, where  $d$  is the gap separation and  $k$  is a constant whose value is given by, for Townsend process,  $k = \ln \left( \frac{\bar{\alpha}}{\gamma\alpha} + 1 \right)$  and for the streamer process by  $k = \ln (N_{\text{crit}})$  where  $N_{\text{crit}}$  is the average number of electrons required for streamer propagation. The equation (1.28) indicates that there is a limiting value for the breakdown gradient  $(E/p)_{\text{lim}} = 88.4 \text{ kV (cm bar)}^{-1}$  at which  $\alpha = \eta$ .

Pedersen [100] extended the uniform field Townsend breakdown criterion to nonuniform fields and obtained the following equation

$$\gamma \int_0^d \exp \left[ \int_0^{x_c} (\alpha - \eta) dx \right] \alpha dx = 1 \quad (1.29)$$

and the corresponding streamer type breakdown criterion may be expressed as

$$\int_0^{x_c} (\alpha - \eta) dx = k \quad (1.30)$$

where  $x_c$  is the critical distance from the surface of the electrode at which the electric field is maximum and  $\alpha = \eta$ .

In the Townsend's mechanism, the secondary processes are very sensitive to condition of electrodes and gas impurity, hence the

criterion expressed in equation (1.29) is realized under well-defined laboratory conditions. The streamer criterion is more applicable to practical conditions than the Townsend type.

Both breakdown criteria have been verified experimentally in different gaps within certain limited experimental conditions. It has been found that the breakdown-voltage characteristics of SF<sub>6</sub> are strongly dependent on the nonuniformity of field, the polarity of the stressed electrode, and the applied voltage type. In nonuniform fields the streamer breakdown criterion only gives the corona inception level and the breakdown voltage will be determined by the space charge conditions. In the case of impulse voltage, the statistical time lag introduces additional difficulty in predicting the breakdown voltage and in nonuniform fields [101] the factors governing the propagation of streamer and leader discharges must be considered.

For mixtures of SF<sub>6</sub> with N<sub>2</sub>, Baumgartner [90] applied the semiempirical streamer criterion for the calculation of breakdown voltage, which states that breakdown or corona onset takes place, depending on the field configuration, when the condition

$$\int_0^{x_c} \bar{\alpha}_m dx = k = \ln (N_{crit}) \quad (1.31)$$

is satisfied, where  $\bar{\alpha}_m = \alpha_m - \eta_m$  is the effective ionization coefficient and given by the equation (1.25) or (1.26),  $x_c$  is the critical avalanche length in which the electron avalanche attains the size of  $(N_{crit})_{mix}$ . The value of  $(N_{crit})_{mix}$  and hence  $k$  is not so critically important in results, but can be best estimated by linearly interpolating between  $k_{SF_6} = (10.5 - 18)$  and  $k_{N_2} = (4 - 8)$  on the basis of partial pressure of respective gases. In many uniform and quasiuniform field configurations a reasonable agreement between measured and

calculated results have been reported [79,90-92]. However, for rod-plane the calculated values of corona onset levels are less than the measured negative corona-onset voltage [97,98].

## 1.6 Experimental Studies in SF<sub>6</sub>

### 1.6.1 General

The knowledge of maximum breakdown voltage of any compressed gas in uniform and nonuniform fields is of practical importance from the insulation consideration. Determination of optimal clearance and pressure, for instance, for a given system voltage requires well-established design data. In SF<sub>6</sub> below atmospheric pressure such data is available for estimating the threshold levels in different geometries. At high pressures, due to the peculiar behaviour of SF<sub>6</sub> in terms of its pressure effect owing to surface microprojections, free particles, etc., uniform and nonuniform breakdown voltages are not readily predictable, and hence there is a need for more investigations to identify some basic design constraints. Also, the effects of corona discharges caused by free conducting particles and by extreme nonuniformities have led to the study of corona stabilized breakdown. In the following sections a brief review of recent uniform, slightly nonuniform and nonuniform field breakdown investigations in SF<sub>6</sub> and its mixtures are given in the extent of relevance to the present work.

### 1.6.2 Breakdown in uniform fields

#### 1.6.2.1 Low-pressure breakdown studies

Several investigators [49,102-105,110] have reported the ac and static breakdown voltage measurements for SF<sub>6</sub> in uniform and quasiuniform fields and the results were compiled by Dakin et al [49]

by plotting the Paschen curve, i.e.  $V_s = f(pds)$ . For two limits of the product  $pd$  defined by the limits  $p \leq 2$  bar and  $d \geq 0.3$  mm, the results are mostly coinciding and the breakdown values of  $E/p$  tends to  $(E/p)_{lim} = 88.4$  kV (cm bar)<sup>-1</sup>. The minimum voltage for ac and dc occurs at about 507 V at  $pd = 3.5 \times 10^{-3}$  bar cm [100].

Dutton et al [105] observed slight discrepancy of 1.5 per cent in breakdown voltage from the Paschen's prediction when the pressure is increased from about 0.25 bar to 0.47 bar for up to  $pd = 29$  bar mm. This deviation was attributed to three-body attachment process of the type given in section 1.5.3., whereas in their precision measurements, Boyd and Crichton [104] observed no deviations in the same pressure range and up to 0.8 bar. Below one bar Chalmers and Tedford [102] obtained the same results in accord with Boyd and Crichton, but at higher pressures up to about 2.6 bar, the breakdown voltage was found to increase by about 2 per cent per 1.5 bar increase in pressure. This was concluded to be due to reductions in the photoionization coefficient  $\gamma_p$  at higher pressures and non-ideal behaviour of the gas [95].

At large gap spacings in excess of about 4 cm, the apparent breakdown voltage value of  $E/p$  was found to lie below  $(E/p)_{lim}$  by several investigators [85, 102-105]. This effect has been indicated [100,102] to be due to the fact that, owing to the field enhancement of the curved part of the electrodes, breakdown takes place outside the uniform portion of the gap.

#### 1.6.2.2 High-pressure breakdown studies

Extensive experimental investigations have shown that in uniform and slightly nonuniform fields, breakdown field strength of SF<sub>6</sub> predicted by the similarity relationship is not readily obtainable

above  $\sim 2$  bar, independent of the applied waveform. In uniform field gaps the corresponding critical field strength attains a value in the range  $150 - 200 \text{ kVcm}^{-1}$  independent of the gap length (up to a critical gap length at which no edge breakdown occurs), whereas in coaxial-cylinder electrode gap this field is a function of the inner electrode radius (Figure 1.2). At higher pressures breakdown can take place when the applied field is less than the limiting value. This means that apparently the applied field is less than the limiting value everywhere in the gap, i.e.  $\alpha < \eta$ . However, in order for the streamer breakdown condition to be satisfied,  $\alpha$  must exceed  $\eta$  at least somewhere in the gap. Several suggestions have been proposed for this anomaly. In general, they are related to electrode processes and sometimes to the ionization behaviour of the gas itself. The suggestions based on the former processes are the most accepted ones and can be listed as:

- (i) electrode surface roughness,
- (ii) free conducting particles,
- (iii) field emission.

Recently, it has been suggested [106] that the statistics of avalanche development are such that there is a possibility of having a critical avalanche leading to breakdown at field strengths below  $(E/p)_{\text{lim}}$ ; however, Tedford et al [107] showed that the statistical probability of achieving such an avalanche of critical size is negligible at even a fraction of a percent below  $(E/p)_{\text{lim}}$ .

The possibility of a deviation from the similarity-law breakdown voltage due to some pressure-dependent gas mechanism other than compressibility was excluded in two recent high pressure studies [108,109] in that up to 12 bar the law is confirmed using highly

polished electrodes of small area and using carefully filtered gas. Further, in these two experiments within the same pressure range, no steady field emission current was detected in the gap prior to breakdown ( $< 10^{-10}$  A up to  $1500 \text{ kV cm}^{-1}$  [108] and  $< 10^{-8}$  A up to  $1800 \text{ kV cm}^{-1}$  [109]).

#### Surface Roughness

In  $\text{SF}_6$  insulated systems, surface roughness can lead to local field enhancement at values above the macroscopic field which either give rise to increased ionization or which cause electron field emission. If the ionization is negligible or too low to initiate a discharge in the gap, the field established by the negative-ion space-charge as a result of attachment of these electrons to  $\text{SF}_6$  molecules is sometimes high enough to initiate a disruptive discharge. This latter process is important in compressed  $\text{N}_2$  and  $\text{H}_2$  [68], while the ionization process is particularly important in  $\text{SF}_6$  where  $\bar{\alpha}/p$  is extremely sensitive to variations in  $E/p$ . Several experimental studies with different electrode surface roughnesses [110-112, 114] and theoretical studies with artificial roughness models [113-116] have revealed the fact that surface microstructure can result in significant reduction in breakdown voltage depending on the gas pressure.

In all theoretical analyses, since it is almost impossible to represent the complex nature of surface roughness, some simplified models such as spheres or hemispheres, ellipsoid or semiellipsoid, and ~~paraboloid~~ have been used where the microscopic field distribution along the geometrical axis can be readily estimated. Pedersen [113] has studied the influence of electrode surface roughness by considering a simple hemisphere of radius  $\rho$  on a smooth electrode. The macroscopic value of  $E/p$  is reduced by the presence of this roughness to

$$E/p = \xi (E/p)_{\text{lim}}, \quad 0 < \xi < 1 \quad (1.32)$$

Where  $\xi$  is the surface roughness factor and is a function of the product pressure  $p$  and radius  $\rho$ , i.e.  $p\rho$ . Threshold voltage for breakdown can be calculated by considering ionization within a critical distance  $x_c$  from the protrusion tip at which  $E/p$  exceeds  $(E/p)_{lim}$ , using the streamer breakdown relationship given in equation (1.30). This gives the maximum permissible  $p\rho$  above which is less than unity, i.e.

$$p\rho \leq 43 \text{ bar } \mu\text{m}$$

For practical electrode surfaces the maximum roughness height  $R_{max}$  can be taken equal to  $\rho$ , thus the roughness becomes effective in reducing the withstand voltage level if  $pR_{max}$  exceeds this figure. Predicted breakdown voltages using this model were shown to agree with the experimental results of Nitta et al [116] for  $R_{max} = 150 \mu\text{m}$  up to 6 bar. Pedersen also suggested that with this model it would be possible to take into account the effect of micro-fields caused by tiny conducting or dust particles in the system.

A similar theoretical model has been developed by Cooke [112] independently. Using the simple streamer process for breakdown in which an avalanche size of  $10^8$  was calculated to be sufficient to initiate a self-sustaining discharge, he found good agreement between the measured breakdown values with those calculated using spherical protrusion placed on the inner conductor of a 76/250-mm diameter coaxial-electrode gap over the pressure range from 0.5 to 15 bar. He applied his model for some other protrusion shapes as well and suggested that when the product of gas pressure times protrusion height,  $ph$ , above a flat electrode exceeds the critical value of  $\sim 80 \text{ bar } \mu\text{m}$ , the breakdown voltage stress decreases with  $ph$  as being independent of protrusion radius. However, a tiny 10  $\mu\text{m}$  height protrusion produced by sparking on surface of the main protrusion was

found to alter the critical value of  $ph$  to 40-50 bar  $\mu\text{m}$ .

With a more generalized approach Somerville et al [115] have estimated tolerable upper limit for surface roughness below which the breakdown voltage is unaffected. For the values above this limit the amount of reduction in the breakdown field strength was found to be determined by the height  $h$  of the protrusion but not with its shape. So, for any rough electrode surface the maximum tolerable value of protrusion was given by  $(ph)_c = k / [K (E/p)_{lim}]$  where for constants  $k = 10.5$  and  $K = 27.8 \text{ kV}^{-1}$ ,  $(ph)_c \lesssim 40 \text{ bar } \mu\text{m}$ . A lower limit of  $\sim 20 \text{ bar } \mu\text{m}$  was estimated by equating the voltage drop across the ionizing region ( $\bar{\alpha} > 0$ ) from the protrusion tip to the Paschen's minimum; for  $\text{SF}_6$  this is 507 V.

Charge simulation technique was used by Berger [114] for the calculation of field distribution in the vicinity of a hemispherically capped rod with height  $h$  and curvature  $r$  placed on a flat electrode surface. Good agreement was achieved for  $h/r = 1$  with the corresponding theoretical results of Pedersen's model, provided the field in a short distance along the axis of the protrusion is not affected by the nonuniformity of the electrode. This method was suggested to be suitable also for slightly nonuniform as well as uniform fields in breakdown field strength predictions in practical systems at moderate pressures and up to  $h/r = 3$ . However, the measured breakdown voltages up to 2.5 bar in a weakly irradiated uniform field gap with a single spherical protrusion of 4-mm in diameter placed on the cathode, was observed to be higher than the computed ones. This discrepancy was related to the lack of initiating electrons in spite of the presence of the radiating source and the protrusion. At high pressures this effect was remarked to be reduced due to intervening effect of field emitted electrons from the protrusion. Also, it was

suggested that roughness measurements after conditioning sparking would provide better knowledge about the role of surface roughness on the onset or breakdown voltage rather than the unsparked surface roughness measurements.

In addition to the effect of local microscopic disturbances in reducing the breakdown voltage as explained above, Shibuya et al [111] proposed that field emitted electrons from the high field sites prior to breakdown may be another factor to be accounted for in the reduction in SF<sub>6</sub> at high pressures. They measured the static breakdown voltage of 2-cm sphere-plane gap with both highly polished ( $\bar{\pm}$  0.5  $\mu\text{m}$ ) and rough ( $\bar{\pm}$  20  $\mu\text{m}$ ) spheres. In the polished case the reduction in breakdown voltage took place at a pressure slightly higher than 5 bar, while this critical pressure was reduced to about 2 bar for the roughened electrode case. Voltage reduction for these two cases was observed to be accompanied with the flow of field emitted electron 'dark' current of  $< 10^{-9}$  A at field strengths exceeding 430 kVcm<sup>-1</sup> and 100 kVcm<sup>-1</sup> for polished and roughened electrodes respectively. Further, it was stated that a negative-ion space-charge layer formed by attachment of field emitted electrons to SF<sub>6</sub> molecules may relieve the local field intensification at the sites resulting in lowering the dark current, and with increasing the applied voltage the local field instability from one of those sites will bring about breakdown.

A more extensive investigation of the influence of prebreakdown processes in a uniform gap in determining the breakdown level in high-pressure SF<sub>6</sub> was presented by Bortnik [75]. Although the process of field emission was accepted as a source of initiating electrons for local discharge formation, it was ruled out in the analysis of observations both because prebreakdown current varied

with the square of the voltage and because the current decreased with decreasing electrode separation. A current of  $10^{-11}$ - $10^{-5}$  A was observed to flow in the gap in the pressure range 2 - 6 bar at field stresses well below the breakdown voltage level. In various experimental observations this current was remarked to have resulted from ionization processes which occur in the vicinity of microscopic inhomogeneities at electrode surfaces: the ionization would either lead to a self-sustained discharge which is limited by its own space charge or to complete breakdown of the gap. The quantitative or qualitative features of the phenomenon from a localized discharge to total breakdown of the gap were found to agree with the observations for prebreakdown effects in a homogeneous field in high pressure SF<sub>6</sub> and on this basis a qualitative picture of the development of a high-pressure discharge was given.

In all the above investigations, with the exception of Bortnik's, the electrode surfaces were modelled by a single isolated protrusion on a flat surface. However, in practice, surfaces are more complex in nature than this model. Another protrusion model of surface roughness associated with manufacturing process was proposed by McAllister [117]; this is a corrugated-surface model with ridges in a semicylindrical form with radius  $\rho$ . With this model  $\sim 30$  per cent reduction of field enhancement is achieved compared with a single ridge protrusion, because of the mutual effects of neighbouring ridges on the perturbing field. In compressed SF<sub>6</sub>, the estimated critical value of  $ph$  for a single ridge was found to be in agreement with previous single protrusion studies (i.e.  $p \leq 43$  bar  $\mu\text{m}$ ) while, owing to proximity effects, the threshold value of  $ph$  with multiple ridges is increased to 370 bar  $\mu\text{m}$ .

## Particle Contamination

The presence of particulate contamination has long been recognised to limit the insulating ability of a compressed gas system. Intensive investigations have been carried out recently to study the effects of the type of the applied field, the gas pressure and the electrode configuration, and some techniques have been suggested to lessen or eliminate particle effects.

Nonconducting particles have been found to exert little or no influence on the breakdown voltage  $V_s$  [55,59]. Gasborne particles of different dielectrics can reduce  $V_s$  by about 30 per cent or more [119]. Conducting particles can have more serious effects by reducing the corona onset and breakdown voltage depending on their sizes and positions in the system.

The main points of recent investigations may be summed up with respect to  $SF_6$  unless otherwise stated:

(i) Excepting a few [123-126] most of the investigations have been conducted in  $SF_6$  in spacer-free systems in pressure range between 2 to 20 bar. Both  $N_2$  and  $SF_6$  insulated gaps have been shown to be affected by free conducting particles [59]. Some of the mixtures of  $SF_6$  with  $N_2$ ,  $He$  and  $CO_2$  were found to be less sensitive to degrading effect of free particles. Cookson and Wootton [124,126] have shown, for instance, in the presence of conducting particles ac strength of 50/50 mixtures of  $SF_6$  and  $N_2$  is about the same as that of  $SF_6$  alone at 2.7 bar, and with the same ratio, the strength of  $SF_6$ -air mixture can exceed that of  $SF_6$  at the same pressure.

(ii) Particle size and shape are also significant factors [120-122] to be noted: irregularly-shaped conducting

particles have more serious effects than the rounded ones.

Cookson and Farish [121] found that, in an SF<sub>6</sub>-insulated coaxial gap, decreasing the length of 0.4-mm diameter wire particles from 6.4 mm to 0.8 mm increased the ac strength by about four times at 17.5 bar. This effect is less pronounced at low pressures. The pressure-dependent limiting value for particle length is  $\bar{r}_p \cdot p = 70 \text{ bar } \mu\text{m}$ . The most deleterious particles are those longer and lighter which are able to cross the gap [130]. Further, conducting particles which would happen to be fixed to high intensity electrode behave as protrusions and have less effect than the free ones [121].

(iii) The type of the applied voltage also affects the type of activity that conducting particles exhibit, and the behaviour is different in different geometries, depending on the pressure and particle size. In coaxial gaps with dc and ac voltages of enough magnitude, the motion of particles is mostly oscillatory, but in the ac case, gap crossover may be achieved in some several cycles of ac waveform. For both dc and ac voltages, breakdown is initiated when the particles are at or near the inner conductor and the breakdown level is usually lower when the inner conductor is positive, contrary to the particle-free breakdown conditions. In SF<sub>6</sub> and N<sub>2</sub> at pressures 3 - 5 bar, the minimum values of positive dc breakdown voltages compared to ac breakdown level, are about 30 per cent higher but are equal or lower at higher pressures [125]. Under impulse conditions, even with long switching pulses, no appreciable particle activity can be noticed although sufficient momentum may be imparted to particles to travel a distance of the gap or more after the pulse is over [119].

(iv) Deleterious effect of particles can be partially

avoided by coating both electrodes with a dielectric film [127,128] or with some adhesives which trap the particles by chemical bonds [127]. The control of particles can also be made by using electrostatic [125] or screen [127] type of traps.

(v) As yet, the breakdown mechanism initiated by particles has not been fully understood. There have been several proposals. The most accepted mechanisms leading to breakdown are field intensification at the particle tip in contact with electrodes [120, 129], rapid change in the local field when a moving charged particle contacts on an electrode due to charge reversal [120, 125] and 'microdischarges' between particle and an electrode [120, 121]. However, in the last two processes it is not yet clear whether breakdown is caused by the shock wave resulting from microdischarges or by an impulse type breakdown from the particle tip.

#### Electrode area and conditioning

The dielectric strength of SF<sub>6</sub>-insulated CGI-system decreases with increasing the active area since the number of microscopic disturbances which are effective in size and shape increases statistically. The influence of the electrode area becomes more pronounced with the increase in pressure and depends on the type and polarity of the applied voltage. Therefore, the knowledge for correlating the effective electrode area to the breakdown field strength is of importance from the reliability point of view in large systems.

Although the area effect has been long noticed in many laboratories in breakdown-voltage measurements [55,110] and in conditioning experiments [118] in various gases, it was first investigated quantitatively by Bortnik and Cooke [129] in small scale

experiments in SF<sub>6</sub>. In a coaxial-cylindrical gap, with and without fine wires wrapped on various inner conductors with different diameters under negative applied field, they found that the area-dependent statistical distribution of extreme breakdown field strengths follows the Weibull-Gnedenko [131] extreme-value probability of the form

$$F(E) = 1 - \exp \left[ - \left( \frac{E - E_0}{E_1 - E_0} \right)^m \right] \quad (1.33)$$

Where  $F(E)$  is the cumulative breakdown probability,  $E_0$  is the minimum breakdown field strength with very large area electrodes for a given pressure, independent of electrode roughness;  $E_1$  is the mode of the distribution, dependent on pressure and electrode roughness; and  $m$  is a constant which is independent of gas pressure and electrode roughness.

The validity of equation (1.33) was verified further by Nitta et al [118] in more extensive ac and dc breakdown experiments in sphere-plane and coaxial cylindrical gaps having areas ranging from 0.2 cm<sup>2</sup> to 3000 cm<sup>2</sup> at pressures between 2 to 10 bars. They performed a series of conditioning tests covering 200 sparks on each gap at different pressures. The results were classified according to their distribution and the conditioning behaviour in several patterns. Small-area electrodes were found to be free from conditioning since the gap characteristic is controlled by the availability of initiatory electrons, but large-area electrodes exhibit considerable conditioning at moderate pressures, due to the presence of large number of radical weak points. Sparking damage was stated to be another source for producing weak points, hence affecting the conditioning characteristic and the distribution.

In another investigation Bortnik et al [132] demonstrated that the statistical distribution of first breakdown voltages and the conditioning breakdown voltage in three coaxial-cylindrical electrodes has the form given in equation (1.33). The lower limit  $E_0$  for a given pressure was suggested as another factor that ought to be accounted for in the design of gas insulated systems, owing to the fact that the mean breakdown field strength usually exhibits area dependence in gas insulated gaps.

The effects of electrode on  $SF_6$  gas breakdown characteristics under practical conditions were determined for dc, ac and impulse voltages on six different gaps by Masetti and Parmigiani [133]. For the electrode areas in the range of 20-6500 cm<sup>2</sup>, a modified version of equation (1.33) was used in which the minimum breakdown field strength  $E_0$  was not included. With this change the statistical distribution of breakdown voltage stresses over an effective surface area was represented in terms of maximum field strength  $E_M$  and the equivalent area  $A_{eq}$  which has the same breakdown probability as the main conductor when it is stressed with  $E_M$ .

Nitta et al [118] suggested that, in discussing changes in breakdown characteristics of different electrode configurations with surface roughness and electrode area, unconditioned electrodes should be used because of practical considerations. What really matters for  $SF_6$ -insulated apparatus is the first breakdown voltage which was found to be considerably smaller and more scattered compared with the conditioned breakdown level for rough electrodes and about the same or slightly higher for etched ones for pressures up to 6 bar [135].

An electrode-area effect for conditioned electrodes

has been substantiated in many investigations for a large range of electrode areas in different configurations. However, in some studies [118,134] for small and moderate-area electrodes this effect was not observed even at high pressures (up to 4 bar in [118]) despite prolonged conditioning. Therefore, the conditions and the processes governing conditioning may be important in interpreting published results in relation to the area effect.

Thom [76] carried out a series of conditioning tests in compressed SF<sub>6</sub>-insulated uniform-field gaps (1.2 cm<sup>2</sup> area) of 2 μm surface finish. Similar conditioning behaviour was observed as in N<sub>2</sub> at the same pressure levels. The importance of capacitive discharges on the conditioning was noted (see section 1.4.3). The influence of capacitive spark energy upon the conditioning characteristic of SF<sub>6</sub> at 3.5 bar was also studied by Mulcahy et al [136] in uniform field gaps with smooth electrodes (600 Grit finish). It was demonstrated that high energy discharges limit the conditioning, with a large scatter, and that subsequent low-energy discharges improve the breakdown level by up to 80%, with less scatter.

Gockenbach [137] performed long conditioning test on negative sphere-plane gaps with different surface finishes in SF<sub>6</sub> at pressures up to 2 bar. He observed that, with a lathe-finished sphere (groove depth = 64 μm), the breakdown voltage attained the same level as for a polished sphere after ~ 7 sparks. However, with the sand-blasted finish (75 μm), the number of conditioning sparks was more than 30 and the breakdown level remained about 13% below the polished -sphere value.

The effects of different surface finishes on the breakdown performance of 1.0 mm uniform-field gap were studied by Spence and Ryan [138] in SF<sub>6</sub> at pressures of 5.15 and 14.8 bar for

dc, ac and impulse voltages. Copper electrodes of  $1.2 \text{ cm}^2$  area were used. Dc and ac conditioning characteristics were compared for initial and conditioned breakdown levels. At both pressures and for both waveforms initial breakdown levels were found to be higher for polished electrodes than for machined electrodes. The conditioned breakdown level under dc voltage was higher for machined electrodes than for polished electrodes at both pressures, but for ac voltage this level was higher at 14.8 bar and lower at 5.15 bar for polished electrodes. For lightning impulse at 14.8 bar machined electrodes were found to have higher first breakdown performance than polished electrodes and less conditioning with small scatter was observed for the machined electrodes.

It can be concluded from the above studies that appreciable changes in the nature of the electrode surface can occur during conditioning, because of the influence of electrode area, gas pressure and experimental circuit parameters on the degree of electrode damage incurred. The influence of electrode area and gas pressure on the breakdown statistics of high-voltage equipment may therefore be accurately elucidated only from the distribution of first breakdown voltages. Nevertheless, the difficulties of obtaining first breakdown data in both laboratory and industrial scale on the one hand, and the interesting outcomes of conditioning processes on the other, have made conditioning experiments attractive from academic and practical points of view.

#### Electrode material effect

In the range of electric field, below  $250 \text{ kVcm}^{-1}$  [139], where Paschen's law is valid, the electrode material is found to have no effect on the breakdown characteristics of  $\text{SF}_6$ , but it does have at

field strengths exceeding the above figure. For the first breakdown voltage, the results show slight dependence on material. With increasing electrode size and surface roughness of the stressed electrode the influence of the material on the breakdown performance of the gap becomes less [140].

In a uniform field gap, since the breakdown voltage is primarily governed by the cathode, the effect of cathode material is partially responsible for determining the breakdown characteristic of the gap as the field and pressure increases. The anode is usually considered to have little or no effect on the breakdown strength of SF<sub>6</sub>.

McAlpine and Cookson [128] showed that covering the electrodes improved the impulse breakdown field strength of SF<sub>6</sub> by about 50% compared with uncovered electrodes at pressures of 15 and 50 bar, and that Paschen's law was maintained with covered electrodes up to 1300 kVcm<sup>-1</sup>. It was observed also that with covered and uncovered electrodes a considerable polarity effect occurs.

Goryunov [139] investigated the effects of electrode material and the method of finishing on the breakdown voltage strength of SF<sub>6</sub> in uniform-field geometry up to 8 bar. The dielectric strength was found to be governed by the mechanical strength of the electrode material and its melting temperature. Cathode materials in the order of decreasing breakdown voltage and increasing in scatter of breakdown voltages were observed to be stainless steel, copper, dural and tin. A similar classification of materials was also given in reference [65]. Whereas the breakdown strength of SF<sub>6</sub> in uniform field gaps at high pressures depends on the material, in coaxial-field gap Kawaguchi et al [110] observed no effect of cathode material for pressures up to 4 bar with dc and impulse voltages.

## Other effects

Apart from the above effects, electrode separation, type of applied voltage, temperature and the amount of radiation also influence the breakdown strength of SF<sub>6</sub>.

In uniform fields in the region where Paschen's law holds any increase of either pressure or gap separation can be balanced by the decrease of the other of these parameters, if the product is kept constant. At high pressures and field strengths, however, increase in gap separation decreases the breakdown field and results in a saturation in the breakdown voltage [110].

The performance of a compressed-SF<sub>6</sub> uniform field gap under dc- and ac-applied voltage under clean conditions is identical; nevertheless the ac breakdown voltage is lower than the dc in particle contaminated gaps, since particles are more active in the ac case [125]. Due to the statistical and formative time lags involved, the impulse breakdown performance is different compared to dc and ac cases.

At pressures up to 4 bar, deviations from Paschen's law begin to occur if the temperature is increased above 450°K. This is attributed to temperature dependency of the electron-attachment process [64].

The amount of irradiation has an important influence on the impulse breakdown characteristic of SF<sub>6</sub> insulated gaps. The statistical time lag,  $t_s$ , which is the time for an initiatory electron to appear in a suitable position, can be varied over many orders of magnitude by varying the amount of irradiation from the source.

### 1.6.3 Quasiuniform-field breakdown

The term 'quasiuniform' is used to apply to situations where the field is nonuniform, but not so nonuniform that breakdown is preceded by corona. This is the condition appropriate to practical applications such as design of contact assemblies for H.V. switchgear and SF<sub>6</sub>-insulated busbars. The dielectric strength of quasiuniform gaps is normally controlled by the conditions at the cathode (in coaxial-electrode geometry, for example, the negative impulse breakdown strength is more critical).

Several investigators have reported dc and ac measurements in different coaxial-electrode gaps. In Figure 1.2 the breakdown results are compiled for convenience in parametric form and associated gap details are presented in Table 1.1. For pressures less than 2 bar the similarity law is generally obeyed, the breakdown field at the inner electrode  $E_b$  is a function of the product of pressure and inner electrode radius  $pr_1$ , and  $E_b/p$  tends to the limiting value ( $E/p_{lim} = 88.4$  kV/cm bar). For higher pressures  $E_b/p$  falls below  $(E/p)_{lim}$  with a rate determined by the nonuniformity factor  $f$  ( $= E_{av}/E_{max}$ ) of the gap. The critical field at which deviation starts is also likely to be dependent on the nonuniformity of the gap (for nonuniformities less than 2.718).

Under carefully controlled experimental conditions Bortnik and Gorjunov [142] investigated the breakdown characteristic of SF<sub>6</sub> in coaxial-field geometry with a 0.6-cm radius copper inner and 0.75-cm radius stainless-steel outer electrode under dc applied voltage up to 20 bar. Breakdown voltages up to 3 bar were observed to be linear and above 3 bar deviation from linearity starts for both polarities with some scatter which is about three times more for the negative polarity than for the positive polarity. The maximum of

scattered values was thought to result from physical processes, particularly field emission on the cathode and the lower values from impurities in the gas or microprojections on the inner electrode. At field strengths more than 300 kV/cm, the reason for deviation from the Paschen's curve was related to the field emission process. In a similar investigation, but in a larger scale of cylindrical geometry comprising several polished inner conductors with different radii of 0.5 to 3.8 cm stainless steel and of 0.8 to 2.6 cm aluminium, and with same 12.5 cm radius outer electrode, Bortnik and Cooke [129] studied the breakdown characteristics of SF<sub>6</sub> for pressures up to 8 bar. Experimental results were compared with the similarity-relation calculations based on the streamer criterion. In clean laboratory conditions, theory and experiment were shown to agree for field strengths of up to ~200 kV/cm with relatively large area electrodes and to even high fields for small-area electrodes. The main factors causing the deviation from the law were qualitatively explained by field amplification and ionisation at microprojections, and conducting particles close to the electrode surface.

The similarity law was checked by Cooke and Velazquez [143] at ultra-high dc voltages with a 38-cm radius outer electrode using several inner electrodes of aluminium or stainless-steel at gas pressures from 1 to 7.8 bar. The following observations were made; up to one bar experimental and theoretical breakdown results were nearly equal while above this pressure deviation with some scatter started; this was explained by the deleterious effect of electrode surface irregularities and particle contamination. The breakdown voltage reduction due to particle contamination was found to be related to the system size. The superior dielectric performance of

SF<sub>6</sub> as compared to N<sub>2</sub> and air were found out to be maintained in the pressure range studied.

Extensive investigations of the dielectric performance of SF<sub>6</sub> in coaxial-cylinder gaps were made in Shibura Electric Company of Japan. The results of standard and switching impulse, and ac voltages, may be summarised as follows.

(i) Breakdown field stress depends to some extent on the non-uniformity of the gap; the smaller the inner conductor radius, the higher the breakdown field stress. This may also be explained by taking into account the electrode area effect [110].

(ii) The influence of the stressed electrode on the negative breakdown gradient is prominent whereas the positive breakdown gradient is less affected at high pressures. This may be due to field-emitted-electron supported discharges growing up from the cathode surface. Also, electrode area, duration of applied voltages and gas pressure are responsible for this discrepancy. Coating the negative electrode might bring the negative breakdown voltage to the same level of the positive one [144].

(iii) There is no effect of electrode material, or of electrode surface microstructure with roughness less than several tens of  $\mu\text{m}$ , on the breakdown of SF<sub>6</sub> [110, 144].

(iv) The surface roughness of the outer electrode does not have any effect on the breakdown characteristics [145].

(v) Breakdown voltages increase almost linearly with pressure up to about 5 bar and thereafter have a tendency to level off. The breakdown voltage gradients are in good agreement with the values achieved by extrapolation from the low pressure results.

(vi) Electrode area, duration of applied voltage and gas

pressure are the main factors causing decrease of negative breakdown gradients.

Over a range of radii ratio  $r_2/r_1$ , varying from 25 to 2.71, Ermel [146] reported dc breakdown characteristic in SF<sub>6</sub> up to 8 bar. The entire breakdown characteristic over the pressure range was divided into three regions depending upon the observed physical phenomena in the spark gap. The third of these corresponds to quasiuniform-field breakdown and in this case deviation from similarity law began with a pronounced polarity effect. The field strength at the deviation point in this region was noted to be a function of radius  $r_1$ , possibly due to effect of electrode surface area. The sharp fall in the breakdown characteristic after the critical field strength was explained by local field disturbances superimposed on the macroscopic field and the polarity effect was considered to be due to the onset of field emission from the cathode.

An estimation of the breakdown characteristic after deviation from the similarity law in coaxial geometry was attempted by Mosch and Hauschild [147] using streamer breakdown theory. They defined a roughness factor by which the allowable maximum field strength is related to the value obtainable with smooth electrodes. Several experimentally determined roughness factors for different surface treatments and pressures were presented.

#### 1.6.4 Corona and breakdown in nonuniform fields

In nonuniform fields in SF<sub>6</sub> breakdown is usually preceded over a pressure range by corona discharge of several forms. In the region where the corona exists, breakdown takes place at a voltage  $V_b$  in excess of the corona-onset voltage  $V_c$ , and outside this region the corona-onset and breakdown voltages coincide. For a fixed gap

length, increasing the pressure from lower values causes the breakdown voltage to pass through a maximum  $V_m$ , corresponding to a pressure  $p_m$ , and then to decrease until a critical pressure  $p_c$  is reached; at pressures greater than  $p_c$  direct breakdown occurs. This feature of breakdown-pressure characteristics is observed for both static and alternating voltages and with impulse voltages. There have been a considerable number of investigations in point-plane gaps of the effects of field nonuniformities, gas pressure and polarity on the V-p characteristics and the associated corona discharge phenomena. The main points of the findings may be summarised as follows.

(i) At pressures below  $p_c$ , corona develops before breakdown, the space charge near the high field electrode reduces the geometric field and results in the increase of breakdown voltage. For the positive point, at low pressures ( $p < p_c$ ), the distortion caused by the primary avalanches, which might facilitate the propagation of streamers across the gap, is quenched by the formation of negative ions by attachment at the rear of the developing streamer which reduces the ionisation. Quenched streamers spread over the point by photo-ionisation to form a self-sustaining corona. This corona effectively extends the point and makes the applied field at the tip of the rod less divergent [149,151] and positive ions created in corona constitute mid-gap space charge which yield additional distortion depending upon the pressure [149-153]. Recently, however, a better understanding of corona discharge phenomena [97,158,159] revealed the fact that the stabilization is rather caused by the positive space charge which stabilizes the tip field and enhances the field in the low-field region [157, 158, 160, 161].

(ii) The positive-ion cloud in the mid-gap establishes a low-field space-charge barrier. At low pressures ( $p < p_m$ ), its

presence is evidenced by the lateral spread of corona discharge activity on the anode surface [158]. Breakdown results when the field at the plane cathode increases sufficiently, allowing intensive streamers to penetrate through this barrier [159]. Sparking channels in this region of pressures are mostly axial. At higher pressures close to or at  $p_m$ , the space-charge field impedes discharge development to the extent that breakdown is initiated by streamers bypassing this region such that curved spark channels are observed [151,157,158,160]. As the pressure is increased from  $p_m$ , the ability of streamer to propagate through the low-field barrier increases [150,158]. The resulting spark channels appear axially [150].

(iii) The transformation from a stable to an unstable corona after the breakdown maximum is not clearly understood. There exists different views on the gas processes taking place: (a) As the pressure is increased the number of both positive and negative ions increase in the streamers; probably the rate at which positive ions increase is greater [149,151]. The gradient at the streamer tip, therefore, increases and is augmented by less diffusion and decreased photon absorption mean free path, all of which bring about continuously extending narrow streamer channels propagating into the gap until all streamers cross the gap [151,152,158]. (b) The transition to unstable corona discharge is possible if the photon absorption mean free path shrinks faster than the effective ionization coefficient with increasing pressure. The critical pressure is reached when a fraction of the secondary electrons produced beyond  $r_c$  falls below a critical value [160]. (c) At the voltage maximum, the field gradient at the rod tip attains values near the detachment threshold which is well above the limiting threshold  $(E/p)_{lim}$ . Two high-affinity ion species,  $SF_5^-$  and  $F^-$ , are most likely to suffer

detachment, since  $\text{SF}_6^-$  has a relatively stable population because of its high capture cross-section. The propagation of an initiating streamer could be facilitated by those high energy electrons along the gap axis due to the high field strength at the streamer head which maintains  $\alpha > \eta$  [153].

(iv) The pressure range over which breakdown is preceded by corona is greater for negative polarity than for positive polarity. The maximum of negative  $V = f(p)$  characteristic is higher and occurs at higher pressures than the positive polarity case. At a given pressure the corona onset level for negative polarity is always lower. The critical pressure is also higher for the negative polarity [118,155,156,161]. From the prebreakdown current measurements, the polarity effect is concluded to be due to differences in space charge density and in mobility of positive and negative ions. An important reason for higher charge densities for negative polarity could also be effective secondary photoemission and field emission from the rod [156]. In another proposal [161], this difference is considered to be as a result of space charge restrictions imposed on positive and negative streamer propagation. In the case of the negative rod-plane gap at low pressures, an initial streamer and its associated secondary avalanches created by photoionization moving ahead of it propagate into a declining field. Further, in the presence of slowly drifting negative space charge, it is rather difficult for streamers to move further into the gap unless the external field is high enough. In the case of positive rod-plane gap initial streamer and secondary avalanches produced by photoionization moving ahead of it travel towards the high field region, leaving behind more positive ion space charge. In this manner, while the positive ion space charge

moves toward the cathode, it maintains the field at the tip of the advancing streamer, resulting in more electrons being created as the streamer advances. This explains the low breakdown voltage as well as low critical pressure in the case of positive rod-plane gaps.

(v) Generally, in  $\text{SF}_6$  the breakdown voltage/pressure characteristics are independent of the rod radius of the stressed electrode at low pressures over the rising part of the curve [97,160]. The breakdown maximum increases and the corresponding pressure decreases with reduction of the rod radius [150,160]. At the critical pressure  $p_c$  the corresponding voltage and also the product  $p_c r$  stay almost constant. The range of corona stabilization increases with the rod radius [97, 161]. The critical pressure is primarily affected by the radius of rod and more or less independent of electrode separation [161].

The data hitherto available for corona stabilized breakdown with impulse voltages is relatively scarce. The identifiable features of these characteristics can be outlined by the following points.

(i) In short and long gaps for both polarities of lightning and switching impulses, the maximum is less pronounced, less affected by nonuniformity of the stressed electrode [166,167] and is less than that for dc or ac voltages under the same experimental conditions [151,152,162,163]. This is because of insufficient time for space charge build-up in the impulse duration. In short gaps, positive impulse characteristics exhibit two maxima, but negative ones do one [163].

(ii) The pressure range over which corona stabilization occurs decreases with increasing rod diameter [165,167] and the range

is larger for the negative polarity.

(iii) Positive or negative breakdown characteristics of nonuniform and extremely nonuniform field gaps over the rising part coincide [165] and negative breakdown voltage is always higher [164-166].

(iv) Breakdown characteristics at pressures between  $p_m$  and  $p_c$  have negative slope and are affected by the impulse waveform and the nonuniformity of the gap [164,166].

(v) In the direct breakdown region of the characteristics, the positive breakdown voltage is higher than the negative and is affected by nonuniformity of the gap.

#### SF<sub>6</sub>/N<sub>2</sub> Mixtures

The breakdown pressure characteristics of mixtures of SF<sub>6</sub> with N<sub>2</sub> in nonuniform fields exhibit similar behaviour to that of pure SF<sub>6</sub> over the corona stabilized region. Particular features observed in different investigations in various mixtures having 10-100% SF<sub>6</sub> are: i) the maximum of the V-p characteristic is less peaked compared to the one achieved in SF<sub>6</sub>, and is reduced by reducing SF<sub>6</sub> concentration [79,97,160]; the corresponding pressure  $p_m$  is almost unaffected.

(ii) In contrast to pure SF<sub>6</sub>, the stepped change after the maximum on V-p characteristics is not observed [97].

(iii) The evidence on the effect of changing SF<sub>6</sub> concentration on the critical pressure is conflicting; as the SF<sub>6</sub>-content is reduced, the critical pressure may be unaffected [79, 156,164] or may be shifted to higher pressures [97,169].

(iv) At higher pressures  $\Delta p_c$ , the dielectric strength of mixtures increases almost linearly with SF<sub>6</sub> concentration [79,97,168].

Positive and negative impulse breakdown characteristics in

$\text{SF}_6/\text{N}_2$  mixtures with  $\text{SF}_6$  concentration less than 1% in various non-uniform field gaps show an additional feature which has not been noticed under steady or alternating conditions in that the corona stabilization over a pressure range is more persistent, resulting in higher breakdown voltages [167,170-171]. The dominant effect is related to charge injection during impulse corona, giving rise to increased shielding of space charge [163,168], although, since the same anomaly has not been observed for other mixtures with  $\text{SF}_6$  content more than 1%, the nature of the mechanism is more complex than that proposed.

#### 1.6.5 Prebreakdown phenomena in $\text{SF}_6$ and $\text{SF}_6/\text{N}_2$ mixtures

Investigations of the nature of the prebreakdown corona discharges have been of interest in recent corona studies, because of the fact that microdischarges occurring in the regions of micro-projections or free conducting particles can lead to reduced breakdown voltages in  $\text{SF}_6$  and  $\text{SF}_6$  mixtures. In an earlier investigation Pollock and Cooper [149] examined positive-corona current-pulse variations over the rising part of V-p characteristics in  $\text{SF}_6$  and in other electronegative gases in a point-plane gap. As the voltage was raised, isolated streamer pulses at the onset were observed to be replaced by burst pulses preceded by streamer pulses at higher voltages giving rise to increased current magnitude. The qualitative explanation given for the phenomenon was similar to that for air, although a space-charge modification to the mechanism was also indicated. A more extensive experimental investigation of anode corona characteristic in  $\text{SF}_6$  over a wide range of pressure and field nonuniformities was performed by Hazel and Kuffel [158] in a point-plane gap. It was observed that the corona in  $\text{SF}_6$  for the range

of pressures and voltages studied is a streamer corona and that the glow discharge noticed in air does not materialise at any phase of the corona. Static cathode corona discharge activity in  $\text{SF}_6$  and  $\text{SF}_6/\text{N}_2$  mixtures was investigated by Malik et al [174] using rod-plane electrodes at constant gap length and at various gas pressures. In  $\text{SF}_6$ , at the corona onset voltage, the corona discharge starts with isolated single pulses, a series of single pulses, or a large pulse immediately followed by a series of small pulses. With increase in the applied voltage, the frequency of pulses and the average current increases; a steady flow discharge was not observed at any of the pressures used. In  $\text{SF}_6/\text{N}_2$  mixtures with low concentrations of  $\text{SF}_6$  (less than 5%), less frequent single or multiple pulses were noticed. At higher concentration of  $\text{SF}_6$  in  $\text{N}_2$ , the current pulses at onset are similar to those in  $\text{SF}_6$ ; however these pulses are smoother in shape and fairly regular in both magnitude and frequency. At higher voltages a steady glow continuing for some periods sets in and is followed by quite regular pulses superimposed on a steady glow.

From a study of image intensifier and current-pulse records of static positive corona discharges in  $\text{SF}_6/\text{N}_2$  mixtures, Farish et al [97,98] reported similar anode corona discharge behaviour as has been noticed in  $\text{SF}_6$  in rod-plane gaps of different nonuniformities; at low gas pressures streamers occur followed by burst pulses which consist of chains of small pulses at  $\sim 1$   $\mu\text{sec}$  intervals, superimposed on a constant luminosity glow discharge which is triggered at the beginning of the chain. At pressures near and beyond the peak, in addition to the continuing burst pulse activity, irregularly occurring, long-duration steady glow-like discharges of filamentary appearance are observed and near the critical pressure the continuous pulse activity disappears.

A semiempirical approach was made for the minimum pressure conditions yielding corona-free breakdown by Aleksandrov and Perlin [173], who attempted to analyze corona discharge behaviour in SF<sub>6</sub>, air and N<sub>2</sub> quantitatively in cylindrical geometry for increasing gas pressures, giving emphasis to the photoelectric effect. In SF<sub>6</sub> in highly divergent fields of cylindrical geometry, it was remarked that at high pressures after a certain pressure the number of electrons in the streamers can reach a level which promotes the formation of a leader discharge, so that the levelling-off after the breakdown minimum exists up to the critical pressure, after which breakdown takes place at the voltage necessary for initiating a self-maintained discharge (i.e. at onset).

The detailed temporal and spatial characteristics of positive switching impulse corona-discharge phenomena were demonstrated by Kurimoto et al [175,176] using photomultipliers and a high-speed camera in long point-plane gaps. At pressures less than  $p_m$  both the initial and successive discharges are diffuse, filling the gap with positive space charge which prevents the formation of a new corona discharge for some tens of microseconds and which is followed by secondary corona consisting of bursts of pulses of similar amplitude at regular intervals of  $\sim 0.1$   $\mu$ sec. Breakdown occurs from one of these pulse trains. At pressure near to  $p_m$ , leader channel propagation commences and is accompanied by a diffuse corona ahead of its tip. Near  $p_c$  and above this pressure, corona is replaced by a filamentary leader. The filamentary leader propagates in steps with the intervals between successive discharges less than 0.1  $\mu$ sec. For the negative switching impulse, at low pressures, the primary corona gives rise to a glow discharge which may be followed by subsequent secondary pulses. At higher pressures secondary pulses always

exist in the form of either single pulse or burst pulses and breakdown follows from one of these bursts.

In  $\text{SF}_6/\text{N}_2$  mixtures for various ratios of  $\text{SF}_6$  in  $\text{N}_2$  at atmospheric pressure a similar corona discharge behaviour to  $\text{SF}_6$  was observed in long point-plane gap [170]. With a small quantity of  $\text{SF}_6$  in  $\text{N}_2$  ( $\sim 0.1\%$  of  $\text{SF}_6$ ) for positive polarity, first, a diffusive luminosity develops from the rod cap; this continues for 1-2  $\mu\text{sec}$  and is followed by bright leaders accompanied by corona streamers at their tips. When the percentage of  $\text{SF}_6$  is increased to 50% intermittently advancing channels appear and stepped leaders occur. For negative polarity, the stepped leaders start with the addition of only  $\sim 0.1\%$   $\text{SF}_6$  into  $\text{N}_2$ . In this case, however, the discharge paths are very irregular in their form and intervals. With increase of the  $\text{SF}_6$  concentration the discharge extends into the gap more regularly and frequently, with increased luminosity at the leader stem. The brighter regions of the corona streamers shrink more as the leader extends giving a ball-like appearance. The different discharge-extension behaviour of positive and negative corona was stated to be due to the difference in the time interval and extension velocity of stepped leaders. In short rod-plane gaps at a pressure of one bar, Kuffel and Yializis [171] demonstrated the temporal growth of ionization before and after breakdown using a photomultiplier and the results were supplemented by current measurements. During the positive breakdown process, following the main leader stroke, a second broad pulse was observed after a few microseconds signifying ion recombination. As  $\text{SF}_6$  concentration in  $\text{N}_2$  was increased the recombination pulse shifted to higher values. The same effect was observed by increasing the gap length. For the negative polarity a similar type of breakdown behaviour was noticed.

Detailed knowledge of the impulse breakdown behaviour as a function of breakdown time is of practical importance for insulation coordination and overvoltage protection of SF<sub>6</sub>-insulated equipment. Although voltage-time characteristics of SF<sub>6</sub>-insulated equipment show a flat variation similar to that for other compressed gases at low pressures, at higher pressures they exhibit 'up curving' at shorter times, which depends upon pressure, polarity and type of applied impulse, and nonuniformity of the gap.

Though sufficient amount of experimental data has been collected for time lags from  $\sim 1$   $\mu$ sec [179-182] up to very long times [177-186] in uniform and slightly nonuniform fields in the pressure range 1 to 6 bar for impulses of different waveforms and some approximate theoretical estimations have been made [177, 182, 184, 185], there still exist some unresolved matters arising from electrode geometry and surface roughness, voltage polarity and waveshape, and circuit parameters, resulting in discrepancies on the behaviour of V-t characteristics.

The distribution of time lags is dependent on the rate of production of primary electrons before the critical field  $(E/p)_{lim^p}$  is reached and on the probability that these electrons will lead to breakdown. Hence, the total probability of an effective electron to bring about breakdown depends on natural radiation, rate of rise of applied field strength, gas pressure, gas volume and the shape of microprojections on the surface of electrodes [184]. To account for so many variables in theoretical estimation would be extremely difficult with the present knowledge on the subject. Assuming natural ionization and field emission [185] as initiatory electron

sources, Knorr has developed a mathematical model known as the volume-time theory, to estimate voltage-time characteristics in quasiuniform fields [181]. Up to 4 bar in 45 mm radius sphere-plane with 40 mm separation [182] and in coaxial cylinders of 50/130 mm in radii [181], good correspondence between estimated and measured values are achieved for both polarities of applied impulse voltages. At higher pressures, due to the disruptive effect of surface microprojections, the predictions of the theory were found to be unsuccessful. Further applications of the theory to account for the changes in the rate of primary electrons [184] and gas volume [188] time delay was carried out by Dreger in uniform and quasiuniform fields. Up to 3 bar good correlation obtained between calculated and measured values. The effect of the damping resistor in the circuit on the voltage-time characteristics in SF<sub>6</sub> was discussed in the experimental work of Lau and Schultz [186] along with the influence of gap separation in the pressure range 1 - 15 bar in sphere-sphere gaps. It was found that a resistor of 900 ohm could provide adequate damping for the discharge current without damaging the electrode surface. The time to breakdown was observed to be unchanging with gap separation up to 5 bar, then afterwards it increases strongly with decreasing gap separation in the 3 - 6 μsec range and slowly in the 6 - 9 μsec range.

In spite of the above theoretical attempts to predict the trend of V-t characteristics for limited electrode geometries and gas pressures in SF<sub>6</sub>, it seems further experimental work is necessary to investigate the effect of various factors such as gap nonuniformity, electrode surface conditions, the presence of free conducting particles, etc, which control the statistical time lag for

practical electrode geometries such that more reliable theoretical estimation of impulse and switching characteristics can be made. Further, the proposals for introducing new multi-component gases as an alternative to SF<sub>6</sub> in CGI systems will require new experimental and theoretical investigations on this complex subject to examine possible factors influencing apparatus design.

In uniform or quasi-uniform gaps in compressed SF<sub>6</sub> the factors contributing to spark conditioning and bringing about deviation from Paschen's law, in spite of the great amount of data in the literature, are not fully understood. This is caused partially by lack of consistency among the existing results, and partially by the lack of data on the fundamental gas parameters at high pressures. The problem is compounded by the uncertainties which arise when the available data is applied to large-scale systems. Similar difficulties are also experienced in gas mixtures.

With all these adverse factors in mind, it was attempted in the present investigation to study insulating properties of SF<sub>6</sub> and its mixtures with N<sub>2</sub>. A coaxial cylindrical electrode geometry was chosen since it facilitates the investigation of one effect at a time, and since it allows the field nonuniformity to be altered, in a controlled manner, from the corona-controlled to the direct breakdown regime. The test system was designed to operate at pressures up to 10 bar and static voltages up to 300 kV, and to allow the study of prebreakdown corona processes.

In the first part of the investigation, it was intended to establish criteria such that insulation performance of SF<sub>6</sub> and SF<sub>6</sub>/N<sub>2</sub> mixtures can be compared consistently. A series of conditioning experiments have been performed to study electrode roughness effects in relation to other effects such as area, material, etc. The results have been also used for prediction of breakdown voltage in large-scale systems using extreme value statistics. A surface roughness model has been proposed and breakdown estimations made for several gap parameters and the results compared with both

the measurements and the results of already existing protrusion models.

The second part of the work is concerned with the study of corona-stabilized breakdown behaviour of  $SF_6$  and of  $SF_6/N_2$  mixtures under static and impulse voltage conditions for a wide range of gap nonuniformities. The effect of an electrode protrusion on dc stabilization and of ion injection on the impulse stabilization process has been examined. The prebreakdown-corona discharge phenomena have been investigated from image-intensifier and current-pulse records for various combinations of gap voltage and gas pressures. Numerical estimations of the space-charge-field have been correlated with field measurements at the outer electrode. Finally, a preliminary study has been made of a method of predicting the transition pressure to corona-free breakdown.

EXPERIMENTAL APPARATUS AND PROCEDURE2.1 General

The dc supply and the components of the smoothing stages were housed in separate screened cabinets and the HV interconnections were made with E.H.T. cable (300 kV) having no metal screen. For earthing connection copper-strips (1/8" x 1/2") were used throughout. When the impulse generator was used, it was also placed in one of those cabinets close to the vessel. All these precautions were taken in order to keep the signal-to-noise ratio to an acceptable level.

Conditioning and breakdown experiments were carried out using microprocessor-controlled automatic voltage and recording systems. Similarly, time-lag measurements were also monitored and recorded by fibre-optic-coupled microprocessor measuring system.

Discharge current variations were determined oscillographically. For current density and field measurement, an analogue electrometer was used in series with a biased type field probe. A photomultiplier adjusted off-axis to the electrode assembly were utilized only for determining impulse-corona inception level. Spatial displacement of corona discharge phenomena were examined by means of an optically-coupled image-intensifier camera.

2.2 Experimental Vessel (Figure 2.1)

The pressure vessel, designed to operate over the gas pressure range from 0.05 torr to 8 bar and up to 300 kV voltage level, is illustrated in Figure 2.1. It was constructed from stainless steel. The overall width and radius of the vessel were

76 cm and 13 cm respectively. The inner surface of the vessel including the surfaces of two side flanges were polished to a dull finish. The vessel was provided with the following access ports:

- (a) A glass viewing port mounted in the main access flange.
- (b) A high-voltage bushing entry port.
- (c) Three electrical high-pressure lead-throughs.
- (d) Two gas entry ports and one pressure measurement port.

The vessel was fitted with a discharge-free resin bushing allowing 300 kV to be applied to the gap. The bushing was designed for pressures up to 15 bar; details of the bushing construction, together with seals, supports for cable connections, etc. are illustrated in Figure 2.2.

#### 2.2.1 Pumping and gas filling systems

A systematic block diagram of the pumping and filling system is illustrated in Figure 2.3. The same figure includes also vacuum and pressure measuring gauges. The two-stage rotary pump and oil diffusion pump were used to evacuate the vessel and the pressure gauges up to 0.05 torr. Two 'Worcester' type high-pressure valves with a mechanical interlock between them to ensure one at a time opening were installed at the vessel inlet and outlet. This was a precaution designed to eliminate the possibility of exposing either the pressurized vessel or gas inlets to the high vacuum system.

The pumping system was provided with two Pirani gauges which were fitted to the inlets of the diffusion and rotary pumps. A high-vacuum Penning gauge was also used at the inlet of the diffusion pump. The locations of the gauges are shown in Figure 2.3.

The gas was supplied to the vessel through a stainless

steel pipe which was fitted with a dust filter (0.08  $\mu\text{m}$ ) and cold trap before the main gas inlet to the vessel.

### 2.2.2 Pressure measurements

Pressure measurements were made by two gauges; for pressures from 0 to 1 bar an aneroid gauge (Wallace and Tiernan) with full scale accuracy of  $\pm 0.2\%$  and for pressures from 1 to 8 bar a similar type gauge (Budenburg) with full scale accuracy of  $\pm 1\%$ . The temperature of the room in which the vessel was located was taken as the gas temperature, owing to the thin wall of the vessel. All quoted temperatures in breakdown experiments were corrected to  $20^\circ\text{C}$ .

### 2.3 Electrode Assembly

Construction details of the electrode assembly are shown in Figure 2.1. The coaxial electrodes composed of either stainless steel or aluminium electrodes having radii ranging from 0.0125 to 0.9725 cm were held concentrically in either 1.27 cm or 2.5 cm stainless steel outer electrodes having an overall length of 33 cm and with profiled ends. The characteristics of electrodes used in the experiments are given in Table 2.1 and Table 2.2.

Both ends of inner electrodes were cone shaped and fitted in two stress relieving rings, similarly shaped at their centres. One of these rings near to the viewing port is specially designed to ease axial observations of the electrodes. The rings, and hence the inner electrodes, were isolated from the outer electrode by means of two PVC insulators fitted tightly to both rings and to the outer electrode, so that concentricity of the inner and outer electrodes was maintained within limits of  $\sim \pm 2 \mu\text{m}$ . The alignment for concentricity was satisfactory in that spark craters were

distributed uniformly over the entire active length of the electrode.

The ends of the outer electrode were profiled in order to avoid edge effects. For a suitable profile design, Maxwell's analysis was applied to calculate the distributions of field and equipotential lines due to a finite plane parallel to an infinitely large plate. Among the other equipotential lines, the curvature of the 40% one was adopted for profiling the edges. The outer electrode incorporated a tension ring at one end to keep inner electrodes of radii less than 0.15 cm concentrically in their position.

The gross capacitance of the gap and ancillary equipment, including the divider, was of interest in conditioning and pre-breakdown current measurement experiments. For electrodes E1 to E13 (Table 2.1) with the outer OE1, the total capacitance variation is given in Figure 2.4, in that

$$C_t = C_g + C_s$$

where  $C_s = 280$  pF and  $C_g$  is the gap capacitance which is given by the equation  $C_g = 2\pi\epsilon_0 / \ln(r_2/r_1)$ .

## 2.4 High Voltage Supplies and Automatic Control Systems

### 2.4.1 Dc voltage supply and gap voltage measurement

A systematic diagram of the overall circuit is shown in Figure 2.5. In static breakdown and conditioning experiments, the high voltage was obtained from a 50-300 kV, 0-1 mA, dc generator which has 40 kHz ripple of 0.1% and a stability of better than  $\pm 0.01\%$  against a change of  $\pm 5\%$  in mains voltage. The control circuit of the generator could be modified to supply voltages in the range 0-50 kV also as needed. The voltage was supplied to the gap through

a two-stage smoothing circuit via a 10-M current limiting resistor. Through successive smoothing the ripple of the generator output voltage was reduced to 1 part in  $10^5$ . For this particular supply, the smoothing stages and the generator were required to be housed in separate screened cabinets as is shown by dotted lines in Figure 2.5.

The input resistor  $R_1$  and the current limiting resistor  $R_3$ , were built from high stability 0.5-M resistors, enclosed in an oil-filled polythene tube; all the other resistors in hv circuit are wire-wound.

In corona discharge experiments, in order to supply high current to the gap, another 0-130 kV, 0-25 mA generator was used. The output of this generator has ripple of 4% and it was reduced to better than 0.05% with a single-stage smoothing circuit which comprised a 10-M carbon resistor in series with 0.01- $\mu$ F capacitor as illustrated in Figure 2.5. It was connected to the gap through a wire wound 0.5-M resistor,  $R_6$ .

The voltage divider that had been used throughout breakdown and discharge experiments is made up of two units of 200 M resistor connected in series, having a 4K resistor in the ground unit. Each unit consists of high-stability carbon resistors immersed in oil-filled bakelite container. The divider ratio was checked from time to time with standard bridge technique and was found to be 101059:1 with an accuracy of  $\pm 0.03\%$ .

Measurement of the divider output voltage was made by a digital voltmeter which had a stated accuracy of  $\pm 0.005\%$  of actual reading, or  $\pm 0.003\%$  of full scale reading. The total error which arises in the measuring circuit for a digital voltmeter reading A on

the scale with maximum reading of 29999 is, therefore, given by

$$0.03 + [0.005 + (0.003 \times 29999/A) ]$$

This amounts to a possible error of 0.038%.

High-voltage interconnections were made by 300-kV plastic insulated cable and joints and terminations were all constructed to be discharge free.

#### 2.4.2 Automatic voltage control and data recording system

The laborious procedure of measuring and recording a large number of breakdowns in static conditioning experiments was avoided by using a microprocessor-controlled system which had been designed for a similar type of investigation [189].

A representation of the whole system is shown in Figure 2.6. The high-voltage supply output is controlled by the microprocessor unit which is programmed to feed the digital information of the required output voltage to the digital-to-analog (D/A) converter. The D/A output drives the HV control circuit which in turn drives the HV supply. The voltage built up at the D/A output is maintained at a preset ramping rate which allows the output voltage of the generator to vary within the same limits.

The binary coded decimal output from the digital voltmeter, which is supplied with the analog gap voltage information from the voltage divider, is continuously sampled at a rate of 50 Hz by the microprocessor unit which picks up the voltage sample, compares with the previously stored sample, checks the difference against a predefined value and stores the highest one in preference to the other during the process of voltage rising. In the case of breakdown the input of DVM is shorted by B/D detector, so that the last stored sample data is directed to teletype for printing.

The second cycle starts in a like manner after the voltage at HV supply output is restored to the preset value.

Two low-pass filters were introduced to both ends of the cable connecting the HV supply to the control system in order to reduce possible hf disturbances which might be transmitted to the control circuit at breakdowns. As a second precaution the control circuit was kept at a distance from the HV supply.

#### 2.4.3 Impulse generator and voltage measuring system

Impulse breakdown and voltage-time characteristics were studied by using a six-stage Marx-type impulse generator which was designed to give impulse voltage of up to 250 kV peak with a fast rise time of 0.2  $\mu$ sec and relatively long tail of 200 ms. A diagram of the generator and the measuring circuit is shown in Figure 2.7. The generator charging circuit, the vessel and gap and the auxiliary equipment are also illustrated in the figure.

The generator was connected to the capacitive divider through resistor  $R_1$  which, together with the front resistors, provides critical damping in the generator. The connection to the test gap is made by the 'switching gap' and the resistor  $R_2$  which prevents possible damages to electrode surfaces.

The generator was triggered by a trigatron in the ground sphere of the first stage, which could maintain reliable triggering for voltages between 6 and 50 kV.

Although the generator circuit was designed originally for 0.2- $\mu$ sec / 0.2-sec waveform, the waveshapes depend on whether the switching gap quenched or not after an operation. For the present experiment, the gap separation was such that quenching was not possible, so that an output waveform of 0.2  $\mu$ s/70 ms was recorded

at the test gap for every impulse application.

The series switching gap was inserted in order to:

- (i) make the wavefront as sharp as possible,
- (ii) eliminate the staircase effect arising from different sparking times of successive stages
- (iii) isolate the generator from the gap for possible current leakages which can cause several volts to appear across the test gap.

The upper arm of the capacitive voltage divider was built from cylindrical electrodes which were enclosed in an oil-filled ceramic post-type insulator. The lower arm consisted of 5 x 0.33 $\mu$ F, 50 V, polystyrene capacitors in parallel and was connected to the CRO by a 5 metre long, 50- $\Omega$  coaxial cable. In order to match the cable to the measuring unit, 50- $\Omega$  matching circuits were added to both ends of the cable.

The generator was calibrated with the test gap connected and it was found that the results were repeatable within  $\pm 2.0\%$ .

The impulse test circuit is also incorporated in a 0-350 V dc bias supply which was connected to the vessel side of the switching gap through a water-filled 400-M resistor, as illustrated in Figure 2.7. A transfer switch was provided to the end of the resistor so that it could be grounded if a bias field was not required.

#### 2.4.4 Automatic time-lag measuring system

The time-interval measurement method described in IEC recommendations [190] was adopted for the representation of voltage-time curves. For this purpose an electronic time interval meter (frequency counter) was used, and the time-lag measurements

were recorded automatically using a microprocessor. The systematic diagram of the control circuit is shown in Figure 2.9.

The breakdown time-lag is measured as the time interval between the start and collapse of the impulse voltage. The light pulse resulting from the start of the impulse voltage at the switching gap is transmitted by a long fibre-optic to a photomultiplier which starts the counter. The stop light pulse is generated at the spark gap SG connected across the current measuring circuit and similarly transferred to the counter.

The MPU (PET 3201) resets the counter first and waits a time delay (60 sec.), fires the generator and reads the count from the counter and stores it. After each 50 counts, it directs the stored data to the magnetic tape for recording.

The light pulse used for triggering the impulse generator is produced from a LED which is fed by a simple circuit connected to MPU. The generator triggering circuit which is coupled to LED through a fibre optic link, comprises a light-sensitive detector whose output drives a relay which in turn triggers the primary of a HV pulse transformer.

There is no direct electrical connection between the HV system and the control system. All monitoring pulses between systems are transmitted by fibre-optic links of 15 metre length.

## 2.5 Ancillary Equipment

In experiments with both dc and impulse voltages, the gap current variations were observed by the voltage appearing across a resistor connected between the outer electrode and the vessel. The link between the resistor and the measuring circuit was maintained through the vessel shell by a 'Conax' type lead-through.

The voltage signal was amplified before entering the CRO amplifier.

The impulse corona inception level in related experiments was determined by using a high-gain photomultiplier positioned at an angle to the discharge gap, whose output was connected to the second channel of the CRO.

Further, in dc corona discharge experiments, the current and voltage relation was recorded by a X-Y plotter which was supplied with output signals of the voltage divider and the preamplifier.

Both CRO and X-Y plotter were protected first by a spark gap across the current measuring circuit and by a transient voltage limiter inserted before the preamplifier, as shown in Figures 2.5 and 2.7.

## 2.6 Optical Recording System

The spatial displacement of corona discharge was observed with the arrangement shown in Figure 2.10. The system basically has optical coupling system, image intensifier and camera.

The coupling system consists of two diverging lenses which in the present arrangement provide a magnification of x5. It has timing and aperture adjusting facilities. The glass used at the viewing port of the experimental vessel is optically polished. The focusing was obtained by means of a bellows arrangement.

The light emitted from the discharge was intensified by a four-stage image intensifier with a gain of  $\sim 30$  per stage, giving an overall gain of  $\sim 10^6$  over four stages when the rated voltage and current was supplied. A standard 35-mm camera with f 2.8, 100 mm lens was mounted at the rear of the intensifier.

The image was focused first on to the front photo-cathode of the intensifier through the optical set. Using different exposure

time and aperture settings, several pictures of the discharge phases were recorded. The corresponding current variations of the same phase were also recorded using an oscilloscope.

## 2.7 Experimental Procedure

The detail of the electrodes and their surface finishes after treatment are given in Table 2.1.

In breakdown experiments, since it was relevant to carry out tests with electrodes having repeatable performance, the following steps were adopted for polishing the inner electrodes:

- (i) Polishing first with 320 Al emery cloth, then with 4/0 emery cloth on a lathe.
- (ii) Extensive lathe polishing with 4/0 emery cloth using 14- and 6-micron diamond paste.
- (iii) Successive hand polishing with 4/0 emery cloth using 3- micron diamond polishing paste, making use of wood guide blocks manufactured for the purpose.
- (iv) Washing the electrode with liquid detergent, then cleaning in an ultrasonic bath for 5 minutes.
- (v) Before inserting into the position, the electrode was rinsed first in acetone and then in ethyl alcohol.

For sand blasted and machined inner electrodes, only steps (iv) and (v) were followed.

Outer electrodes were polished on a lathe, using Grit 240, silicon-carbide-coated cylindrical 'Flex-cone' brushes, and were cleaned as in steps (iv) and (v) above.

After closing the vessel, the system was pumped to 4 torr with  $\sim 10\%$  ballast and to 0.2 torr without it. The oil diffusion pump then evacuated the system to  $< 0.05$  torr in two hours. The

vessel was flushed twice with the test gas before being filled to the required pressure.

In experiments with  $\text{SF}_6/\text{N}_2$  mixtures, a similar pumping and filling procedure was followed but, taking into account the density difference of two gases,  $\text{N}_2$  was filled first to the required pressure, then  $\text{SF}_6$  was admitted gradually to the total procedure. In order to achieve homogeneous mixing, a fan driven by a dc motor placed in the vessel was set to run for about 30 minutes after admixing. Before starting the experiment the gas was allowed to settle down for about 2 hours.

SPARK CONDITIONING CHARACTERISTICS OF SF<sub>6</sub>AND SF<sub>6</sub>/N<sub>2</sub> MIXTURES3.1 General

The insulation performance of compressed gases can be improved by conditioning the electrodes by successive sparkings, whereby reproducible electric field strength measurements are possible, as was explained in section 1.6.2.2. However, due to lack of understanding of the physical nature of the conditioning mechanism, there are discrepancies in the results of different investigators for experiments which were seemingly performed under the same conditions. In general, it has been agreed that, for compressed-gas breakdown in uniform and nearly uniform (sphere-to-sphere) field gaps, the primary reason for spark conditioning is the destruction of microprojections or free conducting microparticles existing on the cathode surface, although an influence of the anode has been occasionally observed.

The existing breakdown theories [113,115] for predicting breakdown field strengths below the Paschen-law value using simple streamer criteria have generally made use of protrusion models situated on the cathode surface in a uniform-field gap. The analytic solution based on this model, however, is more involved owing to the still unknown complex nature of the field emission process from the cathode surface. A more realistic solution, therefore, would be achieved by either analysing the field intensification together with field emission process from a protrusion or investigating the

protrusion model separately. Positive breakdown studies in a coaxial-cylindrical system give this opportunity. In the present investigation spark conditioning and breakdown tests in  $\text{SF}_6$  and  $\text{SF}_6/\text{N}_2$  were made in coaxial geometry with the inner electrode positive in order to separate any field emission mechanism caused by microprojections, dust, oxide layers, etc. (as in the case of cathode conditioning) from the mechanism of high field enhanced ionization from the microprojections, so that a better insight to this important processes could be achieved. It is intended, hence, in this chapter to verify the following objectives:

(i) The conditioning requirements in static breakdown experiments to attain reproducible results over a wide range of pressure and electrode conditions.

(ii) The effects of electrode surface preparation and electrode material on the conditioning sequence for a range of pressures.

(iii) The comparison of conditioning behaviour of  $\text{SF}_6$  and  $\text{SF}_6/\text{N}_2$  mixtures; hence to verify the behaviour of both gases with respect to the electrode surface roughness.

(iv) The correlation of electron microscope records of details of the surface structure of the electrodes before and after conditioning with the conditioning behaviour in both gases.

Before examining the conditioning phenomenon, some initial tests were performed to study the influences of rate of rise of applied voltage and to establish the type of the mixtures to be used throughout this investigation.

The conditioning experiments were conducted at pressures in the range of 1 to 8 bar with the inner electrodes listed in Table 3.1. The physical properties of the electrode materials

used are given in Table 3.2. Two electrode materials having distinct physical features were chosen; the stainless steel electrode has higher mechanical strength, melting temperature and work function than the aluminium.

### 3.2 Experimental Arrangement and Procedure

The experimental vessel, dc supply and hv circuit, and automated voltage control and recording system have been described in section 2.4. The automated system was programmed to record 200 breakdowns and the rate of rise of voltage was kept at 5 kV/sec up to about 90% of the breakdown voltage and, thereafter, at less than 2.5 kV/sec. (The reasons for the choice of rate of rise of voltage will be clear from the following section).

The gap was provided with irradiation from a capsule of 3 m Cr Cs 137 positioned axially just outside the vessel at a 10-cm distance from the end of the electrode assembly. Unless otherwise stated this source was in position.

The arc energy input to the gap was limited by a series resistor  $R_3$  (Figure 2.5) whose value was selected on the basis of some earlier investigations in the Department [76]. Although the use of an external shunt spark gap with a trigatron could be a viable alternative method of limiting the input energy, the operating time of  $\sim 5 \mu\text{s}$  would be too long to allow an appreciable reduction. A 10 M resistor with 0.01  $\mu\text{F}$  storage capacitor was therefore used. The arc energy input to the gap was limited by using optimum values of the hv circuit components  $C_1$  and  $R_3$  (Figure 2.5).

Dc breakdown measurements were performed at pressures of 2, 4, 6 and 8 bar in  $\text{SF}_6$  and  $\text{SF}_6/\text{N}_2$  mixtures of several  $\text{SF}_6$  concentrations, as indicated in section 3.3.3. The inner electrodes

specified in Table 3.1 were used together with a 2.54 cm diameter stainless steel outer electrode. The assembly allows a change of area from  $0.18 \text{ cm}^2$  to  $190 \text{ cm}^2$ . Three electrode finishes were chosen: polished ( $R_{\text{CLA}} = 0.04 \text{ }\mu\text{m}$ ,  $R_{\text{max}} \simeq 0.3 \text{ }\mu\text{m}$ ), sandblasted ( $R_{\text{CLA}} = 2.3 \text{ }\mu\text{m}$ ,  $R_{\text{max}} \simeq 16\text{-}20 \text{ }\mu\text{m}$ ), and machined ( $R_{\text{CLA}} = 2.8 \text{ }\mu\text{m}$ ,  $R_{\text{max}} \simeq 10\text{-}15$ ).

A set of experiments was started using a newly processed and cleaned electrode at the lowest pressure of 2 bar, and at each pressure setting 200 breakdowns were recorded. Since, usually, even for the worst case, the conditioned value could be achieved within the first 50 breakdowns, the conditioning results will be illustrated using only the first 100 conditioning sparks.

### 3.3 Preliminary Conditioning Experiments

#### 3.3.1 Importance of applied voltage waveform

A sketch of the voltage waveform applied to the gap during conditioning experiments is given in Figure 3.1. The parameters describing the waveshape are the reset voltage  $V_r$  to which the voltage is raised from zero at a rate  $r_v'$  within  $t_r$  seconds, and the breakdown voltage  $V_b$  attained by increasing the voltage at a rate  $r_v$  from  $V_r$  within  $(t_b - t_r)$  seconds. The relationship among these parameters over the region of interest,  $t_r \leq t \leq t_b$ , is given by

$$V_b = r_v (t_b - t_r) + V_r \quad (3.1)$$

The breakdown voltage is a function of four independent variables. Before setting the control system with any of these variables, their influences, and hence the relative importance of them in altering the breakdown voltage, must be verified. Keeping  $(t_b - t_r)$  constant by varying  $r_v'$ , for example, the dependence of the breakdown voltage on  $V_r$  and  $r_v$  can be observed simultaneously. In the following

section an attempt has been made to identify the effects of  $V_r$  and  $r_v$  on the breakdown voltage level in  $SF_6$ .

### 3.3.2 Effect of the resetting voltage $V_r$ and the rate of rise of voltage $r_v$

In a series of tests on a 0.5/1.27 cm coaxial-electrode gap in compressed  $SF_6$  the effects of reset voltage  $V_r$  and the rate of rise of voltage  $r_v$  on the static breakdown voltage were studied at pressures 1 and 3 bar for both positive and negative polarity.

For several values of  $r_v$  in between 0.5 to 8.5 kV/sec, at least ten breakdowns were recorded for the values of  $V_r$  which was set to 70%, 80% and 90% of  $V_b$  with and without irradiation. The results with respect to the stated polarity and pressures are illustrated in Figures 3.2 to 3.5.

Since the distribution of breakdown voltages for such a case cannot be explicitly identified with one of the known distributions, the error bars in the figures indicate the maximum and minimum breakdown values in the distribution.

Figures 3.3 and 3.4 show the effect of  $r_v$  on  $V_b$  for positive polarity at 1 and 3 bar respectively. Although, in both figures, there is no striking influence of  $V_r$  on  $V_b$ ,  $V_b$  is reduced with increasing  $r_v$ . The amount of reduction is  $\sim 3\%$  at 1 bar and  $\sim 5\%$  as in the case of 3 bar from the values of  $V_b$  obtained at slower  $r_v$  of less than 2.5 kV/sec. For negative polarity, only at 1 bar is a similar reduction of  $\sim 3\%$  noticeable and at 3 bar the effect of  $r_v$  on  $V_b$  is not apparent. The breakdown level seems to be dominated by the cathode-active field-emission mechanism.

These results are consistent with the finding of Thom

[76] and Coates et al [71] who noticed the same dependency of  $V_b$  or  $r_v$  in compressed  $N_2$  for uniform field gaps. Although the change in  $V_b$  with  $r_v$  was suggested to be due to the time involved for the development of an avalanche, in the present study the slight change in  $V_b$  with irradiation for  $r_v$ , higher than 2.5 kV/sec, implies that the statistical time-lag is another factor to be accounted for in  $SF_6$ . This is confirmed also by the experimental fact that, under negative applied voltage, the dependence of  $V_b$  on  $r_v$  at  $p = 1$  bar, seems to be affected as the pressure is raised to 3 bar, due to the onset of field emission mechanism. This feature in  $SF_6$  merits further statistical study, preferably with rough electrodes.

At slower rates of rise, another reason for having higher  $V_b$  may be the process of 'stress conditioning'. Because of the high current density, the tips of high field sites could be rounded off during the period of voltage rise, hence effectively removing any weak points causing lower breakdown. This point will be also discussed in section 3.5.5.

### 3.3.3 Choice of the type of gas mixture

Since the electron energy distribution in  $SF_6$  gas is highly dependent on the ratio  $E/p$  and since the electron attachment spectrum of  $SF_6$  is limited to electron energies in the range 0 to  $\sim 0.4$  eV,  $SF_6$  exhibits a strong sensitivity to local field intensification due to the presence of microprojections on stressed electrode surface, free conducting particles, etc. This disadvantageous behaviour of  $SF_6$  would be lessened by mixing it with other gases in order that the attachment would be increased. The additive component in this case acts as a buffer, i.e. it modifies the electron energy distribution below gas electronic excitation.

threshold. In recent investigations  $N_2$  has been found [80] to be a relatively efficient substitute for removing electrons of energies ( $\geq 2\text{eV}$ ) to a level at which attachment becomes possible.

In order to determine some specific concentrations of  $SF_6$  in  $N_2$  for some comparative studies of the behaviour with different surface roughness, a series of tests were carried out at a total pressure of 3.5 bar in coaxial geometry having 1.27 cm outer and 0.15-, 0.5- and 0.945- cm inner radii electrodes. The results are shown in Figure 3.6 for polished electrodes and in Figure 3.7 for a sandblasted inner electrode. For the various percentage concentrations of  $SF_6$  studied the mean of at least 10 breakdowns were plotted.

For all the cases studied  $\sim 60\%$  of the inherent dielectric strength of  $SF_6$  is reached with only 10% concentration of  $SF_6$  in  $N_2$ . Similarly, 80% and 90% improvement is achieved with 40% and 75% addition of  $SF_6$  by volume in  $N_2$ . Comparing the rough-electrode data given in Figure 3.6 to that for polished electrodes, the tendency with increasing  $SF_6$  content is the same, except breakdown takes place at lower field strengths. The polarity effect is also more pronounced for the rough-electrode case, which is consistent with the known properties of high field sites in providing initiatory electrons leading to lower breakdown voltages. It can be seen from Figure 3.7 that the scatter is also less with rough electrodes; this also may be associated with the production of initiatory electrodes. As expected, the breakdown field strength of the inner electrode of 0.5-cm radius is the highest as this particular configuration has optimum dimensions, i.e. the ratio of outer electrode radius to inner one is approximately  $e$  ( $=2.718$ ).

The data given in Figures 3.6 and 3.7 also allow one to examine the variation of breakdown field strengths with gap uniformity for different surface roughness for both polarities in SF<sub>6</sub>/N<sub>2</sub> mixtures.

#### 3.4 Initial Spark Conditioning Tests in SF<sub>6</sub> and in 40% SF<sub>6</sub> - 60% N<sub>2</sub> Mixture

A series of spark conditioning tests were made to identify some of the factors affecting electrode performance and hence to realise the requirement for reproducible breakdown results.

Polished 0.5/1.27-cm radii electrodes were used throughout the tests. Pressures were chosen above the critical values at which deviations from the similarity law takes place, which are 3.9 bar for SF<sub>6</sub> and 3.5 bar for the mixture. The results of several conditioning tests are illustrated in Figures 3.8 to 3.10.

In SF<sub>6</sub> the first positive inner conditioning phase starts with an initial low breakdown voltage  $\sim 8\%$  less than the mean breakdown level. This is the lowest of the breakdown voltages recorded in several successive positive-polarity conditioning tests at the same pressure (Figure 3.8). The mean breakdown level is reached after about 5 breakdowns, the scatter thereafter being  $\sim \pm 1\%$ . In positive conditioning sequences made after some periods of negative conditioning, or after leaving the system idle for the times indicated on the figure, no significant change occurs. It is noteworthy that the scatter during the positive conditioning sequences stayed within a few percent of the mean breakdown voltage.

To observe in mixtures the effects of factors such change of polarity and interrupting a conditioning sequence for a

given time, newly polished electrodes of 0.5/1.27-cm radii were tested in a 40% SF<sub>6</sub> - 60% N<sub>2</sub> mixture as shown in Figure 3.9. The general trend of the process is identical to SF<sub>6</sub>; the first breakdown voltage is ~ 12% lower than the mean conditioned level which is reached after a few sparkings. The scatter in the successive sparkings stayed within ~ 2-3% of the mean. Although as shown in Figure 3.9, leaving the system inactive for periods of 2 to 5 hours indicates a slight improvement, this is not a reproducible result. Further, the slight improvement noticed in phase 2 during negative conditioning does not take place at a later stage (phase 8) after a long period of positive conditioning (Figure 3.9).

In order to examine whether the conditioned state of the electrodes could be altered by impurities possibly introduced as the gas sample was replaced, there were several occasions during positive conditioning in a 40% SF<sub>6</sub> - 60% N<sub>2</sub> mixture at 3.5 bar on which new filtered gas samples were introduced into the system. As shown in Figure 3.10 the first breakdown voltages with the new gas samples are lower than the upper limit of conditioning by up to ~ 20%.

To account for the lower first breakdown levels by assuming that spark damage is inflicted on the electrode surface in the course of previous conditioning, newly published electrodes were conditioned in N<sub>2</sub> at 5 bar at small positive voltages (phase 8) before the SF<sub>6</sub>/N<sub>2</sub> gas sample was admitted to the system. No significant change was observed in that the first breakdown voltage was still considerably lower than the upper limit of positive conditioning.

### 3.5 Conditioning in SF<sub>6</sub> and SF<sub>6</sub>/N<sub>2</sub> Mixtures

From the results of the breakdown tests of section 3.3.3 the obvious advantages of using SF<sub>6</sub>/N<sub>2</sub> mixtures containing more than

10% SF<sub>6</sub> by volume suggest that further studies are required in order to identify mixtures which might be less sensitive than SF<sub>6</sub> to the influence of electrode roughness and particles. In this section a quantitative investigation in several mixtures of SF<sub>6</sub> with N<sub>2</sub> is carried out by performing spark conditioning tests to observe the effects of pressure and electrode roughness, area and material.

### 3.5.1 Effect of radiation

To account for the possible effects of radiation on the spark conditioning process, an electrode with radii  $r_1/r_2 = 0.5/1.27$  cm was conditioned by exposing it to 200 breakdowns in 40% SF<sub>6</sub> - 60% N<sub>2</sub> at a pressure of 3.5 bar with and without radiation. The sequence of the first 100 breakdowns is illustrated in Figure 3.11 with the corresponding standard deviation and theoretical breakdown field stress.

For this particular geometry, the effect of radiation on the shot-to-shot scatter during conditioning breakdowns is negligible as the standard deviation and the conditioned level are apparently unaffected. Further statistical analysis of the effect will be given in Chapter 4.

### 3.5.2 Effect of the type of mixture

As was indicated in section 3.3.3, mixtures of SF<sub>6</sub>/N<sub>2</sub> with 10%, 40% and 75% SF<sub>6</sub> content were chosen for possible combinations taking into account the percentage increase in dielectric strength with respect to that of SF<sub>6</sub>. Results of spark conditioning sequences in the mixtures at pressures 4 and 8 bar for electrodes of radii 0.0125/1.27 cm and 0.945/1.27 cm are shown in Figures 3.12 and 3.13 respectively. In the same figures the standard deviation of

the first 100 breakdowns and the estimated theoretical breakdown field strength is also given.

As indicated in Figure 3.12, conditioning sequences of the electrodes with radii 0.0125/1.27 cm at 4 bar are completed after a few sparks, whereas at 8 bar the conditioning period seems to be large and to be extended with increasing  $N_2$  content in the mixtures (note that the nonuniformity factor  $f$  of this gap is 21.7). The frequency of 'breakaways' and the amount of lowering from the conditioned state - although conditioning is performed at low field strengths compared to  $SF_6$  case - is considerably larger for the 10%  $SF_6$  - 90%  $N_2$  mixture.

In Figure 3.13, contrary to above stated conditioning behaviour of the electrode with radius 0.0125 cm in  $SF_6$  and  $SF_6/N_2$  mixtures at 4 bar, the electrode with radius 0.945 cm exhibits a slightly longer conditioning interval (about 10-15 sparks). At 8 bar, in both  $SF_6$  and  $SF_6/N_2$  mixtures, conditioning characteristics of the inner electrode having 0.945 cm radius are similar to that of 0.0125 cm radius, with longer conditioning interval and large shot-to-shot scatter.

For further comparison, the number of breakdowns  $N$  required to achieve the upper limit, and the standard deviation of the last 100 breakdowns have been extracted from the results of Figures 3.12 and 3.13, and are listed in the Table 3.3.

TABLE 3.3

|                     |  | $r_1/r_2$ (cm) |      | 0.0125/1.27 |      | 0.945/1.27 |   |
|---------------------|--|----------------|------|-------------|------|------------|---|
|                     |  | Gas            |      | p(bar)      |      |            |   |
|                     |  |                |      | 4           | 8    | 4          | 8 |
| N                   | SF <sub>6</sub> (A)                          | 1              | 8    | 16          | 13   |            |   |
|                     | 75% SF <sub>6</sub> - 25% N <sub>2</sub> (B) | 4              | 15   | 4           | 44   |            |   |
|                     | 40% SF <sub>6</sub> - 60% N <sub>2</sub> (C) | 1              | 9    | 1           | 23   |            |   |
|                     | 10% SF <sub>6</sub> - 90% N <sub>2</sub> (D) | 1              | 45   | 32          | 15   |            |   |
| $\sigma$<br>100-200 | A  | 4.5            | 25.8 | 7.8         | 21.1 |            |   |
|                     | B  | 4.7            | 8.8  | 6.3         | 24.6 |            |   |
|                     | C  | 1.8            | 12.5 | 10.9        | 16.4 |            |   |
|                     | D  | 6.3            | 23.7 | 8.4         | 23.5 |            |   |

For both gaps, at the same pressure, the number of breakdowns required for conditioning is higher in mixtures than in SF<sub>6</sub> whereas the scatter around the mean in mixtures is less only for the very nonuniform gap ( $f = 21.7$ ).

From the practical point of view, it would be of interest to compare the respective changes in SF<sub>6</sub> and SF<sub>6</sub>/N<sub>2</sub> mixtures as the gap is subjected to successive sparkings over a predefined common range of field strengths. The results obtained in these two gaps were arranged for field strength ranges 300-400 kV/cm and 600-700 kV/cm, as shown in Figures 3.14 and 3.15 respectively. In these two ranges randomly occurring 'bursts' of conditioning states becomes noticeable as the N<sub>2</sub> content in the mixtures is increased and the dispersion from the mean conditioned level similarly gets larger with increasing N<sub>2</sub> content. For further examination of

Conditioning behaviour of these two gaps within the given field ranges N and  $\sigma_{100-200}$  are given in Table 3.4.

TABLE 3.4

|                    | Gas Type | E (kV/cm) |         |
|--------------------|----------|-----------|---------|
|                    |          | 300-400   | 600-700 |
| N                  | A        | 16        | 1       |
|                    | B        | 4         | 4       |
|                    | C        | 1         | 7       |
|                    | D        | 20        | 45      |
| $\sigma_{100-200}$ | A        | 7.2       | 4.5     |
|                    | B        | 6.3       | 6.5     |
|                    | C        | 10.9      | 5.5     |
|                    | D        | 17.7      | 23.7    |

Although at low field strengths (column 1 of the Table 3.4) there is no trend in the behaviour of  $SF_6/N_2$  mixtures relative to pure  $SF_6$ , at high field strengths (column 2) the period of conditioning and shot-to-shot scatter increase as the concentration of  $N_2$  increases. Another point of interest is that the conditioning phenomenon in  $SF_6$  and 75%  $SF_6$  - 25%  $N_2$  mixture is similar at both low and high field ranges.

### 3.5.3 Electrode effects

Breakdown characteristics of compressed gases, as was explained in section 1.6.2.2, exhibit strong dependence on the physical properties of the electrodes of the test gap, such as details of the

surfaces and of the material, and the area of the most highly stressed parts. A reasonable comparison of dielectric strength of various gas samples can be made by examining these properties over well-defined regions of field regions under the same experimental conditions.

In this section such a quantitative comparison is made by analysing the results of conditioning tests for the above-mentioned properties of electrodes in  $\text{SF}_6$  and  $\text{SF}_6/\text{N}_2$  mixtures.

(a) Electrode roughness effect

Results of series spark conditioning tests obtained in  $\text{SF}_6$  and  $\text{SF}_6/\text{N}_2$  mixtures at field strengths in the range of 300-400 kV/cm are illustrated for polished electrode ( $R_{\text{CLA}} = 0.04 \mu\text{m}$ ), in Figure 3.16, for sandblasted electrode ( $R_{\text{CLA}} = 2.3 \mu\text{m}$ ) in Figure 3.17 and for machined electrode ( $R_{\text{CLA}} = 2.8 \mu\text{m}$ ) in Figure 3.18. The radii of electrodes used throughout the experiments were  $r_1/r_2 = 0.945/1.27\text{cm}$ . An alternative presentation of the same results is also given in Figure 3.19 to show the electrode roughness effect for the same gas. For each set of results the gas pressure, the standard deviation of the first 100 breakdowns and the estimated field strengths are also depicted.

Although the apparent overall conditioning trends for these three electrodes are similar, the 'breakaways' from the conditioned state and the shot-to-shot scatter are larger in 10%  $\text{SF}_6$  - 90%  $\text{SF}_6$  mixture than in the other gases.

The mean conditioned level remains slightly below the estimated value for all types of gases and surfaces except in 10%  $\text{SF}_6$  - 90%  $\text{N}_2$  mixture tested in gaps of sandblasted and machined electrodes.

In order to make some further quantitative remarks on the relative conditioning behaviour of electrodes in SF<sub>6</sub> and SF<sub>6</sub>/N<sub>2</sub> mixtures, the number of sparks N required to achieve the conditioned state and the standard deviation of the last 100 breakdowns are tabulated as follows.

TABLE 3.5

|              | Gas | Surface treatment |             |          |
|--------------|-----|-------------------|-------------|----------|
|              |     | Polished          | Sandblasted | Machined |
| N            | A   | 16                | 36          | 42       |
|              | B   | 4                 | 6           | 7        |
|              | C   | X                 | X           | X        |
|              | D   | 20                | 26          | 38       |
| σ<br>100-200 | A   | 7.8               | 8.5         | 8.4      |
|              | B   | 6.3               | 5.5         | 10.0     |
|              | C   | X                 | X           | X        |
|              | D   | 17.7              | 11.7        | 10.3     |

Field range = 300 - 400 kV/cm

Examining the above table and Figures 3.16 to 3.19, the following results can be derived:

- (i) The conditioning interval and shot-to-shot scatter increases with increasing roughness (roughness is the highest for machined electrodes).
- (ii) In 75% SF<sub>6</sub> - 25% N<sub>2</sub> mixture the conditioning is completed by a lesser number of sparks than in SF<sub>6</sub> and 10% SF<sub>6</sub> - 90% N<sub>2</sub> mixture.
- (iii) The conditioning interval and the scatter is noticeably more in 10% SF<sub>6</sub> - 90% N<sub>2</sub> mixture.

(iv) The effect of roughness increases with increasing pressure in SF<sub>6</sub> and SF<sub>6</sub>/N<sub>2</sub> mixtures.

(b) Electrode area effect

Spark conditioning behaviour of gaps with radii  $r_1/r_2 = 0.0125/1.27$  cm (area = 2.4 cm<sup>2</sup>) and  $0.945/1.27$  cm (area = 180 cm<sup>2</sup>) in SF<sub>6</sub> and SF<sub>6</sub>/N<sub>2</sub> mixtures are shown in Figures 3.20 and 3.21 for field strengths in the range 300-400 kV/cm and 500-600 kV/cm respectively.

In both field ranges the conditioned breakdown-voltage level with small-area electrodes is above the estimated value, whereas it is below in the case of large-area electrode.

Sporadic low breakdowns are not observed with small-area electrode for both field ranges. However, the conditioned level for large-area electrodes is interrupted by frequently occurring breakdowns to values as low as 10% of the conditioned breakdown level, and the interruption frequency and minimum level of lowering increase with increasing N<sub>2</sub> content. Further, the shot-to-shot spread of unconditioned and conditioned large-area electrodes is in excess of that for small-area electrodes. 75% SF<sub>6</sub> - 25% N<sub>2</sub> is remarkably less susceptible to these stated variations for field strengths within 300-400 kV/cm range.

The following table gives a comparative list of the conditioning behaviour of both gaps with respect to the conditioning interval N and the standard deviation of the last 100 breakdowns

$$\sigma_{100-200}$$

TABLE 3.6

|         | E(kV/cm)                     | 300 - 400 |      | 500 - 600 |      |
|---------|------------------------------|-----------|------|-----------|------|
|         | Gas \ Area(cm <sup>2</sup> ) | 2.4       | 180  | 2.4       | 180  |
| N       | A                            | 1         | 16   | 1         | 13   |
|         | B                            | 1         | 4    | 4         | 44   |
|         | C                            | X         | X    | X         | X    |
|         | D                            | 1         | 15   | X         | X    |
| 100-200 | A                            | 3.5       | 7.8  | 3.5       | 21   |
|         | B                            | 2.4       | 6.3  | 4.7       | 24.6 |
|         | C                            | X         | X    | X         | X    |
|         | D                            | 6.4       | 23.5 | X         | X    |

In the low field range, the conditioning interval and shot-to-shot scatter are less for the small-area electrode than the large-area one and are increased with the increase of N<sub>2</sub> content in the mixtures.

(c) Electrode material effect

The electrode material, although possibly unimportant in respect of the value of the first breakdown voltage, has considerable influence in determining the lower breakdown limits of gaps if the electrodes are exposed to a number of breakdowns. To investigate this effect, a series of conditioning tests of 200 breakdowns were performed in gaps consisting of stainless-steel and aluminium inner electrodes of 0.945 cm radius in SF<sub>6</sub> and SF<sub>6</sub>/N<sub>2</sub> mixtures. The physical properties of materials used are given in Table 3.2. The conditioning results are illustrated in Figures 3.22(a) and 3.22(b)

for field strengths in the ranges 300-400 and in the range 500-650 kV/cm, in Figure 3.23.

In Figures 3.22(a) and 3.22(b) (field range 300-400 kV/cm for all the spark conditioning cases the conditioned upper limit for both materials remains close to the estimated breakdown value, except for the 10% SF<sub>6</sub> - 90% N<sub>2</sub> mixture. Within the field range of this figure no noticeable influence of electrode material on conditioning phenomena, therefore, on the breakdown level was observed.

In Figure 3.23 the upper limits of conditioning sequences and shot-to-shot scatter are critically dependent on the electrode material. Because of experimental limitations, results in mixtures containing 10% and 40% SF<sub>6</sub> are illustrated only in the 400-500 kV/cm field range. In the case of aluminium electrodes the conditioned state is interfered by irregularly appearing 'burst' of lower breakdowns causing about 30% decrease of the upper limit. The scatter is also wider as compared to stainless-steel electrode.

To account quantitatively for conditioning behaviour of two materials, conditioning interval and standard deviation of results from Figures 3.22 and 3.23 are listed in the following table.

TABLE 3.7

|              | E(kV/cm) | 300-400 |      | 500-650<br>(400-500) |        |
|--------------|----------|---------|------|----------------------|--------|
|              |          | St-St   | Al   | St-St                | Al     |
| N            | A        | 16      | 3    | 13                   | 1      |
|              | B        | 4       | 2    | 44                   | 25     |
|              | C        | 1       | 6    | (23)                 | (9)    |
|              | D        | 15      | 1    | (15)                 | (1)    |
| σ<br>100-200 | A        | 7.8     | 7.5  | 21.1                 | 94.2   |
|              | B        | 6.3     | 6.1  | 24.6                 | 38.3   |
|              | C        | 4.8     | 10.8 | (16.4)               | (15.5) |
|              | D        | 23.5    | 17.6 | (23.5)               | (17.6) |

At field strengths in the range 300-400 kV/cm, the effect of electrode material is not explicit. However, at field strengths above this range the stainless-steel electrode displays a more predictable trend all along its conditioning period (columns 3 and 4 of the table). Another point of interest is that the first breakdown of the aluminium electrode is usually higher after raising the pressure (although the mean value of conditioned state is lower than this) as compared to stainless-steel electrode (column 2).

#### 3.5.4 Polarity effect

The effect of polarity on conditioning was investigated in SF<sub>6</sub> and in a 40% SF<sub>6</sub> - 50% N<sub>2</sub> mixture using polished electrodes with radii  $r_1/r_2 = 0.5/1.27$  cm. Results are shown for field strengths in the range of 100-200 kV/cm in Figure 3.14(a) and in the range of 300-400 kV/cm in Figure 3.14(b).

For both polarities, in the low field range over which the similarity law holds for both gases, conditioning is either non-existent or limited to a few breakdowns, and scatter is, at most, within one per cent of the mean breakdown voltage level.

In the high field range over which the similarity law marginally holds for SF<sub>6</sub> for both polarities and for the mixture only for positive polarity, the conditioning period and the shot-to-shot scatter is affected by the polarity of the applied voltage and the type of gas. The conditioning parameters (i.e. the number of breakdowns to the conditioned level, N, and the standard deviation of the last 100 breakdowns, ) have been extracted from Figures 3.24(a) and 3.24(b) and are tabulated below.

TABLE 3.8

|         | Field Range (kV/cm) | 100-200 |     | 300-400 |      |
|---------|---------------------|---------|-----|---------|------|
|         | Polarity            | ⊕       | ⊖   | ⊕       | ⊖    |
| N       | (A)                 | 5       | 3   | 5       | 10   |
|         | (C)                 | 1       | 1   | 3       | 16   |
| 100-200 | (A)                 | 2.2     | 3.7 | 2.6     | 10.6 |
|         | (C)                 | 1.6     | 2.9 | 10.0    | 17.2 |

In both gases, in the high field range, the conditioning period and scatter are higher for negative polarity and are further enhanced in the 40% SF<sub>6</sub> - 60% N<sub>2</sub> mixture.

Large deviations ('breakaways') from the conditioned breakdown level take place only in the 40% SF<sub>6</sub> - 60% N<sub>2</sub> mixture on negative polarity, and give rise to a decrease of about 30 per cent.

### 3.5.5 Stress conditioning

Although spark conditioning is effective for improving the breakdown level to a certain extent, the process starts usually with a low first breakdown voltage, after replacing the gas or increasing the gas pressure. The first breakdown voltage of a newly polished electrode can be improved by stressing the test electrodes for a certain period of time under voltages of either polarity at voltages about 10% less than the lowest breakdown voltage of the gap.

To observe the effect of 'stressing' the electrodes in giving possible improvements in the value of the first breakdown

voltage, an experiment was performed using a test gap with polished stainless-steel electrodes of  $r_1/r_2 = 0.5/1.27$ - cm radii in a 40%  $SF_6$  - 60%  $N_2$  mixture at a pressure of 3.5 bar. The results of the stress conditioning process, together with spark conditioning, are illustrated in Figure 3.25.

After a period of spark conditioning (phase 1) in which the breakdown voltage improved from an initial level  $\sim 10\%$  lower than the conditioned level, the system was left for 2 hours under positive stress before starting to a new series of sparks (phase 2). At the end of phase 2, the system was left, this time under negative stress, for 2 hours then further sparks were passed (phase 3). In both cases the first breakdown voltages in the spark sequences were found to be at the same level as the conditioned breakdown voltage. This contrasts with the result if the electrodes are left unstressed [196], where it is found that some degree of reconditioning is required. The stressing, therefore, apparently maintains the conditioning of electrodes, possibly by preventing dust from settling on their surfaces.

After changing the gas sample in two subsequent phases (phases 4 and 5), the same electrodes were stressed under negative voltage for 4 and 6 hours respectively. Again the first breakdown corresponded to the conditioned level, and suggests that the effects of dust were being minimised by continuous stressing of the electrodes.

The electrodes were later sparked under negative applied voltage to demonstrate any changes on the conditioned state of the electrodes after a long process of stress and spark conditioning tests (phase 6). No marked variation was observed other than the expected.

Effect of Mixture Content

The pronounced increase for field strengths above 400 kV/cm in the number of conditioning sparks required as the pressure is increased from 4 to 8 bar (as shown for polished electrodes in Figures 3.12 and 3.13) is probably connected with the occurrence of spark damage due to successive breakdowns, as this would be less severe at low pressures but would come into effect as the pressure is increased. This process is more marked as the concentration of  $N_2$  is increased, which is in agreement with earlier investigations in  $SF_6$  and  $N_2$  [71,76]. This is attributable to better cooling of the arc in  $SF_6$  [114] such that residual microprojections on the surface after sparking are smaller. At high pressures, the scatter of successive breakdowns also tends to increase with increasing  $N_2$  content (Table 3.3). This result is in contrast to the observations of Wootton et al [126] who found that in particle contaminated systems the scatter was reduced as the concentration of Nitrogen in  $N_2/SF_6$  mixtures was increased.

At field strengths below 400 kV/cm, the conditioning behaviour of mixtures is relatively insensitive to increasing  $N_2$  concentration (Figures 3.14 and 3.15). This suggests that in  $SF_6/N_2$  mixtures there exists a limit in the field strength below which conditioning is independent of modifications in arc energy input due to variations of the nitrogen content of the mixture.

Electrode Roughness Effect

Although the machined electrode has more overall roughness than the sandblasted one, the scatter obtained with machined electrode is less than with sandblasted one in the field range

300-400 kV/cm (Table 3.5). The conditioning period is, however, longer, which is in agreement with the work of Spence and Ryan [138].

The expected correlation between the scatter of individual shots from the conditioned mean value and the degree of roughness has been found for both SF<sub>6</sub> and SF<sub>6</sub>/N<sub>2</sub> mixtures. However, as discussed above, for polished electrodes, the increase in scatter with increase of N<sub>2</sub> concentration in mixtures for rough electrodes can be explained by the action of factors which enhance the effectiveness of breakdowns in producing microprojections and microparticles.

#### Electrode Area Effect

Although the data given in Table 3.6 for mixtures containing 40% SF<sub>6</sub> and 10% SF<sub>6</sub> is missing for the high field range (because of experimental limitations), the effect of increasing N<sub>2</sub> concentration on the conditioning intervals and on dispersion of the breakdown results may be concluded to be the same as in the case of the low field strength range.

The electrode area effect is generally known to be connected with increase in the probability of effective new sites with increase in electrode area [72,193]. It has also been suggested [76,191] that the area effect is due to the increased gap capacitance, and therefore the enhanced energy-storage capacity of the gap, rather than to an increase in the number of effective sites [192].

On the basis of the above arguments, the area effect in Figures 3.20 and 3.21 might be expected to be caused, at least in part, by the spark damage incurred on the electrode surface due to increased discharge energy. However, the following results, extracted from conditioning data for 2.8 cm<sup>2</sup> and 180 cm<sup>2</sup> area electrodes in SF<sub>6</sub> and SF<sub>6</sub>/N<sub>2</sub>, indicate that the increased statistical appearance of weak points with area, as the pressure is increased, is more

important than the effect of increased stored energy.

Table 3.9 : Standard Deviation of the Final 100 Breakdowns

| V (kv)                                | 50-55 |     | 50-55 |     | 45-50 |     | 30-35 |     |
|---------------------------------------|-------|-----|-------|-----|-------|-----|-------|-----|
|                                       | 6     | 2   | 8     | 2   | 8     | 2   | 8     | 2   |
| Pressure(bar)                         |       |     |       |     |       |     |       |     |
| Area (cm <sup>2</sup> )               | 2.8   | 180 | 2.8   | 180 | 2.8   | 180 | 2.8   | 180 |
| SF <sub>6</sub>                       | 6.8   | 0.9 |       |     |       |     |       |     |
| 75/25-SF <sub>6</sub> /N <sub>2</sub> |       |     | 8.9   | 1.9 |       |     |       |     |
| 40/60-SF <sub>6</sub> /N <sub>2</sub> |       |     |       |     | 12.5  | 0.4 |       |     |
| 10/90-SF <sub>6</sub> /N <sub>2</sub> |       |     |       |     |       |     | 23.7  | 2.9 |

For the given breakdown ranges (30-50 kV), the stored energy in the inter-electrode gap is in the order of 1 joule, which is quite insignificant as compared to the stored energy in the external circuit (250 - 300 joule). Increasing the electrode area from 2.8 cm<sup>2</sup> to 180 cm<sup>2</sup> varies the gap capacitance and hence the stored energy by ~ 12%. However, as shown by the results in the above table, the shot-to-shot spread with the small-area electrode is large compared to that for the large-area electrode. Therefore, in the present work it is difficult to accept the increase in the stored gap energy with area as the major reason for the area effect.

#### Electrode Material Effect

Differences in conditioning characteristics of stainless steel and aluminium electrodes emerged in the present investigation above 400 kV/cm (Table 3.7). The more important limit to be considered, however, is the energy input of individual sparks if it is known quantitatively. In this case more reasonable correlation can be

made between electrode material and the arc energy and, therefore, the corresponding limiting field.

During conditioning, each spark destroys some weak points, originates others and produces contamination. The relative importance of these factors depends very much on the arcing energy and on the electrode material. In the case of aluminium electrodes, increase in the field strength, and hence in the spark energies, above a certain level will result in the possibility of the production of new sites and/or of microparticles from sputtering at the anode. These bring about low and more scattered conditioning breakdowns after slightly higher first breakdown voltages, as was observed during most of the conditioning phases with aluminium electrodes. Stainless steel electrodes, however, because of their higher melting point, are less prone to spark damages at fields which are detrimental to aluminium electrodes.

From the present work, the threshold field for the onset of material effects was about 400 kV/cm. This may be compared with the value of 250-300 kV/cm found for uniform-field breakdown in SF<sub>6</sub> by Goryunov [139] for several electrode materials including stainless steel and aluminium. The difference of fields may be explained by the fact that, in the uniform-field case, the role of the cathode surface is more important owing to the emission, so that the limiting field is relatively less compared to that for the present coaxial-electrode system with the inner electrode positive.

### Polarity Effect

The effect of polarity on conditioning sequences in SF<sub>6</sub> and in a 40% SF<sub>6</sub> - 60% N<sub>2</sub> mixture appeared, under the present experimental conditions, when the field strength at the inner electrode of a gap with radii  $r_1/r_2 = 0.5/1.27$  cm was increased .

above 200 kV/cm; this is within the range of field strengths quoted in the literature for most gases for which deviations from Paschen's Law [49,75] and from the similarity law [141,195] are observed. At field strengths above this limit local field enhancements at microprojections come into effect, resulting in differences in conditioning behaviour for both polarities (Figure 3.24(b)).

The reasons for the polarity effect and for the large scatter in the case of negative polarity may be associated with processes taking place in the gas or at the gas-electrode interface, or both. When the inner electrode is positive the source of initiatory electrons is by detachment of negative ions produced either by the irradiation source, or by microdischarges occurring when microparticles make contact with the cathode. These two sources supply enough initiating electrons to eliminate any time lag which may introduce scatter. When the applied voltage to the inner electrode is negative, the effect of microparticles on the outer conductor (anode) has no bearing in inducing breakdown since any negative ions produced by microdischarges at the contact point are collected at the outer conductor. However, positive charge, or charged dust particles, which accumulate on tarnish layers, may lead to high field between themselves and the cathode giving rise to field emission [79]. Since the size and availability of these sites are statistical in nature, breakdown could be delayed until initiating electrons by field emission from microprojections are released at a slightly higher voltage. The influence of the irradiation source is less important than the field emission process for this polarity.

## Stress Conditioning

Although some conditioning was obtained by continuous stressing of the electrodes, as shown in Figure 3.25, it is not generally as effective as spark conditioning. It has been proposed [65,129] that this process is due to gradual rounding off of the tips of high field sites by melting, because of high current density.

### 3.7 Conclusion

In this chapter the results of positive conditioning phenomena obtained in SF<sub>6</sub> and SF<sub>6</sub>/N<sub>2</sub> mixtures at field strengths at and above the point of deviation from the similarity law have been presented and a comparison has been attempted of results obtained for the same range of field strengths for several gas and electrode conditions. From the foregoing discussions, the following conclusions may be deduced:

- (i) For a given pressure, the period of conditioning is prolonged as the concentration of N<sub>2</sub> in mixtures is increased above ~ 25%. This effect is more pronounced at field strengths above the range 300 - 400 kV/cm.
- (ii) The effect of roughness increases with pressure.
- (iii) In the same field strength range (300-400 kV/cm), the conditioning period increases with both increasing surface roughness and concentration of N<sub>2</sub> in the mixture. The shot-to-shot scatter in the case of a machined inner electrode, although it has greater surface roughness, is less than that for a sandblasted electrode. The 75% SF<sub>6</sub> - 25% N<sub>2</sub> exhibits better conditioning behaviour than SF<sub>6</sub> for rough electrodes.

- (iv)  $\text{SF}_6/\text{N}_2$  mixtures are more polarity dependent with rough electrodes than with polished ones. At field strengths above 200 kV/cm for polished electrodes the dispersion of breakdown voltages around the mean and the conditioning interval are greater for negative polarity in both  $\text{SF}_6$  and  $\text{SF}_6/\text{N}_2$  mixtures, and increasing  $\text{N}_2$  content in mixtures does not improve these characteristics.
- (v) The conditioning interval and the scatter around the mean breakdown value increases with electrode-area.
- (vi) The area effect becomes more marked as the concentration of  $\text{N}_2$  increases.
- (vii) No noticeable effect of material is observed for field strengths up to the range 300-400 kV/cm in  $\text{SF}_6$  and  $\text{SF}_6/\text{N}_2$  mixtures. However, above this range, it is found that aluminium electrodes are more severely affected by spark damage during conditioning, resulting in larger scatter.
- (viii) The first breakdown level of gas insulated systems could be improved more effectively by stress conditioning when the polarity of inner electrode is negative.

STATISTICS OF BREAKDOWN IN SF<sub>6</sub> AND SF<sub>6</sub>/N<sub>2</sub> MIXTURES4.1 General

The reliable operation of compressed-gas insulated systems requires the ability to predict the system withstand voltage  $V_w$  together with its confidence limits. In the case of SF<sub>6</sub>-insulated HV systems,  $V_w$  is determined by the properties of 'weak links' which are in the form of microprojections on electrode surfaces and/or microparticles. The dimensions and distributions of these weak links are statistical in nature and therefore the breakdown characteristics are modified as the gas pressure or the area of the stressed part of the system increases.

The statistical distribution of breakdown voltages for a particular geometry have been shown [118, 129] to follow an extreme value distribution function of the form given in Equation 1.33 when the similarity law fails to hold and it was suggested [118, 194] that, knowing the statistical distribution from laboratory experiments, it should be possible to forecast the breakdown behaviour of a large-scale system.

In the present investigation, a method has been developed for the theoretical estimation of the parameters of the Weibull distribution from experimental data which allows confidence limits for these parameters to be determined. The results of the conditioning experiments of the previous chapter have been analysed on the basis of Weibull extreme-value statistics and the Weibull parameters obtained both by graphical methods and, in some cases,

by the analytical method mentioned above.

#### 4.2 Characteristics of Weak Points

Although the statistical distribution of the first breakdown voltages is of great practical importance for any CGI system, there are difficulties in testing a large scale system for first breakdown voltages. However, a statistical analysis can be made from successive sparking tests on one section of the system if the statistical properties of the gap before and after the test can be maintained unchanged. In this case, the distribution function of successive breakdown voltages becomes identical to that of the first breakdown voltage of the test section, hence the distribution function of the full-scale system can be inferred [118].

In the course of successive sparkings, the initial extremes of weak points will be replaced by new ones whose effect on the breakdown characteristic of the gap is determined by the arc energy involved in each breakdown. If the sparking energy is limited sufficiently, after a limited number of breakdowns, depending on the gas and electrode conditions, breakdowns will take place from new points of high field intensity.

At this point, a distinction ought to be made amongst possible causes of breakdown. Although the largest of the high field points on the electrode surface would be destroyed and new less severe ones may be originated, the disruptive effect of the micro-particles which are produced may or may not diminish depending on the gas and electrode conditions and on the type of applied voltage. In earlier statistical investigations [118, 132, 133, 141, 195] this effect has been disregarded or included in an ensemble of extremes

pertaining mainly to microprojections. In the present investigation, since the electrode assembly is horizontally positioned then, even if conditioning were to result in a uniform distribution of protrusions of similar size, microparticles might still continue to behave as potential extremes in the gap during successive sparkings. In the case of the aluminium electrode, for example, the influence of spark-produced microprojections or microparticles on the statistical distribution cannot be ignored.

#### 4.3 Distribution Function of Extreme-value Breakdown Field Strengths

In the following sections, the reasons are given for the choice of the Weibull distribution in preference to the normal and double-exponential distribution. A new density distribution function is defined and a derivation is made of a Weibull-type cumulative probability distribution function. Weibull parameters are estimated using Maximum Likelihood technique and a method for obtaining confidence intervals in each parameter is also introduced.

##### 4.3.1 Weibull-value distribution function for an elementary region

Due to uncertainties in stochastic breakdown process the necessary approximations to empirical distribution functions determined by experimental investigations must be related in a physically meaningful way to the theoretical distributions. The type of distribution, therefore, will finally be decided by experiment.

The probability of having breakdown from at least one weak link whose breakdown strength is less than  $E$  from an elementary

region of a test gap can be estimated if the following are assumed to be valid: (i) the macroscopic field is constant over the elementary region to be considered, (ii) each breakdown occurs independently of previous ones.

For a given electrode area  $S$ , the probability  $F(S,E)$  of having at least one weak point whose breakdown field strength is less than  $E$  can be expressed as follows.

If the cumulative number density  $D(E)$  of weak points whose breakdown field strength is less than  $E$  is assumed [219] to have the form of

$$D(E) = d_0 \left( \frac{E - E_0}{E_c} \right)^\beta \quad (4.1)$$

where  $d_0$ ,  $\beta$  and  $E_0$  are constants and are dependent upon electrode surface finish and gas pressure, then the probability of having a weak point on an elementary region  $\Delta S$  can be expressed as

$$F(S + \Delta S, E) - F(S, E) = [1 - F(S, E)] \cdot D(E) \cdot \Delta S \quad (4.2)$$

rearranging the terms and

$$\lim_{\Delta S \rightarrow 0} \frac{F(S + \Delta S, E) - F(S, E)}{\Delta S} = [1 - F(S, E)] \cdot D(E)$$

$$\text{or} \quad \frac{dF(S, E)}{dS} = [1 - F(S, E)] \cdot D(E) \quad (4.3)$$

Integrating Equation 4.2 yields

$$F(S, E) = 1 - \exp. [-D(E) \cdot S] \quad (4.4)$$

or

$$F(S, E) = 1 - \exp. \left[ -S \cdot d_0 \left( \frac{E - E_0}{E_c} \right)^\beta \right] \quad (4.5)$$

For some purposes, Equation (4.5) is more conveniently expressed as

$$\bar{l}_n \bar{l}_n \frac{1}{1 - F(S, E)} = \beta \bar{l}_n \left( \frac{E - E_0}{E_c} \right) + \bar{l}_n d_0 S \quad (4.6)$$

In both equations (4.5) and (4.6) the cumulative probability distribution of breakdown field strengths is of Weibull form [131]. The experimental results of conditioning tests can be analysed in more simply if equation (4.6) is rearranged as

$$\bar{l}_n \bar{l}_n \frac{1}{1 - F(S, E)} = \beta \bar{l}_n (E - E_0) + \bar{l}_n q S \quad (4.7)$$

where

$$q = \frac{d_0}{E_c \beta}$$

If a complete assembly comprises N sections, each having distribution function of the form as given in equation (4.5), then the breakdown probability can be expressed using the 'weak link' theory [200], as

$$F(E) = 1 - \exp \left[ - N \cdot d_0 \cdot S \left( \frac{E - E_0}{E_c} \right)^\beta \right] \quad (4.8)$$

This relation holds when each test section and the whole system have identical statistical properties. This means electrode finish, microirregularities, microparticles and contamination must have the same grade throughout the system. For the complete system, this requirement is satisfied. However, for a test section, because of exclusion and/or inclusion of weak links from shot-to-shot, one has to be cautious in applying the data to Equation (4.8). This problem may partly be resolved by keeping the test section long and limiting the breakdown energy as low as possible, or by giving confidence intervals on Weibull parameters and tolerance

bounds on the distribution as will be explained in the following sections.

#### 4.3.2 Other statistical models for extreme-value distributions

The assumptions made for constant field strength over the elementary regions may not always be true in large-scale systems. It would, however, be more practical to assume that the cumulative distribution function is made up of two additive parts [197]. One part,  $F_x(S, E_x)$ , takes into account the statistical nature of the avalanche-to-streamer growth and has the form

$$F_x(S, E_x) = \frac{1}{n} \left( \frac{E_x - E_\alpha}{E_M - E_\alpha} \right)^\beta \quad (4.9)$$

(see Appendix 1 for derivations for SF<sub>6</sub> and SF<sub>6</sub>/N<sub>2</sub> mixtures) where n is the number of elementary surfaces in the complete system and  $E_\alpha$  is the limiting field strength. Exponent  $\beta$  is added to take into account the error involved in this empirical relation. The second part,  $F_y(S, E_y)$  must represent random variations in field strength between different regions caused by unaccountable irregularities and can be described by the normal distribution with zero mean value:

$$F_y(S, E_y) = N(0, \sigma^2) = \frac{1}{\sqrt{2\pi}\sigma} \int_{-\infty}^{E_y} e^{-\frac{t^2}{2\sigma^2}} dt \quad (4.10)$$

where  $\sigma$  is the standard deviation. For the random variable of interest  $E = E_x + E_y$ , the distribution function  $F(S, E)$  can be found by the use of convolution rule.

Since the problem is characterised, on one hand by extreme-values of observation (Equation 4.9) and on the other unlimited variation for random variable (Equation 4.10), a double-

exponential distribution could yield a similar statistical variation

$$F(S,E) = 1 - \exp. \left( - \exp \frac{E - E_0}{\Theta} \right) \quad (4.11)$$

where  $\Theta$  is a measure of the scatter. However, with such a distribution it is possible to have a finite probability of occurrence for negative field strengths, or the possibility of gap breakdown at zero field strength for electrode area of finite value.

If all random errors of measurements and evaluations, and all imaginable random processes independent of each other, are superimposed on the random quantity  $E$ , then the distribution of the sum of these quantities converges towards the normal distribution of the form

$$F(S,E) = \frac{1}{\sqrt{2\pi}\sigma} \int_{-\infty}^E \exp \left[ - \frac{1}{2} \left( \frac{z - E_{50}}{\sigma} \right)^2 \right] dz \quad (4.11)$$

where  $E_{50}$  is the arithmetic mean.

In small area or highly nonuniform field electrodes such as point plane, sphere-sphere, etc., the breakdown process may be affected by several random events, and the distribution of electric field may be normal. In large-area electrodes, where the electric field strength is almost constant over the surface (coaxial-cylindrical, for instance), all elementary regions are identical and similar field enhancement occurs in many elementary regions. For this case, one of the above extreme-value distributions is appropriate.

The three types of distribution are demonstrated in Figures 4.1 to 4.3. In each figure the data plotted is taken from conditioning tests on polished electrodes with radii

$r_1/r_2 = 0.945/1.27$  cm in  $\text{SF}_6$  at pressures 2 and 8 bar. At 2 bar the distributions of three types of plots are linear. The linear variation in the case of normal distribution is expected since it is generally true that the normal distribution applies when the similarity law is obeyed. At 8 bar only the double-exponential and Weibull types of distributions exhibit linear variation.

It is therefore clear that an extreme-value distribution is appropriate for results obtained at high pressure in coaxial geometry. Because of its advantages over the double-exponential type of extreme value distribution, the Weibull distribution has been adopted for use in the present investigation.

#### 4.4 Parameter Estimation for the Weibull Distribution

The Weibull distribution has long been found to fit most of experimental data in life testing of solid insulation better than any other distribution [198]. This flexibility, however, sometimes causes difficulties in assessing the distributions obtained from successive samples from the same population. For instance, two sets of data having different distributions might yield Weibull parameters which differ only slightly; in contrast, apparently similar experimental data may have quite different parameters. This means that parameters are relatively insensitive to the random variable. The inconsistency is further compounded by approximately-estimated parameters and confidence intervals on the parameters.

In the following sections, methods to estimate Weibull parameters and their confidence levels are discussed.

Estimation of the minimum field strength (location  
parameter  $E_0$ )

The minimum field strength  $E_0$  is the asymptotic value of the random variable  $E$  as the effective system area is increased. In Figures 4.4(a) to 4.4(d), field strengths corresponding to 0.5% breakdown probability, extracted from the conditioning results of the previous chapter, are plotted against the effective surface area of polished and rough-finished electrodes. As the area of electrode increases, the minimum breakdown field strength converges to  $E_0$ , independent of surface finish of electrode.

The values  $E_0$  obtained by extrapolation of results of Figures 4.4(a) to 4.4(d) are plotted against pressure in Figure 4.5. In the same figure, the experimental results of Nitta et al [118] are also illustrated for  $SF_6$ . At low pressures the results are in good agreement although the difference increases with increasing pressure; at 8 bar, for instance, the present work gives a value  $\sim 30\%$  below that obtained by Nitta et al.

The variations of  $E_0$  with  $p$  given in Figure 4.5 for  $SF_6$  and  $SF_6/N_2$  mixtures can be expressed by the following approximate empirical relation:

$$E_0 = \left(\frac{E}{p}\right)_{lim} p \cdot (1 + 0.554 p^x) \quad (4.12)$$

where  $x$  has the values given in the table below.

|                        | $(E/p)_{lim}$ | $x$   |
|------------------------|---------------|-------|
| $SF_6$                 | 88.4          | 0.725 |
| 75% $SF_6$ - 25% $N_2$ | 82.5          | 0.814 |
| 40% $SF_6$ - 60% $N_2$ | 71.1          | 0.920 |
| 10% $SF_6$ - 90% $N_2$ | 52.5          | 1.213 |

In some investigations, however,  $E_0$  has been, correctly or wrongly, assumed to be zero [133]. As is illustrated in Fig. 4.4(e), the linearity of the probability distribution is affected by varying its value. This effect was found [194] to be more pronounced as the electrode area increases. Therefore, when Weibull extreme-value statistics are applied for estimation of the scale effect in compressed gas insulated systems, it is appropriate to use the complete form of the relation given by Weibull [131] with a correctly-determined value of  $E_0$ .

#### 4.4.2 Estimation of remaining Weibull parameters

There is no statistically correct and simple method established to calculate the Weibull parameters in Equation 4.5. However, the most commonly employed technique is that of graphical estimation using Weibull probability paper [197]. Other methods include the use of a Maximum Likelihood technique [198] which requires a computer iterative solution and a recently developed 'linear' estimation procedure [199].

In the following sections, a brief review of the graphical estimation method is given and the application of the Maximum Likelihood technique, together with weak link theory, is demonstrated to calculate  $\beta$ ,  $E_0$  and  $\gamma$  for a complete assembly comprising  $N$  identical test sections.

#### Graphical Estimation

This technique makes the use of Weibull graph paper. The vertical axis is scaled for the cumulative probability  $F(E_i)$  of the random variable  $E_i$  ordered according to the estimate [201].

$$F(E_i) = \frac{i}{n+1} \quad (4.13)$$

where  $n$  is total number of breakdowns. The data is plotted on the paper and an approximate straight line is fitted (Figure 4.6). The best estimate of  $\hat{E}_c$  is the value of field strength corresponding to  $F(E) = 63.2$  per cent. The best estimate ( $\hat{\beta}$ ) for  $\beta$  can be found by drawing a line parallel to the fitted line through the point of 'origin'. The estimate  $\hat{\beta}$  is given by the point of intersection of this parallel line and the line of 'small beta estimator'. An estimate of  $\beta$  can also be found from

$$\hat{\beta} = \frac{\ln \ln (Y_2) - \ln \ln (Y_1)}{\ln (X_1 / X_2)} \quad (4.14)$$

where  $(F(E_1), E_1)$ ,  $(F(E_2), E_2)$

$$\text{and } Y_2 = \frac{1}{1 - F(E_2)} \quad ; \quad Y_1 = \frac{1}{1 - F(E_1)} \quad ;$$

$$X_2 = E_2 - E_0 \quad ; \quad X_1 = E_1 - E_0 \quad .$$

Although the graphical estimation technique is easy to apply in representing the data, it has a few drawbacks. Due to the fact that the distribution contains an exponent raised to the power  $\beta$ , small variations in the chosen straight line fit to the data can result in a large error in  $\hat{E}_c$  and  $\hat{\beta}$ . The use of a least-square fit, even if correctly performed, does not yield the true values of  $\alpha$  and  $\beta$ , because of the statistical and double exponential nature of the problem. The second shortcoming of this method is that confidence intervals cannot be obtained, which is a serious defect for analysing experimental data with limited number of observations. The Maximum Likelihood estimate gives more reliable

estimates of  $\alpha$  and  $\beta$ , and also facilitates calculation of confidence intervals on the parameters.

### Maximum Likelihood Estimation

Analytic estimates of three parameters, when all are unknown, could be more accurately determined using the Maximum Likelihood method. First, the Weibull distribution function is rewritten in the form commonly used for iterative solution:

$$F(x; \theta, \beta, \gamma) = 1 - \exp\left(-\frac{(x - \gamma)^\beta}{\theta}\right) \quad (4.15)$$

where  $x = E$  is the random variable,  $\gamma = E_0$  is the minimum breakdown field strength (location parameter) and  $\theta = E_0^\beta / k = \alpha^\beta$  ( $k = d_0 \cdot S$ , where  $S$  is the area of a test section,  $d_0$  is a constant).

If the density function of the variate  $x$  can be written as

$$f(x; \theta, \beta, \gamma) = \frac{\beta}{\theta} (x - \gamma)^{\beta-1} \exp\left(-\frac{(x - \gamma)^\beta}{\theta}\right) \quad (4.16)$$

the Maximum Likelihood function for  $n$  breakdowns becomes [202]

$$L(x; \theta, \beta, \gamma) = \prod_{i=1}^n \frac{\beta}{\theta} (x_i - \gamma)^{\beta-1} \exp\left(-\frac{(x_i - \gamma)^\beta}{\theta}\right) \quad (4.17)$$

Taking the logarithm of equation (4.17) and differentiating with respect to  $\theta$ ,  $\beta$  and  $\gamma$  respectively, equation to zero and eliminating  $\theta$  between the resulting equations yields the following equations for  $\beta > 1$ .

$$\left[ \frac{\sum_i (x_i - \gamma)^\beta \ln(x_i - \gamma)}{\sum_i (x_i - \gamma)^\beta} - \frac{1}{\beta} \right] - \frac{1}{n} \sum_i \ln(x_i - \gamma) = 0 \quad (4.18)$$

$$n \cdot \beta \frac{\sum_i (x_i - \gamma)^{\beta-1}}{\sum_i (x_i - \gamma)^\beta} - (\beta-1) \sum_i (x_i - \gamma)^{-1} = 0 \quad (4.19)$$

If  $\gamma$  is known, Equation 4.18 can be solved for  $\hat{\beta}$  and  $\hat{\alpha}$ . If  $\gamma$  is unknown, simultaneous solution of Equations 4.18 and 4.19 yields  $\alpha$ ,  $\beta$  and  $\gamma$ . Initial estimates are obtainable from either Equation 4.12 or Figure 4.5. The necessary derivations and algorithms for iterative solutions are given in Appendix 2.

#### 4.4.3 Confidence intervals for the Weibull parameters and tolerance bounds

The conditioning behaviour of a test gap, or of several test gaps tested under the same experimental conditions, usually differs owing to the statistical nature of the breakdown phenomenon. This leads to different 'best lines' if data is plotted on Weibull paper. Therefore, any estimates of  $\alpha$ ,  $\beta$  and  $\gamma$  (Equation 4.15) from several such sets of data are unlikely to be equal to the true values of  $\alpha$ ,  $\beta$  and  $\gamma$ . This variability of Weibull distributions, however, can be accounted for by estimating confidence intervals on  $\alpha$ ,  $\beta$  and  $\gamma$ , in addition to computing their values.

The technique for calculating confidence intervals for  $\alpha$  and  $\beta$  is also based on Maximum Likelihood estimation. Estimated confidence intervals for parameters  $\alpha$  and  $\beta$  are tabulated in reference [203]. As yet, confidence intervals for the location parameter  $\gamma$  have not been obtained. Although results are given for censored experiments for a number of samples between 40 and 120, the results of equal sample and censored sizes  $n = r = 100$  (where  $r$  is the number of observations before censoring) are

applicable to the present investigations. The 100 (1 - p) per cent confidence interval for the shape parameter  $\beta$ , if  $(\beta_l, \beta_u)$  indicates lower and upper limiting values, is given by

$$\beta_l = \frac{\hat{\beta}}{E\left(\frac{\hat{\beta}}{\beta}\right) + z_{(1 - \frac{p}{2})} / \sqrt{\eta}}$$

and

$$\beta_u = \frac{\hat{\beta}}{E\left(\frac{\hat{\beta}}{\beta}\right) + z_{\frac{p}{2}} / \sqrt{\eta}}$$

The values of  $E\left(\frac{\hat{\beta}}{\beta}\right)$  and  $Z$  are given in Table 4.1.

The 100 (1 - p) per cent confidence interval for  $\alpha$  which is between the lower  $\alpha_l$  and upper  $\alpha_u$  limits is given by

$$\alpha_l = \alpha \exp\left(-\frac{U_{(1 - \frac{p}{2})}}{\beta \sqrt{\eta}}\right)$$

and

$$\alpha_u = \alpha \exp\left(-\frac{U_{\frac{p}{2}}}{\beta \sqrt{\eta}}\right)$$

The value of  $U$  can be found in Table 4.1

Table 4.1

| $\eta$ | $r$ | $Z_{0.01}$ | $Z_{0.05}$ | $Z_{0.95}$ | $Z_{0.99}$ | $E\left(\frac{\hat{\beta}}{\beta}\right)$ |
|--------|-----|------------|------------|------------|------------|---|
| 100    | 100 | -1.63      | -1.20      | 1.36       | 2.06       | 1.016                                     |

| $\eta$ | $r$ | $U_{0.01}$ | $U_{0.05}$ | $U_{0.95}$ | $U_{0.99}$ |
|--------|-----|------------|------------|------------|------------|
| 100    | 100 | -2.45      | -1.74      | 1.73       | 2.50       |

The application of two methods for estimating Weibull parameters, together with their confidence intervals and tolerance bounds of the distribution, is demonstrated in Fig. 4.6 for the conditioning data obtained in 10% SF<sub>6</sub> - 90% N<sub>2</sub> mixture at a total pressure of 6 bar in  $r_1/r_2 = 0.945/1.27$  cm gap.

The breakdown data is plotted on Weibull paper; the abscissa is the difference between breakdown and minimum possible breakdown field strengths of the gap, and the ordinate is cumulative breakdown probability percentage. A straight line is fitted to these points, and  $\hat{\beta}$  is obtained as 4.9 using graphical method outlined in Section 4.4.2. The estimate of  $\beta$  can also be found by substituting the points  $E_1 = 267$ ,  $F(E_1) = 0.10$  and  $E_2 = 484$  kV/cm  $F(E_2) = 0.99$  into Equation 4.14, which yields  $\beta = 6.94$ . An estimate of the scale parameter ( $E_c$  in Equation 4.5) is given by the field strength corresponding to  $F(E) = 63.2$  per cent, which is 428 kV/cm.

The Maximum Likelihood estimates of  $\alpha$  and  $\beta$ , based on the algorithm given in Appendix 2, are 479 kV/cm and 6.05 respectively, and the 95% confidence intervals ( $F(E) = 0.05$ ) were estimated to be 430-506 kV/cm for  $\alpha$  and 5.25 - 6.74 for  $\beta$ .

#### 4.4.4 Estimation of density distribution parameter $d_0$

The values of the surface density constant  $d_0$  are also evaluated in the above mentioned algorithm. Results in SF<sub>6</sub> and in SF<sub>6</sub>/N<sub>2</sub> mixtures are plotted against pressure in Figures 4.7, 4.8 and 4.9 for polished, sandblasted and machined electrodes respectively. The relation between  $d_0$  and  $p$  can be expressed empirically as

$$d_0 = D_1 \cdot \exp(D_2 \cdot p)$$

where  $D_1$  and  $D_2$  are functions of surface roughness and type of gas, and are given in Table 4.2.

| Surface Treatment<br>Gas                | Polished             |       | Sandblasted          |       | Machined             |       |
|---|----------------------|-------|----------------------|-------|----------------------|-------|
|   | $D_1$                | $D_2$ | $D_1$                | $D_2$ | $D_1$                | $D_2$ |
| SF <sub>6</sub>                         | $1.82 \cdot 10^{-2}$ | 0.810 | $1.10 \cdot 10^{-1}$ | 1.174 | $3.41 \cdot 10^{-1}$ | 1.140 |
| 75% SF <sub>6</sub> -25% N <sub>2</sub> | $1.65 \cdot 10^{-3}$ | 0.780 | $1.98 \cdot 10^{-2}$ | 1.177 | $4.05 \cdot 10^{-2}$ | 1.170 |
| 10% SF <sub>6</sub> -90% N <sub>2</sub> | $1.75 \cdot 10^{-4}$ | 0.705 | $1.78 \cdot 10^{-4}$ | 1.172 | $7.31 \cdot 10^{-3}$ | 1.190 |

Having determined the parameters of the Weibull distribution for the present electrode and gas conditions, it is possible to predict the statistical distribution of breakdown field strengths of a test section by using Equations 4.5 and 4.6. In Figure 4.10 the experimental and calculated (according to Equation A2.26) modal values of breakdown field strengths are plotted as a function of electrode area. The results show clearly the effect of increasing electrode area on breakdown characteristics of polished and sandblasted electrodes in SF<sub>6</sub> at several pressures.

#### 4.5 Weibull Distribution of Field Strengths in Successive Breakdown Tests in SF<sub>6</sub> and SF<sub>6</sub>/N<sub>2</sub> Mixtures

In the following sections, comparisons will be made for the breakdown characteristics of various gaps in SF<sub>6</sub> and SF<sub>6</sub>/N<sub>2</sub> mixtures, making use of the Weibull distribution of breakdown extremes in order to identify any distinct insulating behaviour of SF<sub>6</sub>/N<sub>2</sub> mixtures compared with SF<sub>6</sub>. Since the density distribution function of weak points is dependent on field strength, any comparison of

statistical behaviour for breakdown extremes of several gaps for conditioning, electrode area, polarity and irradiation is meaningful if it will be made for the same field strength or the same range of field strengths.

#### 4.5.1 Conditioning effect

Since the spark conditioning effect is dependent on electrode area, surface finish, pressure and type of gas, in the following statistical investigation, any distinct conditioning behaviour of electrodes for comparison was accounted within the same range of field strengths. In addition, Weibull distributions of successive breakdown test results, obtained in  $\text{SF}_6$  and  $\text{SF}_6/\text{N}_2$  mixtures using the electrodes listed in Table 3.1 are illustrated for 1-20, 21-40 and 41-100 sparks.

#### Area Effect

Conditioning results for small area electrode (E1) and large area electrode (E9) in  $\text{SF}_6$  are depicted for the field ranges 300-400 kV/cm and 500-600 kV/cm in Figures 4.11(a) and 4.11(b) respectively.

In the low field range the conditioning effect is limited to  $\sim 20$  sparks (Figure 4.11(a)). In the high field range, however, both small and large-area electrodes are almost free from conditioning (Figure 4.11(b)). In the low field plots one can observe that, after the first 20 conditioning sparks, the probability distribution of large-area electrode becomes parallel to that for small-area electrode, as is expected. In the case of high-field plots, the small difference in the slopes for electrodes E1 and E9 might be due to slightly better surface finish of the small-area electrode E1 compared to the large-area electrode E9.

Conditioning characteristics of electrodes E1 and E9 are illustrated for 75% SF<sub>6</sub> - 25% N<sub>2</sub> and 10% SF<sub>6</sub> - 90% N<sub>2</sub> in the range of field strengths 300-400 kV/cm in Figures 4.12 and 4.13 respectively.

Conditioning existing in the case of electrode E9 in 75% SF<sub>6</sub> - 25% N<sub>2</sub> (Figure 4.12) is not present in 10% SF<sub>6</sub> - 90% N<sub>2</sub>. This signifies insensitivity of mixtures of less SF<sub>6</sub> content to preceding sparks. For the small area electrode E1 conditioning seems not to be affected by N<sub>2</sub> content in the mixtures.

#### Roughness Effect

Weibull probability distributions for breakdown in SF<sub>6</sub> with stainless-steel polished (E9), sandblasted (E10) and machined (E11) electrodes with radii  $r_1/r_2 = 0.945/1.27$  cm are illustrated in Figures 4.14 and 4.15 for ranges of field strengths 300-400 kV/cm and 500-600 kV/cm respectively. All breakdowns occur at field strengths less than the calculated ones.

As will be clearly observed from the distribution plots in Figure 4.14 (a), (b) and (c), the conditioning process is restricted to the first 1-20 spark period for the three surface finishes and only the sandblasted electrode exhibits distinct distribution for the next 20 sparks. Distribution of polished and machined electrodes are more or less the same after conditioning.

In the high-field range in SF<sub>6</sub> (Figure 4.15) conditioning is extended for polished and machined electrodes to more than 20 sparks giving rise to three separate distributions having different slopes. The distribution for sparks 1-20 with the sandblasted electrode is parallel to that for sparks 41-100, signifying incomplete conditioning within the period of 100 sparks.

In 75% SF<sub>6</sub> - 25% N<sub>2</sub> and 10% SF<sub>6</sub> - 90% N<sub>2</sub> mixtures at the field range of 300-400 kV/cm, the conditioning effect for polished electrodes is almost negligible, resulting in a steeper breakdown probability distribution with the slope decreasing with N<sub>2</sub> content in SF<sub>6</sub>/N<sub>2</sub> mixtures. For both sandblasted and machined electrodes, however, the conditioning probability distribution of sparks 1-20, 21-40 and 41-100 are parallel to each other with some separation between them implying unfinished conditioning processes within 100 sparks.

The conditioning behaviour of three large-area electrodes of different surface finishes in SF<sub>6</sub> and SF<sub>6</sub>/N<sub>2</sub> mixtures is summarised for the low-field range in the following table.

Table 4.3

| Surface Finish | Number of Sparks | A    | B    | D    |
|----------------|------------------|------|------|------|
| Polished       | 1-20             | 5.8  | 9.5  | 8.4  |
|                | 21-40            | 16.4 | 16.8 | 9.8  |
|                | 41-100           | 26.0 | 16.8 | 9.8  |
| Sandblasted    | 1-20             | 5.6  | 13.8 | 12.5 |
|                | 21-40            | 14.0 | 45.2 | 16.2 |
|                | 41-100           | 15.2 | 45.2 | 16.2 |
| Machined       | 1-20             | 3.8  | 11.7 | 13.4 |
|                | 21-40            | 11.4 | 38.0 | 27.4 |
|                | 41-100           | 11.0 | 19.6 | 27.4 |

A - SF<sub>6</sub>

B - 75% SF<sub>6</sub> -  
25% N<sub>2</sub>

D - 10% SF<sub>6</sub> -  
90% N<sub>2</sub>

Field Range =  
300-400 kV/cm.

The following results can be deduced from the above table.

- (i) Initial conditioning results for electrodes limited to 20 sparks exhibit almost the same distribution in SF<sub>6</sub> and SF<sub>6</sub>/N<sub>2</sub> mixtures.
- (ii) The conditioning probability distributions for SF<sub>6</sub>/N<sub>2</sub> mixtures are steeper than those for SF<sub>6</sub>.
- (iii) Fully conditioned states of sandblasted and machined electrodes may usually be attained in SF<sub>6</sub> and in SF<sub>6</sub>/N<sub>2</sub> mixtures within the present experimental limitation of 100 sparks.

#### 4.5.2 Electrode area effect

According to Equations 4.5 and 4.6, the cumulative breakdown probability distribution of Weibull plots of two gaps having electrode areas S<sub>1</sub> and S<sub>2</sub> should be positioned parallel to each other with a vertical distance  $\bar{\ln}(S_1/S_2)$  between them. However, as shown in Figure 4.18, which contains data obtained with several polished stainless-steel electrodes for the range of field strength 300-400 kV/cm, the cumulative-probability plots are not parallel to each other, but get steeper as the electrode area becomes larger. This signifies that the gaps have different conditioning behaviour. For the purpose of prediction of breakdown characteristics, the cumulative-probability distribution of the large-area electrode (E9) gap is more reliable in both SF<sub>6</sub> and 10% SF<sub>6</sub>-90% N<sub>2</sub>. This is because of the fact that there is no significant conditioning during the test sequence. The slopes obtained for large area electrode in SF<sub>6</sub> and 10% SF<sub>6</sub> - 90% N<sub>2</sub> are 7.4 and 13.0 respectively which are within the range of values given in the literature for large-area gaps [118, 132].

### 4.5.3 Electrode roughness effect

Weibull probability plots for gaps with polished (E9), sandblasted (E10) and machined (E11) inner electrodes having radii 0.945/1.27 cm, are shown for SF<sub>6</sub> in Figure 4.19 (a) and in Figure 4.19 (b) for the field ranges 300-400 and 500-600 kV/cm, respectively.

The probability distribution for the first 20 breakdowns in both field ranges are not parallel to each other, as is expected, due to the different conditioning behaviour of polished and rough electrodes. However, the distributions of sparks 21-100 for the three gaps are parallel, which suggests that breakdown characteristics of polished and rough inner electrodes have similar statistical tendencies. In the low field range, the breakdown probability of machined and sandblasted electrodes is 4 and 7 times that of polished electrode respectively at a given voltage. It is noteworthy that, although the average surface roughness of the sandblasted electrode ( $R_{CLA} = 2.3 \mu\text{m}$ ) is less than that of the machined electrode ( $R_{CLA} = 2.8 \mu\text{m}$ ), the breakdown probability with the sandblasted electrode is 4 times that for the machined electrode, which implies different density parameter  $d_0$  under the same pressure and field conditions. Another point of interest is that the Weibull distribution of the first 20 sparks for the polished electrode has less steepness (smaller  $\beta_1$ ) as compared to corresponding distributions for sandblasted and machined electrodes. This suggests effectiveness of isolated microprojections on the polished surface in giving an increased probability of low-voltage breakdowns at elevated pressure or field conditions as compared to sandblasted or machined surfaces.

Weibull probability plots for sparks 1-20 and 21-100

obtained for two mixtures in the field range 300-400 kV/cm are shown in Figures 4.20 and 4.21 respectively. Probability distributions of sparks 1-20 in both mixtures have different tendencies owing to different conditioning features of polished and rough electrodes.

Increasing  $N_2$  content in the mixtures results in changes in the breakdown probability distributions. For instance, the breakdown probabilities with polished and machined electrodes are 4 times and 8 times those with sandblasted electrodes in a 10%  $SF_6$  - 90%  $N_2$  mixture.

#### 4.5.4 Electrode material effect

The change in Weibull probability distributions with material is demonstrated in Figure 4.22 for data obtained in  $SF_6$  and  $SF_6/N_2$  mixtures in the field range 300-400 kV/cm, using gaps having stainless steel (E9) and aluminium (E12) inner electrodes, and stainless steel outer electrode with radii  $r_1/r_2 = 0.945/1.27$  cm. (See Table 3.1 for more details of electrodes).

In  $SF_6$ , the probability distributions of the first 20 sparks are positioned differently for the two materials in spite of a similar surface polishing procedure of both electrodes. This is because of additional microprotrusions produced by spark damage in the case of the aluminium electrode during successive breakdown tests, and because of microinhomogeneties already existing or produced during tests in the case of the stainless steel electrode. The distributions of sparks 21-100 are almost parallel to each other and the breakdown probability for the aluminium electrode is  $\sim 20$  times that for the stainless steel electrode. This indicates the fact that, although the aluminium electrode breakdown characteristic

is affected by each spark, the distribution of weak points -  
excepting the maximum possible ones which are included into the  
distribution of the first 20 sparks - has similar characteristics  
to that of stainless steel electrode.

In the 75% SF<sub>6</sub> - 25% N<sub>2</sub> mixture, the probability  
distributions are parallel and are separated such that breakdown  
probability of the aluminium electrode is about 80 times that for  
the stainless steel electrode. In the case of the 10% SF<sub>6</sub>-90% N<sub>2</sub>  
mixture, the situation is paradoxically reversed, that is, breakdown  
probability of the stainless steel electrode becomes higher than that  
of aluminium electrode; this is due to marginally coinciding  
conditioning behaviour of both electrodes in the given field range.  
Otherwise, it is generally true that the aluminium electrode, under  
the present experimental conditions, possesses distributions with  
higher breakdown probabilities as compared to the distributions for  
the stainless steel electrode.

#### 4.5.5 Effect of polarity and of irradiation

The effect of polarity of applied voltage on the Weibull  
plots is illustrated in Figure 4.23 for the gap consisting of  
polished stainless steel electrodes with radii  $r_1/r_2 = 0.5/1.27$  cm.  
in 40% SF<sub>6</sub> - 60% N<sub>2</sub> mixture. For both polarities, at 2 bar, the  
similarity law holds and the probability distributions are almost  
parallel to each other. The negative breakdown probability is 3  
times higher than the positive one. At 4 bar, however, the negative  
probability plot lies below the value predicted by the similarity  
law and has a distribution with smaller slope than the positive one.  
This is due to the known effect of the cathode in bringing lower  
and erratic breakdowns due to the mechanisms discussed in Section 1.4.2.

Weibull plots of breakdown field strengths obtained with and without irradiation in the above gap in a 40% SF<sub>6</sub> - 60% N<sub>2</sub> mixture at 3.5 bar are shown in Figure 4.24. As is expected, the difference between the distributions is insignificant since the surface area of the inner electrode (E7) is effective in providing initiating electrons during the period of voltage rise.

#### 4.6 Discussion

##### 4.6.1 Theoretical considerations

The breakdown characteristics of gaps insulated with SF<sub>6</sub> or SF<sub>6</sub>/N<sub>2</sub> mixtures have been shown by many investigators to be degraded by the presence of microprojections or microparticles which are introduced during the manufacturing or gas filling process. The spatial distribution [118, 194] and temporal appearance [205] of these weak inhomogeneties in a gap assembly have statistical properties and the probability of breakdown increases with increasing the area of the stressed part. Hence, any estimation of breakdown voltage of any configuration should also be made by statistical means. The relation between the distribution of weak points and the area of electrode was found to be normal [118] at pressures less than that for Paschen deviation and to be one of the extremal types [141], i.e. double exponential (first-order) or Weibull type (third-order) [118] at higher pressures. Since, in the case of double exponential extremal type, there is a possibility of having negative or zero breakdown probability for electrode surface areas of finite value, the Weibull type extreme value distribution is generally accepted and is experimentally confirmed [118, 132, 133] to result in a linear relation for most practical electrode configurations and pressure ranges. Before discussing the

present approach for reliability estimations using Weibull statistics, it seems necessary at this point to summarise the basic conditions for its applications:

- (i) The field should be constant all over the area considered [206],
- (ii) The breakdown process should be defined throughout the gap assembly by the same type of streamer mechanism - mechanism I (for uniform field gaps) or mechanism II (for nonuniform field gaps) [100],
- (iii) There must be sufficient number of observations to establish statistical features of breakdown,
- (iv) Each breakdown should not modify surface conditions and should occur independent of previous ones [206],
- (v) The area of the test section should be sufficiently large,
- (vi) The statistical properties of weak points in the test section and in the whole system should be identical [194].

Conditions (i) and (ii) are important in determining the shape and location of the Weibull distributions and, in the present work, these two requirements are met by choosing coaxial electrode configurations of different sizes. The discrepancy depicted in Figure 4.5 between the present work and the work of Nitta et al [118] for the experimental estimation of  $E_0$  for various pressures in  $SF_6$  is mainly due to failure to satisfy these two conditions. Nitta et al obtained  $E_0$  by extrapolating the minimum (0.5%) breakdown field strengths resulting from successive breakdown tests in gaps of sphere-plane, plane-plane and coaxial-cylinders in which the field is not constant along the electrode surface nor

is the same breakdown mechanism applicable.

Furthermore, a more realistic case for illustrating electrode area effect in the laboratory scale would be to use electrodes fulfilling these two requirements, preferably within the same range of field strengths. If one assumes that the shape parameter  $\beta$  in Equation 4.5 is independent of pressure and, hence, field strength and electrode [118], this last argument would be trivial. However, in Figure 4.25, in  $\text{SF}_6$ ,  $\beta$  is clearly shown to be a function of pressure and electrode for 1st-20th and 21st-100th observations. Even for the same field strength ranges, as illustrated in Figure 4.26, there are considerable differences in the values of  $\beta$ . This inference is also supported by the work of Bortnik [141] who found  $\beta$  to be in between 7.5 and 9 for distributions obtained in  $\text{SF}_6$  in coaxial electrodes of various inner and outer electrodes. In the work of Nitta et al, the value of  $\beta$  was given as 6.3, which is different from the results obtained by Bortnik and from the results of present work, in which  $\beta$  was observed to lie in 15 and 70 for polished and 6 and 20 for rough electrodes. In consequence, the argument of 'independent of electrode and gas pressure' made for  $\beta$  seems to be generally not valid as was evidenced within the scope of the present investigation. As will be mentioned later, any value of  $\beta$  found for a test section must therefore be treated cautiously if the resultant distribution is to be applied to a larger system of similar type.

The requirement (iii) is fulfilled by the use of an automatic voltage control and recording system which made it possible to record up to 200 sparks, which is sufficient to deduce statistical characteristics of large electrode configurations. Although, in the present investigation, only the initial 100 observations of the 200

were used for plotting Weibull distributions, it has been shown that this number is adequate for the present experimental conditions.

The mode of distribution became explicit within 20 sparks for polished electrodes, and within 50 sparks for rough ones (Table 3.5). Any statistical distribution made with a number of observations more than these figures in the present experiment was found to alter the linearity of distributions. In Figure 4.27, for example, it is obvious that distribution of initial 50 observations is more linear as compared to distribution of 100 observations obtained by successive breakdown tests for sandblasted electrode (Electrode E10) in  $SF_6$ . This is partly attributable to the application of Weibull statistics to observations free from extremities and partly to selection of the minimum breakdown voltage  $E_0$ . The nonlinear distribution obtained in Reference [118] for fine finished sphere-plane electrode (Electrode A) was related to the latter effect, although the former one was more important.

The selection of the number of observations should also be incorporated with the requirement stated in (v), as was mentioned previously. Since the number of extremities is limited by electrode area, even for the worst case of roughness  $\sim 50$  sparks was enough to clear the surface extremities of the largest area electrode (area =  $180 \text{ cm}^2$ , electrode E10 or E11) in the present investigation. Thus, in the light of discussions given for requirements (iv) and (v), the number of breakdowns has to be restricted to only those which bring on conditioning and the rest of the observations must be excluded from the distribution.

Although the Weibull probability distribution is flexible enough to represent most dielectric breakdown data, it is

inherently sensitive to large deviations of the random variable [197]. Together with this insensitivity, difficulties of obtaining valid estimates of Weibull parameters result in misjudgment in predicting the breakdown characteristics of a large system. However, by estimating confidence intervals on parameters and hence tolerance bounds of distributions, as was explained in the text, this disability can be partially overcome. What were generally misleading in previous Weibull statistical analyses [118, 132, 194] are straight line or least square approximation to statistically distributed points. In the former, the distribution is observer-sensitive and in the latter confidence bounds are incorrectly underestimated. Moreover, with the method of Maximum Likelihood introduced in this chapter, it was made possible to estimate Weibull parameters  $[\beta, \gamma = E_0, \text{ and } \alpha = E_c / (N.S)^{1/\beta}]$  such that for a system consisting of N-number of test sections for which  $\gamma$  is known or unknown, the distribution can be defined without difficulties arising from the application of Equation 4.5, as was also stated in [194]. The case where  $\gamma$  is known was illustrated in this chapter while, for the case when  $\gamma$  is not known, only the method for estimating the parameters was formulated and the application will be left for future work.

#### 4.6.2 Experimental considerations

1. The Weibull plots for large area electrodes obtained in  $SF_6$  and in  $SF_6/N_2$  mixtures, shown in Figures 4.11 to 4.13, indicate that the distribution for polished electrodes (E9) may be correctly represented with 20 sparks. However, in the case of rough electrodes (E10, E11), the situation is not so clear. Since the density distribution parameter of weak points for rough

electrodes is hardly altered by repeated sparkings, distributions can be represented by any number of observations more than 20. This conclusion is also confirmed by the parallel displacement of the distributions for sparks 1-20, 21-40 and 41-100.

2. In the literature, the surface roughness density parameter,  $d_o$ , of a test section is assumed to be kept constant in successive breakdown tests both by keeping the electrode area large and by keeping the spark energy at a minimum level in order to avoid creating microparticles. In a practical system, it is unavoidable to have microparticles retained on the stressed electrode or on the less stressed one (outer electrode in the case of coaxial electrode configuration). Therefore, the statistical properties of already existing weak points will be altered and, in turn, the Weibull probability distribution will be affected. By stressing, or by appropriately positioning the test section (holding vertically, for instance, in the case of coaxial electrodes) microparticles can be partially eliminated from the gap. In the present investigation, the electrodes were arranged horizontally in order that the results would be comparable with those for practical systems. However, some attempt was made to limit the spark energy by the methods outlined in Section 2.4.1.

3. In large CGI systems, weak links are microprojections and microparticles, and the latter are particularly harmful in affecting the performance of insulators [125, 207, 208]. Therefore, a complete statistical analysis of a system for its probable extremes must include the effects of these weak links.

#### 4.7 Conclusion

From the theoretical and experimental studies of this

chapter the following can be concluded.

(i) The dielectric breakdown characteristics of SF<sub>6</sub> and SF<sub>6</sub>/N<sub>2</sub> mixtures can be evaluated by applying Weibull extreme value statistics to experimental data obtained from laboratory experiments.

(ii) Due to the inherent flexibility of the Weibull probability distributions, it is necessary to estimate the parameters [ $\beta$ ,  $\gamma = E_0$ , and  $\alpha = E_0 / (d_0 \cdot S)^{1/\beta}$ ] of any given distribution with the method of Maximum Likelihood. Confidence intervals to these estimates can then be determined for sample sizes up to 120 observations, and tolerance bounds of a given quantile can be assigned to the distribution.

(iii) The slope of the distributions defined by 100 observations varies between 15 and 70 for polished and between 6 and 20 for rough electrodes. If, however, the number of observations for polished electrodes is reduced to only the number of sparks required for conditioning, the slopes have values in the range of slopes for rough electrodes.

(iv) The shape parameter  $\beta$  is a function of pressure, type of gas and electrode material, so that for any distribution the maximum likelihood estimate of this parameter must be given together with its confidence intervals.

(v) The density distribution parameter of weak points  $d_0$  is dependent strongly on pressure, electrode roughness and type of gas.  $E_0$  is a function of gas pressure and type of gas.

(vi) The parameters of the Weibull probability distribution of a large scale system of N-sections and tolerance bounds of the distribution can be estimated by a simple computer program.

DC AND IMPULSE BREAKDOWN CHARACTERISTICS INSF<sub>6</sub> AND SF<sub>6</sub>/N<sub>2</sub> MIXTURES5.1 General

At moderate pressures, up to 3 bar, and under clean experimental conditions, it has been shown [49, 102, 210] that the breakdown characteristic of SF<sub>6</sub> can well be predicted by the streamer breakdown criterion. At high pressures, however, test results lie below those predicted by the theory; this is caused by surface asperities or by contaminant microparticles. Various models have been proposed to account for field intensification at these inhomogeneities in uniform field [67, 111, 115, 117] and nonuniform field [112, 211, 213] configurations. The main points of these investigations can be summarised as follows.

(i) Local field intensification occurs in the region of surface asperities and, because of the strong field dependence of the effective ionization coefficient  $\bar{\alpha}$ , significant ionization can take place within the region to initiate breakdown [75, 112].

(ii) In SF<sub>6</sub> surface roughness can be tolerated, if  $ph < 43 \text{ bar } \mu\text{m}$  (pressure times the maximum height of projection) [113].

(iii) A lower limit  $(ph)_{\min} \leq 18 \text{ bar } \mu\text{m}$  was estimated [115] in order that the breakdown field is unaffected by electrode protrusion and the upper limit of  $(ph) \geq 85 \text{ bar } \mu\text{m}$  is adequate to ensure breakdown even if the gap field strength is less than  $E_{\lim} = 88.4 \text{ kV}/(\text{cm bar})$ .

(iv) Due to mutual effect of neighbouring protrusions with identical peaks, the effective field strength could be less than the single isolated protrusion [117], resulting in  $(ph)_{\max}$  limit to increase from 43 to 370 bar  $\mu\text{m}$ .

(v) Increasing electrode roughness and hence field amplification factor does not reduce the breakdown voltage in  $\text{SF}_6$  below a certain 'minimum' value, because of 'microcorona' stabilization at microirregularities [213].

(vi) The other important reason reducing the strength of compressed  $\text{SF}_6$  in CGI systems is the contamination in the form of conducting particles. A detailed review of the effects on breakdown was presented in section 1.4.2.3.

(vii) Low pressure discharge parameters may be used at high pressures (above 1 bar) by taking into account the compressibility factor. This was found [95] to yield considerable correction on the breakdown voltage at high pressures.

In  $\text{SF}_6/\text{N}_2$  mixtures, only a few attempts have been made to investigate the effect of roughness and free conducting particles on the breakdown characteristics at high pressures. The main findings are:

(i) Decreasing  $\text{SF}_6$  content in the mixtures results in a gradual increase in the value of tolerable roughness limit  $(ph)_{\max}$  [214].

(ii) In mixtures with more than 50%  $\text{SF}_6$  content, the improvement against surface imperfections is relatively small [215].

(iii) In the presence of conducting particles, an  $\text{SF}_6/\text{N}_2$  mixture having 50%  $\text{SF}_6$  by volume may become as effective as pure  $\text{SF}_6$  [122, 123].

In this chapter the influence of surface roughness on

the breakdown voltage in SF<sub>6</sub> and SF<sub>6</sub>/N<sub>2</sub> mixtures is estimated using a simplified model of surface roughness, taking into account the compressibility factor. In SF<sub>6</sub> a general approach is made to evaluate an upper limit for the parameter (ph) such that the roughness factor,  $\xi (= E_{\max}/E_{\lim})$ , is maintained at unity.

Finally, dc and impulse breakdown data obtained in SF<sub>6</sub> and SF<sub>6</sub>/N<sub>2</sub> mixtures in coaxial-electrode gaps are compared with the proposed theoretical estimations.

## 5.2 Breakdown Voltage Estimation in Compressed SF<sub>6</sub> and SF<sub>6</sub>/N<sub>2</sub> Mixtures

In the following sections, calculations are made of the breakdown voltage for smooth and rough electrodes in SF<sub>6</sub> and SF<sub>6</sub>/N<sub>2</sub> mixtures. The reduction in breakdown voltage due to surface roughness is estimated using both single-protrusion and multiple-protrusion models.

### 5.2.1 Swarm coefficients

The effective ionization coefficient  $\bar{\alpha}$  for SF<sub>6</sub> has been measured by several investigators. Results are depicted in Figure 1.1(a) for the low range  $85 \leq E/p \leq 97$  [83, 85-87] and in Figure 1.1(b) for the range  $88 \leq E/p \leq 500$  [86]. In the former range the relationship between  $\bar{\alpha}$  and E/p can be expressed numerically by

$$\frac{\bar{\alpha}}{p} = K \left[ \frac{E}{p} - \left( \frac{E}{p} \right)_{\lim} \right] \quad (5.1)$$

where  $K = 27.8 \text{ kV}^{-1}$  and  $(E/p)_{\lim} = 88.4 \text{ kV}/(\text{cm bar})$ . In the latter range, due to experimental limitations, deviation occurs

from the above relation. However, the low (E/p) data can be extrapolated to higher ranges by using compressibility factor as will be explained in the following section.

In SF<sub>6</sub>/N<sub>2</sub> mixtures, the measured  $\bar{\alpha}_m$  data was shown [94] to be expressible by the well known partial pressure weighted data of SF<sub>6</sub> and N<sub>2</sub> for a limited range of E/p near (E/p)<sub>lim</sub>. The relation is given by

$$\frac{\bar{\alpha}_m}{p} = \left[ \left( \frac{\bar{\alpha}}{p} \right)_{\text{SF}_6} + x \left( \frac{\bar{\alpha}}{p} \right)_{\text{N}_2} \right] \frac{1}{1+x} \quad (5.2)$$

with  $x = p_{\text{N}_2} / p_{\text{SF}_6}$ , the ratio of partial pressures of two gases. This relation, together with the compressibility factor that will be derived in the following section, can be used to predict  $\bar{\alpha}_m$  at high E/p values.

### 5.2.2 Compressibility effect

Nonideal gas behaviour at elevated pressures can be corrected by knowing the changes in the quality,  $z = pV / (nRT)$  which is known as the compressibility factor, where V is the molar volume of n moles at the pressure p and the temperature T, and R is the gas constant.

In SF<sub>6</sub> it has the form as given in Equation A3.4 and the application to extrapolate low pressure discharge data concerning fundamental gas parameters is demonstrated in Section 1.5.4.

In SF<sub>6</sub>/N<sub>2</sub> mixtures, the compressibility factor can be estimated in terms of partial pressures and 'virial' coefficients of the constituents by assuming that Dalton's law is still valid at high pressures, i.e.  $p = p_1 + p_2$ .

If the compressibility factor for SF<sub>6</sub> or N<sub>2</sub> is expressed in an alternative form as

$$\text{SF}_6 ; \quad \frac{p_1 V}{RT} = n_1 + B_1 \frac{n_1^2}{V} + C_1 \frac{n_1^3}{V^2} + \dots \quad (5.3)$$

$$\text{N}_2 ; \quad \frac{p_2 V}{RT} = n_2 + B_2 \frac{n_2^2}{V} + C_2 \frac{n_2^3}{V^2} + \dots \quad (5.4)$$

where B<sub>1</sub>, C<sub>1</sub> and B<sub>2</sub>, C<sub>2</sub> are virial coefficients of SF<sub>6</sub> and N<sub>2</sub>, the compressibility factor of the mixture then becomes

$$\frac{(p_1+p_2)V}{RT} = (n_1+n_2) + \frac{1}{V} (n_1^2 B_1+n_2^2 B_2) + \frac{1}{V^2} (n_1^3 C_1+n_2^3 C_2) \quad (5.5)$$

Since the total number of moles in the mixture is  $n = n_1+n_2$ , the total pressure  $p = p_1+p_2$ , and the partial pressure ratios of constituent  $i$  are  $x_i = p_i/p$  ( $i = 1,2$ ), the compressibility factor of the mixtures can be written as

$$\frac{pV}{RT} = n \left[ 1 + (x_1^2 B_1+x_2^2 B_2) \frac{n}{V} + (x_1^3 C_1+ x_2^3 C_2) \left( \frac{n}{V} \right)^2 + \dots \right] \quad (5.6)$$

Substituting  $B = (x_1^2 B_1 + x_2^2 B_2)$  and  $C = (x_1^3 C_1 + x_2^3 C_2)$  into Equation 5.6 gives

$$\frac{pV}{nRT} = z = 1 + B \frac{n}{V} + C \left( \frac{n}{V} \right)^2$$

Since the compressibility factor can also be written in terms of gas pressure as  $z = 1 + B' p + C' p^2$

then the coefficients in the two compressibility-factor expressions are related as (see Appendix 3 for the derivation)

$$B' = \frac{1}{RT} (x_1^2 B_1 + x_2^2 B_2) \quad (5.8)$$

and

$$C' = \frac{1}{(RT)^2} [ (x_1^3 C_1 + x_2^2 C_2) - (x_1^2 B_1 + x_2^2 B_2)^2 ]$$

The variation of calculated values of B' and C' with partial pressure ratio of SF<sub>6</sub> at a temperature of 20°C is shown in Figure 5.1 and Table 5.1.

At three gas temperatures (T = 0°C, T = 20°C and T = 67°C) the change in compressibility with pressure is illustrated in Figure 5.2 for SF<sub>6</sub>, N<sub>2</sub> and for mixtures containing 40% and 75% SF<sub>6</sub>. In mixtures having SF<sub>6</sub> concentration less than 40% the compressibility factor is close to that of N<sub>2</sub>, i.e. almost unity.

The effect of temperature variation on the compressibility factor of SF<sub>6</sub>, N<sub>2</sub> and two mixtures is depicted in Figure 5.3 at gas pressures of 5 and 25 bar. Over the temperature range 0 < T < 300°C the compressibility of mixtures having SF<sub>6</sub> concentration less than 40% can also be taken equal to that of N<sub>2</sub>.

The derivation demonstrated above is general and can also be applicable to mixtures containing more than two constituents. The accuracy of the results is restricted by the same conditions that limit the application of Dalton's law and, hence, better accuracy is expected as the pressure of the mixture is decreased.

### 5.2.3 Estimation for smooth electrodes

The minimum breakdown voltage in compressed SF<sub>6</sub> and SF<sub>6</sub>/N<sub>2</sub> mixtures can be readily determined by the streamer breakdown criterion

$$\int_0^{\rho} \bar{\alpha}(r) dr = k \quad (5.9)$$

in which r is the radial distance and ρ is the critical avalanche length from the electrode surface. The parameter  $\bar{\alpha}$  is the

effective ionization coefficient of ionization and, within  $E/p$  range of interest, it is given for  $SF_6$  by Equation 5.1 and for  $SF_6/N_2$  by Equation 5.2. The constant  $k$  is the mean carrier number and for  $SF_6$ , in nonuniform field gaps,  $\ln(k)$  was measured [83, 88] to have a value of  $10.5 \pm 3$ . For  $SF_6/N_2$  mixtures, no experimental data is available; however, it can be extrapolated on a partial pressure basis between  $k(SF_6) = 10.5 \pm 3$  and  $k(N_2) = 5-8$  [49].

#### Estimation for $SF_6$

The breakdown field strength  $E_0$  and the voltage  $V_0$  equations may be derived by substituting the geometric field distribution equation  $E(r) = V/[r \ln(r_2/r_1)]$  into equation 5.1 and solving equation 5.9 together with  $\bar{\alpha}(p) = 0$  yields

$$\frac{E_0}{p} = A \left[ 1 + C \frac{1}{\sqrt{pr_1}} \right] \quad (5.10)$$

and from  $V_0 = E_0 r_1 \ln(r_2/r_1)$ , it follows that

$$V_0 = A (pr_1 + C \sqrt{pr_1}) \ln\left(\frac{r_2}{r_1}\right) \quad (5.11)$$

where  $A = 88.4$  kV/cm and  $C = 0.066$  (bar cm)<sup>1/2</sup>.

Owing to some simplifying assumptions made (Appendix 4), while estimating the critical avalanche length, the results are slightly less than those obtained from the iterative solution of equations  $\int \bar{\alpha} dr = k$  and  $\bar{\alpha} = 0$ . The latter method was adopted for the present investigation.

#### Estimation for $SF_6/N_2$ Mixture

There is no readily available solution in the form of  $E_0/p = \varphi(pr_1)$  unless one makes crude assumptions which are found to result in larger error than that noticed in  $SF_6$ . Hence,  $E_0$  is estimated only by the iterative method. Iteration take place

between equations  $\int_{r_1}^{r_c} \bar{\alpha}_m(r) dr = k$  and  $\bar{\alpha}_m = 0$ . Details of the solution are given in Appendix 4.

#### 5.2.4 Estimation for rough electrodes

The breakdown calculations for rough electrodes is similar to that of smooth ones if the microscopic details of the field distribution is defined. In laboratory experiments, the effect of surface roughness are usually studied with artificial protrusion models placed on a plane and a known axial field distribution. However, inherent surface roughness associated with manufacturing processes are more complex than these representations. Therefore, it is of interest to perform the breakdown estimations with more realistic surface roughness models.

The axial field distribution from the tip of a protrusion of any arbitrary shape can be represented by a polynomial of the following form

$$E(x) = V_0(A_1 + A_2 x + \dots + A_n x^{n-1}) = V_0 \sum_{i=1}^n A_i x^{i-1} \quad (5.12)$$

where  $V_0$  is the potential of the inner electrode, and  $A_i$  ( $i = 1, \dots, n$ ) are the coefficients of the polynomial and are dependent on the gap configuration and protrusion height. This type of representation is suitable for discrete numerical solutions of the field distribution by either finite element or finite difference techniques. The latter method was modified and adapted for the solution of field distribution along the axis of symmetry of the model system.

In the following breakdown estimations, it was assumed that the position coordinate passing through tip of the protrusion

starts from the inner surface of the coaxial electrode geometry.

In SF<sub>6</sub>, breakdown estimation requires successive-iterative solution of equations.

$$kV_0 \int_0^{x_c} \left( \sum_{i=1}^n A_i x^{i-1} \right) dx - k (E/p)_{lim} p x_c = k \quad (5.14)$$

and

$$V_0 \sum A_i x_c^{i-1} - (E/p)_{lim} \cdot p = 0 \quad (5.15)$$

taking into account the property  $E(x_c) = (E/p)_{lim} \cdot p$

In SF<sub>6</sub>/N<sub>2</sub> mixtures, breakdown estimations are similar to that of SF<sub>6</sub>. Substituting E(x) (Equation 5.12) into  $\bar{\alpha}_m$  (Equation 5.2) yields the following relations; the streamer criterion

$$\int_h^{x_c} \left\{ \left[ k \left[ V_0 \sum A_i x^{i-1} - \left( \frac{E}{p} \right) p \right] + \psi p M \exp \left( \frac{Bp}{V_0 \sum A_i x^{i-1}} \right) \right] \right\} dx = k (1 + \psi) \quad (5.16)$$

and limiting value

$$k \left[ V_0 \sum A_i x_c^{i-1} - \left( \frac{E}{p_{lim}} \right) p \right] + \psi \cdot p M \exp \left( \frac{Bp}{V_0 \sum A_i x_c^{i-1}} \right) = 0 \quad (5.17)$$

for the iterative solution.

In all breakdown estimations for smooth and rough electrodes, the effect of gas compressibility has been accounted for by modifying the effective ionization coefficient by including the compressibility factor  $z(p,T)$  as

$$\bar{\alpha} = f [E, p/z(p,T)] \quad (5.18)$$

$z(p,T)$  is given for SF<sub>6</sub> and SF<sub>6</sub>/N<sub>2</sub> mixtures as in Equation 5.8.

The numerical values of the constants are presented in Table 5.1.

#### 5.2.4.1 Protrusion models

In order to predict breakdown characteristic for a rough surface in  $SF_6$  and  $SF_6/N_2$  mixtures, the theoretical roughness model to be selected must be associated with the microsurface profile of the surface produced during manufacturing. The approximate theoretical representation of a machined surface is shown in Figure 5.4(a). It is a model comprising triangular protrusions of identical heights, superimposed on the inner electrode surface of a coaxial gap, or on the cathode in the case of a uniform-field gap. Single and multiple models are illustrated in Figures 5.4(b) and (c). Figure 5.5. shows the microscopic field distribution, for both single and multiple protrusions, for the region  $r \geq 0.15h$  where  $h$  is the height of the protrusion and  $r$  is the position coordinate measured along the line of force from the tip of the protrusion. It is seen that a reduction of field enhancement in the range of 1.3 - 2.2 is achieved by multiple protrusion model that shows the mutual effect of neighbouring protrusions on the effective field distribution.

The field distribution in the vicinity of a protrusion and along its axis was estimated by finite difference method which requires the solution of Laplace's equation  $\nabla^2 \phi (r,z) = 0$  in cylindrical coordinates. The region of interest was divided into a lattice and finite-difference form (of Appendix 4) of Laplace's equation for an irregular-star configuration was solved by iteration at each node under the given boundary conditions. For rapid convergence the extrapolated Liebmann iterative method [218] was adopted. The field distribution along the axis of protrusion was estimated along the axis of protrusion from the relation

$$E(r, z) = \frac{V(r, z) - V(r, z+1)}{h}$$

where  $(r, z)$  are the coordinates of each node and  $h$  is the increment. The field distribution was represented by a  $n$ -degree polynomial of the form given in Equation 5.12 and the coefficients were determined by the method of least square approximation.

An application of the method for solution of the potential distribution for the single-isolated and multiple-protrusion models is illustrated in Figure 5.6. Boundary conditions are determined as follows:

- (i) The potential at the surface of the electrode and of protrusion(s) are kept constant (Region ③).
- (ii) The potential at the outer boundary ① which is at a distance 25 times the height of protrusion, is taken equal to the geometric potential

$$V(m, z) = \frac{\ln \frac{r_2}{r}}{\ln \frac{r_2}{r_1}}$$

- (iii) The potential distribution at discrete nodes at the boundary ② ; for the single protrusion model is the geometric potential at a distance 10 times the height of protrusion and for the multiple protrusion model (a model with six protrusions) it is the geometric potential of a single protrusion model after superimposing the multiple and single protrusion models.
- (iv) The potential at the nodes in region ④ is equated to unity.

The algorithm for the iterative solution is given in Appendix 4.

#### 5.2.4.2 Application of models for estimating the roughness factor in SF<sub>6</sub>

The two types of models are applied to estimate the roughness factor  $\xi$  [ $= (E(r)/p) / (E/p)_{lim}$ ] in SF<sub>6</sub> in coaxial electrodes having radii  $r_1/r_2 = 0.5/1.27$  cm. The results are illustrated in Figure 5.7(a) - (c). In general,  $\xi$  lies below unity for both single and multiple protrusion models, is larger for the multiple - protrusion model - and increases with decreasing h/b ratio. The variation of  $\xi$  with ph is affected both by protrusion height (Figure 5.7(b)) and gap nonuniformity (Figure 5.7(c)). It is interesting to note that for both models  $\xi \approx 1$  can only be attained if the height of protrusion is reduced to zero. In Figure 5.7(b), for instance,  $\xi \approx 0.98$  for  $h = 2 \mu\text{m}$  and it stays more or less the same as ph increases.

### 5.3 Breakdown Voltage Measurements in SF<sub>6</sub> and SF<sub>6</sub>/N<sub>2</sub> Mixtures

In order to check the validity of the presently-suggested model for estimation of the breakdown voltage in SF<sub>6</sub> and SF<sub>6</sub>/N<sub>2</sub> mixtures, a series of experiments were performed under both dc and impulse voltage conditions. The method of estimating breakdown voltages with and without protrusions was explained in sections 5.2.3 and 5.2.4 respectively.

#### 5.3.1 Test conditions

Test results were obtained in laboratory-clean conditions

with electrodes having radii  $r_1/r_2 = 5/12.7$  mm (E7 - See Table 2.1) and  $9.45/12.7$  mm (E9 - E11). In Table 5.2 S.E.M. records and details of the electrode surface condition after successive breakdown tests are shown (see also Table 2.2 for unsparked S.E.M. records for comparison). It is of interest to note that the maximum surface roughness obtained after successive sparking in the case of polished electrodes (E7 and E9) is in the order of  $\sim 2$   $\mu$ m while, as expected, the surface roughness for sandblasted and machined electrodes is unaffected.

Details of dc and impulse voltage supplies, together with measuring circuits, are shown in Figures 2.5 and 2.7 respectively.

Dc results illustrated in several figures of the following sections were obtained from the successive-breakdown tests of Chapter 3. Each breakdown field strength on these figures corresponds to the first mode of the extreme-value distribution of the last 100 breakdowns of the total 200 sparks. For information, the maximum and minimum in the distribution are also depicted.

An impulse voltage waveform of  $0.2$   $\mu$ sec/ $70$  msec was used. Breakdown voltages were determined by up-and-down method with 30 number of voltage applications.

### 5.3.2 Dc breakdown characteristics

#### SF<sub>6</sub>

The breakdown characteristics obtained in gaps with polished electrodes  $r_1/r_2 = 5/12.7$  mm and  $9.45/12.7$  mm are shown in Figures 5.8 and 5.9 respectively. In the same figures, estimated breakdown voltages for smooth electrodes  $E_0$  (calculated from Equation 5.10) and for electrodes having  $\sim 2$   $\mu$ m single protrusion  $E'_0$ .

(estimated by making use of single protrusion method) are also plotted.

The point of deviation (critical point) of positive breakdown characteristics from the similarity law begins for small radius electrode (E7) at 2.3 bar (Figure 5.7(b) ) and for large radius electrode (E9) at 1.9 bar (Figure 5.7(c) ).

In Figure 5.10 breakdown characteristics of SF<sub>6</sub> obtained in gaps having rough inner electrodes with radii  $r_1/r_2 = 9.45/12.7$  mm are illustrated. Surface roughness measurements of electrodes are given in Table 5.2; the range of maximum heights of protrusions for machined electrode is 10 - 15  $\mu\text{m}$  and for sandblasted electrode is 16 - 20  $\mu\text{m}$ . In the same figure, breakdown estimations made for single and multiple protrusion models with the protrusion height  $h = 20$   $\mu\text{m}$  and for hemispherical protrusion model [113] with the radius  $\rho = 20$   $\mu\text{m}$  are also shown. Good correlation is attained for the hemispherical protrusion model over the entire pressure range studied and for the multiple protrusion model up to 6 bar. In the case of machined electrodes, the dispersion of the results is unexpectedly larger than for the sandblasted electrode at pressures  $\geq 6$  bar.

The points of deviation from the similarity law occurs for machined electrode at 1.7 bar and for sandblasted electrode at 1 bar.

#### SF<sub>6</sub>/N<sub>2</sub> Mixtures

Measured positive breakdown characteristics of 75% SF<sub>6</sub> - 25% N<sub>2</sub> and 10% SF<sub>6</sub> - 90% N<sub>2</sub> mixtures obtained in gaps having polished electrodes with radii  $r_1/r_2 = 9.45 / 12.7$  mm are demonstrated in Figure 5.11. Also shown are the calculated breakdown field strengths estimated in accordance with the method of iterative solution for

polished electrodes ( $E_c$ ) (section 5.2.3) and for rough electrodes ( $E'_c$ ) having (section 5.2.4) a single protrusion of height  $h = 2 \mu\text{m}$ . The predicted breakdown field strengths coincide with the experimental ones up to 6 bar for both mixtures. At higher pressures disagreement is least in the case of the 10%  $\text{SF}_6 - \text{N}_2$  mixture. The point of deviation from the similarity law is 2.6 bar for 75%  $\text{SF}_6 - \text{N}_2$  mixture and 4.2 bar for 10%  $\text{SF}_6 - \text{N}_2$  mixture.

The breakdown characteristics of rough electrodes in 10%  $\text{SF}_6 - 90\% \text{N}_2$  and 75%  $\text{SF}_6 - 25\% \text{N}_2$  mixtures are shown in Figures 5.11 and 5.12 respectively. The breakdown field strengths estimated from the multiple protrusion model with protrusion height  $h = 20 \mu\text{m}$  are also plotted in the same figures. The experimental results can be correlated to estimated ones up to 5 bar in both mixtures.

The critical pressure is  $\sim 2$  bar for both machined and sandblasted electrodes in 10%  $\text{SF}_6 - 90\% \text{N}_2$  mixture and is  $\sim 2$  bar for machined electrode and  $\sim 1.5$  bar for sandblasted one in 75%  $\text{SF}_6 - 25\% \text{N}_2$  mixture.

An interesting point to notice in both figures is that the position of the breakdown characteristic for the machined electrode with respect to the sandblasted one is levelled up as the  $\text{SF}_6$  content in mixtures is changed from 10% to 75%.

### 5.3.3 Impulse breakdown characteristics

#### $\text{SF}_6$

The positive and negative impulse breakdown characteristics of  $\text{SF}_6$  obtained for the gap with rough inner electrode with radii  $r_1/r_2 = 5/12.7$  mm are shown in Figure 5.14. Only the positive breakdown field strength characteristic agrees with the similarity .

law up to 3.5 bar: the other prediction from the multiple protrusion model having protrusion height  $h = 20 \mu\text{m}$  lies between the positive and negative breakdown characteristics. The critical pressure for the positive polarity is  $\sim 3.5$  bar and for the negative polarity it occurs at a considerably lower pressure of  $\sim 0.75$  bar.

#### SF<sub>6</sub>/N<sub>2</sub> Mixtures

Impulse breakdown characteristics are presented in Figure 5.15 only for a 40% SF<sub>6</sub> - 60% N<sub>2</sub> mixture in the gap having the same sandblasted inner electrode. Negative breakdown field strengths are marginally predictable by the similarity law and the deviation starts at  $\sim 3.5$  bar. The multiple protrusion estimate lies below both characteristics.

#### 5.4 Discussion

##### SF<sub>6</sub>

The model approach made for estimating the breakdown characteristics of several rough electrodes in SF<sub>6</sub> has indicated that the maximum breakdown field strength on the inner electrode is lower than the limiting field, i.e.  $(E/p)_{\text{lim}}$ . The amount of the reduction is dependent on the protrusion shape (Figure 5.7(a)), the protrusion height (Figure 5.7(b)) and the nonuniformity of the gap (Figure 5.7(c)), and is always higher with the multiple protrusion model. Although these results, at the first instance, seem to contradict what has been evidenced in the uniform field case with a single hemispherical protrusion [113] or multiple ridges [117], one must distinguish properties of gaps and the types of analyses which have been adopted. In the present investigation, since curvature of the inner electrode is accounted for in addition to the effect of

electrode surface roughness, the results demonstrate the existence of no lower limit for the parameter  $ph$  in respect of the effect of surface roughness on the dielectric strength of  $SF_6$ . This theoretical result is also supported by the recent work of McAllister [212] who showed that, for a model having a spherical protrusion superimposed on a spherical electrode, there always results a reduction in breakdown field strength and the size of protrusion is effective only on the amount of the reduction.

In  $SF_6$ , the breakdown characteristics of polished electrodes deviate from the similarity law behaviour at pressures in the range 1.7 - 2.0 bar (Figures 5.8 and 5.9). This range is almost the same for the negative breakdown characteristics. Pedersen [113] estimated a threshold value (see section 1.6.2.2) of 43 bar  $\mu m$  for the parameter  $ph$  in order for surface roughness to affect the breakdown characteristics of  $SF_6$ . This condition implies the presence of  $\sim 20 \mu m$  protrusions that are unrealistic for the polished electrodes. Estimation with this size of protrusion leads to lower breakdown field strengths at higher pressures. However, with the present approach, the breakdown field strength was predicted with sufficient accuracy up to 6 bar for the gap  $r_1/r_2 = 5/12.7$  mm (Figure 5.8) and to 8 bar for  $r_1/r_2 = 9.45/12.7$  mm (Figure 5.9) by assuming a 2  $\mu m$  single isolated protrusion. Above 6 bar, breakdown is governed by some other processes, probably associated with free conducting particles produced by sparking.

In Figure 5.8, at pressures  $\sim 2$  bar, the positive and negative breakdown voltage characteristics coincide with the similarity law. At high pressures, however, the negative breakdown characteristics fall considerably below the positive one. When the applied voltage to the inner conductor is negative, the avalanche starts from

the conductor and leads to a streamer, whereas for the positive polarity a free electron must be found in the gap in order to initiate an avalanche. Due to field emission from the electrode surface when the applied voltage is negative, streamer formation will readily be facilitated. In the case of polarity, one might expect therefore that irradiating the gap sufficiently should at least tend to yield some lower breakdown voltages at the same level as negative ones. As shown in Figure 5.8, out of 100 positive breakdowns, irradiating the gap axially with a  $^{3m}\text{Cr}$   $\text{Cs } 137$  source at a 10-cm distance did not generate any lower positive breakdown voltage falling within the distribution limits of negative breakdown voltage at the same pressure. This experimental evidence implies that in nonuniform gaps either the streamer breakdown criterion must be modified to account for the direction of its propagation or, in  $\text{SF}_6$ , the relation  $\bar{\alpha}/p = f(E/p)$  derived from low pressure data leads to erroneous results at high pressures.

For rough electrodes breakdown field estimation made according to Pedersen's analysis with 20  $\mu\text{m}$  protrusion fits well to experimental breakdown characteristics of sandblasted electrode whose maximum surface roughness is in the range of 15 - 20  $\mu\text{m}$  (Figure 5.10). For the same  $\sim 20 \mu\text{m}$  protrusion, the single protrusion model yields lower results as compared to results of the multiple protrusion model, whose prediction agrees within limited accuracy with the breakdown characteristics of sandblasted and machined electrodes for pressures up to 6 bar. This exhibits the shielding effect of multiple protrusions on rough surfaces. At high pressures, however, there may appear a single protrusion whose effect might become more important than the shielding of other protrusions, and this may result in a lower breakdown voltage.

The positive impulse breakdown characteristic for sandblasted electrodes ( $R_{\max} = 16 - 20 \mu\text{m}$ ) shown in Figure 5.14 coincides up to 2.6 bar with the theoretical one evaluated according to Equation 5.10. This implies that surface roughness of this grade does not affect the breakdown voltage. This result is also confirmed by the findings of Kawaguchi et al [144] who observed no effect of surface roughness less than  $30 \mu\text{m}$  on breakdown characteristics in coaxial-electrode geometry. Moreover, this inference is also indicated by the multiple protrusion estimation which results in lower prediction coinciding with the negative breakdown characteristic up to 3 bar.

The reduction of the positive dc breakdown voltage from the theoretical estimation begins for polished electrodes at field strengths in the range 160 - 180 kV/cm and for rough electrodes in the range 130 - 150 kV/cm. If the area of the electrode is not large field gradients exceeding these figures can still be predicted by Equation 5.10 [195]. For rough electrodes, theoretical breakdown characteristics can be estimated for field gradients up to 450 - 600 kV/cm with the multiple protrusion model.

#### SF<sub>6</sub>/N<sub>2</sub> Mixtures

Together with the multiple-protrusion model approach, an attempt has been made to estimate the breakdown field strength in mixtures for rough electrodes with  $\sim 20 \mu\text{m}$  protrusion in a similar way as was followed in Pedersen's analysis; the effective ionisation coefficient was linearized over a narrow range near the limiting  $(E/p)_{\text{lim}}$  by the relation given in Reference [94]. Results are illustrated in Figure 5.12 for 10% SF<sub>6</sub> - 90% N<sub>2</sub> and in Figure 5.13 for 75% SF<sub>6</sub> - 25% N<sub>2</sub>. Although in a 10% SF<sub>6</sub> - 90% N<sub>2</sub> mixture both

estimates lie above the experimental breakdown characteristics, in a 75% SF<sub>6</sub> - 25% N<sub>2</sub> mixture results obtained from Pedersen's analysis exhibit better correlation with the experimental ones. An experimental threshold for the latter mixture was found to be the same as that of SF<sub>6</sub>.

The deviation of experimental breakdown characteristics from the theoretical estimation seems to be independent of the type of mixture. For example, for polished electrodes, the breakdown characteristics of mixtures with 10% SF<sub>6</sub> - 90% N<sub>2</sub> and 75% SF<sub>6</sub> - 25% N<sub>2</sub>, given in Figure 5.11, deviate at the field strength  $\sim 250$  kV/cm, whereas the corresponding critical pressures are 4.5 and 2.7 bar respectively. For roughened electrodes (Figure 5.12 and 5.13) the critical field strength is also independent on the SF<sub>6</sub> content and is reduced to  $\sim 140$  kV/cm.

## 5.5 Conclusion

A theoretical and experimental investigation has been made of breakdown phenomena for coaxial electrodes in SF<sub>6</sub> and SF<sub>6</sub>/N<sub>2</sub> mixtures. Tests were performed with dc and impulse voltages for various gap nonuniformities and surface finishes. The results can be summarised in the following points.

(i) For SF<sub>6</sub>/N<sub>2</sub> mixtures, a general equation for the compressibility factor was derived from the virial coefficients of the constituents. It was found that the compressibility factor of a mixture containing less than 50 per cent SF<sub>6</sub> can be taken as equal to that of N<sub>2</sub>.

(ii) The breakdown characteristics of SF<sub>6</sub> and SF<sub>6</sub>/N<sub>2</sub> mixtures for a rough surface were derived from a multiple protrusion model comprising juxtaposed triangles. Theoretical analyses with

single and multiple protrusions on electrodes with finite curvature indicated that no upper limit for tolerable surface roughness limit exists. In general, it was found that surface roughness always reduces the dielectric strength of the system and the amount of reduction depends on the protrusion height and shape and on the nonuniformity of the gap.

(iii) For smooth electrodes ( $R_{\max} \approx 2 \mu\text{m}$ ) estimation made with the single-protrusion model is in agreement with the average breakdown field strength up to 6 bar.

(iv) For rough electrodes ( $R_{\max} \approx 20 \mu\text{m}$ ) in  $\text{SF}_6$  at pressures up to 8 bar the single protrusion model suggested by Pedersen yields better agreement than the multiple protrusion model.

(v) Deviation from the similarity law occurs for polished electrodes at field strengths  $>160 - 180 \text{ kV/cm}$  and for rough electrodes  $>130 - 150 \text{ kV/cm}$ .

(vi) Under positive impulse conditions, deviation from the similarity estimation begins in  $\text{SF}_6$  at field strengths  $>450 - 600 \text{ kV/cm}$ .

Positive impulse breakdown characteristics of  $\text{SF}_6$  are not affected for surface finishes with  $R_{\max} \leq 30 \mu\text{m}$ .

CORONA STABILIZED BREAKDOWN IN SF<sub>6</sub> AND SF<sub>6</sub>/N<sub>2</sub> MIXTURES6.1 General

Breakdown characteristics in nonuniform fields are characterised by the existence of a pressure region over which breakdown takes place at levels significantly above the corona threshold level; increasing the pressure causes the breakdown voltage to pass through a maximum  $V_m$ , with a corresponding pressure  $p_m$  and then to decrease until a critical pressure  $p_c$  is reached at which breakdown occurs at onset. This feature of the characteristic appears for dc, alternating and impulse voltages if the gap nonuniformity is appropriate. A brief summary of findings is as follows:

(i) At low pressures ( $< p_m$ ) over the rising part of the curve, the V-p characteristics are independent of the curvature of the stressed electrode and is always higher for negative polarity.

(ii) The breakdown maximum increases and the corresponding pressure decreases with increasing curvature (i.e. decreasing electrode radius). It is less pronounced for impulse voltages and in short gaps, positive impulse characteristics might exhibit two maxima.

(iii) At the critical pressure, the corresponding voltage and the product of critical pressure and radius of the stressed electrode ( $p_c.r$ ) stays almost constant. The critical pressure is almost independent of electrode separation.

(iv) The corona inception voltage is generally less for negative polarity, but corona stabilized breakdown occurs at

significantly higher levels.

(v) The pressure range over which corona stabilization occurs decreases with decreasing curvature and is greater for negative polarity.

For a more comprehensive review of the particular features of V-p characteristics refer to Section 1.6.4.

In this chapter, static and impulse corona-stabilized breakdown behaviour of coaxial electrode configuration in SF<sub>6</sub> and SF<sub>6</sub>/N<sub>2</sub> mixtures have been examined over the pressure range 0-8 bar. The dielectric characteristics of SF<sub>6</sub>/N<sub>2</sub> mixtures have been compared to those of SF<sub>6</sub> for various gap and gas conditions. The effects of factors such as ion injection into the gap or of large protrusions on the inner electrode on corona stabilized breakdown in both SF<sub>6</sub> and SF<sub>6</sub>/N<sub>2</sub> mixtures have been observed.

## 6.2 Experimental Conditions

These investigations have been performed with polished stainless-steel outer electrodes of radii 12.7 and 25 mm and with polished stainless-steel inner electrodes of radii varying from 0.125 - 1.5 mm. Further particulars of the electrodes are tabulated in Table 2.1. The experimental vessel, gas filling and electrode polishing processes are described in Chapter 2.

The dc supplies and measuring circuit are shown in Figure 2.5. Owing to the high current demand in the corona-stabilized breakdown region, a 0-130 kV, 25 mA power supply was used, if required, in addition to the 50 - 300 kV, 1 mA power supply used for corona-free breakdown studies. The corona-onset voltage was detected by measuring pre-breakdown currents in the order of 10<sup>-8</sup> A with a resistor in series with the gap. For each corona-onset or breakdown value .

at least 10 voltage measurements were recorded.

The impulse generator and measuring circuit are illustrated in Figure 2.7. The 50% corona-onset and 50% breakdown voltages were obtained by the "up and down" test method. For each voltage level 30 impulses were applied. The corona-onset level was detected by a photomultiplier or by a 10M resistor in series with the gap.

The gap was irradiated by a 1mCi Cs137 capsule placed axially at a 10 cm distance from the gap.

### 6.3 Dc Corona and Breakdown Voltage Measurements in SF<sub>6</sub>

In order to understand the general behaviour of corona-stabilized breakdown characteristics in SF<sub>6</sub>, especially at low pressures ( $p < p_m$ ) over the rising part and at higher pressures ( $p_m < p < p_c$ ) over the region of negative slope, some initial tests were carried out for repeatability of test results and variation of corona onset and breakdown levels with irradiation. In all the illustrations given in the following sections, a normal distribution of at least 10 breakdowns was assumed and for each point the average of these measurements, together with the maximum and minimum values, is indicated.

#### 6.3.1 Repeatability of test results

Three breakdown characteristics of the gap with  $r_1/r_2 = 0.5/25$  mm obtained in SF<sub>6</sub> at different times are shown in Figure 6.1. Over the rising parts, the measured results are well reproducible, which is the characteristic of breakdown process common to most nonuniform gaps. At and beyond the breakdown maximum ( $V_m$ ) the characteristics are less reproducible. However, unlike the

measurements achieved for rod-plane gaps [220], there are no discontinuities so that the evaluation of mean breakdown voltages on these parts of the characteristics is justified.

For all three trials, the transitions from corona-stabilized breakdown to corona-free breakdown occur at almost the same pressure  $p_c$  and voltage  $V_c$ . Following the transition the characteristics are repeatable within experimental error with some spread in measurements.

On the same figure, the experimental corona-onset level, determined by single pulse discharge, and the theoretical breakdown estimation according to Equation 5.10, are also depicted. The three experimental corona-onset levels overlap and are slightly higher than the theoretical one.

Figure 6.2 shows negative breakdown data obtained in  $SF_6$  for a less nonuniform gap ( $r_1/r_2 = 1/12.7$  mm). All the way up to 1.7 bar the corona onset and breakdown measurements of both characteristics are reproducible. Above this pressure, the breakdown level of the second trial lies considerably below the first one and the corona onset level lies slightly above it. Both characteristics show similar behaviour near and above the critical pressure ( $p_c = 3.4$  bar).

### 6.3.2 Effect of irradiation

For the same experimental conditions of the above section, the test was repeated without irradiation source. The breakdown characteristics are illustrated in Figure 5.3. The plot of non-irradiated gap is characterized only by slightly higher corona-onset level. The description of other particularities of characteristics are the same as mentioned in the preceding section.

### 6.3.3 Effect of gap uniformity

A set of experiments were undertaken to envisage effects of gap nonuniformity on the dc discharge behaviour of SF<sub>6</sub>. Two outer electrodes of radii 12.7 and 25 mm were used together with inner electrodes having radii 0.15, 0.25, 0.5 and 1 mm. The range of gap nonuniformities ( $E_m/E_{ave}$ ) are:

| $r_2$ (mm) \ $r_1$ (mm) | 0.15 | 0.25 | 0.5  | 1   |
|-------------------------|------|------|------|-----|
| 12.7                    | 18.8 | 12.6 | 7.5  | 4.6 |
| 25.0                    | 32.4 | 21.5 | 12.5 | 7.4 |

Figures 6.4 and 6.5 show positive corona onset and breakdown measurements in gaps with outer electrodes of radius 12.7 and 25 mm respectively. For clarity the results are illustrated solely for the pressure range 0-4 bar. The rising part of characteristics, up to 1.2 bar for 12.7 mm outer electrode and 0.8 bar for 25 mm one, are almost independent of the inner electrode radii, but the rate of increase of breakdown voltage with pressure is a function of the outer electrode radius. At higher pressures, the characteristics pass through maxima which exhibit less dependence on the inner electrode radius and which become larger with increasing nonuniformity. The downcurving portion of the characteristics falls off to the corona-free breakdown region by following an irregular pattern and manifest no dependence on any related gap parameters. In gaps with the same outer electrode, the critical pressure  $p_c$  and the corresponding breakdown voltage decreases with decreasing nonuniformity of the gap. The values of  $p_c$  are smaller for gaps with the larger outer electrode (Figure 6.5).

The effect of gap nonuniformity was also investigated for negative polarity. Measurements of breakdown and corona-onset voltages over the pressure range 0 - 4 bar are illustrated in Figure 6.6 for gaps having outer electrode of radius  $r_2 = 12.7$  mm and in Figure 6.7 for gaps with  $r_2 = 25$  mm. In general, at low pressures, the behaviour of the characteristics is similar to that of the positive ones; breakdown voltages are independent of radius of inner electrode over the rising parts of characteristics up to 1.5 bar for gaps with  $r_2 = 12.7$  mm (Figure 6.6) and up to 0.6 bar for ones with  $r_2 = 25$  mm (Figure 6.7). The positions of the breakdown-voltage maxima and critical pressures on characteristics are not well-defined because of experimental limitations. However, the tendency of the characteristics is such that the critical pressure is lower for gaps having least nonuniformity.

As for the positive-polarity case, the corona-onset levels over the corona-stabilized region increase when the inner electrode radius is increased, whereas respective positions of the breakdown levels vary with pressure.

#### 6.3.4 Effect of polarity

Breakdown characteristics of both positive- and negative-polarity gaps having radii  $r_1/r_2 = 1/12.7$  and  $1/25$  mm are shown in Figures 6.8 and 6.9 respectively. Over the corona-stabilized region, the breakdown characteristics coincide up to 1.4 bar for the gap with  $r_1/r_2 = 1/12.7$  mm (Figure 6.8) and up to 0.6 bar for the gap  $r_1/r_2 = 1/25$  mm. Over these pressure ranges, as was explained in previous sections, the breakdown characteristics for each polarity were insensitive to variation of the radii of the inner electrodes.

The figures clearly indicate that the corona-stabilized breakdown region for negative-polarity gaps are wider compared to positive ones. Consequently, the critical pressures for negative gaps are higher than the positive ones. The large pressure range for stabilization in the case of negative polarity results in high breakdown voltages. However, at higher pressures, the direct negative breakdown voltage is lower than the positive one. In general, the negative corona-onset or corona-free breakdown level lies below the estimated threshold level.

#### 6.4 Dc Corona and Breakdown Voltage Measurements in SF<sub>6</sub>/N<sub>2</sub> Mixtures

##### 6.4.1 Effect of mixture ratio

In mixtures the breakdown characteristics are similar to those of SF<sub>6</sub> examined in previous sections: Figure 6.10 and 6.11 show positive-polarity data for  $r_1/r_2 = 0.5/12.7$  and  $0.5/25$  mm obtained in several mixtures. At low pressures,  $V_b$  is dependent upon SF<sub>6</sub> concentration being larger for mixtures with high SF<sub>6</sub> ratio, while at higher pressures the characteristics pass through maxima whose values depend on the mixture ratio. This is less pronounced for the gap with  $r_1/r_2 = 0.5/12.7$  mm (Figure 6.10) compared to the  $0.5/25$  mm gap (Figure 6.11). At pressures higher than  $p_m$ , the breakdown voltages decrease with increasing pressure. However, for the gap with the larger outer electrode (Figure 6.11) this region is more pronounced. The transition pressure ( $p_c$ ) to corona-free breakdown is independent of SF<sub>6</sub> content and is the same ( $\sim 3$  bar) for both gaps: the corresponding breakdown voltages appear to increase with SF<sub>6</sub> content. Over the corona-free breakdown region, as

expected, the breakdown voltage level becomes higher with SF<sub>6</sub> ratio in the mixture.

Negative corona-onset and breakdown voltage data acquired in several SF<sub>6</sub>/N<sub>2</sub> mixtures are illustrated in Figures 6.12 and 6.13 for gaps with  $r_1/r_2 = 0.15/12.7$  and  $0.15/25$  mm respectively. Corona onset and breakdown voltages for both gaps increase with pressure and are higher for the gap with the larger outer electrode (Figure 6.13). Both corona-onset and breakdown levels increase with mixture ratio.

#### 6.4.2 Effect of gap nonuniformity

To illustrate the effect of gap nonuniformity on corona and breakdown characteristics of mixtures, electrode systems having nonuniformity factors varying between 7.5 and 32.4 were chosen. The results of measurements obtained in 10% SF<sub>6</sub>/N<sub>2</sub>, 40% SF<sub>6</sub>/N<sub>2</sub> and pure SF<sub>6</sub> are shown in Figures 6.15 and 6.14 for outer electrodes of radii 12.7 and 25 mm respectively.

At low pressures, characteristics in the same gas are independent of the radius of the inner electrode, and the steepness increases with increasing SF<sub>6</sub> concentration. Similarly, the breakdown maxima and the corresponding pressures increase with increasing gap nonuniformity in the same gas, or with increasing SF<sub>6</sub> percentage in the same gap. Moreover, the corona-inception levels become higher as the gap nonuniformity decreases or as the SF<sub>6</sub> concentration of the mixture increases.

Critical pressures obtained for several gap nonuniformities are plotted against percentage of SF<sub>6</sub> in the mixture in Figure 6.16. It is evident that, for a given gap, the critical pressure is almost independent of SF<sub>6</sub> concentration and increases with increasing gap

nonuniformity. The slight deviation of experimental data from linearity is within the accuracy of measurements.

For the same gap nonuniformity ( $n = 12.5$ ), the corona-stabilized breakdown characteristics of Figures 6.14 and 6.15 are replotted in Figure 6.17. As the concentration of  $SF_6$  in the mixtures increases the following features are apparent:

- (i) The low-pressure parts of the characteristics become steeper.
- (ii) The breakdown maxima increases but the corresponding pressures decrease (except for pure  $SF_6$  in the 0.5/25 mm gap).
- (iii) The critical pressures are not affected and the corresponding voltages increase.

#### 6.4.3 Effect of polarity

Figures 6.18 and 6.19 show the effect of gap polarity on corona and breakdown characteristics of  $SF_6/N_2$  mixtures for gaps having the same nonuniformity factor, but with different outer electrode radii 12.7 and 25 mm respectively. The range of corona-stabilized region for positive-polarity gaps is smaller than the negative ones. This results in higher corona-stabilized breakdown maxima and critical pressures; both also increase with increasing partial pressure of  $SF_6$ . Generally, the negative inception voltage is lower than the positive one and the reverse is true for corona-free breakdown voltages.

It is interesting to note that positive and negative characteristics of the same mixture coincide for pressures up to 1 bar for both gaps.

## 6.5 Impulse Corona and Breakdown Voltage Measurements in SF<sub>6</sub> and SF<sub>6</sub>/N<sub>2</sub> Mixtures

In general, the impulse breakdown characteristics are similar in shape to those for dc conditions while above the critical pressure the breakdown characteristics again vary in accordance with the similarity law. In the following sections some of the important features affecting impulse breakdown characteristics in SF<sub>6</sub> and SF<sub>6</sub>/N<sub>2</sub> mixtures will be given.

### 6.5.1 Effect of mixture ratio

The effect of increasing SF<sub>6</sub> concentration in mixtures on positive impulse corona and breakdown characteristics of the  $r_1/r_2 = 0.5/25$  mm gap are illustrated in Figure 6.20. Over the corona-stabilized breakdown region, increasing percentage of SF<sub>6</sub> in mixtures yields higher stabilization. The negative slopes of the characteristics are not so marked as in dc case. Critical pressures of all three characteristics take place at about 3.2 bar. Corona inception and corona-free breakdown levels increase as SF<sub>6</sub> content in the mixture is increased.

### 6.5.2 Effect of polarity

The corona and breakdown characteristics of the  $r_1/r_2 = 0.5/25$  mm gap are compared for both polarities in a 40% SF<sub>6</sub>/N<sub>2</sub> mixture and SF<sub>6</sub> in Figure 6.21. In general, the corona-stabilized breakdown region is again much wider and the breakdown voltage higher for the negative gap, and both are larger for SF<sub>6</sub>. A wider corona-stabilized region also implies larger critical pressure. For the negative gap, the critical pressure is out of the present experimental capabilities: however, since the critical

pressures for the positive gap are independent of SF<sub>6</sub> content, this is probably also the case for the negative gap (see also Figure 6.19). Further, the corona inception level for negative polarity is lower than for positive and it is less for the 40% SF<sub>6</sub>/N<sub>2</sub> mixture than for pure SF<sub>6</sub>.

#### 6.6 Comparison of dc and Impulse Voltage/Pressure Characteristics

Positive dc and impulse corona onset and breakdown characteristics of the gap with  $r_1/r_2 = 0.5/25$  mm are plotted for 10% SF<sub>6</sub>/N<sub>2</sub>, 40% SF<sub>6</sub>/N<sub>2</sub> and SF<sub>6</sub> in Figures 6.22 (a) to (c) respectively. It was found that in the region of breakdown maxima the impulse breakdown voltages lie below the dc values, i.e. the impulse ratio ( $R_i = V_{50}/V_{dc}$ ) is less than one. Outside this region,  $R_i$  is always greater than one. It is noteworthy that, at lower pressures, at the points of transition from  $R_i \geq 1$  to  $R_i < 1$ , the field at the inner electrode always has the same value of 250 kV/cm. Further, critical pressures in all three figures for both dc and impulse voltages occur at about 3 bar.

Figure 6.23 shows a similar comparison made for a divergent field gap ( $r_1/r_2 = 1.5/12.7$  mm). In this case,  $R_i > 1$  over the whole pressure range. The negative impulse breakdown voltage of this gap, however, remains above the dc one only up to 1.2 bar (Figure 6.24). In addition, there is a tendency for the impulse-corona onset level to fall below the dc onset level at ~ 2.5 bar.

#### 6.7 Factors Affecting the Behaviour of Voltage/pressure Characteristics

Some special tests were performed to understand the corona stabilization phenomenon in coaxial electrode gaps in (a) mixtures .

of SF<sub>6</sub> and SF<sub>6</sub>/N<sub>2</sub> with a small percentage of SF<sub>6</sub>, and (b) SF<sub>6</sub> and SF<sub>6</sub>/N<sub>2</sub> mixtures. Some of these tests involved placing disc-shaped corona-intensifying rings on the inner electrode, and the injection of ions of polarity opposite to that of the inner electrode.

#### 6.7.1 Effect of a small percentage of SF<sub>6</sub> in air and nitrogen

In view of the results of investigations undertaken in point-plane gaps with impulse voltage in mixtures containing a small amount of SF<sub>6</sub> in nonattaching gases such as hydrogen [99] or nitrogen [17], similar tests were carried out in the present coaxial geometry with positive and negative dc voltages in SF<sub>6</sub>/air and SF<sub>6</sub>/N<sub>2</sub> mixtures. Figure 6.25 shows positive dc corona and breakdown characteristics of SF<sub>6</sub>/air mixtures with 0.2% and 1% SF<sub>6</sub>. In the same figure, the characteristics of pure SF<sub>6</sub> and air are also included for comparison. The striking feature of the results is that the addition of a small percentage (0.2% or 1%) of SF<sub>6</sub> in air brings about corona-stabilized breakdown over a wider pressure range than in either pure SF<sub>6</sub> or air. In fact, increasing the SF<sub>6</sub> content from 0.2% to 1% seems to enhance the breakdown maximum by ~ 20 per cent. The increase in the corona inception or corona-free breakdown levels is insignificant. Another point of interest is that the critical pressures for both mixtures are identical to that in air (~ 6 bar) which is much higher than the critical pressure of ~ 2.8 bar in SF<sub>6</sub>.

Voltage/pressure measurements performed in the same gap for a mixture of 1% SF<sub>6</sub>/N<sub>2</sub> together with the results for SF<sub>6</sub> and N<sub>2</sub> are illustrated in Figure 6.26. The corona-controlled breakdown

maximum is not so pronounced as in the case of the 1% SF<sub>6</sub>/air mixture, and the corona-stabilized pressure range is less. However, more pronounced peaks have been reported under impulse conditions in SF<sub>6</sub>/N<sub>2</sub> mixtures with < 1% SF<sub>6</sub> [117]. It is important to note that the critical pressures in SF<sub>6</sub> and in the 1% SF<sub>6</sub>/N<sub>2</sub> mixture are the same ( ~ 2.8 bar).

For the same mixtures of Figures 6.25 and 6.26, experiments were repeated for negative polarity and the results are shown in Figure 6.27. In contrast to the positive-polarity results, the stabilization achieved by adding 1% SF<sub>6</sub> into air or nitrogen is not very effective. Over the pressure range 0-5 bar, corona-onset and breakdown voltages for 1% SF<sub>6</sub>/air are the same as those for the 1% SF<sub>6</sub>/N<sub>2</sub> mixture.

#### 6.7.2 Effect of conducting discs fixed on the inner conductor

To observe the effectiveness of corona stabilization within local field disturbances introduced by single or multiple protrusions made up of circular discs of 3 or 8 mm in diameter, a series of tests were performed in SF<sub>6</sub> and 40% SF<sub>6</sub>/N<sub>2</sub> mixtures. The results of the measurements are shown in Figures 6.28 and 6.29. In the same figures results for the undisturbed gap are also included. The expected nonuniformity-independent breakdown behaviour over the rising part of the characteristics was observed in both gases, and all four characteristics coincide up to 0.8 bar. In SF<sub>6</sub>, the effect of the corona discs is to cause a substantial increase in the breakdown voltage over the corona stabilization region. However, in the case of the 40% SF<sub>6</sub>/N<sub>2</sub> mixture, a decrease was observed with both single and multiple discs. Stabilization seems to be more

effective in both gases with multiple discs than with a single disc. The corona inception level of the gap with multiple 3 mm diameter discs is lower than one having a single disc of 8 mm diameter. Moreover, the critical pressure is dependent upon the diameter of the disc; it is largest for the one having largest diameter. The characteristics of the perturbed gaps do not differ from the original at pressures beyond the critical pressure.

The only conspicuous effect of perturbing the gap with either a single or multiple discs is to shift the critical pressure to higher values and to increase the stabilization slightly.

### 6.7.3 Effect of ion injection

The purpose of these experiments was to determine whether the stabilizing corona could be influenced by the injection of ions of polarity opposite to that of the electrode in corona.

A simple ion injection system was developed as shown in Figure 6.30; a conical probe machined to 1 mm in diameter at its apex was appended to the outer conductor of the coaxial electrode gap having radii  $r_1/r_2 = 0.5/25$  mm. The probe then was connected to a 0-50 kV dc power supply through a 50 M resistor (see Figure 2.7 for the general layout of the experimental circuit). During the course of experiments the amount of power injected into the gap was maintained in the range 0.1 - 0.5 watt. The system was switched on prior to application of impulse voltage and was switched off afterwards to avoid erosion of the probe tip due to heating.

The results of voltage-pressure measurements obtained in  $SF_6$  and  $SF_6/N_2$  mixtures are illustrated in Figures 6.31 and 6.32 respectively. The amount of reduction achieved in the breakdown level over the corona stabilized region in the case of  $SF_6$ .

(Figure 6.31) is considerable as compared to those achieved in 10%  $\text{SF}_6/\text{N}_2$  (Figure 6.32(a)) and 40%  $\text{SF}_6/\text{N}_2$  (Figure 6.32(b)). The corona-free breakdown levels of all three characteristics are also lessened by ion injection; this is due to reduction of the statistical time-lag for the appearance of an initiatory electron near to the stressed electrode.

Contrary to the behaviour of the positive impulse characteristics, the amount of reduction in the negative impulse breakdown level of the 40%  $\text{SF}_6/\text{N}_2$  (Figure 6.34) mixture obtained with ion injection over the corona stabilized region is more than that for pure  $\text{SF}_6$  (Figure 6.33).

## 6.8 Discussion

### 6.8.1 Voltage-pressure characteristics

The familiar positive or negative voltage-pressure characteristics of coaxial-electrode configuration can be divided into three regions, the positive-slope and negative-slope regions of the corona-controlled breakdown regime and the direct-breakdown region above the critical pressure. The results demonstrated in the preceding sections for  $\text{SF}_6$  and  $\text{SF}_6/\text{N}_2$  for various gap nonuniformities will be discussed under these headings. A summary of the results is given in Table 6.1.

#### a) Positive-slope region and the breakdown maximum:

In all cases this part of the characteristics is repeatable within the experimental error. The breakdown characteristics exhibit a constant rate of increase with pressure and, for gaps with a fixed outer electrode radius, a single curve is obtained which is a function only of the type of gas and is independent of the radius and polarity of the inner electrode; on increasing either the

radius of the outer electrode or the SF<sub>6</sub> content in SF<sub>6</sub>/N<sub>2</sub> mixtures, the characteristics become steeper. These findings imply that the breakdown regime is controlled by a constant average gap field which is independent of the inner electrode field and is determined by the properties of the gas employed and the radius of the outer electrode. The existence of such a field was suggested [157 - 162] to be due to the presence of a space charge sustained in the gap by the corona. The space charge causes the field in the gap or at the outer electrode to increase to a value  $(E/p)_{str}$  sufficient for streamer breakdown to occur [159]. The gap-spacing-dependent feature of the characteristics (compare Figure 6.4 and 6.5) raise the question of whether the cathode field is maintained the same or not as the space charge zone is varied by varying the gap spacing. Field measurement at the cathode is valuable in explaining this behaviour. A detailed analysis of the space-charge modified gap and cathode fields were made using the results of static biased field probe [221] measurements which will be introduced in Chapter 7.

In the same gap, the reduced stabilization when the applied voltage is impulse (Figure 6.22(a) to (c)) suggests that radial displacement of the space charge and the extension of the space-charge zone from the corona electrode is important in sustaining stabilization.

The pressure range in which the radius-independent behaviour of the positive-slope region is upheld is the same for both polarities: this allows one to conclude that the corona discharge process, and mechanism supporting stabilization, is the same and is independent of the electronic charge carrier. However, at higher pressures the more extensive stabilization in the case of negative

polarity suggests a more stable negative-ion carrier with lesser mobility in the drift region. Further measurements were undertaken to explain the implications of the type of corona discharge and the effect of carrier mobility on the anomalous behaviour of attaching gases; these will be discussed in Chapter 7.

Both positive and negative-polarity breakdown voltage/pressure characteristics pass through a maximum with increasing pressure. As would be expected, in a gap with a fixed outer electrode the maximum breakdown voltage  $V_m$  (Figure 6.4 and 6.5) increases with increasing gap nonuniformity and with the ratio of  $SF_6$  concentration in mixtures (Figures 6.10 and 6.11). However, surprisingly, the latter seems not to hold for pure  $SF_6$  in the gap having the larger outer electrode (Figure 6.11); for instance, in a 75%  $SF_6/N_2$  mixture,  $V_m$  is larger than that in pure  $SF_6$ . This result also contradicts that obtained in point-plane gaps [97,160]. Further, the pressure  $p_m$  decreases with increasing  $SF_6$  content, in agreement with other works in point-plane gaps [97,160].

Although, near  $p_m$ , the predischARGE process near to breakdown has been observed [98] to alter its mode, the main mechanism causing this change is still unknown. In the following chapter, mechanisms involved in stabilization phenomenon and the associated gas processes bringing about destabilization after  $p_m$  will be elaborated in the light of experimental observations.

The corona inception level or the start of single pulse activity in  $SF_6$  and  $SF_6/N_2$  mixtures was found to increase with decreasing gap uniformity (Figures 6.4 and 6.5) and with increasing the ratio of  $SF_6$  in the mixture (Figure 6.10 and 6.11). Theoretical estimations with the methods given in Chapter 5 result in good agree-

ment over the pressure range studied.

b) Negative-slope region and critical pressure:

Test results over this region exhibit considerable scatter. However, unlike point-plane gaps, there is no transitional region yielding discontinuity (Figures 6.1). Although the breakdown levels appear to be enhanced by increasing the gap nonuniformity and the partial pressure of SF<sub>6</sub> in SF<sub>6</sub>/N<sub>2</sub> mixtures, the behaviour of characteristics is generally difficult to predict, owing to overlap of characteristics at some parts.

The large scatter in breakdown values observed in sphere-plane [79] and point-plane [97,220,222] gaps in compressed SF<sub>6</sub> or SF<sub>6</sub>/N<sub>2</sub> was not noticed for a wide range of field and gas conditions. This part of the characteristic becomes smoother and flatter with decreasing the gap nonuniformity. It can be inferred that the type of corona discharge started near  $p_m$  persists through this region up to the critical pressure  $p_c$ .

At pressures before corona-free breakdown takes place (i.e.  $p < p_c$ ), the voltage-pressure characteristics of SF<sub>6</sub> and SF<sub>6</sub>/N<sub>2</sub> either pass through a minimum or are unaltered up to  $p_c$  with increasing pressure (for SF<sub>6</sub> Figures 6.4 and 6.5, for mixtures Figures 6.10 and 6.11). This situation was also observed in point-plane gaps in SF<sub>6</sub> [79,97,155-157,161] and in SF<sub>6</sub>/N<sub>2</sub> mixtures [79,97,222]. The active gas processes associated with this change are of academic interest and require further investigation.

A point of practical interest over this region is the transition pressure,  $p_c$ , to corona-free breakdown region. It is a function of the gap nonuniformity and of spacing. In Figure 6.35(a) the variation of critical pressures obtained in several gap

configurations (point-plane, sphere-plane, coaxial-cylinder) together with those of the present investigation, are plotted against the gap nonuniformity  $f$ . Since critical pressures of negative voltage-pressure characteristics are always higher, results in this figure is only compiled from positive-voltage characteristics of radiated or nonirradiated gaps. The limiting transition boundary from corona-controlled breakdown to the direct breakdown regime can be represented in terms of gap nonuniformity by the following empirical relation

$$p = 0.063 f + 2.75 \text{ bar}$$

A similar transition is defined as a function of inner electrode radius in Fig.6.35(b) including both  $\text{SF}_6$  and  $\text{SF}_6/\text{N}_2$  mixtures for the present experimental conditions. In accordance with the findings in sphere-plane [155] and point-plane [97,160] gaps for  $\text{SF}_6$ , it is evident that the critical pressure varies inversely with the radius of the corona electrode. The gas-composition-independent behaviour of the critical pressure in the same gap (illustrated in Figure 6.16) seems to be a property of coaxial-electrode geometry that was not observed in point-plane gaps [97,160,220]. The proposed condition for direct-breakdown,  $(p_c r)_{\min} \geq 0.05 \text{ bar cm}$  in nonuniform fields [159] was also confirmed for the present experimental conditions (Figure 6.36). The lower limit in this figure is determined for different gap configurations by the similarity law.

In general, over the corona-controlled breakdown region, the maximum field strength in the gap decays with  $p.r$  and saturates at  $\sim 120 \text{ kV/cm}$  (Figure 6.37), although this limit for most of the electrode configurations differs depending upon the gap nonuniformity and the presence of irradiation.

c) Direct-breakdown region:

At pressures higher than  $p_c$ , breakdown follows the occurrence of the first streamer. The breakdown level is higher for the least nonuniform gaps and for mixtures with high  $SF_6$  concentration. Unlike point-plane gaps [220] the breakdown values are unaffected by the presence of an irradiation source, which is a characteristic of coaxial electrode gaps due to the large area of the stressed electrode. Although the breakdown level can be accurately predicted by using the methods proposed in Chapter 5, over a range of pressures in this region, at higher pressures, deviation from the estimated values starts. The pressure ( $p_d$ ) at the point of deviation increases with increasing gap nonuniformity and in mixtures with increasing partial-pressure ratio of  $SF_6$  (Table 6.1).

6.8.2 Factors affecting the voltage-pressure characteristics

The present results indicate that under dc voltage conditions the presence of a small amount of  $SF_6$  (~ 1%) in air or in nitrogen enhanced the positive or negative breakdown characteristics to a great extent over a range of pressures. The addition of 1.0%  $SF_6$  in air (Figure 6.25), for example, resulted in an increase of the breakdown maxima of air from 50 kV to 100 kV which is higher than that of pure  $SF_6$ . The critical pressures of mixtures, however, remained at the same value as that of air, which is considerably larger than that for  $SF_6$ . In the same gap, with 1%  $SF_6$  in nitrogen, the corona-free breakdown characteristic was modified to the form shown in Figure 6.26, but for this mixture the breakdown maximum is less than that of  $SF_6$ . It is interesting to note that the negative corona-controlled breakdown characteristics of both mixtures of air and nitrogen with 1%  $SF_6$  almost coincide and take values intermediate

between those of SF<sub>6</sub> and air (Figure 6.27).

This anomalous behaviour of both mixtures signifies increased spread of ionization around the inner electrode, and hence, an enhanced shielding effect of the space charge. This space charge is due to the yield of collisional ionization initiated by photoionization in the gas [172]. In SF<sub>6</sub>/N<sub>2</sub> mixtures, though no chemical interactions between SF<sub>6</sub> or its ions and nitrogen molecules are known to take place, enhanced dissociation of pure nitrogen with the presence of 1% SF<sub>6</sub> [225] could be suggested to contribute the space-charge stabilization by charge transfer or three body reactions or by causing reduction of ion mobilities. In addition, the decreased effective ionization coefficient of nitrogen could be counted as a possible process along with the other factors.

Although recently a few qualitative analyses were made of the behaviour of impulse voltage-pressure characteristics obtained in (0.01 - 1.0)% SF<sub>6</sub>/N<sub>2</sub> [171,172] and 1% SF<sub>6</sub> - air [167], the fundamental mechanisms involved in the processes still lack interpretation. It requires quantitative study of corona chemistry as well as basic gas processes.

Another interesting observation which provided a better insight into the role of stressed electrode during the processes of corona stabilization was the effects of conducting discs upon the behaviour of positive voltage-pressure characteristics of SF<sub>6</sub> (Figure 6.28) and of the 40% SF<sub>6</sub>/N<sub>2</sub> mixture (Figure 6.29). Although the presence of discs having diameters 3 or 8 times that of the inner electrode does not affect the rising part of the characteristics at low pressures, it appears that stabilization is slightly improved in SF<sub>6</sub> and unchanged in 40% SF<sub>6</sub>/N<sub>2</sub> mixture near to and beyond the

breakdown maxima. This suggests that predischARGE conditions leading to breakdown is still independent of field conditions at the inner electrode over this part of the characteristics and the space-charge field in the drift region is the dominating factor in determining the breakdown. Owing to change in the type of corona regime [97,158], the density of space-charge is probably reduced and, in turn, the length of the effective space-charge zone might shrink toward the inner electrode.

The presence of space-charge in the gap and its ionic constituents were substantiated in ion injection experiments. As shown in Figures 6.31 to 6.34, considerable reduction was obtained in breakdown levels of positive voltage-pressure characteristics of SF<sub>6</sub> (Figure 6.31) and negative voltage-pressure characteristics of 40% SF<sub>6</sub>/N<sub>2</sub> (Figure 6.34) when ions of opposite polarity to that of the stressed electrode were injected into the gap. The possible processes that could be accounted for in the reductions are: abated space-charge effect due to extensive neutralization, or ionization started in the midgap due to photons radiated from the charge exchange processes taking place at points close to ion injection rod, or both. Although the measured photon absorption coefficient in SF<sub>6</sub> and SF<sub>6</sub>/N<sub>2</sub> mixtures [226] favours the latter process, since the reduction in stabilization does not hold for every case, the mechanisms involved may be more complex than those suggested. It is sufficient to state that, with the present experimental evidence, both processes are likely to cause reductions. However, some photographic records of the phenomenon would be helpful to identify the effective mechanism.

### 6.8.3 Comparison of voltage-pressure characteristics of point-plane and coaxial-electrode gaps

Due to negligible diffusion, self-confined photoionization processes and multiple reflection of photons from the outer electrode, the stabilization process in coaxial geometry should be more pronounced compared to the point-plane gap. Here, a question arises concerning the conditions under which these two gaps should be compared, i.e. whether gap nonuniformity, gap separation or radius of the inner electrode should be taken as a constraint. In Figure 6.38, the voltage-pressure characteristic of a 10 mm rod-plane gap with 1.0 mm rod radius is compared with the characteristics of 0.25/12.7 and 0.5/25 mm coaxial gaps in SF<sub>6</sub>. All three gaps have the same non-uniformity factor of ~7.5. The stabilization of the coaxial-electrode gap with the large outer electrode is superior to that of point-plane gap. This means that under the same dimensional conditions, as expected, the coaxial-electrode gap will yield more stabilization. It is interesting to notice that, although the rod diameter of the point-plane gap is the largest, its corona inception level is the same as that of the  $r_1/r_2 = 0.25/12.7$  mm gap and considerably less than that of the 0.5/25 mm gap, despite its having the same gap nonuniformity factor.

The enhanced stabilization with increasing radius of the outer electrode suggests again the importance of gap separation in both gaps for the sustenance of the stabilization process rather than the gap divergence.

### 6.9 Conclusion

The qualitative studies of dc and impulse breakdown behaviour of coaxial-electrode gaps in SF<sub>6</sub> and SF<sub>6</sub>/N<sub>2</sub> mixtures in

the pressure range 0-8 bar revealed the following experimental facts.

1. The rising parts of dc voltage-pressure characteristics for the same outer electrode is independent of radius of inner electrode and polarity of the gap. The breakdown voltage measurements are highly reproducible. The impulse breakdown voltages lie slightly above the dc ones and the polarity-independent property is not valid.

The steepness increases as the radius of the outer electrode, or in mixtures as the ratio of SF<sub>6</sub> content, is increased.

2. In the negative-slope region of voltage-pressure characteristics the measurements are still reasonably reproducible in contrast to observations in rod-plane geometry.

3. Voltage values at the part of characteristic lying in between the pressure minimum and the critical pressure remains unchanged in most cases with increasing pressure. The variation of the minimum voltage, unlike the point-plane gap case, does not show any regular dependence upon gap nonuniformity or inner electrode radius.

For a given gap nonuniformity, the critical pressure remains unchanged and the corresponding voltage increases with increasing partial pressure of SF<sub>6</sub> in the mixture. Also, for the same inner electrode, both critical pressure decreases and the critical voltage increases with increasing the outer electrode radius. In SF<sub>6</sub> the minimal limit for the critical field strength  $E/p_c$  varies inversely with  $\sqrt{p_c r}$ . The minimum pressure and inner electrode-radius condition for corona-free breakdown in extremely nonuniform field gaps is determined by  $p_c r < 0.05$  bar.cm. In negative-polarity gaps, the critical pressure and voltage are always higher as compared

to those obtained in the positive-polarity gaps. The dc critical pressure of a gap is the same as that for impulse conditions.

4. The corona inception and/or direct breakdown voltage levels can be predicted reasonably well by the streamer criterion. The pressure at which the deviation from the similarity law occurs gets larger as the radius of the inner electrode decreases, i.e. as the electrode area decreases.

5. The process of corona stabilization is more pronounced with dc voltage than with impulse voltage. For the same gap, the voltage maximum increases and the corresponding pressure decreases with increasing SF<sub>6</sub> concentration. However, the case of pure SF<sub>6</sub> is an exception to this.

6. Stabilization is more extensive in coaxial-electrode gap with large outer electrode than in a point-plane gap for equal nonuniformities.

CORONA CHARACTERISTICS AND CORONA STABILIZATION PROCESSIN SF<sub>6</sub> AND SF<sub>6</sub>-N<sub>2</sub> MIXTURES7.1 Introduction

In view of the practical applications of compressed SF<sub>6</sub>, the corona discharges occurring at extreme microinhomogeneities (e.g. around particles or sharp protrusions) and, in particular, the space-charge supported corona-stabilization process have become the subject of many recent investigations. Although a considerable amount of qualitative information has been obtained with positive polarity dc and impulse voltages, there exists still some difficulties for a quantitative description of the phenomena because of the dearth of data on some gas-swarm parameters and uncertainties arising in applying low-pressure data at high pressures.

Corona in SF<sub>6</sub> and SF<sub>6</sub>-N<sub>2</sub> mixtures appears primarily to be pulsative over a range of pressures for both positive and negative polarity. In earlier investigations, attempts had been made to observe the phenomena electrically and optically; recently, some new investigations have been undertaken to characterize corona discharges as a function of electrode configuration, gas pressure and polarity in short and long gaps by using high speed photographic techniques in addition to electrical and optical means [97,158,171,228,233]. Also there have been some attempts to determine the optical spectra, intensity distribution and correlation with simultaneously observed electric pulse in SF<sub>6</sub> and SF<sub>6</sub>/N<sub>2</sub> mixtures [237]. The salient points derived from these investigations are:

### Positive-polarity corona characteristics

- (1) At pressures below  $p_c$ , the corona starts initially as low level avalanche activity then develops into randomly appearing streamer - pulse activity [97, 158, 162].
- (2) Over the rising part of the voltage-pressure characteristics at very low pressures ( $< 0.2$  bar), a diffuse glow-like discharge appears and covers the corona-active electrode as the gap voltage is increased [97]. It consists of current pulses occurring in "bursts" of up to a few milliseconds. In  $SF_6/N_2$  mixtures, the glow becomes more diffuse and homogeneous and occupies a wider pressure with reducing  $SF_6$  concentration [227].
- (3) At slightly higher pressures, the diffuse discharge is replaced by a more filamentary discharge. The current pulse activity again appears as a burst of streamer-type pulses, the first pulse in the chain being somewhat larger than the succeeding ones [97, 98]. Bursts appear at random repetition rates and the average pulse level and the average time duration of the growth phase increase with increasing gap voltage [158]. The corona consists of distinct discharges which are distributed over the stressed electrode, and it has been shown [98] that each 'burst' of current pulses is associated with the restriking of one of these filaments. Further increase of the voltage resulted in the appearance of continuous discharge activity. The waveform associated with this activity appears to be similar to that of the burst of pulses after the growth phase [158]. The structure of the pulse activity appears to be dependent on the  $SF_6$  concentration in  $SF_6/N_2$  mixtures [98]. Breakdown follows the appearance of a streamer capable of penetrating the low field barrier. The spark develops axially out of this corona through the

space charge region [155, 158, 220].

(4) At and beyond the breakdown maximum ( $> p_m$ ), the discharge still comprises the bursts of current pulses, but the activity, this time, is characterized by the appearance of a large current pulse-breakdown streamer [97, 98] at the start of each current burst. At pressures close to  $p_c$ , the continuous spatially-restricted discharge disappears, and only large infrequent discharge pulses occur. In highly divergent fields this phase corresponds to that at which the breakdown voltage is suddenly reduced to a minimum. The corona inception voltage coincides to the breakdown voltage at pressure slightly above this pressure [97]. At  $p_m$  and over a part of the downcurved part of the characteristic the curved spark trajectories are replaced by the axial ones at pressures near to  $p_c$  [158].

#### Negative polarity corona characteristics

(1) At very low pressures ( $\sim 0.2$  bar), the current bursts consist of a chain of regular pulses at a frequency of up to  $\sim 100$  kHz.

(2) At higher pressures ( $p < p_m$ ), the current is intermittent at first with burst of current pulses, then with increasing gap voltage the burst duration is reduced and the discharge becomes continuous. Except at very low pressures, in  $SF_6$ , there appears to be no Trichel-like pulse activity [162, 227].

In  $SF_6/N_2$  mixtures, at voltages slightly above the corona onset transition to a continuous discharge occurs, so that the corona burst and the continuous corona appears as intermittent and steady flow discharge respectively. At low pressure, also an incipient onset pulse is followed by pulses similar to Trichel corona in air, having a constant amplitude and a regular frequency of  $\sim 20$  kHz.

The frequency increases with increasing the voltage [227].

For the development of the various forms of corona discharges in  $\text{SF}_6$  and  $\text{SF}_6/\text{N}_2$  mixtures, two factors are of most importance; the absorption of photons in the gas or at the cathode (major secondary mechanism for negative polarity discharges), and the distribution of space charges in the gap. The data on the absorption coefficients of  $\text{N}_2$ ,  $\text{SF}_6$  and their mixtures is very scarce, and is obtained under low field and pressure conditions. Over a radiation spectrum of wavelengths ranging between 800 - 1800Å the measured absorption coefficients were found to be, for  $\text{N}_2$  [229,230] between 0 - 1.3  $\text{mm}^{-1}$  and for  $\text{SF}_6$  [229] between 0.06 - 24  $\text{mm}^{-1}$ . The absorption coefficients of  $\text{SF}_6/\text{N}_2$  mixtures with 10% and 20%  $\text{SF}_6$  were also measured for the same radiation frequencies [226]. It was observed that the absorption coefficients increase with increasing  $\text{SF}_6$  content. It lies between 0.6 - 4.55  $\text{mm}^{-1}$  for 10%  $\text{SF}_6/\text{N}_2$  and between 3.5 - 14.8  $\text{mm}^{-1}$ .

Although some attempts have been made to estimate the space charge field through the gap and to measure the space-charge-induced field on the plane of a point-plane gap in  $\text{SF}_6$  under dc conditions for short gaps [98] and under impulse conditions for long gaps [175,176], the role of gap field modified by the space charge for corona stabilization is not yet well understood.

In the present work, corona discharge phenomena were studied in  $\text{SF}_6$  and 40%  $\text{SF}_6/\text{N}_2$  mixture, with the spatial growth of the discharge being observed using an image intensifier and the discharge currents recorded for different gas pressure and field conditions. The space-charge field was measured at the outer electrode and was correlated with the estimated one. The effect of space-charge on .

different modes of corona discharge was examined. In addition, the results of the field measurements were used to calculate ion mobilities in proximity to the outer electrodes.

## 7.2 Experimental Conditions

The visual appearance of the corona phenomena were recorded using an image intensifier camera as shown in Figure 2.10 (see section 2.6 for further details). In order to fix the location of the discharge and thus to facilitate focusing, a 1 mm thick disc 4 mm in radius was placed on the inner electrode 8 cm from the view side of the electrode. Since, as was explained in section 6.7.2, the presence of the conducting disc, in contrast to expectation, did not cause any change in stabilization, the visual records of the discharge from the disc should be comparable with the actual phenomena taking place in the vicinity of the inner electrode. The corresponding space-charge displacement and its magnitude through the gap was recorded by using the circuit given in Figure 2.5.

The measurement of field at the collector (outer electrode) boundary was made employing a biased static probe described by Tassicker [231] and later developed by Selim and Waters [221]; the details of the probe and its connecting circuit are given in Figure 7.1. The calibration and the application of the probe for current density and field measurement at the outer conductor, and hence the method for estimating the mobilities, will be dealt with in later sections. No disc was present for these measurements.

## 7.3 The Role of the Coaxial Electrode Configuration in Corona Studies

Although the corona discharge phenomena are more clearly

observable in asymmetrical systems such as point-plane, confocal paraboloids, sphere-plane, etc. because of its axial symmetrical property, the coaxial cylinder configuration allows calculation of the space-charge distortion introduced during the discharge. In other geometries, after the first discharge threshold, the gap field is almost impossible to calculate correctly owing to the presence of space charge.

There are also differences in corona manifestations between the asymmetrical gaps and the coaxial-cylindrical configuration. In the point type geometries, since the discharge is concentrated in a small local region, one has the advantage to observe and to study the phenomena more easily. In addition, certain effects are intensified more, so that some gas discharge mechanisms are more easily recognised. In coaxial-electrode gaps the discharge can start at any point along the inner electrode, and can spread radially and laterally. If the diameter of the outer electrode is not large enough, it contributes to the discharge by reflecting photons. Also, due to its confined geometry, it has the advantage of conserving the space-charge. However, this property has the disadvantage of allowing less ventilation causing some chemical reactions [24] to occur. By employing a disc on the central conductor the discharge is considerably intensified without disturbing the influence of the space charge on the phenomena. By circulating the gas with a small electric-motor-driven propeller, the effect of heating was partly eliminated.

#### 7.4 Corona Characteristics in Positive-Inner Coaxial-Electrode Gaps

Prebreakdown discharge development in SF<sub>6</sub> and in a 40% .

SF<sub>6</sub>/N<sub>2</sub> mixture was examined by obtaining still photographs of the spatial appearance of the discharge and the current pulse waveforms for varying pressure and voltage conditions. Shutter speeds in the range 1/2 - 1/125 sec. were used and the current was recorded using a 1 MHz bandwidth system.

#### 7.4.1 SF<sub>6</sub>

The records of prebreakdown discharge activity were taken at the positions given in Figure 7.2. and are illustrated in the sequence of records shown in Figures 7.2 (i) to 7.2 (v). In Figure 7.2 the inception level of sustained corona is also delineated.

At low pressures ( $p \leq 0.2$  bar), at voltages near corona inception and slightly above it, the discharge starts with a glow-like luminous phenomenon which envelops the disc homogeneously (Figure 7(i) - Frame (A)). The current oscillograms indicate low level avalanches or streamer pulses superimposed on a continuous dc level. At higher voltages, the discharge becomes slightly more intense, appearing at random on the perimeter of the disc superimposed on the diffused discharge (Frame (B) and (C)). The small current pulse activity disappears and is replaced by a sustained succession of streamers.

Over the rising part of the curve, increasing the pressure results in separately emerging constricted and intense discharges at the inception level (Figure 7(ii) - Frame (D)). Their rate of occurrence increases with increasing voltage and their lengths are spatially limited to the vicinity of the disc. At slightly higher voltages (Frame (E) and (F)) the presence of a diffuse discharge is still noticeable. The associated current pulses are intermittent,

consisting of packets of pulses whose amplitude go through several sequential phases. These phases are illustrated in the current oscillograms of Frame (D). Each 'burst' exhibits a growth-phase, lasts 100 - 300  $\mu$ sec, and undergoes a sudden extinction. The individual pulses of the burst sequence are superimposed on a dc level and their magnitudes and duration varies from pulse to pulse. The burst of pulses appear randomly and their repetition rate and average pulse level increases with increasing voltage.

At, and slightly beyond, the peak of the curve, the discharge at the corona inception voltage and above it is similar to those of the cases given in the previous figure (Frames (G), (H) and (J) of Figure 7.2(iii)), but the streamer activity seems to be more frequent and to occur more closely to the perimeter (compare Frames (F) and (J)). Further, the sequence of pulses in the current waveforms displays a decaying phase and a continuous dc component after being extinguished. A new burst activity is initiated by a large streamer pulse which is followed by pulses with slightly reduced amplitude. As the voltage is increased the rate of occurrence of current, bursts and of the streamer pulses comprising them, is increased.

Over the negative slope part of the curve, a new type of discharge appears which extends a considerable distance into the gap and which becomes more filamentary in appearance (Figure 7.2(iv)). This behaviour was also reported for ac corona in point-plane gaps by Farish and Ibrahim [98] who identified the long, off-axis discharge with a leader discharge. The present author considers that there is insufficient evidence to show the occurrence of the leader in such short gaps in SF<sub>6</sub>, and in the present work the term 'breakdown

streamer' will be used to describe these discharges. The burst of pulses in this pressure range is initiated with a very large pulse which probably corresponds to one of these filamentary breakdown streamers. As the voltage is increased above inception, the filamentary discharges become more vigorous and extend more into the gap. The average value of the current burst increases and a new burst activity can recur in the middle of another burst (Figure 7.2(iv) - Frame (M)). At higher voltages, streamers and filamentary discharges merge in time and space such that the discharge appears as a continuously luminous phenomenon (Frame (N)).

Towards the end of the corona-controlled breakdown regime, the discharge activity becomes more filamentary and isolated (Frame (O) of Figure 7.2(v)), and extends more into the gap as the voltage is increased. The associated current waveforms are intermittently appearing bursts of pulses whose average value increases with voltage (Frame (P)).

#### 7.4.2 SF<sub>6</sub>/N<sub>2</sub> Mixture

In the description of the corona discharge phenomena in 40% SF<sub>6</sub>/N<sub>2</sub>, the observations are made at the points of the voltage-pressure characteristic given in Figure 7.3. In the same figure onset levels for single pulses and for sustained corona discharge are also depicted. The illustrations of the discharge phenomenon for various voltage and pressure combinations are given in Figures 7.3(i) to 7.3(v).

Over the rising part of the characteristic, at low pressures ( $\leq 0.3$  bar), similar to the case of SF<sub>6</sub>, the discharge consists of a diffused glow-like phenomenon with concurrent luminous abortive

discharge channels, Frame (A) in Figure 7.3(i). The current waveforms of this discharge activity is a sequence of streamer pulses superimposed on a constant dc component. The dc component is probably associated with the continuous glow discharge. At higher voltages the discharge channels extend into the gap further and their roots on the perimeter become brighter (Frame (B)). Near to the breakdown voltage, the glow becomes more diffuse and less bright. The channels shrink in length and localized discharge spots appear on the perimeter. Breakdown takes place from one of these spots (Frame (C)). At higher pressures over the rising part of the characteristics, although the glow discharge is still present, it is less extensive as compared to the low-pressure case. The concurrent discharge channels become more filamentary. The current waveforms indicate the formation of a succession of lower amplitude 'secondary' streamers in addition to the irregular large streamer activity (Frame (D) in Figure 7.3(ii)). As the voltage is increased gradually, the streamer growth becomes more pronounced and yet is spatially restricted. Also, the number of streamers to the disc increases (Frames (E) and (F)).

At pressures near to  $p_m$ , although the glow discharge is still noticeable in the image intensifier records together with constricted streamer channels (Frame (G) in Figure 7.3(iii)), it is not as luminous as that observed at low pressures. The secondary streamer current activity noticed at 0.8 bar (Frame (D)) is not present in this case. However, primary streamer activity becomes more frequent. With increasing voltage, the number of streamer channels developing out of the perimeter of the disc increases and their lengths stay almost unchanged (Frames (H), (J) and (K)).

Over the negative-slope region of the curve ( $p > 1.5$  bar) the discharge has the same spatial appearance but the streamer channels become more filamentary. Their number increases with increasing voltage. Although there is a small dc offset current at voltages slightly above the corona inception level, it disappears as the voltage is increased above the corona sustained voltage (see Figure 7.3). Moreover, the isolated current pulse activity of previous phases is replaced by intermittently appearing bursts of pulses as the voltage is increased from the inception level (Frame (M)). Each burst comprises a succession of streamers. The rate of occurrence and the average value of bursts increases with the applied voltage.

Close to the critical pressure, a transition to a new discharge regime takes place; the restricted filamentary streamers extend into the gap considerably with glaring brush-like terminations. Along a propagation channel two or more of these luminous phenomena may appear either branched or unbranched (Frame (P) and (Q) of Figure 7.3(v)). The corresponding current pulse activity comprises only successive burst pulse activity whose average value and repetition rate increase with voltage.

## 7.5 Corona Characteristics in Negative-inner-coaxial Electrode Gaps

Because of experimental limitations, the discharge phenomena were recorded only over the rising part of the characteristics at points shown in Figure 7.4 for  $\text{SF}_6$  and in Figure 7.5 for 40%  $\text{SF}_6/\text{N}_2$  mixture. In the same figures, the inception levels of both single pulse and sustained corona discharge activities are also shown. The details of the observations are given in the following

sections.

### 7.5.1 SF<sub>6</sub>

At low pressure, the corona starts as a succession of blurred and isolated luminous spots at the boundary of the disc: each corresponds to a streamer current pulse of 2-3  $\mu$ sec in duration at random repetition rate (Frame  $\textcircled{A}$  in Figure 7.4(i)). As the voltage is increased, these spots become more frequent and merge in space, and near breakdown a glow-like luminosity is observed.

With increasing pressure, although the spatial displacement of the spots is maintained, they become brighter (Frame  $\textcircled{D}$  in Figure 7.4(ii)). In the accompanying current oscillograms, in addition to the primary streamers, low level secondary streamers appear in succession. It is interesting to notice that in the millisecond-time-scale oscillograms of Frame  $\textcircled{D}$  the primary streamers exhibit regular variations having frequency of  $\sim 120$  MHz. At higher voltages, the only conspicuous change is the increase in the number of localized discharge spots around the perimeter (Frames  $\textcircled{E}$  and  $\textcircled{F}$ ) and subsequently an increased rate of occurrence of primary and secondary streamers.

At  $p = 1.6$  bar, apart from the slightly intensified luminous spots, the intermittent burst activity shown in the current oscillograms of Frame  $\textcircled{G}$  and  $\textcircled{H}$  of Figure 7.4(iii) is the only additional noticeable change in this phase of the corona. The dc component of the burst changes from pulse to pulse and it can appear in series with primary streamer over a range of voltages. The streamer-burst activities become very irregular in magnitude and frequency as the voltage is increased gradually (Frame  $\textcircled{H}$ ).

### 7.5.2 SF<sub>6</sub>/N<sub>2</sub> Mixture (40% SF<sub>6</sub>/N<sub>2</sub>)

Generally, the luminous manifestations of the corona discharge have the same appearance as those observed in SF<sub>6</sub>. However, the discharge is more constricted and brighter (compare Frames (A) and (B) of Figure 7.4(i) with Frames (B) and (C) of Figure 7.5(i)). The current-pulse oscillograms show more regular streamer pulse activity for pressures  $\leq 1.0$  bar (Figure 7.5 (i) and 7.5(ii)) and regular streamer-burst pulse activity at higher pressures (Figure 7.5 (iii)).

### 7.6 Current-Voltage Relation in SF<sub>6</sub> and SF<sub>6</sub>/N<sub>2</sub> Mixtures

The space-charge controlled current measurements was carried out in SF<sub>6</sub> and in a 40% SF<sub>6</sub>/N<sub>2</sub> mixture to determine the relation between the gas pressure, the magnitude of the corona current and the applied voltage. The current measurements were recorded by using a digital voltmeter or an XY-recorder connected across a 1 K resistor in series with the  $r_1/r_2 = 0.5/25$  mm gap (see Figure 2.5).

#### SF<sub>6</sub>

The average corona current variations with voltage for several gas pressures are shown for positive polarity in Figure 7.6 and for negative polarity in Figure 7.7. A comparison of the characteristics for the effect of polarity is given in Figure 7.8. In both figures the voltage levels for sustained corona and breakdown are also indicated.

Generally, for both polarities the characteristics exhibit similar variations; in that the slopes are steeper at low pressures and gradually decrease at high pressures. The current at any given voltage reduced with increasing pressure. At pressures over the

rising part of the related voltage pressure characteristics, current-voltage hysteresis was noted, although it is shown only for one pressure in Figure 7.7. At high pressures this effect was negligible. Another point of interest is that, over a pressure range up to  $\sim 0.8$  bar, positive and negative I - V characteristics coincide, as is shown in Figure 7.8.

The distribution of equal current lines over the stabilization region for both positive and negative voltage-pressure characteristics are illustrated in Figures 7.9 and 7.10 respectively. Since the stabilizing characteristic of the drift region is more pronounced over the rising part of the curve, the space charge or the associated current lines as is expected are higher in this pressure range. Although the stabilization region is greater for negative polarity than for positive, it should be noted that, at a given voltage and pressure, the corona current, and hence the energy input to the gap, is the same for either polarity. With the data supplied in Figures 7.9 and 7.10, the gap field may be estimated easily in order that more information may be extracted for modelling the ion behaviour in the drift region or the propagation processes leading to breakdown.

#### SF<sub>6</sub>/N<sub>2</sub> Mixtures

In Figures 7.11 and 7.12 the current-voltage characteristics of 40% SF<sub>6</sub>/N<sub>2</sub> mixture as a function of gas pressure are illustrated for positive and negative polarities respectively. The sharp increase in current magnitudes with voltage at low pressures decreases slightly at high pressures (a similar behaviour to that observed for SF<sub>6</sub>). A comparison between the positive and negative I - V characteristics up to 1.8 bar is illustrated in

Figure 7.13. The small differences at high pressures decrease as the pressure is reduced to subatmospheric. In this pressure range, as one can easily perceive, the positive voltage-pressure characteristics given (in Figure 7.14 for the positive polarity and in Figure 7.15 for the negative polarity) rise linearly, independent of the radius of the inner conductor. In these latter figures the distribution of the constant current lines are also shown. Comparing the related current lines at the same pressures, before breakdown is reached, larger current values can be achieved in the case of positive polarity.

As a final remark, although the average value of current corresponds to the total current collected at the outer electrode, one should be cautious while using the results illustrated here, since the effective length of the inner electrode is varying, dependent on the pressure and the voltage. In the coming sections, a more accurate technique will be illustrated.

## 7.7 Space-Charge Induced Field Measurements at the Outer Electrode

### 7.7.1 Probe characteristics

In nonuniform field gaps when the corona discharge occurs the field distribution in the mid-gap and around the most stressed electrode may be altered from the Laplacian field. In attaching gases the parabolic increase in current with voltage (Equation 1.23) and the different modes of discharge observed at different pressures, are due to the self-regulating influence of the space-charge field. The knowledge of the field at any boundary of the corona gap affords an analytic solution for the field distribution in the gap.

In SF<sub>6</sub>, it was pointed out [159] that the field strength in the drift region is definitive for determining the breakdown, rather than the field at the electrode in corona, and the minimum value of this field in the point-plane gap was estimated [98] to have values between 39 and 47 kV/cm, depending on the pressure.

In this section, the application of the static-field probe introduced by Tassicker [231] and developed by Selim and Waters [221] for the measurement of the field at the outer electrode will be described. The probe also makes it possible to measure; (i) the current density at the outer electrode, (ii) ionic mobility and (iii) the spatial potential distribution.

Figures 7.1(a) and 7.1(b) show the probe assembly and biasing and measuring circuits. The bias voltage is applied to the probe as in the original version, i.e. the power supply is connected to the probe via an ammeter. The variation of the normalized current ( $I/I_0$ ) as a function of the boundary field ( $E_0$ ), determined according to the method suggested in [221], is shown in Figure 7.17. In the same figure the positive-corona current measured at several bias voltages, in the gap with  $r_1/r_2 = 0.5/25$  mm filled with air at atmospheric pressure, is also depicted. All the points except those on the  $\mp 200$ V bias curves lie in line, thus verifying the correct operation of the probe in a limited range of probe-bias voltage. The slight deviation at  $\mp 200$  V implies the start of nonlinearity in the probe characteristics from those estimates of Selim and Waters, and of Tassicker, as illustrated in Figure 7.18. The bias voltage was therefore limited to  $\mp 150$  V. The fluctuation in ammeter reading was damped using an integrating capacitor (0.1  $\mu$ F) connected across it.

### 7.7.2 Field measurements in SF<sub>6</sub>

The electric field measurements obtained for both positive and negative corona voltages for pressures up to 1 bar are shown in Figures 7.19 and 7.20. Each point corresponds to a mean of 8 test results achieved at several bias voltages.

For both polarities, the field at the outer electrode increases linearly with increasing gap voltage. For a given gap voltage, the field is higher at low pressures. The comparison of positive and negative field strengths at the outer electrode is given in Figure 7.2.1. Generally, the negative field strength characteristics lie below their positive counterparts.

The characteristics in SF<sub>6</sub>/N<sub>2</sub> mixtures are expected to resemble those of SF<sub>6</sub> so that the field strength should increase with increasing the partial pressure of SF<sub>6</sub>. However, the lengthy procedure for extracting field strengths results from the probe measurements has not been carried out.

### 7.8 Determination of Ion Mobilities in SF<sub>6</sub>

The electric field in the interelectrode gap in the presence of ionic space charge is described by the well-known field relation under the steady-state conditions

$$\bar{\nabla} \cdot \bar{E} = \frac{\rho}{\epsilon_0} \quad (7.2)$$

The solution of this equation together with the current density equation  $j = \mu \rho \bar{E}$  in coaxial electrode geometry yields the following approximate relation (see Appendix 5).

$$E = \left[ \frac{j r}{\epsilon_0 \mu} \right]^{1/2} \quad (7.3)$$

where  $j$  is the current density and  $\mu$  is the ionic mobility. This equation allows one to estimate positive and negative ion mobilities if the current density and the local electric field at the collector surface are measurable. The field data given in Figures 7.19 and 7.20, together with the zero-bias-voltage probe-current measurements, yield the ion mobilities, as shown for  $V_c = 40$  kV in Figure 7.22. Although the results in this figure are obtained for the same corona voltage, it would be more correct to illustrate the results for the same field conditions, due to the known slight field-dependent nature of ion mobilities. This inference is confirmed in Figure 7.23. At 0.4 bar, both mobilities exhibit considerable dependence on the field.

Ion mobilities extracted from Figures 7.19 and 7.20 for the field strengths in the range 8 - 12 kV/cm are demonstrated in Figure 7.24. Although mobilities in this field range may be represented as varying with pressure, as  $\mu_{\pm} \propto p^{-2.25}$ , at other field strengths, a slight variation in the exponent of the pressure is expected.

## 7.9 Estimation of Gap Field Distribution with Space Charge

In attaching gases, the influence of the space charge on the development of the corona discharge and on the subsequent stabilization in the enclosing space of the stressed electrode is well known. In an early work, the analytic solution (Equation 1.23) of the ionic field was illustrated by Townsend [12] for the coaxial-electrode system under steady state conditions. The solution depends on the symmetry of the geometry and several rigorous assumptions [24]. Although a similar solution suits the purpose of the present work, the estimation for the ionic space charge can

be done more accurately with an iterative computational procedure. This is due to the difficulties of obtaining accurate current readings and the field life-time dependent nature of ionic mobilities [242], and the assumption of constant ion densities.

In the present iterative technique [241], the solution is liable to the following assumptions only; the electric field at the surface of the electrode in corona remains constant at the onset level and concurrent with this the thickness of the ionization zone is negligible. The amount of reduction in air in the corona onset voltage was measured [243] as 15% and 30% for positive and negative coronas respectively. The error caused by this assumption is quoted [241] to be in the order of 0.5 - 2%. Although a few theoretical attempts have been made [244, 245] to include the variations in  $V_0$ , as yet no satisfactory solution is available. The boundary field measurements illustrated in the next section, however, show that the error in the estimated results with this assumption remains safely within the experimental one.

The iterative numerical procedure requires simultaneous solution of Poisson's equation

$$-\bar{\nabla} \cdot \bar{\nabla} \phi = \frac{\rho}{\epsilon_0} \quad (7.4)$$

and the continuity equation

$$\bar{\nabla} (\rho \bar{\nabla} \phi) = 0 \quad (7.5)$$

with the boundary conditions; (i) the space charge density at the corona sheet is taken as the value  $\rho_e$  at the electrode, (ii) the surface potential of the inner electrode is  $V$ , and (iii) the potential of the outer electrode is zero.

The details of the derivation and related algorithm are given in Appendix 5.

A typical illustration of the potential, field and space charge density functions estimated for the gap  $r_1/r_2 = 0.05/2.5$  cm in  $\text{SF}_6$  for pressures 0.2 and 0.6 bar is shown in Figure 7.25. It is important to note that the gap field distribution remains almost constant after a distance  $10r_1$  and its level increases with pressure.

#### 7.9.1 Comparison of experimental data with estimated results

In Figure 7.26 the estimated field distributions are compared with the measurements obtained with the boundary biased-field probe for several values of gap voltage. The other particulars are given in the legend of the figure. The measured boundary field at breakdown is obtained by extrapolation of the field measurements made at various gap voltages. Except at breakdown, excellent agreement is achieved.

Further comparisons are given in Figures 7.19 and 7.20 for positive and negative corona voltages respectively. In both figures the deviation starts at pressures above atmospheric, although the agreement is still within the experimental error. For positive polarity, the pressure ( $p = 1$  bar) at which the deviation occurs, corresponds to  $p_m$  of the voltage pressure characteristic, whereas it is over the rising part of the characteristic for negative polarity.

For various inner electrode radii, the calculated boundary fields or minimum gap fields as a function of the pressure is shown in Figure 7.27. Up to the pressures marked with arrows, the characteristics exhibit almost no variation with pressure and  $(E/p)_{\min}$  increases slightly with the inner electrode radius. The pressures at these turning points correspond to pressures at which .

deviation from the linearity of the voltage-pressure characteristics over the rising parts start. For the gap having the smallest electrode radius  $(0.015\text{cm})(E/p)_{\min}$  does not exhibit any considerable change up to 1 bar, since the deviation from linearity sets in at about 1.3 bar (see Figure 6.7).

#### 7.10 Model Approach for the Prediction of Critical Pressure

Since corona-free conditions are required for the operation of gas insulated high voltage equipment, it is therefore necessary to predict the upper pressure limit for corona-free operation for worst nonuniformities present in the system. This critical pressure limit, as was explained in Chapter 6, is a function of the type of the gas, the voltage polarity and the geometric parameters. For the same gap nonuniformity,  $p_c$  is always higher in the case of negative polarity. However, since the insulation level is determined largely by the positive-dc and impulse-voltage performance, most of the previous theoretical attempts [158,160,176,250] in  $\text{SF}_6$  to predict  $p_c$  were undertaken for positive polarity.

In the present work, image-intensifier and current-pulse studies in  $\text{SF}_6$  have revealed the fact that the critical pressure is approached with extensive streamer discharge activity. At the critical pressure, it can be inferred that any initiating streamer from the active electrode is expected to cross the gap and lead to breakdown. Any model approach should therefore fulfil these two requirements of streamer initiation and propagation.

In the present model approach, the simple streamer criterion [100] and the growth model suggested for air by Gallimberti [251] have been used. The simplified model adapted

for the iterative procedure is shown in Figure 7.28. For convenience in numerical computations only, the secondary avalanche axial to the streamer is considered.

After the streamer is launched into the gap, the propagation is maintained if each avalanche initiated within the active region will have a number of ion pairs equal to  $N_1 = N_{\text{crit}}$ . The continuation of the streamer growth at any instant is determined by the resultant electric field and the probability of obtaining photoelectrons in the right place within the active region. If the field conditions are favourable and if the photoionizing mean path ( $\mu_p^{-1}$ ) becomes comparable to the critical avalanche formation length, the streamer develops to breakdown.

If the space charge distortion of the developing avalanche on the resultant field at the point P in Figure 7.28 is assumed to be less as compared to the geometric field ( $E_g$ ) and to the field of the developing streamer head ( $E_s$ ), the field at the point P(r) is

$$E(r) = E_g(r) + E_s(r) \quad (7.6)$$

where r is measured from the axis of the coaxial electrode.

If the space charge field of the positive ions is assumed to be contained in a spherical volume of radius  $R_0$  and situated at distance  $R_x$  from the electrode axis, then

$$E(r) = \frac{V}{r \ln \frac{r_2}{r_1}} + \frac{e N_0}{4\pi E (r - R_x)^2} \quad (7.7)$$

for  $r > R_x$ ,

where V is the potential difference across the gap and e is the electronic charge.

As the avalanche drifts distance x under the

influence of the resultant field toward the tip of the streamer, it will have the radius [24]

$$R_a = \sqrt{6 D_e / v_e} \quad (\text{cm}) \quad (7.8)$$

where  $D_e$  is the electron diffusion coefficient and  $v_e$  is the electron drift velocity.

In  $\text{SF}_6$  [252],

$$v_e = (0.03 \frac{E}{p} - 1.64)^{107} \quad (\text{cm/sec}) \quad (7.9)$$

where  $E$  and  $p$  have the dimensions of (V/cm) and (bar) respectively, and

$$D_e = 1240 \quad (\text{cm}^2/\text{sec})$$

In order for the streamer to develop, the conditions

$$\begin{aligned} x &= x_c \\ x_c &= \mu_p^{-1} \\ R_a &= R_o \end{aligned} \quad (7.10)$$

must be satisfied throughout its growth phase. Therefore, in any iterative computational procedure, the length of the avalanche initiated at the distance  $x_c$  where  $\bar{\alpha} = 0$  must be checked against the photoabsorption mean free path (see Appendix A5.3) for the computational algorithm).

In uniform field gaps, streamer propagation is possible at low applied field because of the effect of its own field[16,24, 255]; in nonuniform fields the condition for the propagation would be achieved if the initial resultant field is maintained throughout the gap. Consequently, in the present model approach, any solution for  $R_x > r_1$  yields a description of an isolated streamer in corona discharge mode and corresponds to the negative-slope region of the voltage-pressure characteristic. At the critical pressure,

breakdown is assumed to occur if, when the applied voltage reaches the inception level,  $R_x = R_a$  (i.e. the spherical positive space charge is touching the axis of symmetry).

The accuracy of the solution depends upon the value of the photoabsorption coefficient  $\mu_p$ . Unfortunately, the available data is scarce and is conflicting. As referred to atmospheric pressure, Blair et al [229] reported a value of  $246.6 \pm 5.4 \text{ cm}^{-1}$  using a monochromator technique, but in their measurements the photoionizing component of radiation ( $< 780 \text{ \AA}$ ) were absent. In their current-pulse analysis Crichton et al [253] found absorption coefficients in the ranges  $10.3 \pm 1.4 \text{ cm}^{-1}$ , and  $17.3 \pm 1.6$ , while Alexandrov [254] quoted  $6 \text{ cm}^{-1}$ . The value of the photoabsorption coefficient used in the present work is taken to be  $6 \text{ cm}^{-1}$ .

By defining the length of the active region at critical pressure by  $x_{cc}$ , the effect of the position of the streamer head at the inception voltage on the critical length with respect to the photoabsorption length as a function of pressure is shown in Figure 7.29. The crossing point of  $x_{cc}$  and  $\mu_p^{-1}$  curves corresponds to the critical pressure. In order to have breakdown for  $R_x = 0.1 \text{ cm}$  (i.e. at  $2r_1$ ), the voltage applied to the gap should be increased such that  $x_c$  characteristic at breakdown will cross the  $\mu_p^{-1}$  curve.

Estimated results according to the present model show good agreement with the measurements in  $r_1/r_2 = 0.05/2.5 \text{ cm}$  and  $0.025/1.27 \text{ cm}$  gap as is illustrated in Figure 7.30.

## 7.11 Discussion

### 7.11.1 Positive corona characteristics

Over the corona-controlled breakdown regime, at the

inception level, the corona discharge starts with anode-directed avalanches which are initiated by electrons produced from the detachment of negative ions. At voltages above the inception level, several possibilities are feasible for avalanche instabilities leading to subsequent discharge growth, depending upon the pressure and voltage conditions.

#### In SF<sub>6</sub>

At low pressures, certain of the avalanches growing radially from the anode wire are likely to reach critical size to form streamers (commonly known to be 'pre-onset streamers') which develop until the stored energy in the space charge has been dissipated in the gap by electron collision. At the same time, the positive space charge accumulated in the gap outside the ionization zone diminishes the anode field such that this field restricts the formation of subsequent generation of streamers in the wake of the original one. The inception of a new pre-onset streamer is only possible after the extinction of the 'quasicontinuous' current. The spread of the discharge along the periphery of the inner wire is maintained through the 'diffusive dispersion' of photons supplied by feedback to the gas layer close to the ionization region, either by photodetachment [25] or by photo-ionization [24]. At higher voltages the discharge becomes more unstable and the glow-like appearance is replaced by randomly occurring luminous streamers. This is because the anode field clears the space charge of the pre-onset streamer as fast as it builds up, such that the growth of subsequent streamers occurs in a space-charge free gap. Breakdown follows when one of these streamers traverses the entire gap. In air, in short gaps, when 'breakdown streamers' approach

the ground electrode, a luminous secondary streamer channel is initiated at the electrode in corona, facilitating the formation of the arc [36]. In  $\text{SF}_6$  the role of the ground electrode on the propagation of the breakdown streamers and final jump to breakdown is not known. Time resolved pictures and analysis of the spectral emission of the primary and secondary streamers would be helpful to explain the processes involved.

At higher pressures, over the rising part of the characteristic, the discharge begins with restricted filaments near the inception voltage (Figure 7.2(ii), Frame (D)). The filamentary appearance of the discharge is associated with the increased photoabsorption [98,162,175] and low diffusion [175] coefficients in  $\text{SF}_6$ . This means that, with increasing pressure, the photons are absorbed more closely to the avalanche head, hence facilitating the extension of the streamer channel into the gap. Afterwards, secondary streamers are launched into the gap through the wake of the primary one. In the current oscillograms each channel is accompanied by a train of pulses each consisting of streamers superimposed on a permanent glow, and has the same characteristics as the primary one, as indicated in current pictures of Frame (D) of Figure 7.2(ii). The similarity in magnitudes of the primary and secondary streamers in a current burst suggests the strong self-governing influence of the space charge of every restricting streamer on its growth. Further, occasionally the current burst shows a growth phase, as was observed in the work of Hazel and Kuffel [158]. Although this was accounted for by a gradual field enhancement mechanism active near the anode due to a negative-ion space charge, the presence of such a negative charge cloud in the

proximity of the anode has already been disputed [29]. The influence of the current-limiting resistor  $R$  and the total gap capacitance  $C$  (including the stray capacitance) can be given as a possible reason for this phase; since the instantaneous current is generally larger than the current available from the source the extra energy must be supplied from the gap capacitance, which recharges between each pulse with time constant  $RC$ , hence giving rise to the growth phase. A current pulse at this level continues over a short period of time and suffers an extinction. Though the reasons causing this are still not known, the following can be suggested: (a) the field reduction at the anode resulting from the accumulation of positive space charge, (b) the reduction of the field at the inner electrode surface owing to field enhancement at the cathode, and (c) the limited energy stored in the gap capacitance [25]. As the voltage is increased further, the filaments in the discharge become numerous and are superimposed on a luminous glow. The average value of the current bursts and the frequency of their occurrence increase with the voltage.

At or near to  $p_m$ , even though the appearance of the discharge is slightly different with more frequently occurring filamentary channels, the current waveforms possess almost the same properties as those observed in the previous cases, i.e. secondary streamers in each burst have similar features to the primary one. At slightly higher pressures, the interdependence between primary streamers and subsequent pulses becomes clearer in that each burst is initiated by the appearance of a primary streamer having slightly larger amplitude (Frame (L) Figure 7.2 (iv)).

At higher pressures, over the negative slope region of

the characteristic, the primary streamer is able to advance well into the gap, due to an increase in the photoabsorption coefficient and to increased negative ion detachment as the positive space charge is pushed further into the gap. The associated current pulse may or may not give way to the formation of a sequence of pulses. The magnitude of the primary streamer pulse is remarkably larger (shown in dotted lines in Frames (L) and (M) in Figure 7.2(v) than the succeeding secondary streamers in the burst. This distinctive feature of primary streamers in this phase was also observed by Farish and Ibrahim [98] in their point-plane gap studies.

At higher pressures, near to the critical pressure, large streamers occur without any secondary successors. Visually, the discharge achieves a long and filamentary appearance. The breakdown follows from one of these filamentary streamers when thermal detachment starts throughout its channel such that rapid electron liberation provides higher conductivity [36].

As a whole, the positive dc corona discharge phenomenon is basically a streamer activity whose spatio-temporal development is governed by the gap pressure and the gap voltage. At low pressures, over the rising part of the voltage-pressure characteristic, while the current-burst activity is initiated by restricted pre-onset streamers having similar amplitudes as the succeeding streamer, over the negative-slope region breakdown streamers are distinguished by their very large amplitudes. At pressures close to the critical pressure, only extensive isolated breakdown streamers are present.

In point-plane gaps, in the prebreakdown current studies of Kuffel and Hazel [158] although the streamer-discharge activity

was recognised, no distinction was quoted on the pressure dependent nature of pre-onset streamers. In their comprehensive, prebreakdown current and image-converter camera studies Farish et al [97,98,227] observed similar interrelation to that in the present work between the pre-onset streamers and subsequent secondary streamers over different regions of the characteristic. Over the negative slope region, although the large amplitude breakdown streamers concurrent with the secondary streamers were identified as leaders - after the recognition of leader discharge development in  $\text{SF}_6/\text{N}_2$  mixture under impulse voltage conditions [227] - the present author considers that there is not enough evidence to verify the complete development of a leader in pure  $\text{SF}_6$  in short gaps. Further experimental observations are necessary to characterize the nature of the large-amplitude pulses associated with the long filamentary channels.

#### In $\text{SF}_6/\text{N}_2$ Mixtures

Though the appearance of the positive corona and the type of the current pulse activity observed in a 40%  $\text{SF}_6/\text{N}_2$  mixture (Figure 7.3(i) to (v)) are similar to those found in  $\text{SF}_6$ , the discharge channels are more filamentary and brighter. This is because, according to the findings of Blair et al [226], the photo-absorption coefficient ( $\mu_p$ ) is reduced which enhances the effects of the secondary photoionization mechanism and alters the distribution of the space charge field, so that the discharge develops locally in more constricted and longer channels. The current-burst duration is longer than the corresponding one in  $\text{SF}_6$  under the same pressure and voltage conditions. This is probably due to the stronger space-charge field in mixtures which sustain the predischarges for a longer period.

Another point of interest is that, at pressures close to  $p_c$ , the discharge development to breakdown takes place through stepwise elongation of the channel with brushlike flaring steps, (Frames (P) and (Q) of Figure 7.3(v)). A similar form of discharge development was also observed in short [232, 233] and long [170] gaps and was identified as a leader discharge. Owing to the enhanced energy loss by electron attachment and photo-absorption [233] the growth of the streamer is possible only with high field strength. Since the space charge build-up in front of the ionization zone of the streamer is sufficient to stop the ionization, the streamer propagation temporarily is delayed pending field recovery caused by the diffusion and recombination. The field at the tip of the streamer increases and allows further extension of the streamer and hence advance of the leader into the gap. Flares at each step along the leader channel signifies the start of ionization process which give way to pre-onset streamers avalanching axially into the main streamer branch. The extension of the channel takes place from one of these pre-onset streamers and the process repeats itself. As is expected, increasing the  $SF_6$  concentration causes the length of the leader steps to be reduced.

#### 7.11.2 Negative corona characteristics

##### In $SF_6$

Over the rising part of the voltage pressure characteristic (Figure 7.4) up to 1.6 bar, two types of corona regime were observed, namely at low pressures, irregular avalanche activity replaced by streamer bursts at high pressures.

The formation of irregular pulse activity at low pressures is similar to what was observed by Trichel [37].

Immediately after the initiation of an avalanche from the inner electrode surface at voltages slightly above the inception, photons produced in the ionization zone of the first avalanche and positive ions returning to the cathode, cause a group of electron avalanches to be liberated from the cathode. In the meantime, the field between the positive-ion charge cloud and the cathode gradually increases as the positive ion accumulates, and the field exceeds the original cathode field. This enhances the initial ionization process and accelerates the formation of avalanches. All this process brings in the rapid growth of the current. Electrons proceed out into the gap beyond the positive space charge and form a negative ion cloud which drifts toward the anode. All this process results in a rapidly growing current pulse limited by locally developing space-charge field [25]. The current growth is accompanied by a 'transfer discharge contraction' resulting in a constricted glow spot. The number of spots on the perimeter of the disc is determined by the magnitude of the applied voltage. Moreover, the negative space charge and the positive space charge clouds yield a field-free region in the gap, blocking the ion transit and bringing the negative charge cloud closer to the cathode. In a slightly longer time scale, while the negative space charge continues to accumulate near to the positive space charge, the positive ions shorten the zone of the effective field region thereby reducing the ionization. Eventually, further multiplication ceases and the positive space charge disappears. It is believed that the generation of a dipole field in the gap, together with the strong spatial concentration of negative space charge, prevents streamer formation so that higher stabilization can be realized as compared with the positive stabilization process.

When the negative ions clear away sufficiently to raise the ionization voltage to the self-sustaining value, a new negative-glow pulse occurs and the process repeats itself. The irregular behaviour of pulses in both time and amplitude signifies the fact that initiation of pulses are delayed due to lack of initiatory electrons as was also suggested by Sigmond et al [48].

At higher pressures, the rapid growth of the pulse current is accompanied by a chain of low amplitude pulses at an enhanced current level. The initial pulse has the properties of a streamer that were observed for the positive-polarity corona. The streamer formation process was shown [234] to occur at the transition phase from avalanche to Trichel pulse when the number of electrons created in the avalanches gives rise to the initiation of a streamer. The formation of the intermittent pulse activity is due to field relaxation which brings about the spread of the discharge along the cathode surface.

Over the negative-slope region of the curve, although not investigated, avalanche instabilities, at lower voltages, would be expected to develop into extensive streamer activity at higher voltages. It would be of interest to examine the type of discharge growth bringing about breakdown so that the conditions for a corona-free breakdown can be predicted for negative polarity.

#### In SF<sub>6</sub>/N<sub>2</sub> Mixtures

The overall picture of the corona phases over the corona stabilized region for different pressures and voltages resembles those observed in SF<sub>6</sub>, due to low diffusion and high absorption [175], the development is more restricted and brighter.

### 7.11.3 Current-voltage characteristics

For both polarities of the corona electrode, the current above corona onset increases nearly proportional to voltage (Ohm's law) over a certain voltage range, and afterwards increases parabolically, following the well known Townsend's law [12]

$$I = 8 \pi E \mu V (V - V_i) / p \cdot r_2^2 \ln \frac{r_2}{r_1} \quad (1.23)$$

where  $V_i$  is the onset voltage and  $\mu$  is the ion mobility.

Over the Ohm's law region, at constant gap voltage, the increase in the average current is limited by a decrease in the mean electric field in the ionization zone and this, in turn, stabilizes the discharge current [24]; the voltage range of this regime increases with the gas pressure. For instance, in the positive current-voltage characteristics of  $SF_6$  given in Figure 7.6, this range increases from 2 kV to 10 kV with increase in the pressure from 0.5 to 1.4 bar. After the inception of the continuous-corona regime, the discharge current varies rapidly with the gap voltage, i.e. the I-V characteristics exhibit the parabolic variation given by Equation 1.23. The theoretical limit for the current increase after which the differential resistance  $\Delta I / \Delta V$  of the drift region becomes negative is given [235] by

$$J_{\max} = C \mu E_0 \frac{V^2}{(r_2 - r_1)^3} \quad (7.1)$$

where C is a constant determined by the gap configuration.

The average current estimate made using Equation 1.23 on a typical XY-record of I-V characteristic is illustrated in Figure 7.16; for  $\mu = 1.0 \text{ cm}^2 / (\text{V} \cdot \text{sec})$  [236] and for the voltage value given at point A ( $I = 0.40 \text{ mA}$ ) the estimate (point A') is

$I = 0.48$  mA. Similarly, using Equation 7.1 for  $C = 1.5$ , the limiting current value was calculated as  $I = 0.57$  mA (point B).

The current-voltage hysteresis effect illustrated in Figure 7.16 was also noticed in most of the low-pressure current-voltage characteristics of both polarities in  $SF_6$  and  $SF_6/N_2$  mixtures. Though there is yet no experimental evidence, it may result from the enhanced effective average secondary coefficient and the increased cathode field, and this will necessitate lesser energy requirement as the voltage is reduced. Moreover, due to the confined geometry of the coaxial gap, thermal energy evolved as the voltage is raised may also be another reason, by bringing about density changes and thus additional ionization and excitation.

Another point of interest in Figure 7.16 is that, although the breakdown is expected to occur just after the differential resistance of the drift region becomes negative, the characteristic continues over a current range. This behaviour is known from the Townsend discharge stability studies of Sigmond [235] and is attributed to instability due to self-inductance and capacitance of the drift region when the series circuit resistance is less than the absolute value of the discharge negative resistance.

Figures 7.8 and 7.13 show that at low pressure the I-V characteristics of both polarity are similar although differences arise with increasing pressure. This is simply due to the same factors which bring in the drift-region resistance. One possibility for this behaviour was suggested [238] to be the differences in ion mobilities. In Figure 7.8, for instance, at  $p = 0.8$  bar and  $V = 50$  kV the ratio of the negative to positive corona currents is 1.16, which is consistent with the ratio of

negative to positive ion mobilities (1.21) in SF<sub>6</sub>.

#### 7.11.4 Space charge field distribution and ion mobility

The field measurements obtained by means of the biased-field probe at the outer electrode exhibit good correlation with the estimated results over the rising part of the voltage-pressure characteristics for both polarities (Figures 7.19 and 7.20). This is expected within assumptions made for the estimations, i.e. that corona consists of a sheath of negligible thickness under steady state conditions. Beyond the peak of the characteristics, due to the outset of extensive streamer activity, the assumptions are no longer valid. Estimated results agree with measurements only in a limited range of voltages above the inception level. In the case of negative polarity, the parallel displacement of the estimated results from the measured ones probably indicates the amount of error introduced due to the assumption that the field at the electrode surface remains at the onset value during corona. This is in agreement with measurements of Waters et al [243] who observed a 30% reduction at the inner electrode surface-field in the glow corona-mode in air. Since the field results were obtained by fitting an approximate least-square line to the data points, this could bring about an additional error.

An interesting comparison is given in Figure 7.21 which demonstrates the fact that the space-charge-induced field on the outer boundary is consistently higher at all pressures for the positive polarity; similar observations were made in non-cylindrical coaxial geometry in air at atmospheric pressure [257]. This result is consistent with the total current (charge) measurements at the outer boundary; at the same gap voltage, the negative

current always being higher than the positive current and the difference increasing with pressure (Figure 7.8). This difference is due to the difference in ionic mobilities as shown in Figure 7.22; in that ionic mobilities are smaller for the negative ions than for the positive ions up to 1.2 bar. In a 90% SF<sub>6</sub>/N<sub>2</sub> mixture a similar variation was also observed for pressures up to 1.4 bar by Dzhubarly et al [236] using ion decay technique, while Schmidt et al [258], employing the same technique, observed no differences between ionic mobilities in SF<sub>6</sub> at field strengths of 1 kV cm<sup>-1</sup> at 0.25 bar and 6 kV cm<sup>-1</sup> at 21 bar. In the latter work, a strong dependence on pressure was also noticed. This seems to be contrary to the present results in which at pressures above 1.2 bar both mobilities tend to have values in the range 0.3 - 0.4 cm<sup>2</sup>V<sup>-1</sup>cm<sup>-1</sup>. The lower ionic mobilities at high pressures (> 1 bar) are due to the abundance of heavy SF<sub>6</sub><sup>-</sup> and SF<sub>5</sub><sup>-</sup> ions and possibly also to the presence of cluster ions such as SF<sub>6</sub><sup>-</sup> (SF<sub>6</sub>), SF<sub>6</sub><sup>-</sup> (SF<sub>6</sub>)<sub>2</sub> and SF<sub>5</sub><sup>-</sup> (SF<sub>6</sub>)<sub>2</sub> [259].

In view of the low mobilities of negative ions, a corresponding space-charge accumulation near the outer electrode and, hence an increase in the field strength, was expected for negative polarity. However, the higher field strengths were measured in the presence of positive ions as illustrated in Figure 7.8. As is shown by the I-V characteristic, the space charge density or the current density at the outer electrode is slightly higher in the case of negative inner electrode. The lower electric field strength at the outer electrode is only possible by having lower negative ion drift velocity. Although no experimental data related to the positive ion velocities in SF<sub>6</sub> is known presently, this inference is justifiable from the known drift velocity data

in common gases [14].

The present experimental technique is simple and efficient for space-charge-induced field measurements. However, since the measurements are limited to the corona stabilized breakdown regime, the ion mobility measurement is consequently limited to this region. Due to the wide pressure range of the corona-stabilized - breakdown region in the case of negative polarity, negative ion mobilities can be obtained for higher pressures than positive.

#### 7.11.5 Critical pressure estimation

In several nonuniform field gap studies, it has been substantiated that the critical pressure exhibits dependence on geometric parameter and type of gas. Hence, any method for predicting the critical pressure must account for the factors related to these two requirements.

Several empirical and semiempirical formulae have been proposed for predicting the critical pressure in SF<sub>6</sub> in short and long gaps. Hazel and Kuffel [158] proposed a semi empirical relation, based on the suggestion of Pollock and Cooper [149] which relates the rate of decrease of the geometric field to the rate of increase of positive charge in the streamer tip in the direction of propagation. The predicted results were in approximate agreement with the measurements and were limited to a number of gap geometries. A somewhat more realistic method was suggested by Farish et al [160] who derived an expression for the critical pressure in terms of gas and gap parameters by proposing that at the critical pressure an equivalence will be reached between the critical ionizing distance and the mean photo radiation path length. This method, however, requires the critical pressure data for the value of the constant

in the expression. A more rigorous mathematical approach was made by Kurimoto et al [176] who compared the mean radiation path length to the radius of the critical avalanche head. However, this consideration is not in accordance with the accepted mechanism of propagation of a streamer.

The present method of estimation for predicting the critical pressure results in good agreement with measurements. However, its accuracy is limited by the photoabsorption coefficient data; the lower values yield the lower limit for the critical pressure.

#### 7.12 Conclusion

Dc corona discharge phenomena has been studied in SF<sub>6</sub> and in a 40% SF<sub>6</sub>/N<sub>2</sub> mixture. The significance of the space charge field on the various corona modes observed at different parts of the voltage-pressure characteristic has been pointed out. The estimated space-charge field has been correlated with the boundary field measurements and a preliminary model has been proposed for critical pressure estimation. The main points to be concluded are:

#### SF<sub>6</sub>

(1) Over the corona controlled breakdown region, for both polarities, the corona discharge is mainly a streamer corona. However, at low pressures ( $\leq 0.2$  bar), a glow discharge occurs for positive polarity, while in the case of negative polarity regular Trichel pulse activity was observed.

(2) Over the rising part of the voltage-pressure characteristics the corona-controlled breakdown voltage is determined by the space charge field which is slightly dependent on the radius of the inner

electrode and, for positive polarity, was found to vary between 35 - 45 kV/cm for inner electrode radii of 0.05 - 0.1 cm, in good agreement with the value previously determined for point-plane geometry by Farish et al [98].

(3) The space-charge-induced field at the outer electrode is higher when the applied voltage to the inner electrode is positive.

(4) The mobility of the negative ions is less than that of the positive ions at pressures < 1.0 bar.

(5) The ionic mobilities at low pressures (< 1.0 bar) are dependent on field.

(6) High stabilization in the case of negative polarity is believed to be due to low ionic mobilities of clustered negative ions of the form  $SF_6^-(SF_6)_n$ .

(7) The downcurving region of the voltage-pressure characteristics starts with extensive filamentary-streamer activity. The reason for this change of corona mode is believed to be associated with the enhanced detachment process.

(8) At the same values of voltage and pressure, the energy input to the gap for both polarities is the same.

(9) A model has been proposed for predicting the transition pressure to corona-free breakdown. The results have shown good agreement with the measurements.

#### 40% SF<sub>6</sub>/N<sub>2</sub> Mixture

(10) The discharge activity over the rising part of the voltage-pressure characteristics is a streamer activity.

(11) At the downcurving part of the characteristic a stepwise streamer-leader discharge activity takes place.

(12) A similar tendency to  $SF_6$  is expected in the space-charge field variation and hence in the ion mobilities.

GENERAL CONCLUSION AND RECOMMENDATIONS FOR THE FUTURE WORK8.1 General

Although there has been a considerable amount of useful data collected on breakdown characteristics of SF<sub>6</sub> in uniform and nonuniform field gaps, some discrepancies and even conflicts still exist among the results obtained in different laboratories.

The deleterious effect of surface roughness has been successfully accounted for in breakdown predictions. However, there are yet some problems to be resolved, such as inclusion of the curvature of the active electrode and the application of the data obtained in the laboratory in large-scale systems. Corona discharge formation at high field sites has added new dimensions to the investigations in this field.

Similar investigations have been undertaken in multi-component gases having desired breakdown properties as an alternative to SF<sub>6</sub>. Because they have no problems with toxicity, breakdown products, etc., simple mixtures such as SF<sub>6</sub>/air, SF<sub>6</sub>/Co<sub>2</sub> and SF<sub>6</sub>/N<sub>2</sub> are presently more attractive for practical applications than complex mixtures which may have higher dielectric strength.

In the present study, experimental and theoretical breakdown and corona-controlled breakdown characteristics of SF<sub>6</sub> and SF<sub>6</sub>/N<sub>2</sub> mixtures were investigated over a wide range of gap nonuniformities (0.03 - 38) and of pressure (0 - 8 bar) in coaxial cylindrical geometry under dc and impulse voltages.

8.2 Conditioning and Electrode Area Effects

Conditioning experiments were undertaken in SF<sub>6</sub> and

and SF<sub>6</sub>/N<sub>2</sub> mixtures at and above the points of deviation from the similarity law in order to compare the insulating performance of SF<sub>6</sub> to that of the mixtures.

In mixtures containing N<sub>2</sub> concentration above ~25% and at field strengths at and above the range 300 - 400 kV/cm, the conditioning period has been found to be prolonged both by increasing the surface roughness and the N<sub>2</sub> concentration. However, SF<sub>6</sub>/N<sub>2</sub> mixtures having SF<sub>6</sub> concentration larger than 75% exhibit better conditioning behaviour than SF<sub>6</sub> for rough electrodes. Moreover, SF<sub>6</sub>/N<sub>2</sub> mixtures are more polarity dependent with rough electrodes than with polished electrodes.

In both SF<sub>6</sub> and SF<sub>6</sub>/N<sub>2</sub> mixtures, the lowest breakdown voltage and the greatest scatter were obtained with aluminium electrodes at field strength above the range 300 - 400 kV/cm.

In almost all the conditioning experiments, it has been generally found that the breakdown voltage distributions above ~2 bar are exponential; hence, in studies of breakdown of gas insulated gaps, it would be more correct to quote the mode of the distributions rather than the averages.

The area effect has been shown to be more pronounced with increasing N<sub>2</sub> content in SF<sub>6</sub>/N<sub>2</sub> mixtures. The distribution of extreme values of breakdown voltage has been related to the area effect by the Weibull type extreme value distribution. The method of Maximum Likelihood has been adopted to estimate the parameters ( $\alpha$ ,  $\beta$ ). The confidence intervals on these parameters and the tolerance bounds for a given quantile have been included in the computational estimations. The estimations have been extended to systems consisting of N sections.

The slope of the distributions for rough electrodes lies in the range 6 - 20 quoted in the literature. However, in the case of polished electrodes, values outside this range are obtained if the number of observations exceed that required for conditioning, since the data can no longer be assumed to be consistent with first breakdown levels.

### 8.3 Breakdown Characteristics

The deviation from the similarity law has been found to occur for polished electrodes at field strengths larger than 160 - 180 kV/cm and for rough electrodes for fields greater than 130 - 150 kV/cm. In SF<sub>6</sub>, with positive impulse voltage the deviation occurs at field strengths greater than 450 - 600 kV/cm, and the breakdown characteristics are not affected for surface finishes  $\leq 30 \mu\text{m}$ .

The breakdown characteristics of electrodes with rough surfaces have been estimated from a multiple protrusion model comprising juxtaposed triangles. It has been shown that there exists no upper limit for tolerable surface roughness; the surface roughness always reduces the dielectric strength of the gap and the amount of reduction is determined by the protrusion height, shape and the nonuniformity of the gap.

In SF<sub>6</sub>, for polished electrodes ( $R_{\text{max}} \simeq 2 \mu\text{m}$ ), a single protrusion model has been found to agree with the average breakdown voltage values up to 6 bar. For rough electrodes ( $R_{\text{max}} \simeq 20 \mu\text{m}$ ) up to 8 bar, the single protrusion model suggested by Pedersen has been shown to result in better agreement than the multiple protrusion model.

For SF<sub>6</sub>/N<sub>2</sub> mixtures, a general equation has been derived for the compressibility factor from the virial coefficients of the constituents. It has been shown that the compressibility factor of mixtures containing less than 50 per cent SF<sub>6</sub> can be taken as equal to that of N<sub>2</sub>.

#### 8.4 Corona-Stabilized Breakdown and -Discharge Phenomena

The voltage-pressure characteristics have been found to behave similarly to those of point-plane gaps in that the rising part of the characteristics for the same outer electrode are independent of the radius of the inner electrode and of the polarity of the gap. The results are highly reproducible, and the impulse breakdown voltages lie slightly above the dc ones. In SF<sub>6</sub>, the positive space-charge field at breakdown has been shown to vary between 35 - 45 kV/cm for inner electrode radii of 0.05 - 0.1 cm. The steepness of the rising part of the characteristics has been observed to increase with the radius of the outer electrode and the ratio of the SF<sub>6</sub> content.

The negative-slope parts of the voltage-pressure characteristics have been found to be reproduced reasonably well, but do not exhibit any regular dependence on gap parameters and the type of the gas.

The parts of the characteristics lying in between the pressure minimum and the critical pressure remain unaffected with increasing the pressure in most cases.

The critical pressure has been observed to be unchanged with increasing N<sub>2</sub> concentration in SF<sub>6</sub>/N<sub>2</sub> mixture and to be decreased with increasing the outer electrode radius. The critical

pressures obtained in the case of negative polarity are always higher than those of positive polarity. The impulse voltage-pressure characteristics have the same critical pressures as the dc ones for the same gap.

The process of corona stabilization is more pronounced with dc voltages than with the impulse voltage, and is more extensive in a coaxial electrode gap with larger outer electrode than in a point-plane gap for the same nonuniformities.

The dominant corona discharge mode over the corona-controlled breakdown region of the voltage-pressure characteristic of SF<sub>6</sub> is a streamer corona. However, at low pressures ( ≤ 0.2 bar) in the case of positive polarity, a glow discharge, and in the case of negative polarity, regular Trichel pulse activity have been observed. In SF<sub>6</sub>/N<sub>2</sub> mixtures, over the downcurving part of the characteristic, a stepwise streamer/leader discharge activity has been noticed.

For the same applied voltage, the space-charge-induced field at the outer electrode is higher in the case of positive polarity.

Ion mobilities exhibit pressure and field dependence at pressures less than 1.0 bar, and the negative ion mobility is less than the positive ion mobility in this range of pressure.

A preliminary attempt at developing a model for predicting the critical pressure, based on the conditions required for streamer propagation at onset, has shown good agreement with the measurements.

## 8.5 Recommendations for the Future Work

As was pointed out in the review chapter and in Chapter 3, in compressed gas studies discrepancies existing among

the results obtained in different laboratories are due to gap and circuit parameters which are not fully recognised, and to uncontrollable factors such as gas-borne dust or free conducting particles. Therefore, it is necessary to standardize test conditions in uniform and nonuniform breakdown experiments such that effects of various mechanisms can be analysed separately. Such studies will afford a better understanding of the factors which result in differences among different investigators.

In gas-insulated HV systems, the factors influencing breakdown are interrelated and intermixed. The use of probabilistic methods which take into consideration the basic breakdown mechanisms which are operative will be essential for predicting the insulation characteristics of practical systems.

In the present study, the area effect was considered as an effect related to the surface roughness using the Weibull type extreme value statistics. In practical systems, however, the insulators, free conducting particles, etc. are also important 'weak links' to be accounted for. In laboratory experiments, tests should be extended to include all these effects in the same system.

The quantitative information related to the voltage-pressure characteristics for a large range of gap nonuniformities are almost complete. However, the type of corona discharge mechanisms at very low pressures ( $< 0.2$  bar) and over the downcurving part of the characteristic are still not clear. Moreover, the gas processes bringing about downcurving should be explained.

## ACKNOWLEDGMENTS

The author wishes to express his sincere appreciation to Professor D.J.Tedford for the opportunity to undertake the present work and for his keen interest throughout.

The author is indebted to Dr.O.Farish for his invaluable supervision during the research and preparation of the thesis. Thanks are due to Mr.I.Somerville and other staff members for their interest and many useful discussions.

He acknowledges the help of Mr.J.Dickson, Chief Technician, and all his staff for their help in the constructional work.

The patient and careful typing of the manuscript by Miss J.Baird is appreciated.

Receipt of a M.E.T.U. Research Studentship is gratefully acknowledged with thanks.

## REFERENCES

1. Camili, G. and Chapman, J.J., AIEE Trans., 66, 1463, 1947.
2. Camili, G., Gordon G.S. and Plump, R.E., AIEE Trans., 71, 348, 1952.
3. Lingal W. and Owens, P., AIEE Trans., 72, 293, 1953
4. Nitta, T., Trans. IEE of Japan, 92-B, 523, 1972.
5. Graybill, H.W. and Cronin, J.C., IEEE Tr. 73 366-2, 1973.
6. Takagi, T., Kenmochi, H., Saba, S. and Sakata, K., CIGRE, Paper No.23-02 0, 1976.
7. Boeck, W. and Troger, H., CIGRE, Paper No.23-08 0, 1976.
8. Pedersen, B.O., et al, IEEE PES Winter Power Mtg, Paper 71 TP 193-PWR, 2631, 1971
9. Srivastava, K.D., Conf. Elect. Ins. and Dielect. Phen., Annual Rep., Washington, 448, 1977.
10. Cookson, A.H., Garrity, T.F. and Sann, R.W., CIGRE, Paper No. 21-09 0, 1978.
11. Hampton, B.F., Browning and Mayes, R.M., Proc. IEE, 123, 159, 1976.
12. Townsend, J.S., Electricity in Gases, Oxford Univ. Press, 1915.
13. Llewellyn-Jones, F., Ionization and Breakdown in Gases, London, Methvens, 1957.
14. Meek, J.M. and Craggs, J.D., Electrical Breakdown of Gases, Oxford, 1953.
15. Geballe, R. and Reeves, M.L., Phys. Rev., 92, 867, 1953.
16. Raether, H., Arch. Elektrotech, 34, 49, 1940
17. Meek, J.M., Phys. Rev. 57, 722, 1940.
18. Loeb, L.B. and Meek, J.M., The Mechanism of the Electric Spark, Stanford Univ. Press, 1941.
19. Pedersen, A., Trans. IEEE, PAS-86, 200, 1967.
20. Cookson, A.H., Ph.D. Thesis, University of London, 1965.

21. Muller, E.K., Z.ang.Phys., 21, 554, 1966.
22. Meek, J.M., J.Franklin Inst., 230, 229, 1940.
23. Raether, H., Ergebnisse d. exakten Naturwiss, 22, 73, 1949.
24. Loeb, L.B., Electrical Coronas: Their Basic Physical Mechanism, UCLA Press, 1965.
25. Beattie, J., Ph.D.Thesis, University of Waterloo, Canada, 1975.
26. Bondel, H.W., Phys.Rev., 84, 92, 1951.
27. Peek, F.W., Dielectric Phenomena in High-Voltage Engineering, McGraw-Hill, New York, 1929.
28. Hermstein, W., Arch. fur Elek, 45, 209 and 279, 1960.
29. Buchet, G. and Goldman, M., 9th Int. Conf. on Phen. in Ion. Gas, Bucharest, 291, 1969.
30. Beattie, J.E. and Cross, J.D., 3rd Int.Conf. Gas Discharges, IEEE Publ. 118, 279, 1974.
31. Das, M.K., Z. angew Phys. 13, 410, 1961
32. Waters, R.T., Rickard, T.E. and Stark, W.B., Proc.IEE, 119, 717, 1972.
33. Kondo, K. and Ikuta, N., J.Phys.D: Appl.Phys., 13, 133, 1980.
34. Marode, E., J.Appl. Phys., 46, 2005, 1975.
35. Lama, W.L. and Gallo, C.F., J.Appl. Phys. 45, 103, 1974
36. Hirsh, M.N. and Oskam, H.J., Gaseous Electronics: Electrical Discharges, v.1., Academic Press, London, 1978.
37. Trichel, G.W., Phys. Rev. 54, 1078, 1938.
38. Bugge, C., and Sigmond, R.S., Proc.9th Int.Conf. on Phenomena in Ionized Gases, Bucharest, 289, 1969.
39. Sigmond, R.S., and Torsethaugen, K., Proc.11th Int.Conf. on Phenomena in Ionized Gases, Prague, 194, 1973.
40. Loeb, L.B., Phys.Rev. 86, 256, 1952.

41. Aleksandrov, G.N., Sov.Phys.-Tech.Phys. 8, 161, 1963.
42. Zentner, R., Z.angew, Phys., 29, 294, 1970.
43. Ikuta, N., and Kondo, K., 4th Int.Conf.Gas Discharges, IEE Publ.  
143, 227, 1976.
44. Goldman, A., Goldman, M., Rautureau, M. and Tchoubar, C.,  
J.Phys., 26, 486, 1965.
45. Suzuki, T., J.Appl. Phys., 44, 4534, 1973.
46. James, A.G., Ryan, H.McL., and Powell, C.W., Nature, 210, 403  
1966.
47. Lewis, T.J., J.Appl. Phys. 26, 1405, 1955.
48. List, G., Exp. Technik der Physik, 7, 118, 1959.
49. Dakin, T.W., Luxa, G., Oppermann, G., Vigreux, J., Wind, G. and  
Winkelkemper, H., Electra, 32, 61, 1974.
50. Muller, E.K., Zeit, F., Physik., 102, 734, 1936.
51. Boulloud, A., Ann.Phys., 8, 909, 1953.
52. Boulloud, A., CR Acad. Sci., 231, 514, 1950.
53. Llewellyn-Jones, F. and De La Parrelle, E.T., Proc.Roy.Soc.,  
216, 267, 1953.
54. Macalpine, J.M.K. and Cookson, A.H., Proc.IEE, 117, 642, 1970.
55. Philp, S.F. and Trump, J.F., Ann.Rep. of Conf. on Elect.  
Insulation, 100, 1966.
56. Goldspink, G.F., Cookson, A.H. and Lewis T.J., IEE Colloq. on  
Gaseous Insulation, ch.4, 1966.
57. Trump, J., IEEE Trans. NS-14, 113, 1967.
58. Berecz, C., KFKI Kozlemenyek, 16, 137, 1968.
59. Doepkin, H.C., IEEE Trans., PAS-88, 364, 1969
60. Cobine, J.D., and Easton, E.C., J.Appl.Phys, 14, 321, 19, 1943.
61. Theobald, J.K., J.Appl. Phys., 24, 123, 1953.

62. Goldspink, G.F. and Lewis T.J., Proc. 8th Int. Conf. on Phenomena in Ionized Gases, Vienna, 1, 211, 1967.
63. Llewellyn Jones, F. and Morgan, C.G., Phys. Rev., 80, 223, 1950.
64. Sharbaugh, W.H. and Watson, P.K., Ann. Rept. Conf. on Elec. Insulation, 57, 1960.
65. Cookson, A.H., Proc. IEE, 117, 1970.
66. List, G., Ann. Phys., 20, 238, 1957.
67. Agapov, V.G. and Razevig, D.V., Elektrichestvo, No. 5, 32, 1972.
68. Avrutskii, V.A., Goncharenko, G.M. and Prokhorov, E.N., Sov. Phys. Tech. Phys. 18, 386, 1973.
69. Berger, S., 5th Int. Conf. Gas Discharges, IEEE Publ. 165, 173, 1978.
70. Philp, S.F., IEEE Trans. PAS-66, 356, 1963.
71. Coates, R., Dutton, J. and Harris, F.M., 3rd Int. Conf. Gas Discharges, IEEE Publ. 118, 403, 1974.
72. Felici, N. and Marchal, Y., Rev. Gen. Elect. 57, 155, 1948.
73. Young, D.R., J. Appl. Phys., 21, 222, 1950.
74. Cohen, E.H., Proc. IEE, 103A, 57, 1956.
75. Bartnik, I.M., Sov. Phys. Tech. Phys., 23, 156, 1978.
76. Thom, J., Ph.D. Thesis, University of Strathclyde, 1976.
77. Naidu, M.S. and Prasad, A.N., J. Phys. D.: Appl. Phys. 3, 951, 1970.
78. Ahcarn, A.J. and Hannay, N.B., J. Chem. Phys., 21, 119, 1953.
79. Ermel, M., ETZ-A, 96, 231, 1975 (Translation).
80. Pace, M.O., Chan, C.C. and Christophorou, L.G., ORNL Report on breakdown strength of gaseous and liquid insulators, 1979.
81. McAfee, K.B. Jun. and Edelson, D., Proc. Phys. Soc., 81, 382, 1963.
82. Fehsinfeld, F.C., J. Chem. Phys. 45, 4634, 1966.
83. Boyd, H.A. and Crichton, G.F., Proc. IEE, 118, 1872, 1971.
84. Loeb, L.B., Basic Processes of Gaseous Electronics, UCLA Press, 415, 1955.

85. Bhalla, M.S. and Craggs, J.D., Proc. Phys. Soc., 80, 151, 1962.
86. Kline, L.E., Davies, D.K., Chen, C.L. and Chantry, P.C., J. Appl. Phys., 50, 6789, 1979.
87. Teich, T.H. and Branston, D.W., 3rd Int. Conf. Gas Discharges, IEE Publ. 118, 109, 1974.
88. Karlson, P.W. and Pederson, A., IEEE Trans., PAS-91, 1597, 1972.
89. Nitta, T. and Shibuya, Y., IEEE, Trans. PAS-90, 1065, 1971.
90. Baumgartner, R.G., 3rd Int. Conf. Gas Discharges, IEE Pub. 118, 366, 1974.
91. Wieland, A., ETZ-A, 94, 370, 1973.
92. Brand, K.P. and Kopainsky, J., ISH, Paper 31-05, Milan, 1979.
93. Itoh, H., Shimozurna, M., Tagashira, H. and Sakamoto, S., J. Phys. D: Appl. Phys, 12, 2167, 1979.
94. Aschurnden, Th., 6th Int. Conf. Gas Discharges, IEE Pub. 189, 24, 1980.
95. Crichton, B.H. and Tedford, D.J., J. Phys. D. 9, 1079, 1976.
96. Abhurn, S. and Mollerup, J., 6th Int. Conf. Gas Discharges, IEE Pub. 189, 278, 1980.
97. Farish, O., Ibrahim, O.E. and Korasli, C., 5th Int. Conf. Gas Discharges, IEE Publ. 165, 320, 1978.
98. Farish, O., Ibrahim, O.E. and Kurimoto, A., ISH paper 31-01, Milan, 1979.
99. Farish, O., Dale, S.J. and Sletten, A.M., Trans. IEEE PAS-95, 1639, 1976.
100. Petersen, A., IEEE Trans., PAS-89, 2043, 1970.
101. Farish, O., Int. Symp. Gaseous Dielectrics, Publ. Conf. 780301, 1978.
102. Chalmers, I.D. and Tedford, D.J., Proc. IEE, 118, 1893, 1971.
103. Dutton, J., Harris, F.M. and Jones, G.J., Proc. IEE, 118, 732, 1971.
104. Boyd, H.A. and Crichton, G.E., Proc. IEE, 119, 275, 1972.
105. Opermann, G., Int. Symp. H.V. Tech., Munich, 378, 1972.
106. Rein, A., Arnesen, A. and Johansen, I., IEEE Trans. PAS-96, 945, 1977.

107. Tedford, D.J., Crichton, B.H. and Somerville, I.C., 1977 Ann.Rep. Conf. Elec. Insul. Dielectric Phenom., NAS Publ. 2866, 370, 1979.
108. Baumgartner, R., ETZ-A, 98, 369, 1977.
109. Somerville, I.C., 3rd Int. Symp. H.V. Tech. Paper 32.13, Milan, 1979.
110. Kawaguchi, Y., Sakata, K. and Menju, S., IEE Trans, PAS-90, 1072, 1971.
111. Shibuya, Y., Yamoda, N. and Nitta, T., 2nd Int. Conf, Gas Discharges, IEE Publ. 90, 320, 1972.
112. Cooke, C.M., IEEE Trans., PAS-94, 1518, 1975.
113. Pederson, A., IEEE Trans., PAS-94, 1749, 1975.
114. Berger, S., IEEE Trans., PAS-95, 1073, 1976.
115. Somerville, I.C., Tedford, D.J. and Crichton, B.H., Proc. 13th Conf. Ion. Phen. in Gases, Berlin, 429, 1977.
116. Le Ny, R., Charrier, J. and Boulloud, A., 4th Int. Conf. on Gas Discharges, IEE Publ. 143, 121, 1976.
117. McAllister, I.W., ETZ-A, 99, 283, 1978.
118. Nitta, T., Yamada, N. and Fujiwara, Y., IEEE Trans. PAS-93, 623, 1974.
119. Farish, O., IEE Colloquium, London, 1977.
120. Cookson, A.H., Farish, O. and Sommerman, G.M.L., IEEE Trans. PAS-91, 1329, 1972.
121. Cookson, A.H., Farish, O. PAS-92, 871, 1973.
122. Ganger, E.B. and Leibold, A.A., IEEE PES Winter Power Meeting, Paper A-7, 152, 1976.
123. Cookson, A.H. and Wooton, R.E., 3rd Int. Conf. Gas Discharges, IEE Publ. 118, 385, 1974.
124. Cookson, A.H. and Wooton, R.E., Int. Symp. H.V. Tech., Zurich, 416, 1975.
125. Cooke, C.M., Wooton, R.E. and Cookson, A.H., IEEE Trans. PAS-96, 768, 1977.

126. Wooton,R.E. and Cookson,A.E., 1st Int.Symp.on Gaseous Dielectrics, Tennessee,U.S.A., 1978.
127. Diessner,A. and Trump,J.G., IEEE Trans. PAS-89, 1970,1970.
128. MacAlpine,J.M.K. and Cookson,A.H.,Proc.IEE, 117, 646, 1970.
129. Bortnik,J.M. and Cooke,C.M.,IEEE Trans.PAS-91, 2196, 1972.
130. Mosch,W., Hauschild,W., Speck,J.and Schierig,S.,3rd Int. Symp. H.V.Engin., Paper 32.01, Milan, 1979.
131. Gumbel,E.J., Statistical Theory of Extreme Values and Some Practical Applications, U.S.Government Printing Office, 1954.
132. Bortnik,J.M., Gurjunov, B.A.,and Panov,A.A., 2nd Int.Conf. Gas Discharges, IEE Publ.90, 326, 1972.
133. Massetti,C. and Parmigiani,B., 3rd Int.Symp.H.V.Eng.32.15,1979.
134. Goldspink,G.F.,Cookson,A.H. and Lewis,T.J., IEE Colloquium on Gaseous Insul., ch.1, 1, 1966.
135. Hampton,B.F. and Browning,D.N., 5th Int.Conf.Gas Discharges, IEE Publ.165, 169, 1978.
136. Mulcahy,M.J. et al, 4th Int.Conf.Gas Discharges, IEE Publ.113, 16, 1976.
137. Gockenbach,E., 4th Int.Conf.Gas Discharges, IEE Publ.143,113,1976.
138. Spence,G. and Ryan,H.M.,4th Int.Conf.Gas Discharges,IEE Pub.143,157,1976.
139. Guryunov,B.A.,Sov.Phys.Tech. Phys.20, 66, 1975.
140. Bortnik,J.M., Elektrichestvo, 12, 20, 1974.
141. Bortnik, J.M., and Gorjunov,B.A.,9th CIPIG,Bucharest,263,1969.
142. Husbands,A.S., Insulation Conf.,Brighton,Paper No.5.4,205,1974.
143. Cooke,C.M. and Velazquez,R., IEEE Trans.PAS-96, 1491, 1977.
144. Kawaguchi,Y. and Menju,S., EE in Japan, 90, 197, 1970.
145. Menju,S.,Aoyagi,H.,Takahashi,K. and Ohno,H, IEEE.Trans. PAS-93, 1706, 1974.

146. Ermel, M., ETZ-A, 96, 505, 1975 (Translation).
147. Mosch, W. and Hauschild, W., Elektrichestvo, 5, 50, 1974.
148. Menju, S. and Takahashi, K., IEEE Trans. PAS-97, 217, 1977.
149. Pollock, H.C. and Cooper, F.S., Physical Review, 56, 170, 1939
150. Foord, T.R., Nature, 166, 688, 1950.
151. Works, C.N. and Dakin, T.W., AIEE Trans., 72, 682, 1953
152. Howard, P.R., Proc. IEE, 104, 139, 1957.
153. Eccles, M., Prasad, A.N. and Craggs, J.D., Electronics Letters, 3, 410, 1967.
154. Azer, A.A. and Comsa, R.P., IEE Trans., EI-8, 136, 1973.
155. Sangkasaad, S., Int.Symp. H.V.Tech., Zurich, 379, 1975.
156. Sangkasaad, S., 4th Int.Conf. on Gas Discharges, IEE Publ.143, 145, 1976.
157. Liapin, A.G., Popkov, V.I. and Shevtsov, E.N., 4th Int.Conf. on Gas Discharges, IEE Publ.143, 169, 1976.
158. Hazel, R. and Kuffel, E., IEEE Trans. PAS-95, 178, 1976.
159. Bortnik, I.M., 13th Int.Conf. Ionized Phen. in Gases, Berlin, 426, 1977.
160. Farish, O., Davidson, R.C. and Tedford, D.J., Conf. Elect. Ins. on Dielectric Phen. (CEIDP) New York, Oct. 1977.
161. Malik, N.H. and Qureshi, A.H., IEE Trans., EI-14, 327, 1979.
162. Steiniger, E., ETZ-A, 86, 583, 1965.
163. Klewe, R.C. and Tozer, B.A., 1st Int.Conf. Gas Discharges, IEE Publ.70, 36, 1970
164. Takuma, T. and Watanabe, T., EE in Japan, 90, 166, 1970.
165. Takumo, T. and Watanabe, T., EE in Japan, 91, 733, 1971.
166. Takumo, T. Watanabe, T. and Kita, K., IEEE Paper C-72, 534-6, PES Summer meeting, San Francisco, July, 1972.

167. Ryan,H.M. et al, CIGRE, paper 15-02, 1976.
168. Foord,T.R., Proc.IEE, 100, 585, 1953.
169. Camili,G., Liao,T.W. and Plump,R.E., Elect.Eng., 580, 1955.
170. Watanabe,T. and Takuma,T., J.Appl.Phys.48, 3281, 1977.
171. Kuffel,E. and Yializis,A., IEEE paper F-78-183-6, PES Winter Power Meeting, New York, Jan -Feb., 1978.
172. Yializis,A. et al, IEEE Trans. PAS-98, 1832, 1979.
173. Aleksandrov,G.N. and Perlin,A.S., Soviet Phys.Tech.Phys. 17, 1846, 1973.
174. Malik,N.H., Qureshi,A.H., Theophilus,G.D.and Raghuv eer,M.R., IEEE Trans. PAS-97, 140, 1978.
175. Kurimoto,A., Aked,A. and Tedford,D.J., 3rd Int.Conf. Gas Discharges, IEE Publ. 143, 162, 1976.
176. Kurimoto,A., Aked,A. and Tedford,D.J., 4th Int.Conf. Gas Discharges, IEE Publ. 165, 324, 1978.
177. Nitta,T., Shibuya,Y. and Fujiwara,Y., IEEE Trans.,PAS-94, 108,1975.
178. Ryan,H.M.and Watson,W.L.,Int.Symp.H.V.Tech.Zurich,12, 1975.
179. Taschner,W., ETZ-A, 97, 118, 1976 (Translation-Tr.)
180. Taschner,W., ETZ-A, 98, 153, 1977. (Tr.)
181. Knorr,W., ETZ-A, 98, 549, 1977 (Tr.).
182. Specht,H., ETZ-A, 97, 675, 1977. (Tr.)
183. Ryan,H.M. and Watson,W.L., CIGRE, Paper 15-01, 1978.
184. Dreger,G., ISH. paper 31.06, Milan, 1979.
185. Knorr,W., ISH, paper 31.11, Milan, 1979.
186. Lom,H. and Schultz,H., ISH, paper 32.02, Milan, 1979.
187. Somerville,I.C. and Tedford,D.J., ISH, paper 53.02,Milan, 1979.
188. Dreger,G., 6th Int.Conf.Gas Discharges, IEE Publ.189, 188, 1980
189. Somerville,I.C., Private communication.

190. IEC Publication 60-2 High Voltage Test Techniques, 2, 1973.
191. Berger, S., IEEE Trans. PAS-96, 1179, 1976.
192. Berger, S., 4th Int. Conf. on Gas Discharges, IEE Pub. 143, 98, 1976.
193. Mulcahay, M.J., Proc. 8th Elec. Inst. Conf. IEEE Publ. C6-E1, 216, 1968.
194. Nitta, T. et al, Symp. on Gaseous Dielectrics, Oak Ridge, Nat. Lab. Tennessee, U.S.A., 338, 1978.
195. Bortnik, I.M., and Cooke, C.M., Sov. Phys. Tech. Phys. 17, 1850, 1973.
196. Tait, R.A.R., Ph.D. Thesis, Univ. of Strathclyde, 1975.
197. Mosch, W. and Hauschild, W., Hochspannungsisolierungen mit Schwefelhexafluorid, Veb Verlag Technik, Berlin, 1979.
198. Stone, G.C. and Heeswijk, R.G., IEEE Trans. EI-12, 253, 1977.
199. Cohen, A.C., Technometrics, 7, 579, 1965.
200. Mann, N.R., Schafter, R.E. and Singpurwalla, Methods for Statistical Analysis of Reliability and Life Data, Wiley-Interscience, New York, 1974.
201. Treson, W.G., Reliability Handbook, McGraw-Hill, 2-2, 1966.
202. Cohen, A.C., Technometrics, 17, 347, 1975.
203. Billmann, B.R. and Antle, C.E., Technometrics, 14, 831, 1972.
204. Chatfield, C., Statistics for Technology, Penguin Books, 1970.
205. Nitta, T. and Kuwahara, H., IEEE paper 80-SM, 703-9, PES Summer meeting, Minneapolis, July, 1980.
206. Weber, K.H. and Endicott, H.S., AIEE, 75-III, 371, 1956.
207. Karner, H and Voß, H-J, ISH paper 32.04, Milan, 1979.
208. Cookson, A.H. et al, SIGRE paper 15-09, 1976.
209. Ikeda, C. and Yoda, B., EE in Japan, 91, 67, 1971.
210. Idenzl, W. and Baumgartner, R., ETZ-A, 96, 510, 1975 (Tr.).
211. Saha, B.B. and Pratt, J.M.K., 6th Int. Conf. Gas Discharges, IEE Publ. 189, 196, 1980.

212. McAllister, I.W., Arch.F.Electrot. 62, 43, 1980.
213. Borin et al, CIGRE, Paper No.15-06, 1976.
214. Farish, O. et al, Proc.IEE 123, 1047, 1976.
215. Pedersen, A., 1977 Ann.Rep.Conf. El.Insul. and Dielectric Phenomena, NAS, Washington, D.C., 373, 1977.
216. Dymond, J.H. and Smith, E.B., The Virial Coefficient of Gases, A Critical Compilation. Clarendon Press, Oxford, 1969.
217. Mears, W.H., Rosenthal, E. and Sinko, J.W., J.Phys.Chem., 73, 2254, 1969.
218. Storey, J.T. and Billings, M.J., Proc.IEE, 114, 1551, 1967.
219. Nitta, T. et al, CIGRE, paper 15-04, 1976.
220. Korasli, C., First year Rep., Univ. of Strathclyde, 1978.
221. Selim, E.O. and Waters, R.T., IEEE-IAS, Meeting on Electrostatics, Conf.Records 78, CH 1346-61A, 136, 1978.
222. Malik, N.H. and Qureshi, A.H., ISH paper 31.03, Milan, 1979.
223. Howard, P.R., PIEEE, 104, 123, 1957.
224. Berg, D. and Works, C.N., AIEE Trans., 77, 820, 1958.
225. Young, R.A. et al, J.Chem.Phys., 40, 111, 1964.
226. Blair, D.T.A., MacLeod, N.M., 4th Int.Conf.Gas Discharges, IEEE Publ.143, 401, 1976.
227. Ibrahim, O.E. and Farish, O., IEE Colloquium on corona discharges, London, 1979.
228. Ibrahim, O.E. and Farish, O., 6th Int.Conf.Gas Discharges, IEEE Publ.189, 161, 1980.
229. Blair D.T.A., MacLeod, N.M. and Orr, J.S., 3rd Int. Conf. Gas Discharges, IEEE Publ.No.118, 68, 1974.
230. Govinda Raju, G.R., Harrison, J.A. and Meek, J.M., Brit.J.Appl. Phys., 16, 933, 1965.

231. Tassicker, O.J., Proc. IEEE, 121, 213, 1974.
232. Ibrahim, O.E. and Farish, O., Gaseous Dielectrics II, Pergamon Press, New York, 83, 1980.
233. Voß, W., ISH paper 31.13, Milan, 1979.
234. Hosokawa, T., Kondo, Y. and Kiyoshi, Y., Elec. Eng. Japan, 90, 1123, 1970.
235. Sigmond, R.S. in Meek and Craggs (Eds.) Electrical Breakdown of Gases, Ch.4, Wiley, 1978.
236. Dzhuvarly, Ch., M., et al, Sov. Phys. Tech. Phys., 22, 314, 1977.
237. Van Brunt, R.J., Minutes of Workshop on Gaseous Dielec. for use in future Elec. Power Systems, Report No. NBSIR 80-1966, Jan. 1980.
238. Mulcahy, M.J. and Zumich, Z., 8th Int. Conf. Phen. in Ionized Gases, paper No. 3.1.2.7, Vienna, 1967.
239. Spence, D.A., Proc. Cambridge Phil. Soc., 68, 529, 1970.
240. Popkov, V.I., Elektrichestvo, 1, 33, 1949, (Trans.)
241. Janischewskyj, W. and Gela, G., IEEE Trans., PAS-98, 1000, 1979.
242. Vereshchagin, I.P. and Litvinov, V.E., Elect. Tech. USSR, No. 1, 101, 1979.
243. Waters, R.T., Rickard, T.E. and Stark, W.B., 1st Int. Conf. on Gas Discharges, IEEE Publ. 90, 188, 1972.
244. Khalifa, M. and Abdel-Salam, M., Proc. 2nd Int. Symp. on H.V. Tech., Zurich, 30, 1975.
245. Khalifa, M. and Abdel-Salam, M., Proc. IEEE, 120, 1574, 1973.
250. Chatterton, P.A., ISH paper 31.07, Milan, 1979.
251. Galimberti, I., J. Phys. D: Appl. Phys, 5, 2179, 1972.
252. Naidu, M.S. and Prasad, A.N., J. Phys. D.: Appl. Phys, 5, 1090, 1972.
253. Crichton, B.H., Blair, D.T.A. and Lee, D.L., 6th Int. Conf. Gas Discharges, IEEE Publ. 189, 5, 1980.

254. Alexandrov, G.N., 2nd Int. Conf. on Gas Discharges, IEEE Publ. 90, 398, 1972.
255. Puether, H., Electron Avalanches and Breakdown in Gases, Butterworths, London, 1964.
256. Dutton, J., Haydon, S.C. and Llewellyn Jones, F., Proc. Royal Soc., A213, 203, 1952.
257. Canadas, P. et al, ISH paper 12.04, Milan, 1979.
258. Schmidt, W.F. and Jungblut, H., J. Phys. D.: Appl. Phys. 12, 1979.
259. Patterson, P.L., Bull. Amer. Phys. Soc. 14, 459, 1969
- 260 Clegg, H.P. et al, Trans. Faraday Soc., 51, 1327, 1955.
- 261 Hamann, S.D. et al, ibid, 49, 351, 1953.
- 262 Dymond, J.H. and Smith, E.B., The Virial Coefficients of Gases. A Critical Compilation, Oxford Univ. Press, England, 1969.

# APPENDICES

APPENDIX 1

A1.1 Distribution Function of Electric Field Strength  
for an Elementary Region

The analysis will become valid if the following will hold for an elementary surface: (i) field strength is constant, (ii) only one initiating electron is provided, (iii) breakdown takes place only by the streamer mechanism. The critical probability [196] defined as  $p_{cr} = 1 - \frac{\eta}{\alpha}$  depends on field strength, and for  $N_{crit} = 10^8$  this field strength is equal to the electric field strength  $E$  of the gap. In the presence of an initiating electron  $p_{cr}$  can also be interpreted as breakdown probability of elementary region:

$$F_x(\Delta S, E) = p_{cr}(E) = p(\max_{0 < x \leq s} N(x) \geq 10^8 / N(0)) = \frac{\bar{\alpha}(E)}{\alpha(E)} \quad (A1.1)$$

that is, breakdown probability of an elementary surface whose breakdown field strength is lower than  $E$ .

For  $SF_6$ , swarm coefficients  $\bar{\alpha}$  and  $\alpha$  are given by:

$$\bar{\alpha} = K_{\bar{\alpha}} [E - (\frac{E}{p})_{\bar{\alpha}} \cdot p] ; \quad \alpha = K_{\alpha} [E - (\frac{E}{p})_{\alpha} \cdot p] \quad (A1.2)$$

and for  $SF_6/N_2$   $\bar{\alpha}_m$  is linearized over a narrow region near to the limit  $(E/p)_{\bar{\alpha}}$  [94] and  $\alpha_m$  could be assumed to be linearized similarly,

$$\bar{\alpha}_m = K_{\bar{\alpha}} \cdot C^{0.25} [E - (\frac{E}{p})_{\bar{\alpha}} \cdot p \cdot C^{0.2}] \quad (A1.3)$$

$$\alpha_m = K_{\alpha} C^q [E - (\frac{E}{p})_{\alpha} \cdot p \cdot C^r]$$

where  $k_{\bar{\alpha}} = 27 \text{ kV}^{-1}$  and  $(E/p)_{\bar{\alpha}} = 88.4 \text{ kV}/(\text{cm bar})$ ,  $K_{\alpha} = 24 \text{ kV}^{-1}$  and  $(E/p)_{\alpha} = 56 \text{ kV}/(\text{cm bar})$ ,  $q$  and  $r$  are to be determined.

Equations given in (A1.2) are valid for  $0.05 < c < 1$ .

Substituting (A1.2) and (A1.3) into equation (A1.1), the distribution function for an elementary region becomes:

For  $SF_6$

$$F(S,E) = \begin{cases} 0 & \text{for } E < E_{\alpha}^- \\ K_R \frac{E - E_{\alpha}^-}{E - E_{\alpha}^-} & \text{for } E > E_{\alpha}^- \end{cases} \quad (A1.4)$$

and for  $SF_6/N_2$

$$F(S,E) = \begin{cases} 0 & \text{for } E \leq E_{\alpha_m}^- \\ (K_{Rm} \frac{E - E_{\alpha_m}^-}{E - E_{\alpha_m}^-}) & \text{for } E > E_{\alpha_m}^- \end{cases} \quad (A1.5)$$

where  $K_R = K_{\alpha}^- / K_{\alpha}$  and  $K_{Rm} = K_{\alpha_m}^- / K_{\alpha_m}$ .

If the complete system consists of  $n$  elementary surfaces, in order to have a meaningful physical result as  $n \rightarrow \infty$  and  $E \rightarrow E_{\alpha}^-$ , the distribution function of elementary surface can be rewritten as

$$F(\Delta S, E) = \begin{cases} 0 \\ \frac{1}{n} \left( \frac{E - E_{\alpha}^-}{E_M - E_{\alpha}^-} \right) \end{cases} \quad (A1.6)$$

where  $E_M$  is the mode of the distribution.

A2.1 Parameter Estimation for the Weibull Distribution

The cumulative Weibull distribution function is given by

$$F(x) = 1 - \exp \left[ -\left(\frac{x - \gamma}{\alpha}\right)^\beta \right] \quad (\text{A2.1})$$

where  $\alpha$  is the scale parameter

$\beta$  is the shape parameter

$\gamma$  the location parameter, and

$x$  the random variable, usually the b/d voltage or electric field strength.

$F(x)$  indicates the probability of failure at the  $i$ -th stage of the test of the  $n$ -sample. The scale parameter  $\alpha$  represents the field strength required for  $(1 - e^{-1})$  or 63.2 per cent. of the tests to fail. The shape parameter ( $\beta$ ) is a measure of dispersion of the failure field strengths from  $x = \alpha$ . The parameter  $\gamma$  indicates the field strength for which breakdown is not possible. Therefore the Equation A2.1 is written for  $x \geq \gamma$

$$F(x) = 0 \quad \text{for} \quad 0 < x \leq \gamma$$

The units of  $\alpha$  and  $\gamma$  are electric field, when this is a random variable, while  $\beta$  is dimensionless. The location parameter  $\gamma$  is sometimes taken to be zero (a two-parameter distribution) although finite values have been used in most of the analysis [118, 132, 196, 197].

If it is known that the observations are from a population of Weibull variates with known shape and location parameters  $\beta$  and  $\gamma$  respectively, and the unknown scale parameter  $\alpha$ , then  $y_1 = (x_1 - \gamma)^\beta \dots, y_n = (x_n - \gamma)^\beta$  can be considered

ordered observations with unknown scale parameter  $\theta = \alpha^{\frac{1}{\beta}}$  from an exponential distribution [B12]. Then to make such a transformation it is necessary to have enough breakdowns in a sample that the Weibull shape parameter is independent of the (rate of rise voltage and the radiation) way of voltage application for breakdown and that  $\beta$  and  $\gamma$  can be assumed to be known for given environmental conditions. In such a case the Equation A2.1 will take the form:

$$F(x; \theta, \beta, \gamma) = 1 - \exp\left(-\frac{(x - \gamma)^\beta}{\theta}\right) \quad (\text{A2.2})$$

Thereby the three parameter Weibull distribution, the density function can be written as:

$$f(x; \theta, \beta, \gamma) = \frac{\beta}{\theta} (x - \gamma)^{\beta-1} \exp\left[-\frac{(x - \gamma)^\beta}{\theta}\right] \quad (\text{A2.3})$$

When Equation A2.3 is the applicable density function. The likelihood function of random sample of  $n$  observations is [201]

$$L(x; \theta, \beta, \gamma) = \prod_{i=1}^n \frac{\beta}{\theta} (x_i - \gamma)^{\beta-1} \exp\left[-\frac{(x_i - \gamma)^\beta}{\theta}\right] \quad (\text{A2.4})$$

On taking the logarithms of Equation A2.4 and differentiating with respect to  $\theta$ ,  $\beta$  and  $\gamma$  in turn and equating to zero, we obtain the maximum likelihood estimating equations as follows

$$\begin{aligned} \frac{\partial \bar{\ln L}}{\partial \theta} &= -\frac{n}{\theta} + \frac{1}{\theta^2} \sum_{i=1}^n (x_i - \gamma)^\beta = 0, \\ \frac{\partial \bar{\ln L}}{\partial \beta} &= \frac{n}{\beta} + \sum_{i=1}^n \bar{\ln}(x_i - \gamma) - \frac{1}{\theta} \sum_{i=1}^n (x_i - \gamma)^\beta \bar{\ln}(x_i - \gamma) = 0 \\ \frac{\partial \bar{\ln L}}{\partial \gamma} &= \frac{\beta}{\theta} \sum_{i=1}^n (x_i - \gamma)^{\beta-1} - (\beta - 1) \sum_{i=1}^n (x_i - \gamma)^{\beta-1} = 0 \end{aligned} \quad (\text{A2.5})$$

The limitations on the shape parameter  $\beta$  leads to the

following cases [201]. For  $\beta < 1$ , the likelihood function given in Equation A2.4 becomes infinite as  $\gamma \rightarrow \gamma_0$ , where  $\gamma_0$  is the smallest sample observation. Accordingly, in this case, the applicable estimating equations consist of the first two equations of (A2.5) plus  $\gamma = \gamma_0 - \frac{\eta}{2}$ , where  $\eta$  is the unit of precision with which observations are made and  $\gamma$  is the max. likelihood estimate of  $\gamma$ .

For  $\beta = 1$ , the distribution achieves the exponential form, the applicable estimators are

$$\theta = \sum_i \frac{x_i - \gamma_0}{n} \quad \text{and} \quad \gamma = \gamma_0$$

For the case  $\beta > 1$ , solving  $\theta$  from the first equation of (A2.5) and substituting into the last two equations of (A2.5) yields:

$$\left[ \frac{\sum_i (x_i - \gamma)^\beta \ln(x_i - \gamma)}{\sum_i (x_i - \gamma)^\beta} - \frac{1}{\beta} \right] - \frac{1}{\eta} \sum_i \ln(x_i - \gamma) = 0 \quad (\text{A2.6})$$

$$n \cdot \beta \frac{\sum_i (x_i - \gamma)^{\beta-1}}{\sum_i (x_i - \gamma)^\beta} - (\beta-1) \sum_i (x_i - \gamma)^{-1} = 0 \quad (\text{A2.7})$$

### $\gamma$ - Known

When  $\gamma$  is known and also in those cases where  $\gamma_0 + k$  is an applicable estimator for  $\gamma$ , we need only to solve Equation A2.6 to obtain  $\beta$ . This can be accomplished using (trial and error technique) described by Cohen [198] or iterative technique for the solution of  $f(\beta) = 0$ , Equation A2.6, using Newton-Raphson method the  $(j + 1)$  successive approximation  $\beta_{j+1}$  to  $\beta$  is given by

$$\hat{\beta}_{j+1} = \hat{\beta}_j - \frac{f(\hat{\beta}_j)}{f'(\hat{\beta}_j)} \quad (\text{A2.8})$$

With thus  $\hat{\beta}$  determined,  $\hat{\theta}$  follows from the first equation of A2.5

as

$$\hat{\theta} = \frac{1}{n} \sum_{i=1}^n (x_i - \gamma)^{\hat{\beta}} \quad (\text{A2.9})$$

The procedure for calculating the parameters formulated above can be put into the ALGORITHM which calculates  $\beta$ ,  $\theta$  and  $\alpha$ .

Equation A2.5 can be simplified as:

$$f(\hat{\beta}) = \frac{A_2}{A_1} - \frac{1}{\beta} - c = 0 \quad (\text{A2.10})$$

with

$$A_k = \frac{1}{n} \sum_{i=1}^n (x_i - \gamma)^{\hat{\beta}} [\ln(x_i - \gamma)^{k-1}] \quad k=1,2,3 \quad (\text{A2.11})$$

and

$$c = \frac{1}{n} \sum_{i=1}^n \ln(x_i - \gamma) \quad (\text{A2.12})$$

while 
$$\theta = \frac{1}{n} \sum_{i=1}^n (x_i - \gamma)^{\hat{\beta}}$$

$$\theta = \frac{A_1}{n} \quad \text{and} \quad \alpha = \left( \frac{A_1}{n} \right)^{(1/\hat{\beta})}$$

Using the Newton-Raphson iterative rule, with  $\hat{\beta}_\rho$  representing the iteration number

$$\hat{\beta}_{\rho+1} = \hat{\beta}_\rho - \frac{f(\hat{\beta}_\rho)}{f'(\hat{\beta}_\rho)} \quad (\text{A2.13})$$

where

$$f'(\hat{\beta}) = \frac{A_3}{A_1} - \left( \frac{A_2}{A_1} \right)^2 + \frac{1}{\beta^2} \quad (\text{A2.14})$$

The simple algorithm showing the procedure for estimating  $\hat{\beta}$ ,  $\hat{\theta}$  and  $\hat{\alpha}$  is as follows. Initial estimate of  $\hat{\beta}$  was obtained from the graphical estimate.

(i) input; initial estimate of  $\hat{\beta}$  and data.

- (ii) Calculate  $A_k$  ( $k = 1, 2, 3$ ) and  $C$  from Equations A2.11 and A2.12.
- (iii) Calculate  $f$ ,  $f'$  and  $\hat{\beta}$  (Equations A2.10 and A2.14)
- (iv) If  $f$  is sufficiently small, go to step (vi).
- (v) If  $f$  is not small enough, replace  $\hat{\beta}$  with the new one and go to step (ii).
- (vi) Calculate  $\hat{\theta}$ ,  $\hat{\alpha}$  and print  $\hat{\alpha}$  and  $\hat{\beta}$ .

$\gamma$  is unknown

Method A

In the more general case of concern here, we choose a first approximation  $\gamma_1$ . Then assuming  $\gamma = \gamma_1$ , we proceed as described above and determine first approximations to  $\beta_1$  and  $\theta_1$ . With these approximations substituted into the third equation of (A2.5), we calculate the first approximation  $(\partial \bar{\ln} L / \partial \gamma)_1$ . If this value differs from zero, we select a second approximation  $\gamma_2$  and repeat. The procedure is continued until we obtain two values,  $\gamma_i$  and  $\gamma_j$  with a difference that is sufficiently small and such that  $(\partial \bar{\ln} L / \partial \gamma)_i > 0 > (\partial \bar{\ln} L / \partial \gamma)_j$ , whereupon we interpolate for the required estimates [201].

Convergence of this method of solution depends on the initially selected values of constants and it is slow. The following method was found to be more effective.

Method B

If  $\gamma$  is unknown, simultaneous solution of Equations A2.6 and A2.7 provides  $\alpha$ ,  $\beta$  and  $\gamma$ . For numerical iterative solutions, the approximate (including first degree terms only) Taylor series expansion of functions  $f(\beta, \gamma)$  and  $g(\beta, \gamma)$  can be written at points  $\beta = \beta_0 + h$  and  $\gamma = \gamma_0 + k$  as:

$$f(\beta_0 + h, \gamma_0 + k) = f(\beta_0, \gamma_0) + \left( h \frac{\partial}{\partial \beta} + k \frac{\partial}{\partial \gamma} \right) f_{\beta_0, \gamma_0} \equiv 0 \quad (\text{A2.15})$$

and

$$g(\beta_0 + h, \gamma_0 + k) = g(\beta_0, \gamma_0) + \left( h \frac{\partial}{\partial \beta} + k \frac{\partial}{\partial \gamma} \right) g_{\beta_0, \gamma_0} \equiv \theta \quad (\text{A2.16})$$

where  $\beta_0$  and  $\gamma_0$  initial estimates,  $h$  and  $k$  are increments. The necessary algorithm for the iterative solution is

- (i) Input; initial estimates  $\beta_0$  and  $\gamma$  increments  $h$  and  $k$ .
- (ii) Calculate new increments from equations A2.15 and A2.16.
- (iii) Calculate new estimates and replace with old ones.
- (iv) Check whether  $|h| / |\beta|$  and  $|k| / |\gamma|$  are less than
- (v) If the answer is 'no', go to step (ii).
- (vi) If the answer is 'yes', calculate  $\alpha$ .
- (vii) Print  $\alpha$ ,  $\beta$  and  $\gamma$

## A2.2 Application of Weakest Link Theory to Three Parameter Weibull Distribution

In the previous section, derivations were made for a subcomponent of the complete assembly. As a whole, the breakdown characteristic of the system is equivalent to the breakdown characteristic of the weakest subcomponent. Assuming all  $N$  subcomponents are identically prepared and their breakdown field strengths are distributed with some p.d.f. =  $f(x)$  and c.d.f. =  $F(x)$ , the breakdown field strength of the component would be distributed according to the smallest order statistic [200]: thus

$$F_1(x) = 1 - [1 - F(x)]^N \quad (\text{A2.17})$$

$$f_1(x) = N [1 - F(x)]^{N-1} f(x) \quad (\text{A2.18})$$

For the three parameter Weibull distribution:

$$F_1(x; \theta, \gamma, \beta) = 1 - \{1 - \exp[-(x-\gamma)^\beta / \theta]\}^N \quad (\text{A2.19})$$

$$f_1(x; \theta, \gamma, \beta) = \frac{N\beta}{\theta} (x-\gamma)^{\beta+1} \exp[-N(x-\gamma)^\beta / \theta] \quad (\text{A2.20})$$

also the parameterization in which  $\theta = \alpha^\beta$ ,  $\alpha = \theta^{1/\beta}$  can be used alternatively.

The likelihood function with density function Equation A2.20 is

$$L(x; \beta, \gamma, \theta) = \prod_{i=1}^n f_1(x_i) = \left(\frac{N\beta}{\theta}\right)^n \prod_{i=1}^n (x_i - \gamma)^{\beta-1} \exp[-N(x_i - \gamma)^\beta / \theta] \quad (\text{A2.21})$$

and the logarithm of Equation A2.21

$$\bar{\ln L} = n \cdot \bar{\ln(N\beta)} - N \cdot \bar{\ln \theta} + (\beta-1) \sum_{i=1}^n \bar{\ln}(x_i - \gamma) - \frac{N}{\theta} \sum_{i=1}^n (x_i - \gamma)^\beta \quad (\text{A2.22})$$

on differentiating Equation A2.22 with respect to  $\beta$ ,  $\theta$  and  $\gamma$  in turn, and equating to zero. We obtain

$$\frac{\partial \bar{\ln L}}{\partial \beta} = \frac{n}{N\beta} + \sum_{i=1}^n \bar{\ln}(x_i - \gamma) - \frac{N}{\theta} \sum_{i=1}^n (x_i - \gamma)^\beta \bar{\ln}(x_i - \gamma) = 0$$

$$\frac{\partial \bar{\ln L}}{\partial \theta} = -\frac{n}{\theta} + \frac{N}{\theta^2} \sum_{i=1}^n (x_i - \gamma)^\beta = 0 \quad (\text{A2.23})$$

$$\frac{\partial \bar{\ln L}}{\partial \gamma} = -(\beta-1) \sum_{i=1}^n (x_i - \gamma)^{-1} + \frac{N\beta}{\theta} \sum_{i=1}^n (x_i - \gamma)^{\beta-1} = 0$$

For the case for which  $\beta > 1$  we eliminate  $\theta$  between the first two equations of equation A2.23 to obtain

$$f(x; \beta, \gamma, N) = \left[ \frac{\sum_{i=1}^n (x_i - \gamma)^\beta \bar{\ln}(x_i - \gamma)}{\sum_{i=1}^n (x_i - \gamma)^\beta} - \frac{1}{N\beta} \right] - \frac{1}{n} \sum_{i=1}^n \bar{\ln}(x_i - \gamma) = 0 \quad (\text{A2.24})$$

When  $\gamma$  is known experimentally, Equation A2.24 is needed to be

solved to obtain  $\beta$ . The method for solution was described previously for single component system.

When  $\gamma$  is unknown, the second nonlinear equation for simultaneous solution together with Equation A2.24 can be derived similarly, eliminating  $\theta$  between second and third equations of A2.23, which has the same form as Equation A2.7. The method of iterative solution for the estimates  $\alpha$ ,  $\beta$  and  $\gamma$  (i.e.  $E_c$ ,  $\beta$  and  $E_o$  respectively) is the same as was described for one test section.

### A2.3 Modal Value of a Statistical Distribution [194,204]

Breakdown probability density function is given by differentiating of Equation 4.5 with respect to E.

$$f(E) = \frac{\beta \cdot d_o}{E_c} \cdot S. \left( \frac{E-E_o}{E_c} \right)^{\beta-1} \exp \left[ - S \cdot d_o \left( \frac{E-E_o}{E_c} \right)^\beta \right] \quad (A2.25)$$

Modal value of the statistical distribution is obtained by equating the differentiation of the density function  $p(E)$  by E which gives

$$\frac{E_m - E_o}{E_c} = \left( \frac{\beta - 1}{S \cdot d_o \cdot \beta} \right) \frac{1}{\beta}$$

or

$$\frac{E_m}{E_c} = \frac{E_o}{E_c} + \left( \frac{\beta - 1}{S \cdot d_o \cdot \beta} \right) \frac{1}{\beta} \quad (A2.26)$$

Calculation of Compressibility Factor in SF<sub>6</sub>/N<sub>2</sub> Mixtures

A3.1      General

The deviation from the ideal gas behaviour is due to changes in the quantity  $z = PV/nRT$  as the pressure is raised. This quantity exhibits more complex behaviour as pressure and temperature are varied and can be expressed in the form of a polynomial, as

$$z = \frac{pV}{nRT} = 1 + B'(T).p + C'(T)p^2 + D'(T).p^3 + \dots \quad (A3.1)$$

This is known as the virial equation and the coefficients  $B'(T)$ ,  $C'(T)$ ... as virial coefficients.

Another equivalent form of equation (A3.1) which is useful for experimental purposes for finding the coefficients is the expansion of the compressibility in reciprocal powers of the mole volume,  $n/V$

$$\frac{pV}{nRT} = 1 + B\left(\frac{n}{V}\right) + C\left(\frac{n}{V}\right)^2 + D\left(\frac{n}{V}\right)^3 + \dots \quad (A3.2)$$

These coefficients can be related to the coefficients  $B'$ ,  $C'$ ,  $D'$ ... as follows. Equation (A3.1) may be written as

$$\frac{n}{V} = \frac{p}{RT} (1 + B'p + C'p^2 + \dots)^{-1}$$

or after neglecting higher order terms having power greater than two

$$\frac{n}{V} = \frac{p}{RT} (1 - B'p - C'p^2 + B'^2p^2)$$

and simplifying,

$$\frac{n}{V} = \frac{p}{RT} - \frac{B'p^2}{RT} - \frac{(C' - B'^2)p^2}{RT} \quad (A3.3)$$

Substituting equation (A3.3) into (A3.2) yields the following equation

$$\frac{pV}{nRT} = 1 + \frac{B}{RT} p + \left[ \frac{C}{R^2T^2} - \frac{B'B}{RT} \right] p^2 \quad (A3.4)$$

Comparing equation (A3.4) to (A3.1), we obtain:

$$B' = \frac{B}{RT} \quad \text{and} \quad C' = \frac{C}{R^2 T^2} - \frac{B'B}{RT}$$

The virial equations of state are not useful at pressures near or above the critical pressure (i.e. near the liquification point).

### A.3.2 Virial Coefficients of SF<sub>6</sub> and N<sub>2</sub>

The compressibility factor in SF<sub>6</sub> working at 20°C and for  $0 \leq p \leq 10$  bar may be expressed with second order polynomial approximation as

$$z = 1 + B'p + C'p^2 \quad (\text{A3.5})$$

In order to find out the coefficients B' and C' the experimental data collected for B and C in Equation (A3.4) from several sources [216, 217] is as depicted in Figure A3.1, was extrapolated to include the temperature of interest, which was found to be

$$B_1(293) = -291 \quad (\text{cc/mole})$$

$$C_1(293) = 23,500 \quad (\text{cc/mole})^2$$

and hence,

$$B_1'(293) = -1.1938 \cdot 10^{-2} \quad (\text{bar})^{-1}$$

$$C_1'(293) = -1.0198 \cdot 10^{-4} \quad (\text{bar})^{-2}$$

Similarly, for N<sub>2</sub>, at 20°C, the virial coefficients obtained from the extrapolation of the experimental data (Figure A3.2), given in reference [216], can be written as:

$$B_2(293) = -5.4 \quad (\text{cc/mole})$$

$$C_2(293) = 1430 \quad (\text{cc/mole})^2$$

and

$$B_2'(293) = -2.2154 \cdot 10^{-4} \quad (\text{bar})^{-1}$$

$$C_2'(293) = 2.3578 \cdot 10^{-4} \quad (\text{bar})^{-2}$$

Calculation of Compressibility Factor ofSF<sub>6</sub>/N<sub>2</sub> Mixtures

The compressibility factor of SF<sub>6</sub>/N<sub>2</sub> mixtures of varying mixing ratios can be deduced by making use of Dalton's law for mixtures of gases.

Since the compressibility factor for the constituents SF<sub>6</sub> and N<sub>2</sub> may be written as in Equation A3.2 as for SF<sub>6</sub>:

$$z_1 = \frac{p_1 V}{n_1 RT} = 1 + B_1 \left(\frac{n_1}{V}\right) + C_1 \left(\frac{n_1}{V}\right)^2 + D_1 \left(\frac{n_1}{V}\right)^3 + \dots \quad (\text{A1.6})$$

$$z_2 = \frac{p_2 V}{n_2 RT} = 1 + B_2 \left(\frac{n_2}{V}\right) + C_2 \left(\frac{n_2}{V}\right)^2 + D_2 \left(\frac{n_2}{V}\right)^3 + \dots \quad (\text{A1.7})$$

Where  $p_i$  is the partial pressure and  $n_i$  is the number of moles of the constituent  $i$  occupying the volume  $V$  alone.

Rearranging equations (A3.6) and (A3.7)

$$\frac{p_1 V}{RT} = n_1 + B_1 \frac{n_1^2}{V} + C_1 \frac{n_1^3}{V^2} + \dots \quad (\text{A3.8})$$

$$\frac{p_2 V}{RT} = n_2 + B_2 \frac{n_2^2}{V} + C_2 \frac{n_2^3}{V^2} + \dots \quad (\text{A3.9})$$

Adding Equations (A1.8) and (A1.9)

$$\frac{(p_1 + p_2)V}{RT} = (n_1 + n_2) + \frac{1}{V} (n_1^2 B_1 + n_2^2 B_2) + \frac{1}{V^2} (n_1^3 C_1 + n_2^3 C_2) + \dots \quad (\text{A3.10})$$

Assuming that molecules do not interact with one another, and they all behave ideally, total pressure of constituents according to Dalton's law

$$p = p_1 + p_2 \quad (\text{A3.11})$$

and since the number of moles does not change after mixing two

gases, the number of moles in the mixture becomes

$$n = n_1 + n_2 \quad (\text{A3.12})$$

Defining the mole fractions  $x_i$  of the constituents of the mixture as

$$x_i = \frac{n_i}{n} \quad (\text{A3.13})$$

the partial pressure  $p_i$  of the constituent  $i$  is then given by

$$p_i = x_i p \quad (\text{Note } \sum x_i = 1) \quad (\text{A3.14})$$

Substituting Equations (A3.11), (A3.12) and (A3.13) in (A3.10)

we obtain

$$\frac{pV}{RT} = n + \frac{1}{V} [(x_1 n)^2 B_1 + (x_2 n)^2 B_2] + \frac{1}{V^2} [(x_1 n)^3 C_1 + (x_2 n)^3 C_2] \quad (\text{A3.15})$$

Arranging the parentheses on the right hand side of the equation for  $n$ , we have

$$\frac{pV}{RT} = n \left[ 1 + (x_1^2 B_1 + x_2^2 B_2) \left(\frac{n}{V}\right) + (x_1^3 C_1 + x_2^3 C_2) \left(\frac{n}{V}\right)^2 + \dots \right] \quad (\text{A3.16})$$

If we call  $B = x_1^2 B_1 + x_2^2 B_2$  and  $C = x_1^3 C_1 + x_2^3 C_2$ , we will obtain the familiar compressibility equation (A3.2). The virial coefficients in the pressure dependent compressibility factor (Equation (A3.1)) can therefore be written for the mixtures as

$$B' = \frac{B}{RT} = \frac{1}{RT} (x_1^2 B_1 + x_2^2 B_2) \quad (\text{A3.17})$$

$$C' = \frac{1}{(RT)^2} (C - B^2) = \frac{1}{(RT)^2} [(x_1^3 C_1 + x_2^3 C_2) - (x_1^2 B_1 + x_2^2 B_2)^2] \quad (\text{A3.18})$$

The derivation is also applicable for mixtures having more than two constituents up to pressures less than the critical pressure of the mixture.

Breakdown Field and Voltage Calculations for  
Smooth and Rough Electrode Gaps in  
SF<sub>6</sub> and SF<sub>6</sub>/N<sub>2</sub> Mixtures

A4.1 Estimation for Smooth Electrode GapsA4.1.1 In SF<sub>6</sub>Method of Substitution

In coaxial electrode configuration, the geometric field distribution is given by  $E(r) = V/r \ln(r_2/r_1)$ . If the field strength of the inner conductor at breakdown is  $E_0$ , then the following simple relation can be written for the geometric field

$$E(r) = E_0 \frac{r_1}{r} \quad (\text{A4.1})$$

Since  $r = r_1 + \rho$  (Figure A4.1), the new form of Equation (A4.1)

$$E(r) = E_0 \frac{1}{1 + \frac{\rho}{r_1}} \quad (\text{A4.2})$$

Substituting Equation (A4.2) into  $\bar{\alpha} = f(E/p)$  and in turn into

$\int_0^{\rho} \bar{\alpha}(\rho) d\rho = k$  yields the following

$$E_0 \int_0^{\rho} \frac{d\rho}{1 + \frac{\rho}{r_1}} - \left(\frac{E}{\rho}\right)_{\text{lim}} \rho = \frac{k}{K} \quad (\text{A4.3})$$

or

$$E_0 r_1 \ln\left(1 + \frac{\rho}{r_1}\right) - \left(\frac{E}{\rho}\right)_{\text{lim}} \rho = \frac{k}{K} \quad (\text{A4.4})$$

Since  $\ln(1+x) = x - \frac{x^2}{2} + \frac{x^3}{3}$ , it follows that

$$\ln\left(1 + \frac{\rho}{r_1}\right) = \frac{\rho}{r_1} - \frac{1}{2} \left(\frac{\rho}{r_1}\right)^2 + \frac{1}{3} \left(\frac{\rho}{r_1}\right)^3$$

Neglecting higher order terms and substituting into Equation (A4.4) gives

$$E_0 \rho - \left(\frac{E}{p}\right)_{\text{lim}} p \rho = \frac{k}{K} \quad (\text{A4.5})$$

Also, from  $\bar{\alpha}(\rho) = 0$ , we have

$$E_0 \frac{1}{1 + \frac{\rho}{r_1}} - \left(\frac{E}{p}\right)_{\text{lim}} \rho = 0 \quad (\text{A4.6})$$

and solving for the critical avalanche length  $\rho$

$$\rho = r_1 \left[ \frac{(E_0/p)}{\left(\frac{E}{p}\right)_{\text{lim}}} - 1 \right] \quad (\text{A4.7})$$

Substituting Equation A4.7 into Equation A4.5 and solving for  $E_0/p$

$$\frac{E_0}{p} = A \left( 1 + C \frac{1}{\sqrt{pr_1}} \right) \quad (\text{A4.8})$$

where  $A = \left(\frac{E}{p}\right)_{\text{lim}}$  and  $C = \left(\frac{k}{A \cdot K}\right)^{1/2}$

and  $V_0 = E_0 r_1 \ln \frac{r_2}{r_1}$

or

$$V_0 = A (pr_1 + C \sqrt{pr_1}) \ln \frac{r_2}{r_1} \quad (\text{A4.9})$$

#### Method of Iteration (computer solution)

This method of solution is performed by solving Equations (A4.4) and (A4.6) simultaneously.

Although results of both methods of solutions exhibit reasonable agreement for electrodes with inner radii  $r_1 > r_2$  . e, for smaller radii electrodes there exists considerable differences, as shown in Figure A4.2

#### A4.1.2 In SF<sub>6</sub>/N<sub>2</sub> Mixtures

Only the iterative method of solution is applied for

the estimation of  $E_0$  and  $V_0$ .

The effective ionization coefficient according to partial pressure approximation can be expressed as

$$\frac{\bar{\alpha}_m}{p} = \left[ \left( \frac{\bar{\alpha}}{p} \right)_{\text{SF}_6} + x \left( \frac{\alpha}{p} \right)_{\text{N}_2} \right] \frac{1}{1+x} \quad (\text{A4.10})$$

with  $x = p_{\text{N}_2} / p_{\text{SF}_6}$ . Substituting  $\left( \frac{\bar{\alpha}}{p} \right)_{\text{SF}_6} = k \left[ \frac{E(r)}{p} - \left( \frac{E}{p} \right)_{\text{lim}} \right]$  and  $\left( \frac{\alpha}{p} \right)_{\text{N}_2} = M \exp [-Np/E(r)]$ , where  $M = 6.6 \times 10^3 \text{ (bar cm)}^{-1}$  and  $N = 215 \text{ kV (bar cm)}^{-1}$ , into Equation A4.10, setting it to zero and iterating it yields  $(E/p)_x$ , i.e. limiting field strength of a mixture with partial pressure ratio  $x$ .

The critical avalanche length for any mixture can be estimated from Equation A4.1 that is given by

$$r_c = \frac{(E_0/p) r_1}{(E/p)_x} \quad (\text{A4.11})$$

Simultaneous solution of equations

$$\frac{1}{1+x} \int_{r_1}^{r_c} K \left[ E(r) - p \left( \frac{E}{p} \right)_{\text{lim}} \right] + x M e^{-N/pE(r)} dr = k \quad (\text{A4.12})$$

and

$$K \left[ E(r) - p \left( \frac{E}{p} \right)_{\text{lim}} \right] + x M e^{-N/pE(r)} = 0 \quad (\text{A4.13})$$

Taking into account Equation A4.11 yields  $E_b$  and  $V_b$ .

## A4.2 Application of Finite Difference Method to Breakdown Estimation in a Coaxial Gap having Rough Inner Electrode

### A4.2.1 A review of finite difference method

The finite-difference form of Laplace's equation, modified for rapid convergence, is given for an irregular rectangular mesh (Figure A4.3) in cylindrical coordinate system as [218].

$$\begin{aligned}
V_{(r,z)}^{n+1} = & V_{(r,z)}^n + \left(\frac{\alpha}{k}\right) V_{(r+1,z)}^n \left[ \frac{1+\omega h/2R_{r,z}}{q(q+\omega)} \right] + \\
& V_{(r-1,z)}^{n+1} \left[ \frac{1-qh/2R_{r,z}}{\omega/q+\omega} \right] + \\
& V_{(r,z+1)}^n \left[ \frac{1}{p(\rho+s)} \right] + \\
& V_{(r,z-1)}^{n+1} \left[ \frac{1}{s(\rho+s)} \right] - k V_{(r,z)}^n \quad (A4.14)
\end{aligned}$$

where  $R_{r,z} = r_1 + (r - 1) c x h$

|                         |                           |
|-------------------------|---------------------------|
| $c, \rho, q, s, \omega$ | are constants             |
| $h$                     | mesh length               |
| $\alpha$                | accelerating factor       |
| $n$                     | order of iteration        |
| $r_1$                   | radius of inner electrode |

$$k = \frac{1}{\omega q} + \frac{1}{sp} + \frac{h(\omega-q)}{2\omega q R_{r,z}}$$

The optimum value of  $\alpha$  when the number of nodes in  $r$ -direction  $t$  and in  $z$ -direction  $y$  are large is given by

$$\alpha_{opt} = 2 - \pi \sqrt{\left[ \frac{1}{(t-1)^2} + \frac{1}{(y-1)^2} \right]} \quad (A4.15)$$

For the first two iterations,  $\alpha$  is taken to be unity.

#### A4.2.2 Algorithm for iterative solution

1. Read data: radii  $r_1$  and  $r_2$ , protrusion height  $h_p$ , mesh size constants  $p$  and  $s$ , radial and axial node numbers.
2. Store boundary conditions; boundaries (A), (B), (C) and (D) (see section 5.4.2.1).

3. Set values in reference meshes.
4. Calculate  $\alpha_{\text{opt}}$  and start iteration.
5. Calculate  $R_{(r,z)}$  and  $V_{(r,z)}$  (Equation A4.14).
6. Calculate  $|V_{(r,z)}^{n+1} - V_{(r,z)}|$  and store the maximum value.
7. If the convergence is achieved 'go to 8', if the convergence is not achieved 'go to 5', and continue.
8. Print  $V_{r,z}$  and  $R_{r,z}$ .

Estimation of the Space Charge Field DistributionA.5.1 Mathematical Model

Unipolar dc corona starts in any nonuniform electrode system when the applied voltage is increased above the corona onset in the form of a steady ion flow of one polarity in the interelectrode space, the ions polarity being the same as the polarity of the electrode in corona. The direction and magnitude of the local electric field  $\bar{E}$  is not only determined by the applied potentials and the geometry of the electrodes but also by the distribution of local space charge, while the ionic flow itself is a function of electric field.

Due to axial symmetry, the divergence of the electric field  $\bar{E}$  is related to volume charge density  $\rho$  by the permittivity  $\epsilon_0$  of free space as

$$\nabla \cdot \bar{E} = - \frac{\rho}{\epsilon_0} \quad (\text{A5.1})$$

and to the ionic flow (or current density) vector  $\bar{j}$  along the line of force by

$$\bar{j} = \mu \rho \bar{E} \quad (\text{A5.2})$$

where  $\mu$  is the mobility of ions. The condition for current continuity under steady state conditions

$$\nabla \cdot \bar{j} = 0 \quad (\text{A5.3})$$

The electric field in terms of potential  $\phi$

$$\nabla \phi = - \bar{E} \quad (\text{A5.4})$$

substituting (A5.4) into (A5.1)

$$- \nabla \cdot \nabla \phi = \frac{\rho}{\epsilon_0} \quad (\text{A5.5})$$

Also using (A5.4) in (A5.2) and substituting into (A5.3)

$$\bar{\nabla} \cdot (\rho \bar{\nabla} \phi) = 0 \quad (\text{A5.6})$$

(A5.5) and (A5.6) are two coupled differential equations describing unipolar corona mechanism. This set must be solved for the potential function  $\phi$  and the volume charge density. However, they are nonlinear in nature and for general cases the solution is possible with the simplifying assumption given in section 7.9.

#### A.5.2 Equations for Field and Charge Distributions

Basing on the above assumption, the analytic solutions of the coupled differential (Equations A5.5 and A5.6), hence potential and space charge functions for the concentric cylindrical geometry is as follows. The Poisson's Equation A5.5 in the radial direction, assuming charge density and electric field is unidirectional, becomes

$$\frac{d^2\phi}{dr^2} + \frac{1}{r} \frac{d\phi}{dr} = - \frac{\rho(r)}{\epsilon_0} \quad (\text{A5.7})$$

and

$$j = 2 \pi r \mu \rho(r) E(r) \quad (\text{A5.8})$$

where  $r$  is the radial space coordinate in cylindrical coordinates.

Substituting  $\frac{d\phi}{dr} = - E(r)$  in Equation A5.7

$$\frac{dE(r)}{dr} + \frac{1}{r} E(r) = \frac{j}{\epsilon_0} \quad (\text{A5.9})$$

and integrating Equation A5.9 for  $E$  by making use of the boundary conditions and Equation A5.8, the field strength at any radius

becomes

$$E(r) = \frac{1}{r} [r_1^2 E_0^2 + \frac{j}{2\pi\epsilon_0\mu} (r^2 - r_1^2)]^{1/2} \quad (\text{A5.10})$$

$$E(r) = \frac{1}{r} \left[ r_1^2 E_0^2 + \frac{r_1 \rho_e E_0}{\epsilon_0} \left( 1 - \frac{r_1^2}{r^2} \right) \right]^{1/2} \quad (\text{A5.11})$$

where  $E_0$  is the corona onset field strength and  $p_e = p(r_1)$ , using the relation

$$\phi(r) = V - \int_{r_1}^r E(r) \cdot dr \quad (\text{A5.12})$$

and substituting for  $E(r)$  as in Equation A5.11, the potential function becomes

$$\phi(r) = V - z_1 \left\{ h(r) - z_2 + z_3 \left[ \ln \frac{r}{r_1} + \ln(z_2 + z_3) - \ln(h(r) + z_3) \right] \right\} \quad (\text{A5.13})$$

where

$$z_1 = \sqrt{\frac{r_1 E_0 \rho_e}{\epsilon_0}} \quad ; \quad z_2 = \sqrt{\frac{r_1 E_0 \epsilon_0}{p_e}} \quad ; \quad z_3 = \sqrt{z_2^2 - r_1^2}$$

$$h(r) = \sqrt{r^2 + z_2^2 - r_1^2}$$

$$\rho(r) = \sqrt{\frac{r_1 E_0 \epsilon_0 \rho_e}{h(r)}} \quad (\text{A5.14})$$

$$E(r) = \frac{z_1}{r} h(r) \quad (\text{A5.15})$$

#### A5.2.1 Computational Algorithm

Conferring to the section A5.1, the numerical solution to the simultaneous equations A5.5 and A5.6 can be achieved through the following computational steps:

- (i) Assume an initial non-zero emitter charge density  $\rho_e$  and calculate the charge distribution from Equation A5.4.
- (ii) Obtain a solution  $\phi_A$  for the potential function from Equation A5.13.
- (iii) Since the initially chosen  $\rho$  (or  $\rho_e$ ) step(i) is not correct, substitution of  $\rho$  into the Equation A5.6

will yield another potential function  $\phi_B$  other than  $\phi_A$ .

(iv) This disagreement between potential functions is due to the error present in  $\rho$ . The difference between potential functions  $\delta\phi = |\phi_A - \phi_B|$  should be related to the density correction factor  $\delta\rho$  as:  $\rho^{\text{new}} = \rho^{\text{old}} + \delta\rho$ .

(v) Repeating the procedure with  $\rho^{\text{new}}$  and returning to step (ii) until convergence is achieved.

The convergence was tentatively obtained as both following conditions are satisfied simultaneously:

- (i) In two successive iterations a change in  $\rho$  is less than 0.5% of  $\rho$ , i.e.  $\delta\rho < 0.005\rho$
- (ii) In any one iteration the agreement between  $\phi_A$  and  $\phi_B$  is also less than 0.5% of their average, i.e.  $|\delta\phi| < 0.005 \left( \frac{\phi_A + \phi_B}{2} \right)$

### A5.3 Algorithm for Estimation of the Critical Pressure

The steps in the iterative solution are as follows:

- (i) Input data: Electrode radii and related SF<sub>6</sub> data  
 $(r_1, r_2; (E/p)_{\text{lim}} = 88.4 \text{ kV}/(\text{cm}\cdot\text{bar}), K = 27 \text{ kV}^{-1},$   
 $N_{\text{crit}} = 10^8; e, D_e = 1240 \text{ cm}^2/\text{sec};$
- (ii) First iteration for  $V$  and  $r_c$  (or  $x_c$ ) for determination of the corona inception level (without streamer model).
- (iii) Second iteration with streamer model for  $x_c$  using  $\bar{\alpha} = 0$  at the active discharge boundary. An initial  $R_o = 0.35E - 04$  was assumed.
- (iv) Initial estimate for  $v_e$  and  $R_o^{\text{new}}$ .

(v) Check  $R_o$  :

$$R_o^{\text{new}} = R_o^{\text{old}} + \delta R_o$$

and repeat the procedure going through steps (iii) to (v) until convergence is achieved.

# FIGURES

Table 1.1 Reference Table to Figure 1.2

| Critical Pressure (bar) | Symbol | Inner Elec Radius (cm) | Material (Inner Elec) | Outer Elec. radius (cm) | Material Outer Elect | $\frac{r_p}{r_{av}} \frac{E_{av}}{E_{max}}$ | Effective Elec. length (cm) | Effective Elec. area (cm <sup>2</sup> ) | Critical Field Stren kV/cm | Applied Voltage | Reference            |
|-------------------------|--------|------------------------|-----------------------|-------------------------|----------------------|---|-----------------------------|---|----------------------------|-----------------|----------------------|
| 1.6                     | ◇      | 6.6                    | Cr-Ni                 | 7.6                     | AL                   | 1.07  | 11.6                        | 480                                     | 160                        | AC              | Nitta et al [118]    |
| 2.0                     | ⊖      | 0.5                    | Cr-Ni                 | 12.5                    | St-St                | 7.4   | 91.5                        | 257                                     | 190                        | DC              | Bortnik, Cooke [129] |
| 1.0                     | ⊖      | 2.6                    | AL                    | 12.5                    | St-St                | 2.42  | 91.5                        | 1340                                    | 94                         | DC              |                      |
| 1.1                     | ⊖      | 3.8                    | Cr-Ni                 | 12.5                    | St-St                | 1.92  | 91.5                        | 1960                                    | 114                        | DC              |                      |
| 1.7                     | □      | 0.33                   | Cr-Ni                 | -                       | -                    | -   | -                           | -                                       | -                          | DC              | Popkov et al [*]     |
| -                       | ⊕      | 1.6                    | AL                    | 4.3                     | AL                   | 1.71  | 27                          | 244                                     | -                          | AC              | Husbands [142]       |
| -                       | x      | 2.5                    | AL                    | 4.8                     | St-St                | 1.41  | 25                          | 392                                     | -                          | AC              | Menju [145]          |
| 0.57                    | ●      | 7.0                    | AL                    | 12.5                    | AL                   | 1.35  | 75                          | 3300                                    | 57                         | AC              | Ermel [146]          |
| 0.7                     | ⊙      | 4.0                    | -                     | 10                      | -                    | 1.63  | 20                          | 1256                                    | 84.5                       | DC              | Menju [217]          |
| 1.0                     | ⊕      | 4.0                    | -                     | 10                      | -                    | 1.63  | 20                          | 1256                                    | 103.6                      | AC              |                      |
| 1.0                     | ⊗      | 0.6                    | Cu                    | 0.75                    | St.                  | 1.12  | -                           | -                                       | 240                        | DC              | Bortnik [140]        |

\* Popkov, V.I., Conf. of Ionization Phen. in Gases, Prag, p.185, 1973

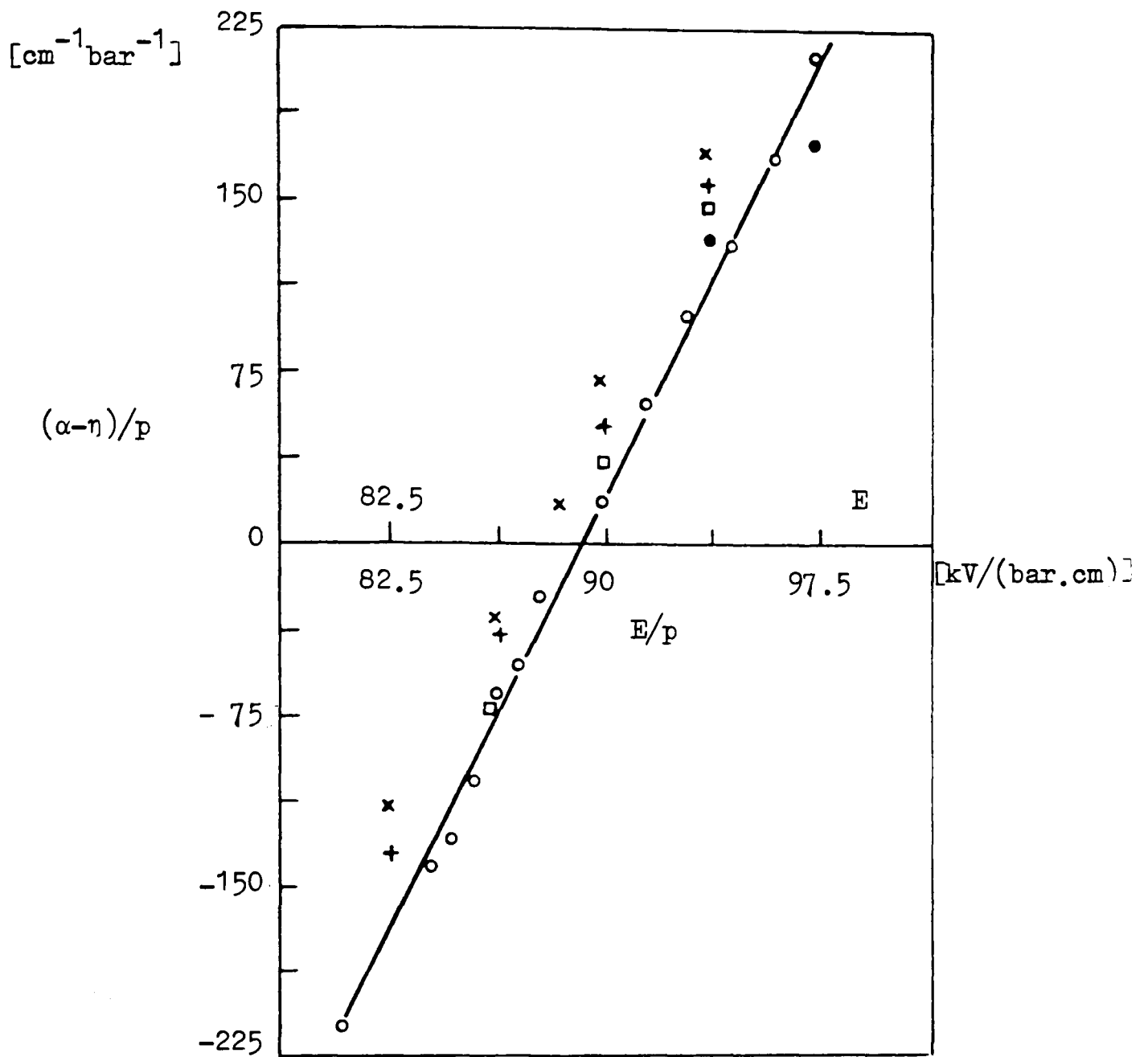


Figure 1.1(a) Graph of  $(\alpha-n)/p$  against  $E/p$  in  $\text{SF}_6$ , measured by several investigators.

|                                      | <u>p(bar)</u> | <u>kV/(cm bar)</u>                |
|--------------------------------------|---------------|-----------------------------------|
| o Teich and Branston [87]            | 0.0066        | $81 \leq \frac{E}{p} \leq 98$     |
| x Bhalla and Craggs [85]             | 0.0066-0.133  | $3.75 \leq \frac{E}{p} \leq 75$   |
| + Harrison and Geballe [cited in 86] | 0.146 -0.166  | $82.5 \leq \frac{E}{p} \leq 93.7$ |
| □ Boyd and Crichton [83]             | 0.006 -0.533  | $3.75 \leq \frac{E}{p} \leq 300$  |
| • Sangi [cited in 86]                | 0.166 -2.66   | $93.7 \leq \frac{E}{p} \leq 1500$ |

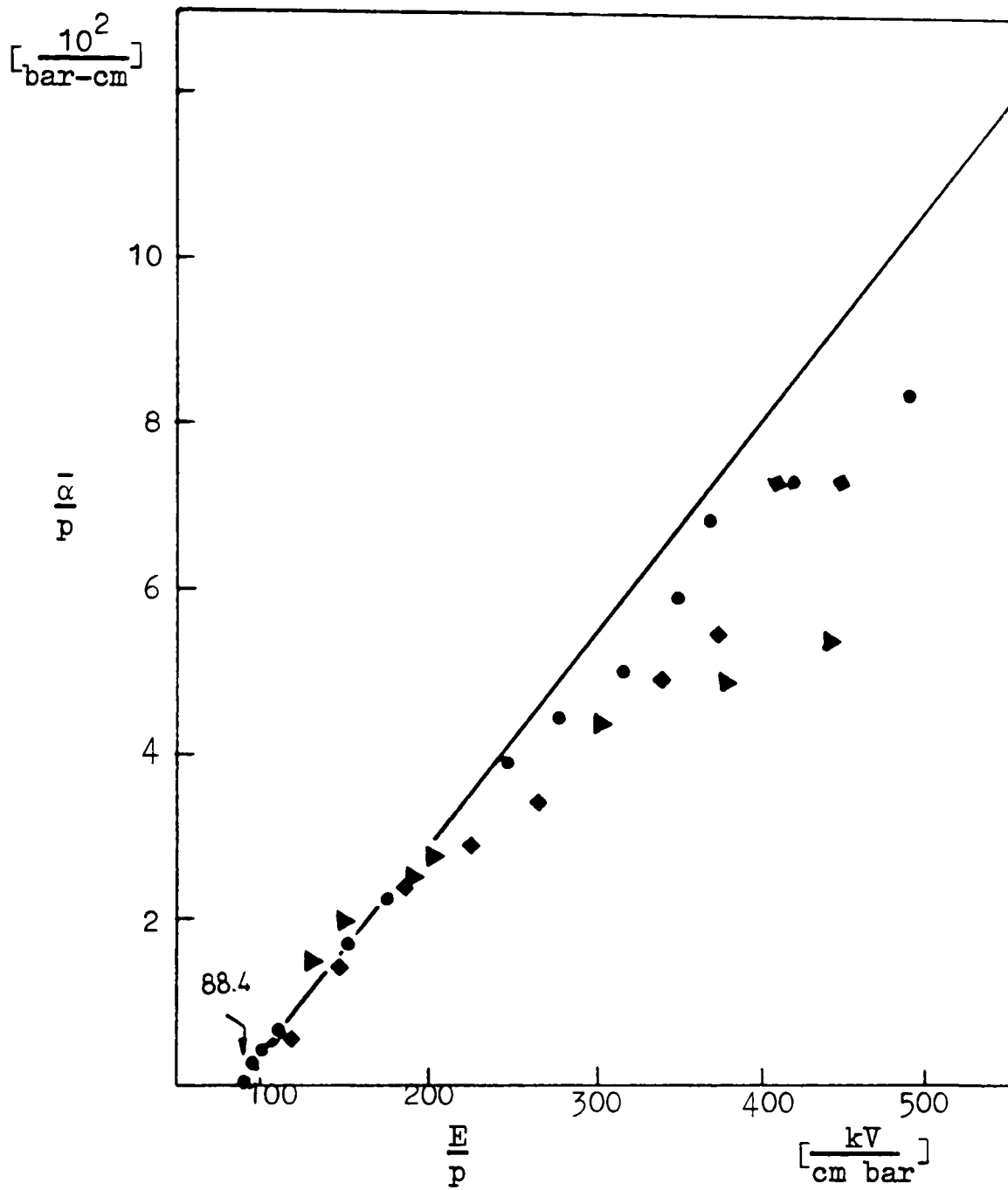


Figure 1.1(b) Comparison of  $\bar{\alpha}/p$  as a function of  $E/p$  of various investigators in  $SF_6$  above  $(E/p)_{lim}$

|                                  | $p(\text{torr})$ | $E/p$                    | $V(\text{cm torr})$ |
|----------------------------------|------------------|--------------------------|---------------------|
| ● Kline et al [86]               | 1 - 27           | $157 \leq E/p \leq 600$  |                     |
| ◆ Teich and Sangi [cited in 86]  | 125 - 2000       | $110 \leq E/p \leq 650$  |                     |
| ▶ Maller and Naidu [cited in 88] | 1 - 10           | $110 \leq E/p \leq 1000$ |                     |

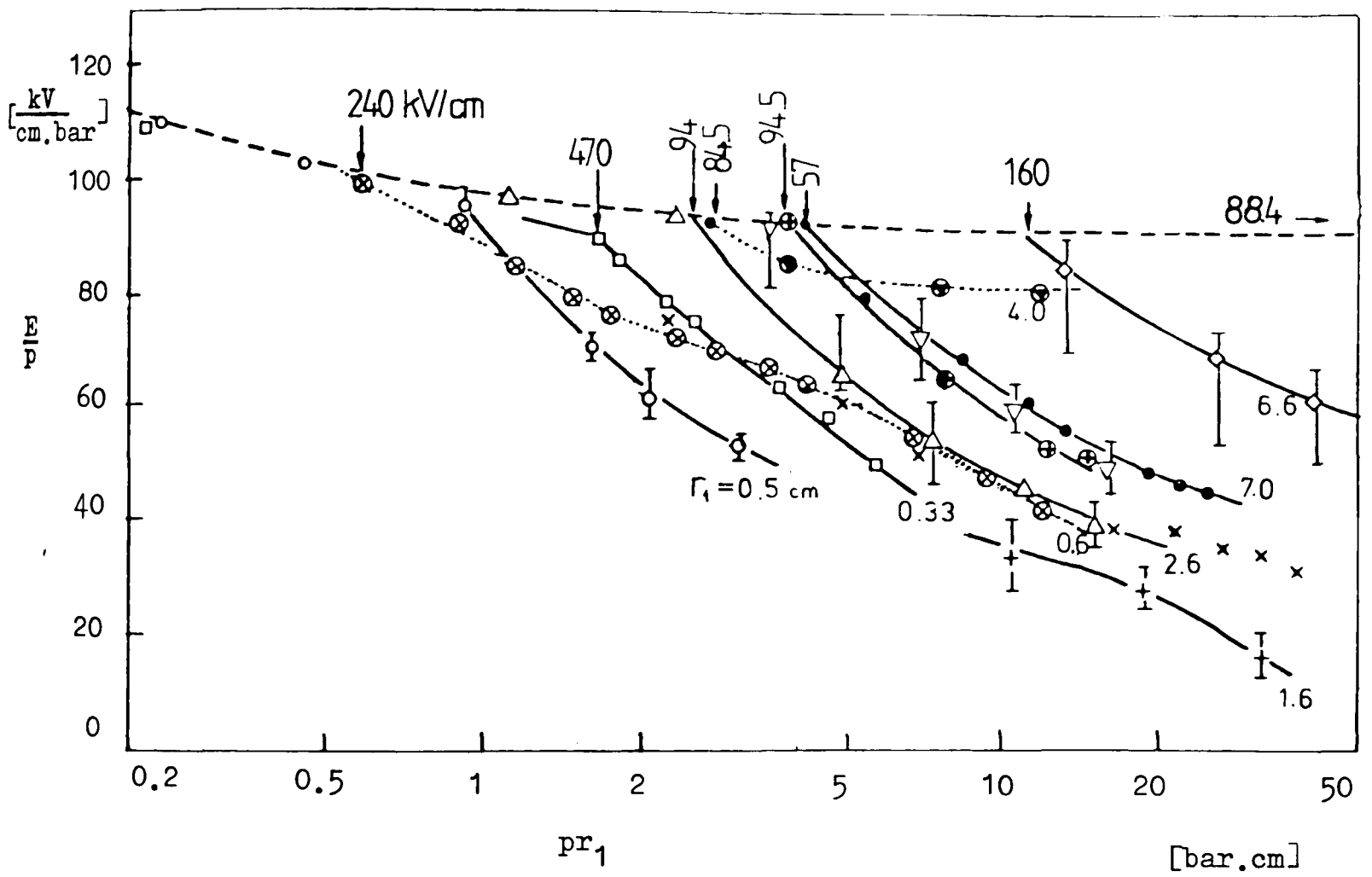


Figure 1.2  $E/p$  against  $pr_1$  in  $\text{SF}_6$  obtained in various investigations

Table 2.1

Characteristics of Electrodes

| Symbol | Radius<br>cm | Roughness, $\mu\text{m}$ |                  | Finish      | Material           |       |
|--------|--------------|--------------------------|------------------|-------------|--------------------|-------|
|        |              | $R_{\text{CLA}}$         | $R_{\text{MAX}}$ |             |                    |       |
| E1     | 0.0125       | 0.07                     | 0.6              | Polished    | Stainless<br>Steel | Inner |
| E2     | 0.015        | 0.08                     | 0.5              |             |                    |       |
| E3     | 0.025        | 0.06                     | 0.4              |             |                    |       |
| E4     | 0.05         | 0.07                     | 0.8              |             |                    |       |
| E5     | 0.1          | 0.06                     | 0.6              |             |                    |       |
| E6     | 0.15         | 0.05                     | 0.7              |             |                    |       |
| E7     | 0.5          | 0.07                     | 0.4              | Polished    | Stainless<br>Steel |       |
| E8     |              | 2.5                      | 14.25            | Sandblasted |                    |       |
| E9     | 0.945        | 0.1                      | 0.5              | Polished    | Stainless<br>Steel |       |
| E10    |              | 2.9                      | 15-25            | Sandblasted |                    |       |
| E11    |              | 1.8                      | 10-15            | Machined    | Aluminium          |       |
| E12    |              | 0.15                     | 0.5              | Polished    |                    |       |
| E13    |              | 2.8                      | 12-20            | Sandblasted |                    |       |
| OE1    | 1.27         | 0.04                     | 0.6              | Polished    | Stainless<br>Steel | Outer |
| OE2    | 2.5          | 0.06                     | 0.7              |             |                    |       |

Effective length = 30 cm

- |   |                    |         |                       |    |                          |
|---|--------------------|---------|-----------------------|----|--------------------------|
| 1 | Vessel             | 4 and 5 | Gas entry ports       | 8  | Main access flange       |
| 2 | Gap assembly       | 6       | Gauge connection port | 9  | Bushing                  |
| 3 | Insulator supports | 7       | Viewing port          | 10 | H.V.bushing entry flange |

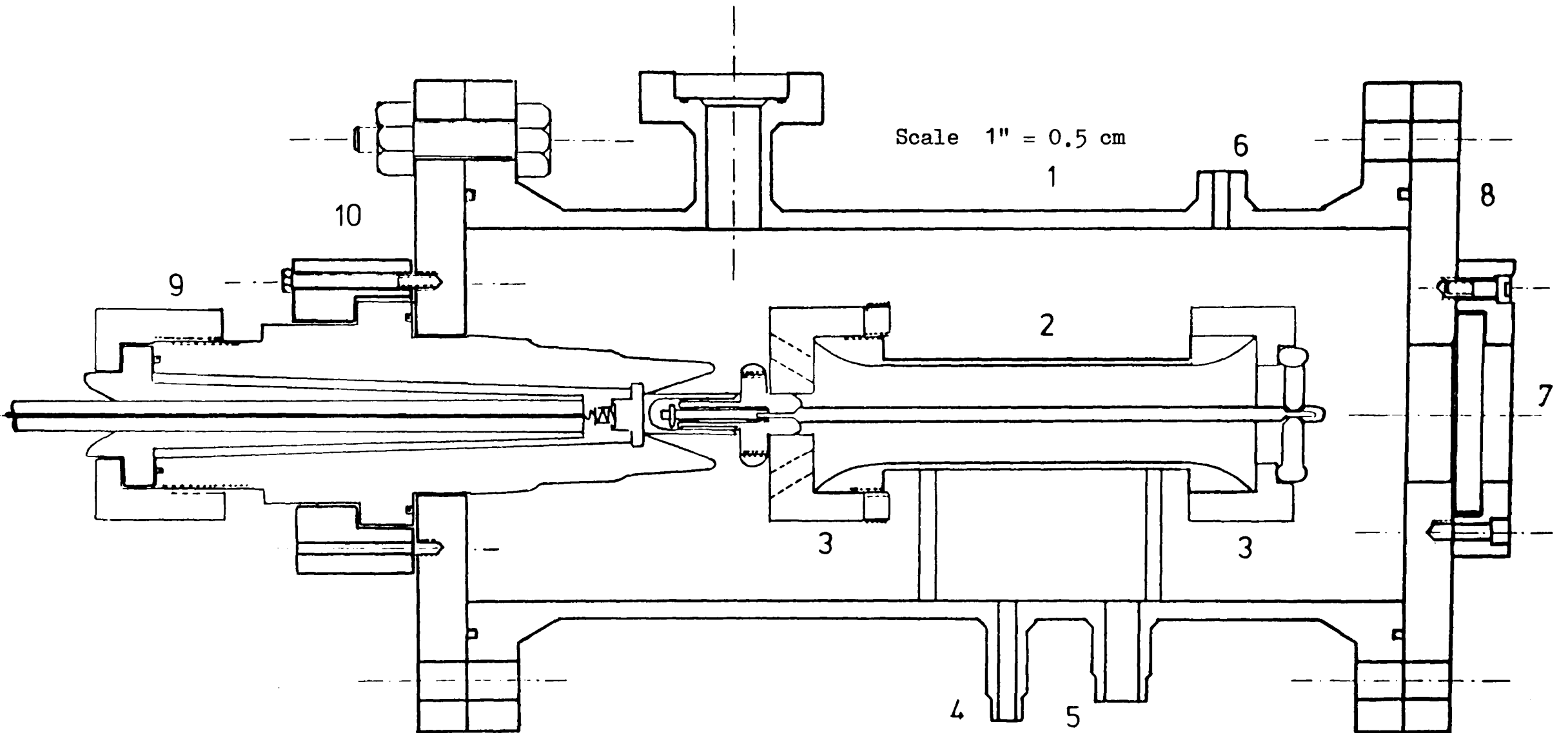
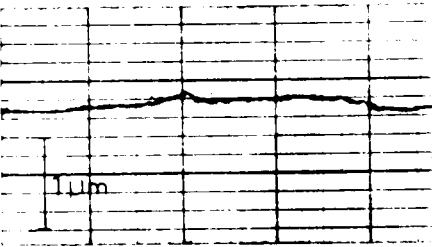
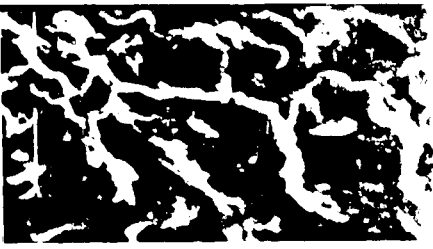
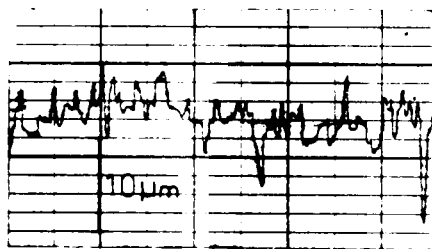
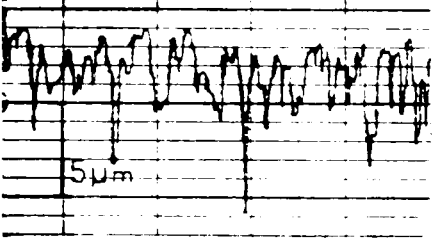
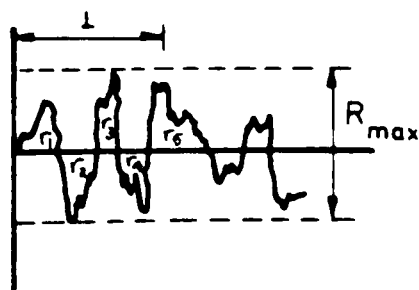


Figure 2.1 Illustration of the vessel and the electrode assembly.

Table 2.2 Electronmicroscope Pictures and Roughness Profiles of inner electrodes before sparking (Material: Stainless steel)

|             | Electronmicroscope Pictures<br>(Magnification)  |  | Roughness Profiles  | $R_{max}$<br>( $\mu m$ ) | $R_{CLA}$<br>( $\mu m$ ) |
|-------------|---|--|---|--------------------------|--------------------------|
| Polished    | X 80<br>   | X 2500<br>   |    | 0.8                      | 0.03                     |
| Sandblasted | X 40<br> | X 1250<br> |  | 15                       | 2.3                      |
| Machined    | X 80<br> | X 1250<br> |  | 18                       | 2.8                      |



$$R_{CLA} = \frac{1}{L} \sum r_i$$

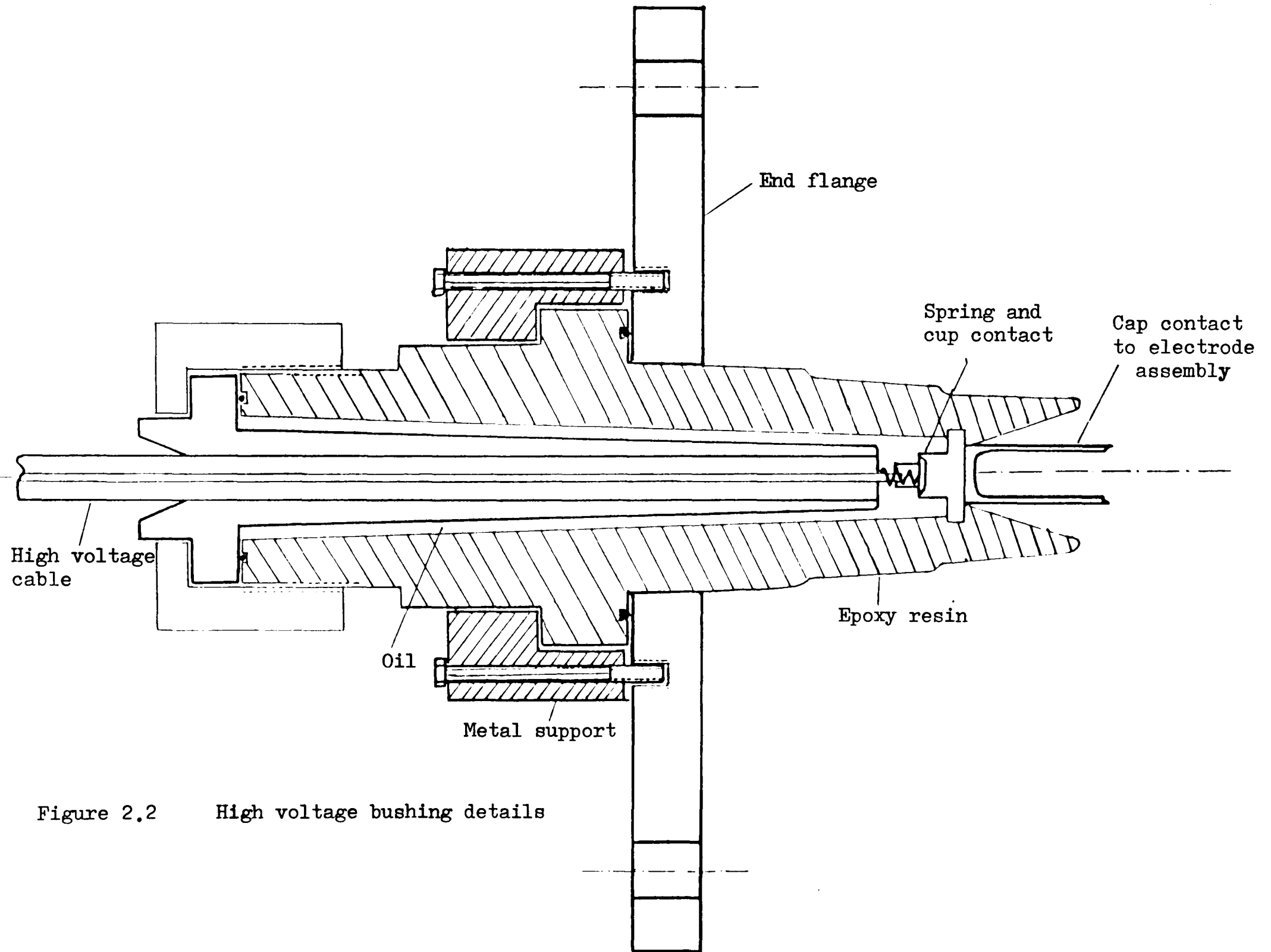


Figure 2.2 High voltage bushing details

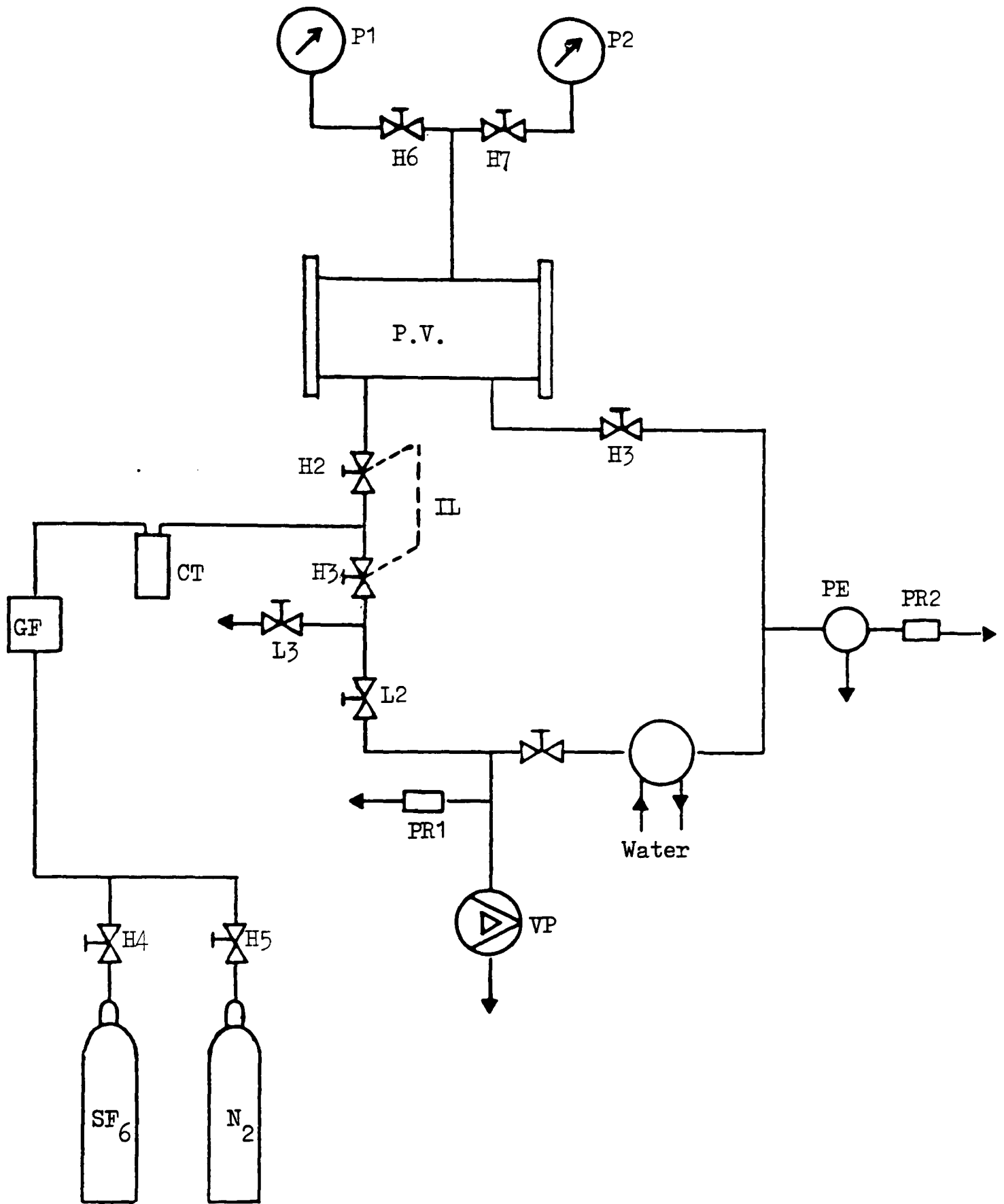


Figure 2.3 The pumping and gas filling systems

- |        |                                 |             |                                    |
|--------|---------------------------------|-------------|------------------------------------|
| P1     | Barometer (0 - 1 bar)           | PR1 and PR2 | Pirani gauges (supply not shown)   |
| P2     | Barometer (1 - 8 bar)           | PE          | Penning gauge                      |
| H1..H7 | High Pressure valves (< 25 bar) | VP          | Vacuum pump (rotary)               |
| L1..L3 | Low Pressure valves (0-3.5 bar) | DF          | Diffusion pump (with water supply) |
| CT     | Cold trap                       | IL          | Interlock                          |
| GF     | Gas filter                      |             |                                    |
| PV     | Pressure vessel                 |             |                                    |

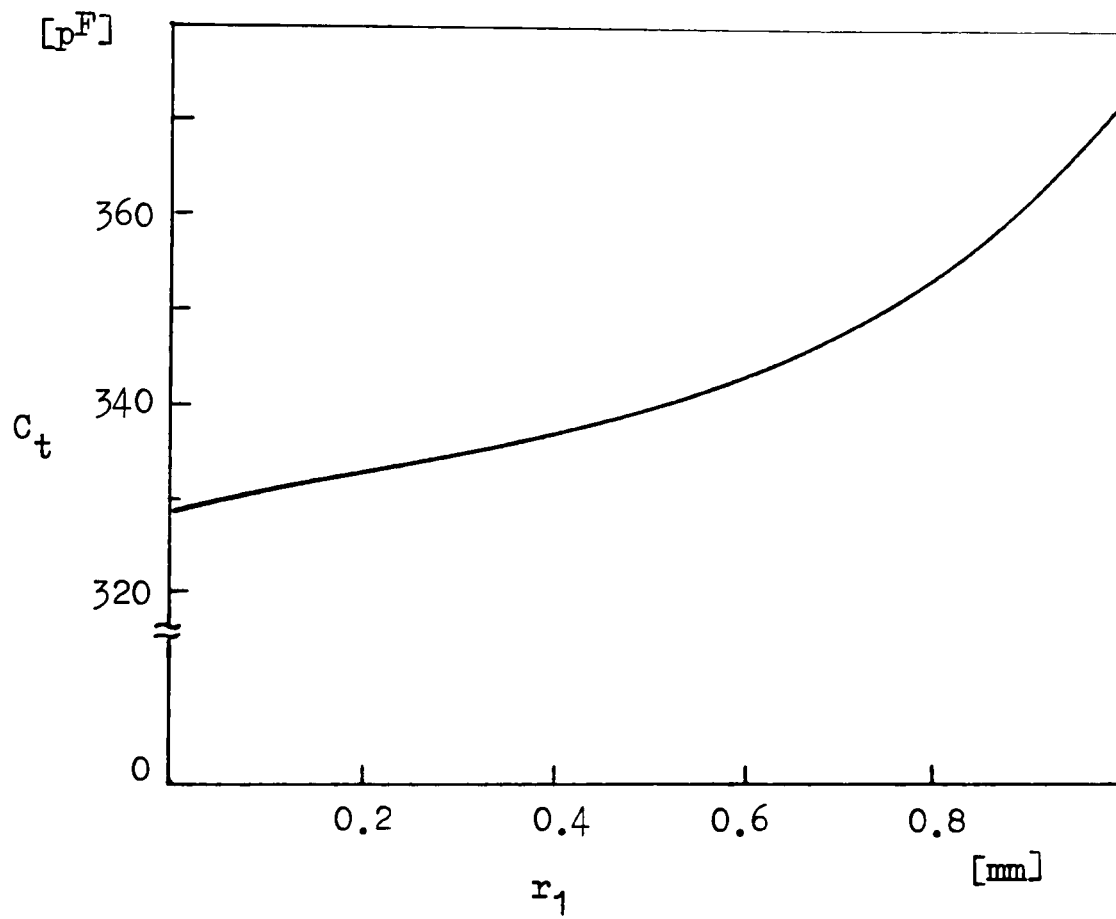


Figure 2.4 Gross capacitance variation with inner electrode radius.  
( $r_2 = 1.27$  cm)

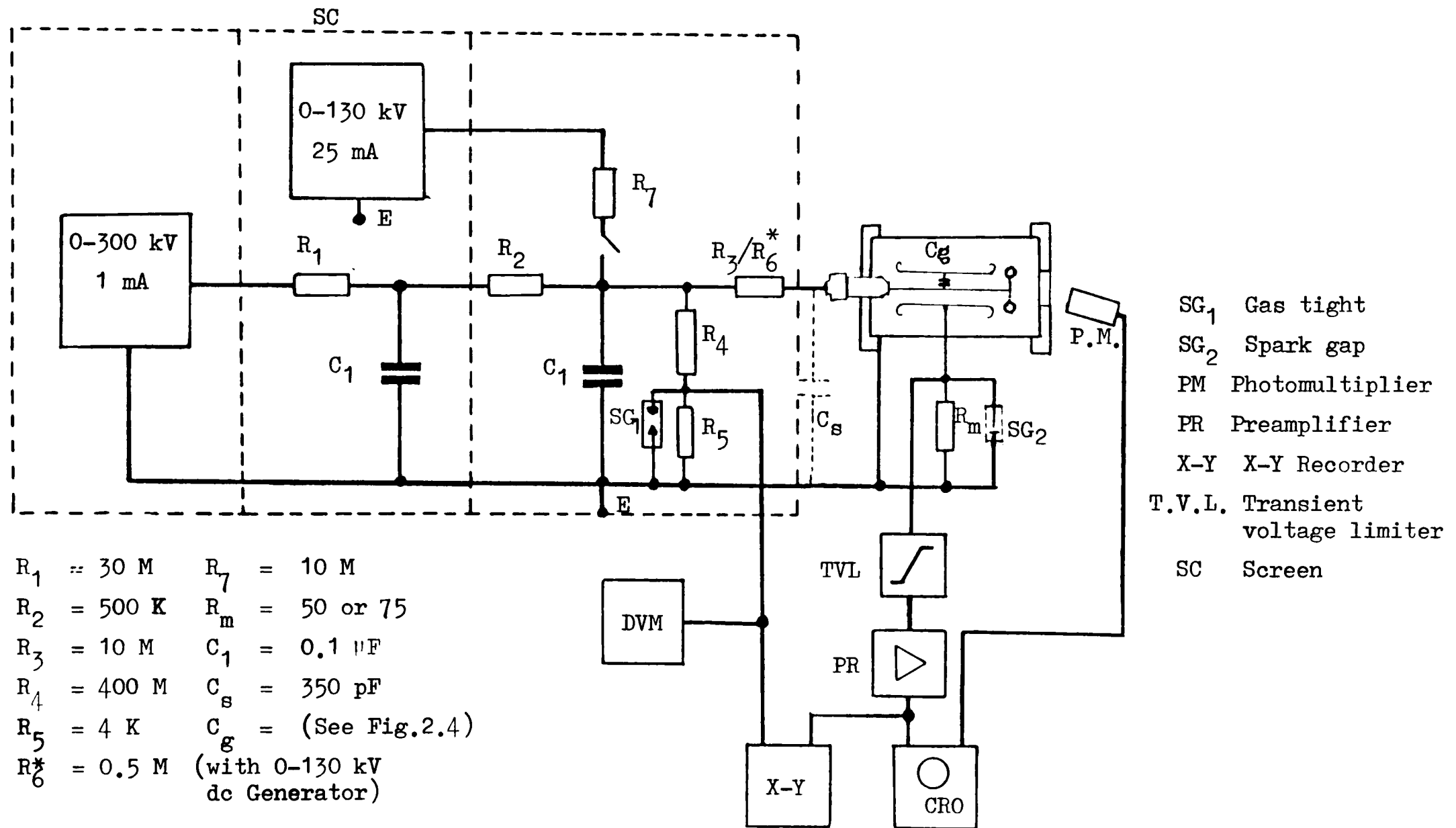


Figure 2.5 High-voltage dc supplies and measuring circuit

|     |                             |     |                     |
|-----|-----------------------------|-----|---------------------|
| DVM | Digital voltmeter           | B/D | Breakdown           |
| D/A | Digital to Analog Converter | MPU | Microprocessor Unit |
| F   | Filter                      |     |                     |

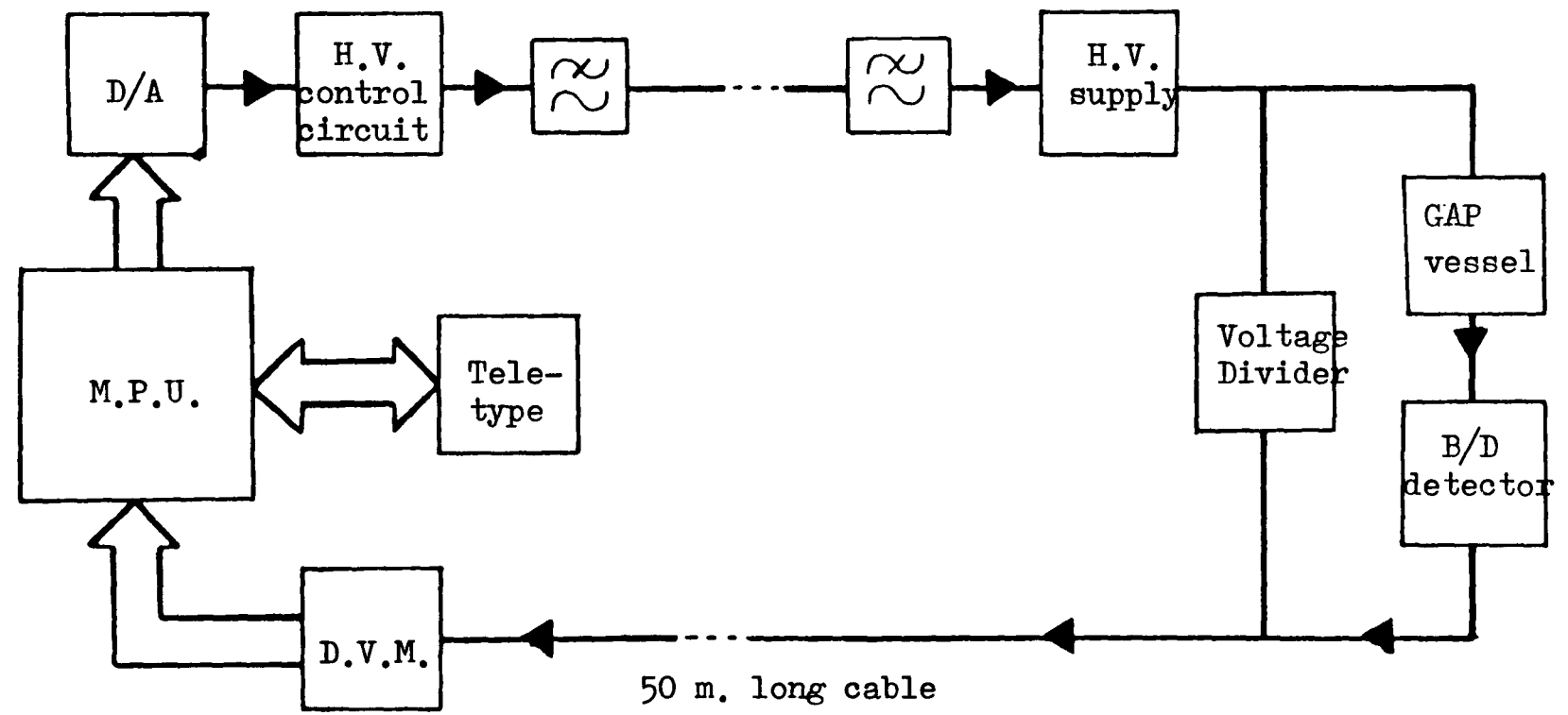


Figure 2.6 Systematic illustration of the control circuit for static breakdown voltage measurements

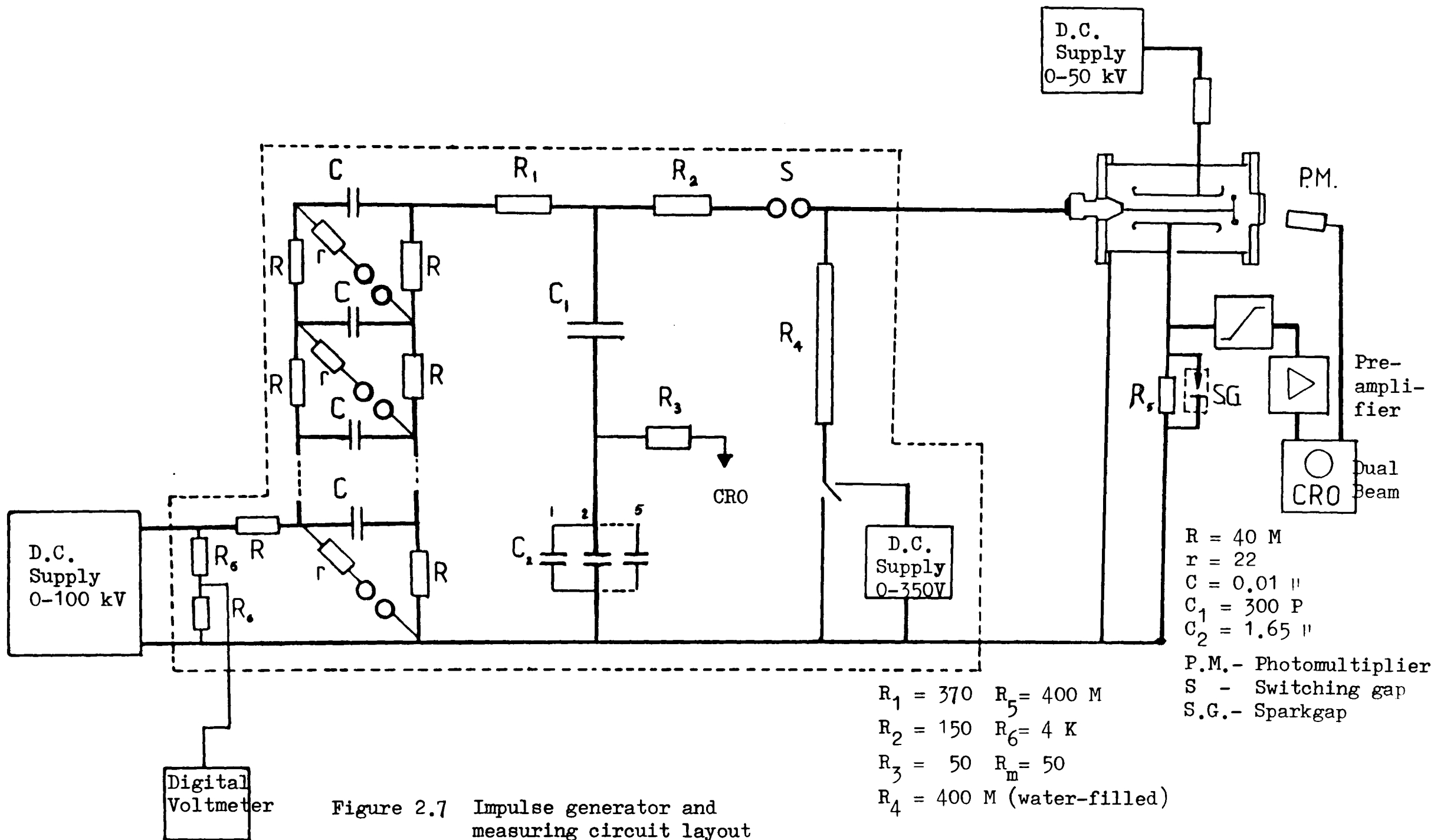


Figure 2.7 Impulse generator and measuring circuit layout

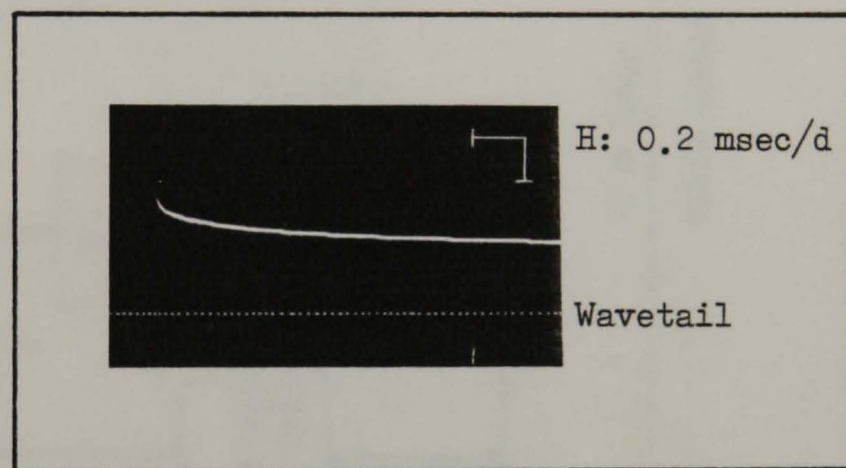
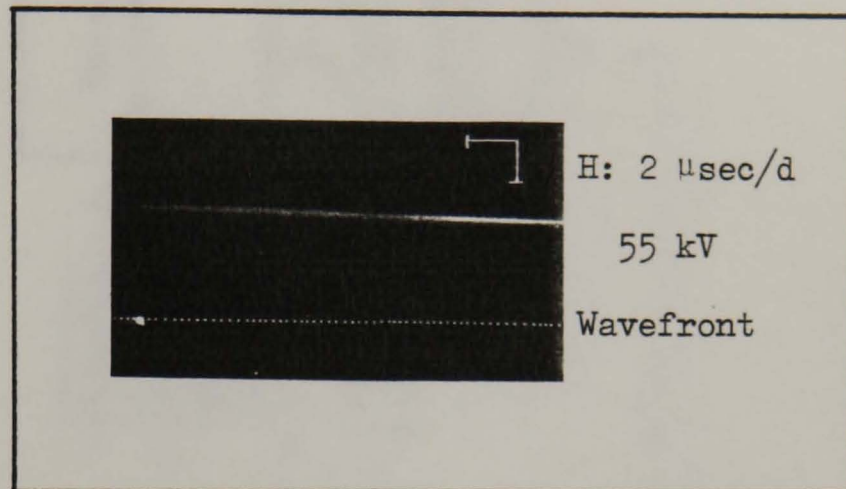


Figure 2.8 Impulse generator waveforms  
(V = 55 kV)

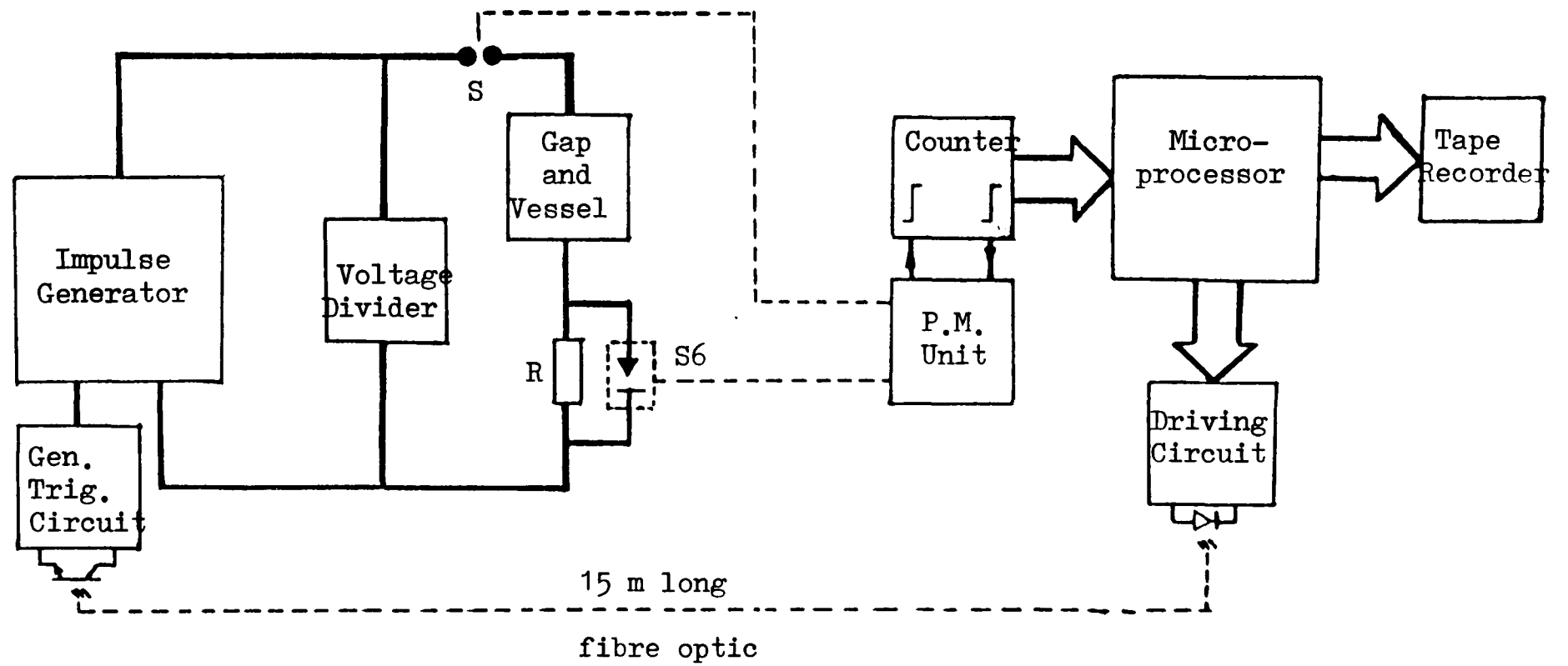


Figure 2.9 Systematic illustration of control circuit for time-lag measurements

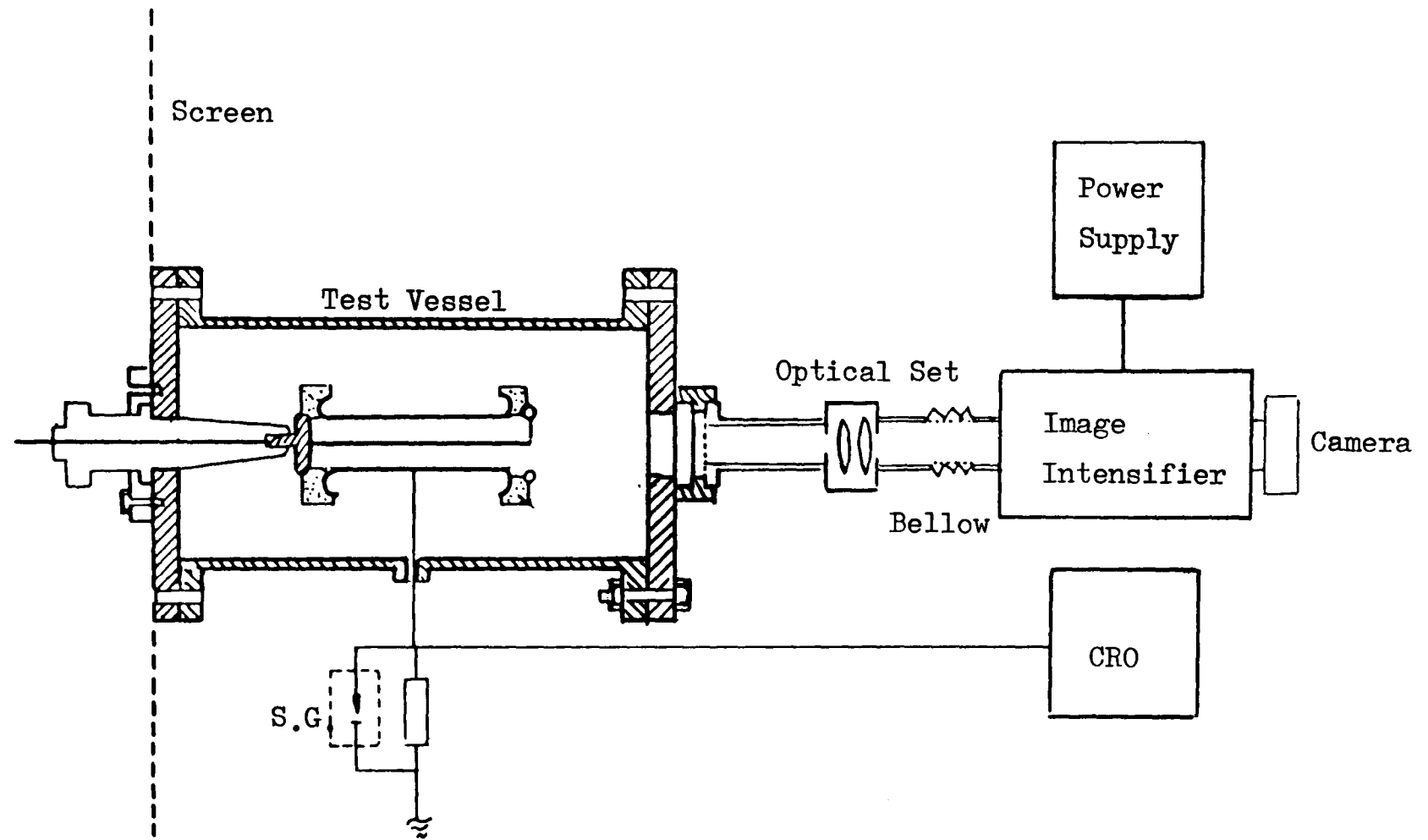


Figure 2.10 Experimental apparatus for optical recording

TABLE 3.1 Inner electrodes used in conditioning breakdown experiments

| Symbol | Radius (cm) | Ratio | Non-Uniform Factor $\eta$ | Area (cm <sup>2</sup> ) | Ratio of Area | Surface Treatment | Roughness        |                  | Material  |
|--------|-------------|-------|---------------------------|-------------------------|---------------|-------------------|------------------|------------------|-----------|
|        |             |       |                           |                         |               |                   | R <sub>CLA</sub> | R <sub>MAX</sub> |           |
| E7     | 0.0125      | 37.3e | 21.7                      | 2.35                    | 40.5          |                   |                  |                  |           |
| E8     | 0.5         | 0.93e | 1.65                      | 95.2                    | 1             | Polished          | ~0.04            | ~0.3             | St.St.    |
| E9     | 0.945       | 0.49e | 1.16                      | 179.9                   | 1.88          |                   |                  |                  |           |
| E10    | 0.945       |       |                           |                         |               | Sand-blasted      | ~2.3             | ~15.2            |           |
| E11    | 0.945       | 37.3e | 1.16                      | 179.9                   | 1.88          | Machined          | ~2.8             | ~10.15           | St.St.    |
| E12    | 0.945       |       |                           |                         |               | Polished          | ~10.04           | ~0.3             |           |
| E13    | 0.945       | 37.3e | 1.16                      | 179.9                   | 1.88          | Machined          | ~2.8             | ~10.15           | Aluminium |

Outer electrode: radius  $r_2 = 1.27$  cm, stainless steel, polished

$$R_{CLA} = 0.04 \mu\text{m} \quad R_{MAX} = 0.25 \mu\text{m}$$

Effective length of electrodes,  $L = 30.3$  cm.

TABLE 3.2 Properties of materials given in Table 3.1

| Material  | $\phi$ , eV | T, °C | H <sub>B</sub> (kgf/mm) <sup>2</sup> |
|-----------|-------------|-------|--------------------------------------|
| St. St.   | 3.91-4.77   | 1450  | 52                                   |
| Aluminium | 2.98-4.36   | 650   | 21                                   |

$\phi$  - work function, H<sub>B</sub> - tensile strength

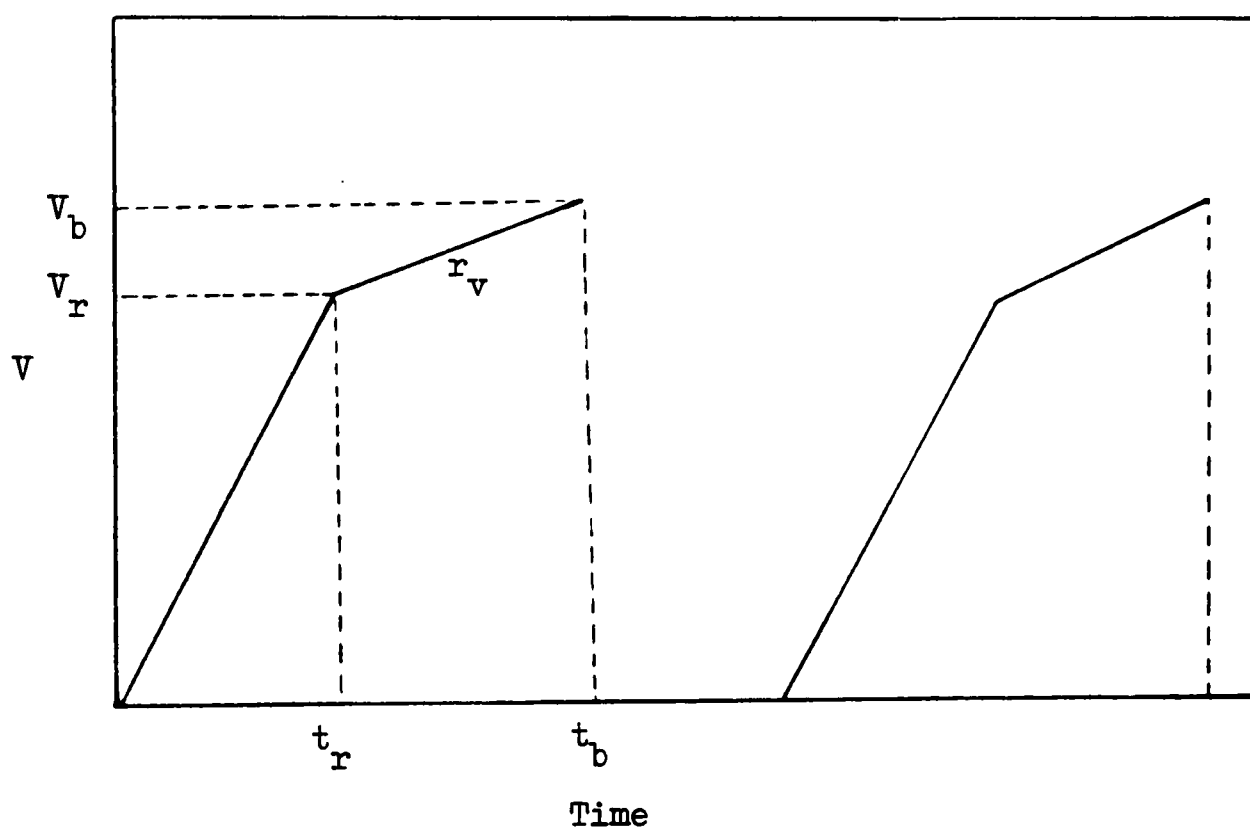


Figure 3.1 Typical variation of voltage waveform applied to the gap

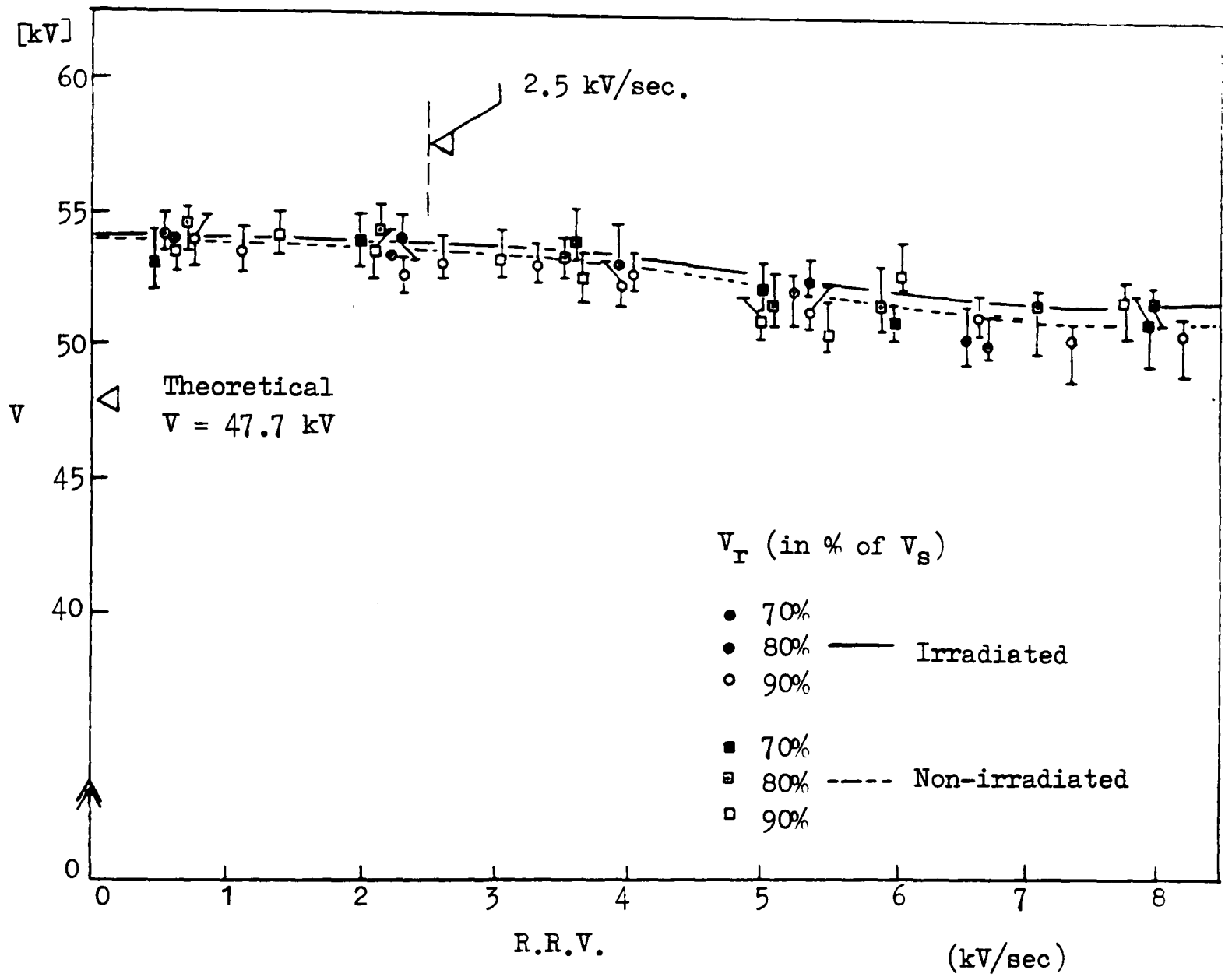


Figure 3.2 Effect of rate of rise of voltage on positive breakdown voltage of  $SF_6$  at  $p = 1.0$  bar ( $n/r_2 = 0.5/1.27$  cm)

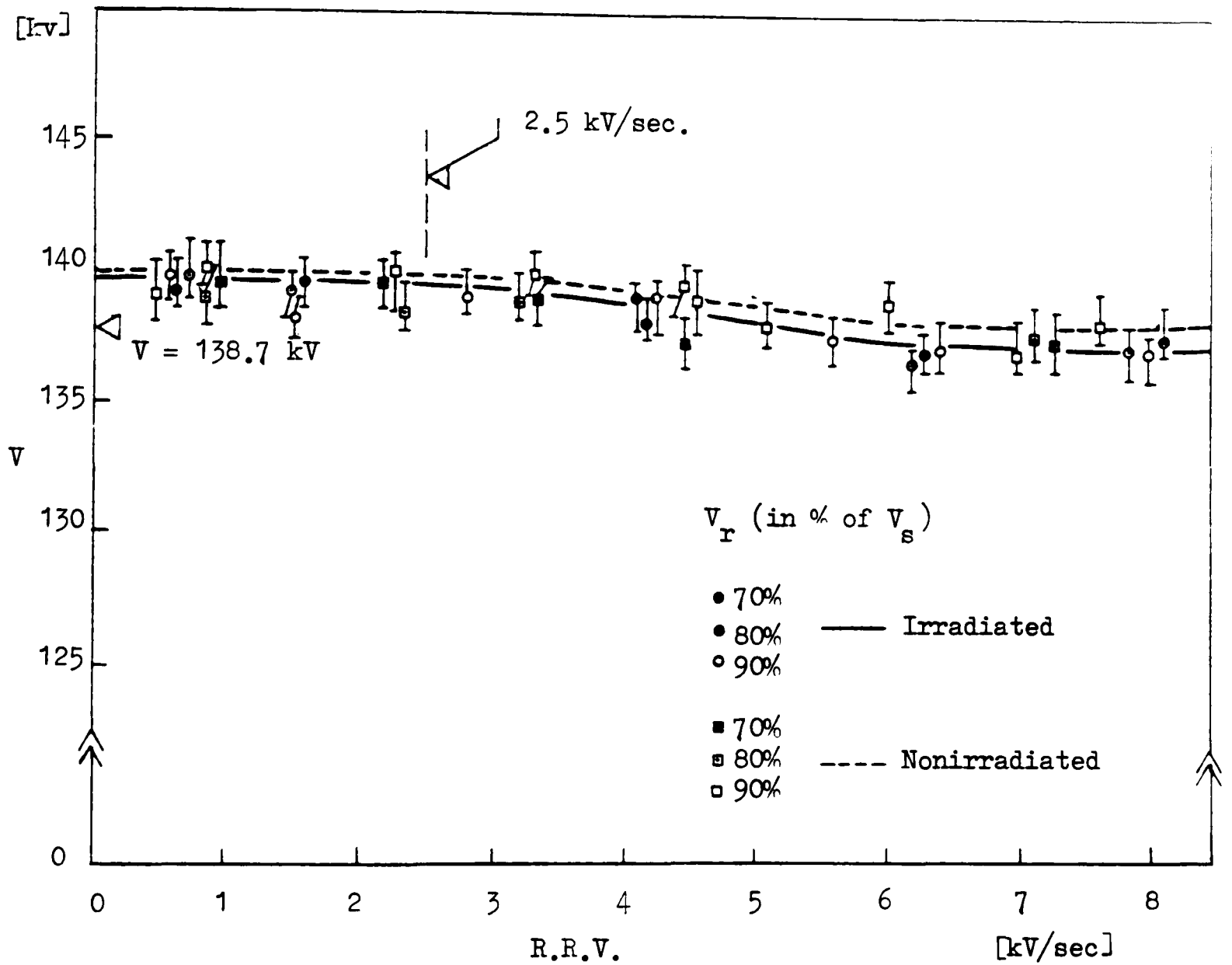


Figure 3.3 Effect of rate of rise of voltage on positive breakdown voltage level in  $\text{SF}_6$  at  $p = 3.0$  bar ( $r_1/r_2 = 0.5/1.27$  cm)

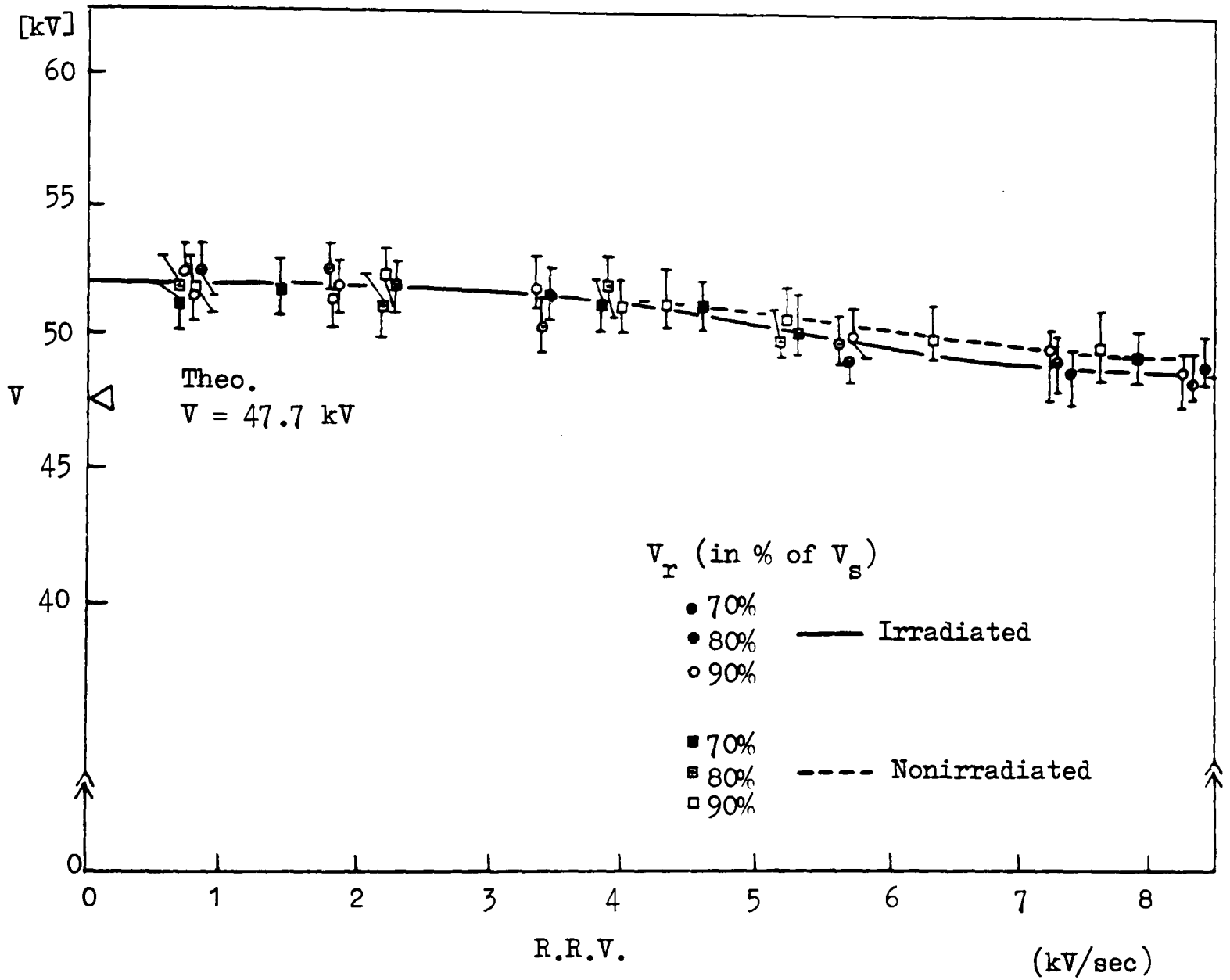


Figure 3.4 Effect of the rate of rise of voltage on negative breakdown level of  $\text{SF}_6$  at  $p = 1.0$  bar ( $r_1/r_2 = 0.5/1.27$  cm)

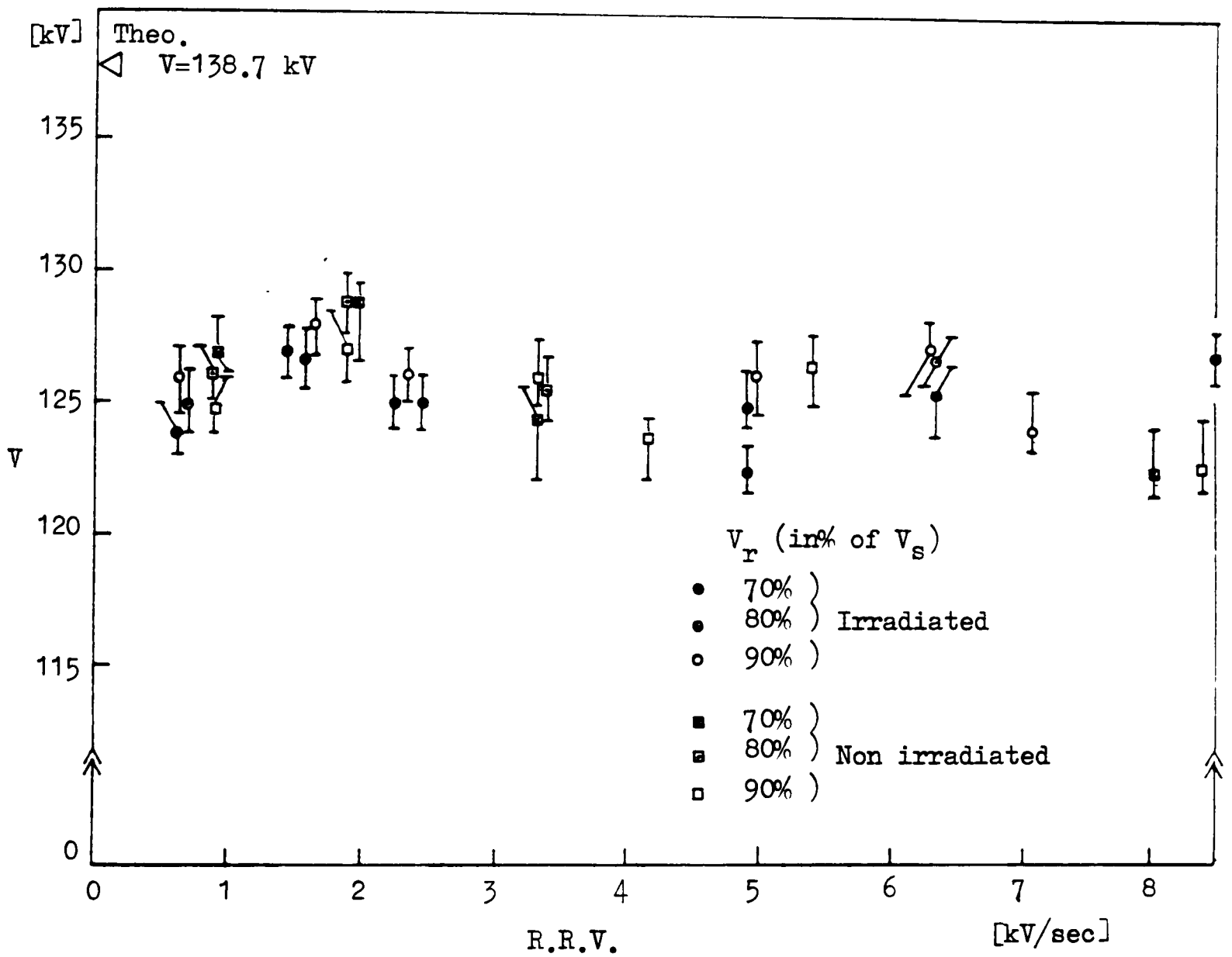


Figure 3.5 Effect of rate of rise of voltage on negative breakdown level of SF<sub>6</sub> at p = 3.0 bar ( $r_1/r_2 = 0.5/1.27$  cm)

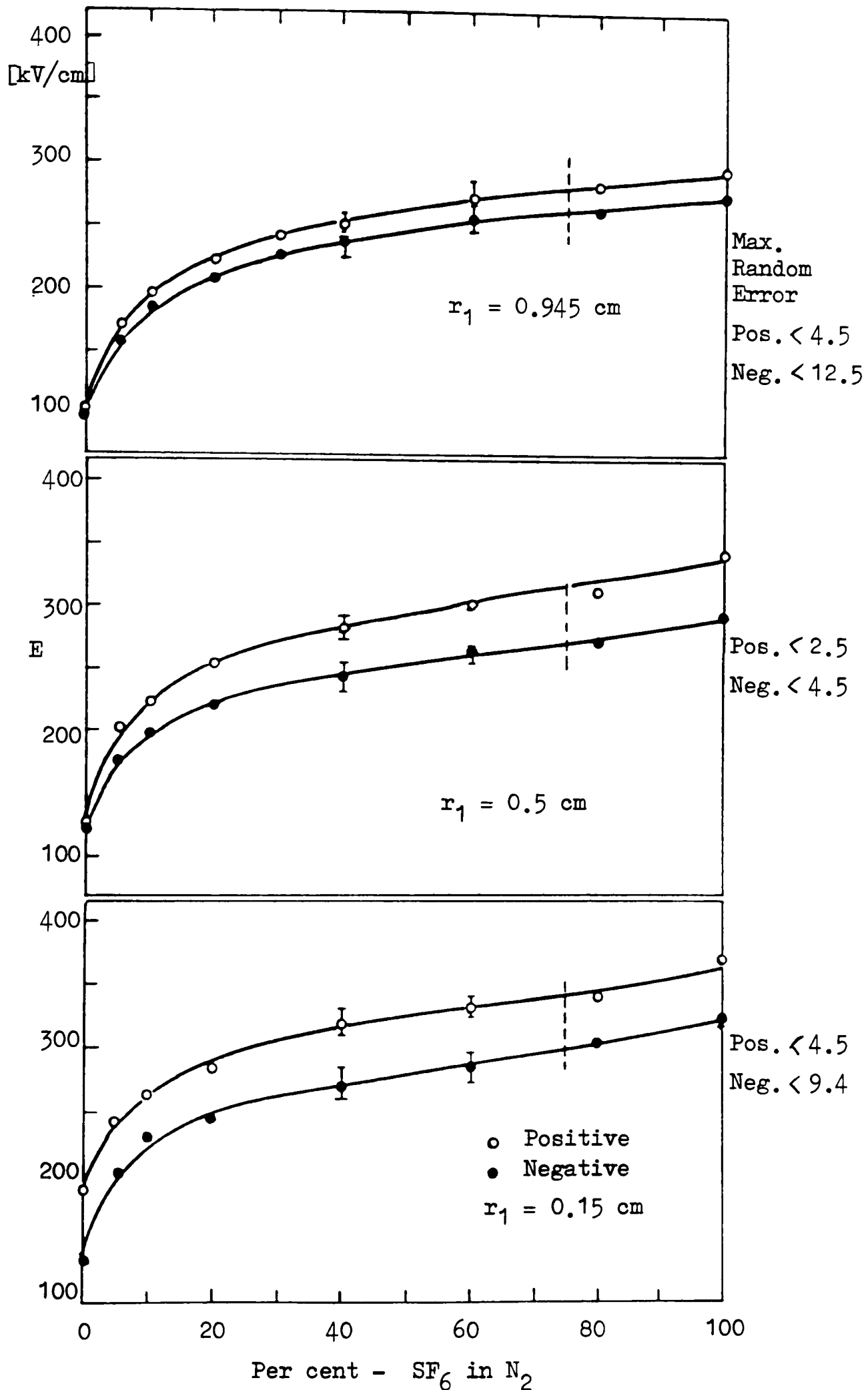


Fig. 3.6 Breakdown versus percentage of SF<sub>6</sub> in N<sub>2</sub> at p = 3.5 bar in polished cylindrical electrode geometry (r<sub>2</sub> = 1.27 cm)

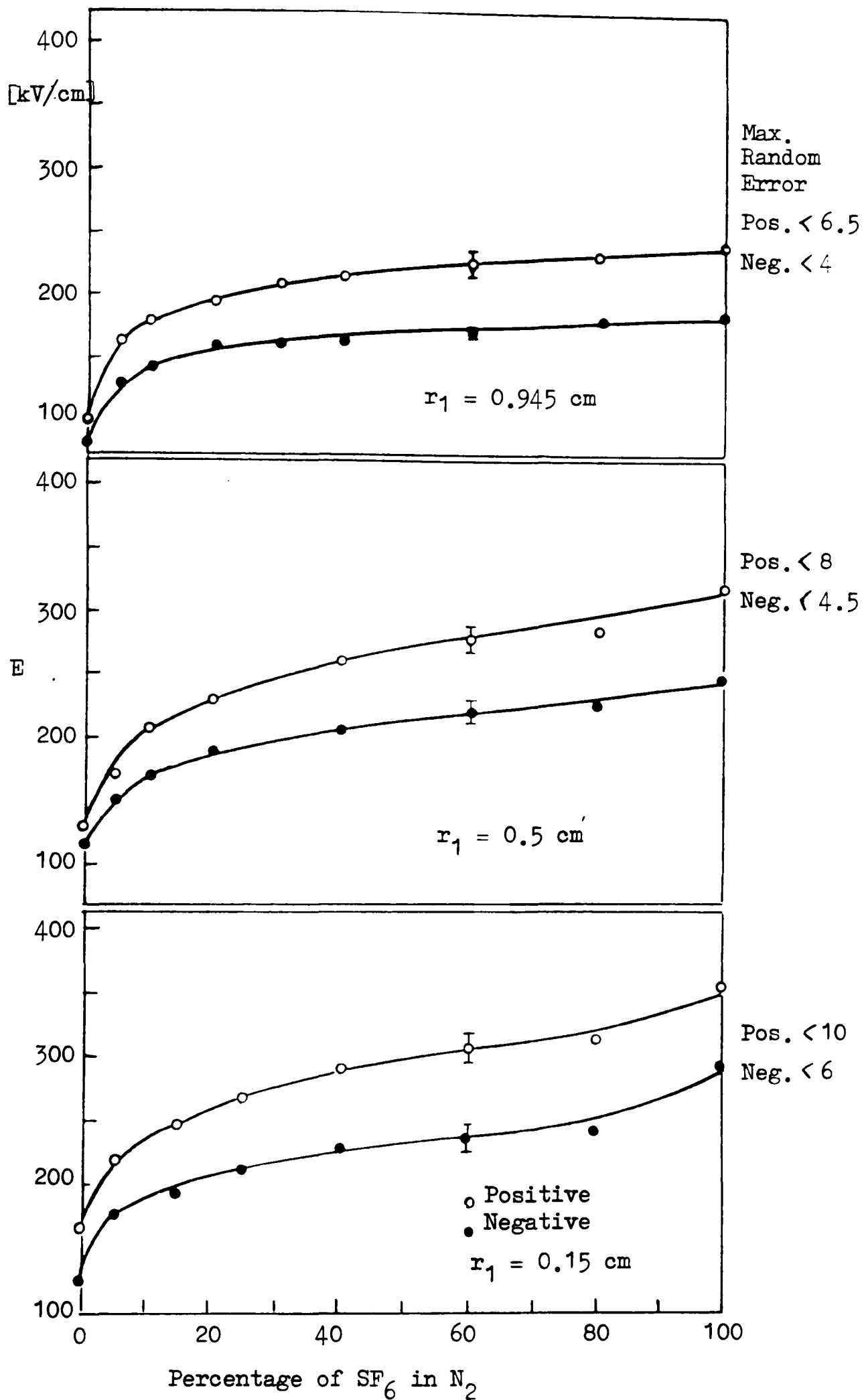


Figure 3.7 Breakdown versus percentage of SF<sub>6</sub> in N<sub>2</sub> at p = 3.5 bar in cylindrical geometry with sand-blasted inner (r<sub>2</sub> = 1.27 cm)

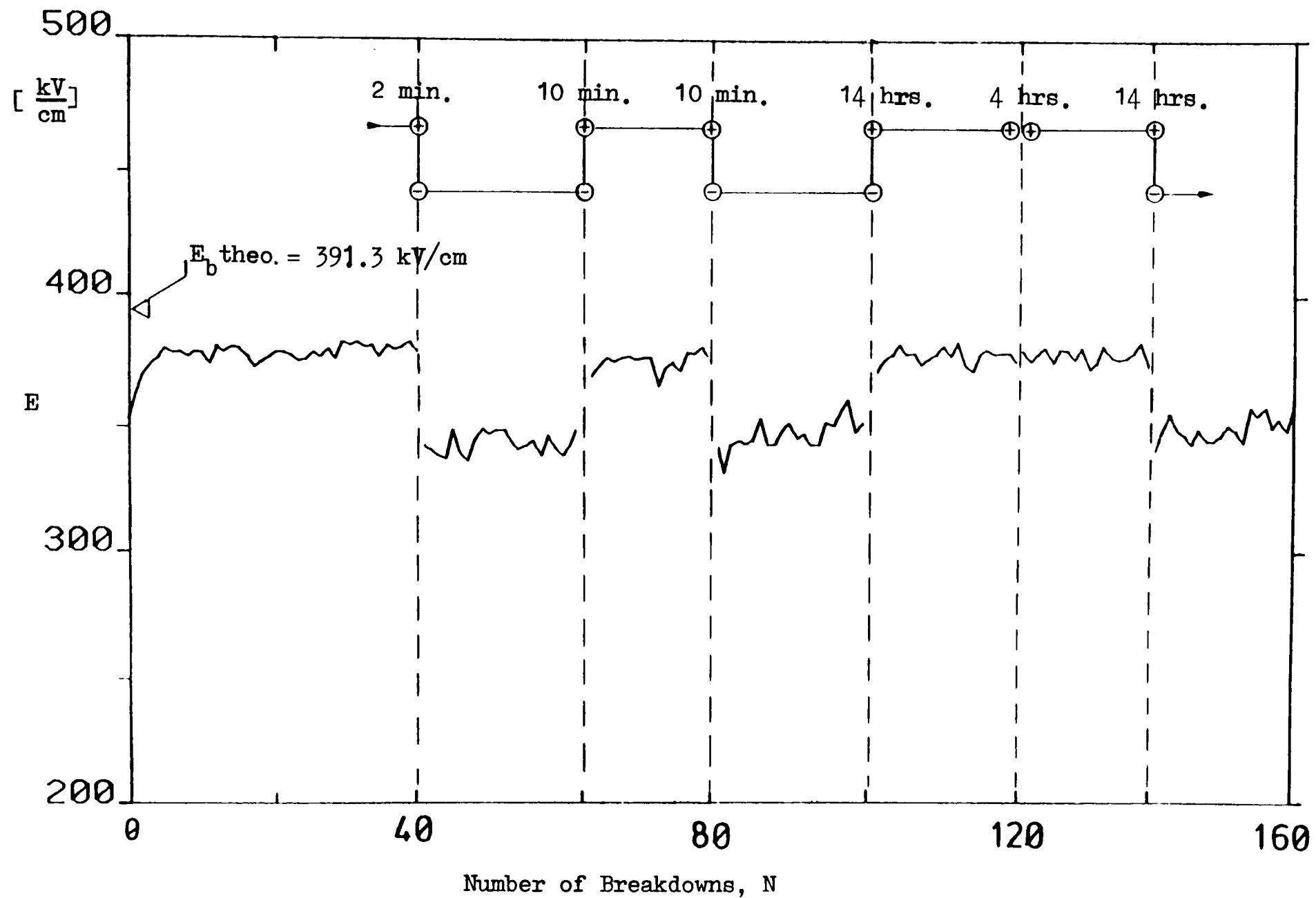


Figure 3.8 Spark conditioning phases in  $\text{SF}_6$  at  $p = 3.9 \text{ bar}$   
 $(r_1/r_2 = 0.5/1.27 - \text{cm radii, polished})$

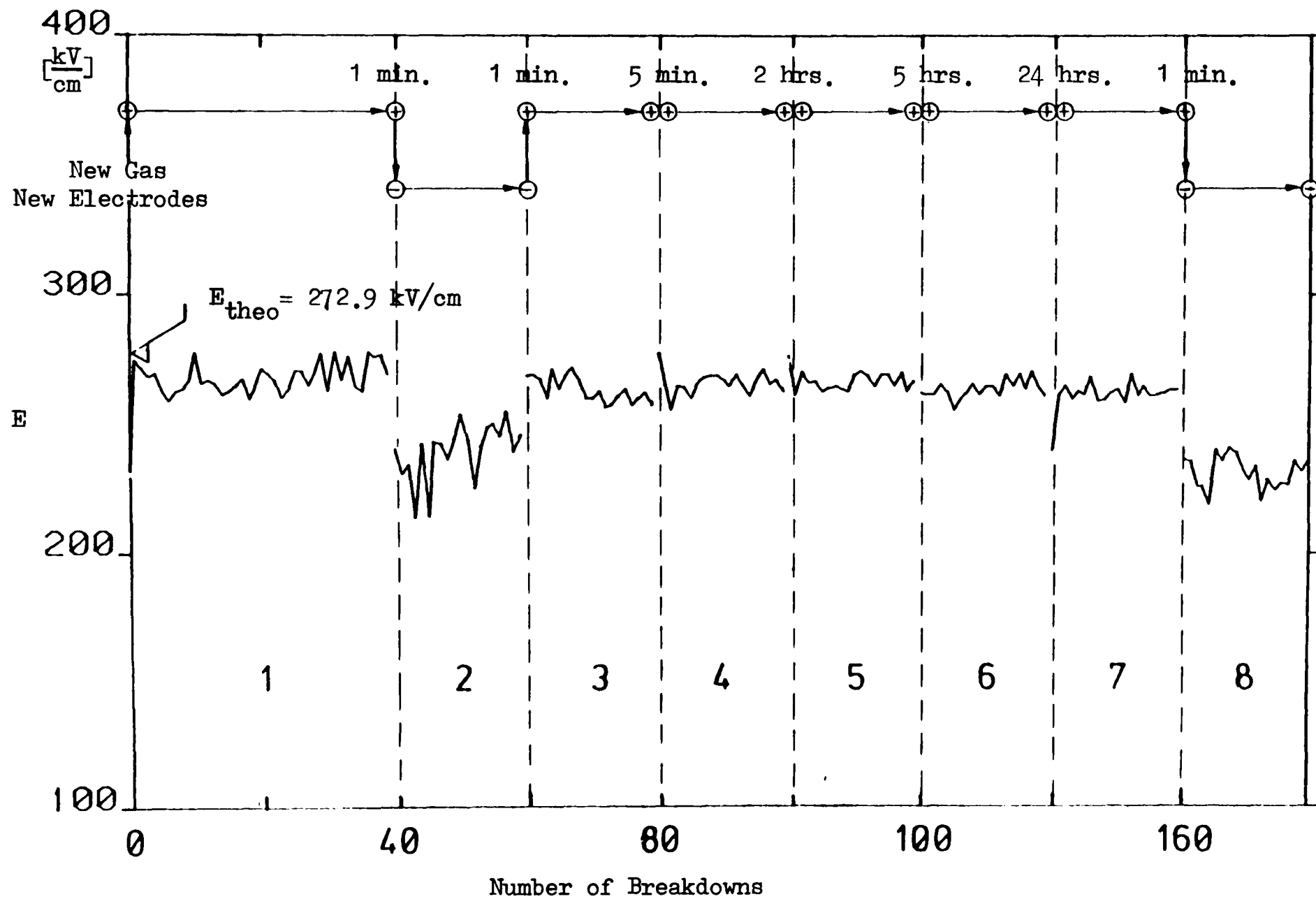


Figure 3.9 Spark Conditioning Phases in 40%  $\text{SF}_6$  - 60%  $\text{N}_2$  at  $p = 3.5$  bar  
 ( $r_1/r_2 = 0.5/1.27$  cm. radii, polished)

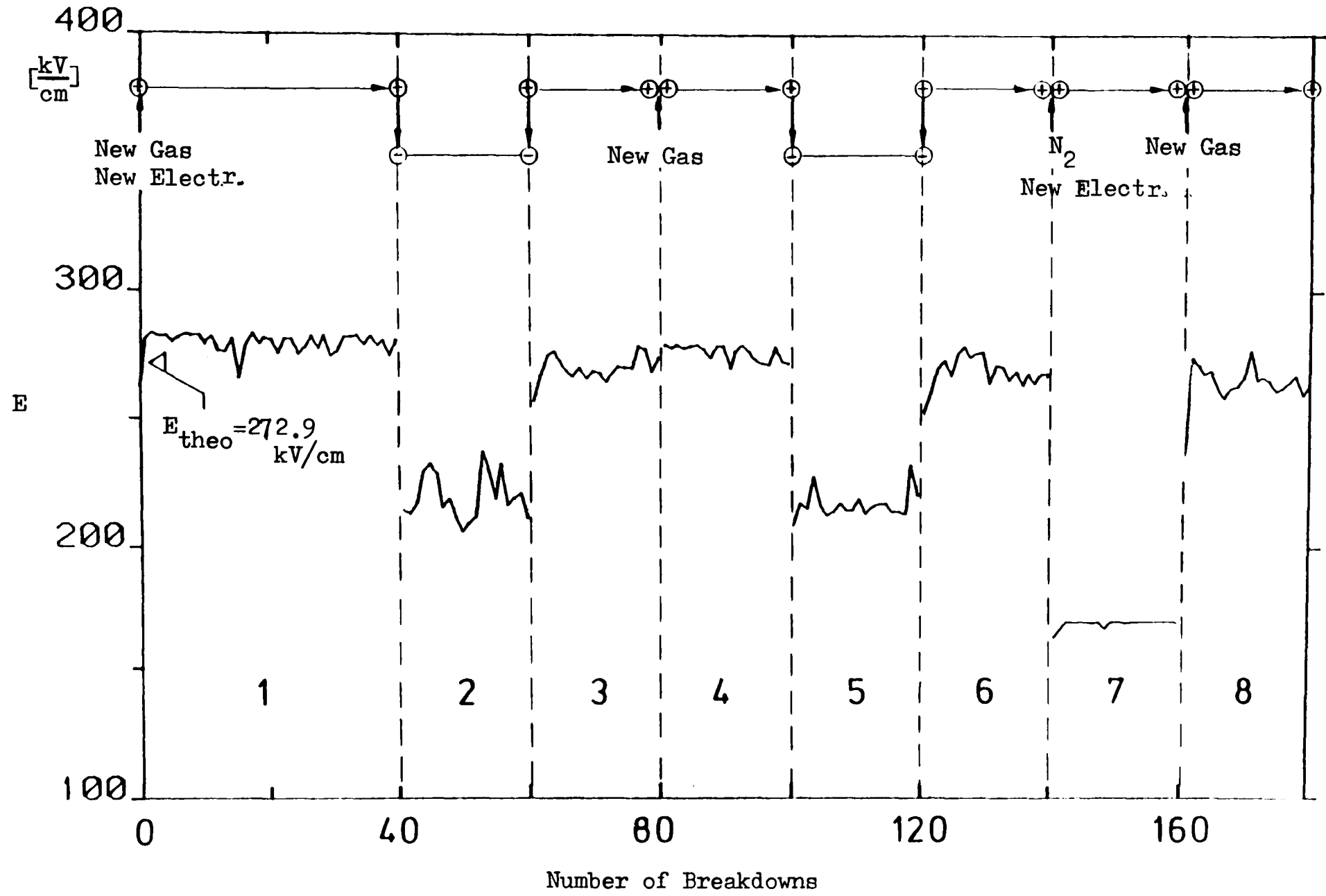


Figure 3.10 Spark conditioning phases for various gas and electrode conditions  
 ( $r_1/r_2 = 0.5/1.27$  cm. radii, polished)

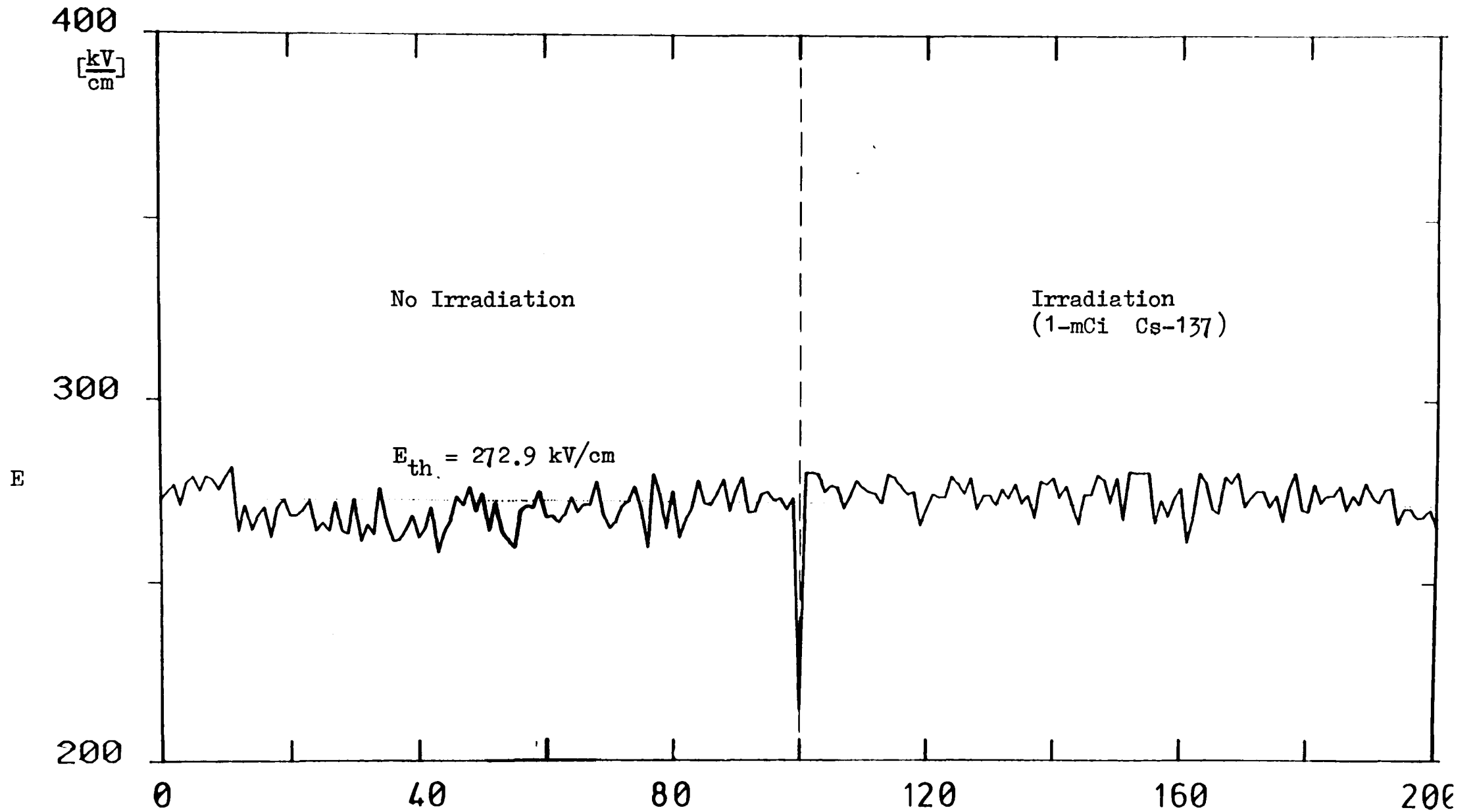
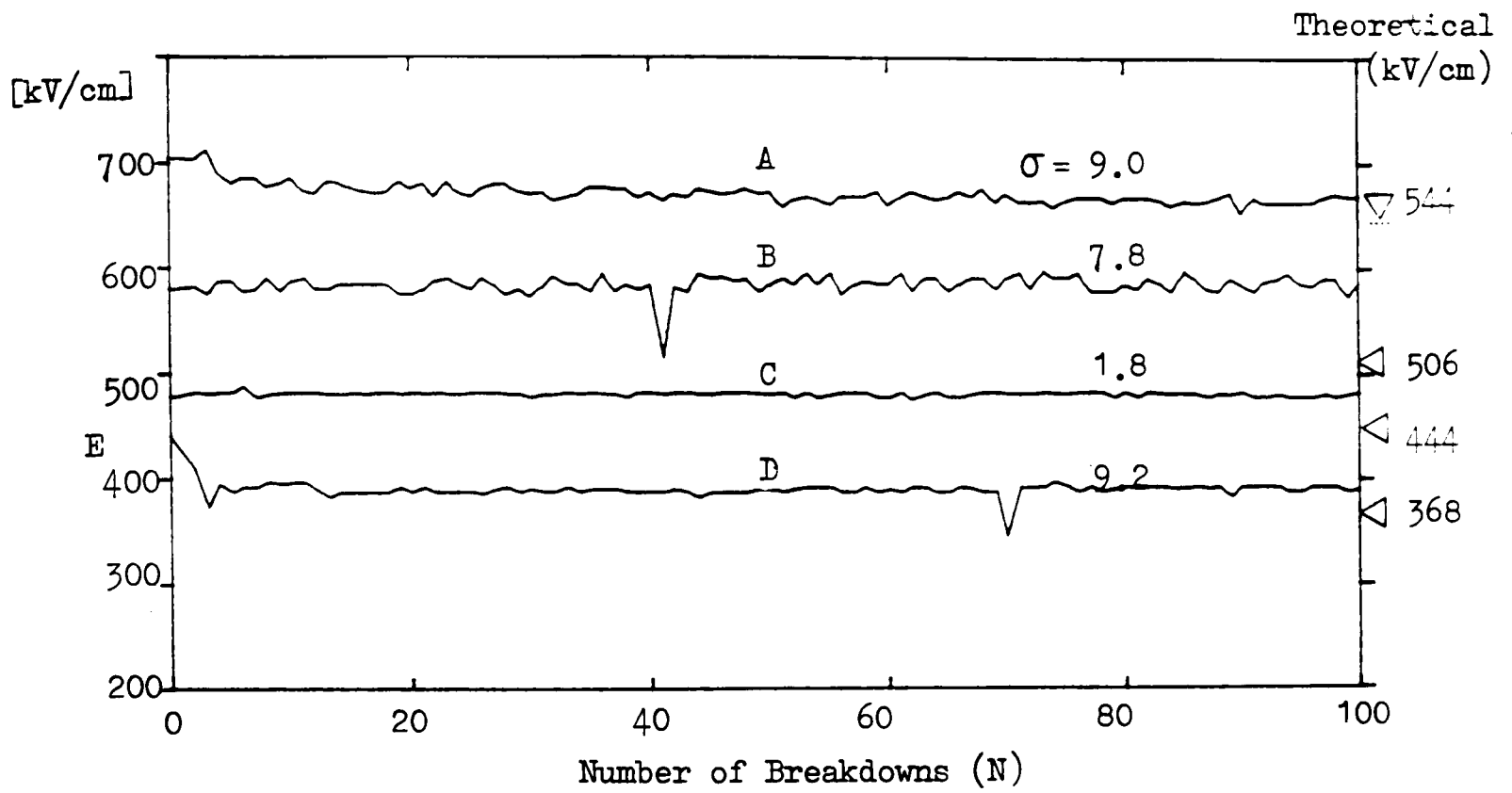
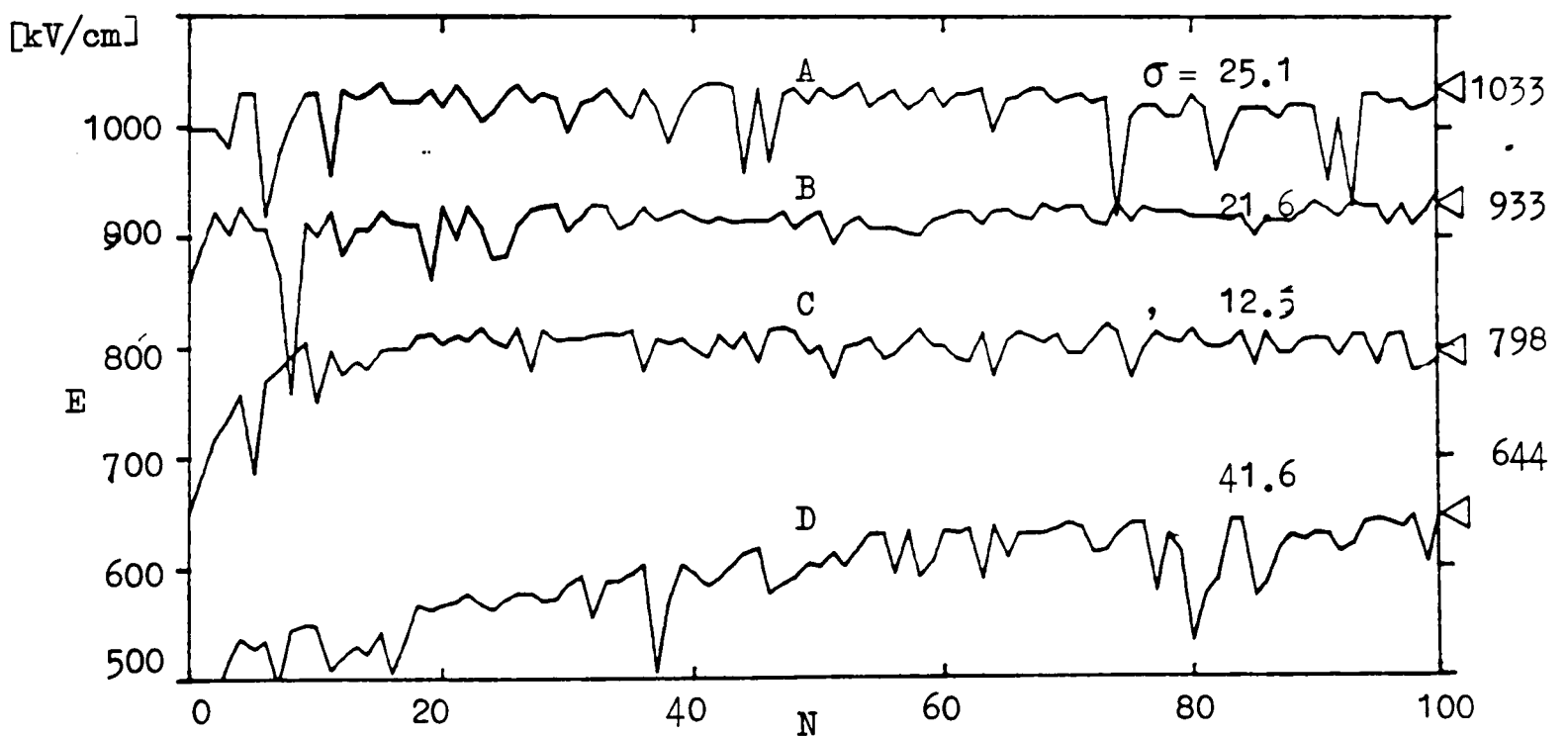


Figure 3.11 Effect of radiation in 40%  $\text{SF}_6\text{-N}_2$  at  $p = 3.5$  bar  
 ( $r_1/r_2 = 0.5/1.27$  cm. radii)



(a)  $p = 4$  bar

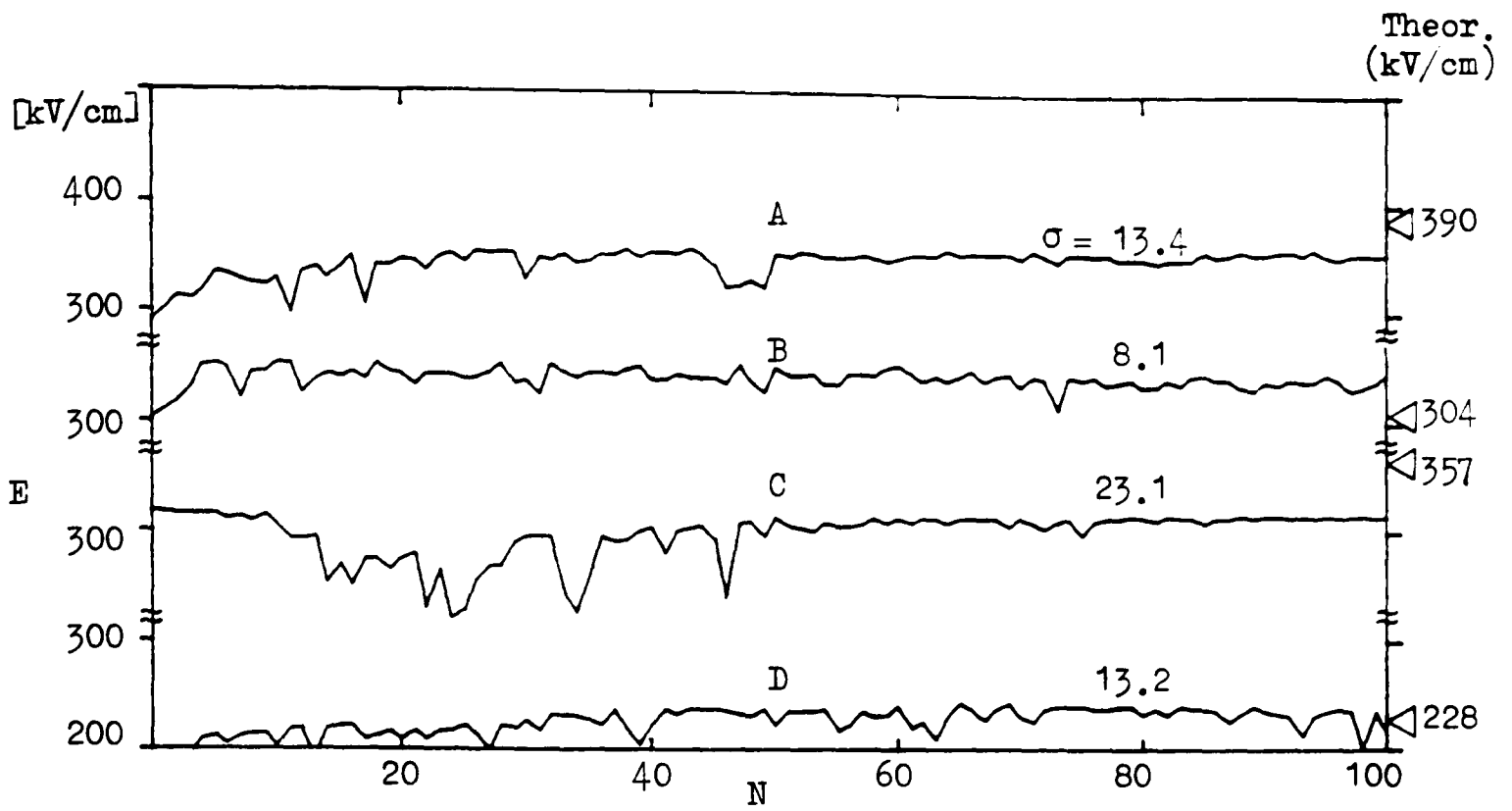


(b)  $p = 8.0$  bar

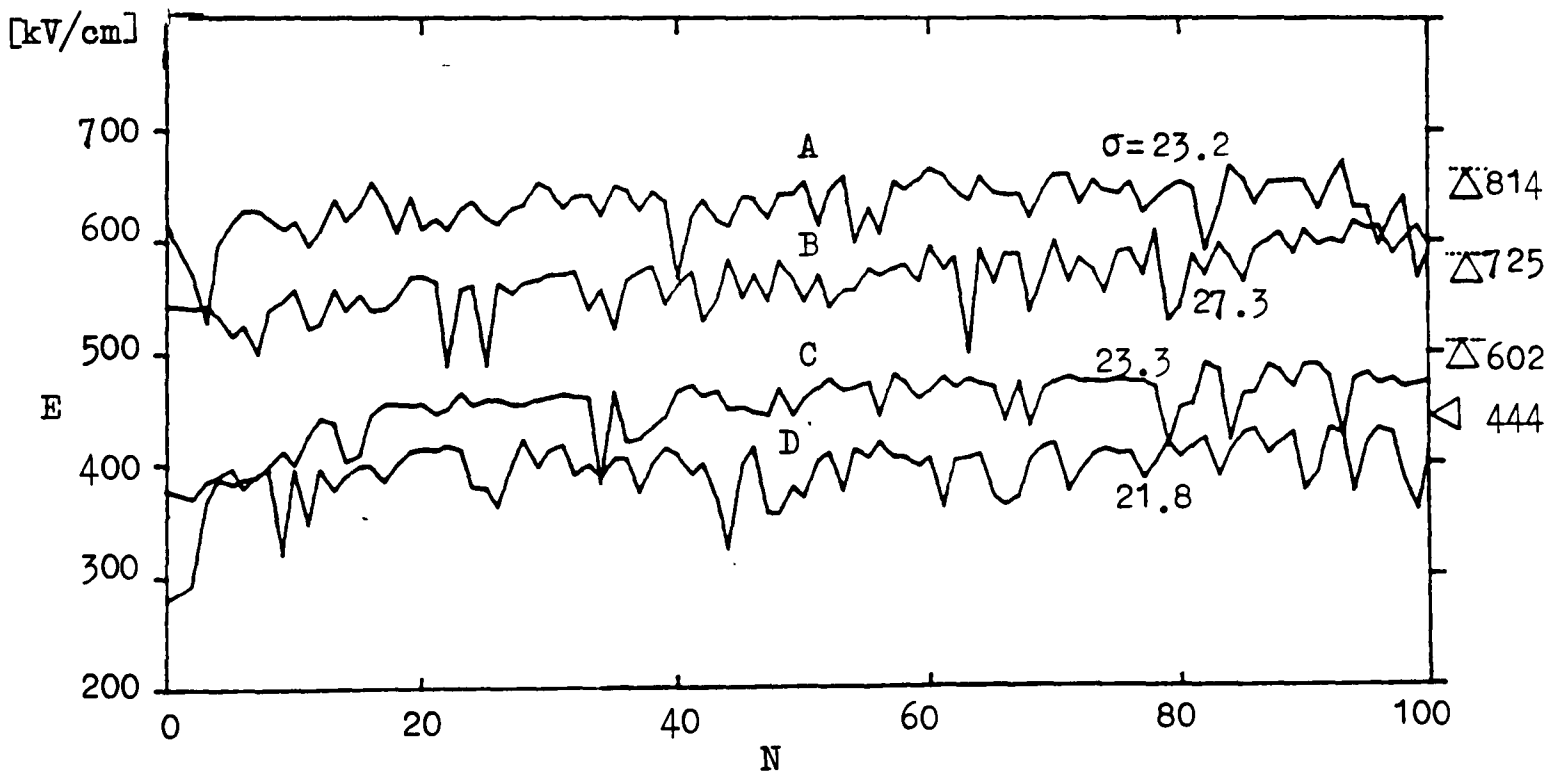
Figure 3.12 Spark conditioning sequences in mixtures at pressures of 4 bar (Figure (a)) and 8 bar (Figure (b))

(Gap  $r_1/r_2 = 0.0125/1.27$  cm, nonuniformity factor( $f$ ) = 21.7, polished).

A -  $\text{SF}_6$ , B - 75%  $\text{SF}_6/\text{N}_2$ , C - 40%  $\text{SF}_6/\text{N}_2$ , D - 10%  $\text{SF}_6/\text{N}_2$



(a)  $p = 4.0$  bar



(b)  $p = 8.0$  bar

Figure 3.13 Spark conditioning sequences in several mixtures at pressures 4 bar (Figure (a)) and 8 bar (Figure (b)) (Gap  $r_1/r_2 = 0.945/1.27$  cm,  $f = 1.16$ , polished)

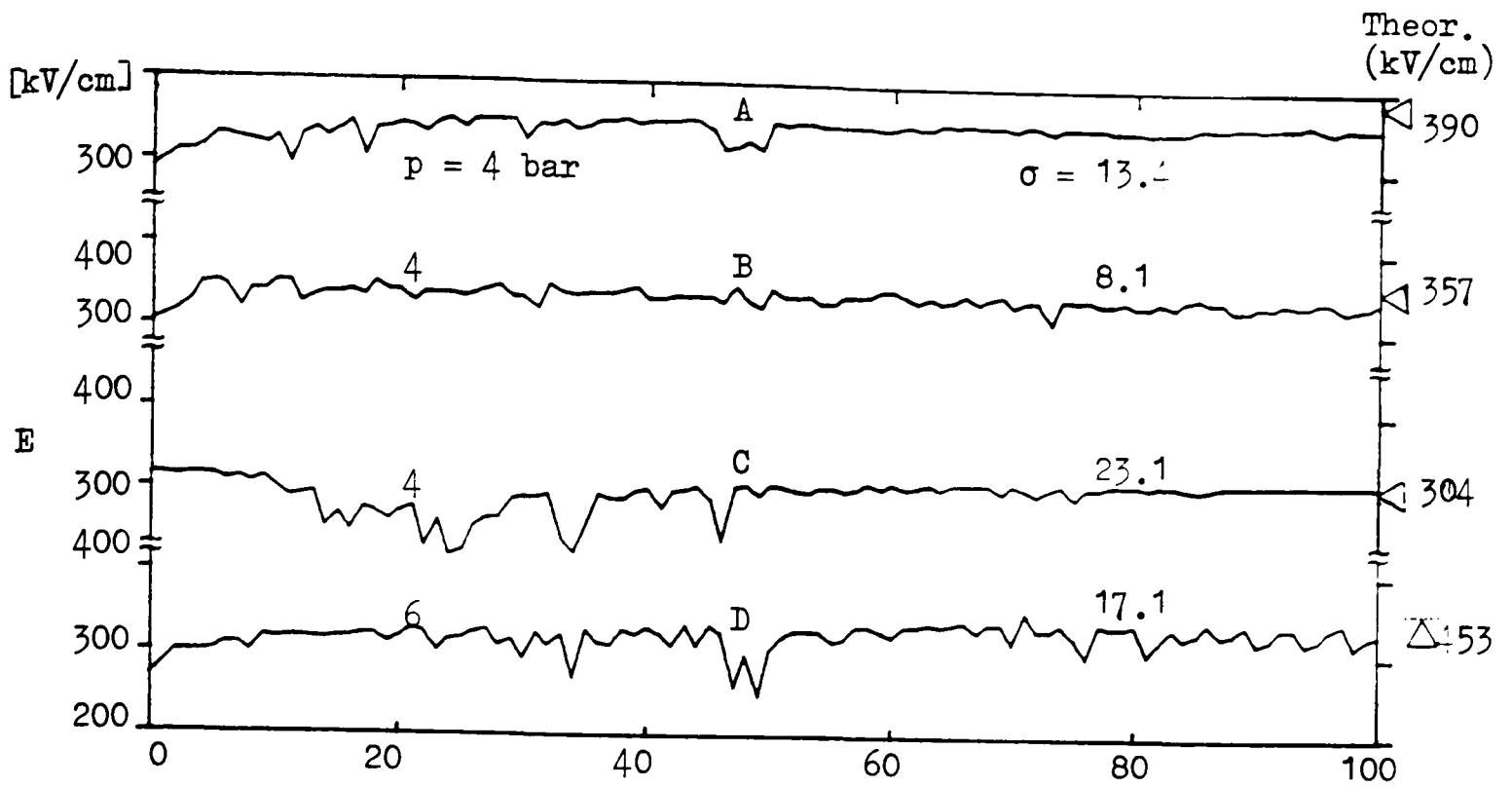


Figure 3.14 The effect of varying SF<sub>6</sub> content on spark conditioning for positive field intensities in the range 300-400 kV/cm (Gap  $r_1/r_2 = 0.945/1.27$  cm, polished)

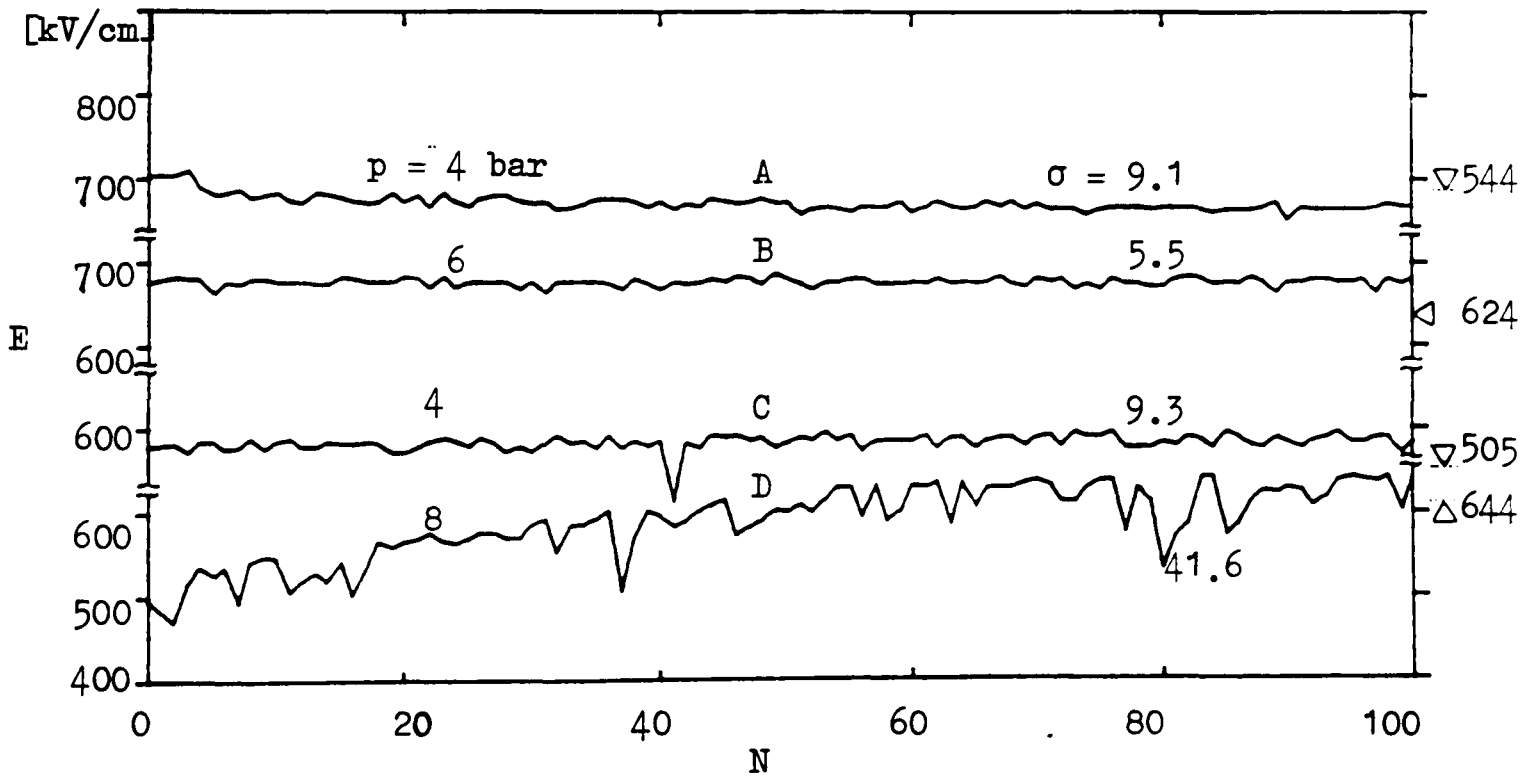


Figure 3.15 The effect of varying SF<sub>6</sub> content on spark conditioning for positive field intensities in the range 600-700 kV/cm ( $r_1/r_2 = 0.0125/1.27$  cm, polished)  
 A- SF<sub>6</sub>, B-75% SF<sub>6</sub>-N<sub>2</sub>, C-40% SF<sub>6</sub>-N<sub>2</sub>, D-10% SF<sub>6</sub>-N<sub>2</sub>

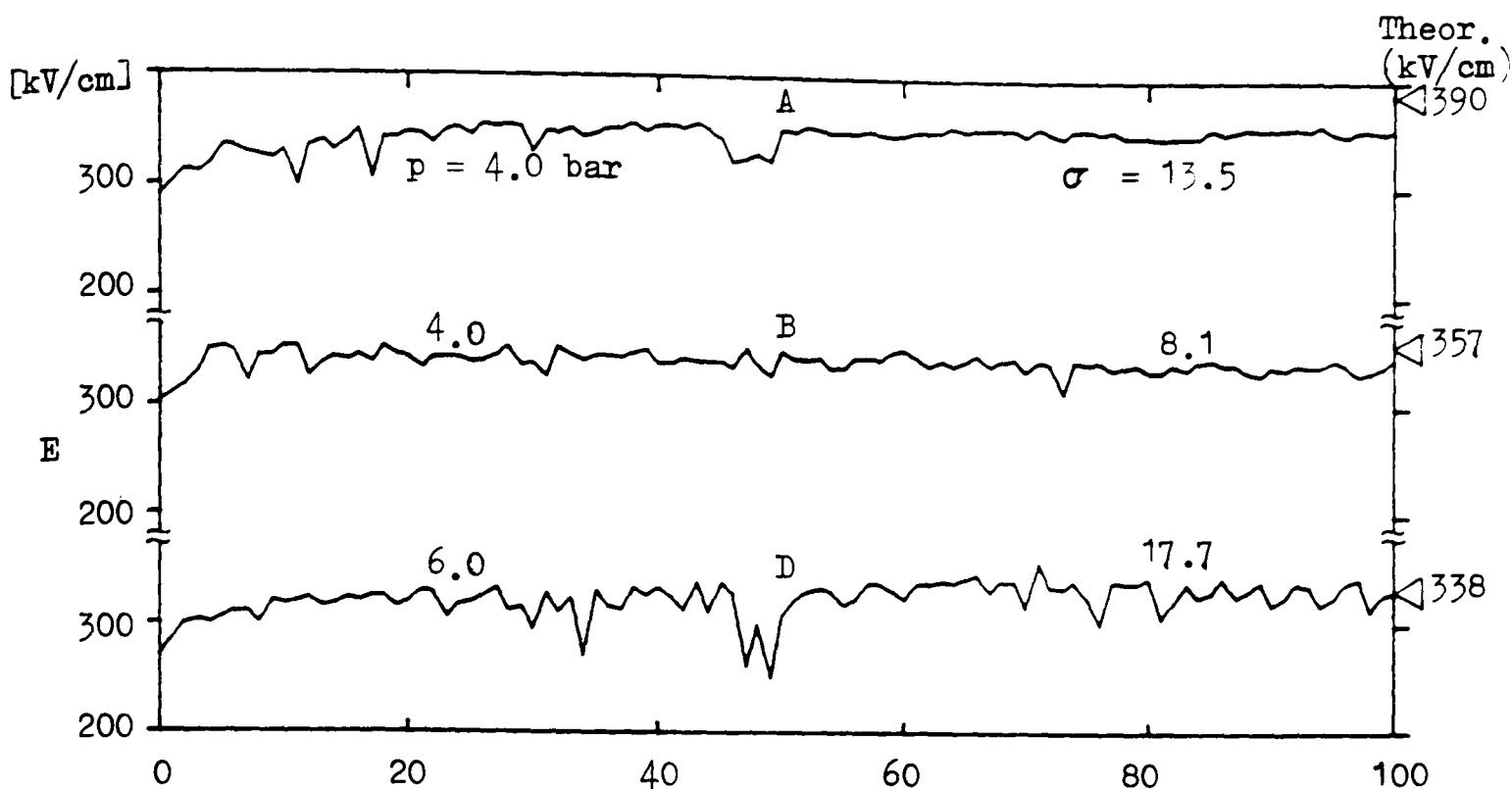


Figure 3.16 Spark conditioning sequences for polished electrode ( $R_{CLA} = 0.04 \mu\text{m}$ ) for field strengths in the range 300-400 kV/cm (Gap  $r_1/r_2 = 0.945/1.27$  cm)

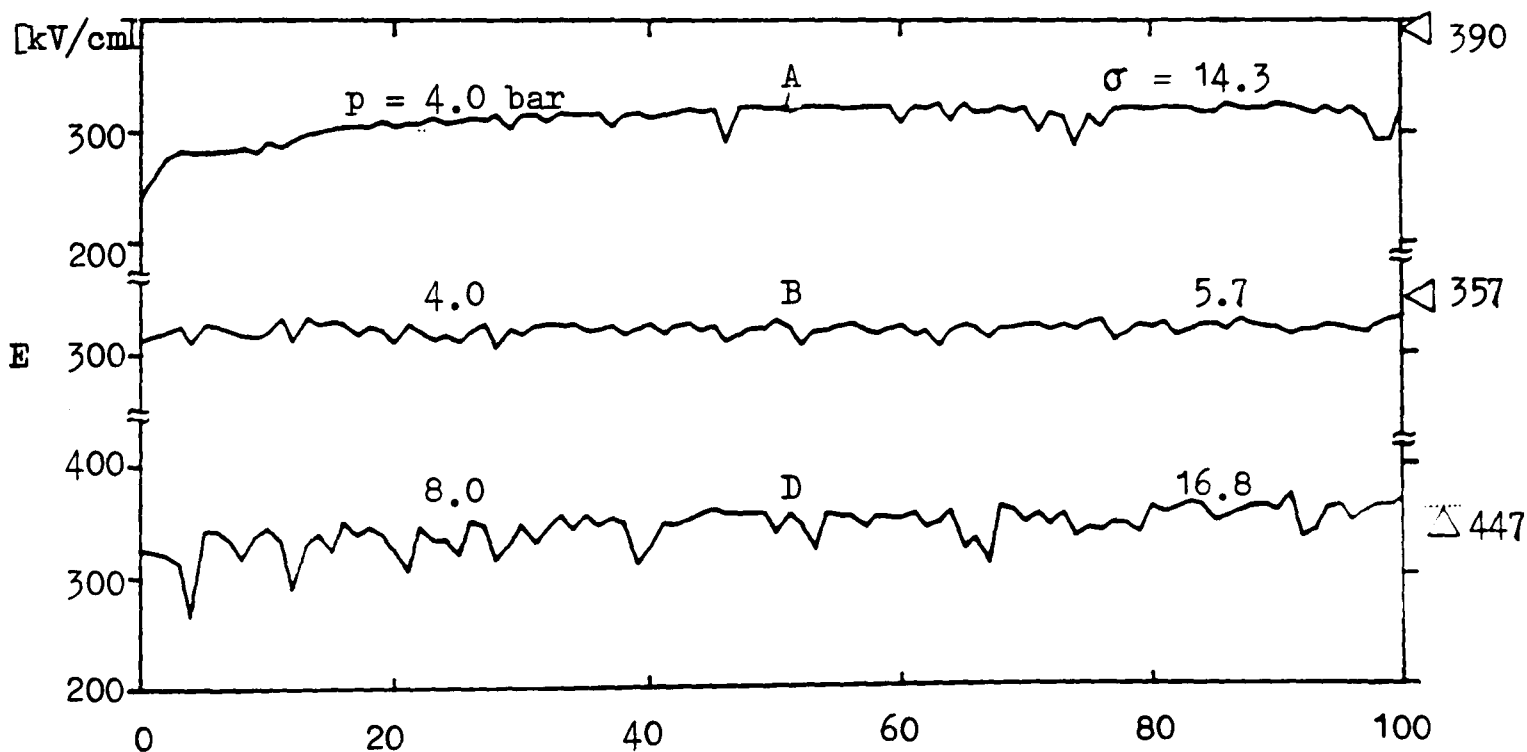


Figure 3.17 Spark conditioning sequences for sandblasted electrodes ( $R_{CLA} = 2.3 \mu\text{m}$ ) for field strengths in the range 300-400 kV/cm (gap  $r_1/r_2 = 0.945/1.27$  cm)

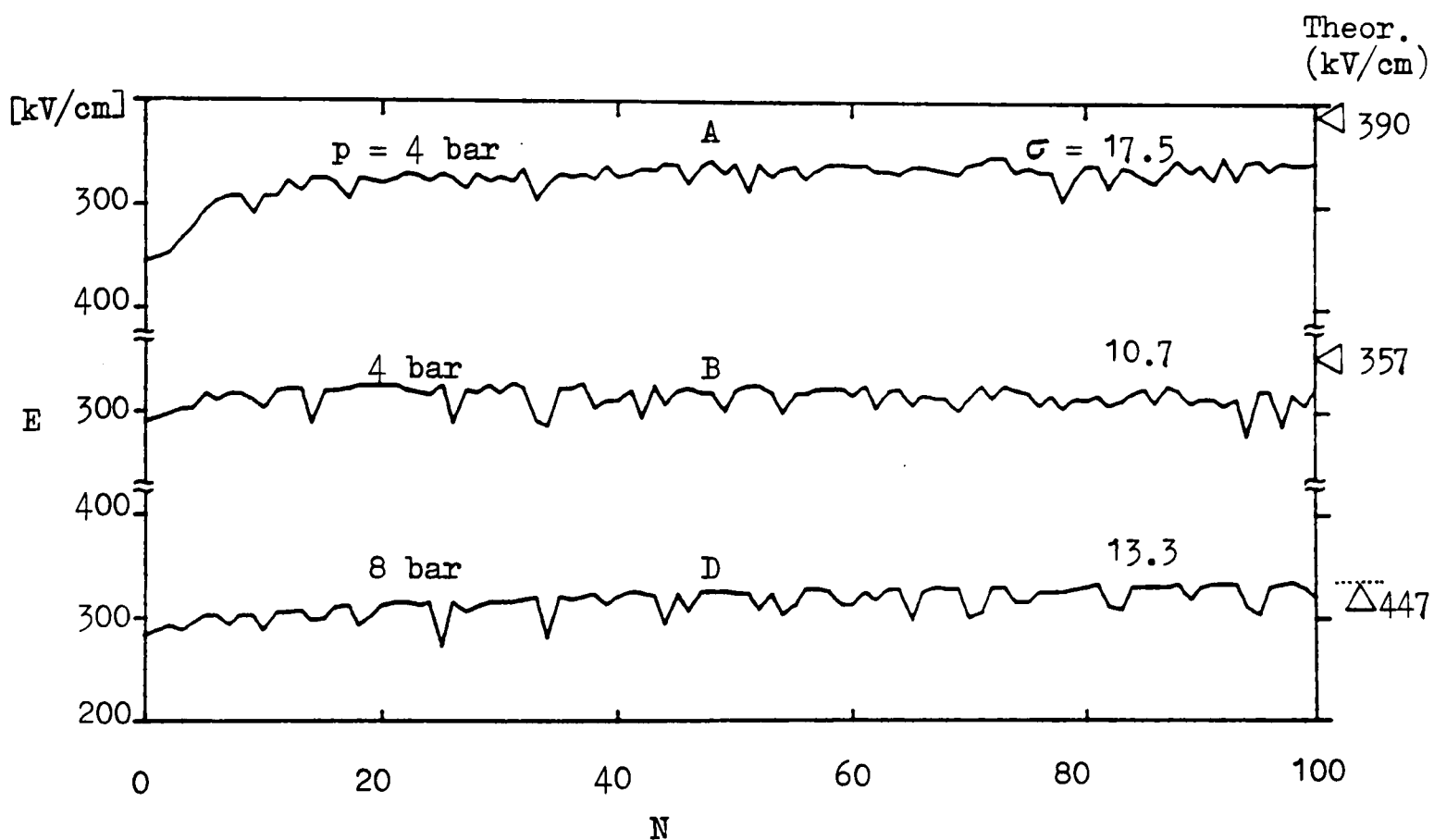


Figure 3.18 Spark conditioning sequences of machined electrode ( $R_{\text{CLA}} = 2.8 \mu\text{m}$ ) for field strengths in the range 300–400  $\text{kV/cm}$  (Gap  $r_1/r_2 = 0.945/1.27 \text{ cm}$ )

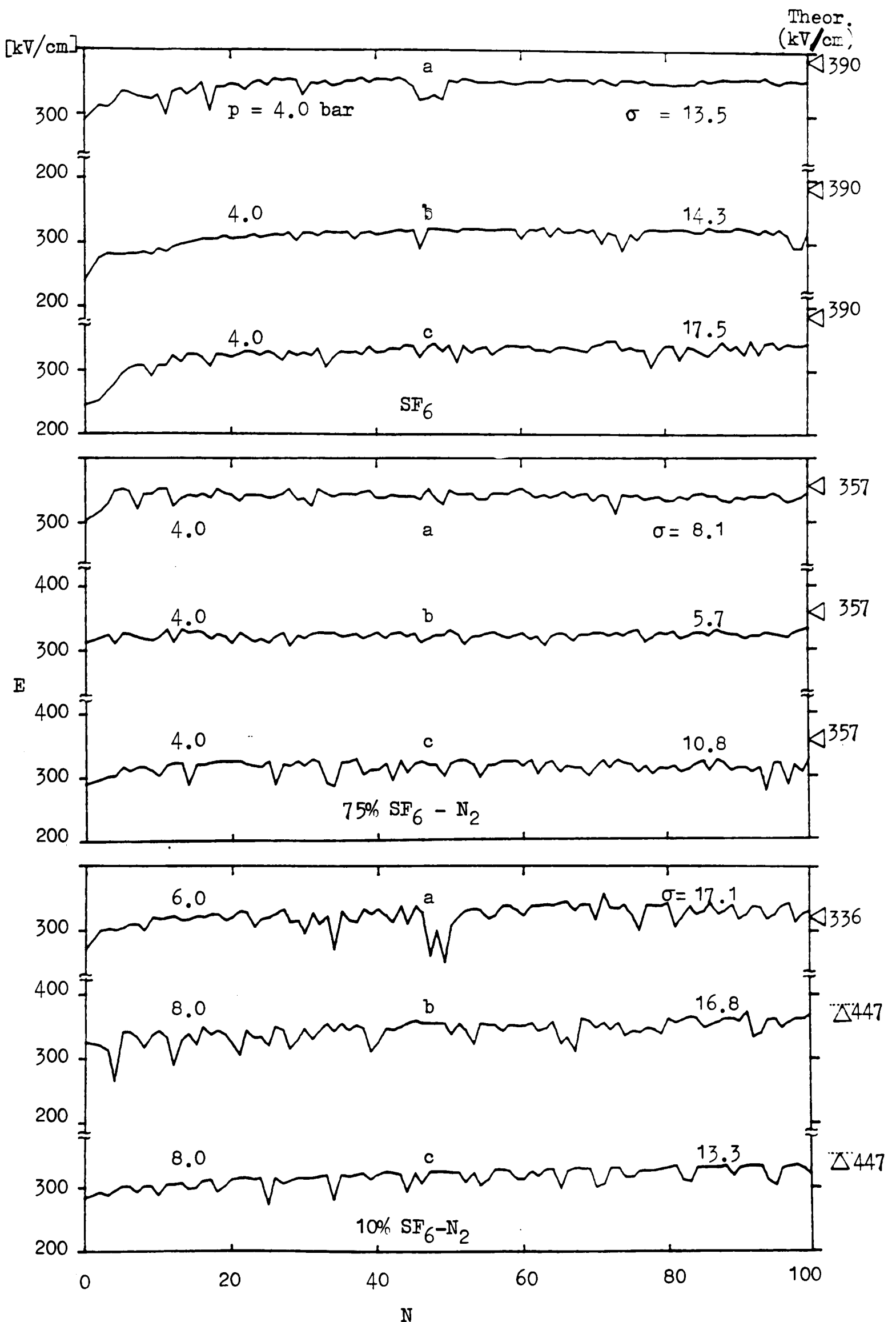


Figure 3.19 Effect of electrode surface roughness in mixtures for field strengths in the range 300–400  $\text{kV/cm}$  ( $r_1/r_2 = 0.945/1.27$  cm).  
 a - Polished, b - Sandblasted, c - Machined

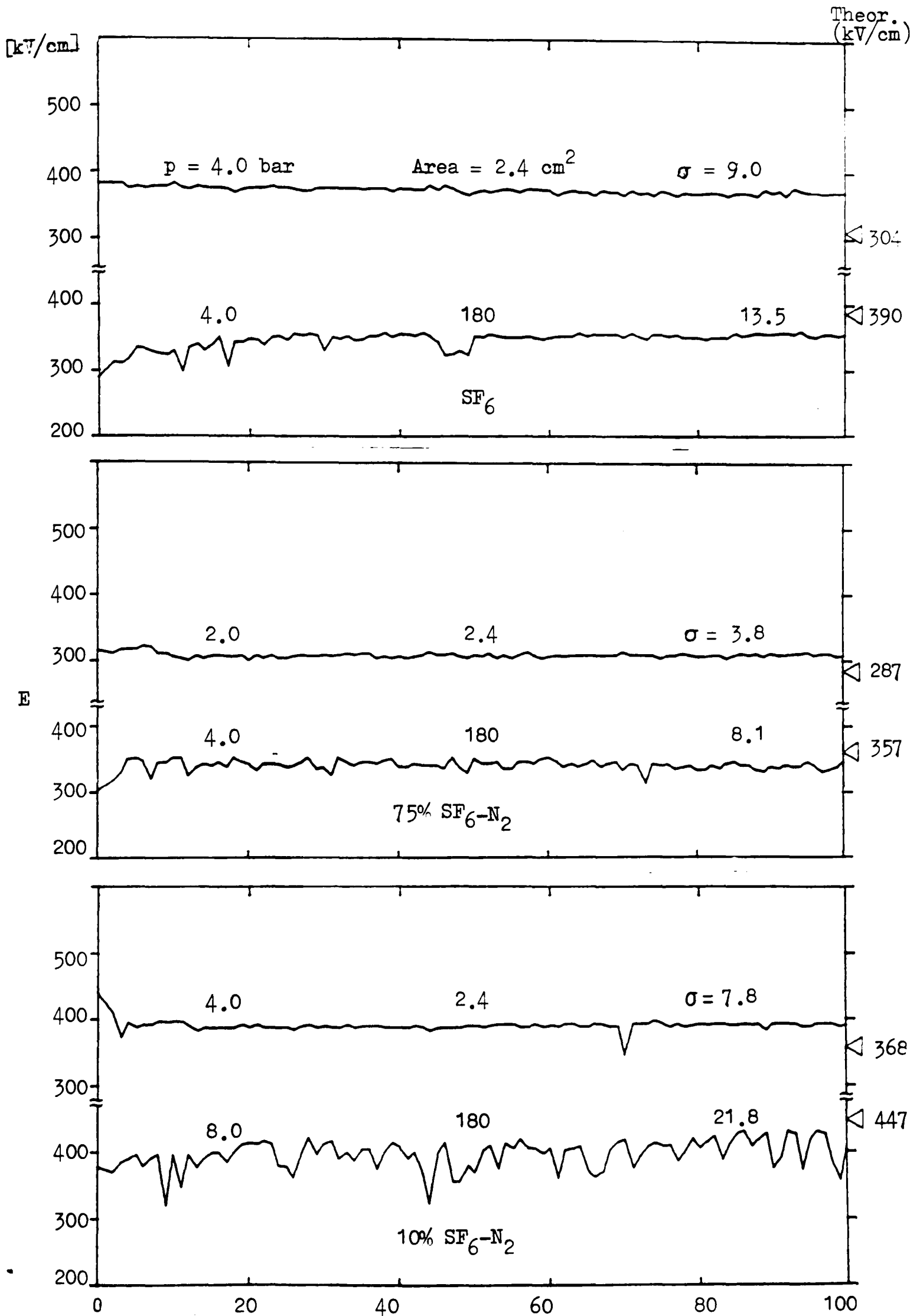
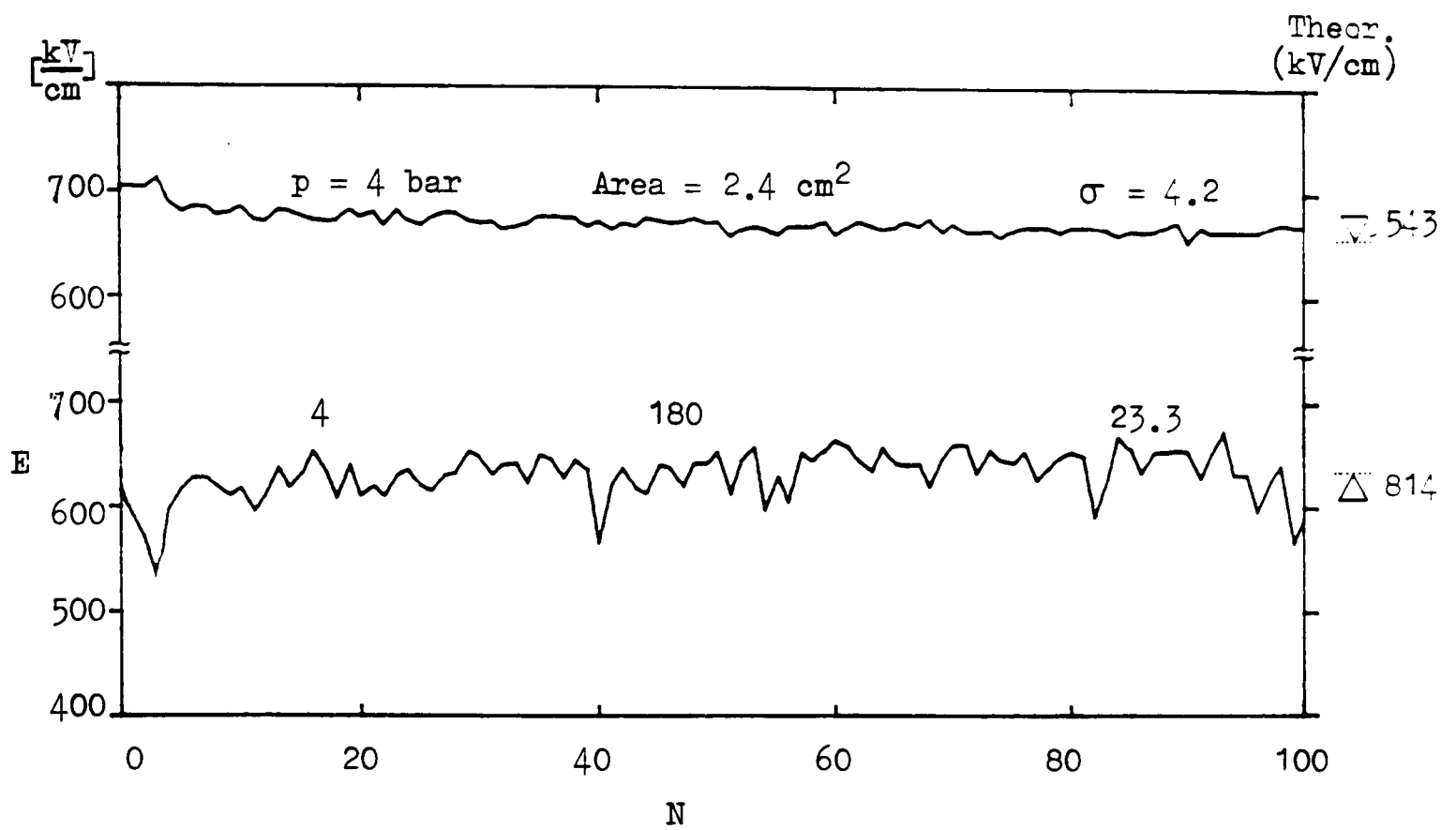
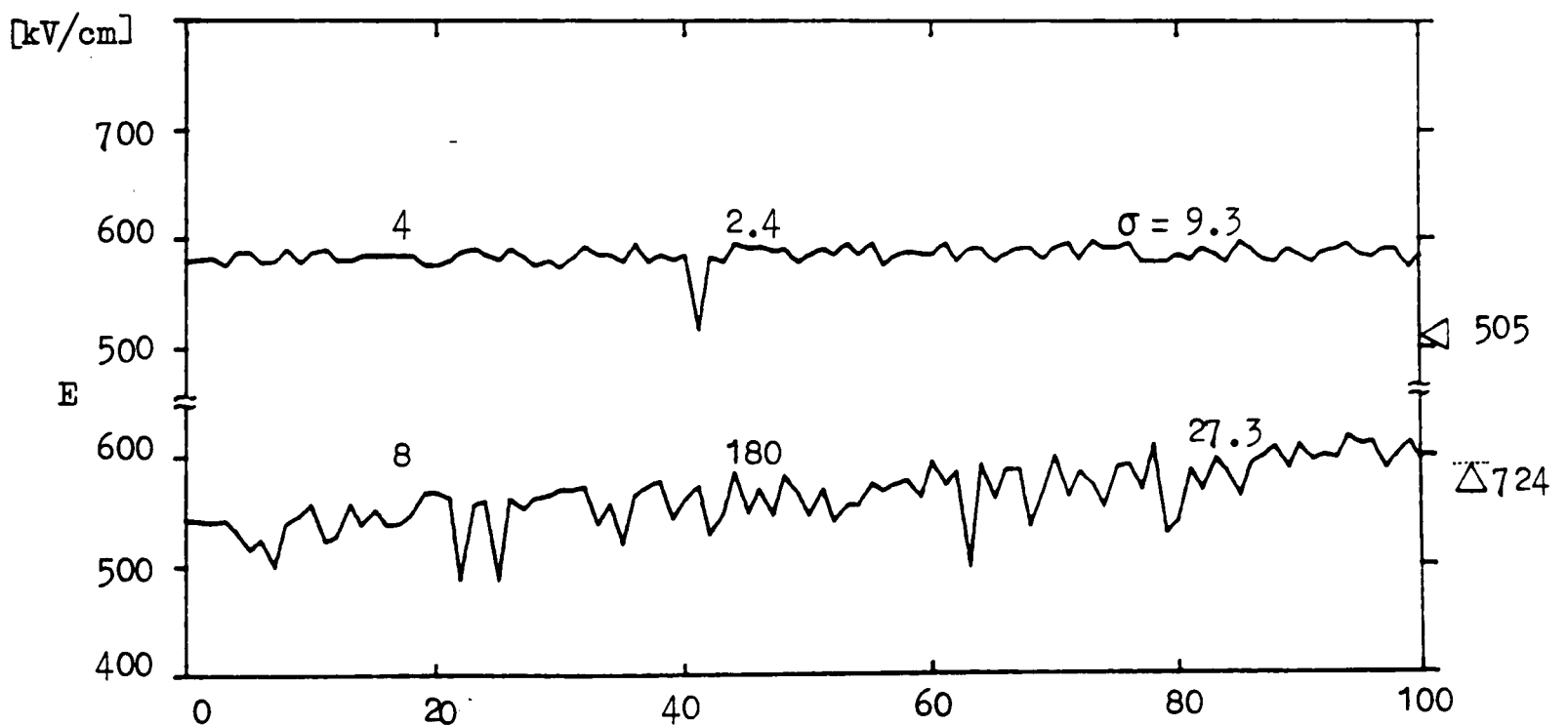


Figure 3.20 Effect of electrode area on spark conditioning in mixtures for field strengths in the range 300-400  $\text{kV/cm}$



(a)  $\text{SF}_6$



(b) 75%  $\text{SF}_6$ - $\text{N}_2$

Figure 3.21 Effect of electrode area on spark conditioning in  $\text{SF}_6$  and in a 75%  $\text{SF}_6$ - $\text{N}_2$  mixture for field strengths in the range 500-600  $\text{kV/cm}$

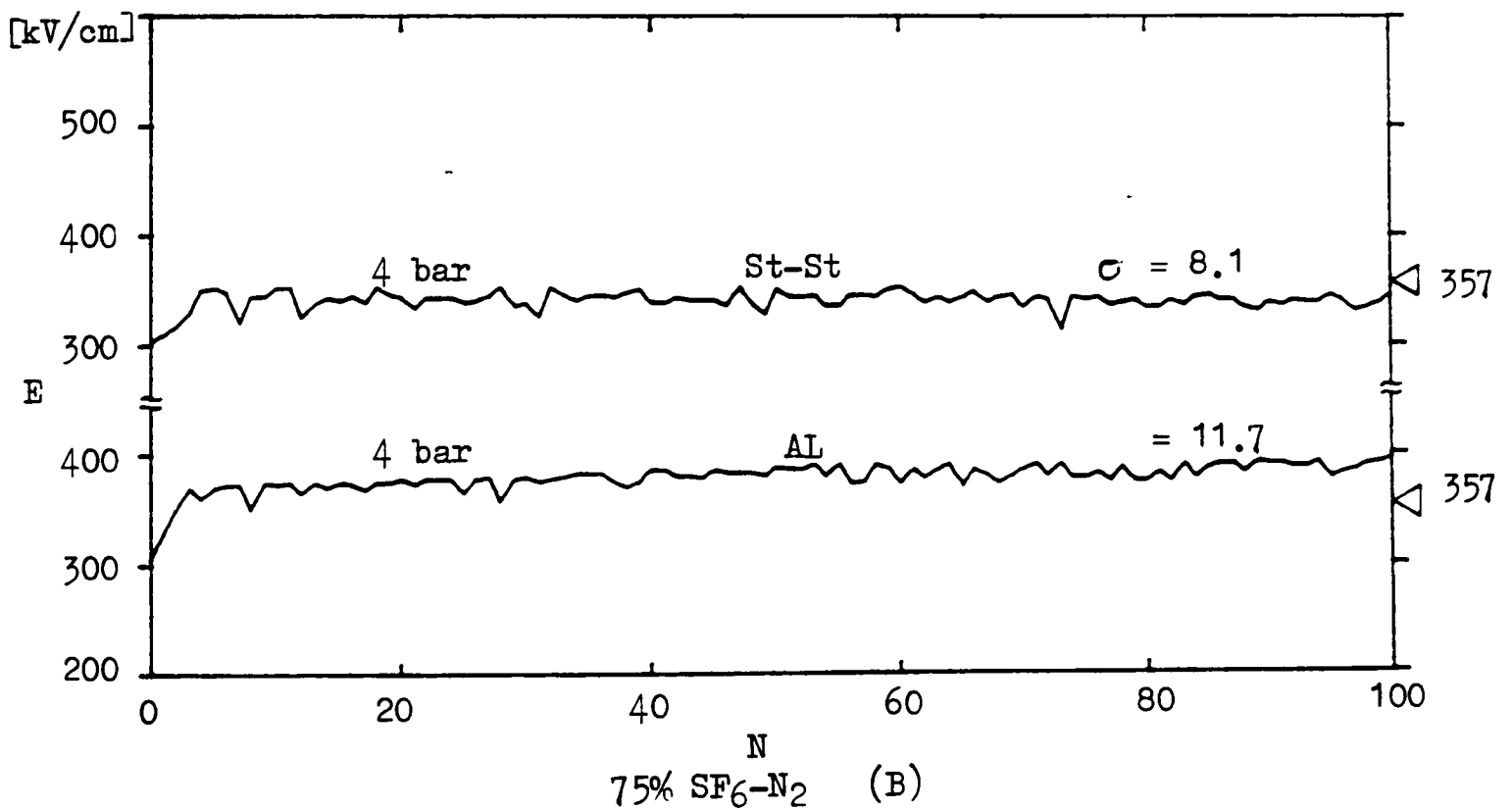
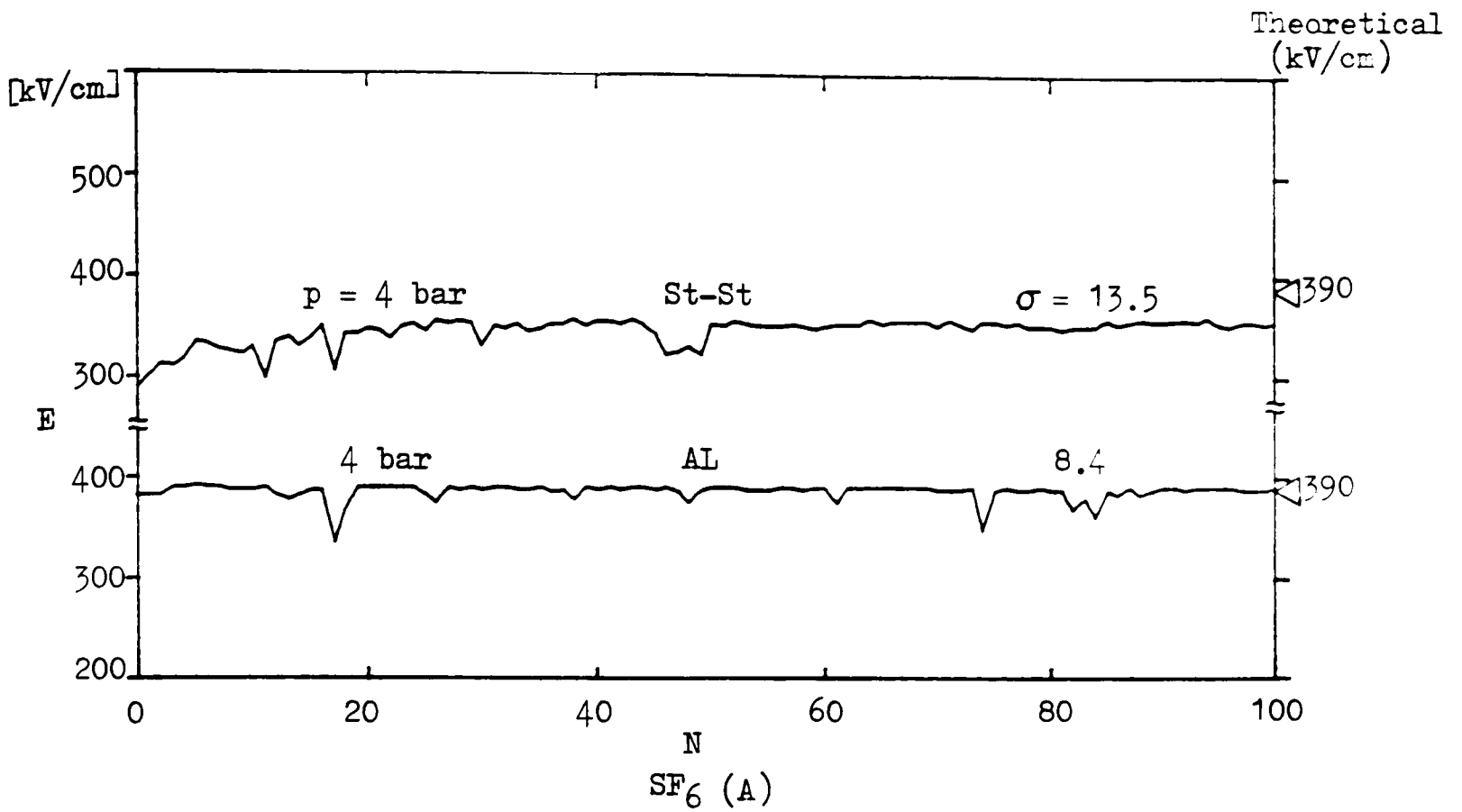


Figure 3.22(a) Effect of electrode material on spark conditioning in SF<sub>6</sub> and in a 75% SF<sub>6</sub>-N<sub>2</sub> for field strengths in the range 300-400 kV/cm ( $r_1/r_2 = 0.945/1.27$  cm, polished)

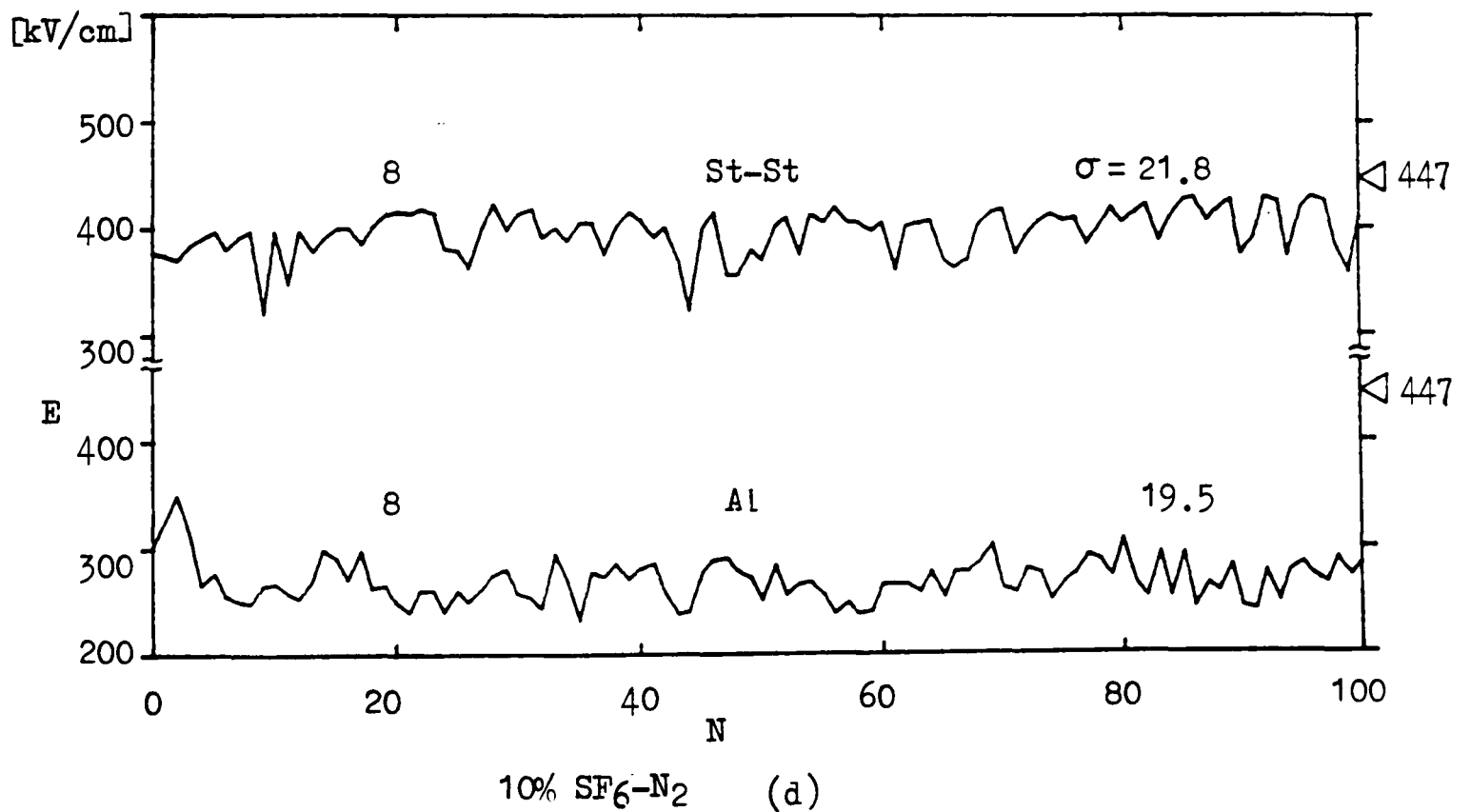
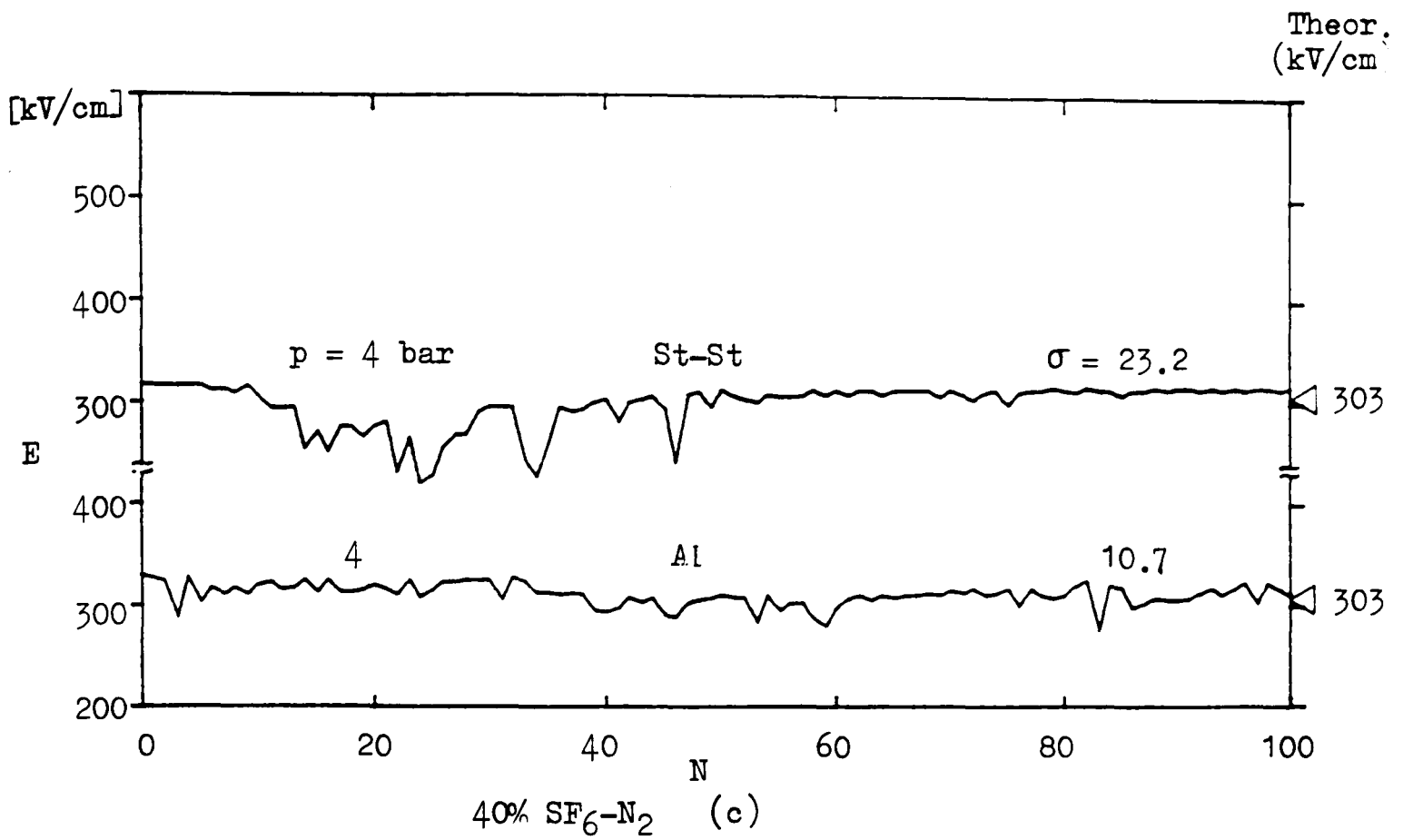


Figure 3.22(b) Effect of electrode material on spark conditioning in 40% SF<sub>6</sub>-N<sub>2</sub> and 10% SF<sub>6</sub>-N<sub>2</sub> for field strengths in the range 300-400 kV/cm ( $r_1/r_2 = 0.945/1.27$  cm, polished)

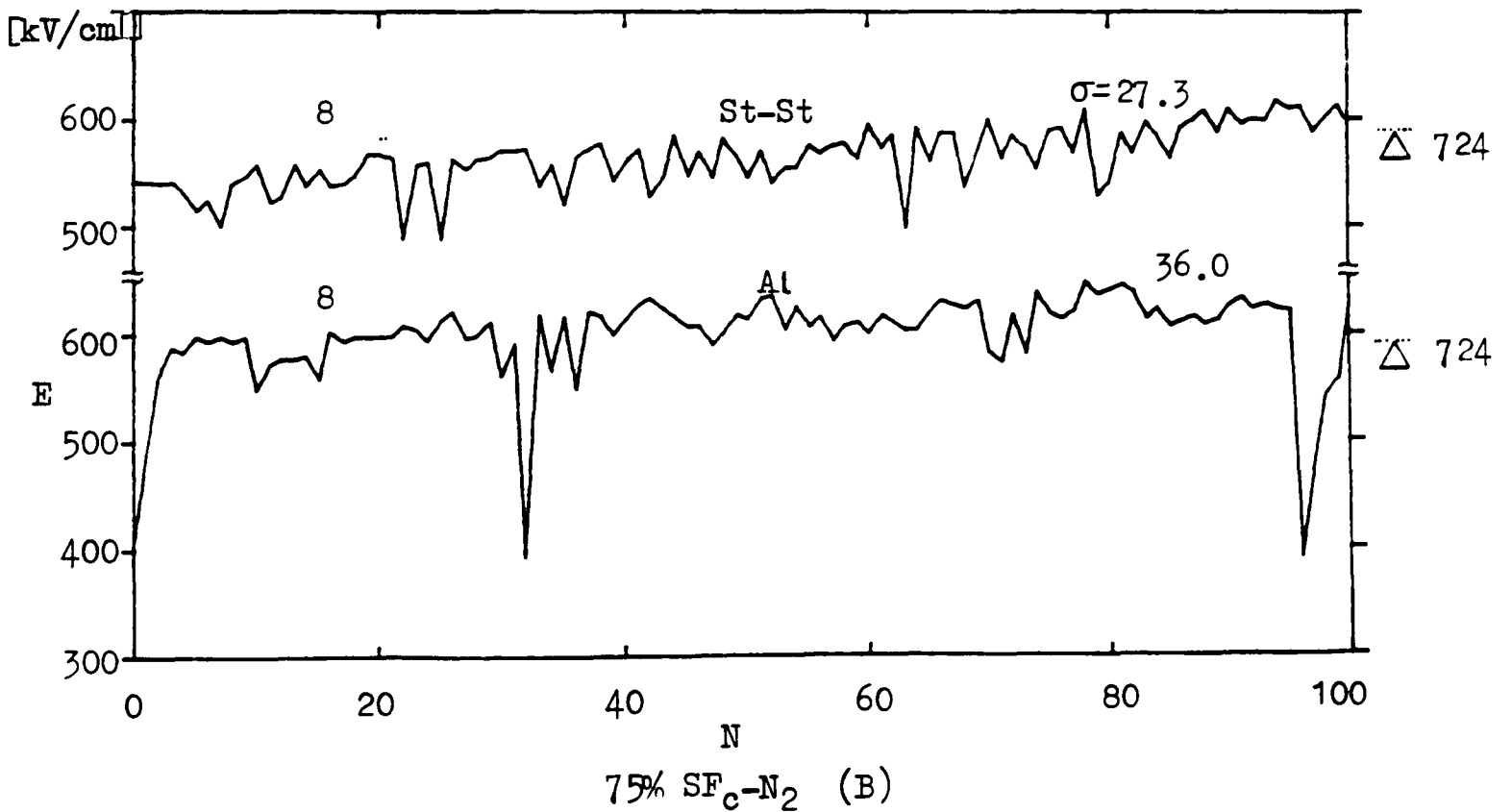
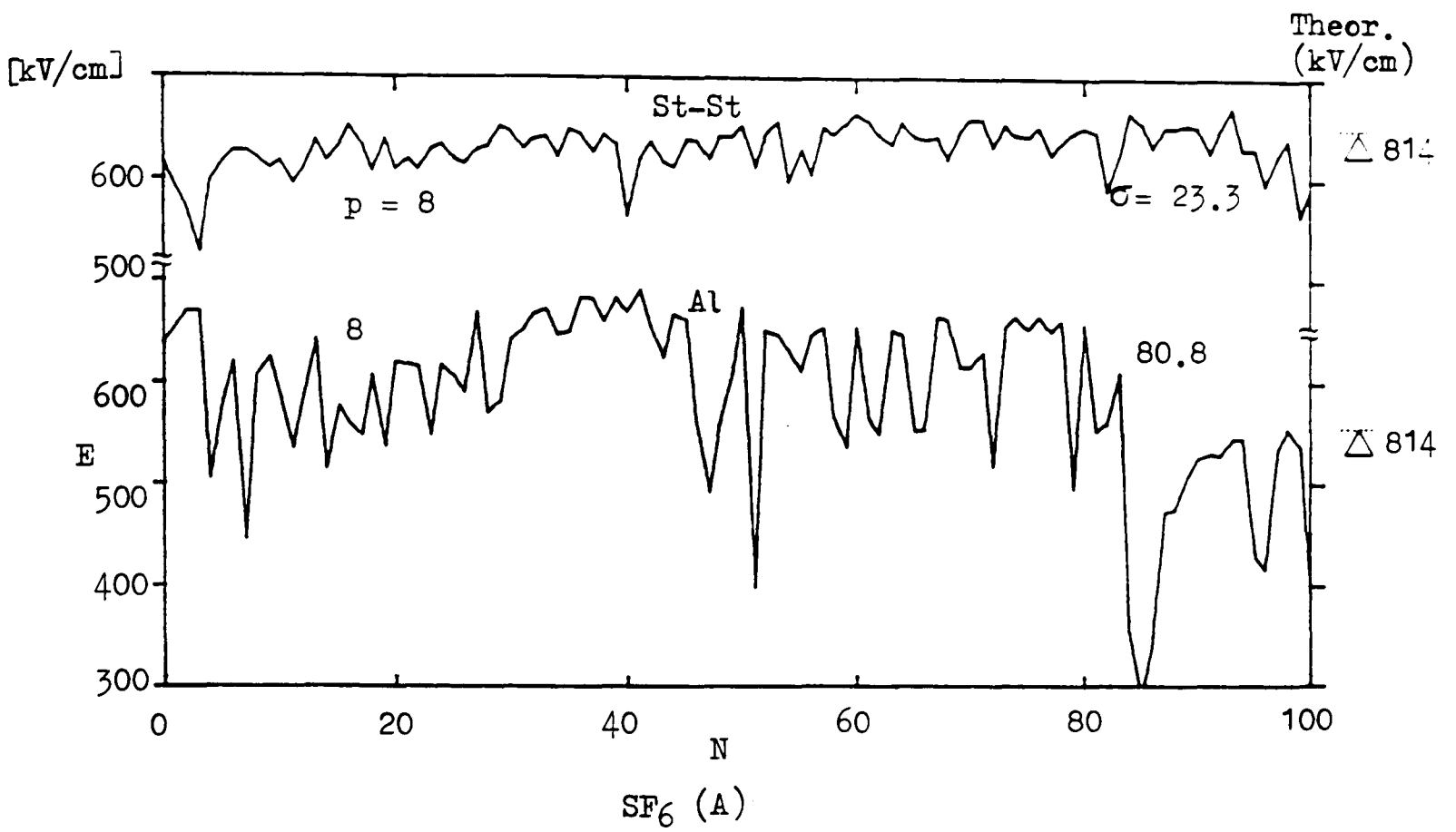


Figure 3.23 Effect of electrode material on spark conditioning for field strengths in the range 500-600 kV/cm in  $SF_6$  and in a 75%  $SF_6-N_2$  mixture ( $r_1/r_2 = 0.945/1.27$  cm)

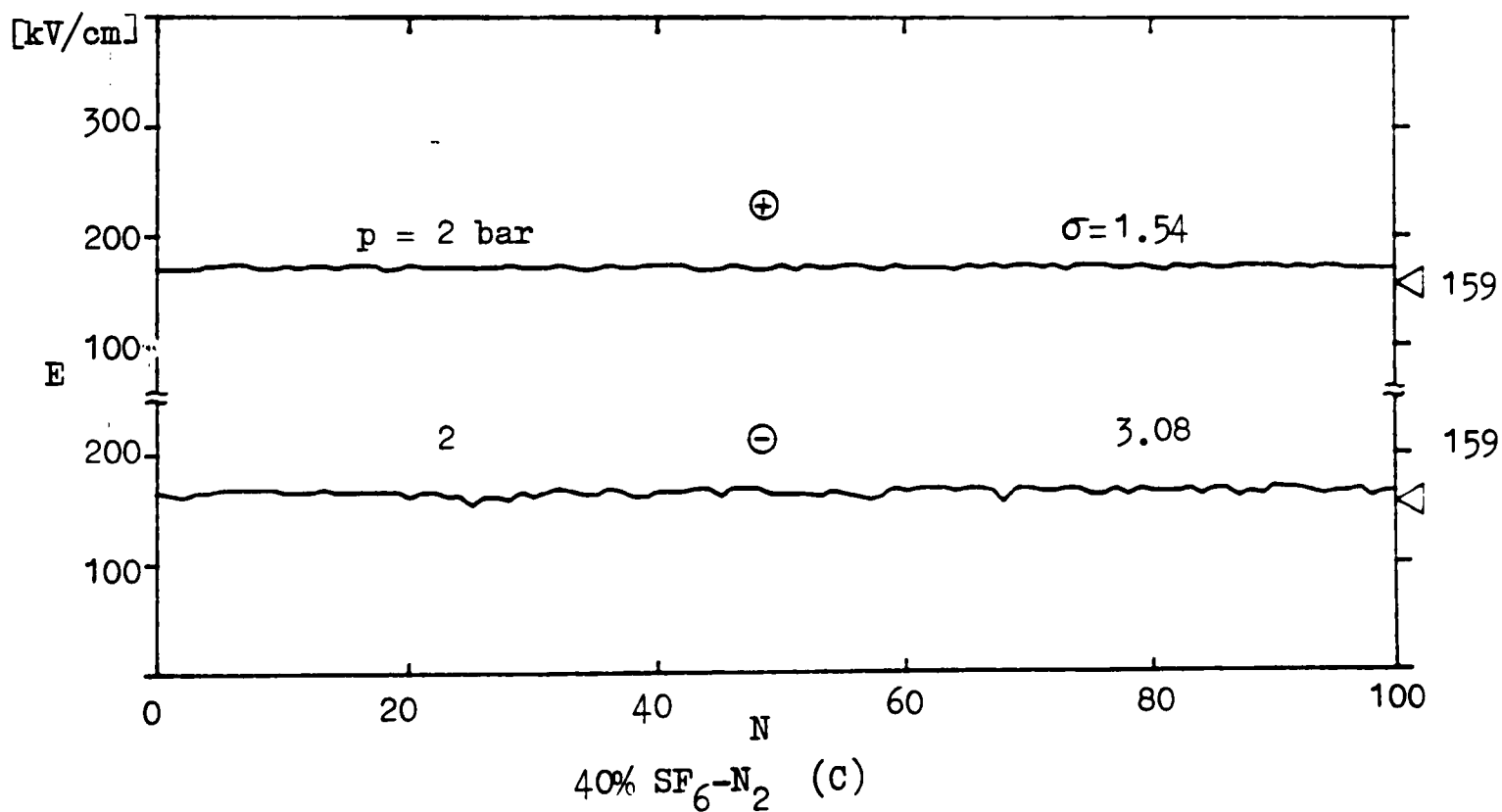
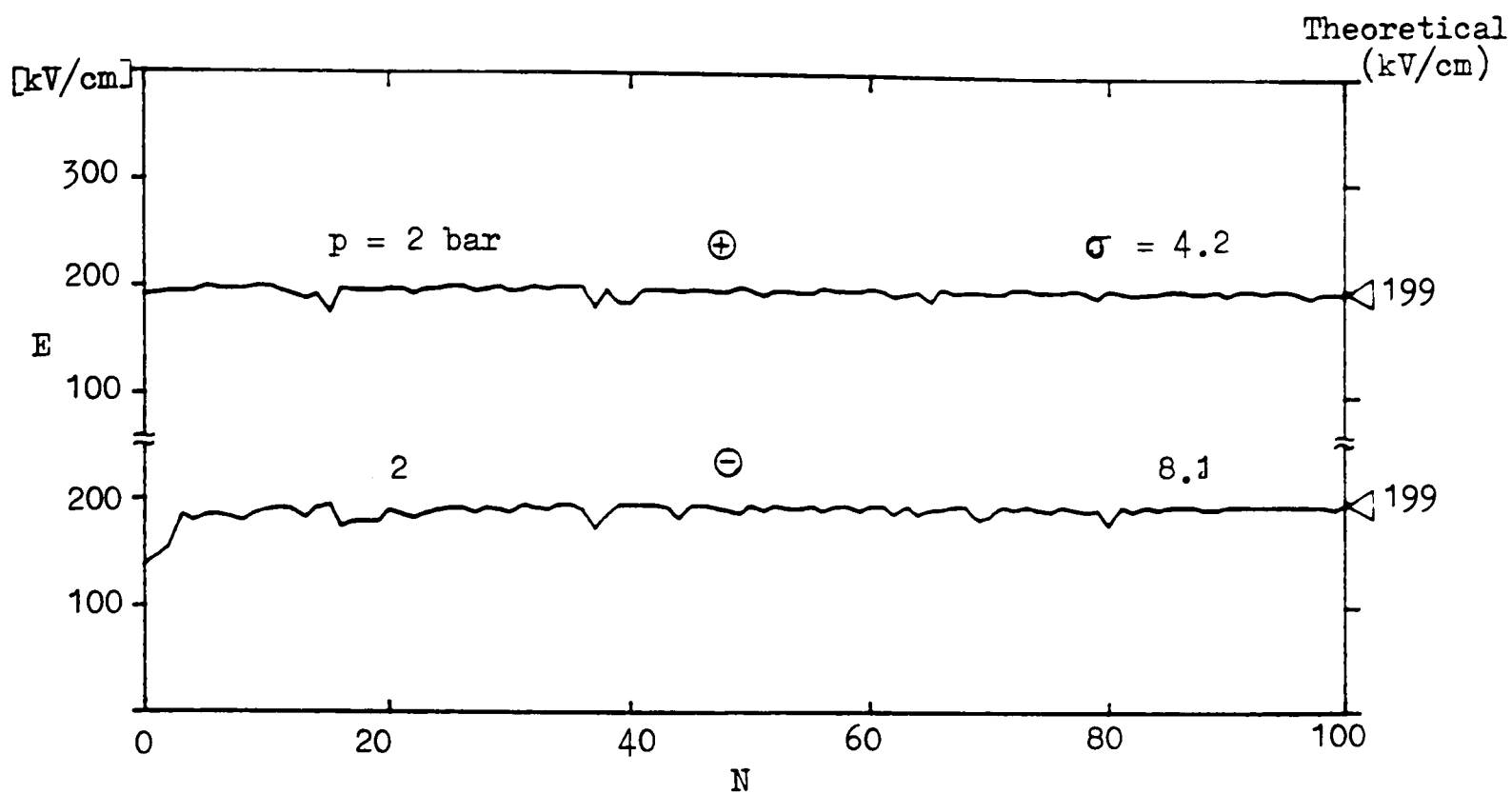


Figure 3.24(a) Effect of polarity on spark conditioning for field strengths in the range 100–200 kV/cm in  $\text{SF}_6$  and 40%  $\text{SF}_6/\text{N}_2$  mixture ( $r_1/r_2 = 0.5/1.27$  cm, polished)

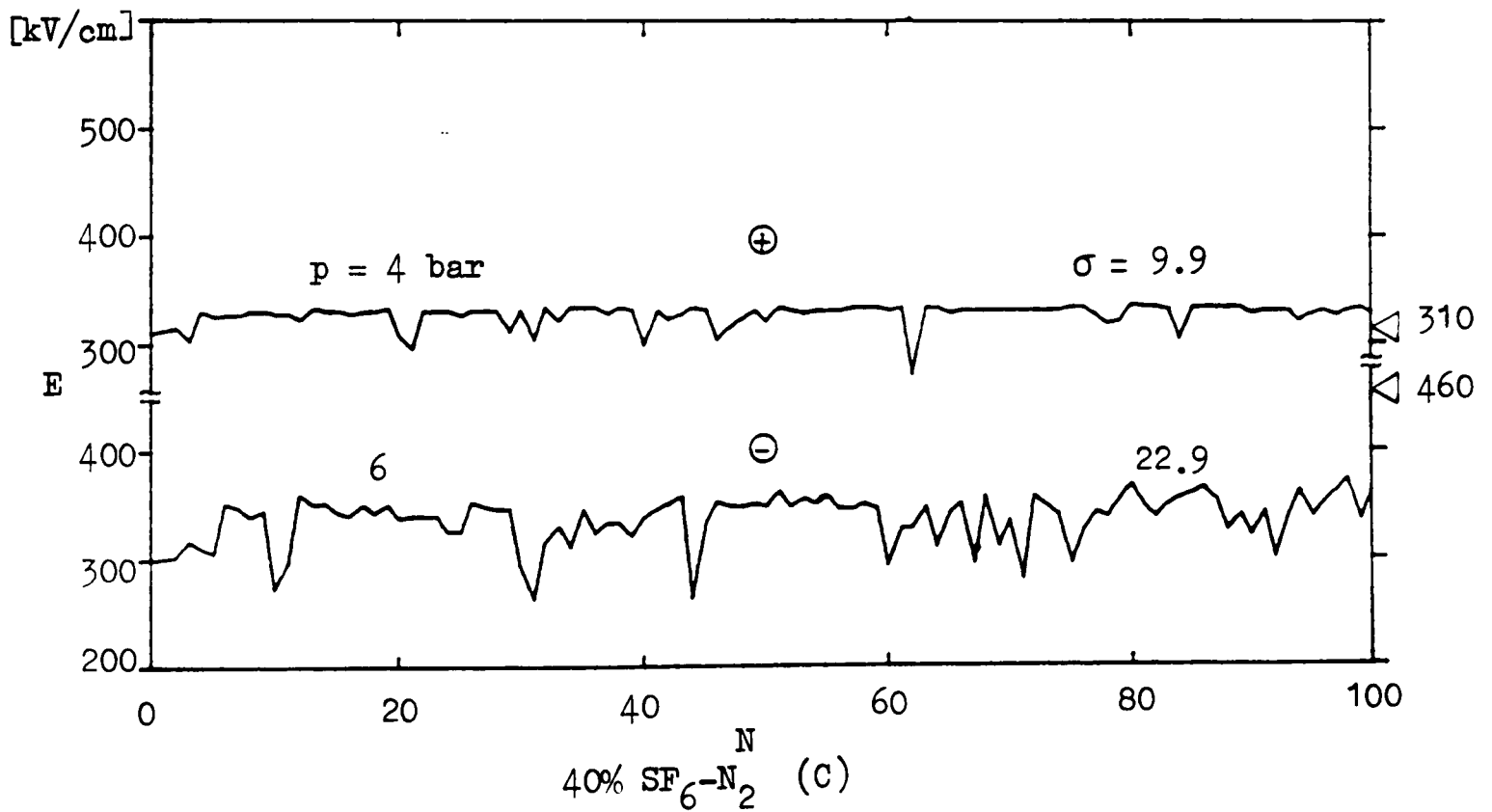
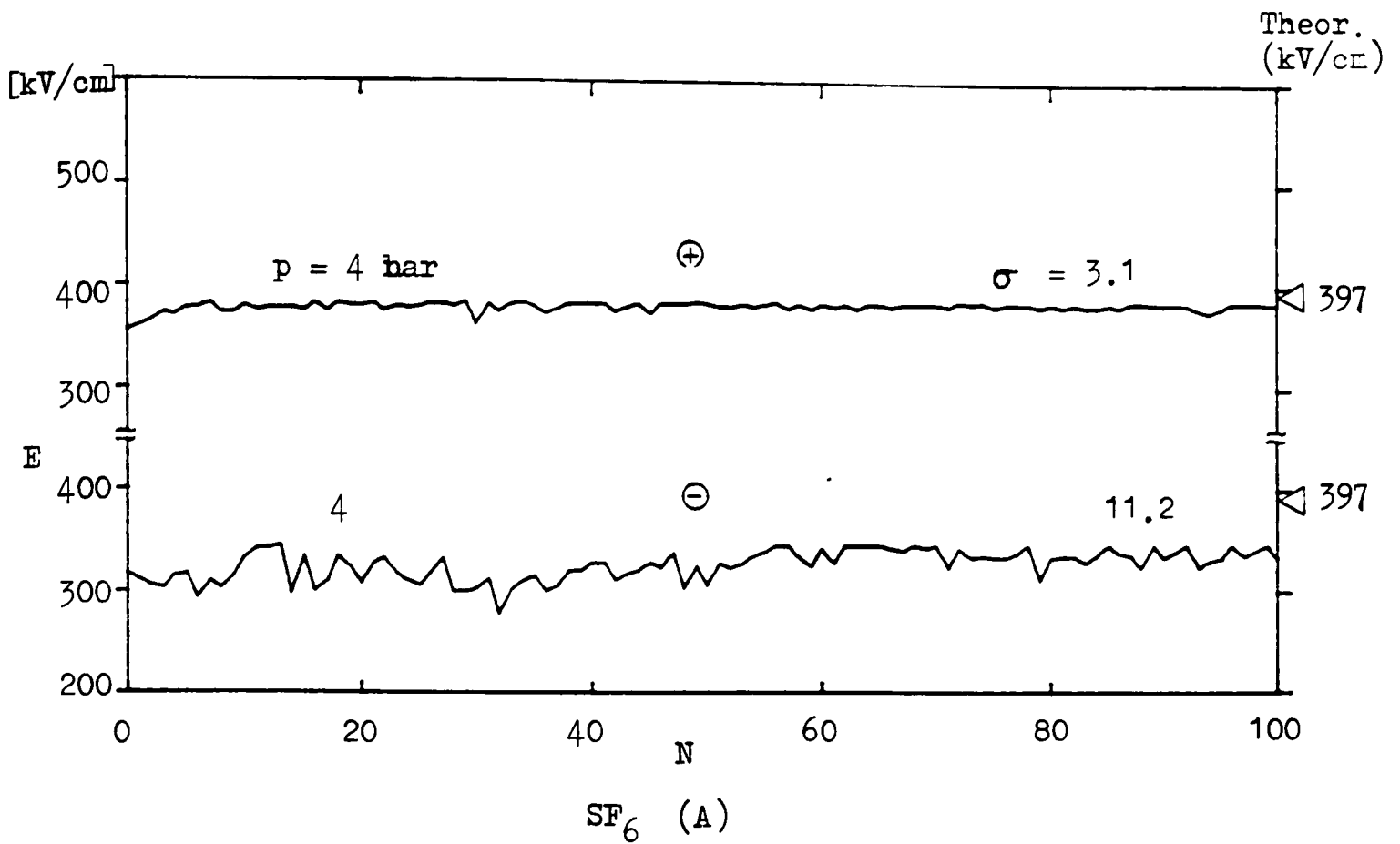


Figure 3.24(b) Effect of polarity on spark conditioning for field strengths in the range  $300\text{--}400$  kV/cm in  $\text{SF}_6$  and  $40\% \text{SF}_6/\text{N}_2$  mixture. ( $r_1/r_2 = 0.5/1.27$  cm, polished)

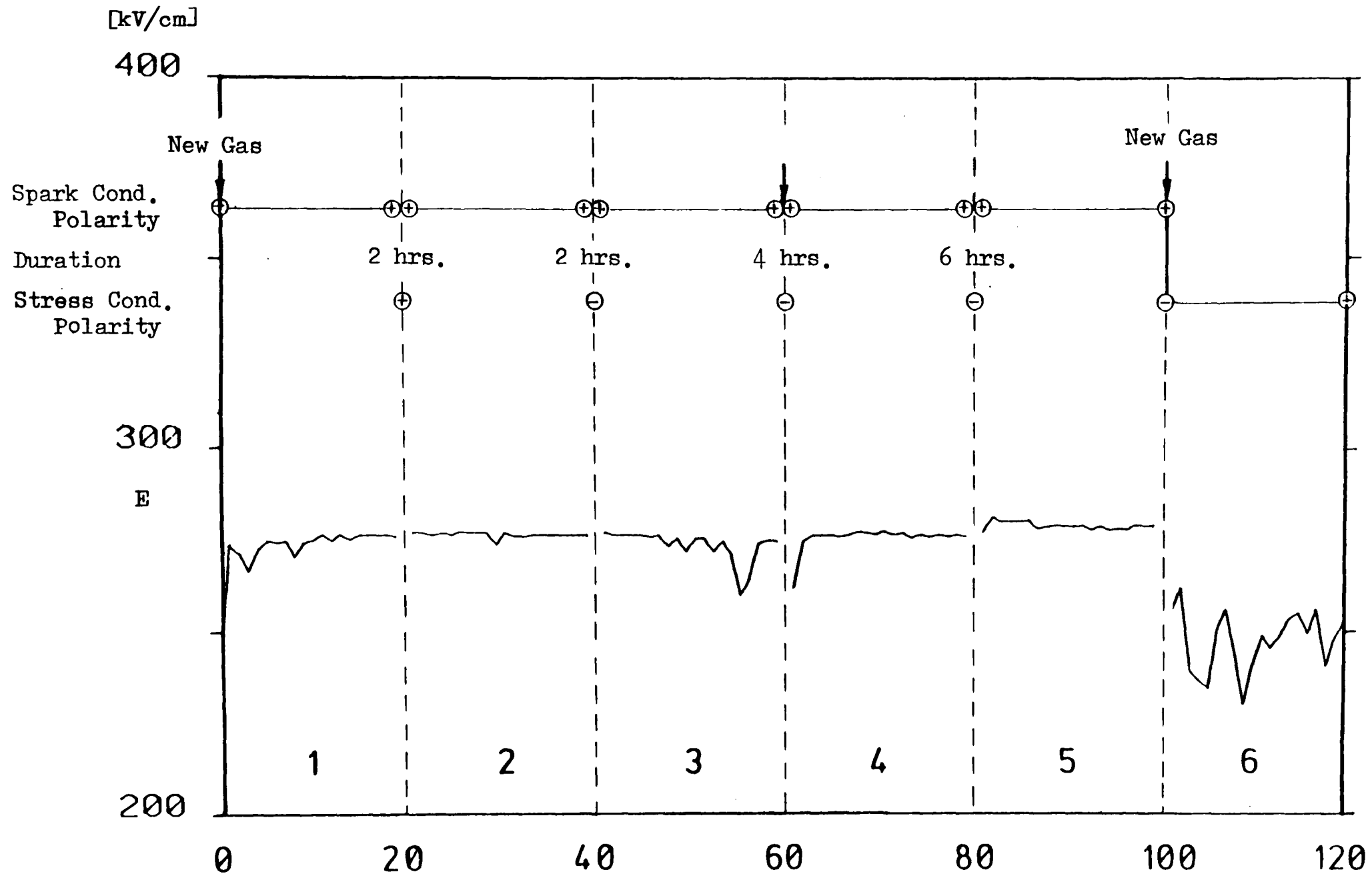


Figure 3.25 Stress Conditioning Phases of 0.5/1.27 cm. radii electrode in 40% SF<sub>6</sub>/N<sub>2</sub> mixture at 3.5 bar

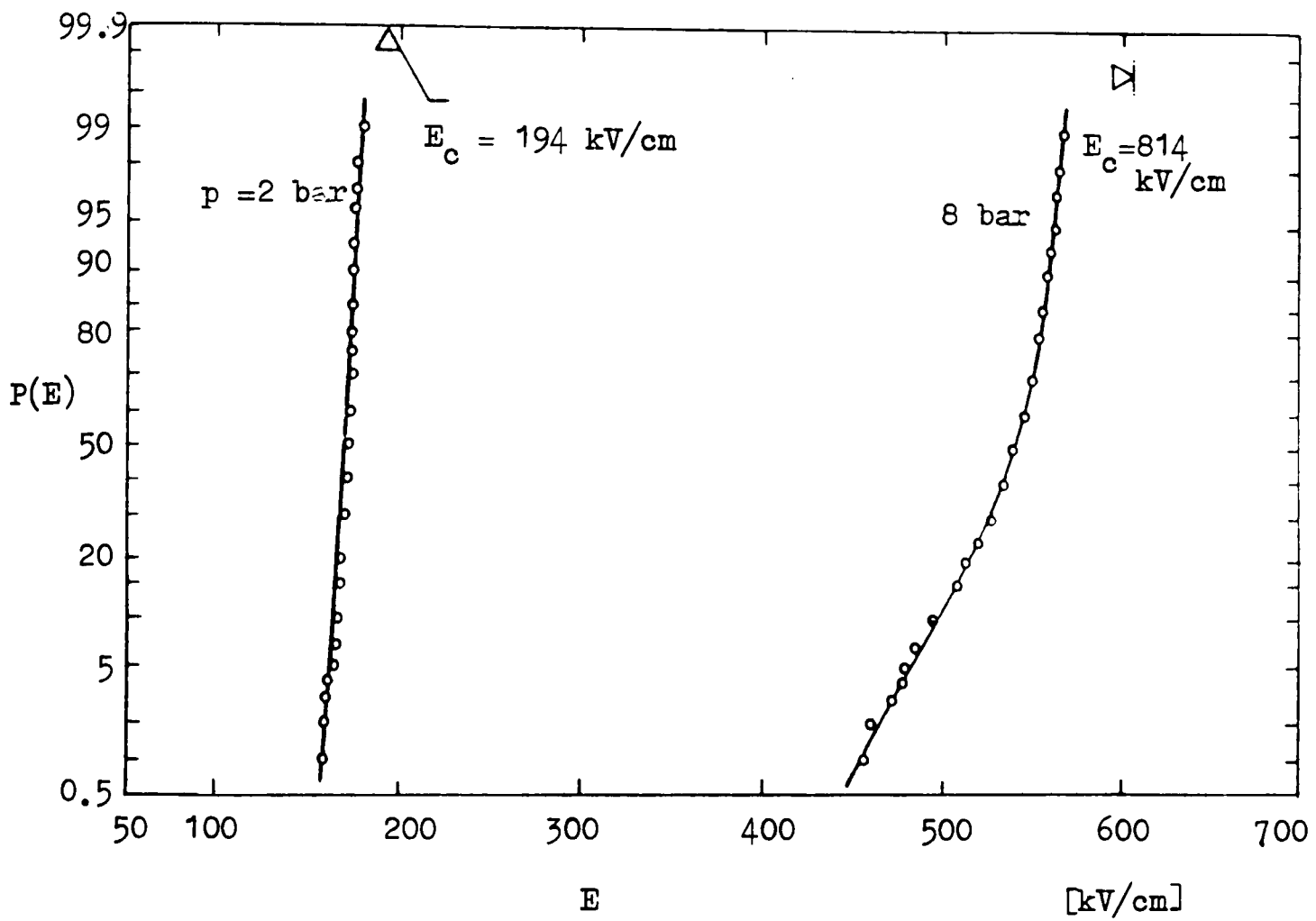


Figure 4.1 Normal cumulative probability distribution of breakdown field strengths of machined electrode in  $SF_6$  ( $r_1/r_2 = 0.945/1.27$  cm)

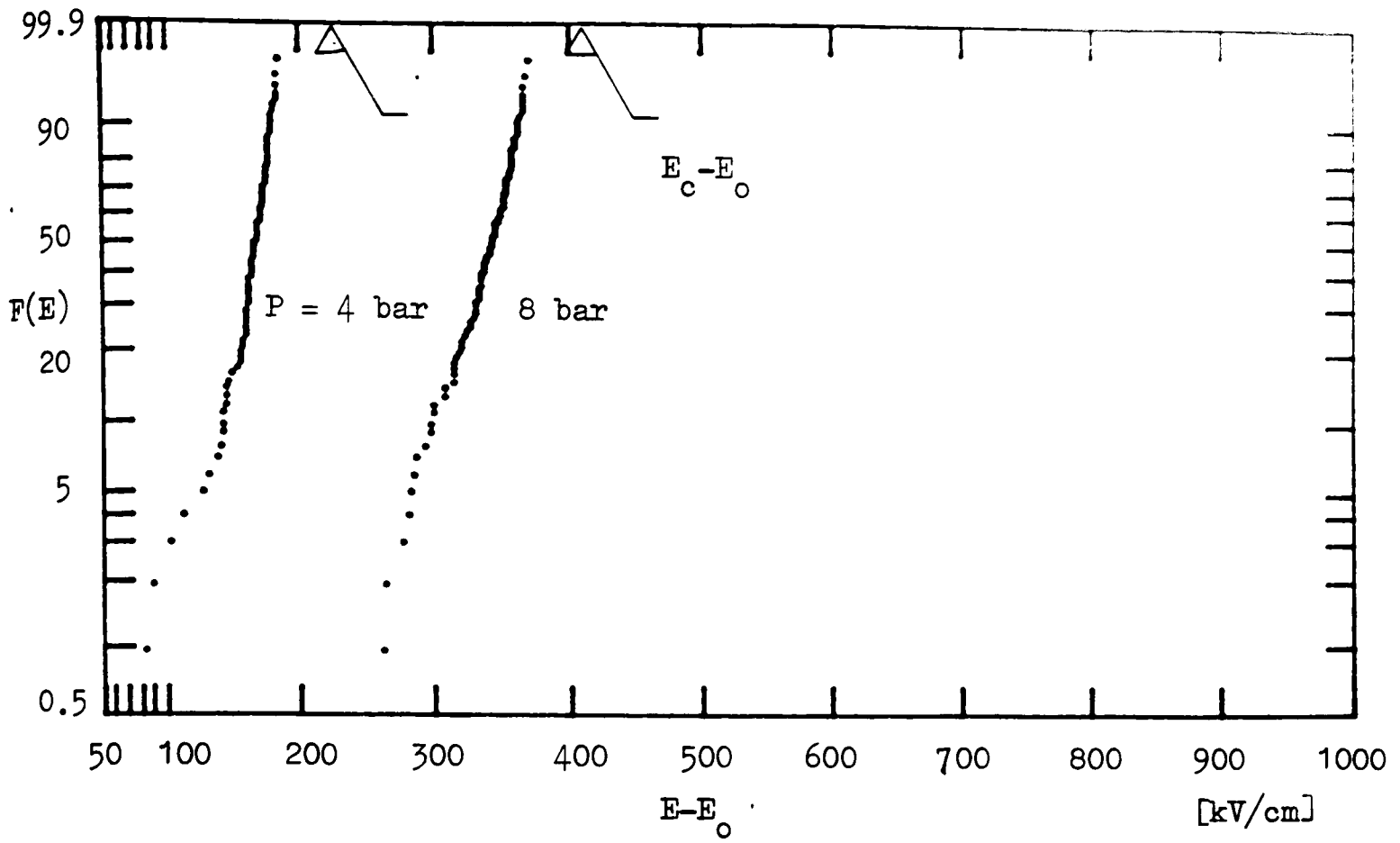


Figure 4.2 Double exponential probability distribution of breakdown field strengths of machined electrode in  $\text{SF}_6$  ( $r_1/r_2 = 0.945/1.27$  cm)

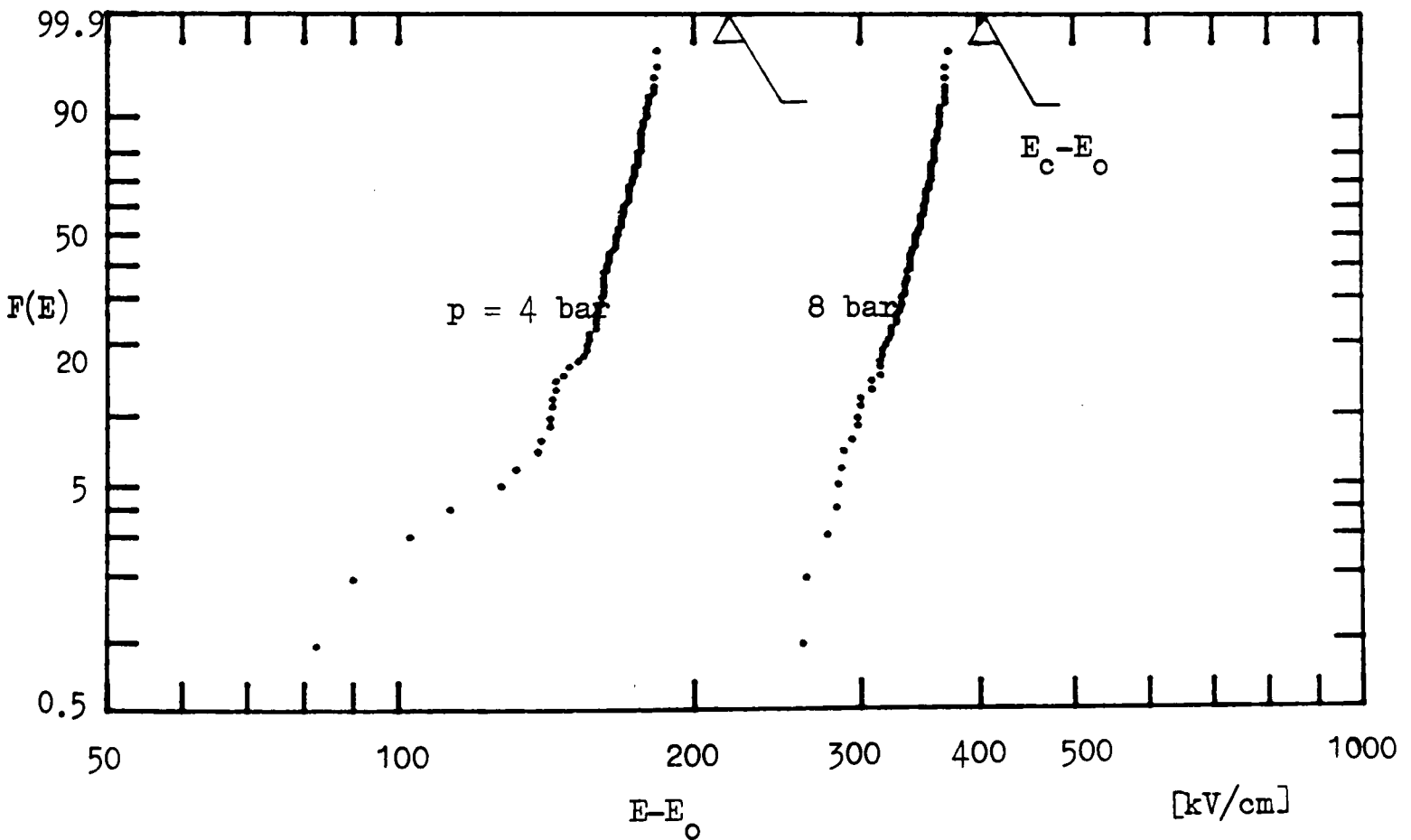


Figure 4.3 Weibull probability distribution of breakdown field strengths of machined electrode in  $\text{SF}_6$  ( $r_1/r_2 = 0.945/1.27$  cm)

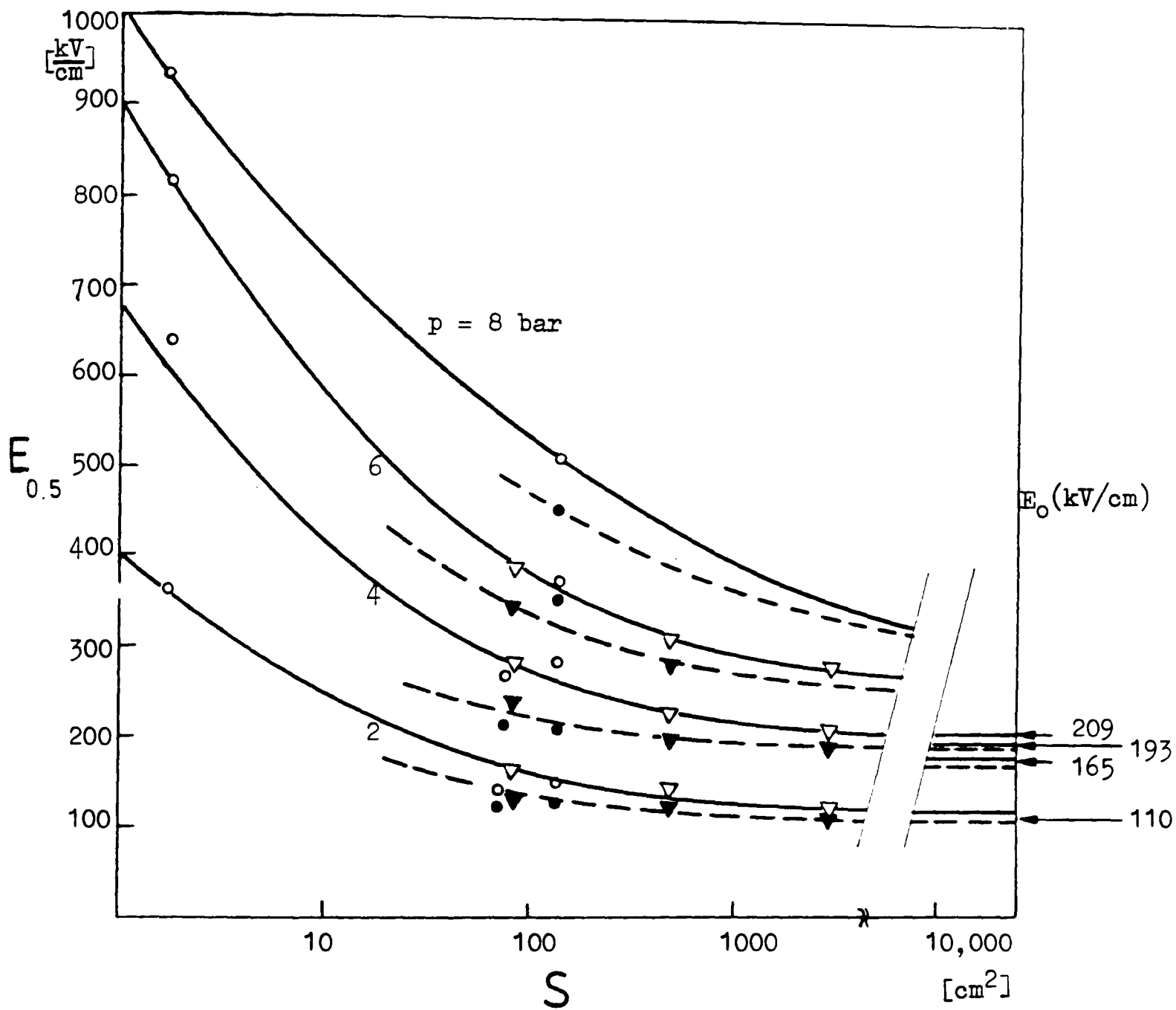


Figure 4.4(a) Variation of minimum breakdown field strength with electrode area in  $\text{SF}_6$ .

- Polished ( $\bar{\pm} 0.3 \mu\text{m}$ )
- Rough (sand-blasted) ( $\bar{\pm} 15 \mu\text{m}$ )
- ▽ Polished ( $\bar{\pm} 0.5 \mu\text{m}$ ) Nitto et al [118]
- ▼ Rough ( $\bar{\pm} 20 \mu\text{m}$ )

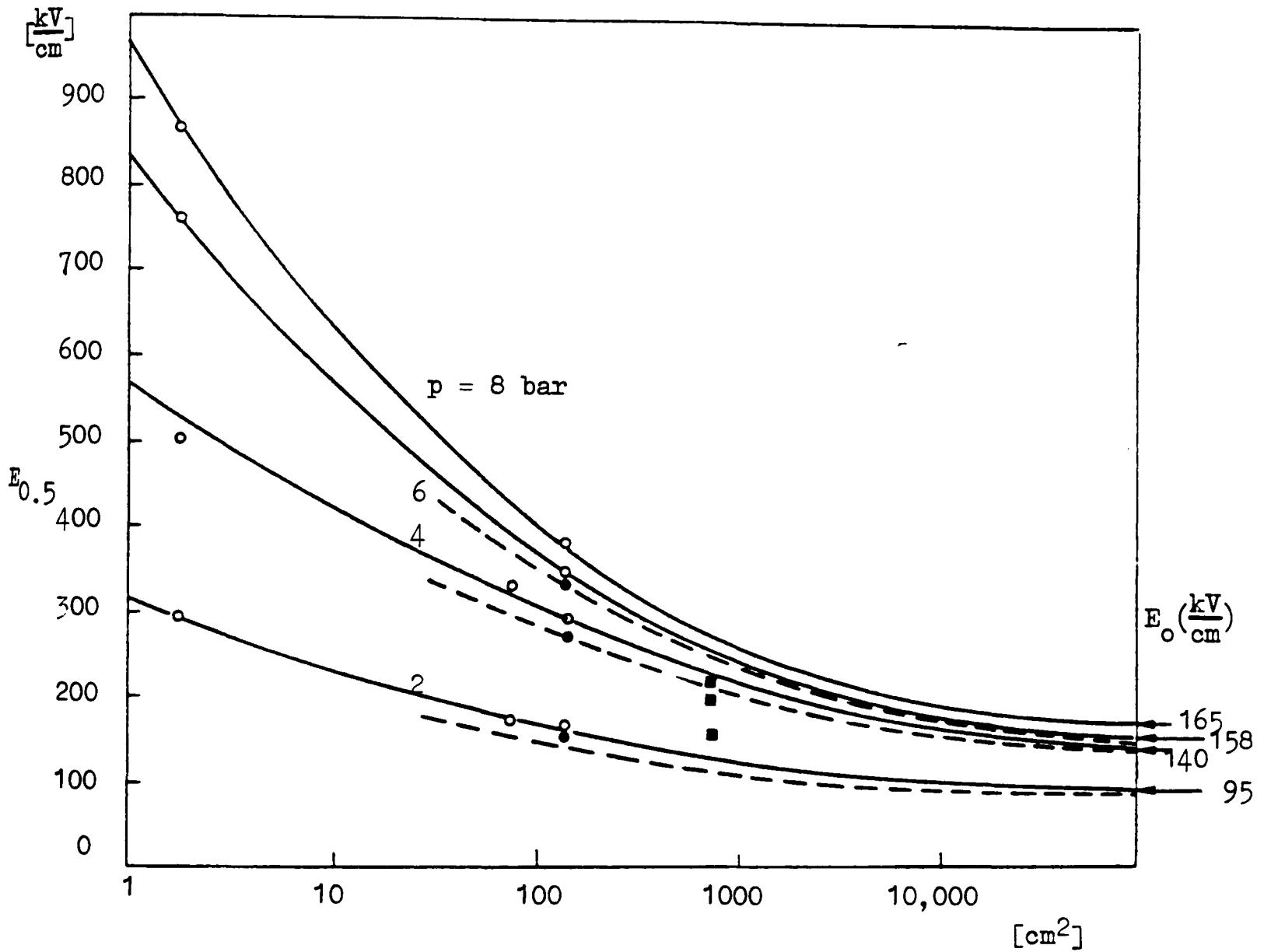


Figure 4.4(b) Variation of minimum breakdown field strength with effective electrode surface in 75%  $SF_6-N_2$  mixture.

- Polished ( $\bar{\mu} = 0.3 \mu m$ )
- Rough ( $\bar{\mu} = 15 \mu m$ )
- Ermel [146]

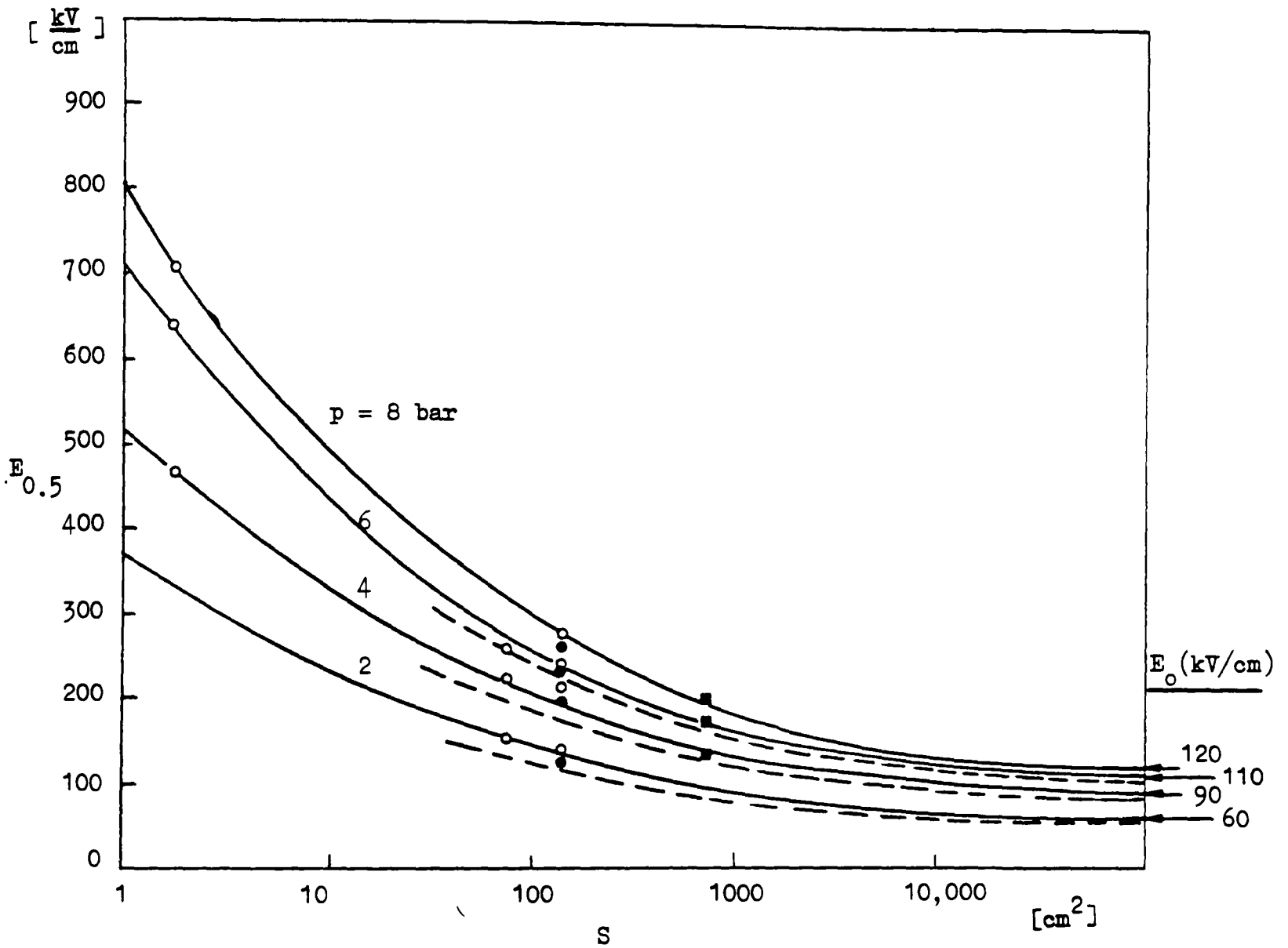


Figure 4.4(c) Variation of minimum breakdown field strength with effective electrode area in 40%  $\text{SF}_6/\text{N}_2$  mixture

- Polished ( $\bar{r} = 0.3 \mu\text{m}$ )
- Rough ( $\bar{r} = 15 \mu\text{m}$ )
- Ermel [146]

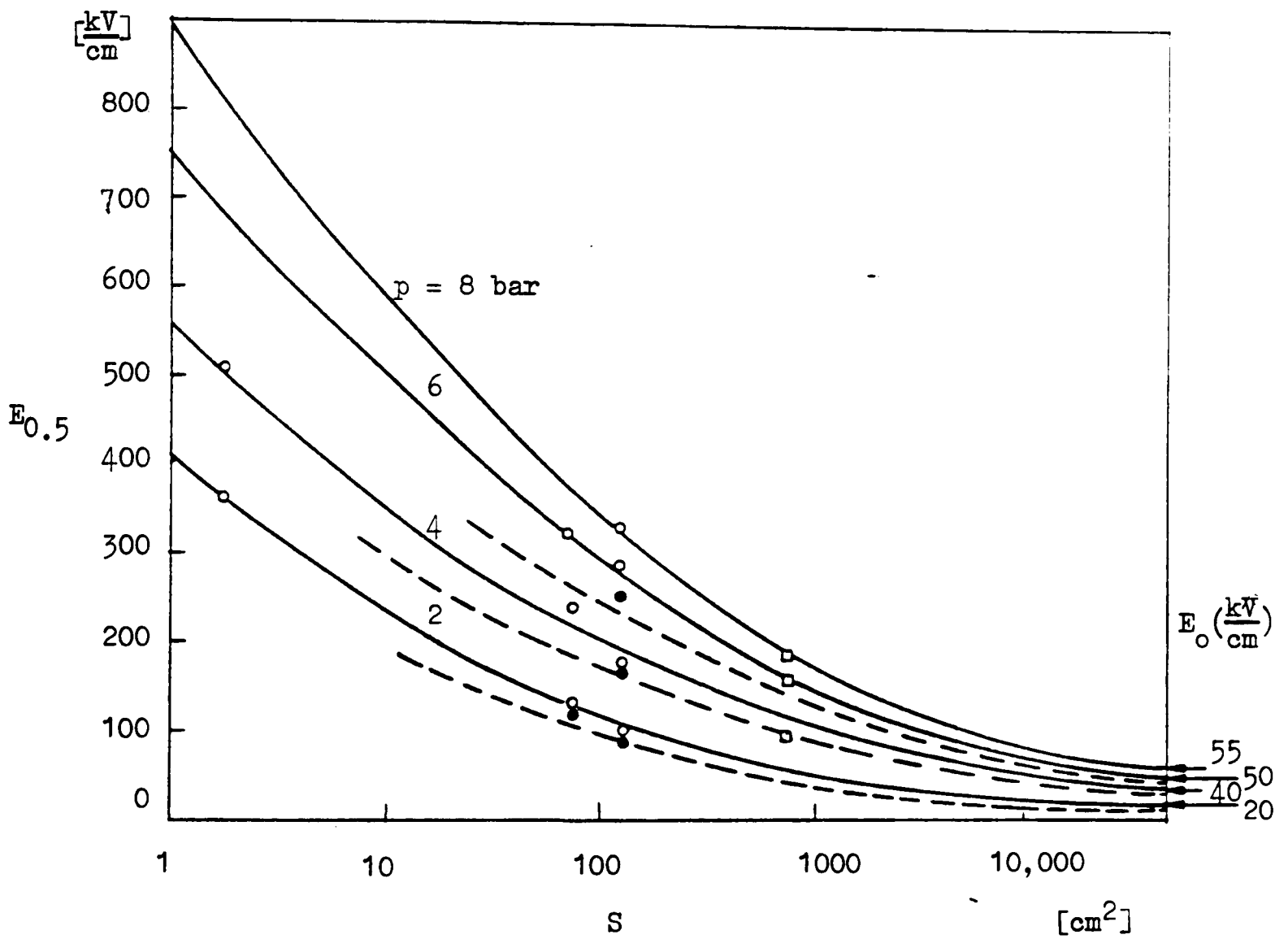


Figure 4.4(d) Variation of minimum breakdown field strength with effective electrode area in 10%  $SF_6-N_2$  mixture

- Polished ( $\mp 0.3 \mu m$ )
- Rough ( $\mp 15 \mu m$ )
- ◻ Polished ( $\mp 0.3 \mu m$ )
- Rough ( $\mp 16 \mu m$ )

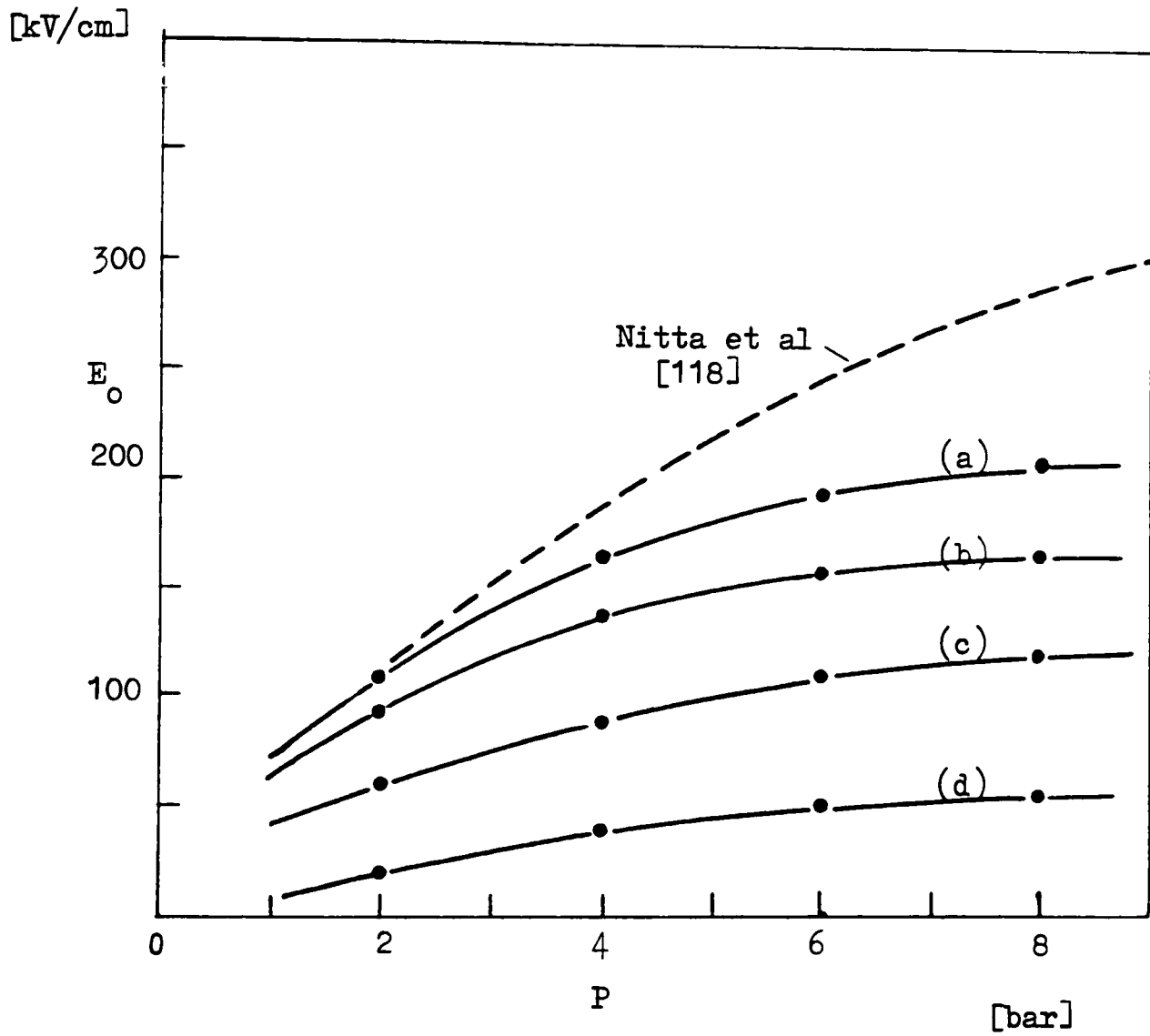


Figure 4.5 Minimum breakdown field strength of large-area electrodes in  $\text{SF}_6$  and  $\text{SF}_6/\text{N}_2$  mixtures at different pressures (including irradiated and non-irradiated positive and negative breakdown voltage results).

(a)  $\text{SF}_6$  ; (b) 75%  $\text{SF}_6\text{-N}_2$  ;

(c) 40%  $\text{SF}_6\text{-N}_2$  ; (d) 10%  $\text{SF}_6 - \text{N}_2$

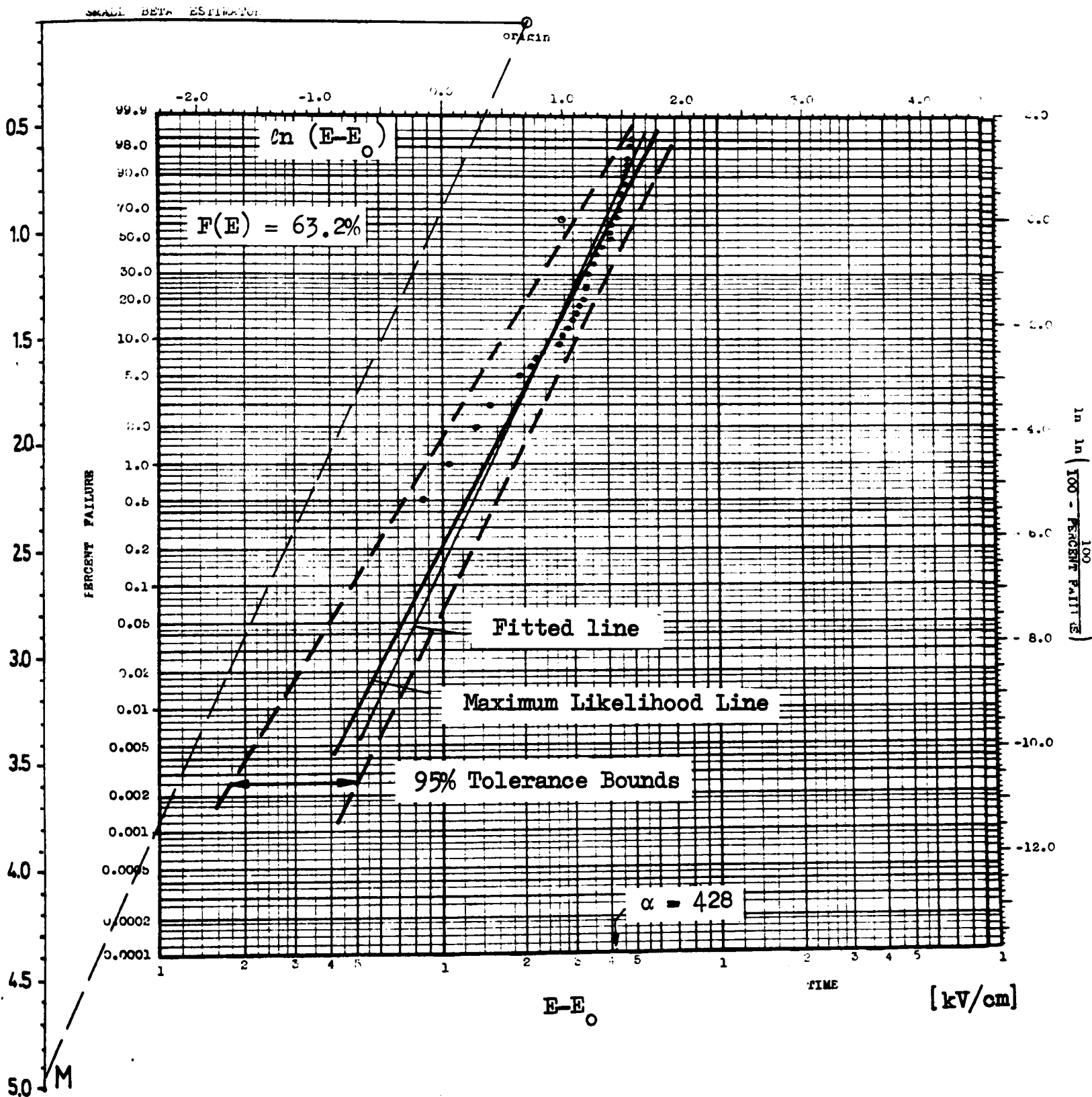


Figure 4.6 Weibull probability plot of aluminium polished electrode having radii  $r_1/r_2=0.947/1.27$  cm in  $SF_6$  at  $p = 8$  bar

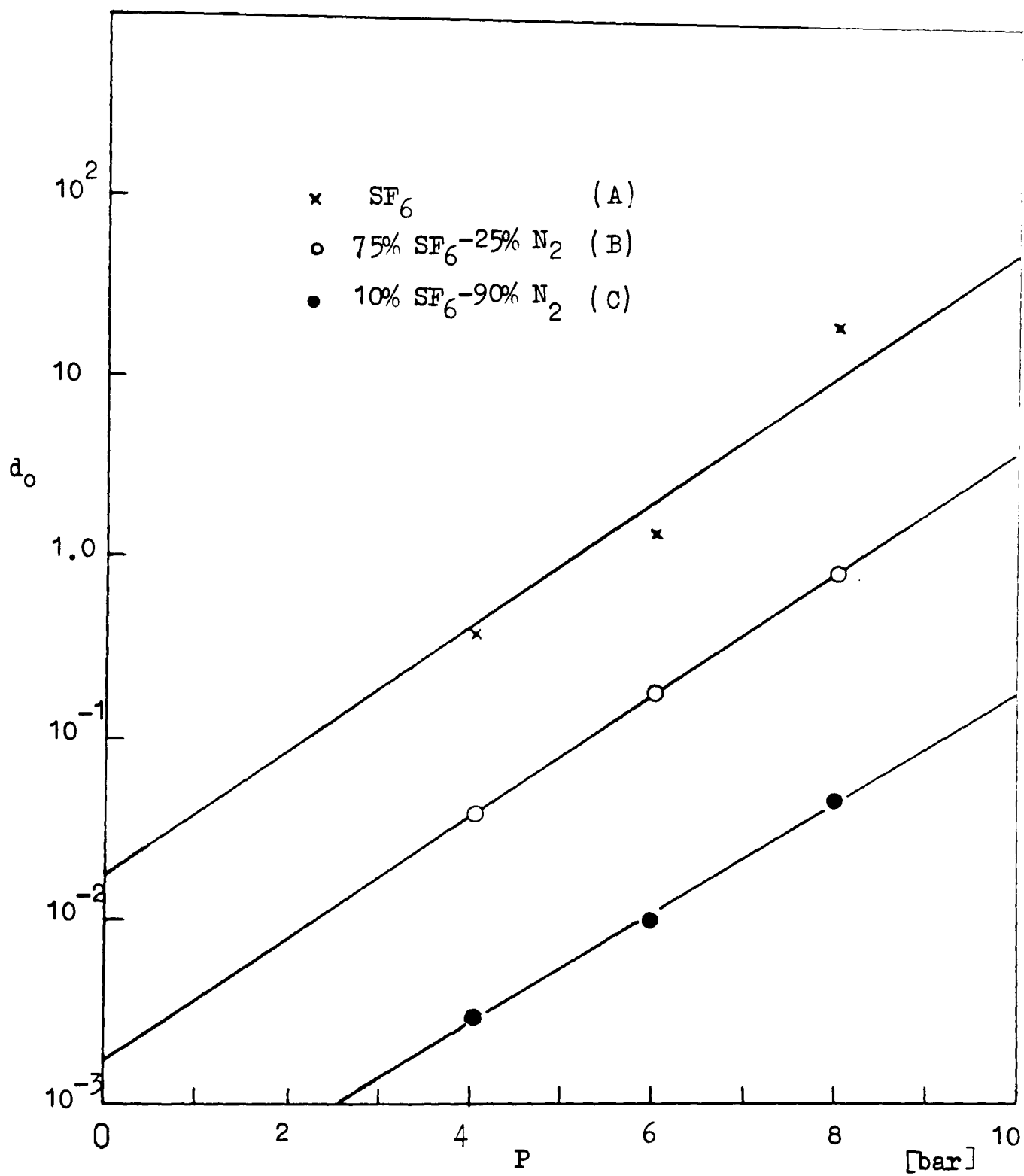


Figure 4.7 Maximum likelihood estimate of the density function for polished electrodes

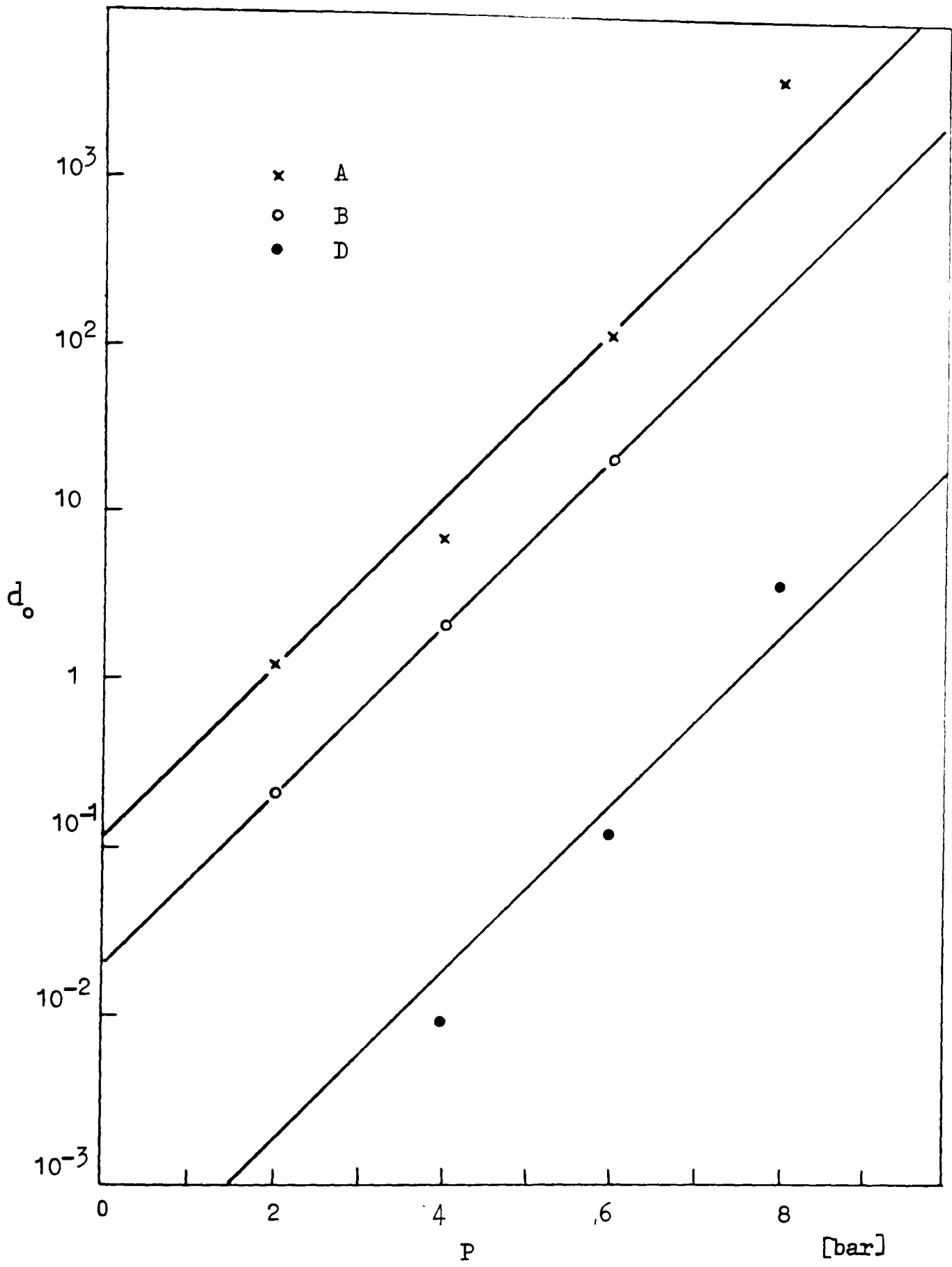


Figure 4.8 Maximum likelihood estimate of the density function for sandblasted electrodes

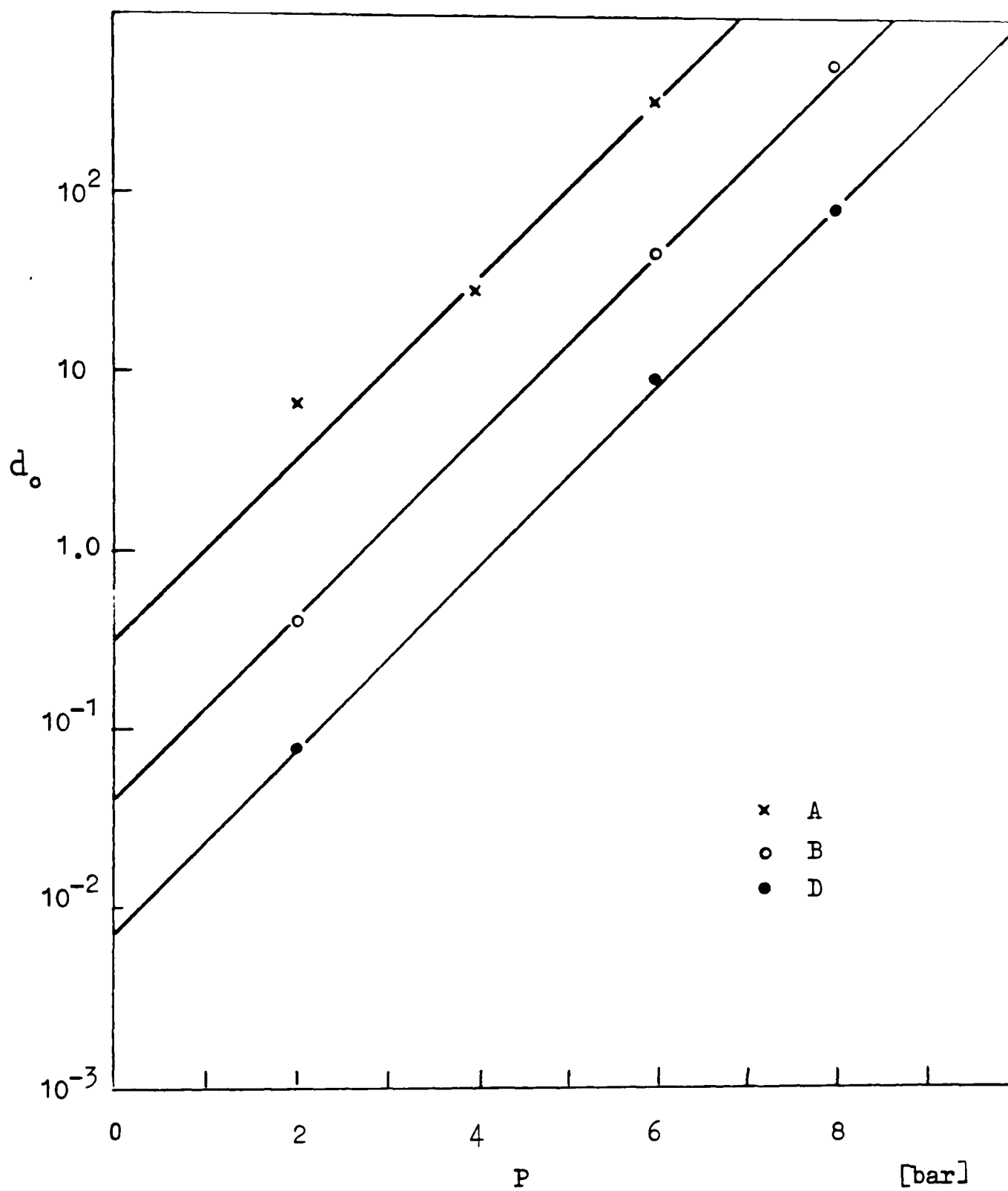


Figure 4.9 Maximum likelihood estimate of the density function for machined electrodes

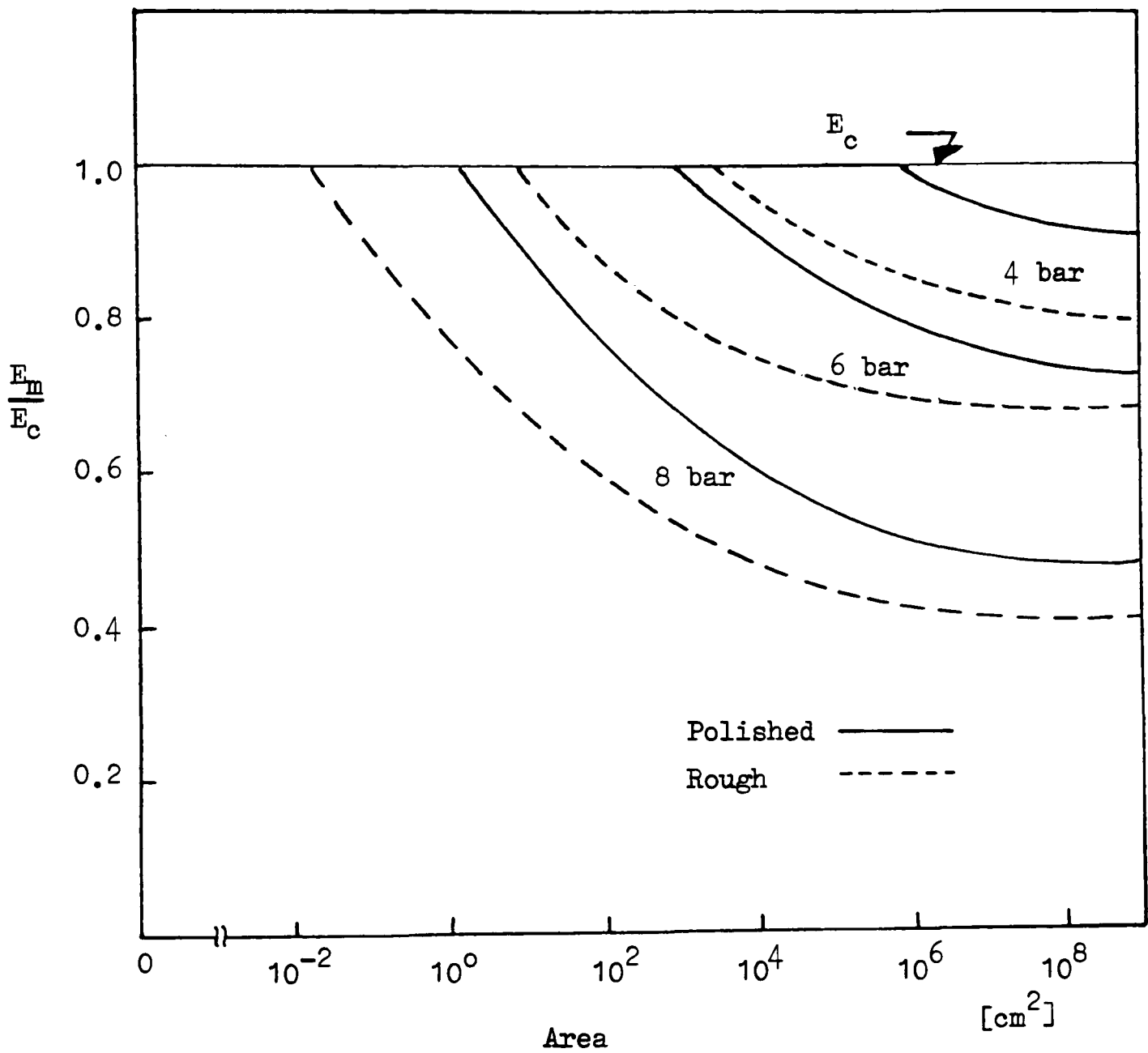
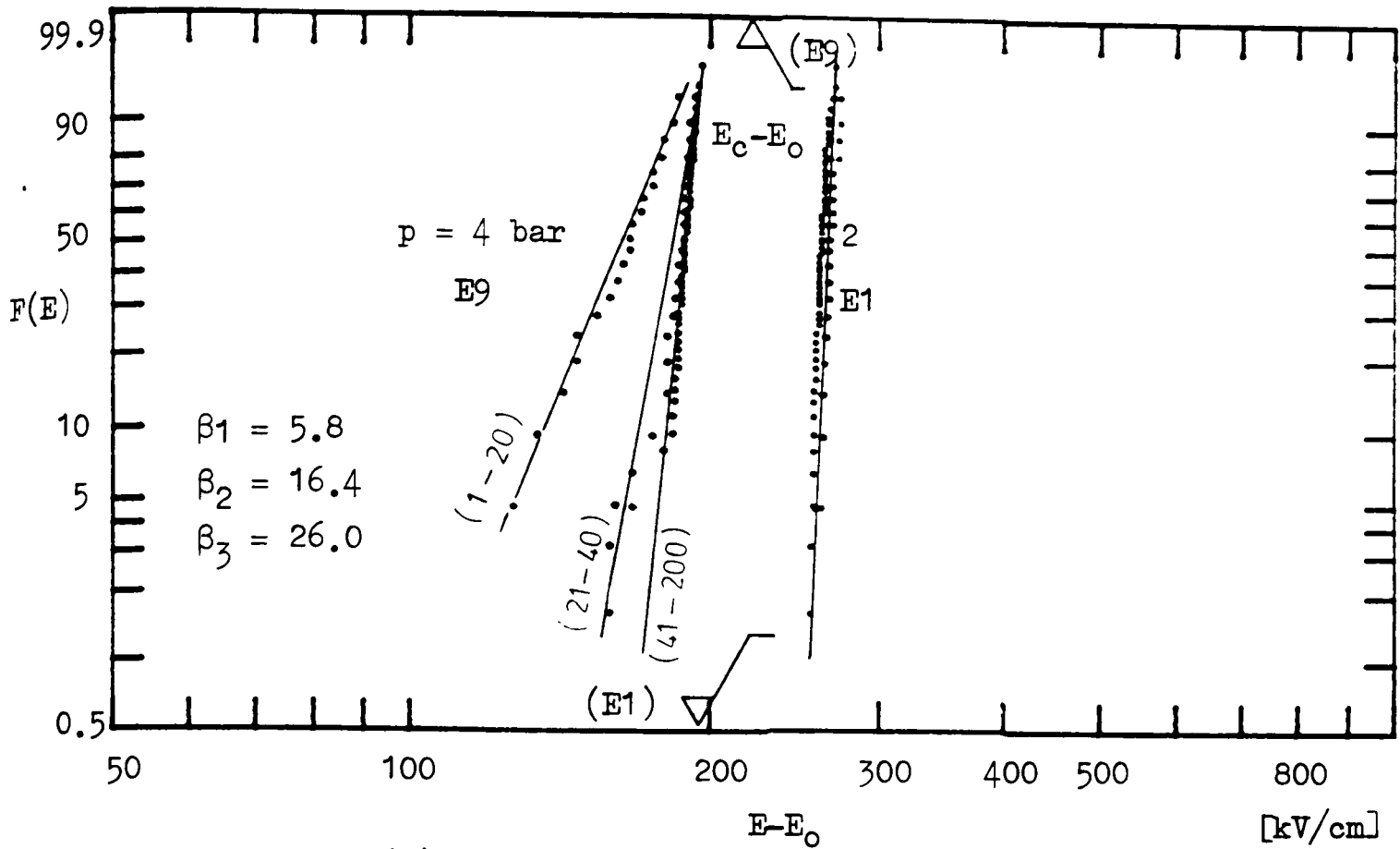
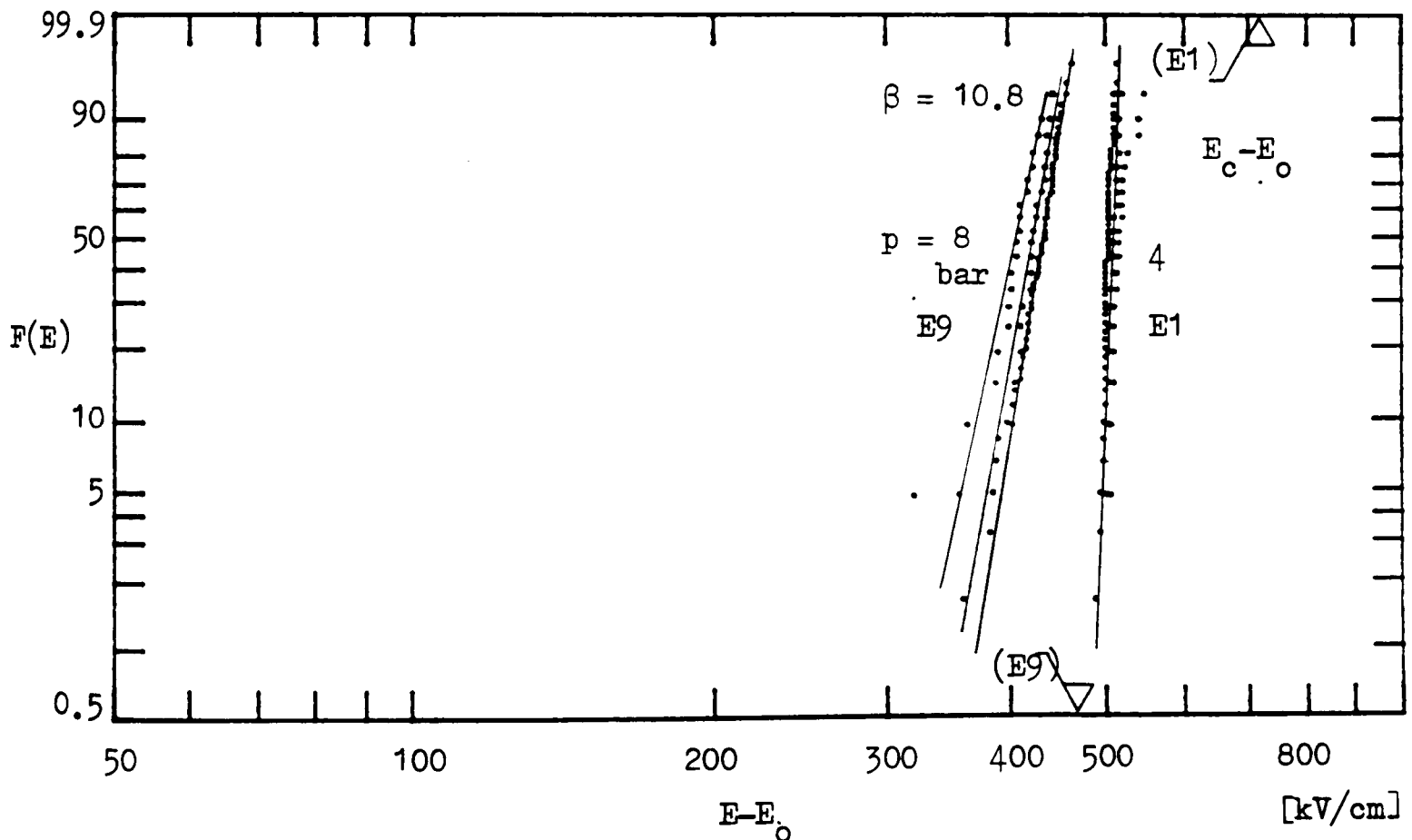


Figure 4.10 Variation of calculated modal value of field strength for polished and rough electrodes in  $\text{SF}_6$



(a) Field range : 300-400 kV/cm



(b) Field range : 500-600 kV/cm

Figure 4.11 Effect of conditioning on Weibull probability distribution in  $\text{SF}_6$  for different electrode areas.  
 (Area  $(E_1) = 1.8 \text{ cm}^2$  ; Area  $(E_9) = 180 \text{ cm}^2$ )

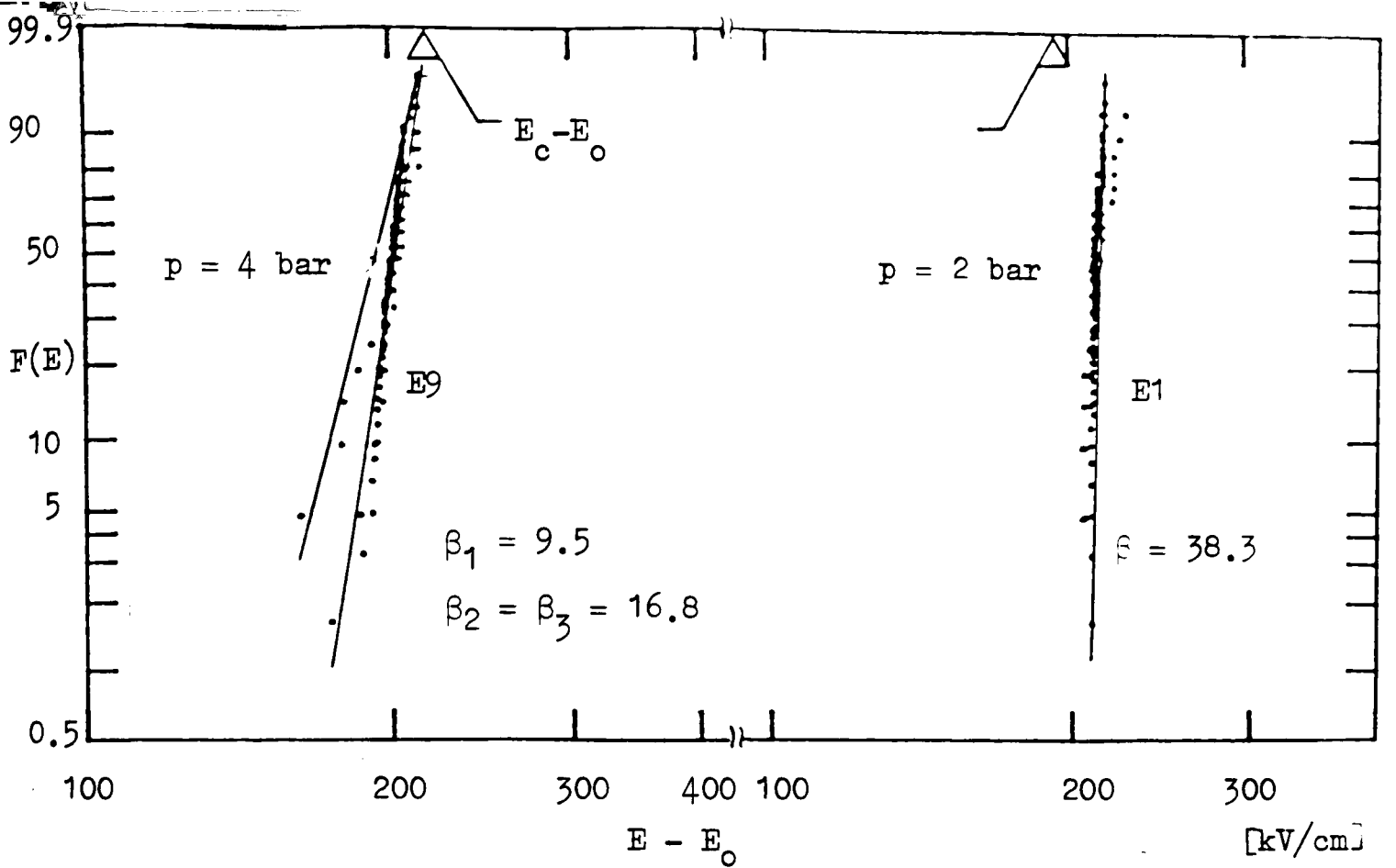


Figure 4.12 Effect of conditioning on Weibull probability distribution in 75% SF<sub>6</sub>-N<sub>2</sub> mixture for different electrode areas in the field range 300-400 kV/cm.

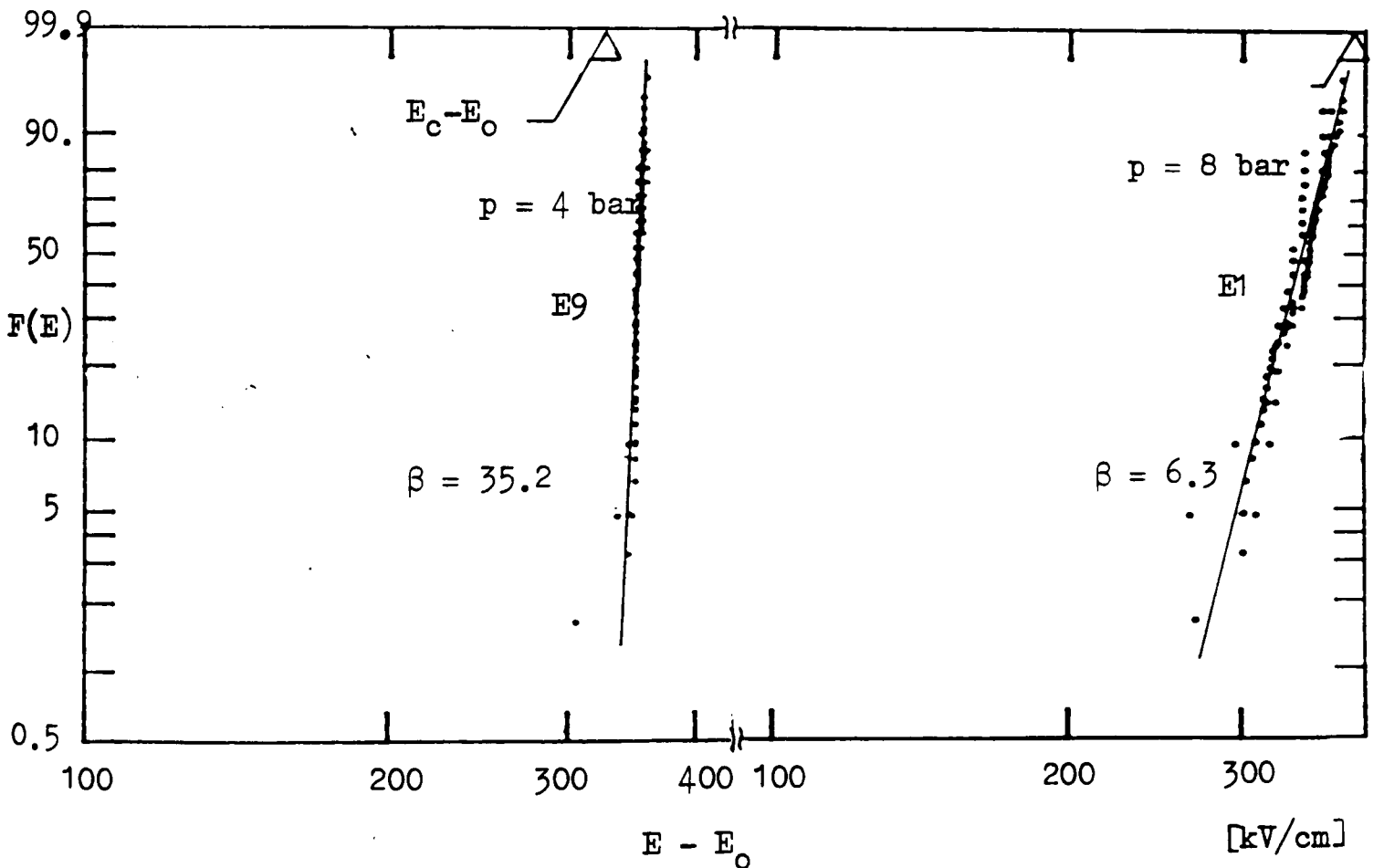


Figure 4.13 Effect of conditioning on Weibull probability distribution in 10% SF<sub>6</sub>-N<sub>2</sub> mixture for different electrode areas in the field range 300-400 kV/cm (Area (E1) = 1.8 cm<sup>2</sup> ; Area (E9) = 180 cm<sup>2</sup>)

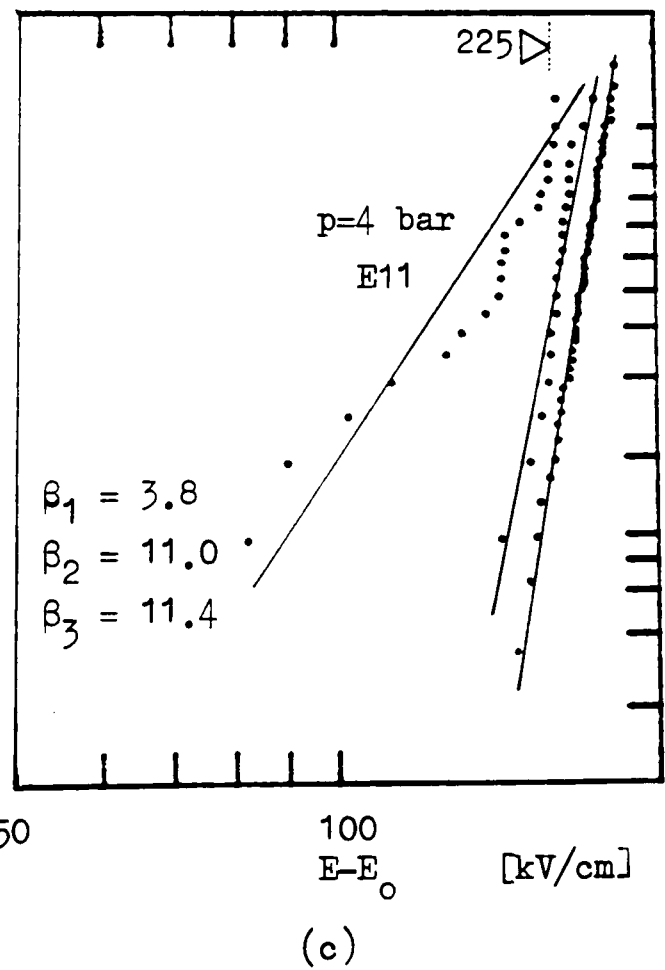
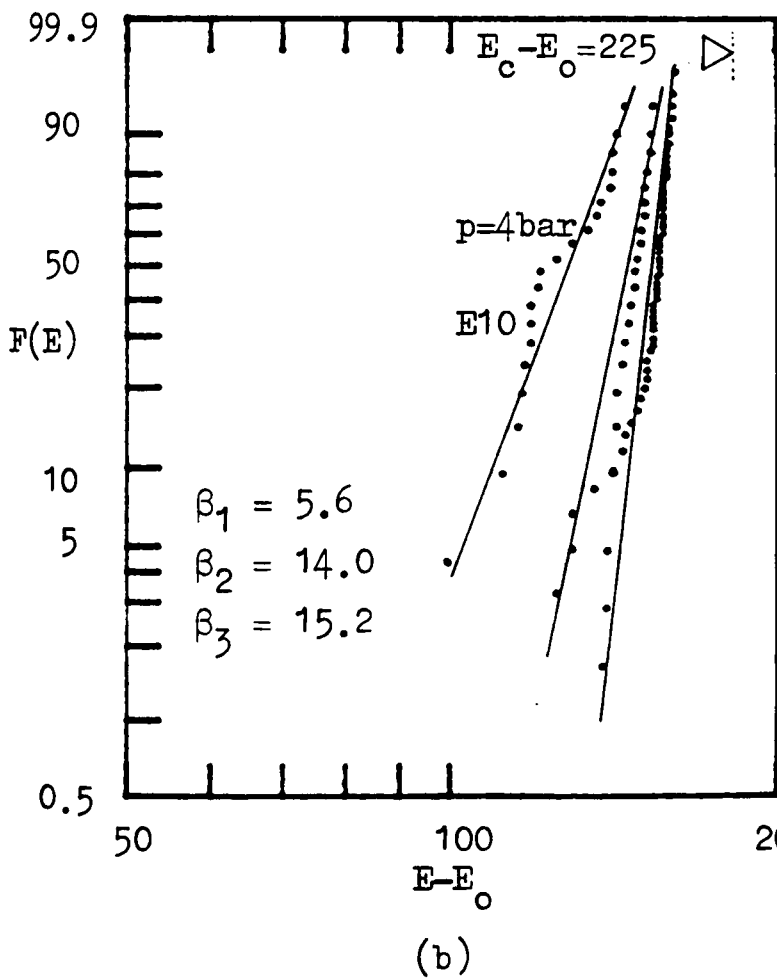
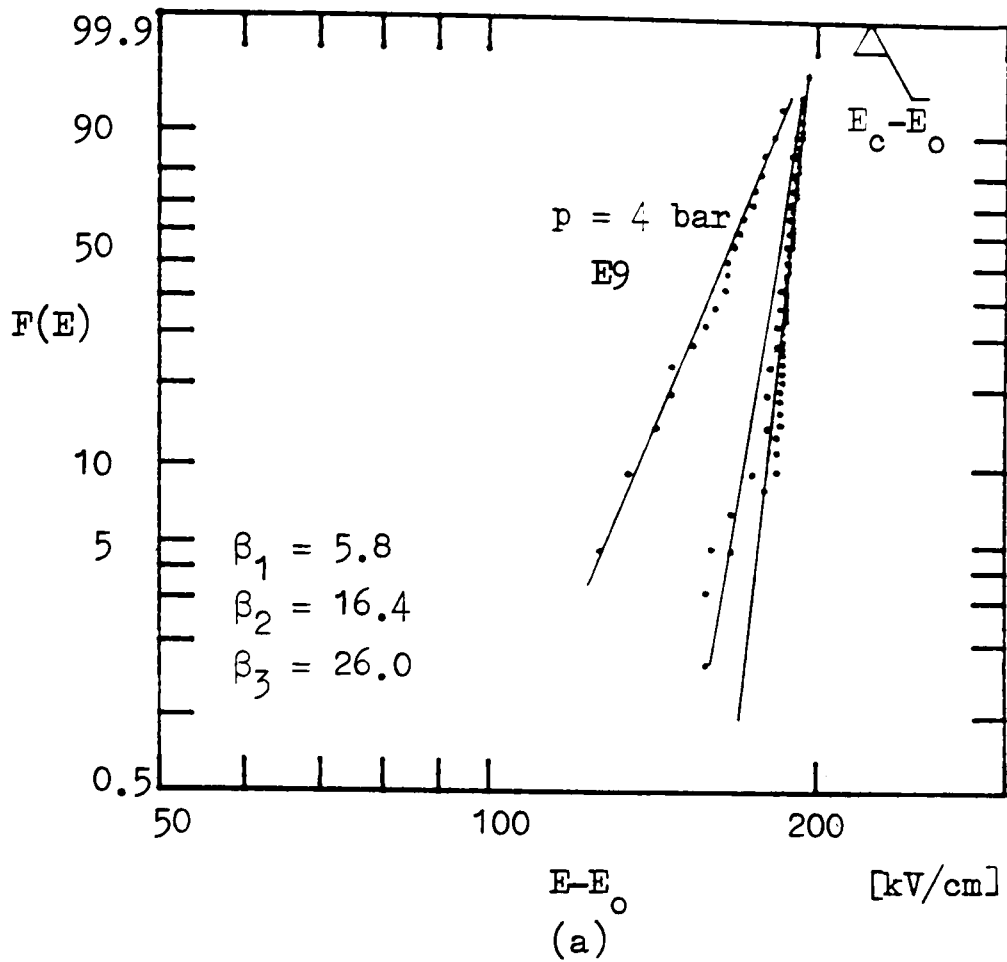
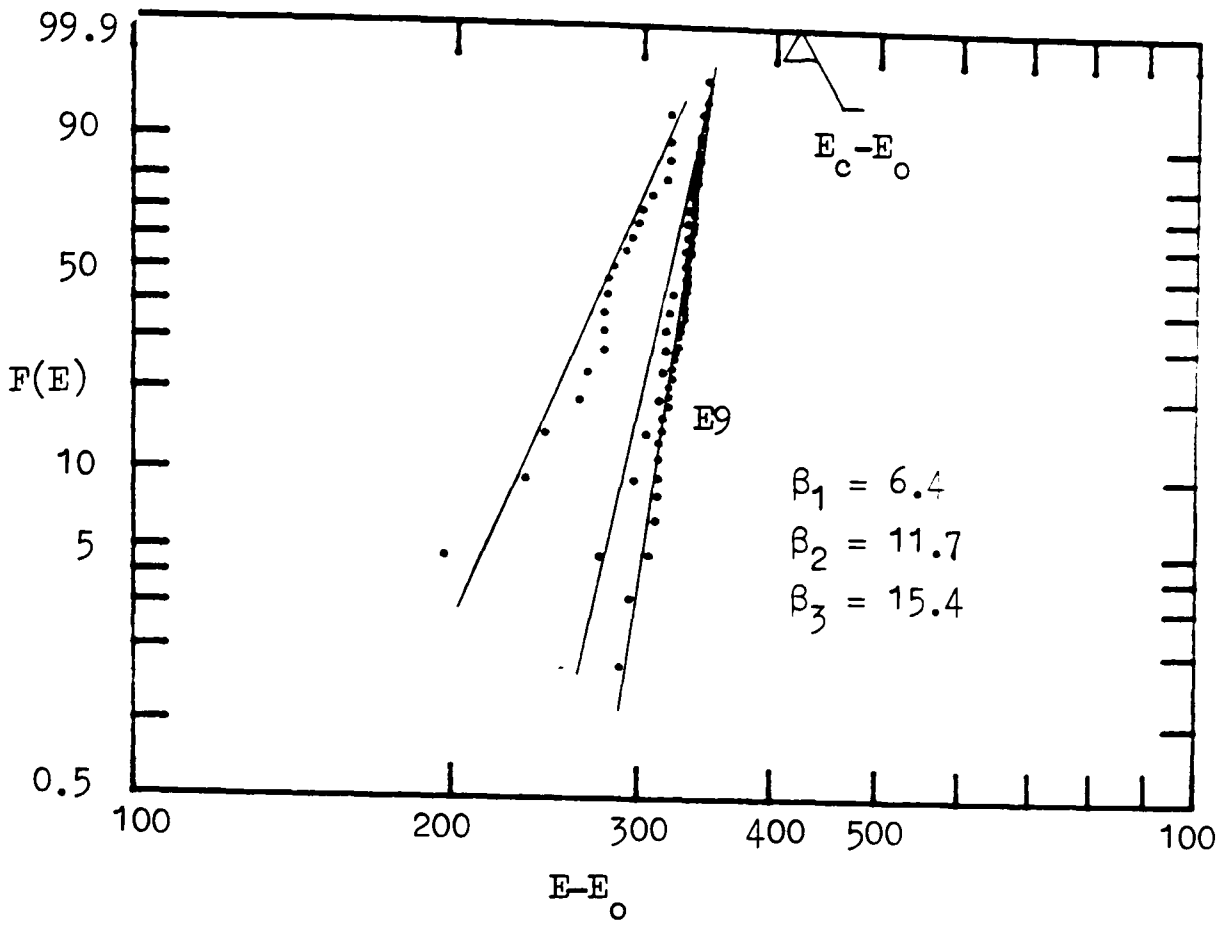
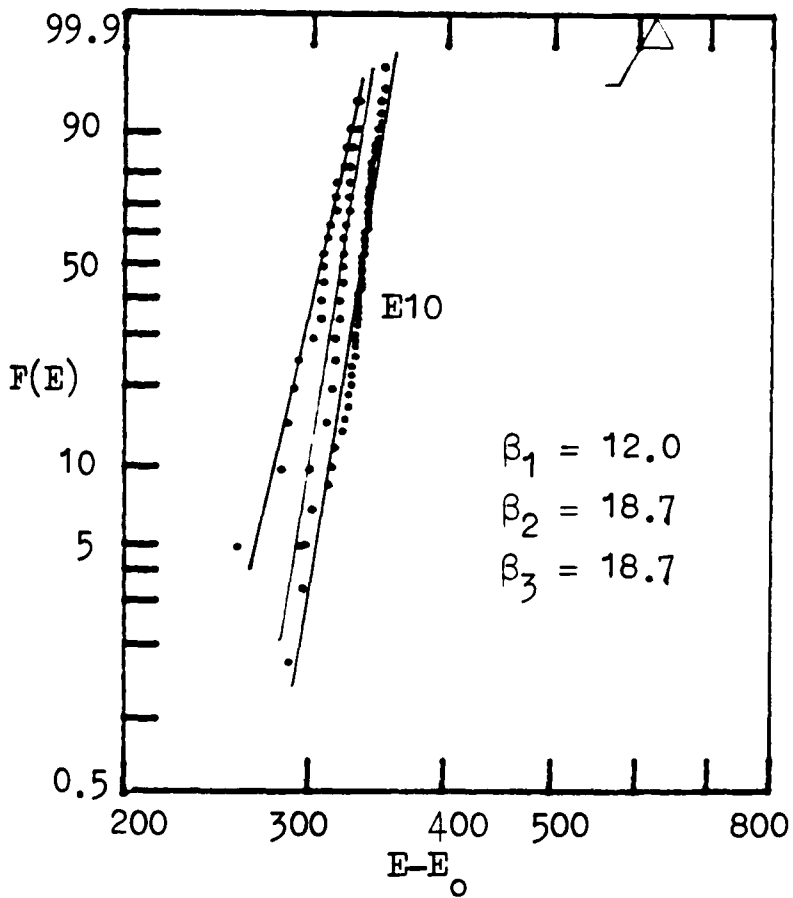


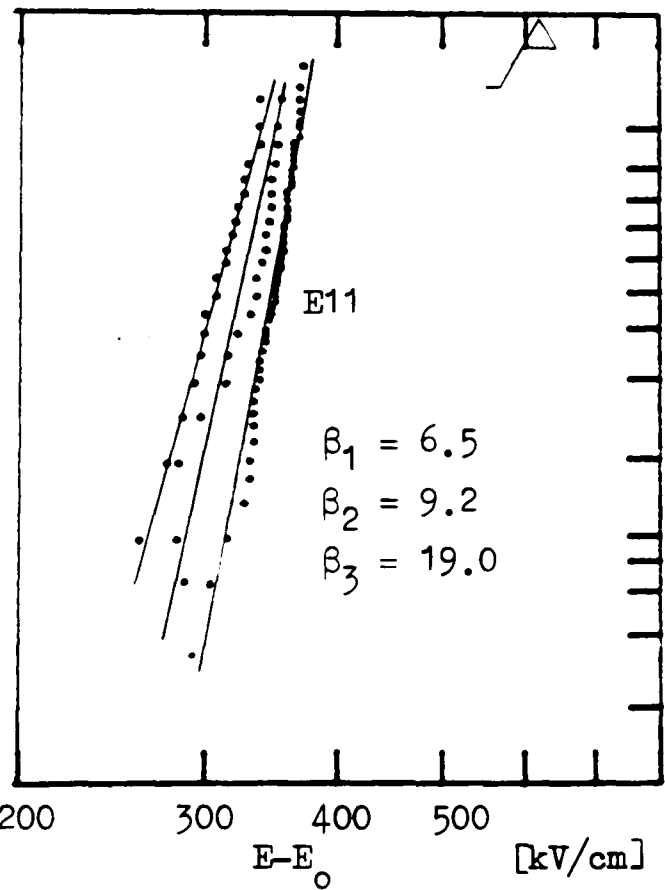
Figure 4.14 Effect of surface roughness on Weibull probability distribution in  $\text{SF}_6$  for field strengths in the range 300–400 kV/cm.  
 (a) Polished (E9) ( $R_{\text{CLA}} = 0.04 \mu\text{m}$ )  
 (b) Sandblasted (E10) ( $R_{\text{CLA}} = 2.3 \mu\text{m}$ )  
 (c) Machined (E11) ( $R_{\text{CLA}} = 2.8 \mu\text{m}$ ).



(a)



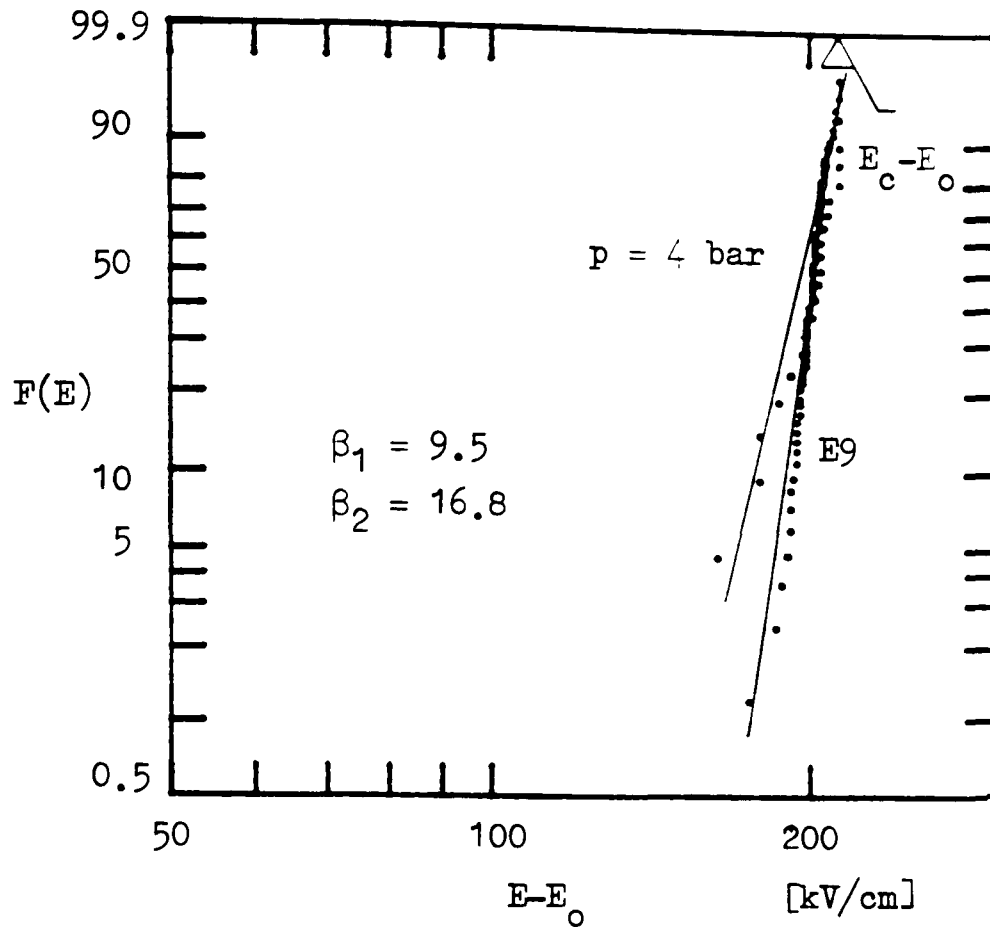
(b)



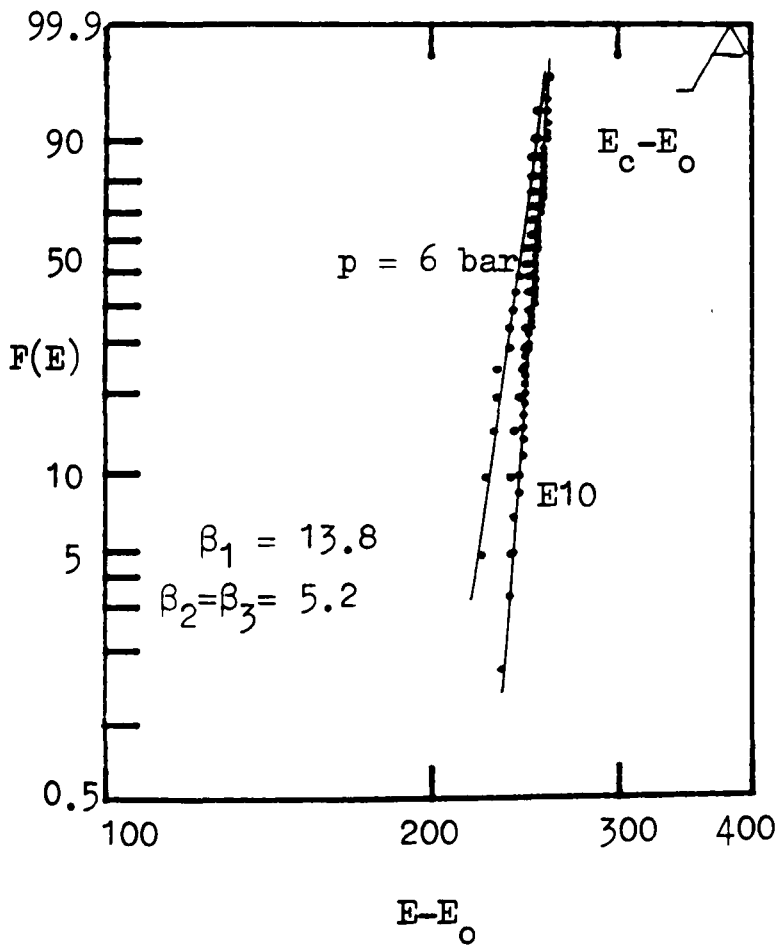
(c)

Figure 4.15 Effect of surface roughness on Weibull probability distribution in  $\text{SF}_6$  for field strengths in the range 500-600 kV/cm.

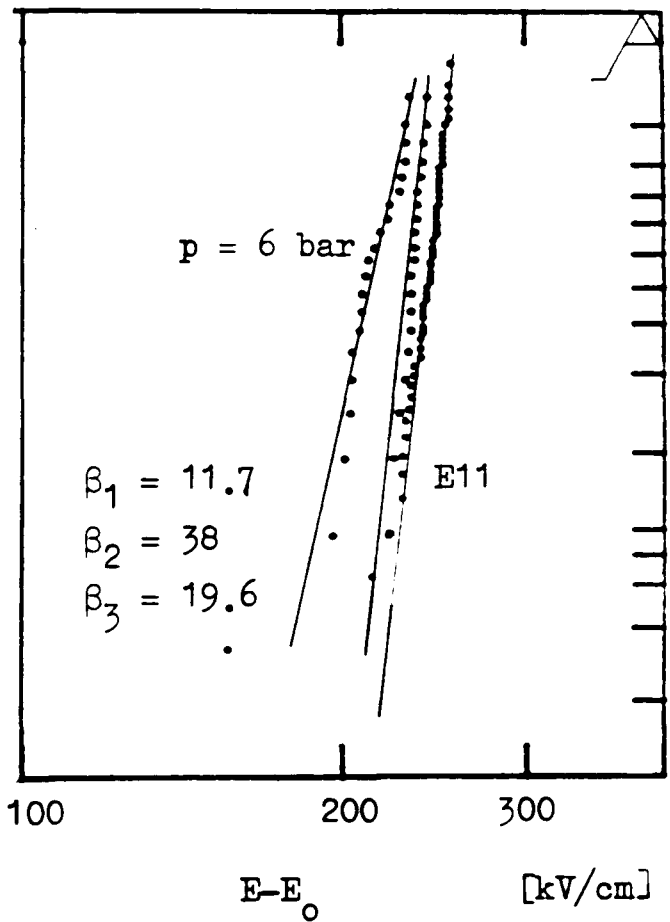
- (a) Polished (E9); (b) Sandblasted (E10);  
 (c) Machined (E11).



(a)

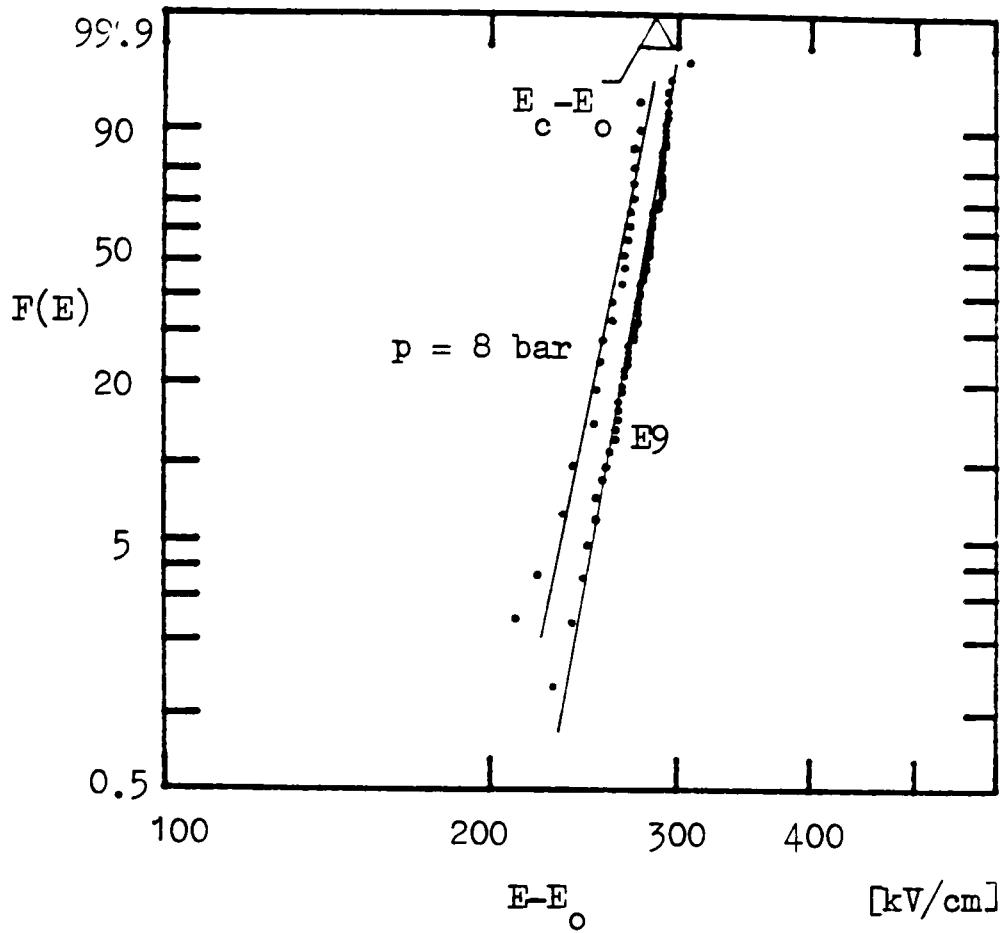


(b)

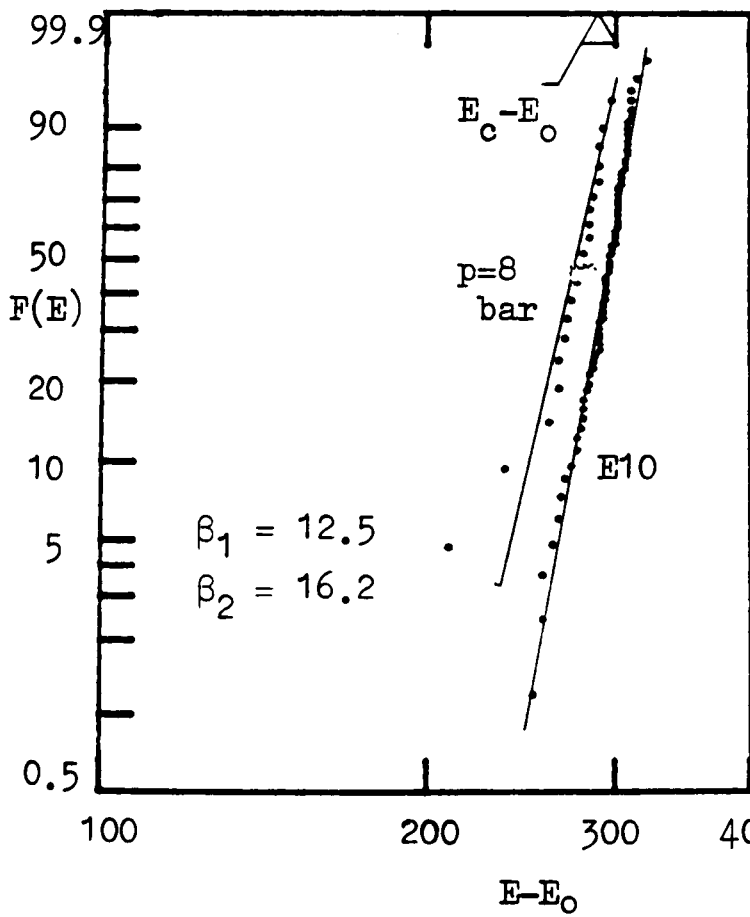


(c)

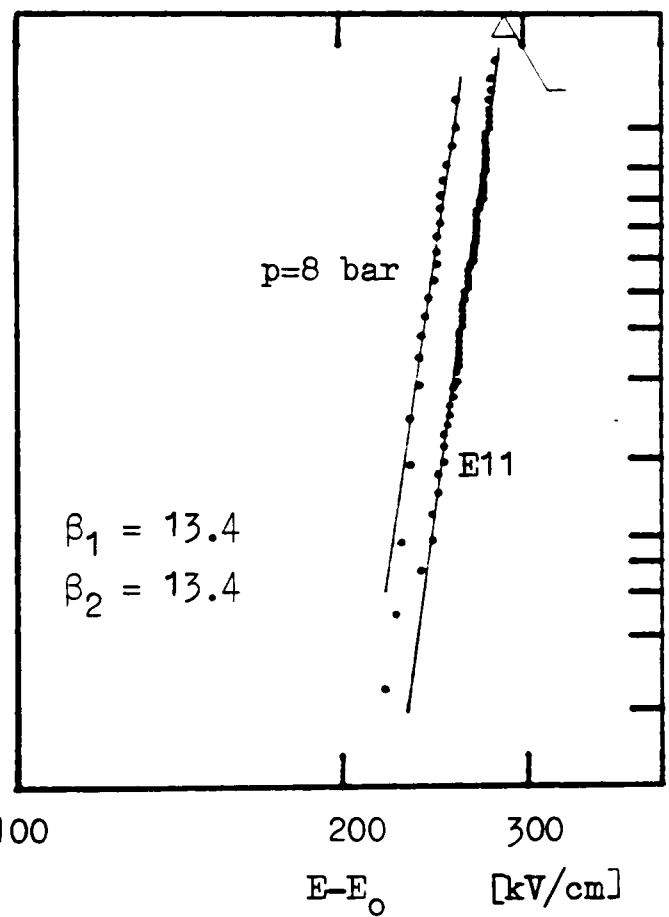
Figure 4.16 Effect of roughness on Weibull probability distribution in a 75% SF<sub>6</sub>-N<sub>2</sub> mixture in the field strength range 300-400 kV/cm.  
 (a) Polished (E9); (b) Sandblasted (E10);  
 (c) Machined (E11).



(a)



(b)



(c)

Figure 4.17 Effect of roughness on Weibull probability distribution in a 10%  $SF_6-N_2$  mixture in the field range 300-400 kV/cm.  
 (a) Polished (E9); (b) Sandblasted (E10);  
 (c) Machined (E11).

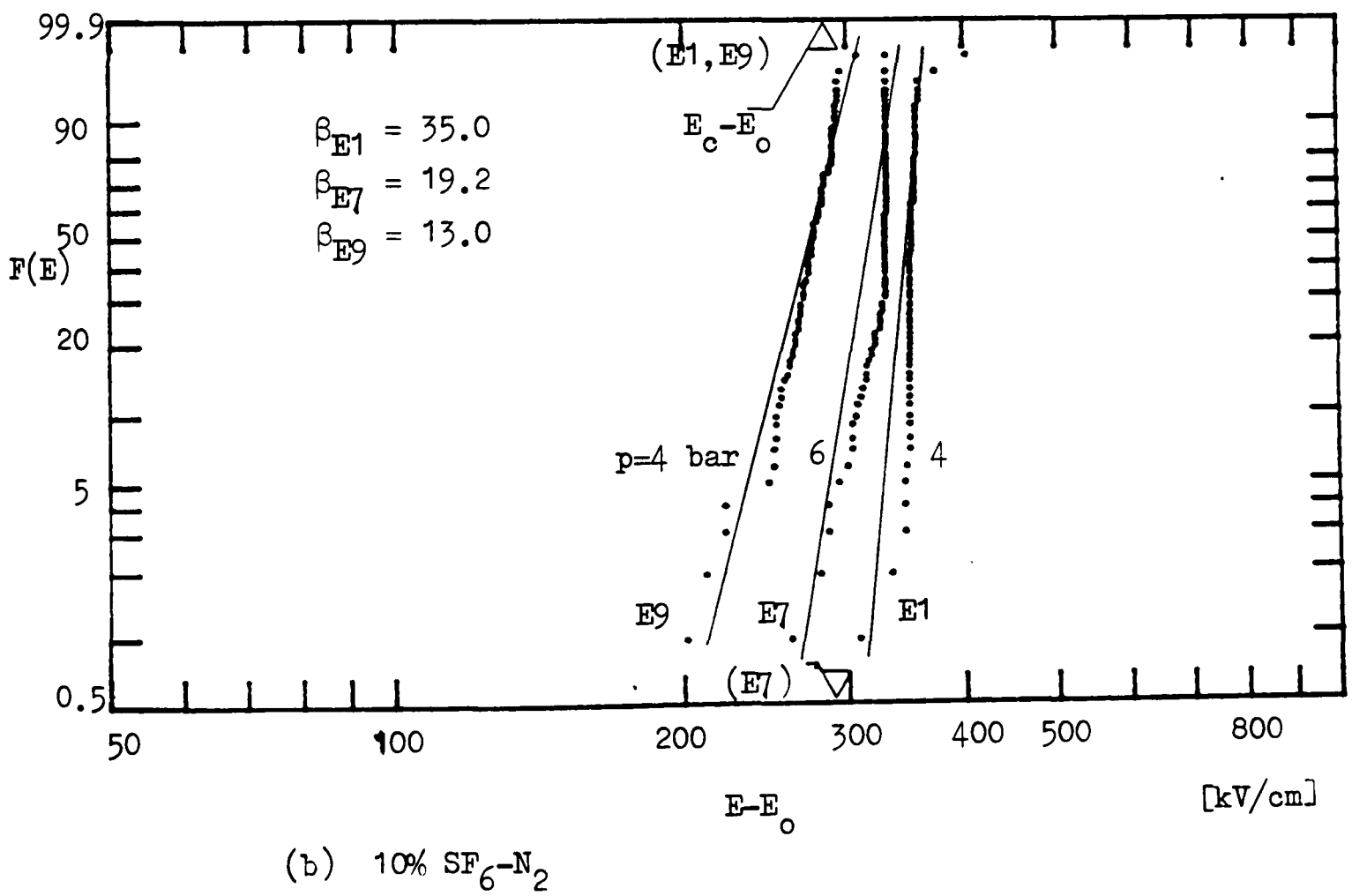
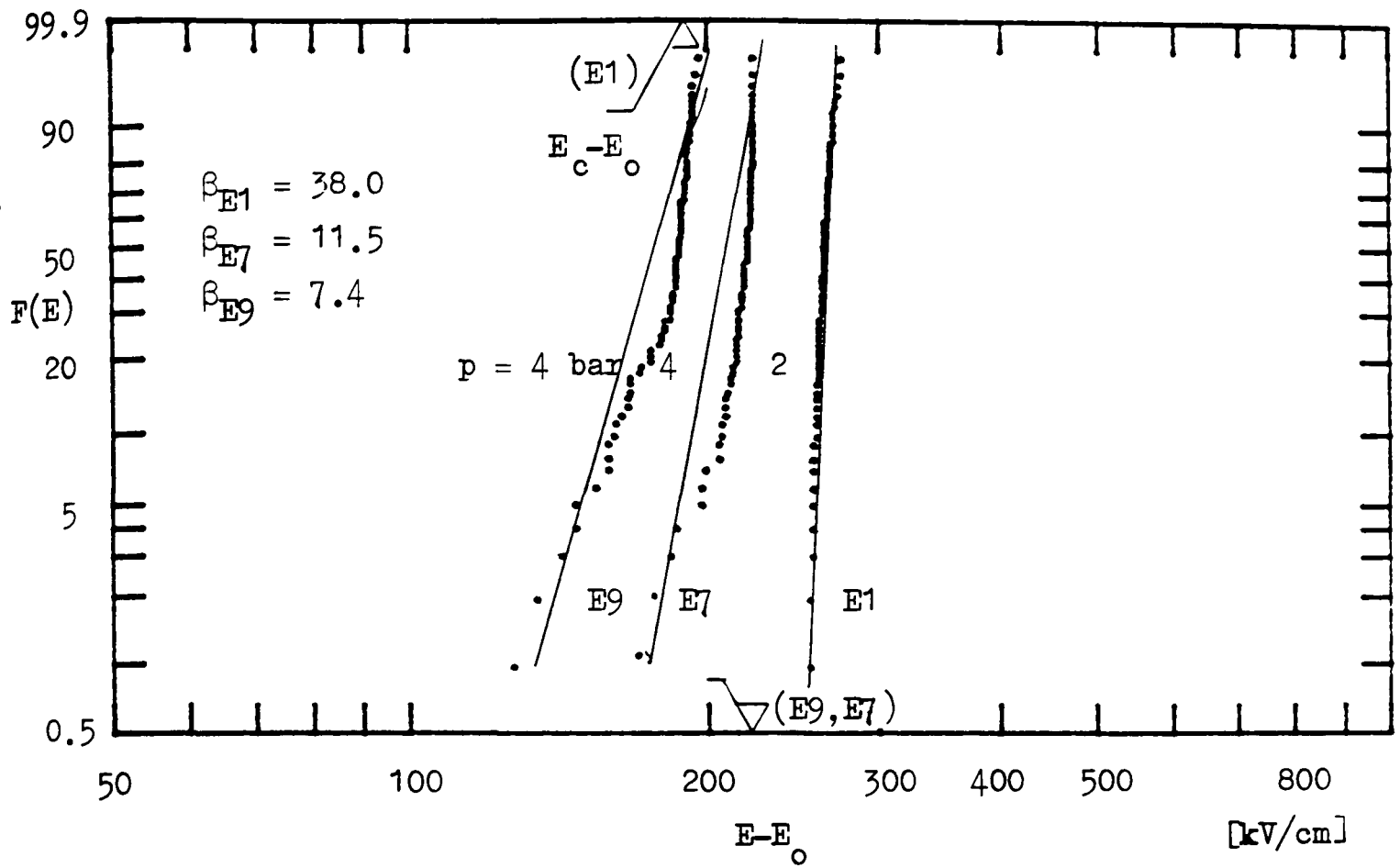
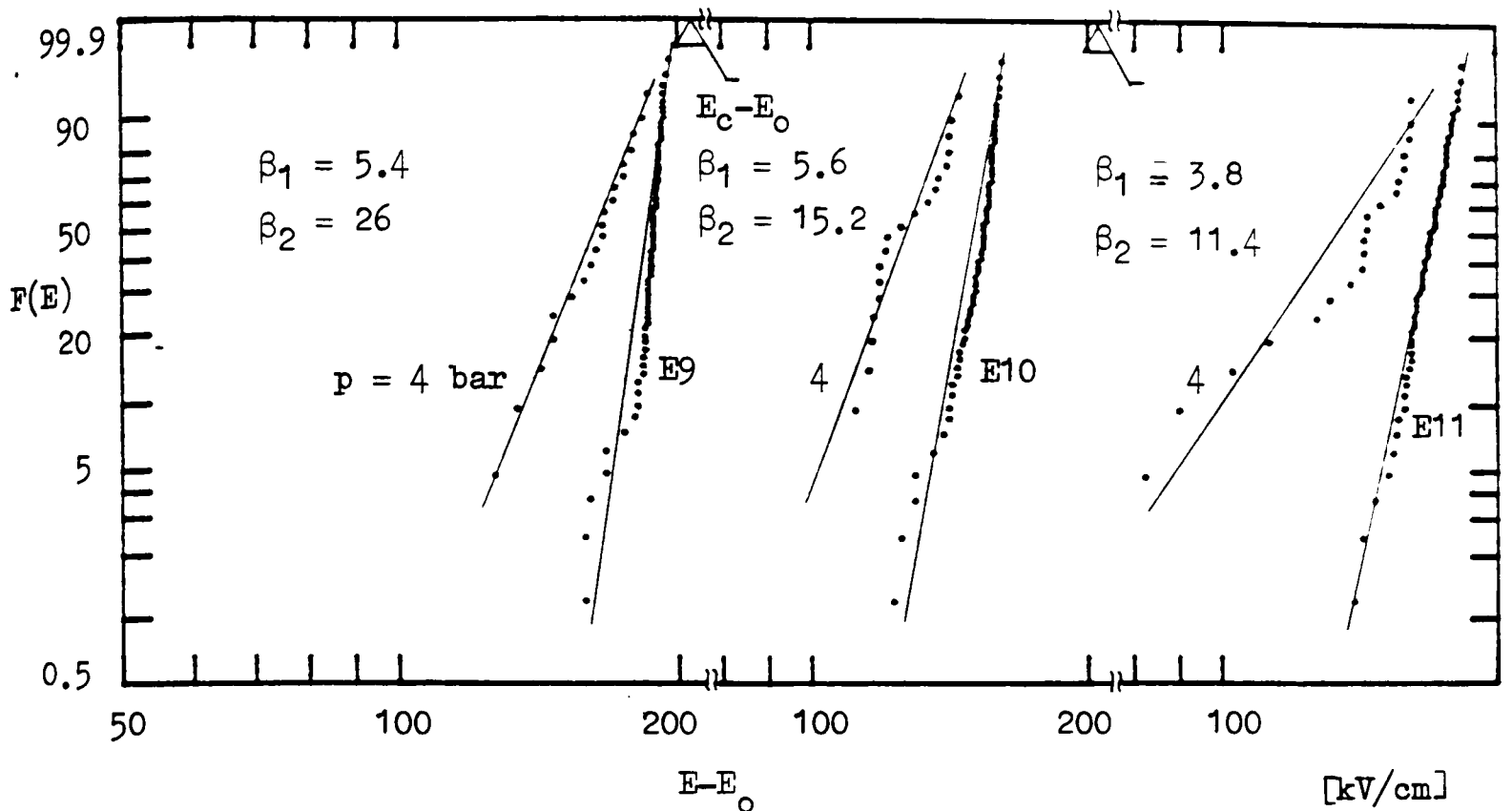
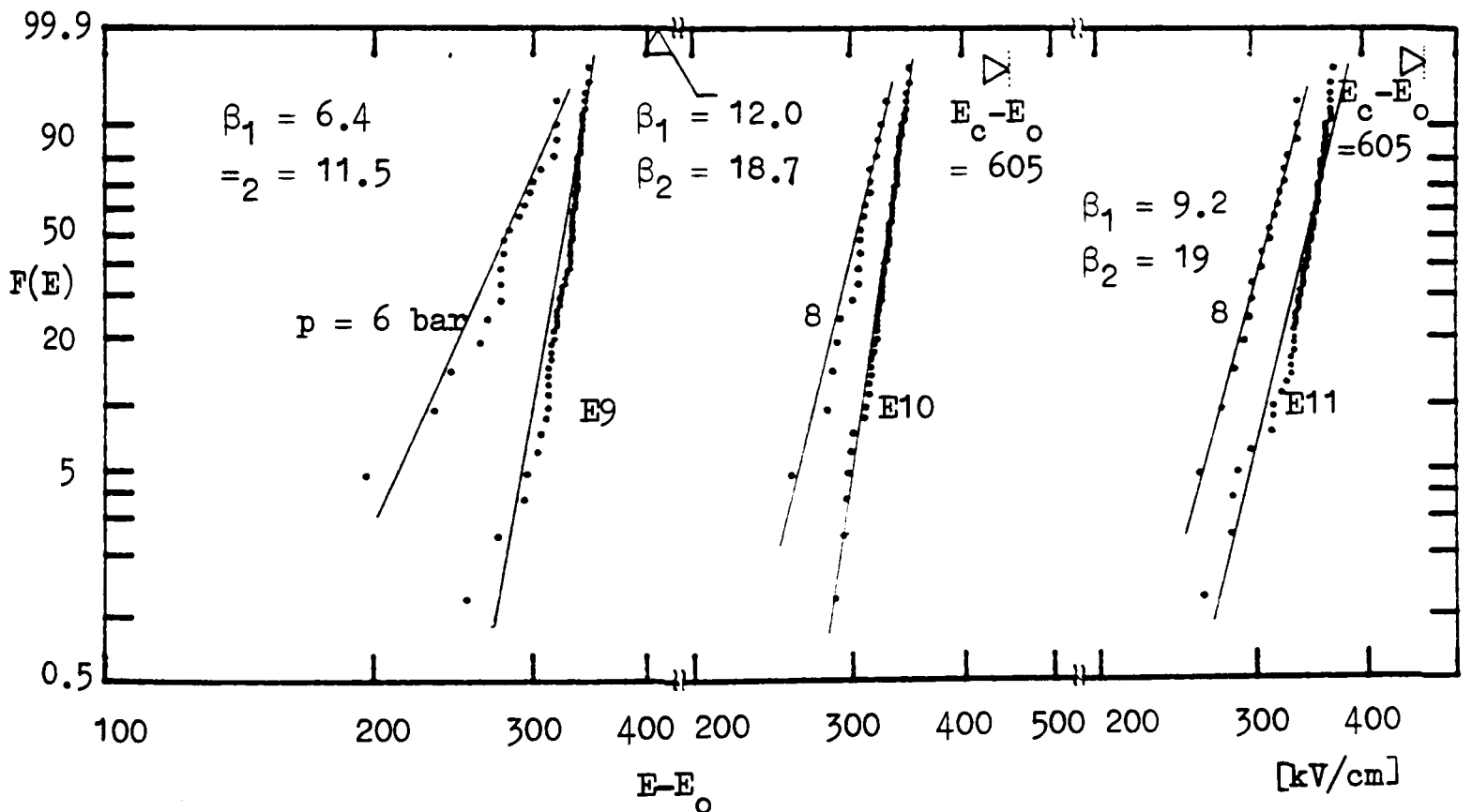


Figure 4.18 Effect of electrode area on Weibull probability distribution in SF<sub>6</sub> and a 10% SF<sub>6</sub>-N<sub>2</sub> mixture

Electrode areas  $S_{E1} = 1.8 \text{ cm}^2$ ;  
 $S_{E7} = 95 \text{ cm}^2$ ;  
 $S_{E9} = 180 \text{ cm}^2$ .



(a) Field range = 300-400 kV/cm



(b) Field range = 500-600 kV/cm

Figure 4.19 Effect of roughness on Weibull probability distribution for field strengths in ranges 300-400 kV/cm (Figure 4.19(a)) and 500-600 kV/cm (Figure 4.19(b)) in SF<sub>6</sub>

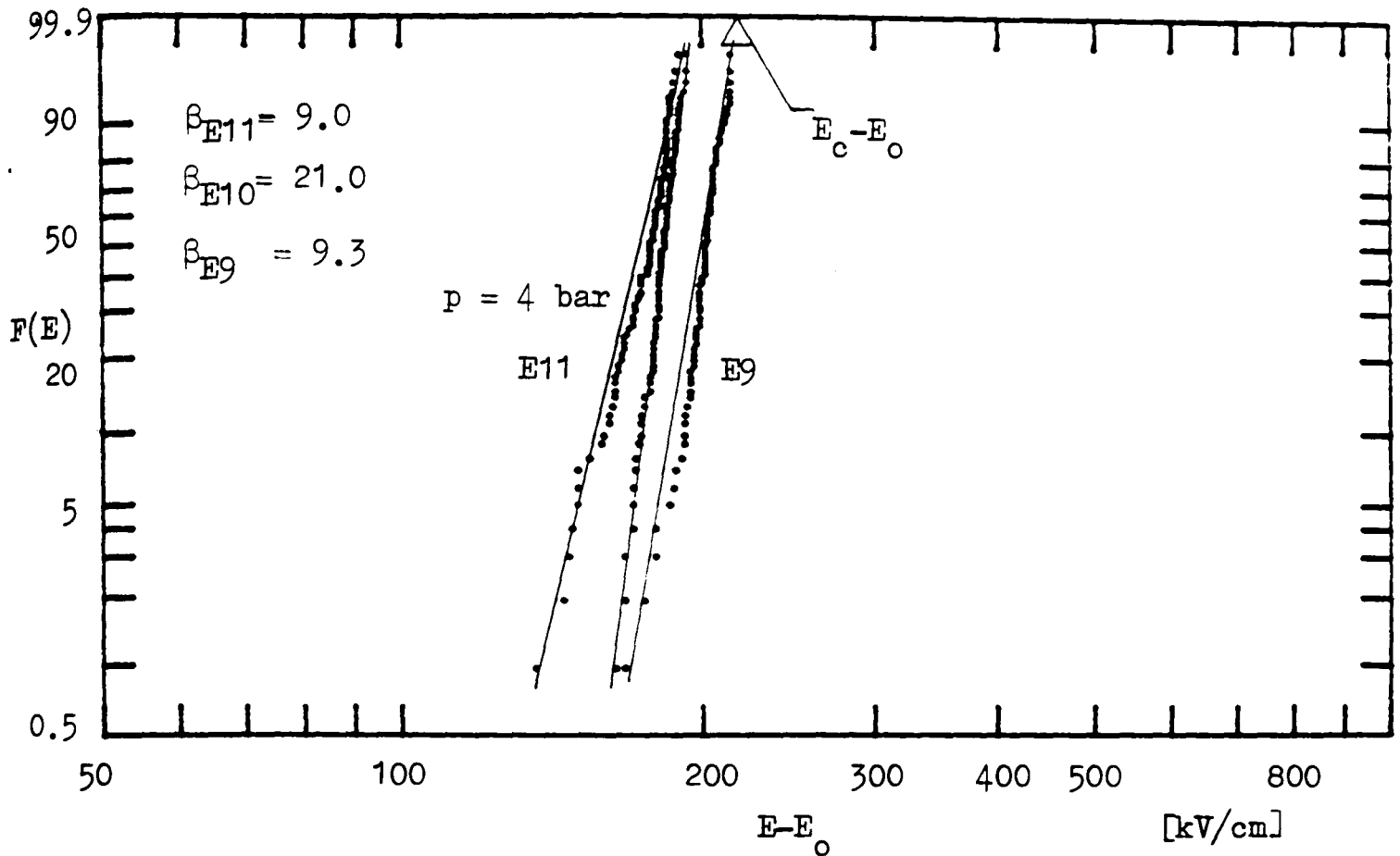


Figure 4.20 Effect of roughness on Weibull probability distribution in the field strength range 300-400 kV/cm in 75% SF<sub>6</sub>-N<sub>2</sub>

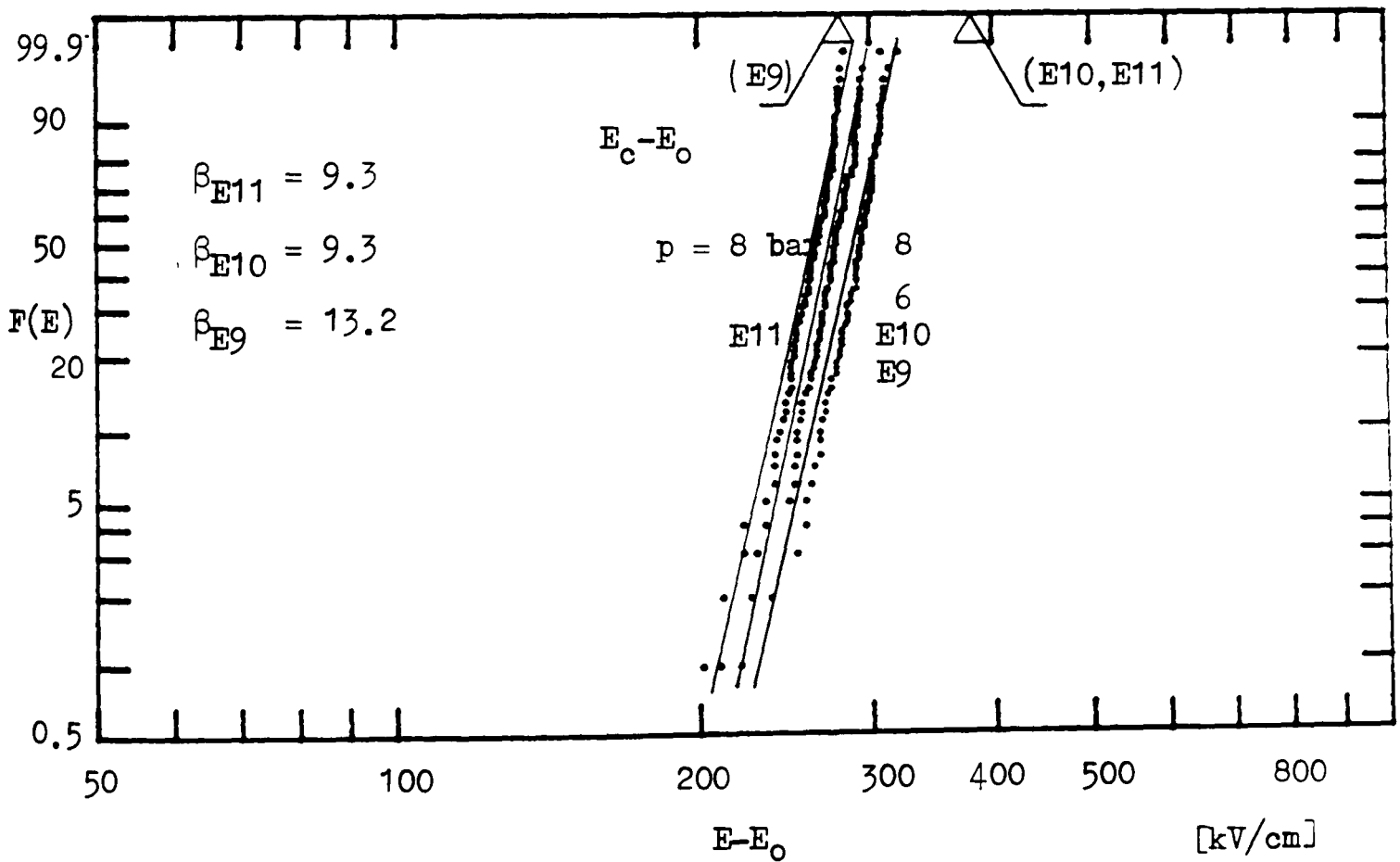


Figure 4.21 Effect of roughness on Weibull probability distribution in the field strength range 300-400 kV/cm in 10% SF<sub>6</sub>-N<sub>2</sub>

Electrodes: E9 polished ( $R_{CLA}=0.04 \mu\text{m}$ ), E10 Sandblasted ( $R_{CLA}=2.3 \mu\text{m}$ )  
 E11 Machined ( $R_{CLA}=2.8 \mu\text{m}$ )

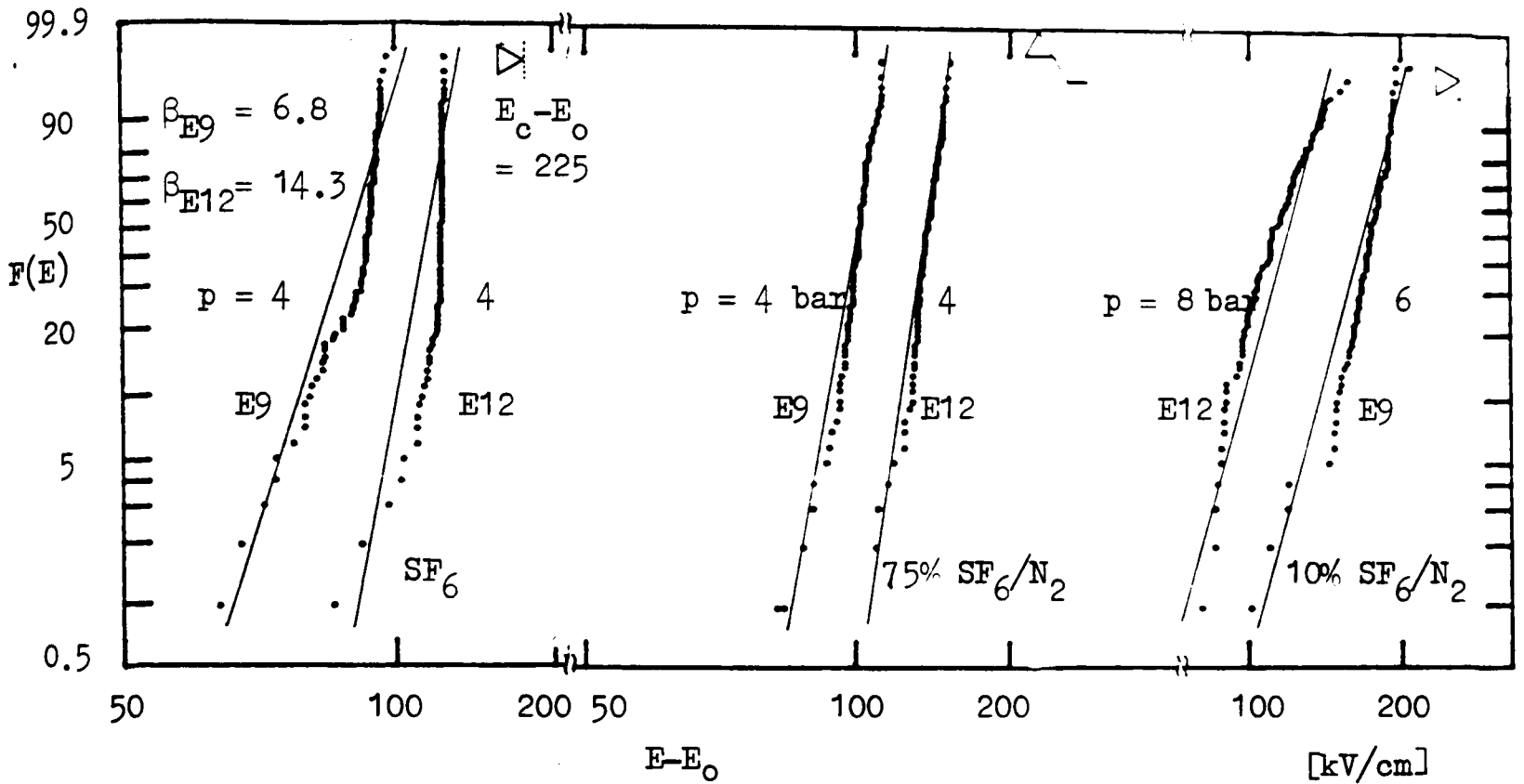


Figure 4.22 Effect of electrode material on Weibull probability distribution in SF<sub>6</sub> and SF<sub>6</sub>/N<sub>2</sub> mixture for the field strength range 300-400 kV/cm (Gap r<sub>1</sub>/r<sub>2</sub> = 0.945/1.27 cm, polished, E9 - stainless steel, E12 - Aluminium)

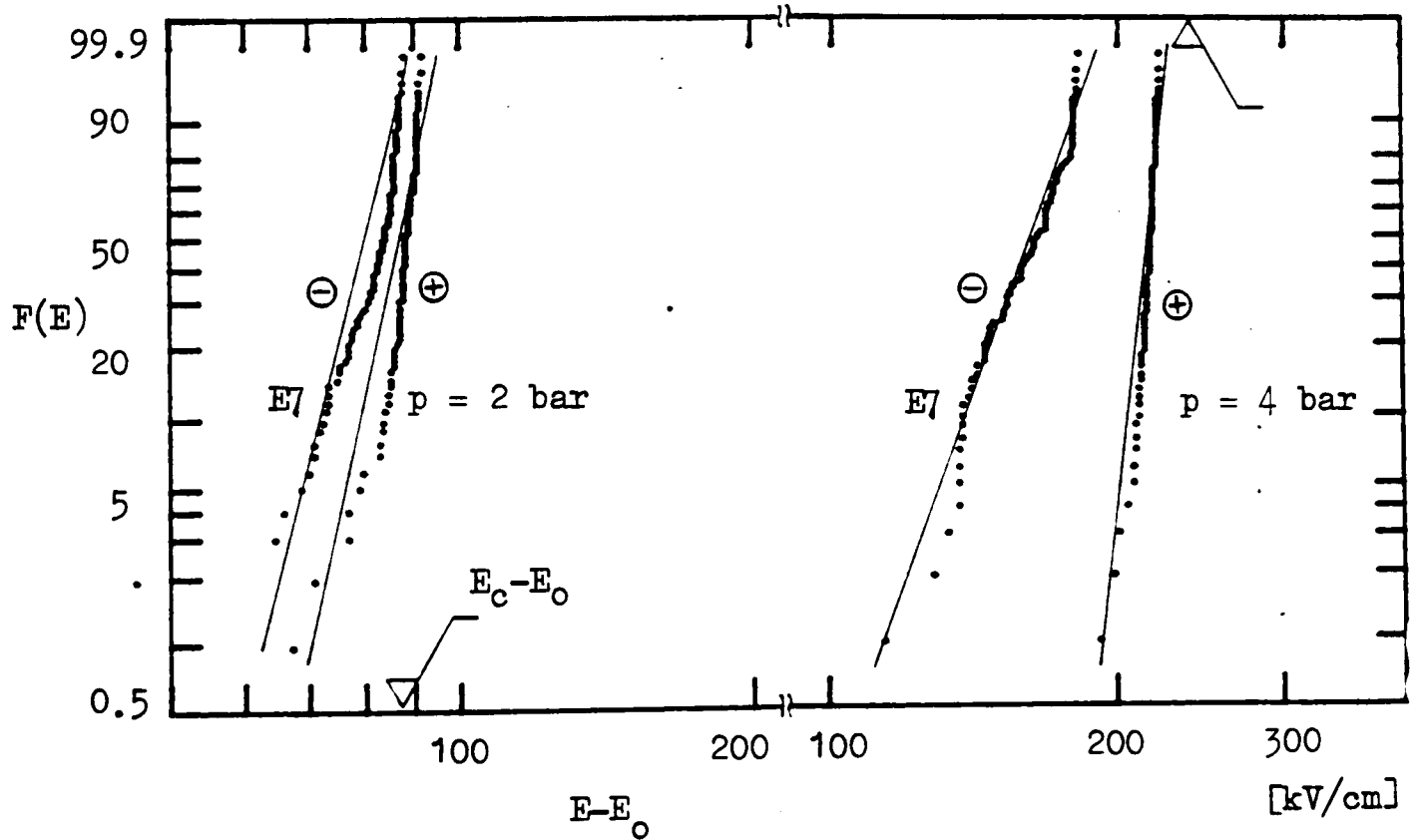


Figure 4.23 Effect of polarity on Weibull probability distribution in SF<sub>6</sub> (r<sub>1</sub>/r<sub>2</sub> = 0.5/1.27 cm, polished)

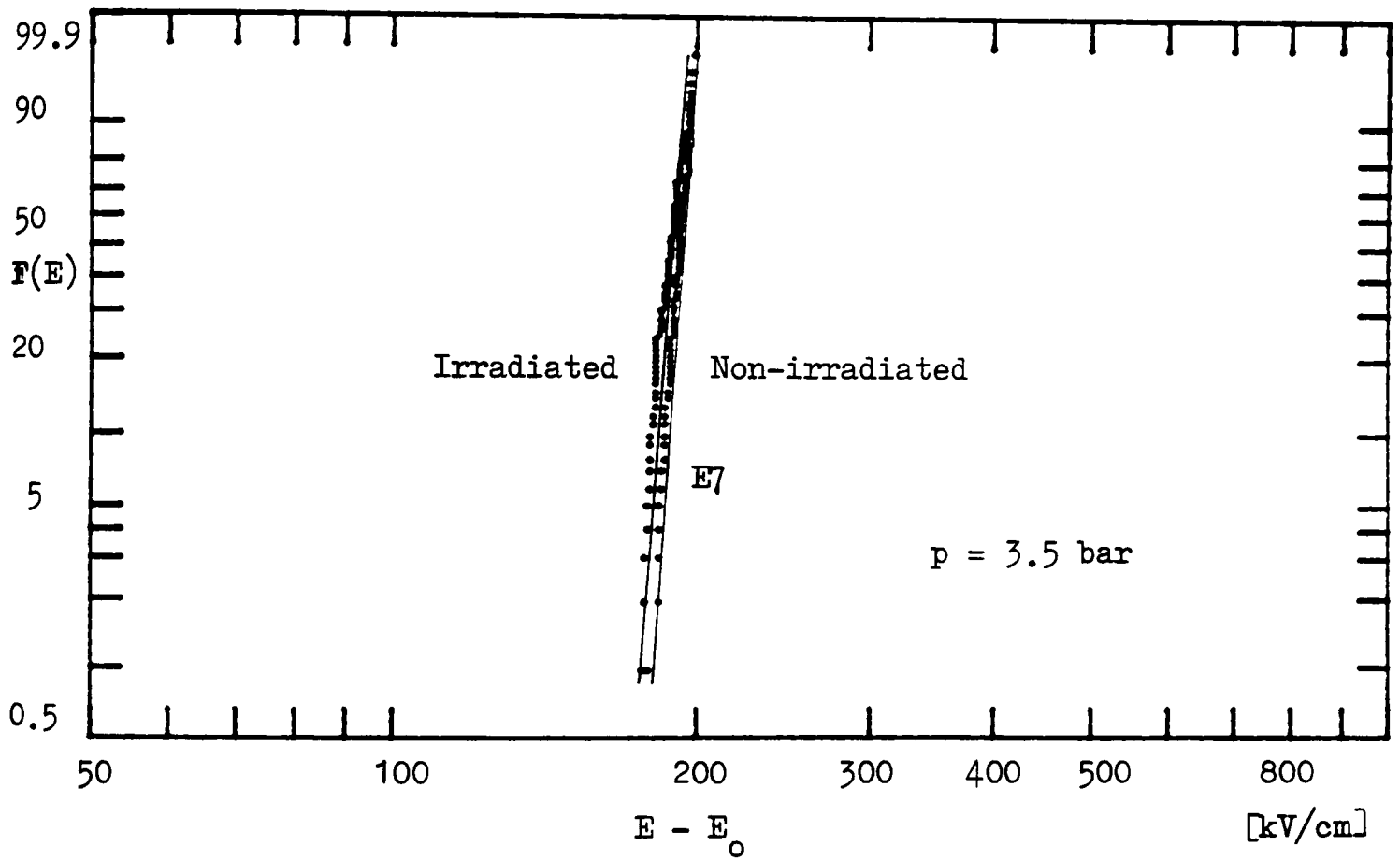


Figure 4.24 Effect of irradiation on Weibull probability distribution in a 40%  $\text{SF}_6/\text{N}_2$  mixture (Gap:  $r_1/r_2 = 0.5/1.27$  cm, polished)

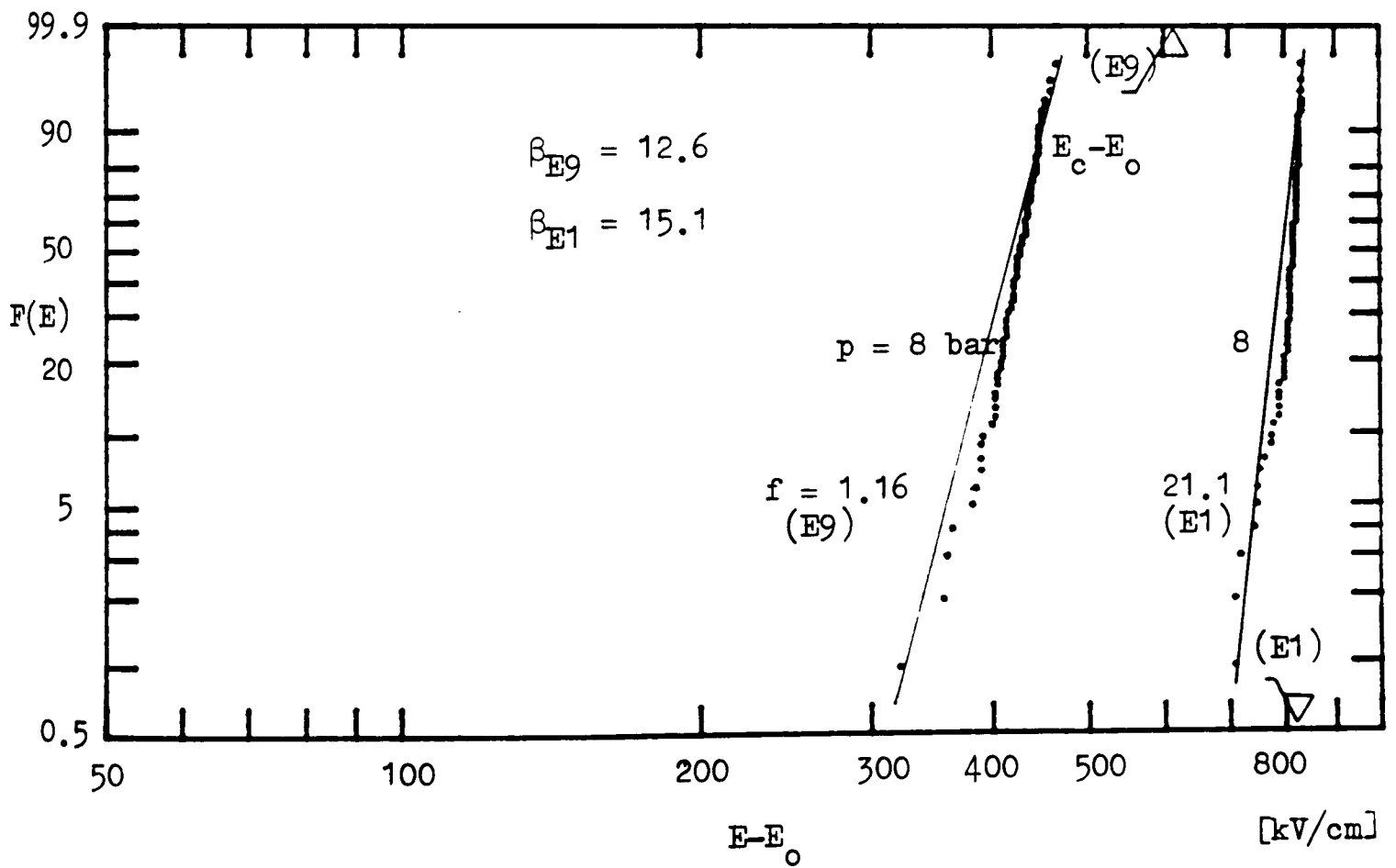
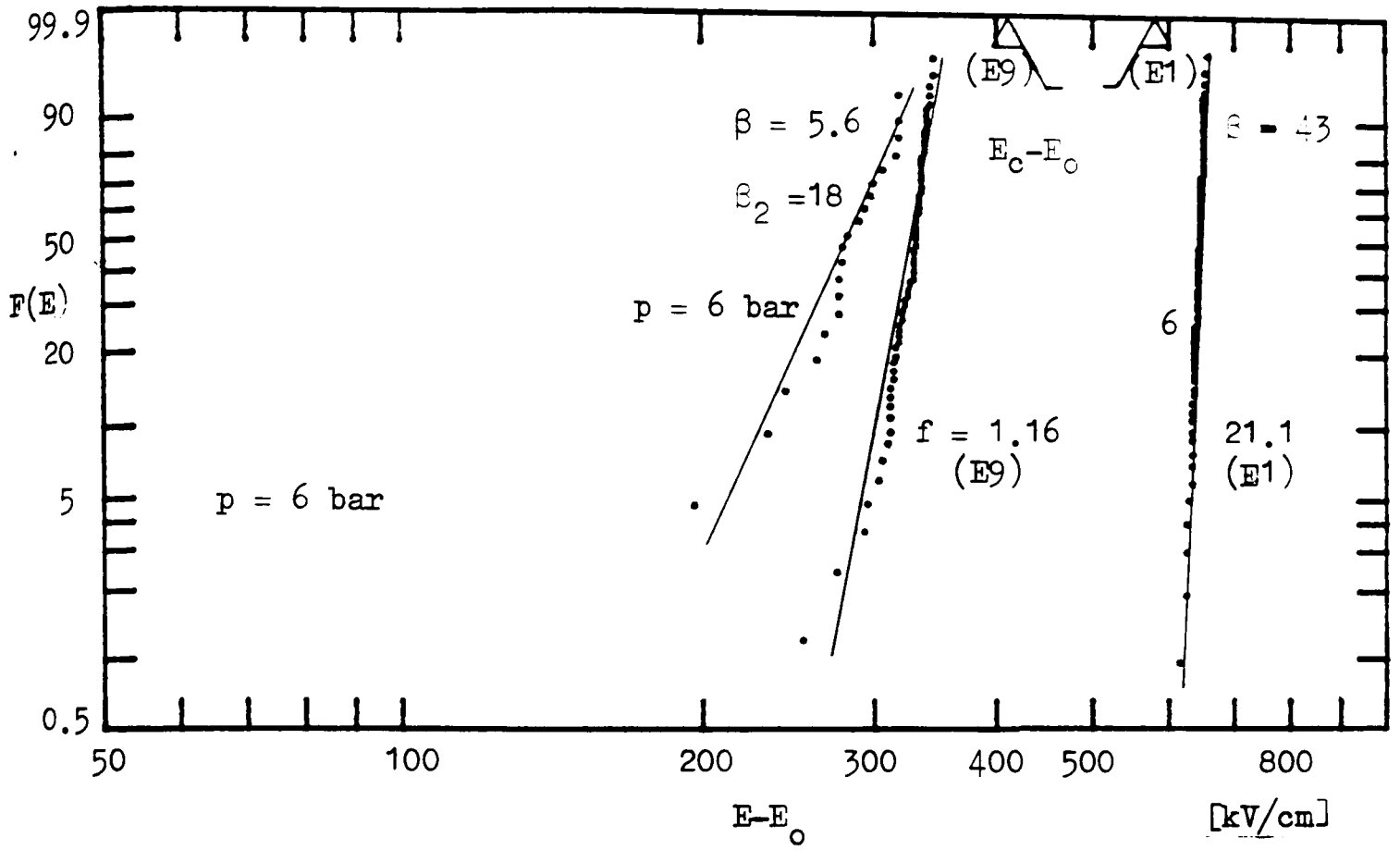
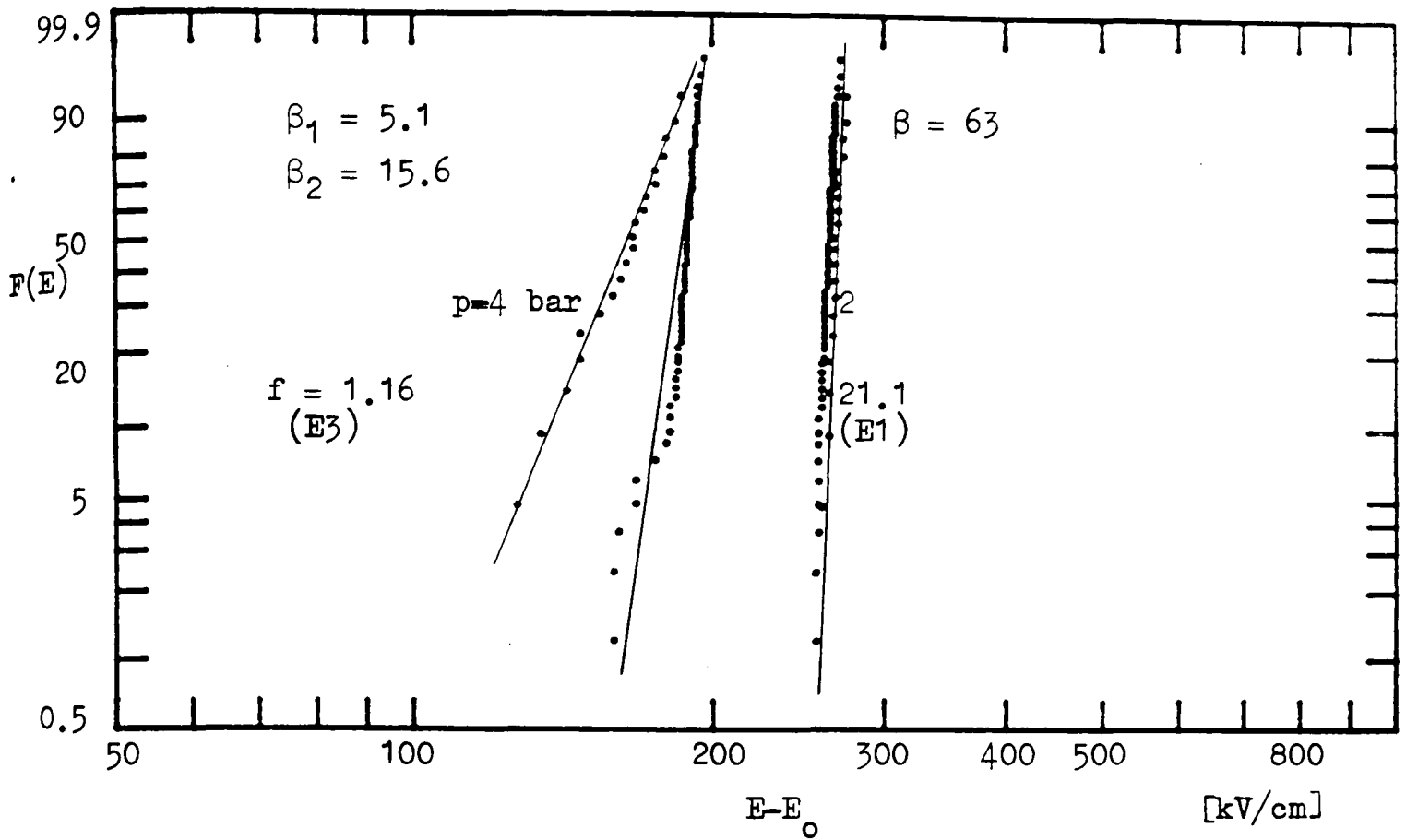
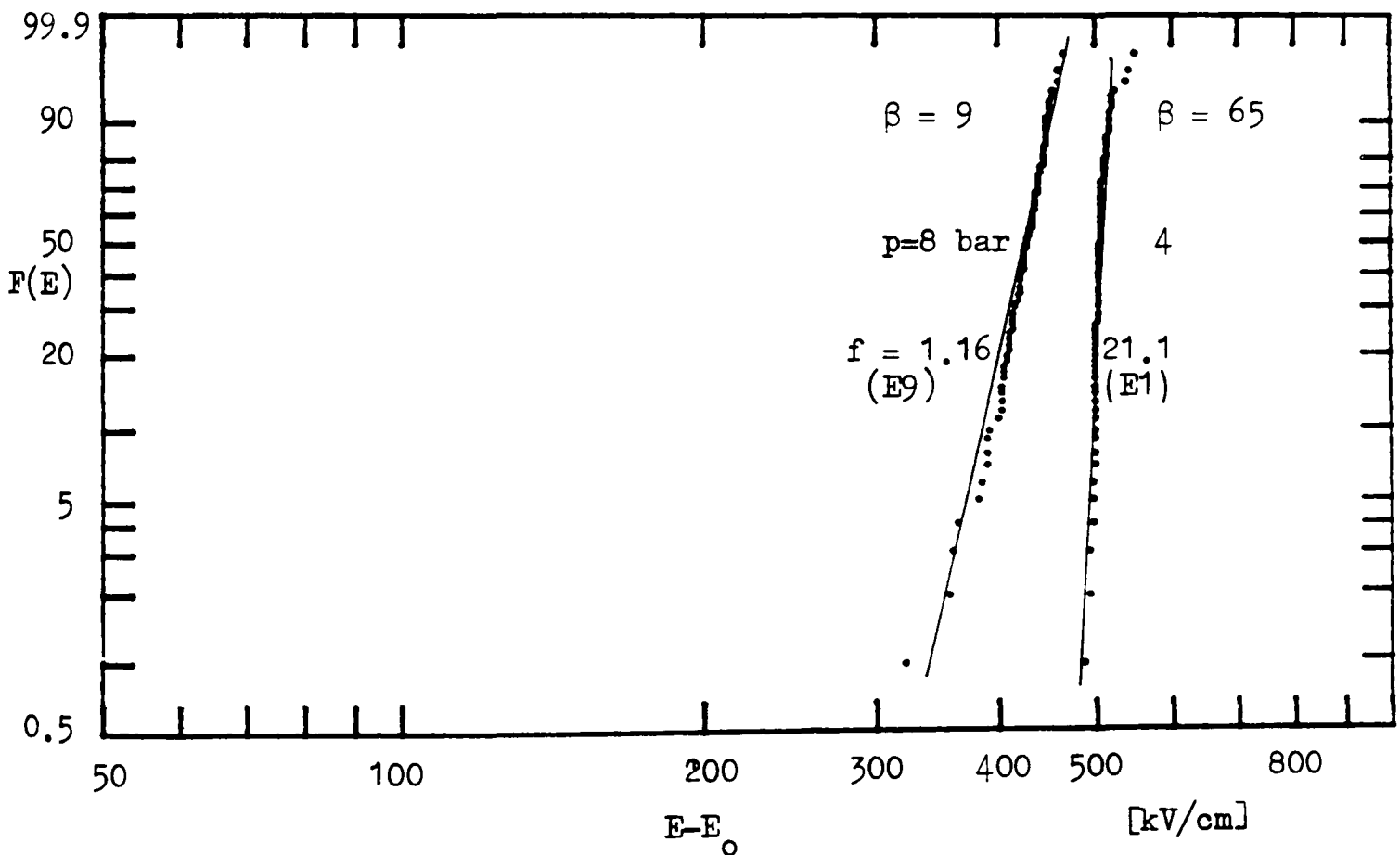


Figure 4.25 Effect of gas pressure on Weibull probability distribution in  $\text{SF}_6$  in gaps having nonuniformities  $f_{E1} = 21.1$  (E1) and  $f_{E9} = 1.16$  (E9)



(a) Field range : 300-400 kV/cm



(b) Field range : 500-600 kV/cm

Figure 4.26 Change in Weibull probability distribution with gap nonuniformities in  $SF_6$ . (Nonuniformities)

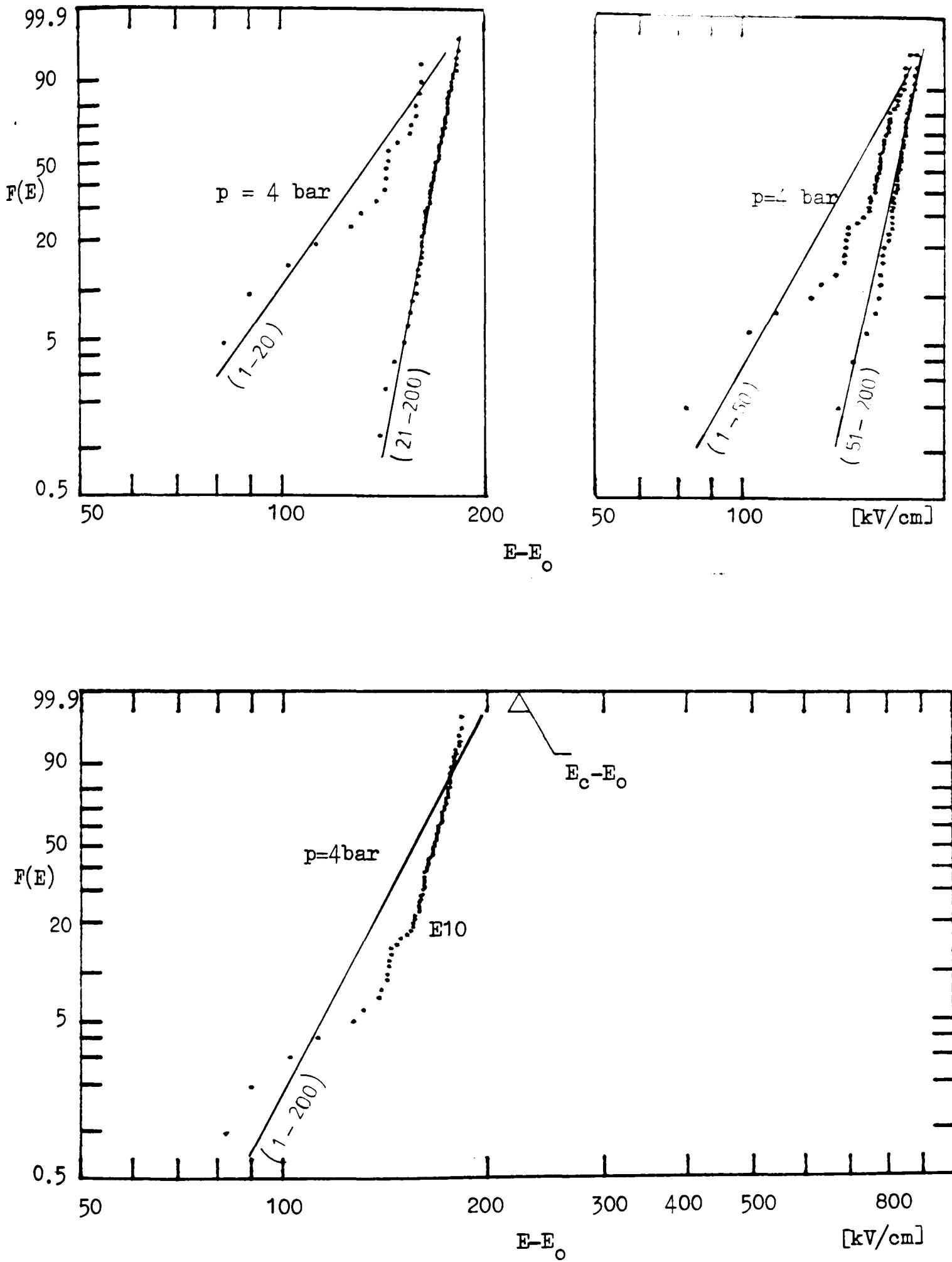


Figure 4.27 Effect of number of observations on Weibull probability distribution obtained for sandblasted electrode (E10) in  $SF_6$

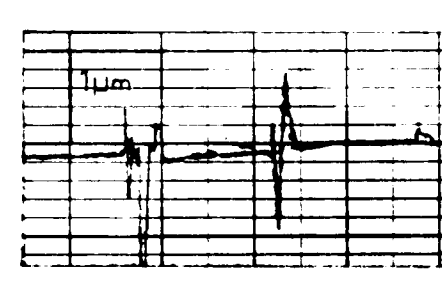
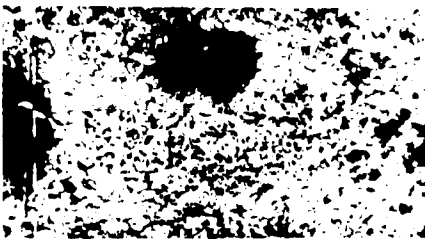
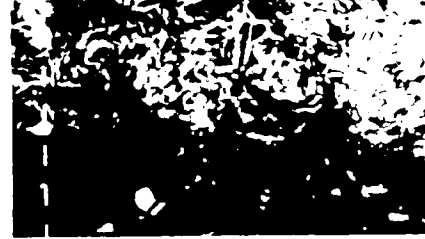
Table 5.1 Virial coefficients of SF<sub>6</sub>/N<sub>2</sub> for varying SF<sub>6</sub> concentration at T = 20°C (= 293.16)

| % of SF <sub>6</sub><br>in the mixture | B <sub>m</sub><br>(cc/mole) | C <sub>m</sub><br>(cc/mole) <sup>2</sup> | B <sub>m</sub> <sup>i</sup><br>(bar) <sup>-1</sup> | C <sub>m</sub> <sup>i</sup> x 10 <sup>-5</sup><br>(bar) <sup>-2</sup> |
|--|-----------------------------|--|--|---|
| 10                                     | - 7.28                      | 1065.97                                  | -2.988x10 <sup>-4</sup>                            | 0.170   |
| 20                                     | - 15.09                     | 920.16                                   | - 6.193  | 0.116   |
| 30                                     | - 28.83                     | 1124.99                                  | - 11.830   | 0.049   |
| 40                                     | - 48.50                     | 1812.88                                  | - 19.899   | - 0.091   |
| 50                                     | - 74.10                     | 3116.25                                  | - 30.401   | - 0.399   |
| 60                                     | -105.62                     | 5167.51                                  | - 43.334   | - 1.008   |
| 70                                     | -143.07                     | 8099.11                                  | - 58.699   | - 2.082   |
| 80                                     | -186.45                     | 12040.34                                 | - 76.496   | - 3.825   |
| 90                                     | -235.76                     | 17132.92                                 | - 96.726   | - 6.472   |
| 100                                    | -291.00                     | 23500.00                                 | -119.387   | -10.297   |

$$Z = 1 + B_m^i \cdot p + C_m^i \cdot p^2 \quad p \text{ in bar}$$

where  $B_m^i = B_m / RT$  ;  $C_m^i = (C - B_m^2) / RT$

Table 5.2 Electronmicroscope pictures and roughness profiles of inner electrodes after sparking.  
(Material : Stainless Steel)

|             | Electronmicroscope Pictures<br>(Magnification)  |   | Roughness Profiles   | $R_{max}$<br>( $\mu m$ ) | $R_{CLA}$<br>( $\mu m$ ) |
|-------------|---|---|--|--------------------------|--------------------------|
| Polished    | X 80<br>  | X 640<br>  |  | 2                        | 0.08                     |
| Sandblasted | X 40<br> | X 320<br> |  | 15                       | 2.3                      |
| Machined    | X 80<br> | X 320<br> |  | 18                       | 2.8                      |

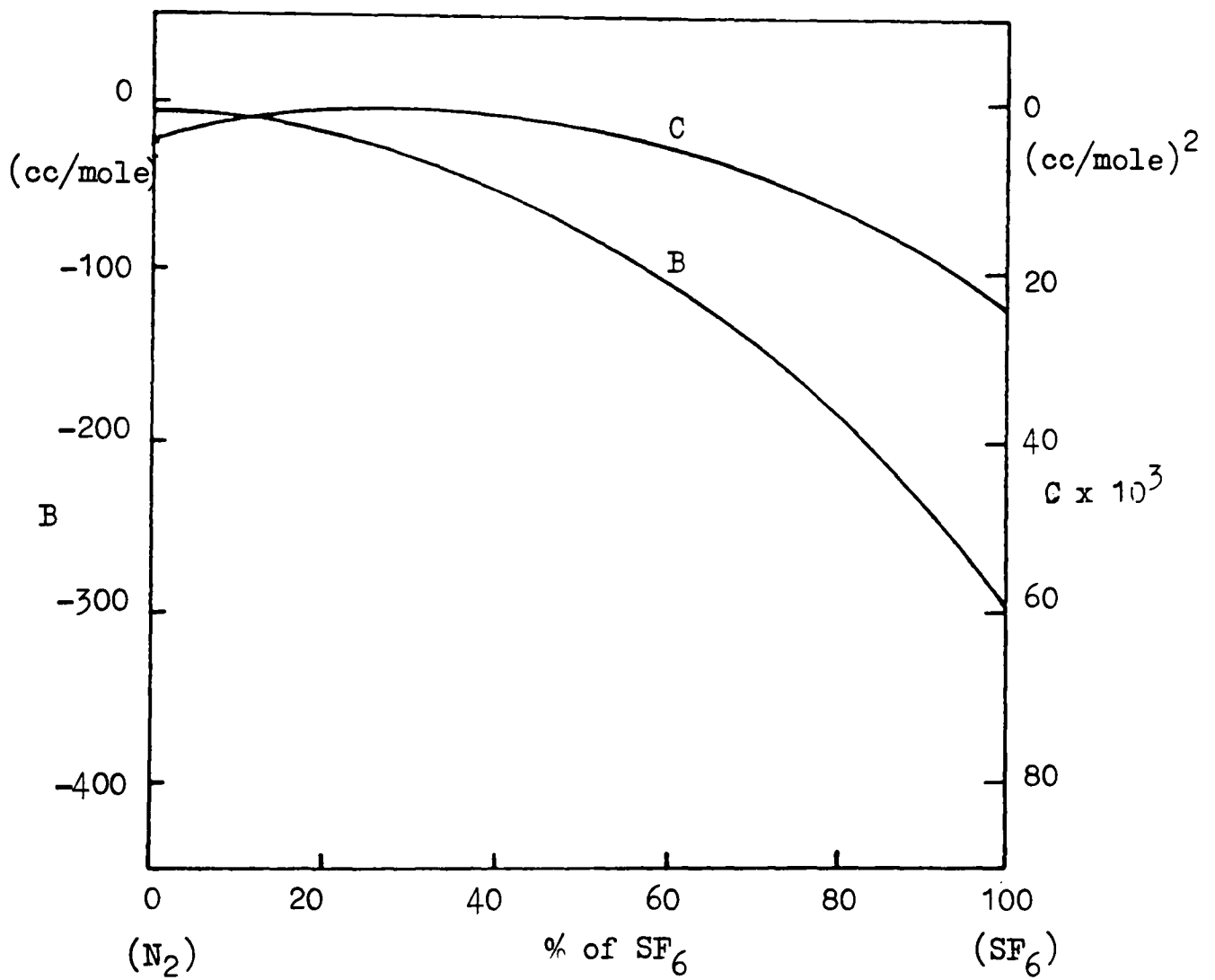


Figure 5.1 Variation of the virial coefficients of SF<sub>6</sub>/N<sub>2</sub>-mixtures as a function of SF<sub>6</sub> concentration (T = 293.16°K)

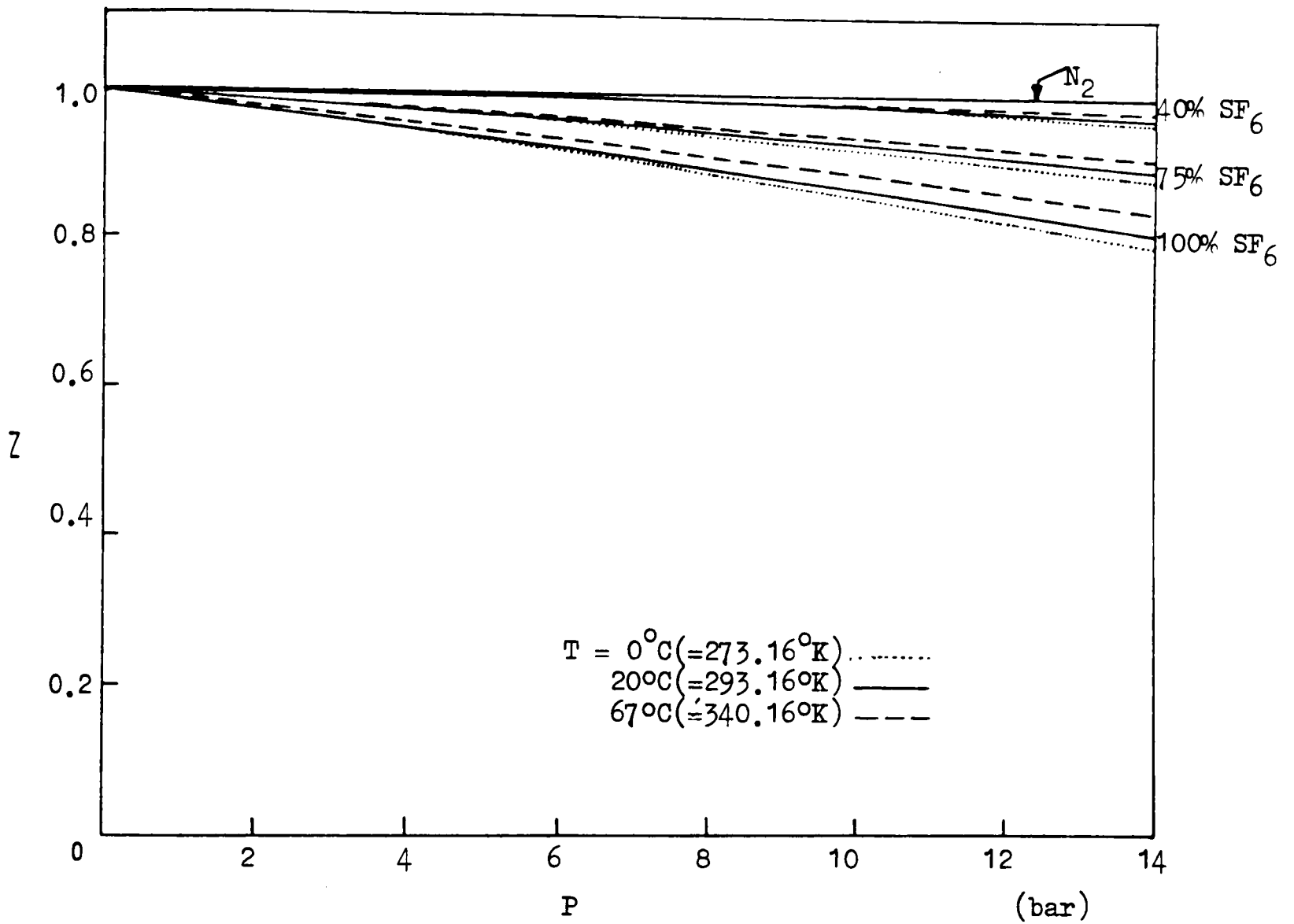


Figure 5.2 Variation of the compressibility factor with pressure in  $\text{SF}_6$ ,  $\text{N}_2$  and  $\text{SF}_6/\text{N}_2$  mixtures for several temperatures.

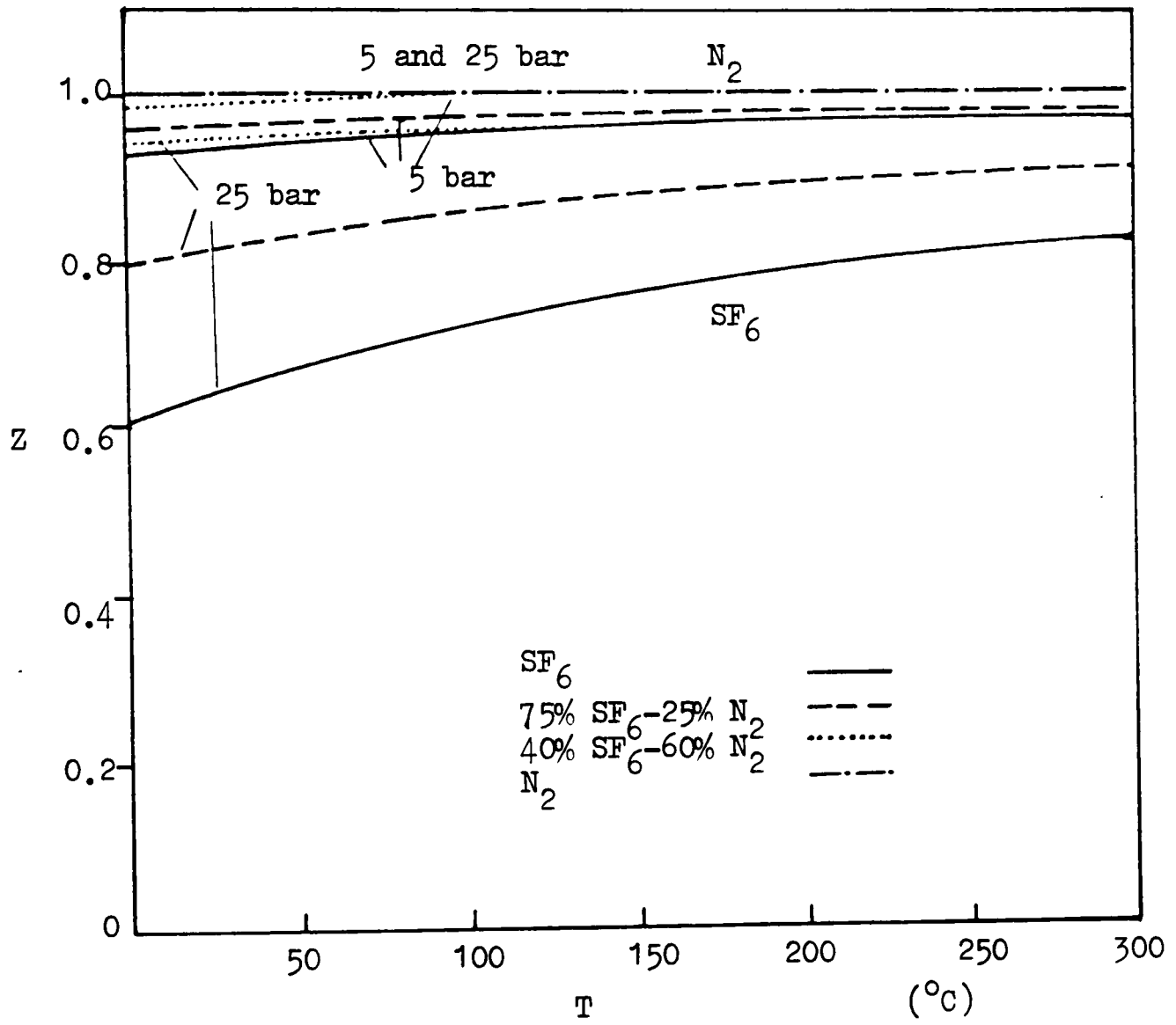


Figure 5.3 Variation of the compressibility factor with temperature in SF<sub>6</sub>, N<sub>2</sub> and SF<sub>6</sub>/N<sub>2</sub> mixtures for several pressures.

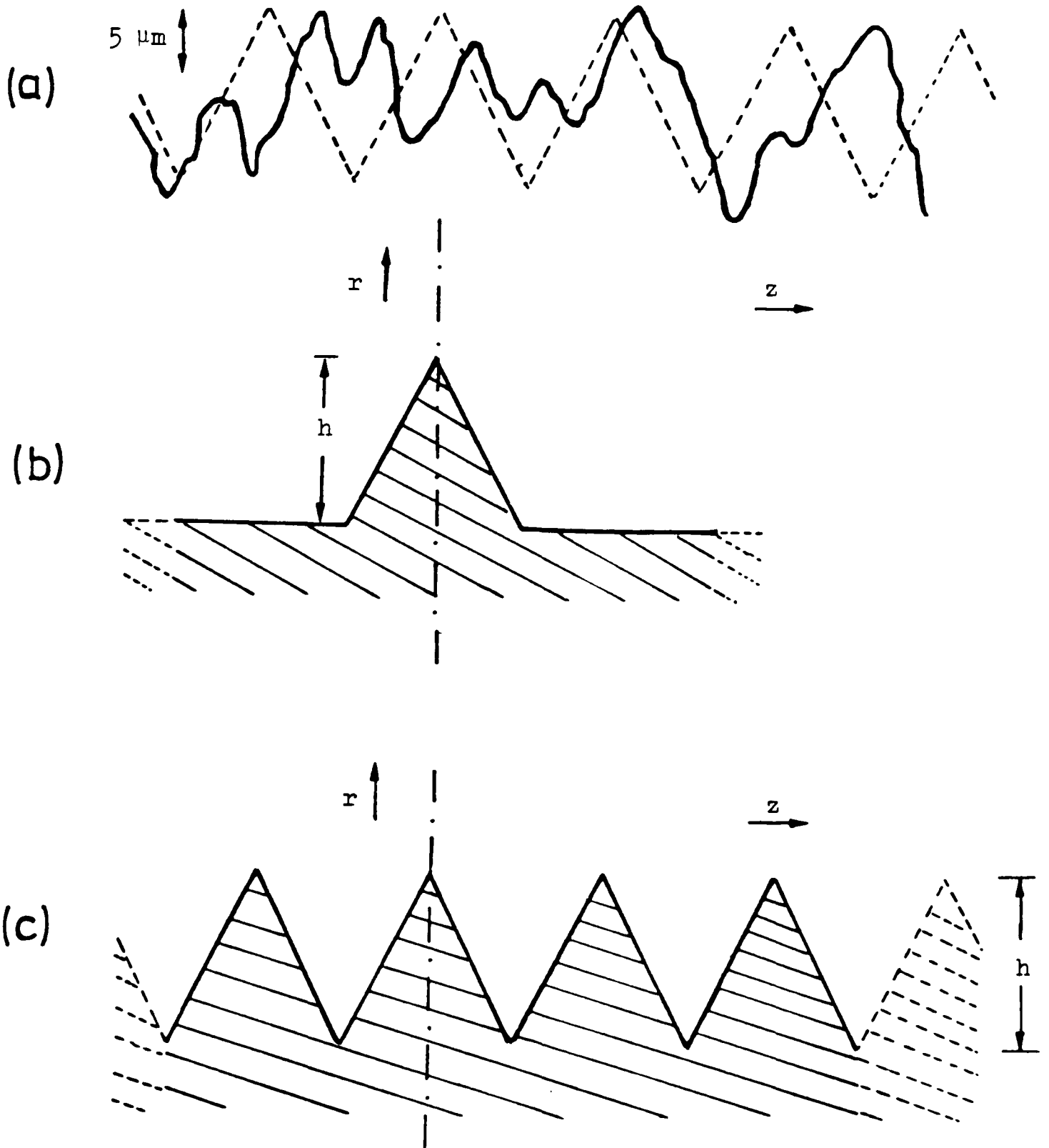


Figure 5.4 Surface roughness models of a machined electrode.

- a) Representation of surface roughness (machined electrode)
- b) Single protrusion
- c) Multiple protrusion

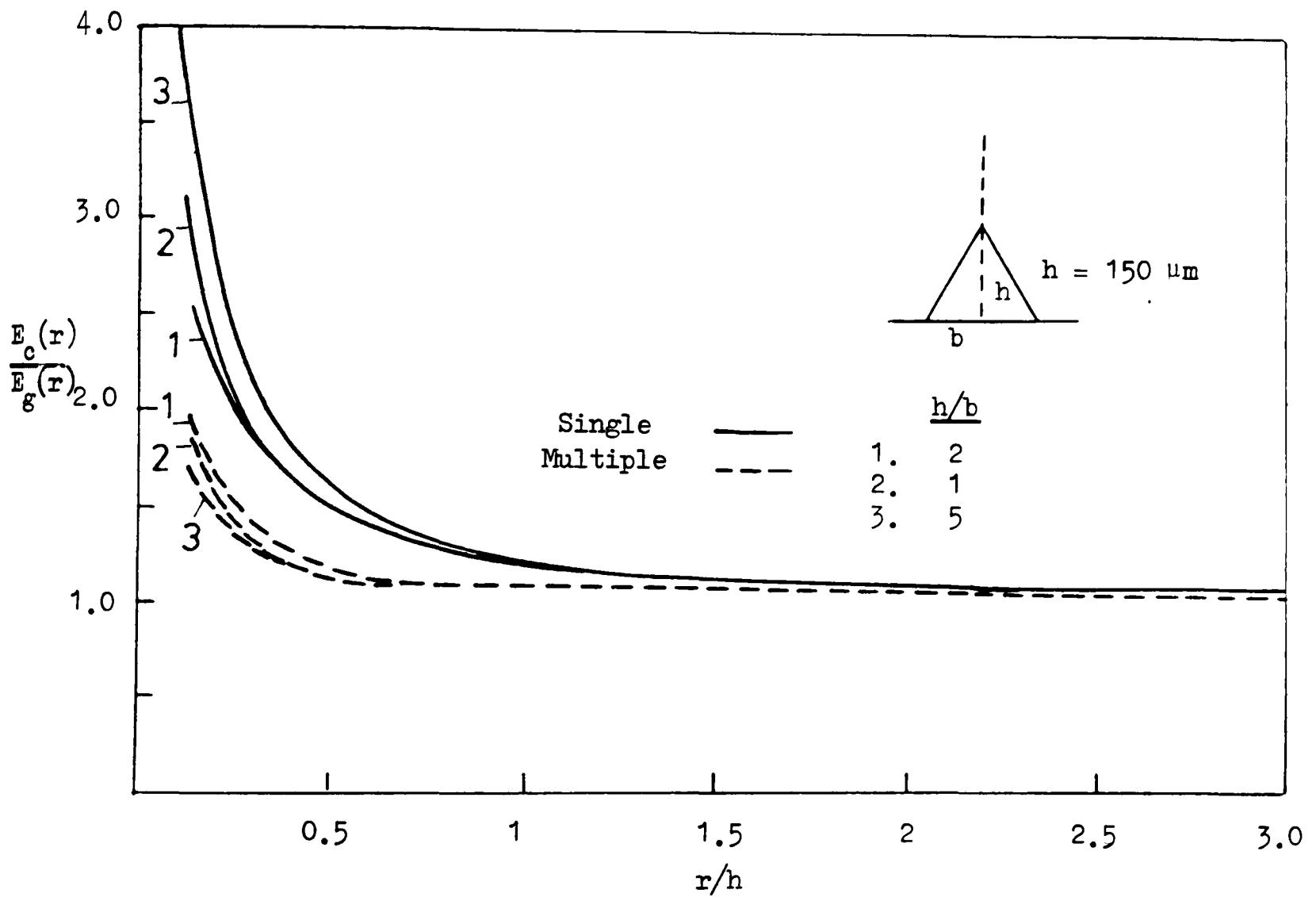


Figure 5.5 Radial field distributions along the axis of single and multiple protrusions models for several  $h/b$  ratios.

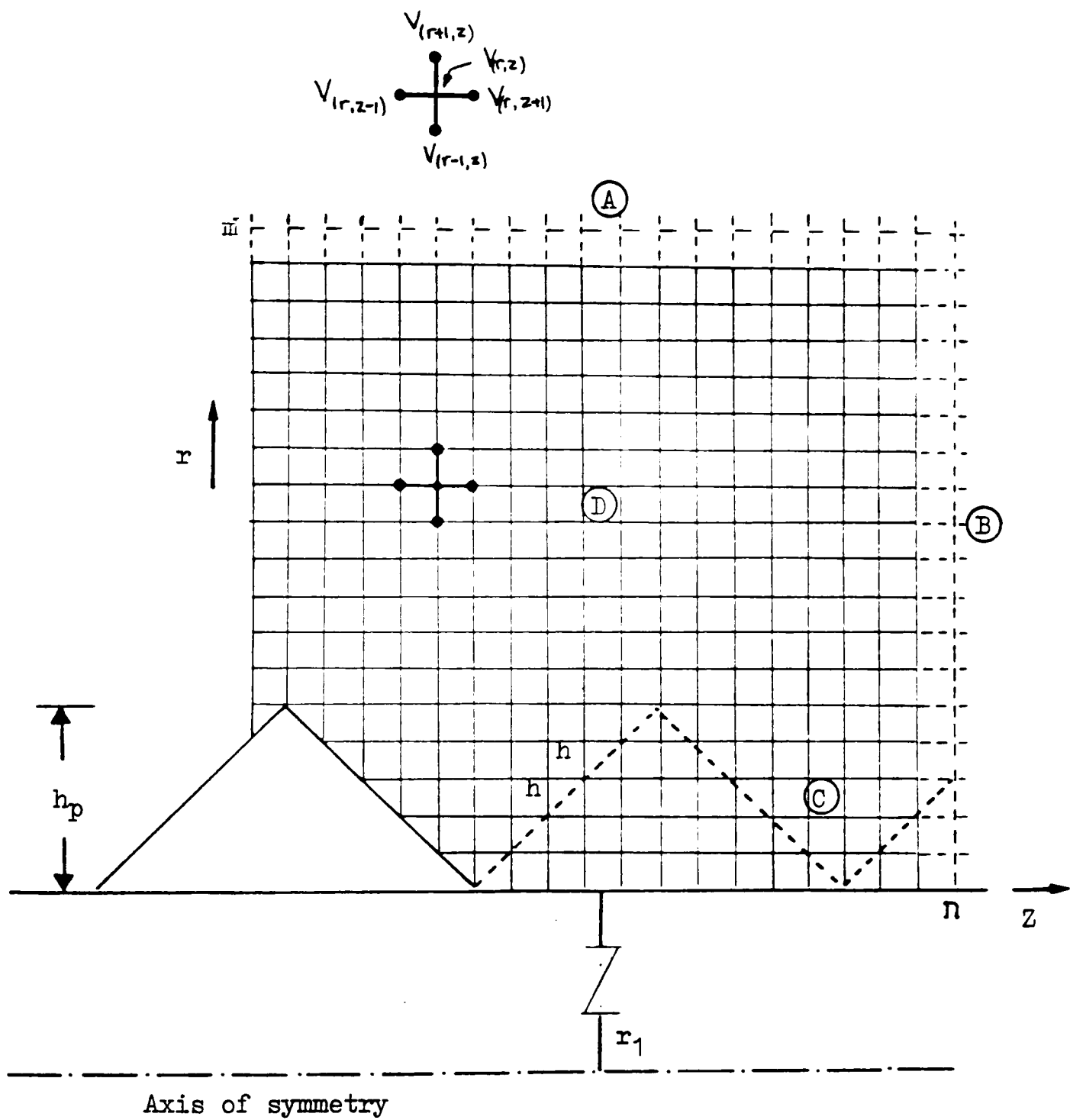


Figure 5.6 Region of solution for a regular mesh

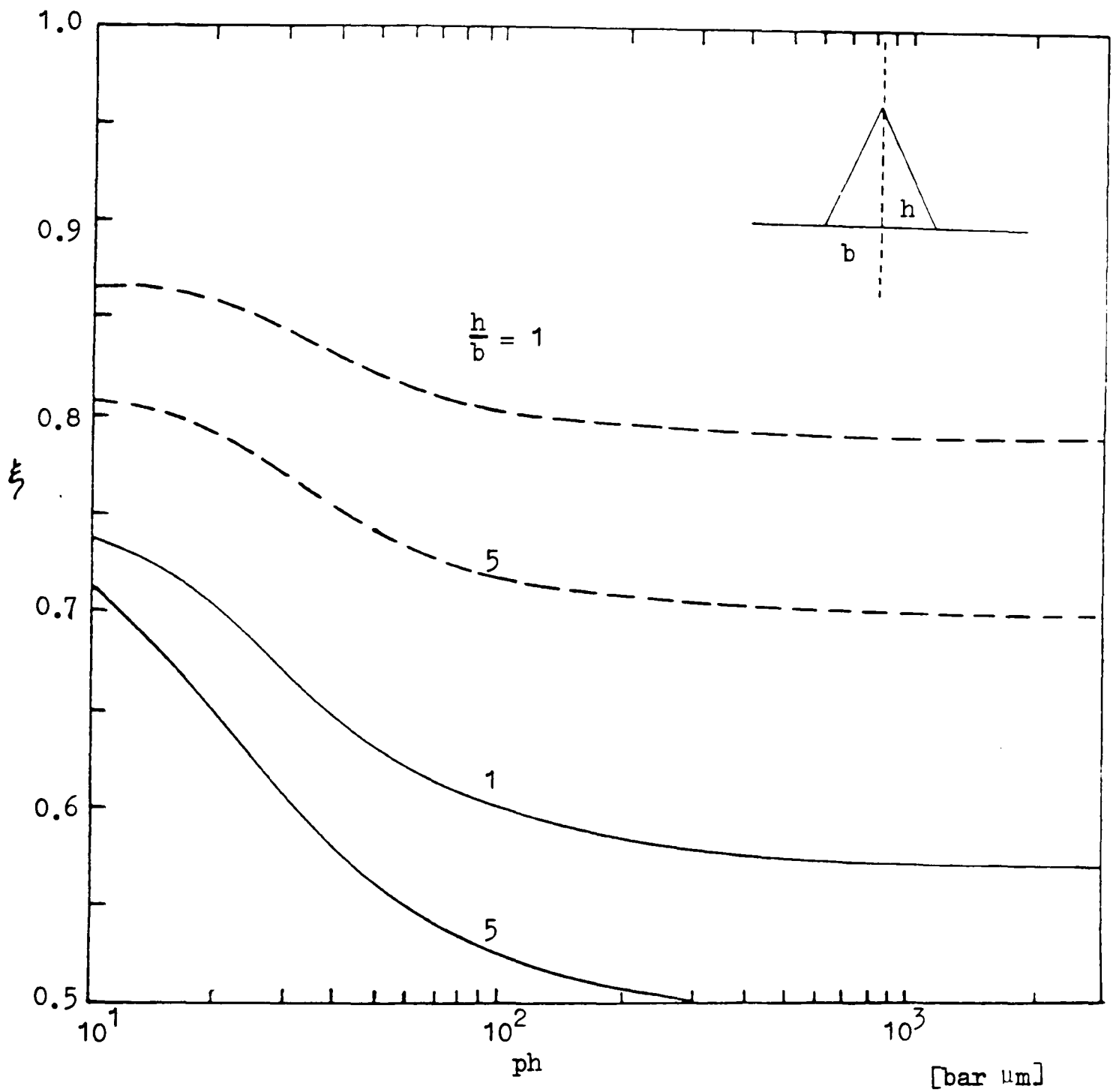


Figure 5.7(a) Roughness factor variation in  $\text{SF}_6$  ( $r_1/r_2 = 5/12.7$  mm;  $h = 150$   $\mu\text{m}$ )

— single protrusion; --- multiple protrusions

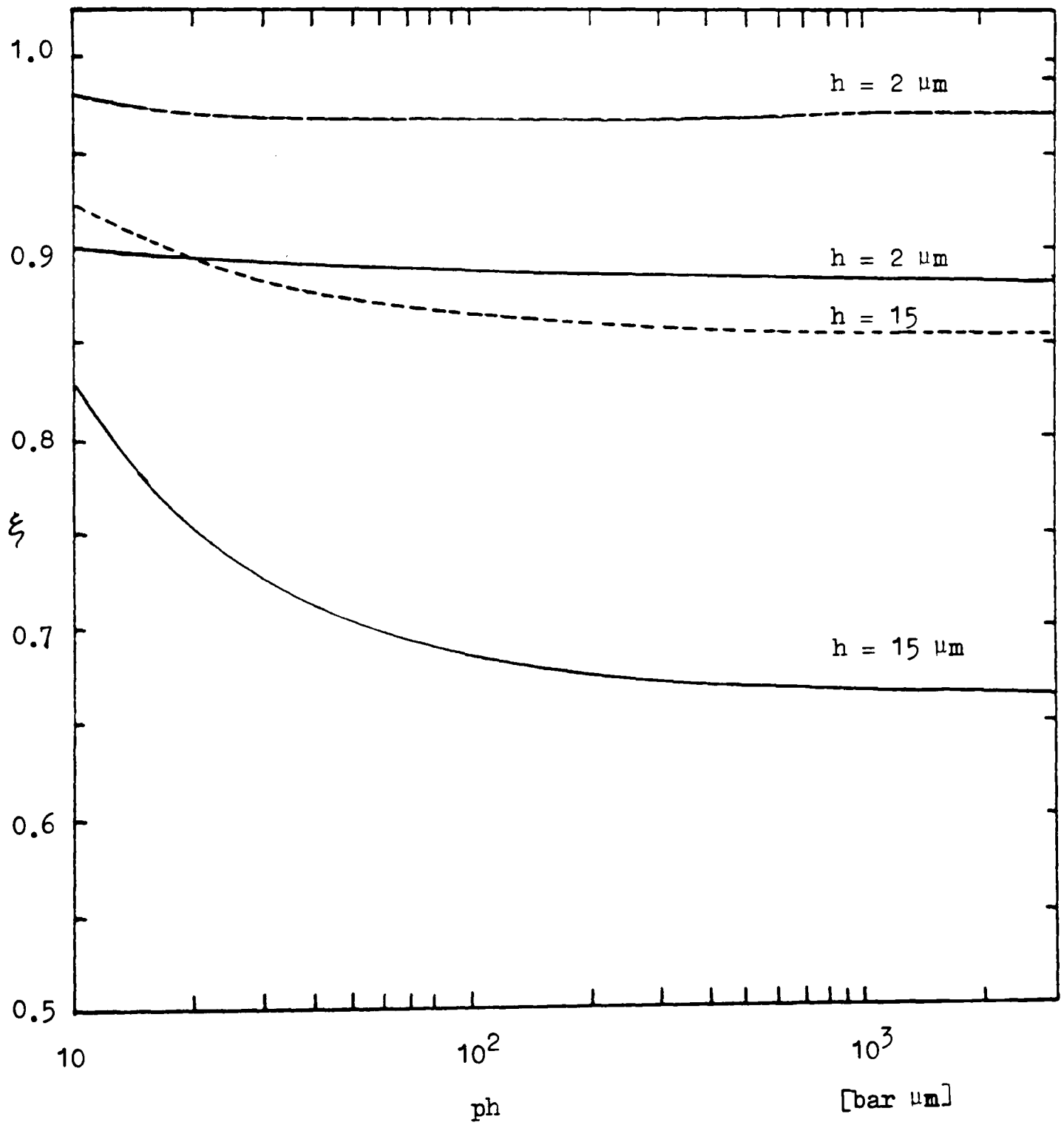


Figure 5.7(b) Effect of protrusion height ( $h/b = 1$ ) on roughness in  $\text{SF}_6$  ( $r_1/r_2 = 9.45/12.7 \text{ mm}$ )

— single protrusion;    - - - multiple protrusions

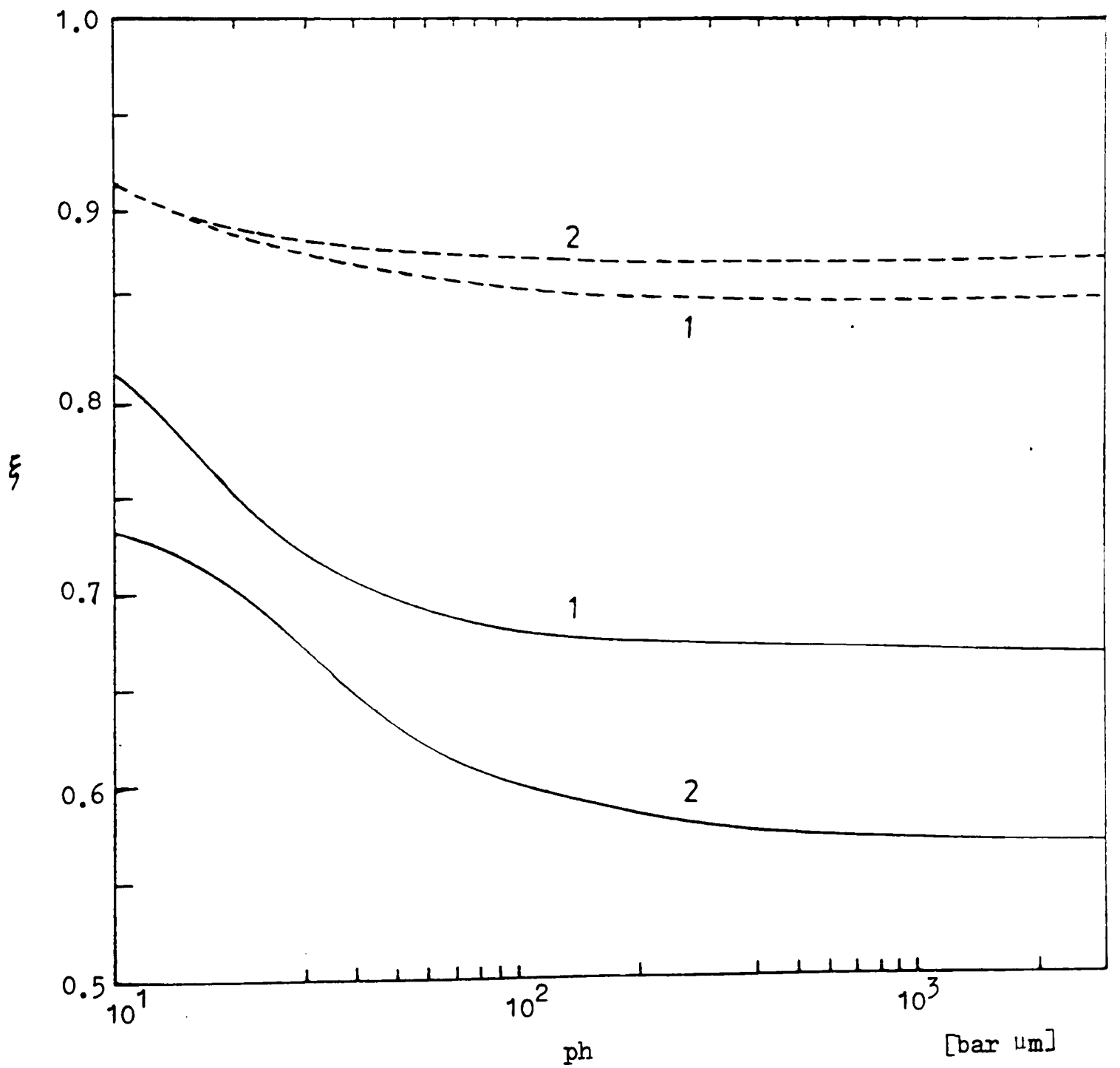


Figure 5.7(c) Effect of nonuniformity factor  $\eta F$  on surface roughness in  $SF_6$  ( $h = 20 \mu m$ )

—— Single protrusion;      ——— Multiple protrusions.

|    | $r_1/r_2$ (mm) | $\eta$ |
|----|----------------|--------|
| 1. | 9.45/12.7      | 1.16   |
| 2. | 5.0/12.7       | 1.65   |

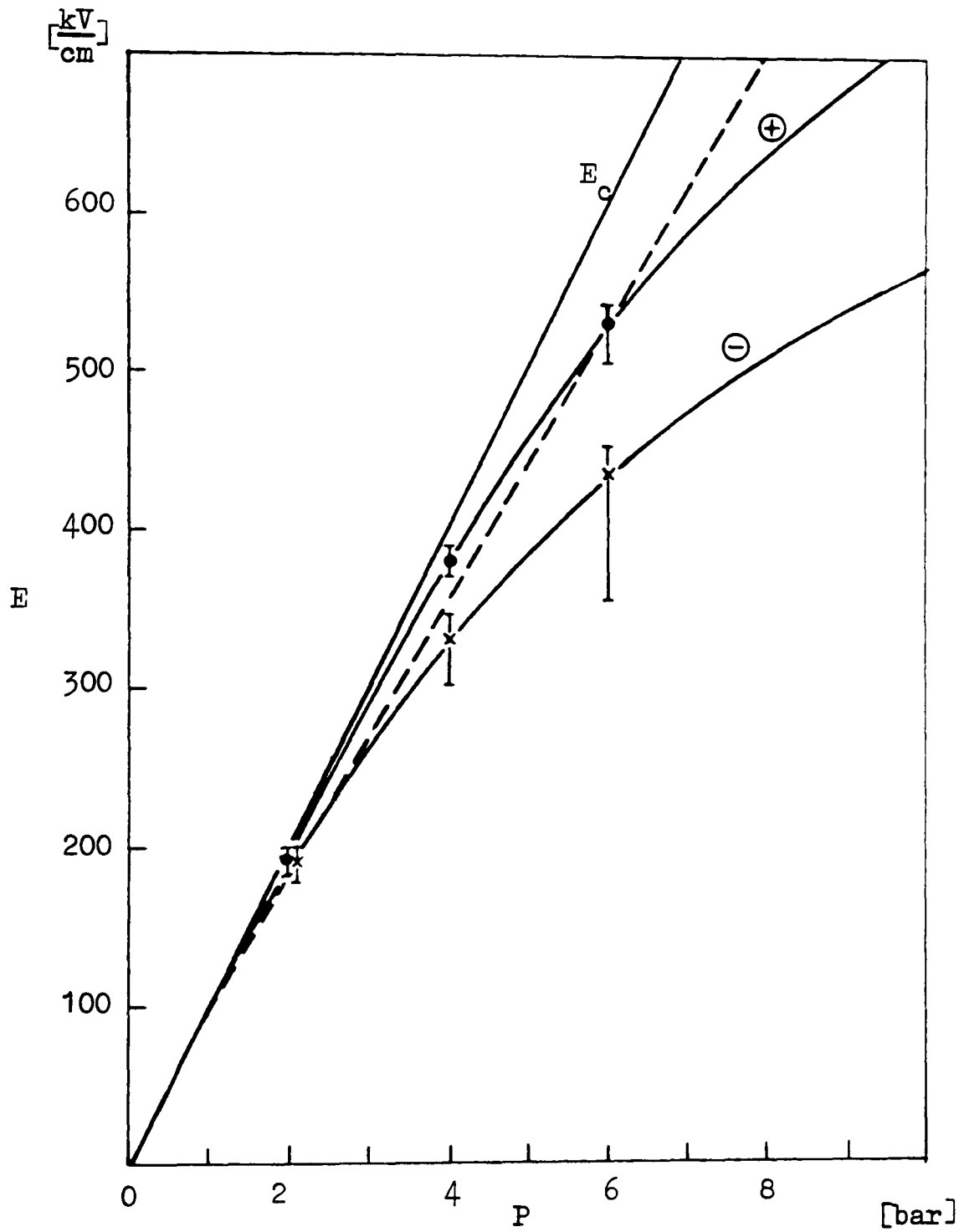


Figure 5.8 Positive and negative breakdown voltage characteristics in  $\text{SF}_6$  ( $r_1/r_2 = 5/12.7$  mm, polished (E7))

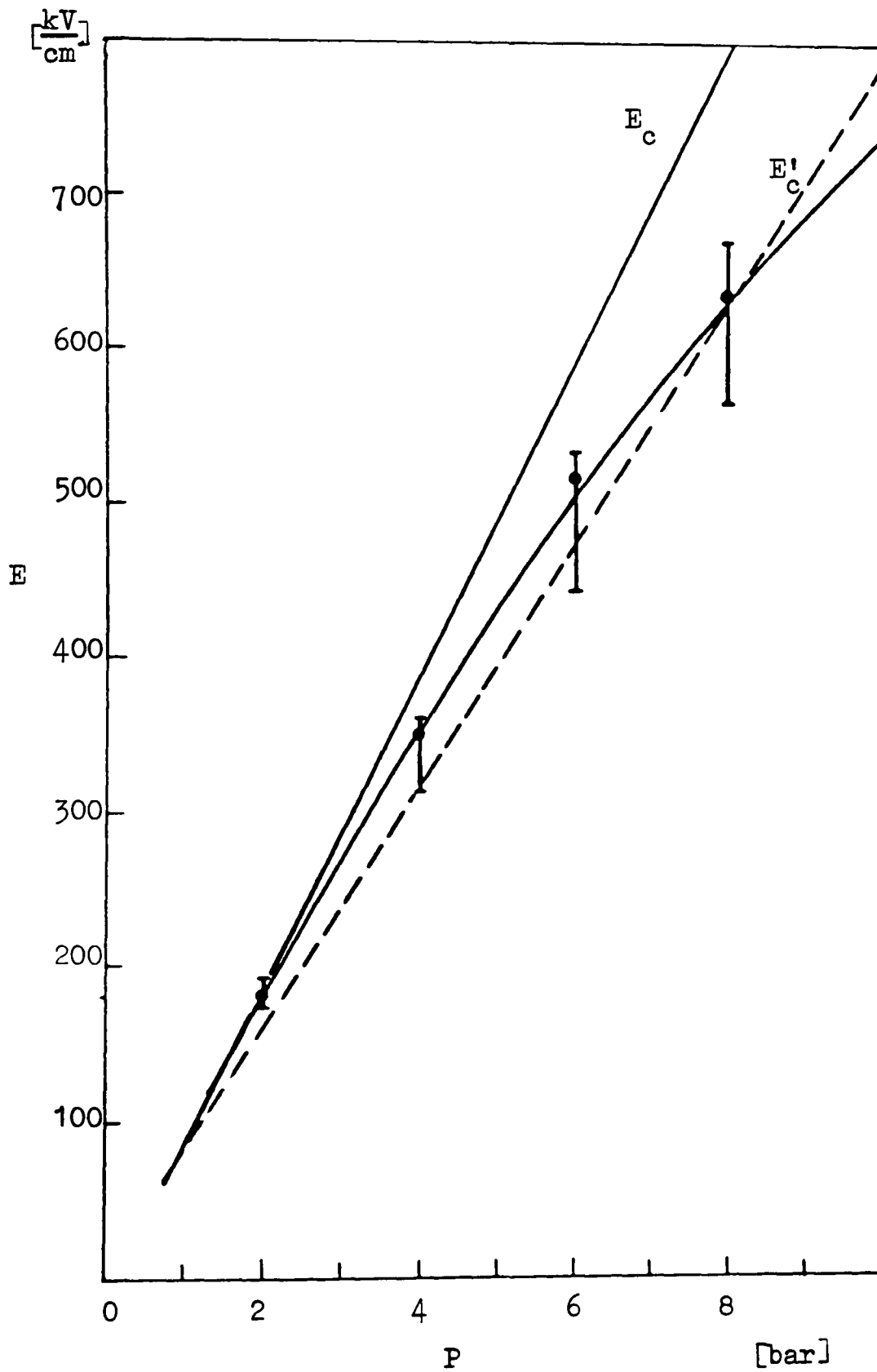


Figure 5.9 Positive dc breakdown characteristic in SF<sub>6</sub> ( $r_1/r_2 = 9.45/12.7$  mm, polished (E9))

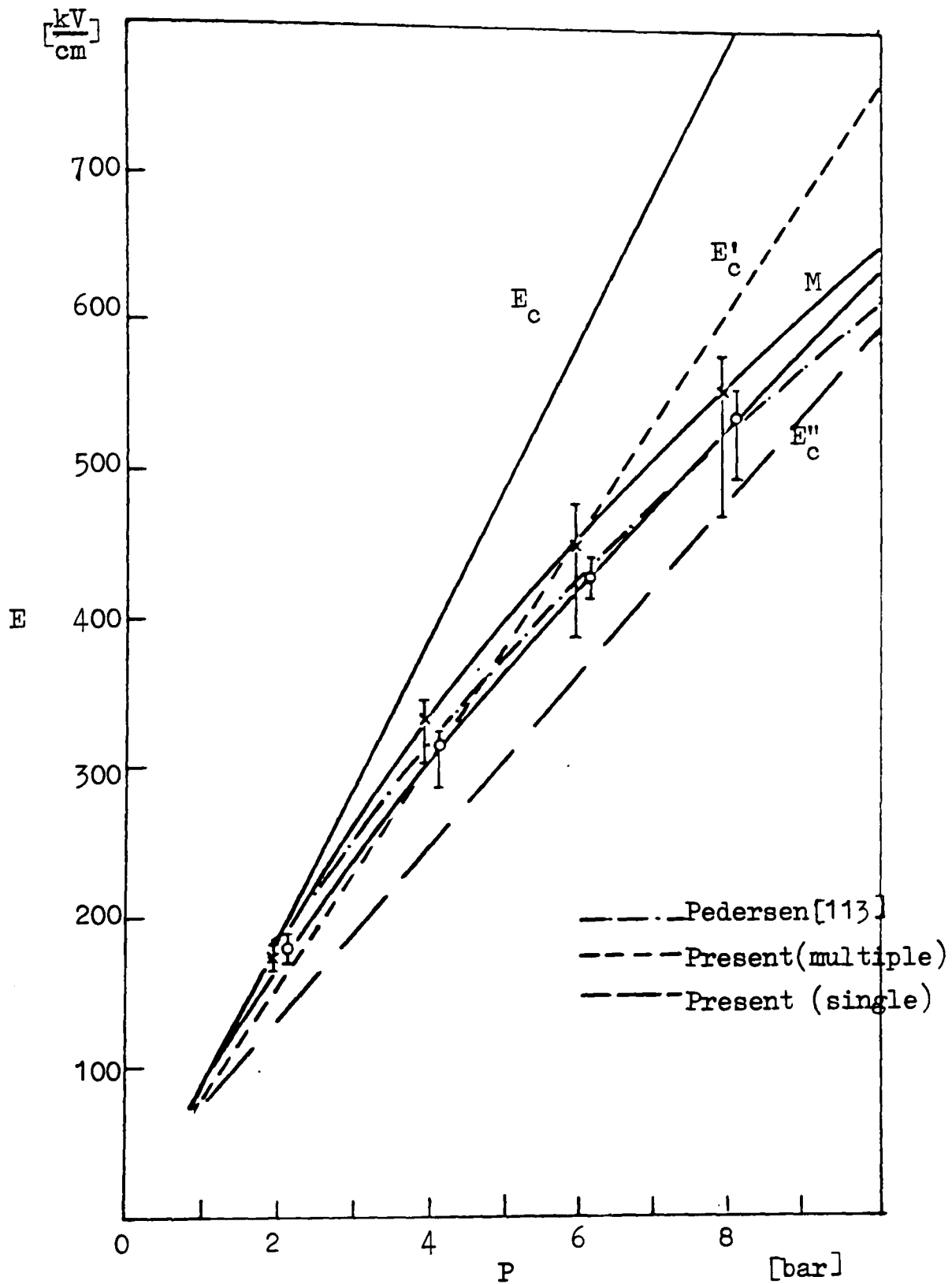


Figure 5.10 Positive dc breakdown characteristic in  $\text{SF}_6$  for rough electrodes ( $r_1/r_2 = 9.45/12.7 \text{ mm}$ )  
M-machined(E10), S-Sandblasted(E11)

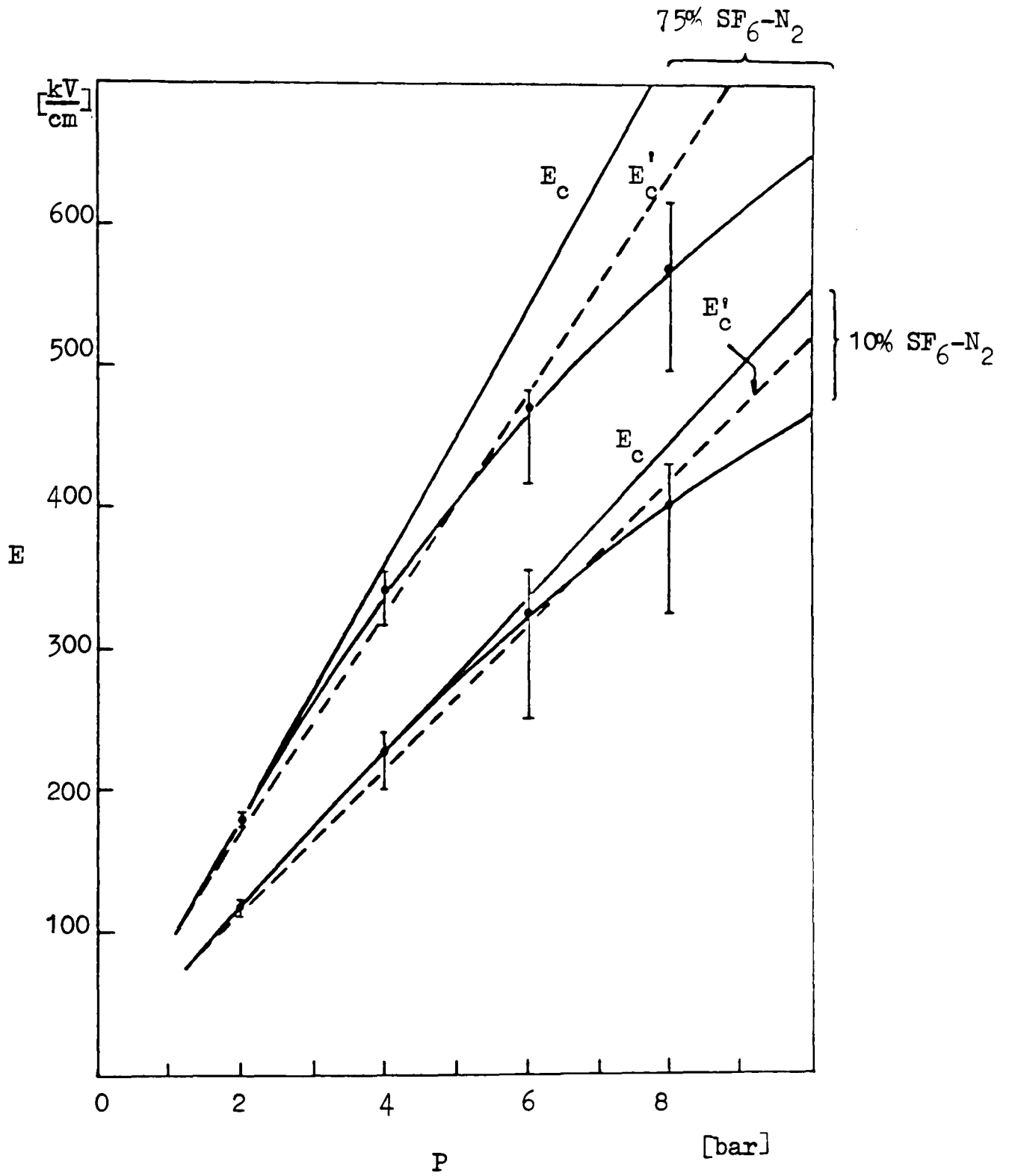


Figure 5.11 Positive breakdown characteristics in  $\text{SF}_6/\text{N}_2$  mixtures for polished electrodes.  
 ( $r_1/r_2 = 9.45/12.7$  mm, polished (E9))

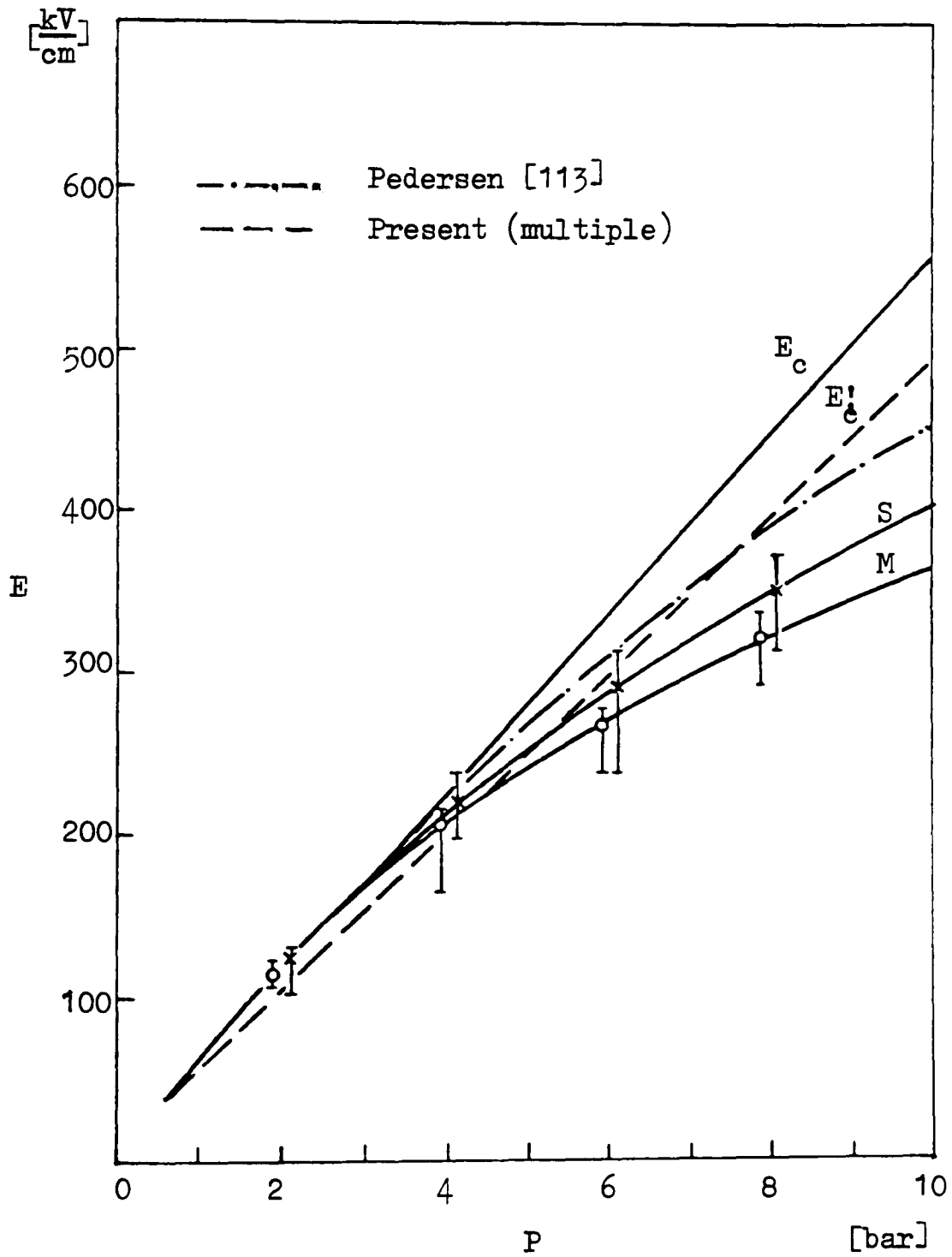


Figure 5.12 Positive breakdown characteristics in 10%  $\text{SF}_6$ -90%  $\text{N}_2$  mixtures for rough electrodes ( $r_1/r_2 = 9.45/12.7$ ; M-machined(E11); S-Sandblasted (E12))

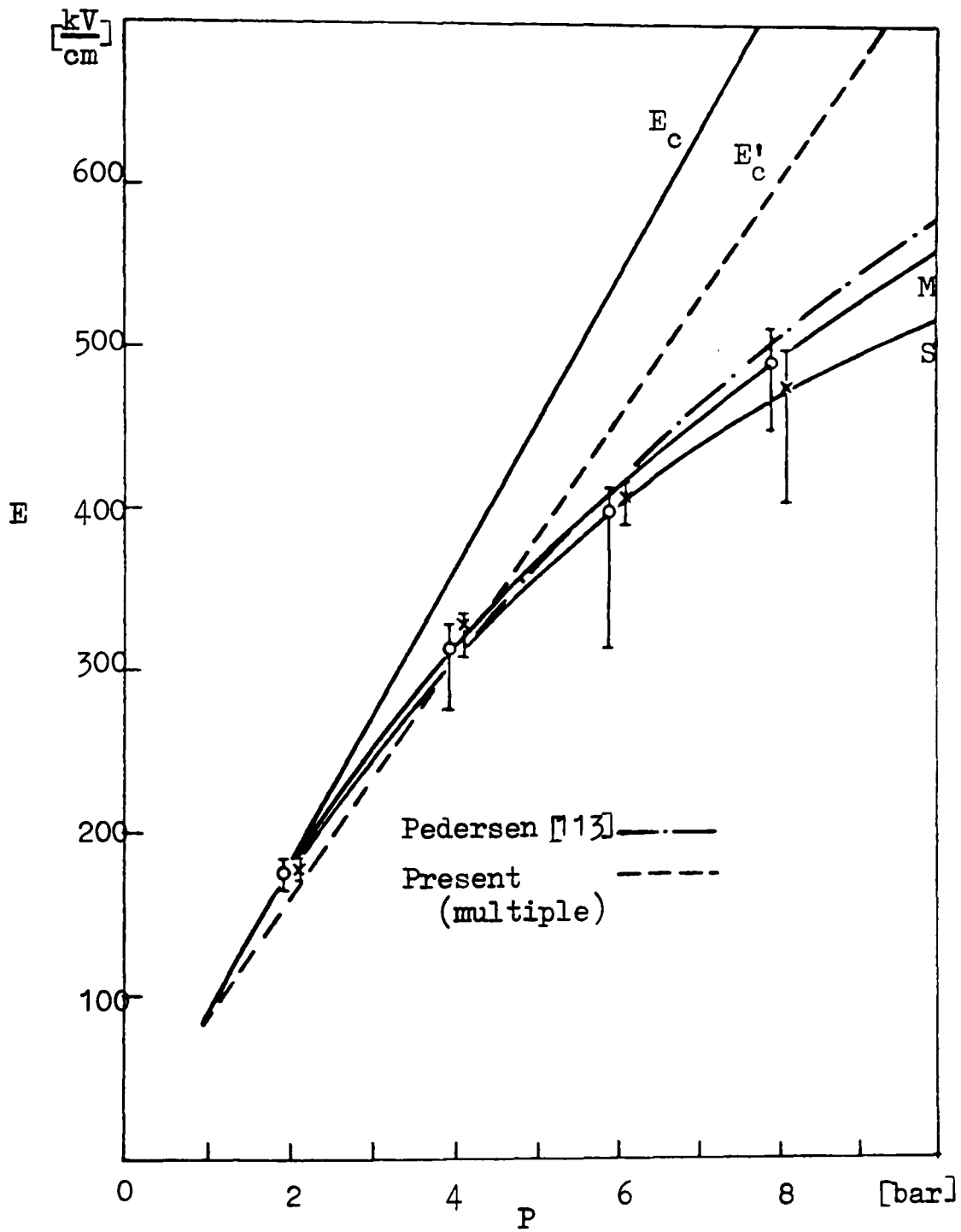


Figure 5.13 Positive breakdown characteristics in 75%  $\text{SF}_6$  - 25%  $\text{N}_2$  mixture for rough electrodes ( $r_1/r_2 = 9.45/12.7$  mm; M - machined; S - sandblasted)

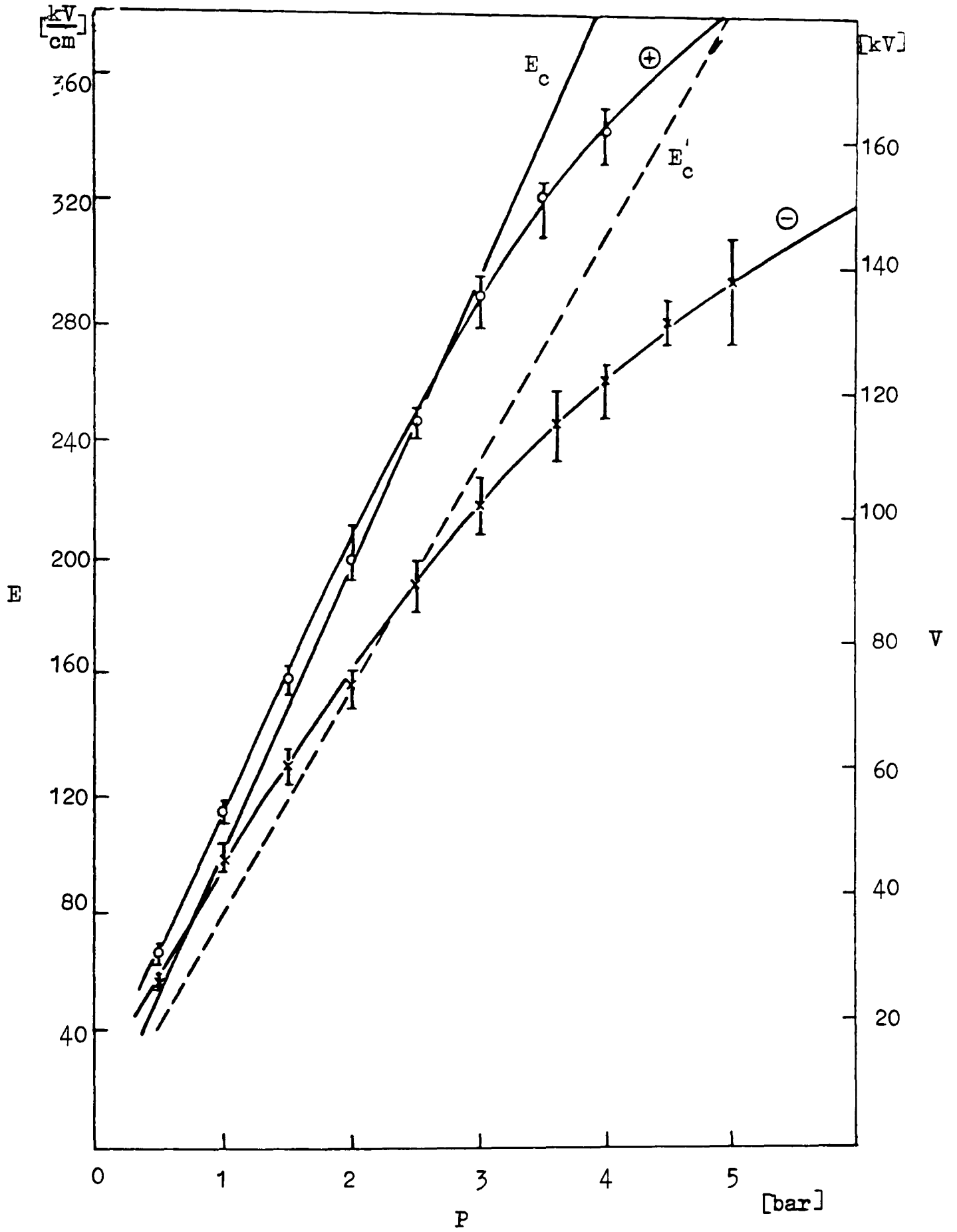


Figure 5.14 Impulse breakdown characteristics of SF<sub>6</sub> ( $r_1/r_2 = 5/12.7$  mm, sandblasted (E8))

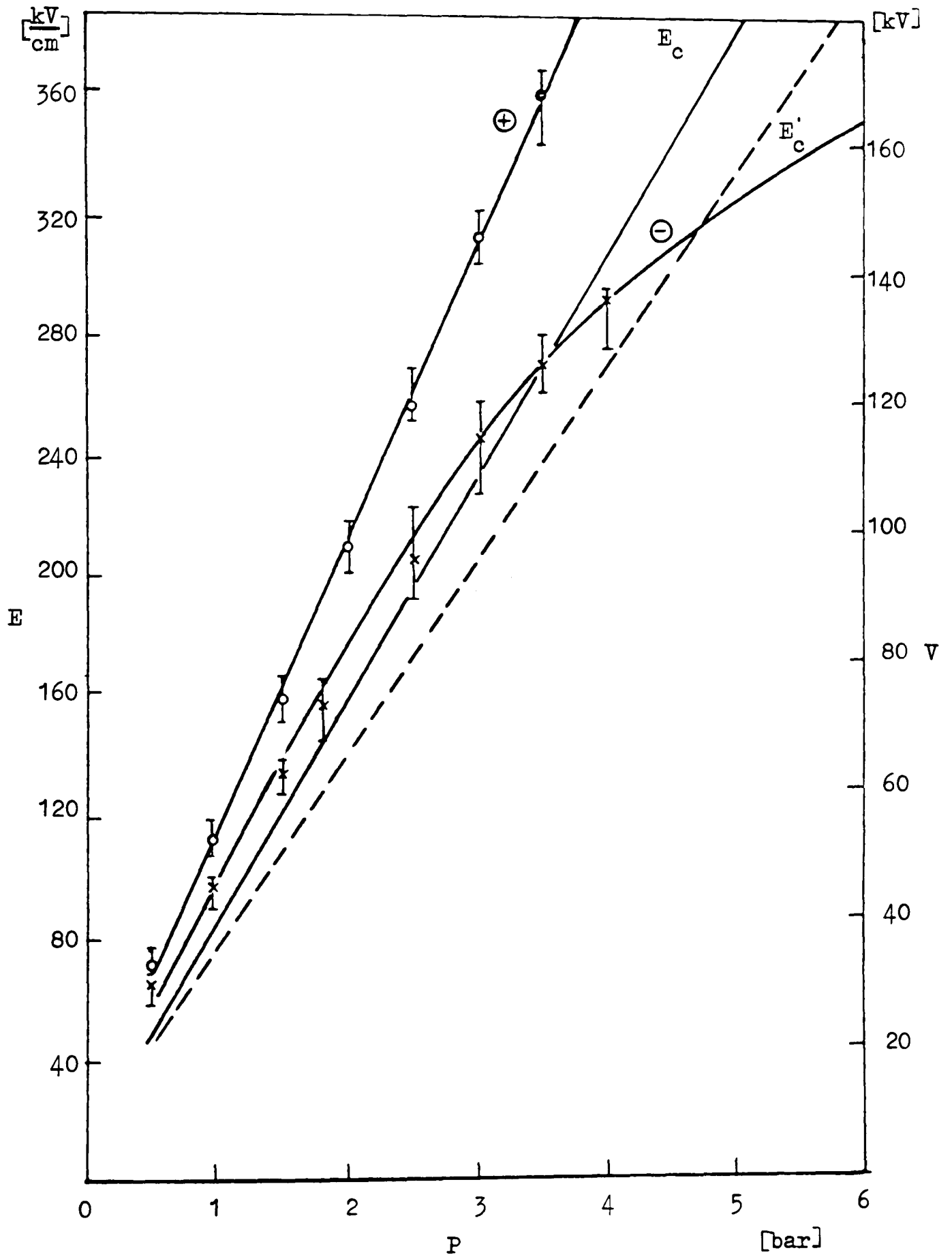


Figure 5.15 Impulse breakdown characteristics of 40% SF<sub>6</sub> - 60% N<sub>2</sub> mixture  
( $r_1/r_2 = 5/12.7$  mm, sandblasted)

Table 6.1 Some of the important features of positive corona stabilized breakdown characteristics  
 $V_o$  - corona inception voltage at  $P_m$ ;  $V_d, P_d$  - voltage and pressure at the point of deviation from the similarity law

|                         | GAS                                 | $r_1$<br>(mm) | $\eta$ | $dV/dp$<br>(kV/cm) | $P_m$<br>(bar) | $V_m$<br>(kV) | $V_o$<br>(kV) | $P_o$<br>(bar) | $V_o$<br>(kV) | $P_d$<br>(bar) | $V_d$<br>(kV)  | Comments on negative<br>breakdown region   |
|-------------------------|-------------------------------------|---------------|--------|--------------------|----------------|---------------|---------------|----------------|---------------|----------------|--|--|
| $r_2 = 12.7 \text{ mm}$ | 10% SF <sub>6</sub> -N <sub>2</sub> | 0.15          | 18.8   | 15                 | 3.5            | 47            | 24            | 5              | 32            | 6.0            | 37   | Cont., narrow (1 bar), gradual decay<br>Cont., narrow (1 bar), gradual<br>Cont., very narrow (0.2 bar), flat<br>Cont., very narrow (0.2 bar), flat |
|                         |                                     | 0.25          | 12.6   | 16                 | 2.8            | 42            | 28            | 4              | 37            | 5.5            | 47   |  |
|                         |                                     | 0.5           | 7.5    | 23                 | 2.2            | 38            | 31            | 3.2            | 43            | 3.6            | 48   |  |
|                         |                                     | 1.0           | 4.6    | 27                 | 1.7            | 29            | 26            | 2.2            | 36            | 2.8            | 50   |  |
|                         | 40% SF <sub>6</sub> -N <sub>2</sub> | 0.15          |        | 25                 | 2.8            | 43            | 24            | 5.5            | 42            | 6.0            | 45   | Cont., wide (2 bar), flat<br>Cont., wide (1.5 bar) flat<br>Cont., narrow (0.2 bar)<br>No max.  |
|                         |                                     | 0.25          | "      | 22                 | 2.4            | 44            | 29            | 4.2            | 45            | 5.7            | 60   |  |
|                         |                                     | 0.5           |        | 24                 | 1.8            | 43            | 31            | 3.2            | 53            | 4.0            | 62   |  |
|                         |                                     | 1.0           |        | 32                 | x              | x             | x             | 2.6            | 56            | 4.0            | 87   |  |
|                         | 75% SF <sub>6</sub> -N <sub>2</sub> | 0.15          |        | -                  | -              | -             | -             | -              | -             | -              | -  | -  |
|                         |                                     | 0.25          | "      | -                  | -              | -             | -             | -              | -             | -              | -  |  |
|                         |                                     | 0.5           |        | 32                 | 2.2            | 51            | 44            | 3.0            | 57            | 4.5            | 80   |  |
|                         |                                     | 1.0           |        | -                  | -              | -             | -             | -              | -             | -              | -  |  |
| SF <sub>6</sub>         | 0.15                                |               | 35     | 2.8                | 60             | 34            | 5.0           | 56             | 5.0           | 56             | Cont., narrow (1 bar), $P_o = P_d$<br>Cont., narrow (0.4 bar), $P_o = P_d$ , sharp<br>Cont., narrow (0.2 bar), flat<br>No max. |  |
|                         | 0.25                                | "             | 31     | 2.5                | 70             | 41            | 4.0           | 56             | 4.0           | 56             |  |  |
|                         | 0.5                                 |               | 33     | 2.4                | 57             | 47            | 3.2           | 61             | 3.6           | 66             |  |  |
|                         | 1.0                                 |               | 42     | x                  | x              | x             | 2.4           | 68             | 3.2           | 88             |  |  |
| $r_2 = 25 \text{ mm}$   | 10% SF <sub>6</sub> -N <sub>2</sub> | 0.15          | 32.4   | 47                 | 2.7            | 107           | 22            | 6.5            | 41            | 7.0            | 42   | Cont., wide (2 bar), gradual<br>Cont., wide (1.5 bar), gradual<br>Cont., narrow (0.4 bar), flat  |
|                         |                                     | 0.5           | 12.5   | 49                 | 1.7            | 71            | 31            | 3.0            | 50            | 6.0            | 89   |  |
|                         |                                     | 1.0           | 7.4    | 42                 | 1.4            | 54            | 38            | 2.4            | 62            | 2.8            | 70   |  |
|                         | 40% SF <sub>6</sub> -N <sub>2</sub> | 0.15          |        | 63                 | 2.0            | 103           | 21            | 6.8            | 53            | 6.8            | 52   | Cont., stepwise, wide (4 bar), gradual<br>Cont., wide (1.5 bar), sharp<br>Cont., narrow (0.4 bar) sharp  |
|                         |                                     | 0.5           | "      | 65                 | 1.4            | 88            | 32            | 3.0            | 60            | 5.5            | 102  |  |
|                         |                                     | 1.0           |        | 62                 | 1.1            | 69            | 38            | 2.5            | 80            | 3.5            | 104  |  |
|                         | 75% SF <sub>6</sub> -N <sub>2</sub> | 0.15          |        | -                  | -              | -             | -             | -              | -             | -              | -  | -  |
|                         |                                     | 0.5           | "      | 93                 | 1.2            | 100           | 32            | 3.0            | 72            | 4.0            | 90   |  |
|                         |                                     | 1.0           |        | -                  | -              | -             | -             | -              | -             | -              | -  |  |
|                         | SF <sub>6</sub>                     | 0.15          |        | 110                | 3.0            | 160           | 35            | 7.2            | 68            | 7.4            | 70   | Cont., wide (2.5 bar), gradual<br>Cont., stepwise, wide (?), gradual<br>Cont., narrow (0.4 bar)  |
|                         |                                     | 0.5           | "      | 116                | 0.8            | 97            | 25            | 2.6            | 67            | 3.0            | 70   |  |
|                         |                                     | 1.0           |        | 95                 | 1.2            | 78            | 50            | 2.0            | 83            | 3.2            | 112  |  |

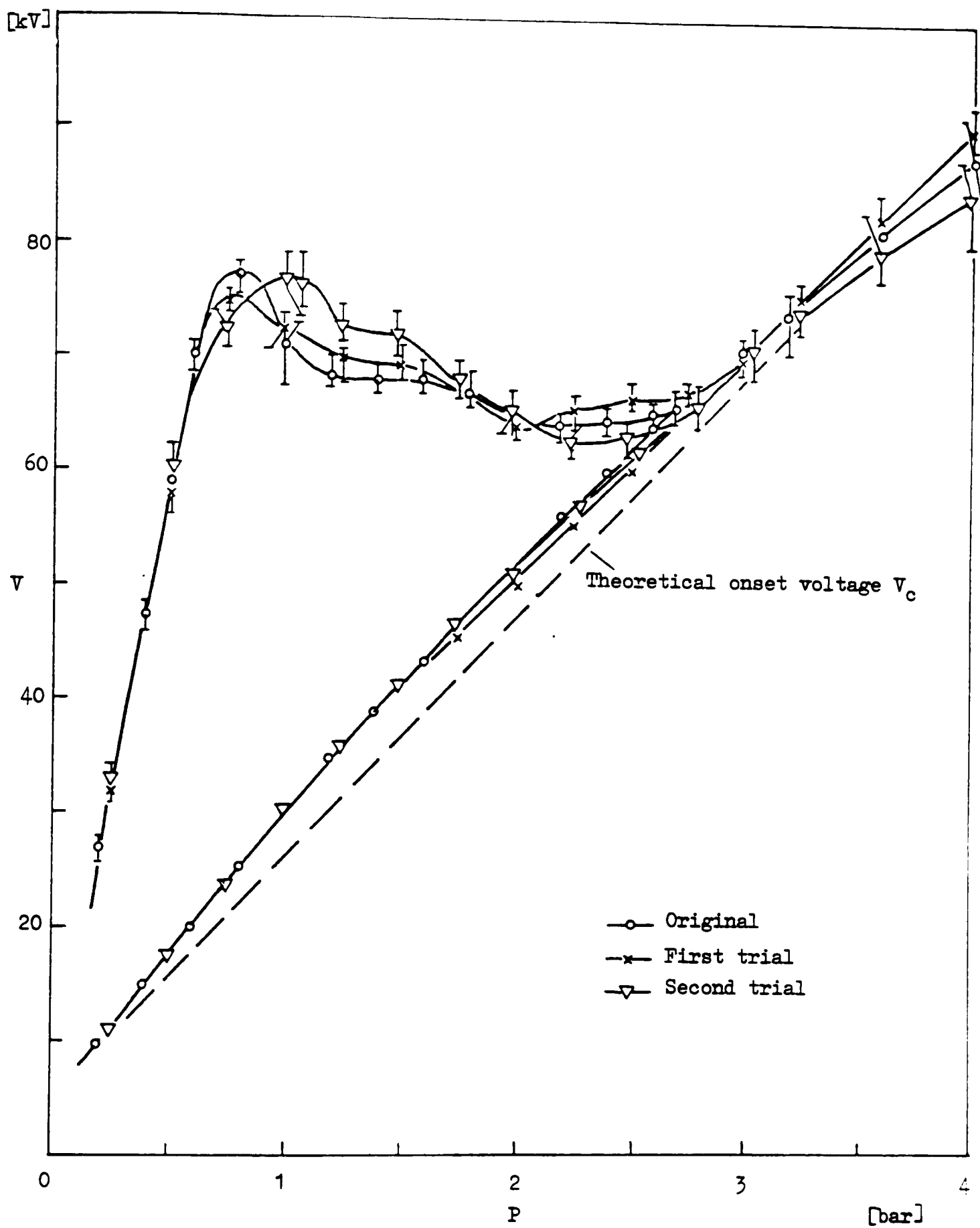


Figure 6.1 Influence of repeated trials on positive dc breakdown characteristics of  $SF_6$  ( $r_1/r_2 = 0.5/25$  mm)

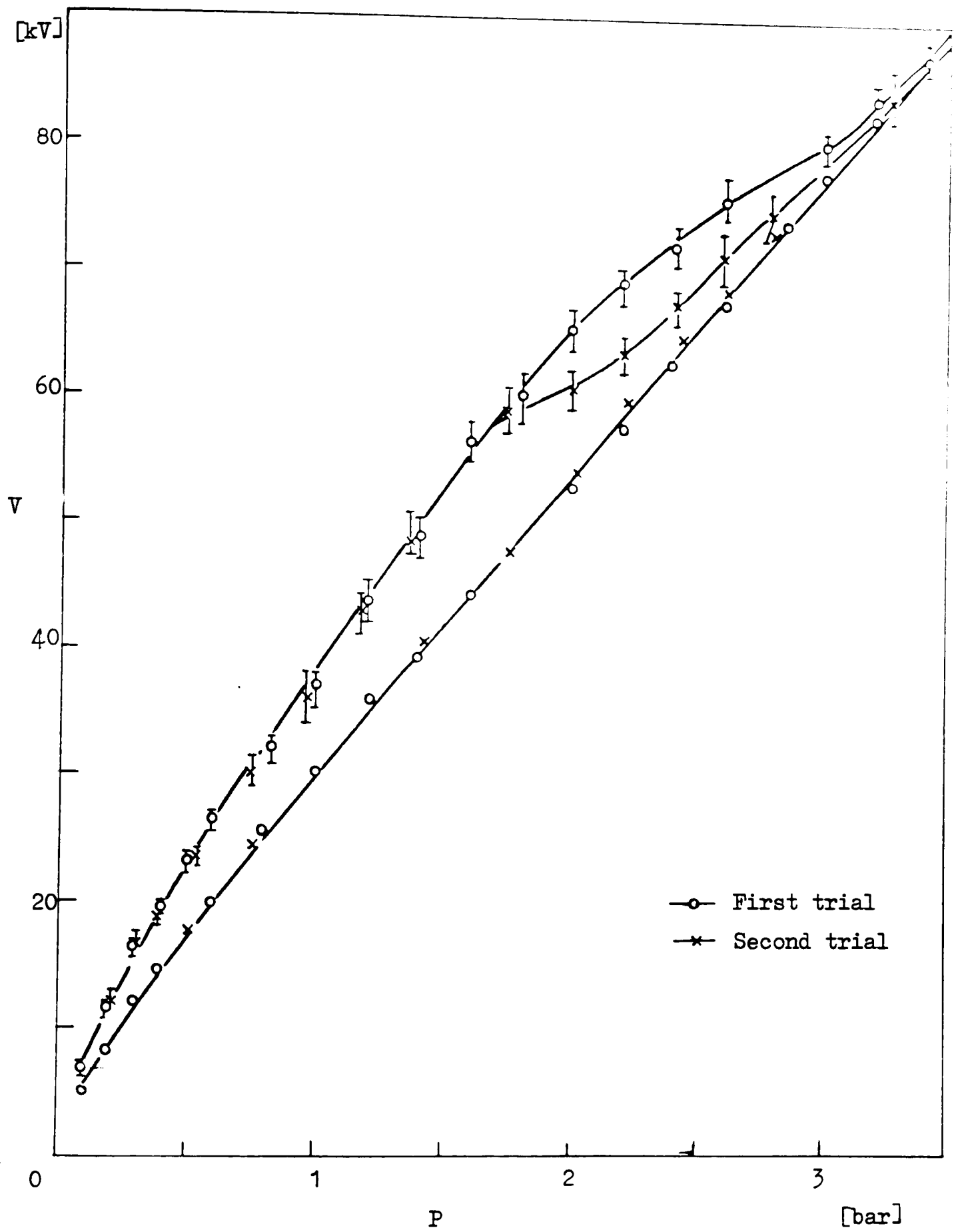


Figure 6.2 Effect of repeated trials on negative dc breakdown characteristics of SF<sub>6</sub>.  
 ( $r_1/r_2 = 1/12.7$  mm)

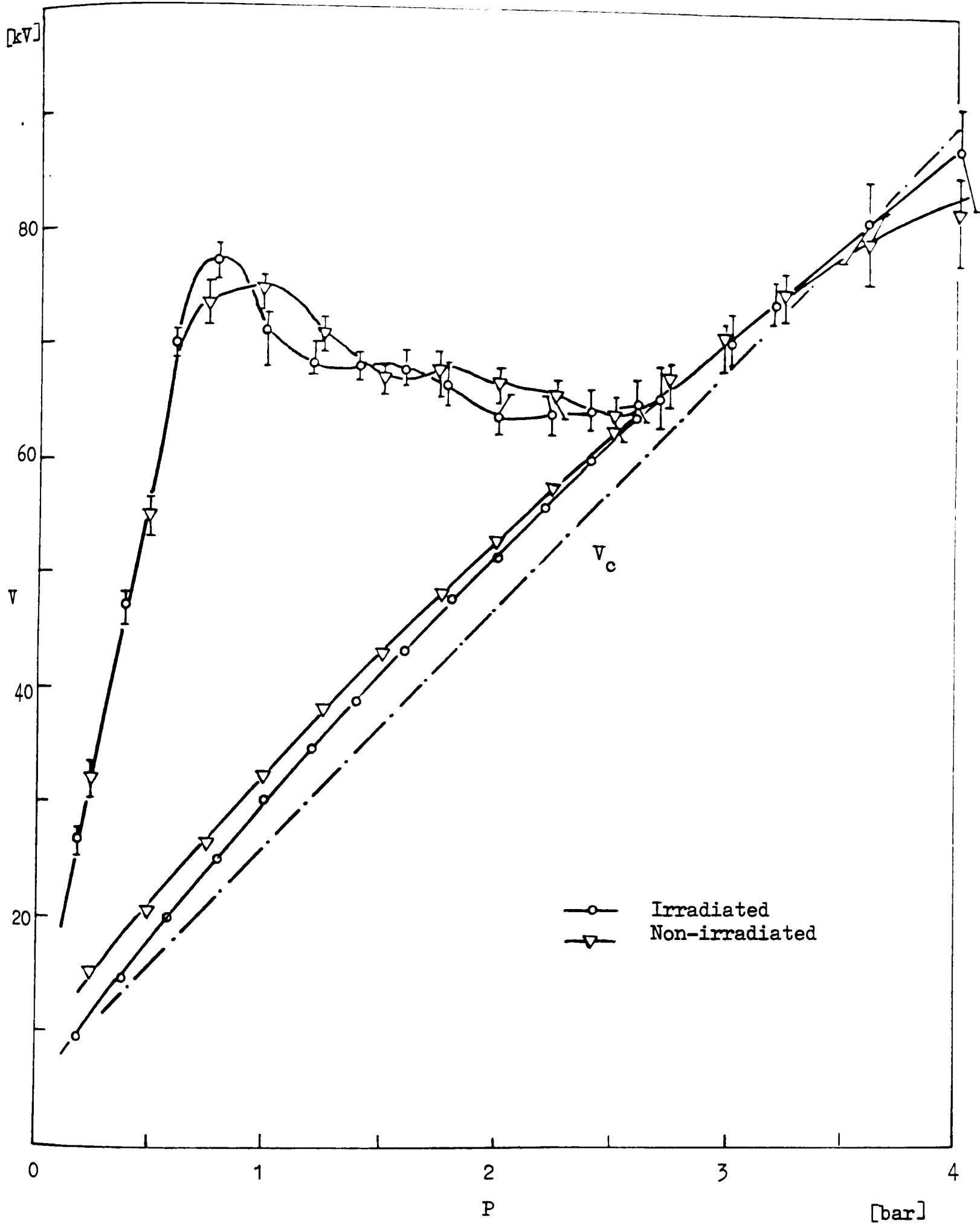


Figure 6.3 Effect of irradiation on positive dc breakdown characteristic of  $\text{SF}_6$ . ( $r_1/r_2 = 0.5/25$  mm)

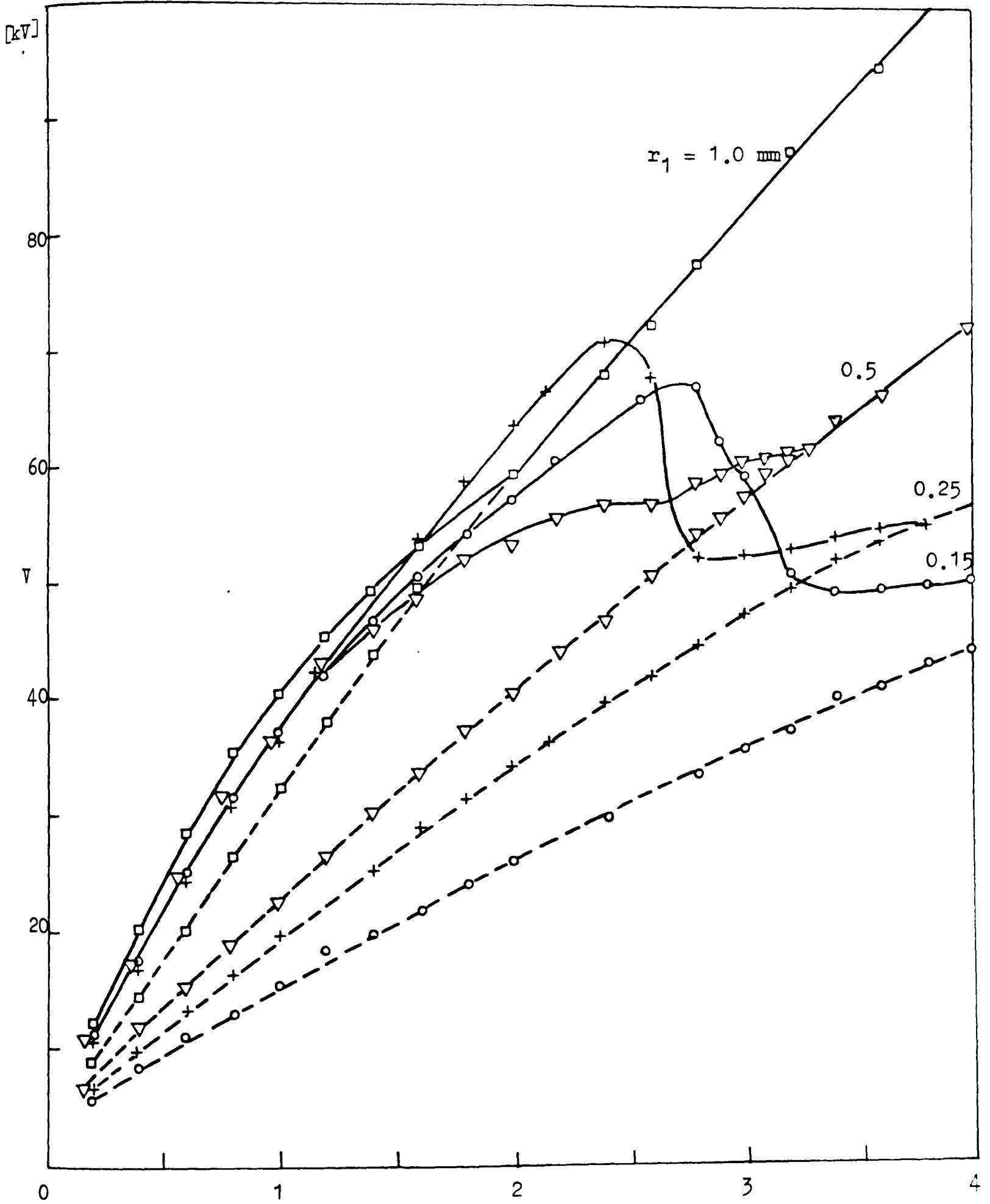


Figure 6.4 Influence of gap nonuniformity on the positive dc breakdown voltage behaviour of SF<sub>6</sub>. ( $r_2 = 12.7 \text{ mm}$ )

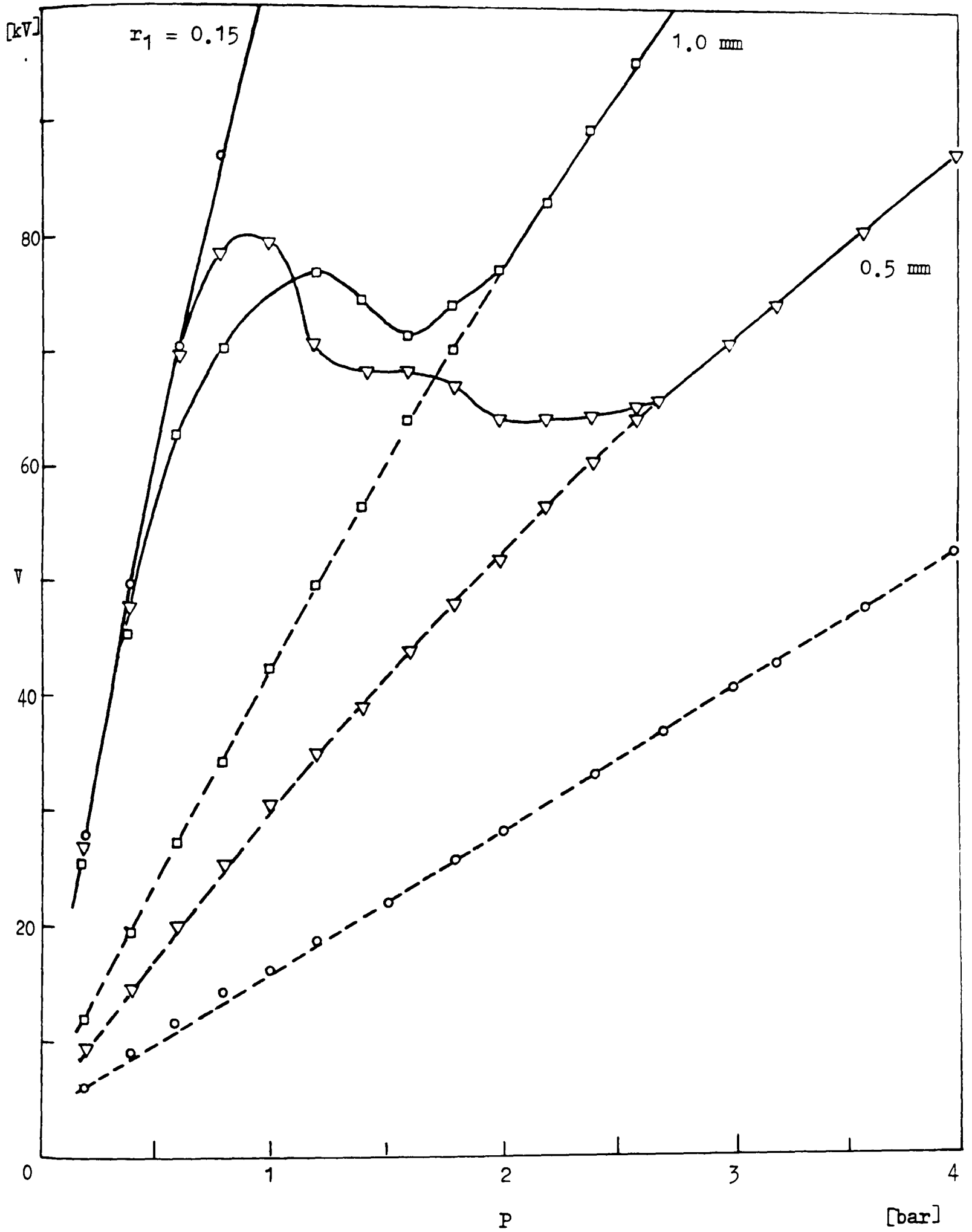


Figure 6.5 Influence of gap nonuniformity on the positive dc breakdown behaviour of  $\text{SF}_6$  ( $r_2 = 25$  mm)

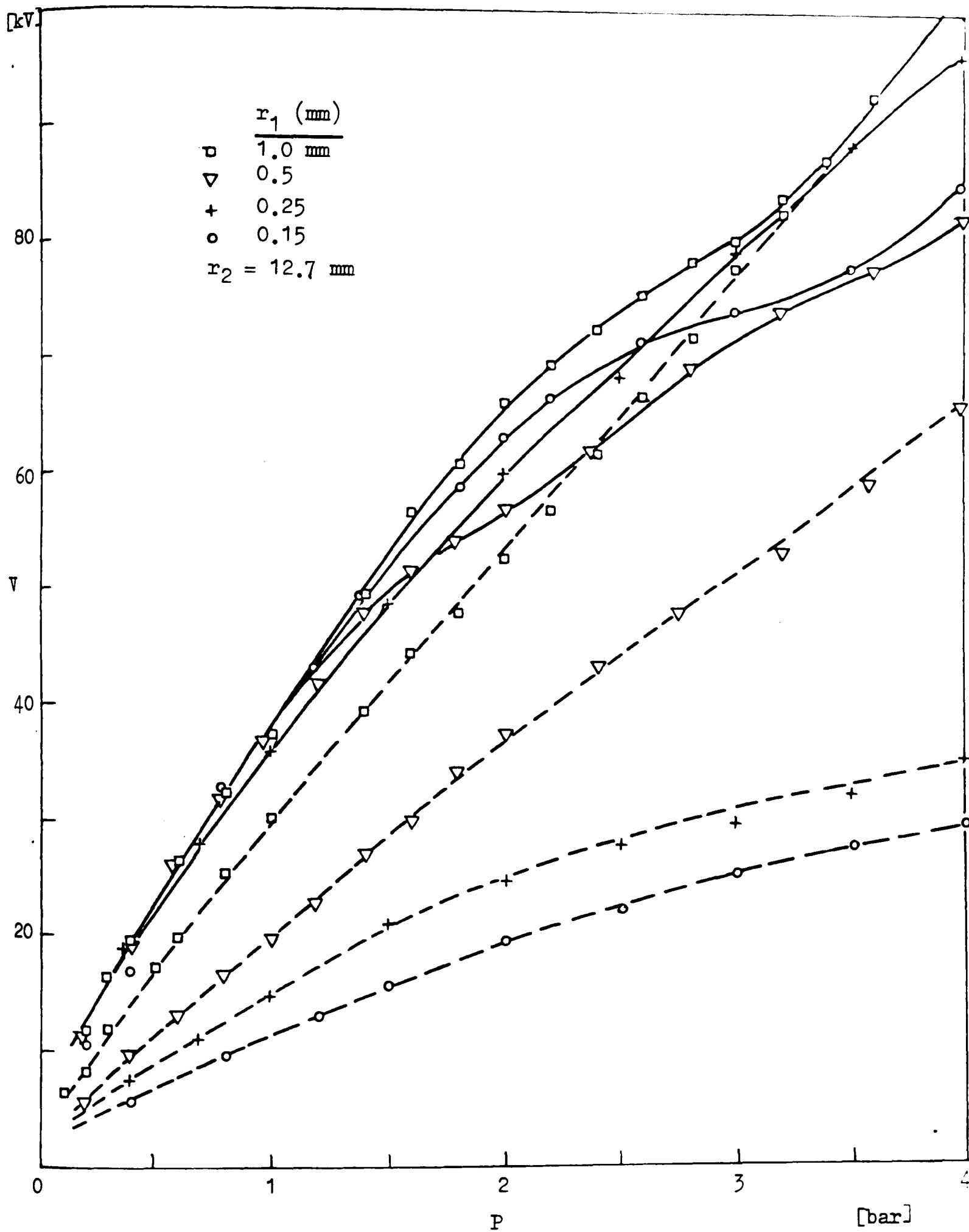


Figure 6.6 Effect of gap nonuniformity on negative dc breakdown characteristic of SF<sub>6</sub> ( $r_2 = 12.7$  mm)

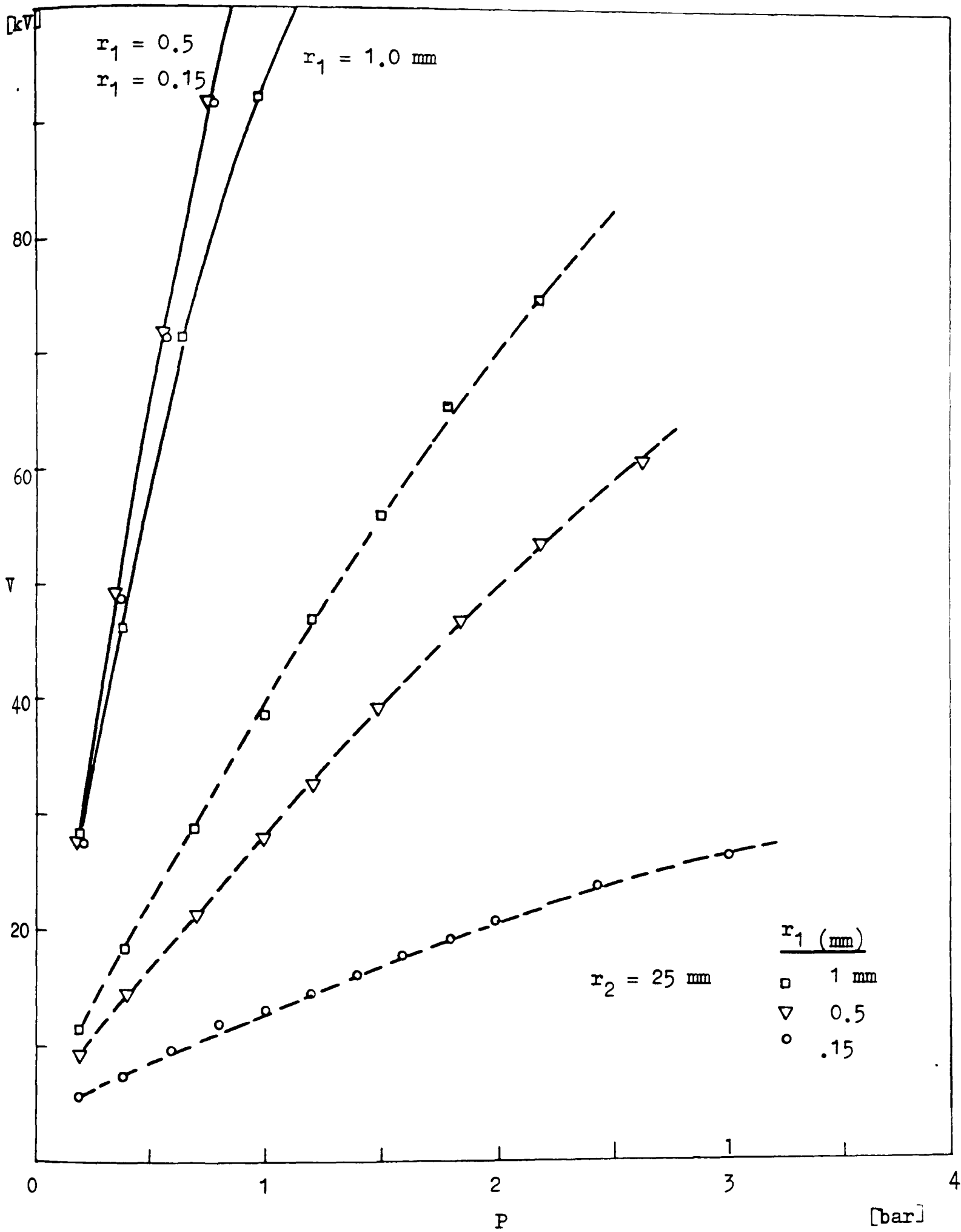


Figure 6.7 Effect of gap nonuniformity on negative breakdown characteristic of SF<sub>6</sub> ( $r_2 = 25 \text{ mm}$ )

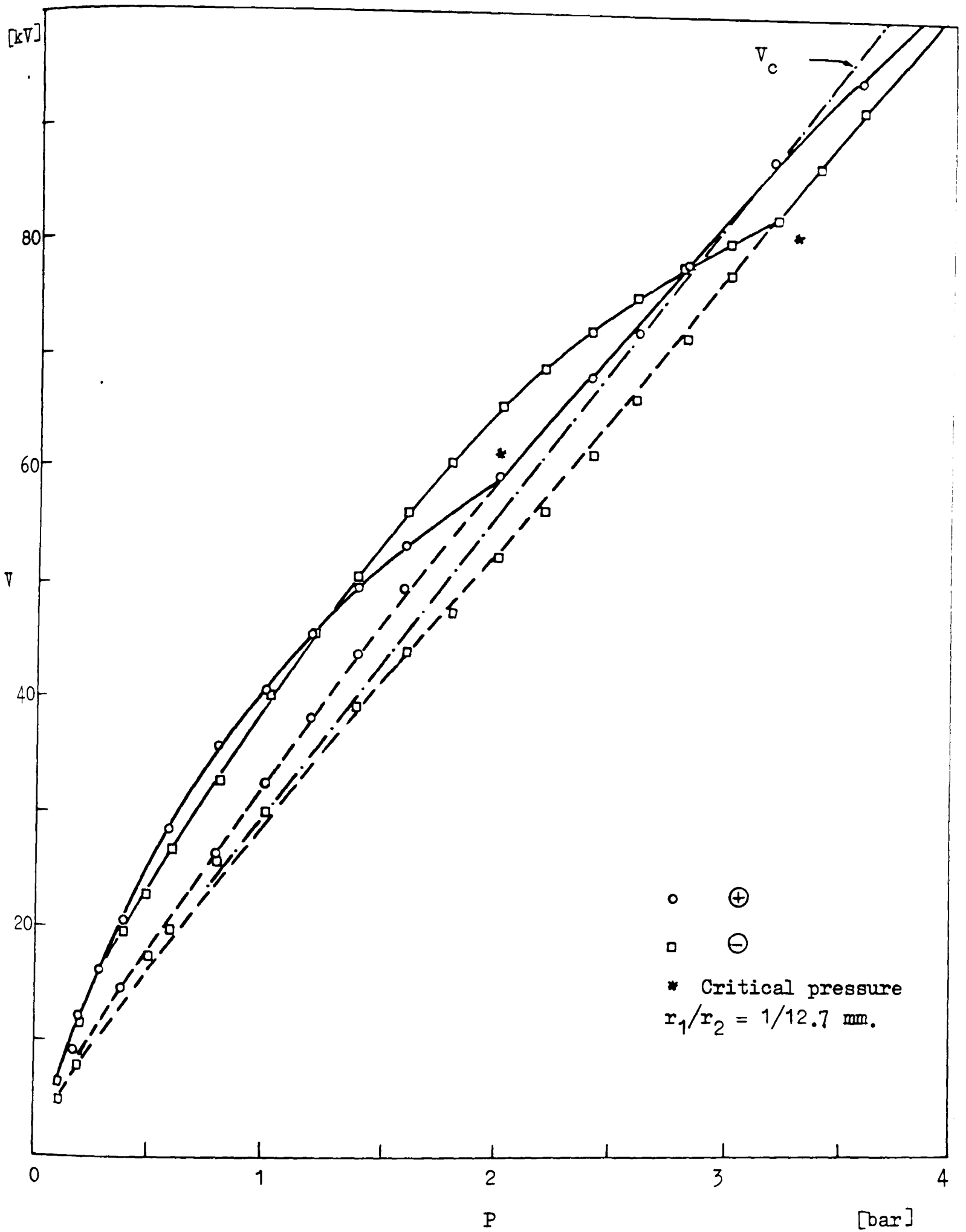


Figure 6.8 Influence of polarity on breakdown behaviour of  $\text{SF}_6$  in the gap having electrodes with radii  $r_1/r_2 = 1/12.7$  mm

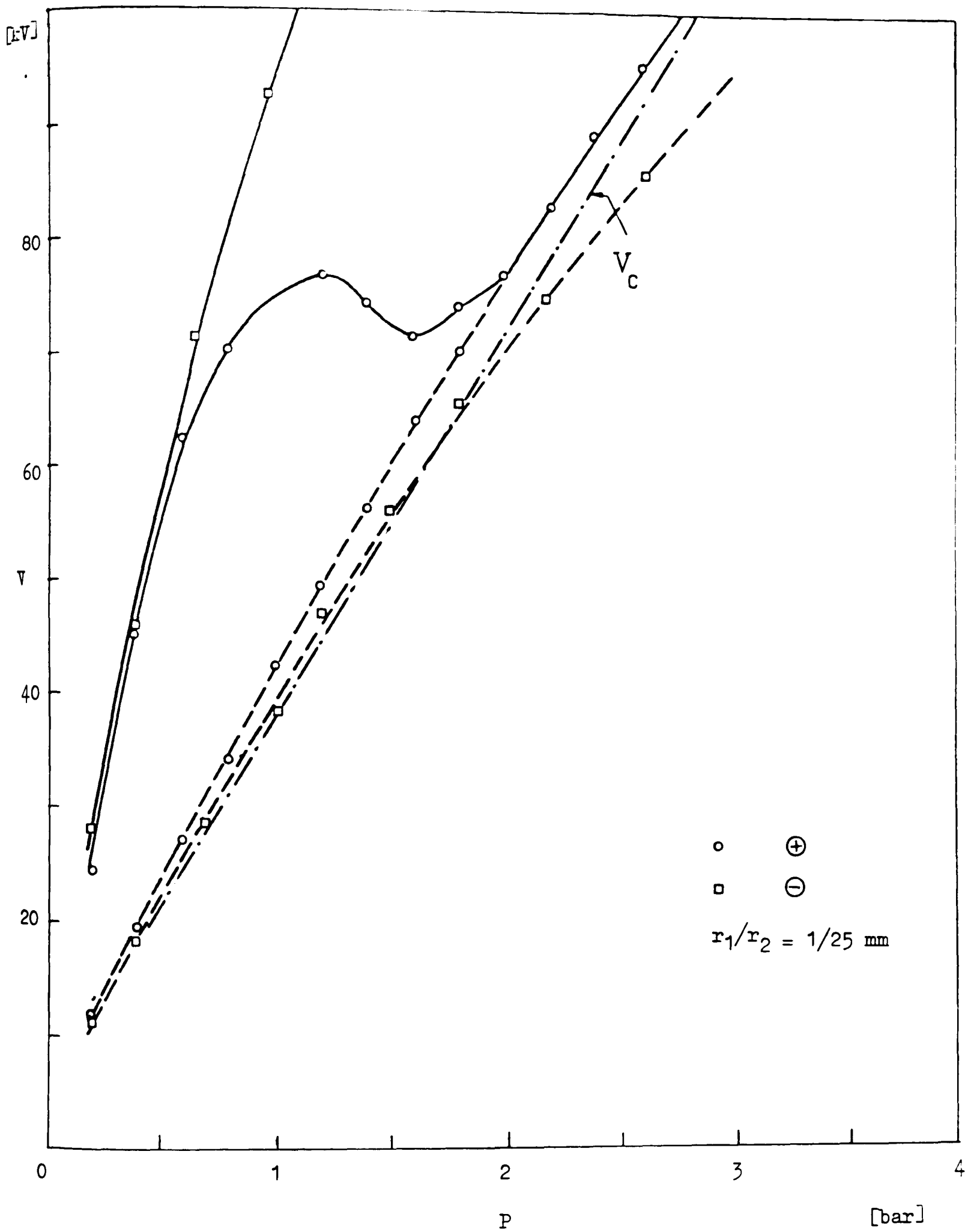


Figure 6.9 Influence of polarity on breakdown behaviour of  $SF_6$  in the gap having electrodes with radii  $r_1/r_2 = 1./25$  mm.

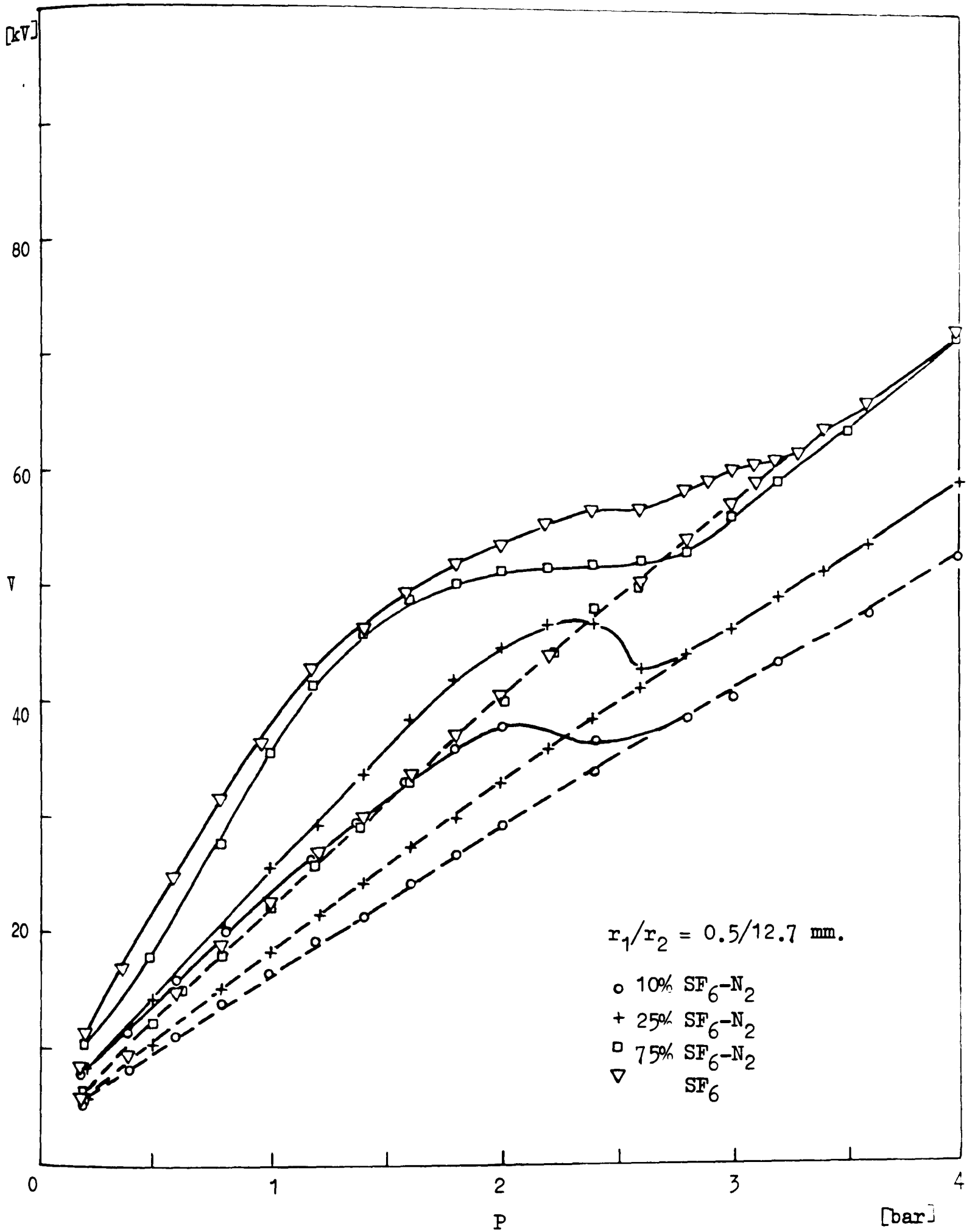


Figure 6.10 Influence of concentration of SF<sub>6</sub> on positive breakdown characteristics of SF<sub>6</sub>/N<sub>2</sub> mixture in the gap with electrodes having radii  $r_1/r_2 = 0.5/12.7 \text{ mm.}$

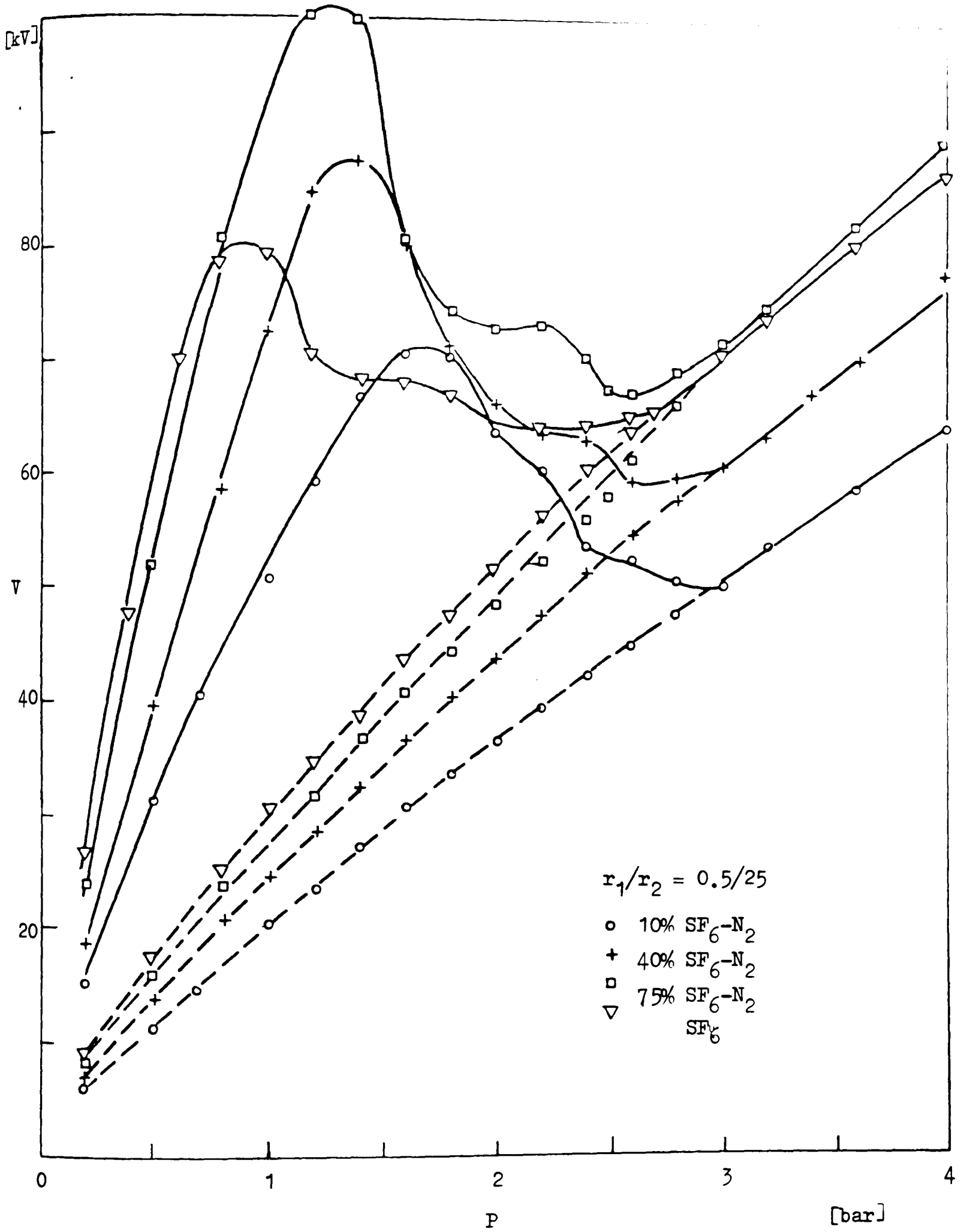


Figure 6.11 Influence of concentration of SF<sub>6</sub> on positive breakdown characteristics of SF<sub>6</sub>/N<sub>2</sub> mixtures in the gap with electrodes having radii  $r_1/r_2 = 0.5/25$  mm.

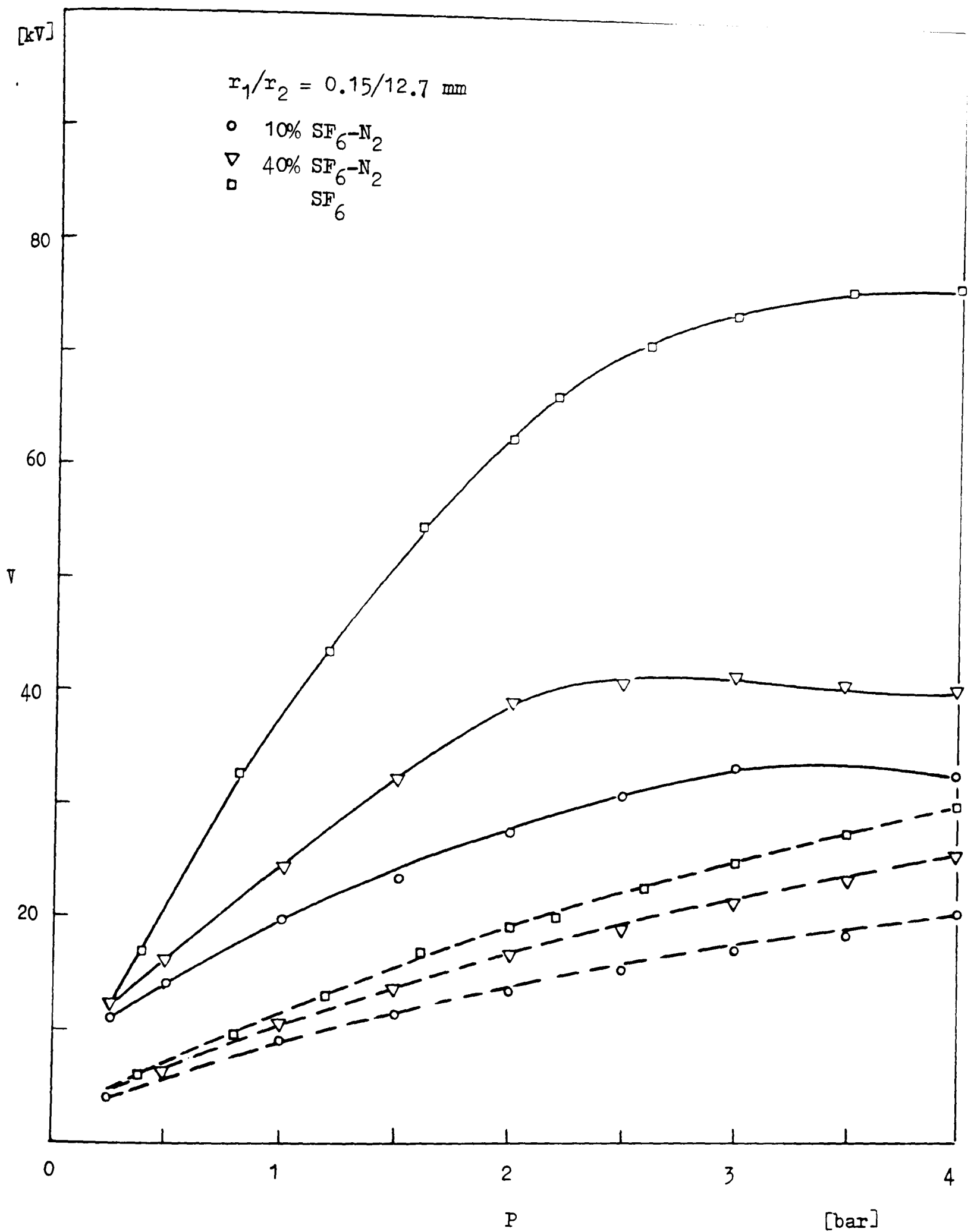


Figure 6.12 Influence of concentration of SF<sub>6</sub> on negative breakdown characteristics of SF<sub>6</sub>/N<sub>2</sub> mixtures in the gap having electrodes of radii  $r_1/r_2 = 0.15/12.7 \text{ mm}$ .

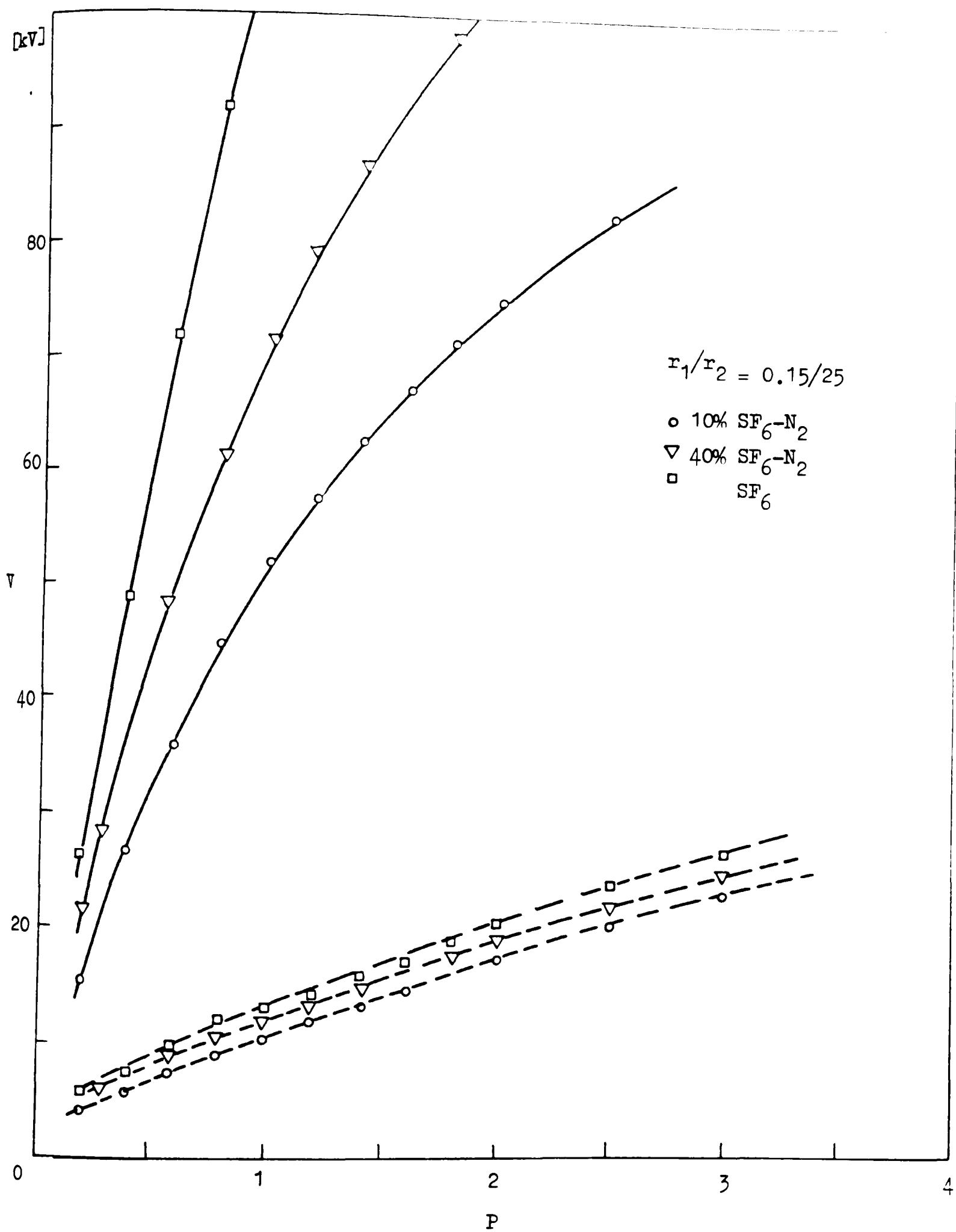


Figure 6.13 Effect of concentration of SF<sub>6</sub> on negative breakdown characteristics of SF<sub>6</sub>/N<sub>2</sub> mixtures in the gap having electrodes of radii  $r_1/r_2 = 0.15/25$  mm.

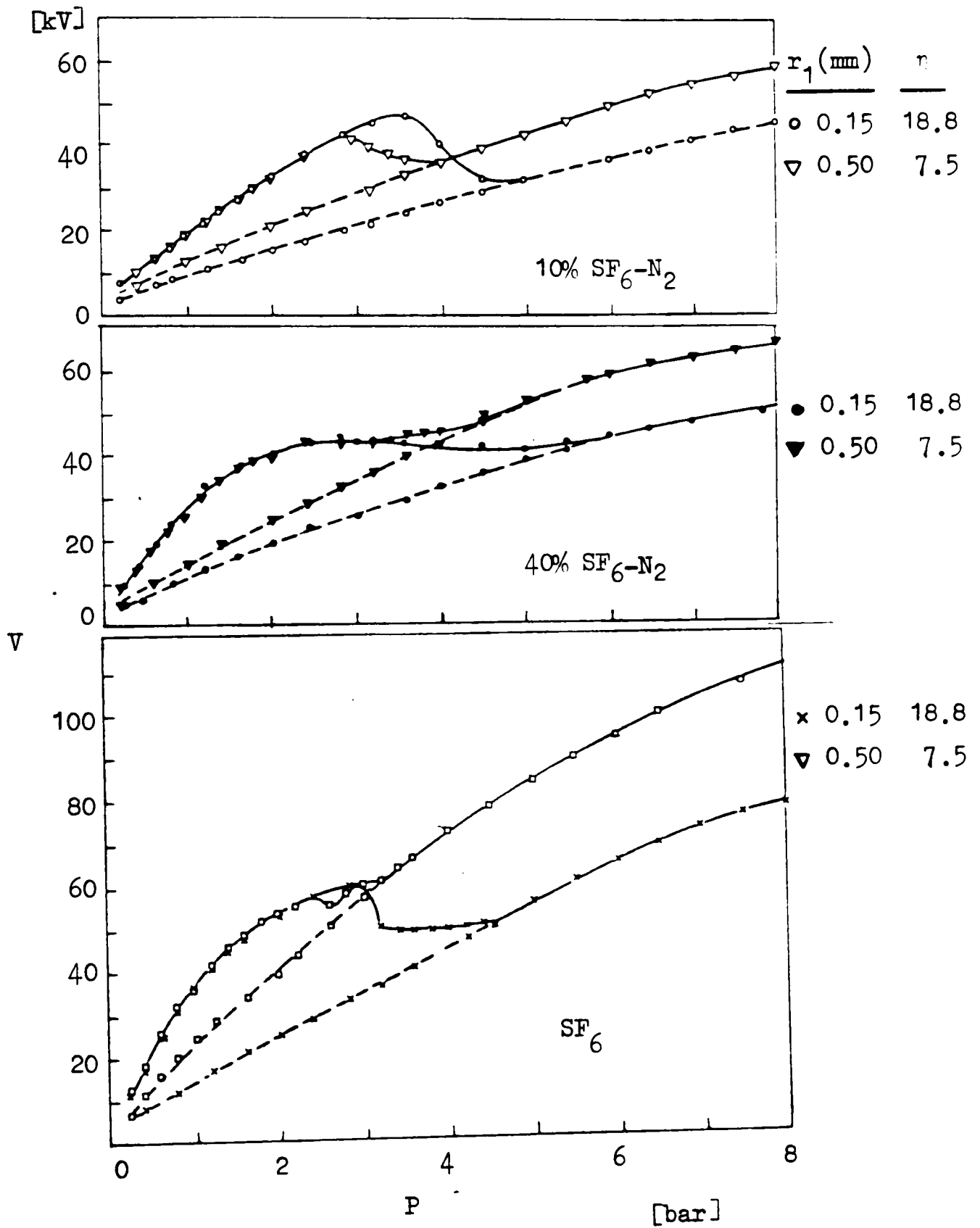


Figure 6.14 Effect of gap nonuniformity on breakdown characteristics of mixtures ( $r_2 = 12.7$  mm)

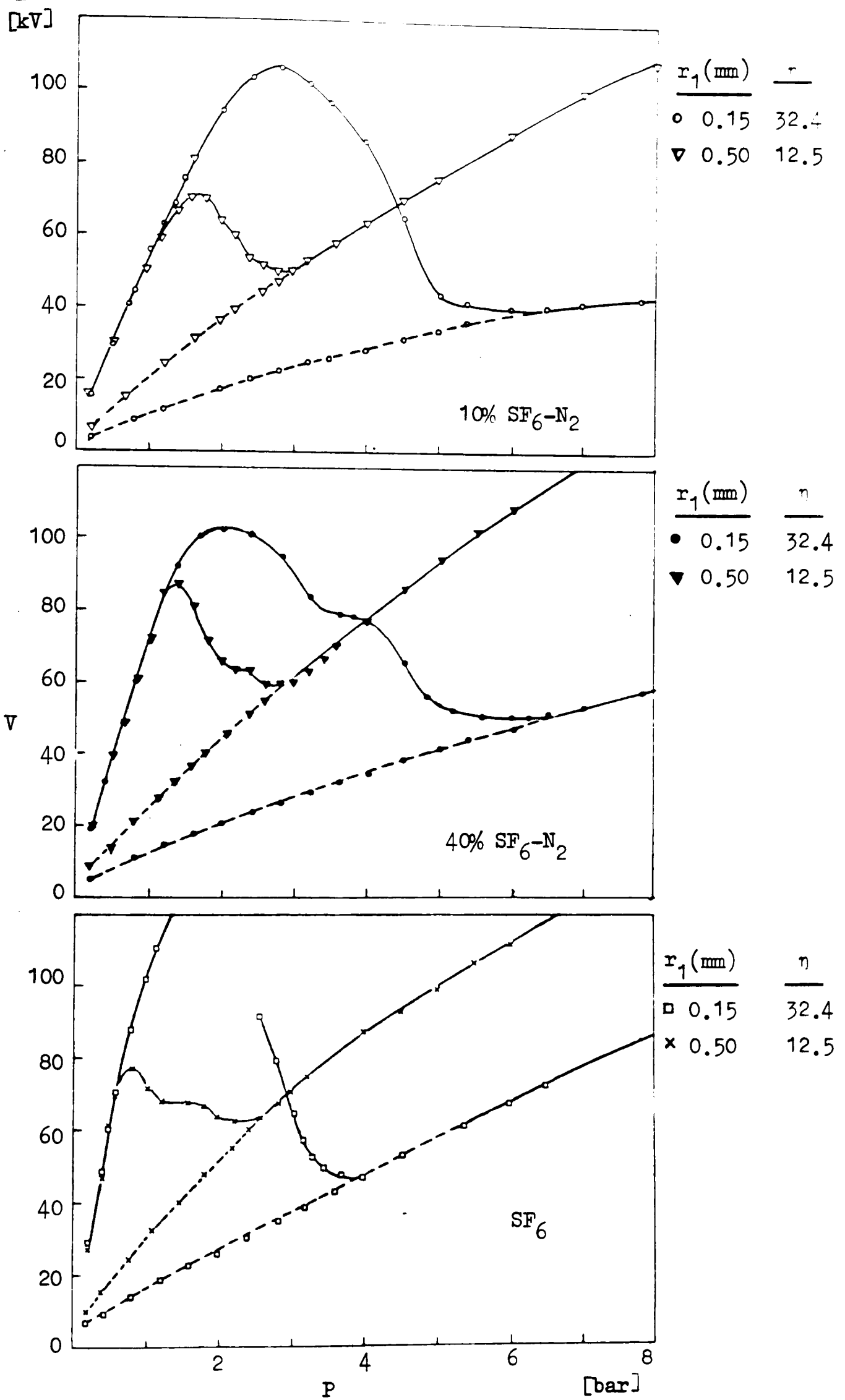


Figure 6.15 Effect of gap nonuniformity on breakdown characteristics of mixtures (r<sub>2</sub> = 25 mm)

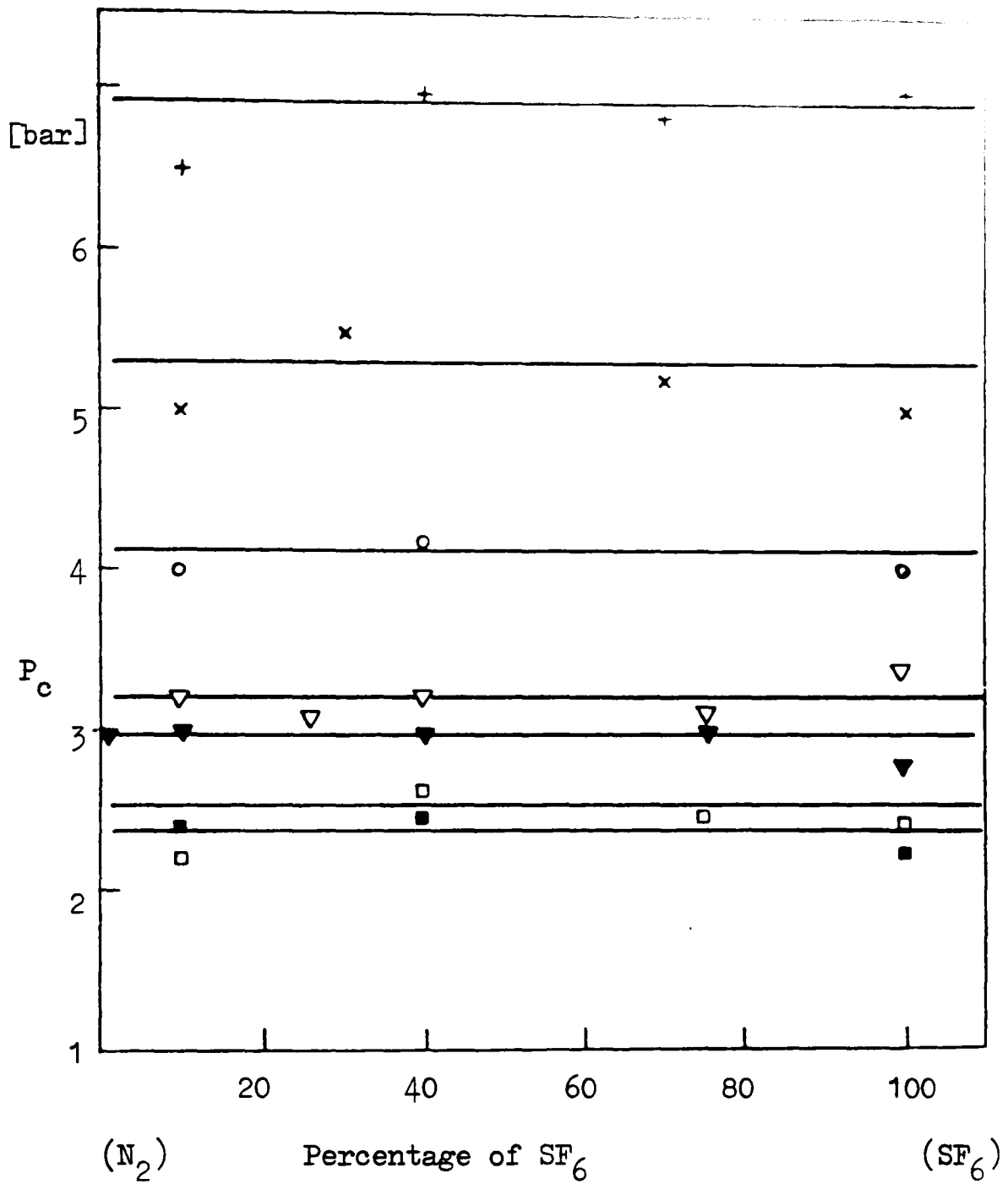


Figure 6.16 Variation of critical pressure with  $SF_6$  concentration for several gap nonuniformities

| $r_1$ (mm) | $\eta$ |                 |
|------------|--------|-----------------|
| x 0.15     | 18.8   | $r_2 = 12.7$ mm |
| o 0.25     | 12.6   |                 |
| ▽ 0.50     | 7.5    |                 |
| □ 1.00     | 4.6    |                 |
| <hr/>      |        |                 |
| + 0.15     | 32.4   | $r_2 = 25$ mm   |
| ▽ 0.50     | 12.5   |                 |
| □ 1.00     | 7.4    |                 |

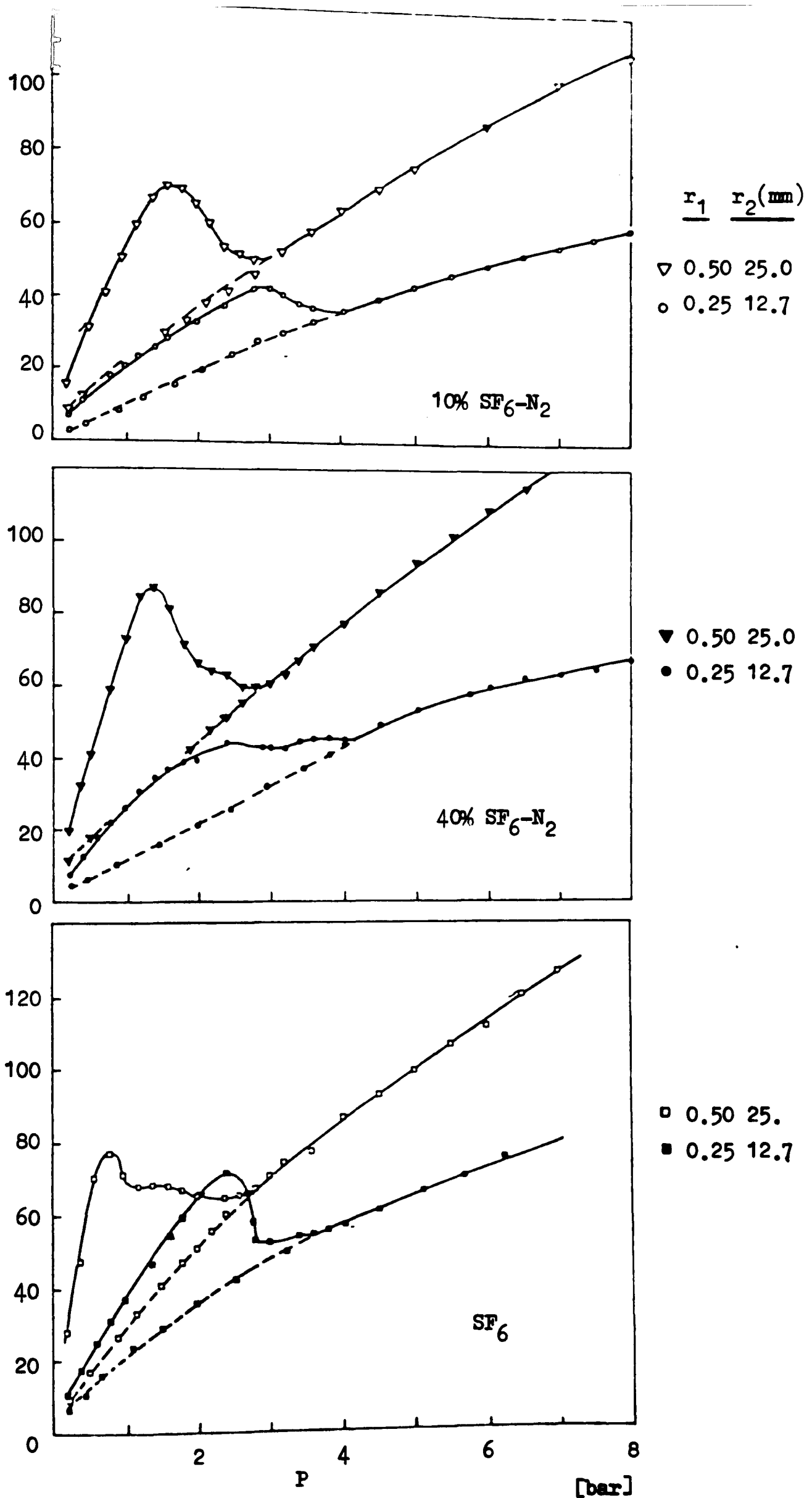


Figure 6.17 Effect of SF<sub>6</sub> content on positive breakdown characteristics of gaps having the same nonuniformity factor ( $\eta = 12.5$ )

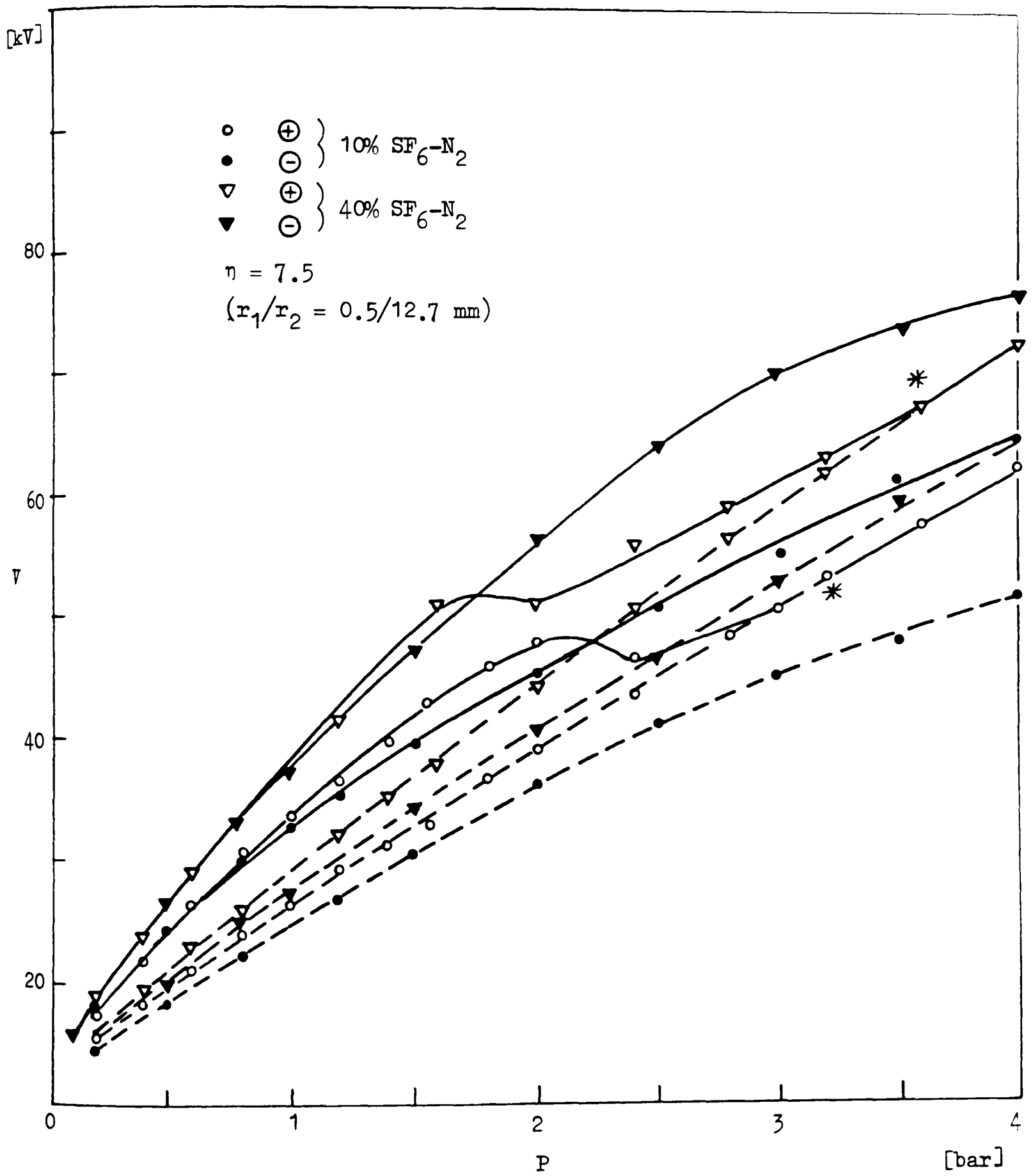


Figure 6.18 Effect of polarity on corona inception and breakdown voltage of mixtures for a gap with electrodes.  
 $r_1/r_2 = 0.5/12.7 \text{ mm}$  ( $\eta = 7.5$ )

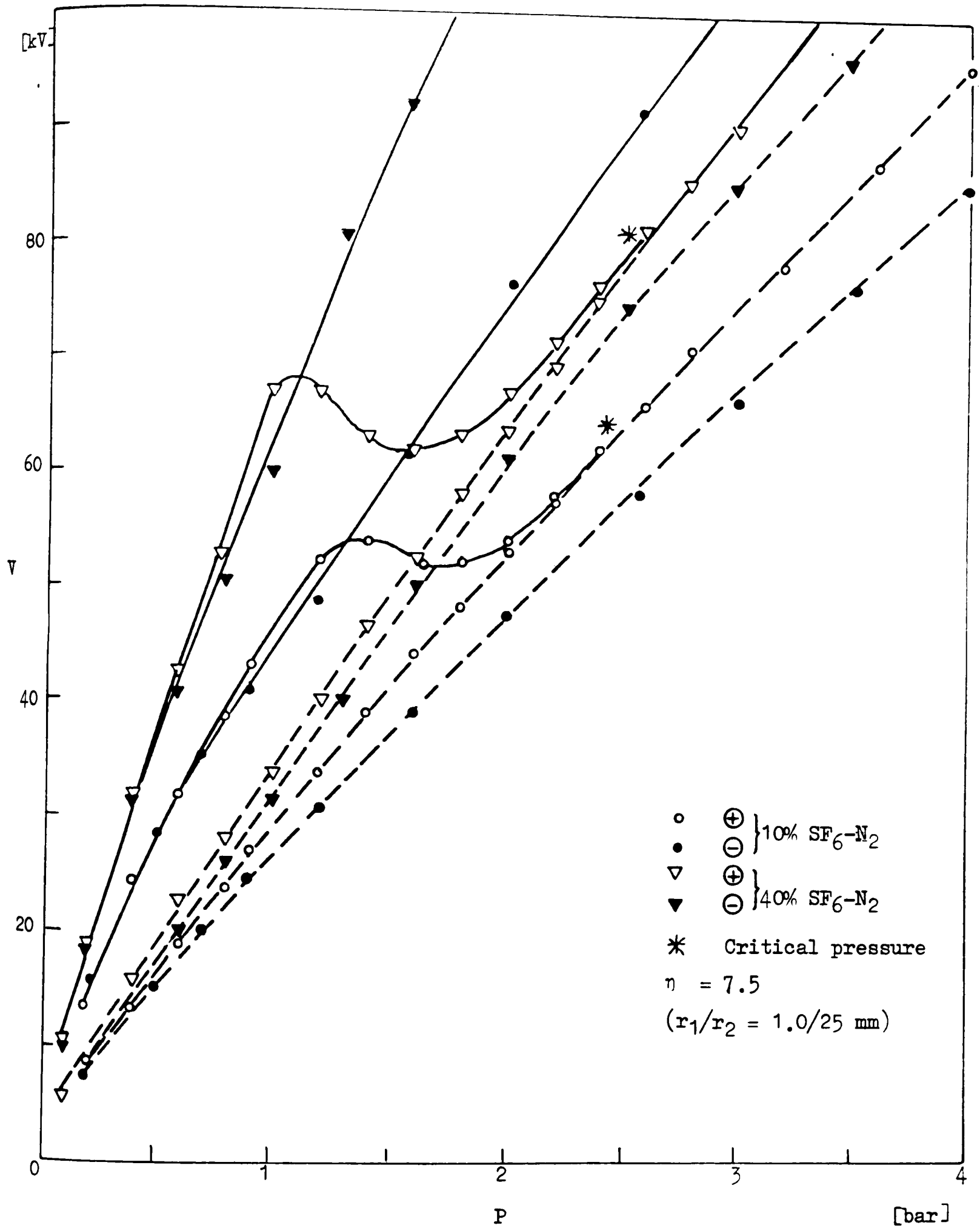


Figure 6.19 Effect of polarity on corona inception and breakdown voltage of mixtures for a gap with electrodes  $r_1/r_2 = 1.0/25 \text{ mm}$  ( $\eta = 7.5$ )

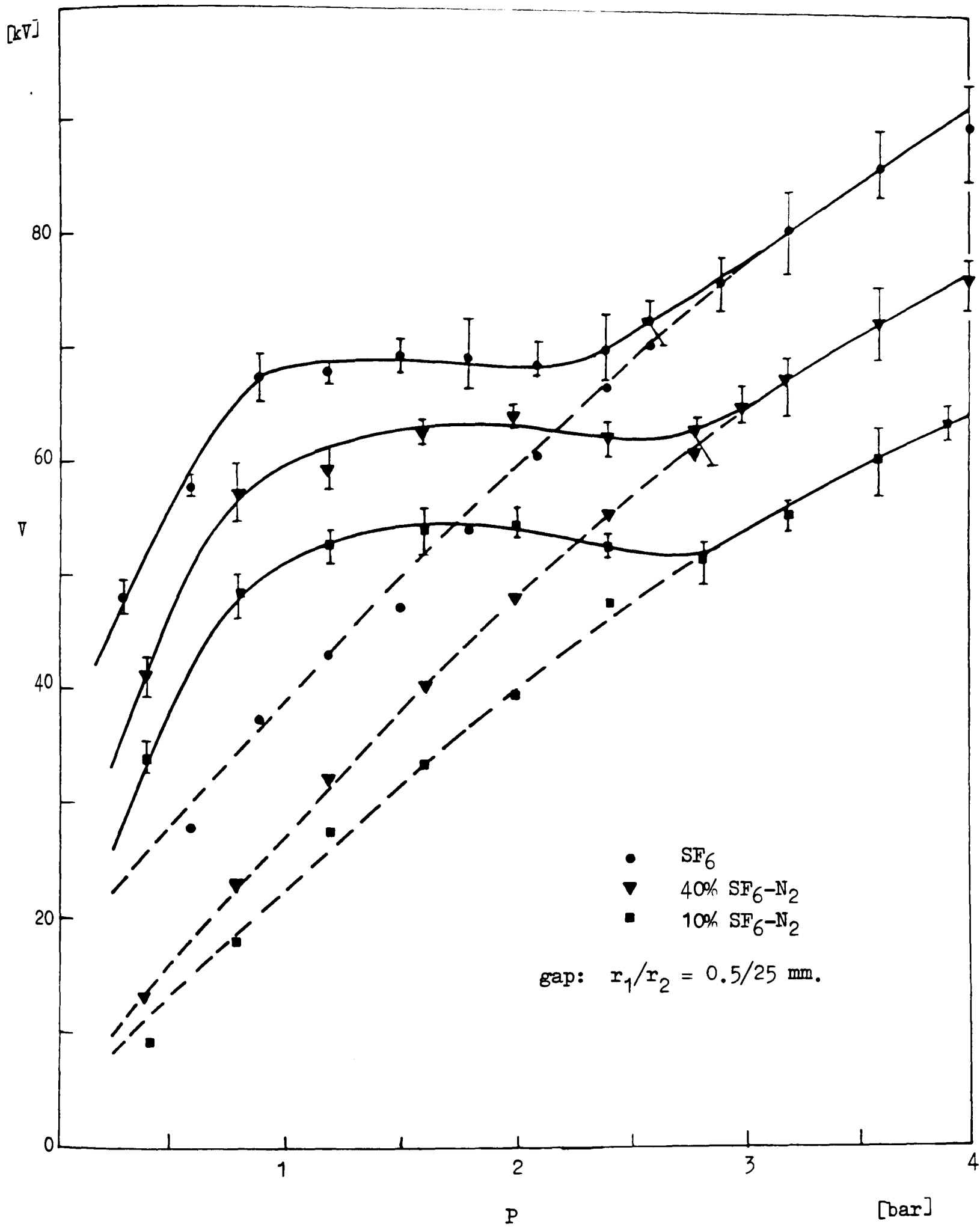


Figure 6.20 Effect of  $SF_6$  concentration on positive impulse corona and breakdown characteristics ( $r_1/r_2 = 0.5/25$  mm)

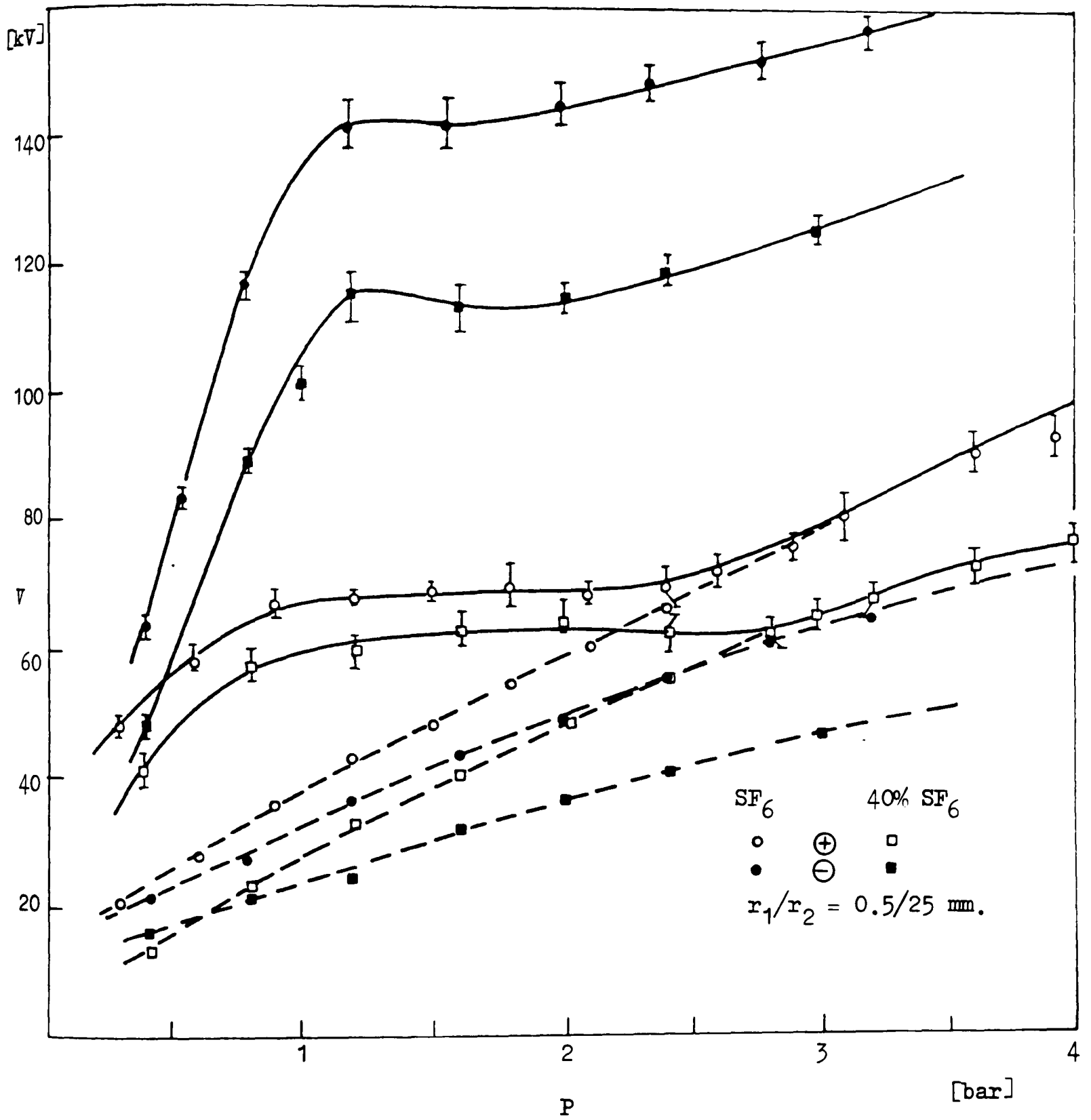


Figure 6.21 Effect of polarity on the impulse breakdown characteristics of SF<sub>6</sub> and 40% SF<sub>6</sub>-N<sub>2</sub> mixture ( $r_1/r_2 = 0.5/25$  mm)

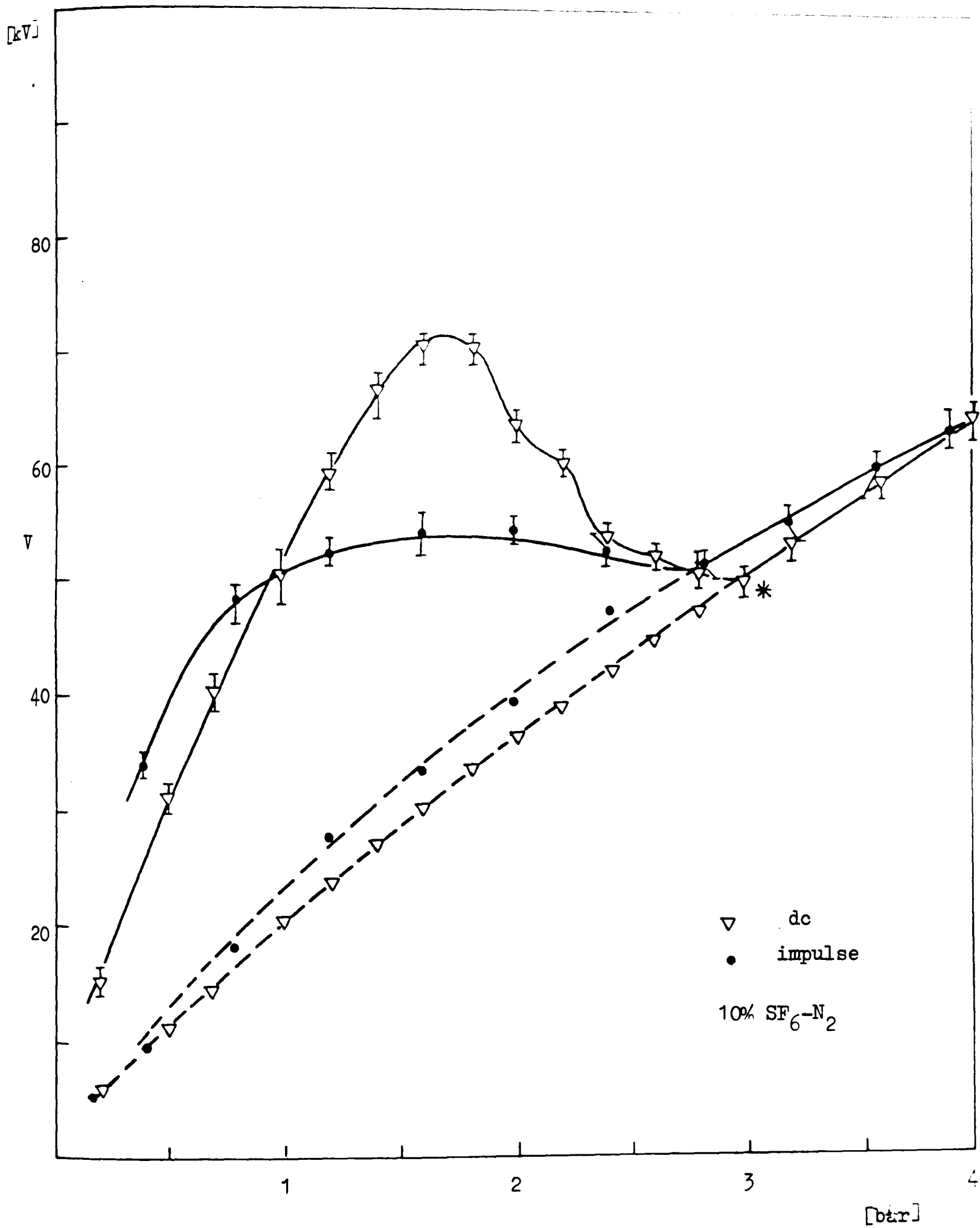


Figure 6.22 (a) Comparison of positive dc and impulse breakdown/pressure characteristics of a 10% SF<sub>6</sub>-N<sub>2</sub> mixture ( $r_1/r_2 = 0.5/25$  mm)

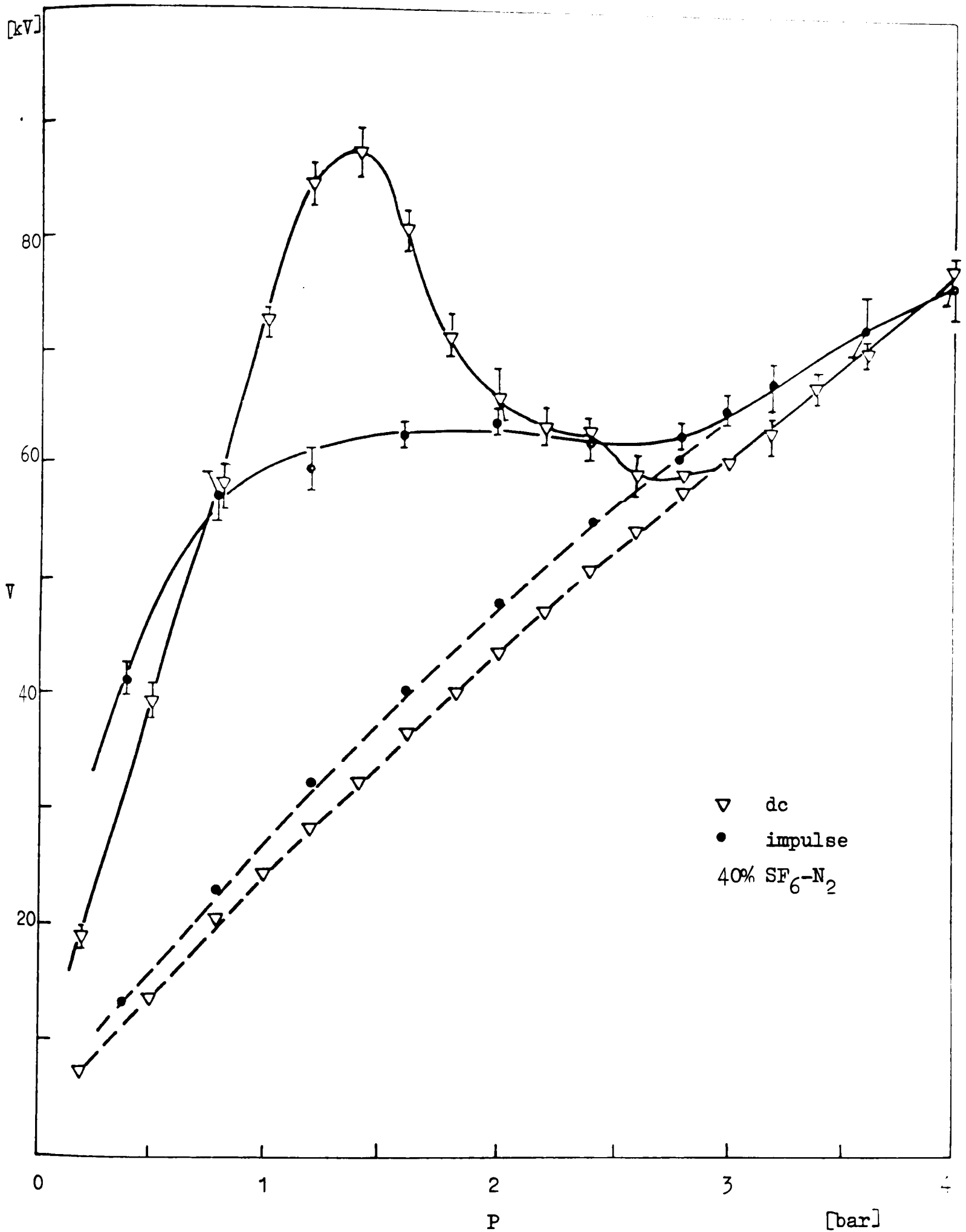


Figure 6.22(b) Comparison of positive dc and impulse breakdown/pressure characteristics of a 40% SF<sub>6</sub> - N<sub>2</sub> mixture  
 ( $r_1/r_2 = 0.5/25$  mm)

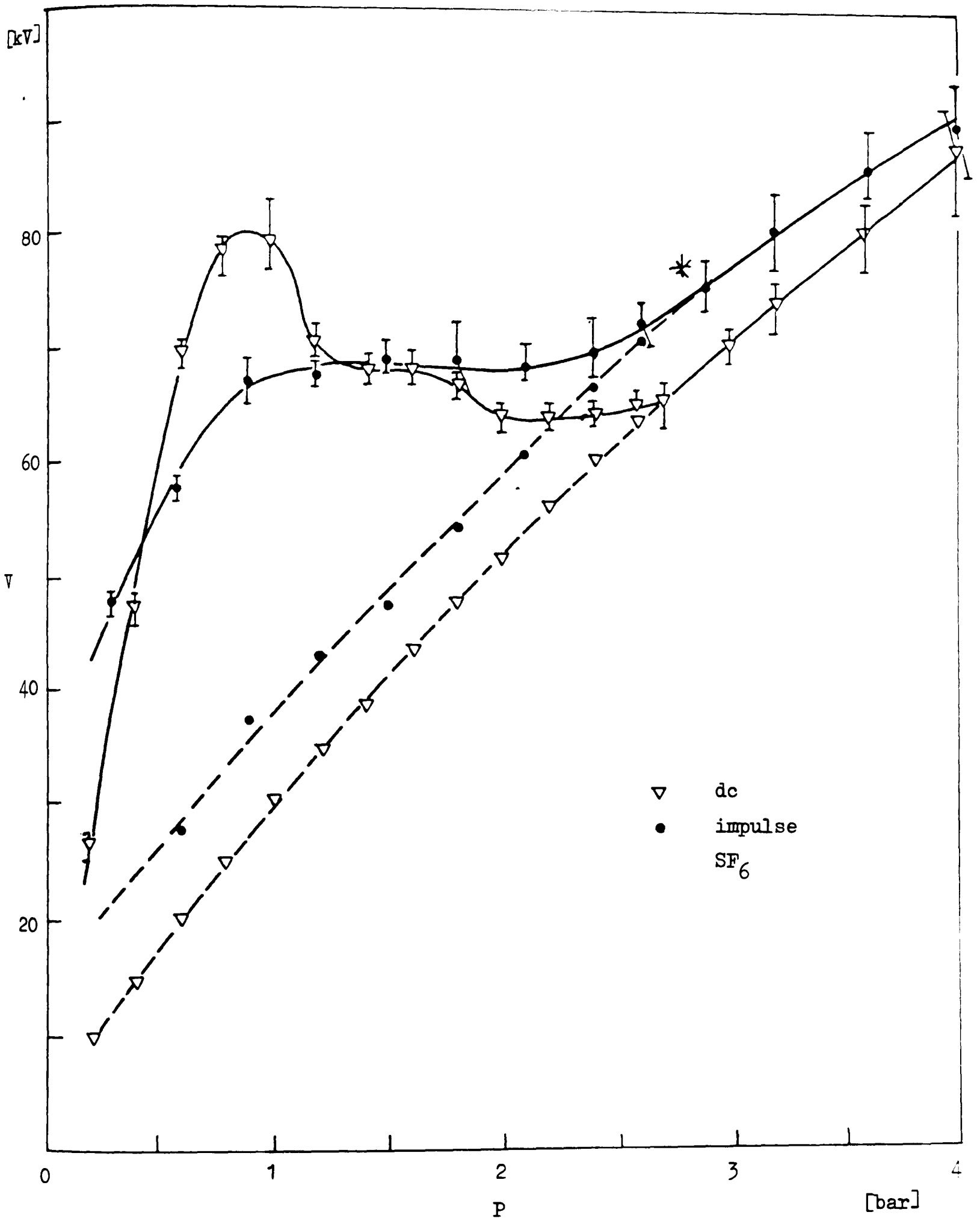


Figure 6.22(c) Comparison of positive dc and impulse voltage/pressure characteristics of SF<sub>6</sub> ( $r_1/r_2 = 0.5/25$  mm)

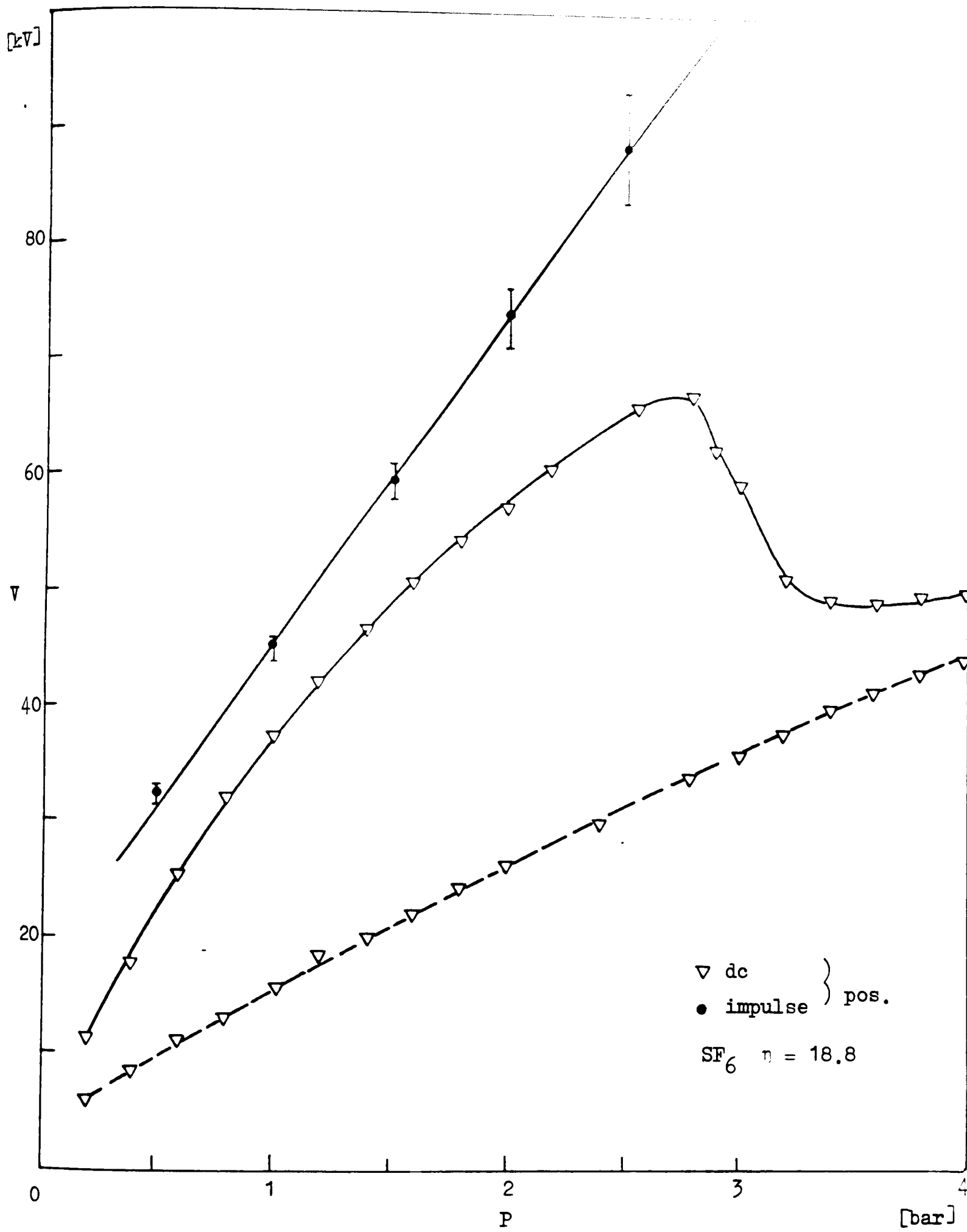


Figure 6.23 Comparison of positive dc and impulse voltage/pressure characteristics of  $SF_6$  ( $r_1/r_2 = 1.5/12.7$  mm)

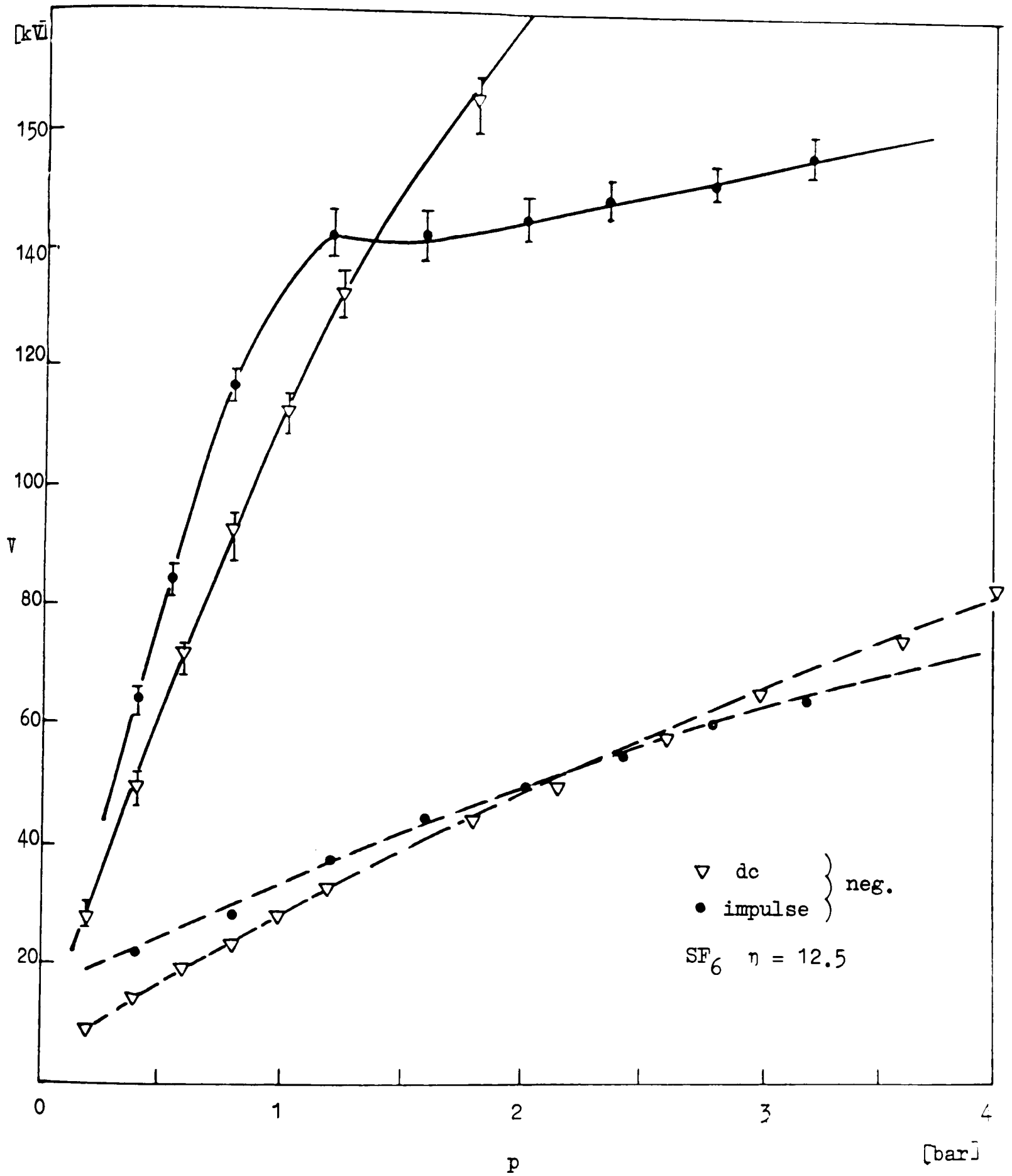


Figure 6.24 Comparison of negative dc and impulse voltage/pressure characteristics of SF<sub>6</sub> ( $r_1/r_2 = 0.5/25$  mm.)

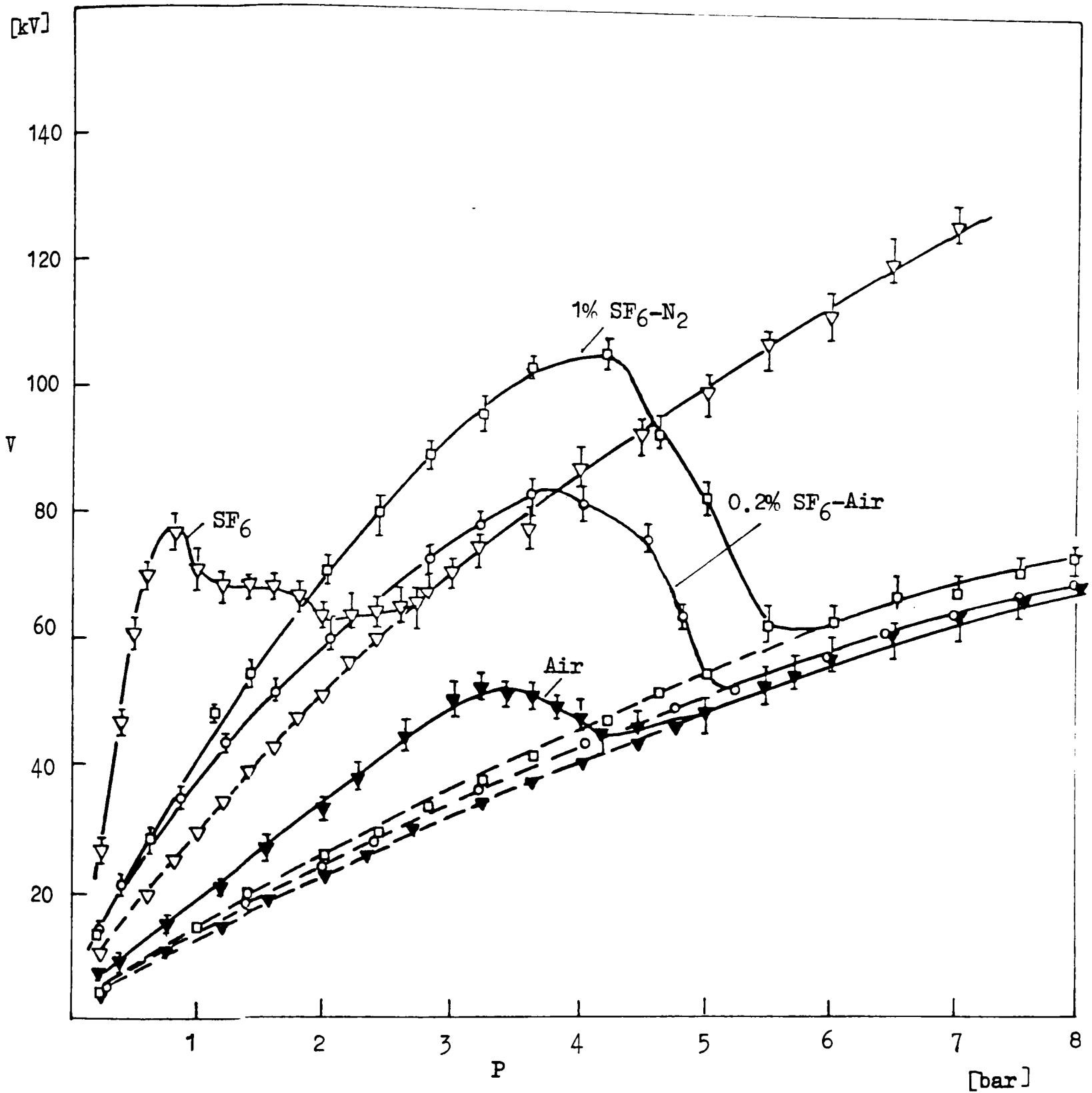


Figure 6.25 Positive dc voltage/pressure characteristics in SF<sub>6</sub>/Air mixtures ( $r_1/r_2 = 0.5/25$  mm)

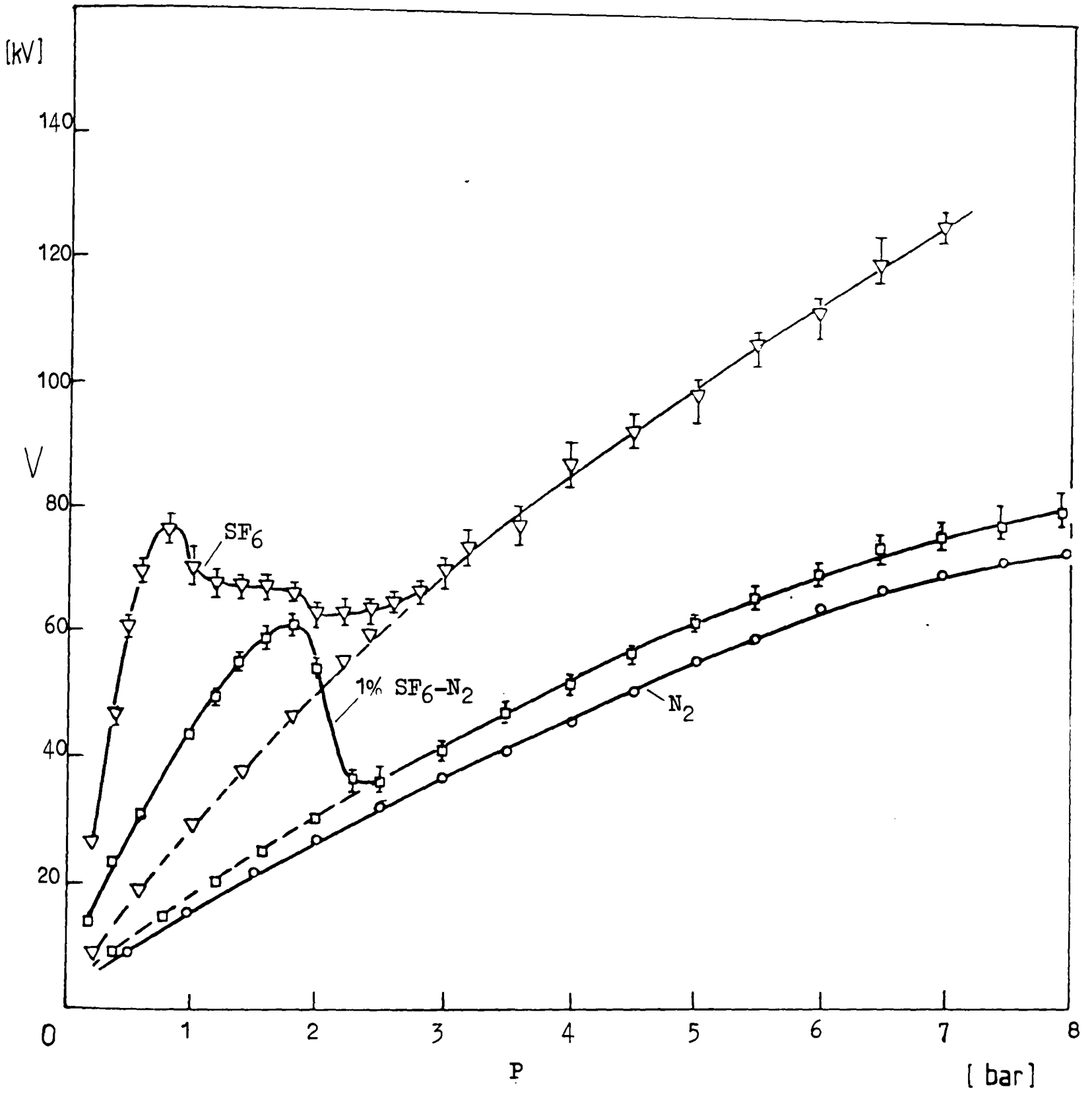


Figure 6.26 Positive dc voltage/pressure characteristics in SF<sub>6</sub>/N<sub>2</sub> mixtures ( $r_1/r_2 = 0.5/25$  mm)

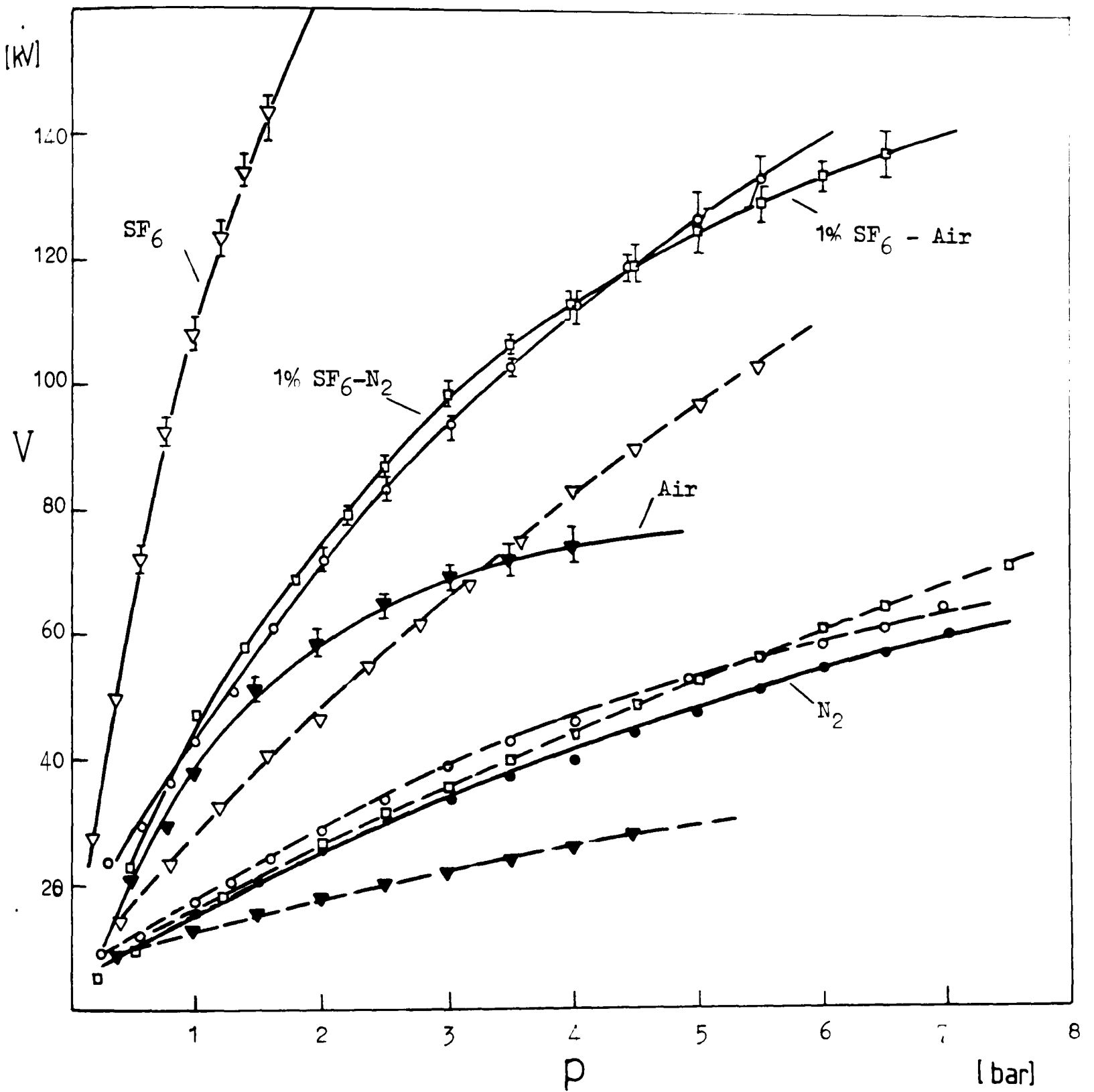


Figure 6.27 Negative dc voltage/pressure characteristics in SF<sub>6</sub>/Air and SF<sub>6</sub>/N<sub>2</sub> mixtures ( $r_1/r_2 = 0.5/25$  mm)

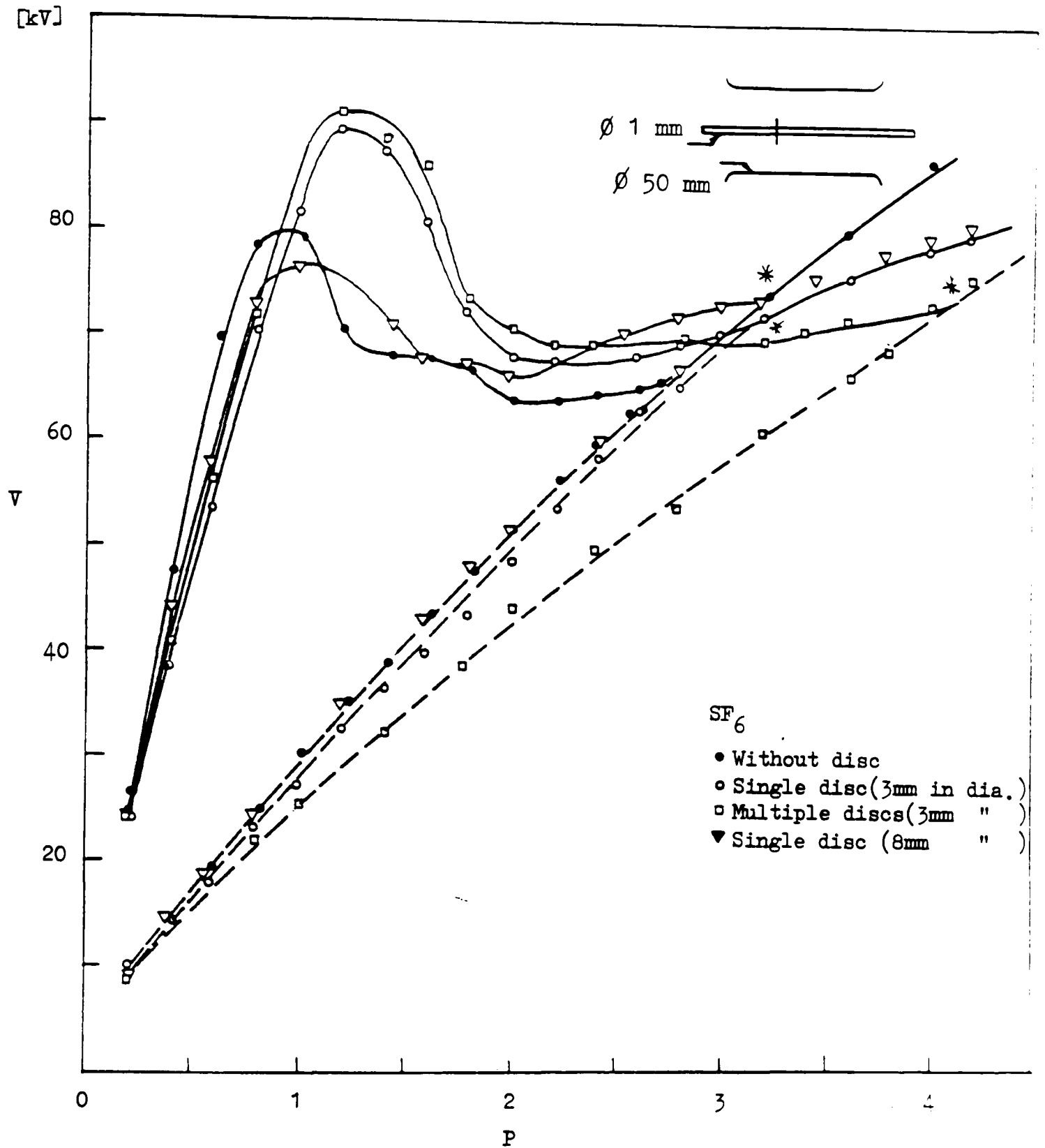


Figure 6.28 Positive dc voltage/pressure characteristics of the gap  $r_1/r_2 = 0.5/25$  mm protruded with single and multiple discs in  $\text{SF}_6$

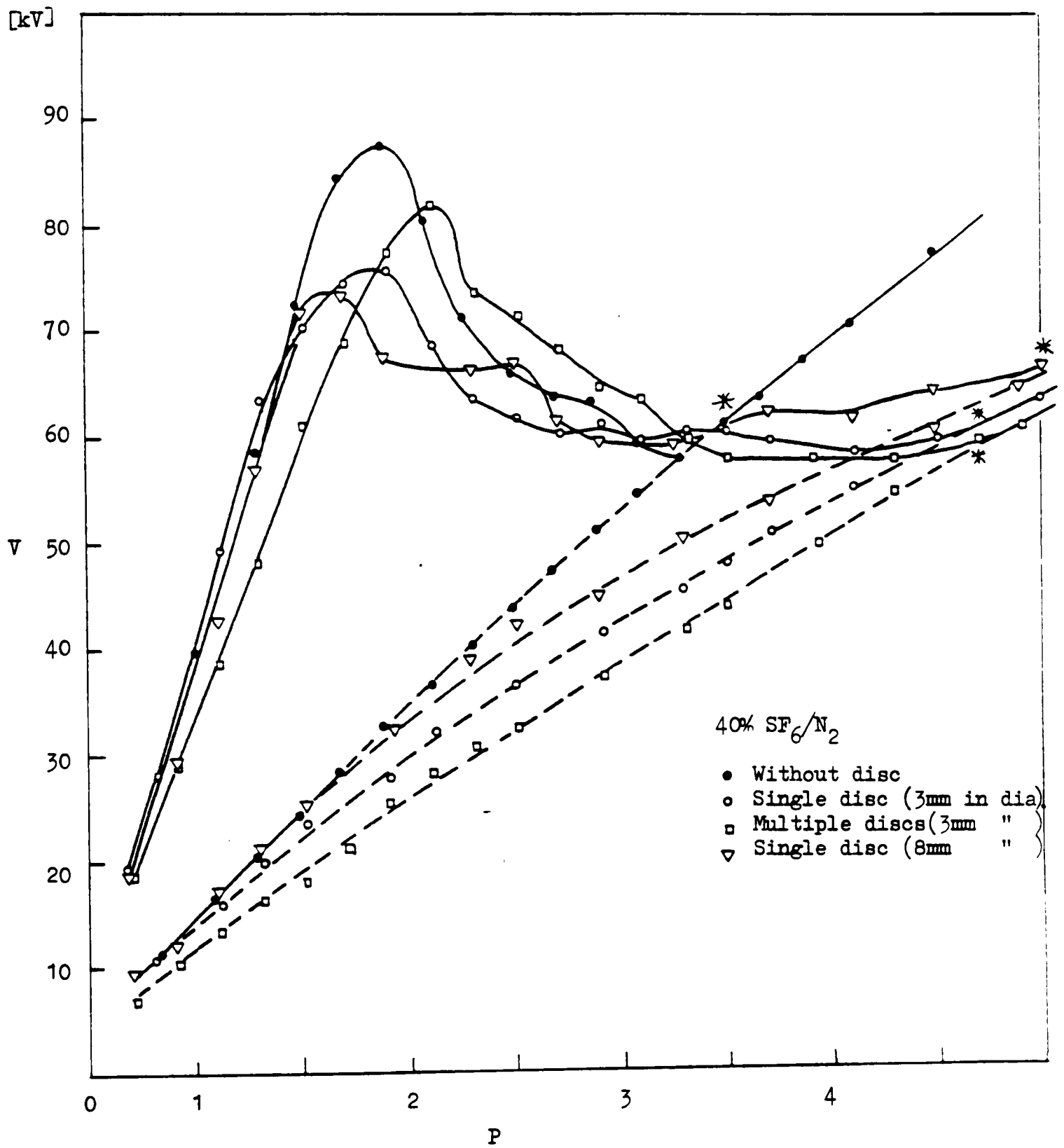
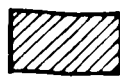
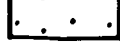
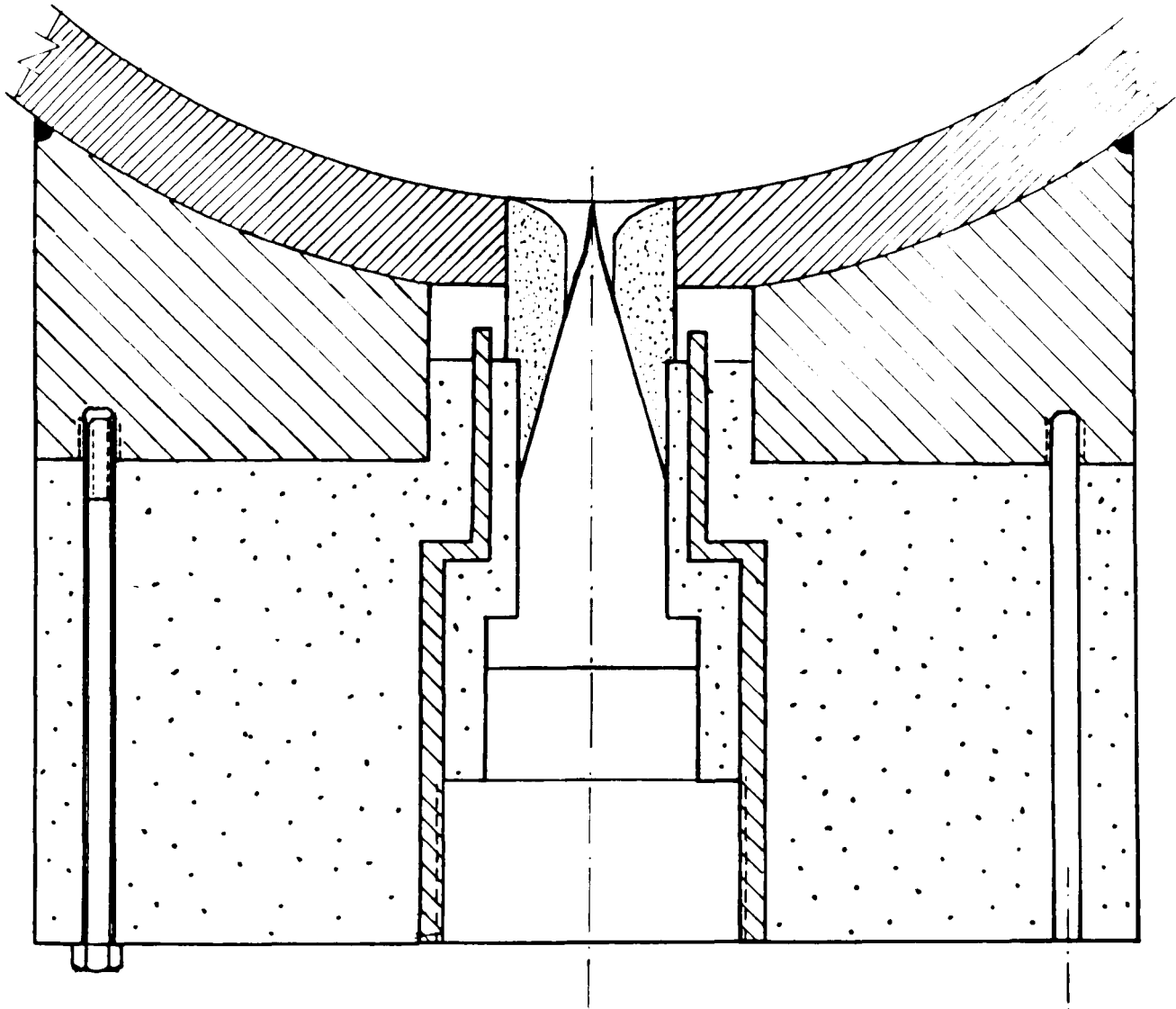


Figure 6.29 Positive dc voltage/pressure characteristics of the gap  $r_1/r_2 = 0.5/25$  mm protruded with single and multiple discs in 40% SF<sub>6</sub>/N<sub>2</sub>

-  St-St
-  St-St
-  Nylon
-  P.T.F.E



Scale : 1 cm = 0.24 mm

Figure 6.30 Details of ion injection system

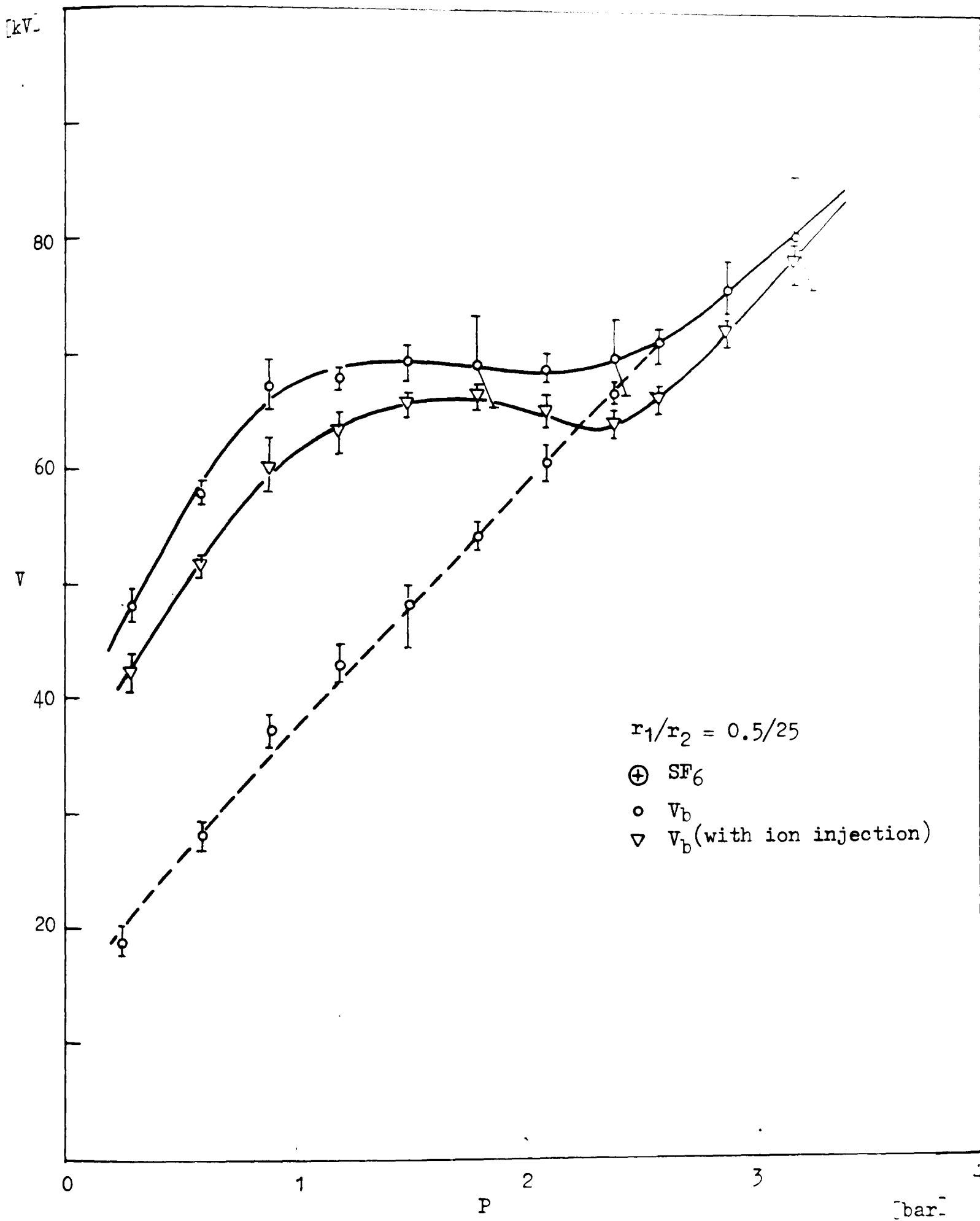


Figure 6.31 The variation of positive impulse voltage-pressure characteristic of  $\text{SF}_6$  with ion injection ( $r_1/r_2 = 0.5/25$  mm)

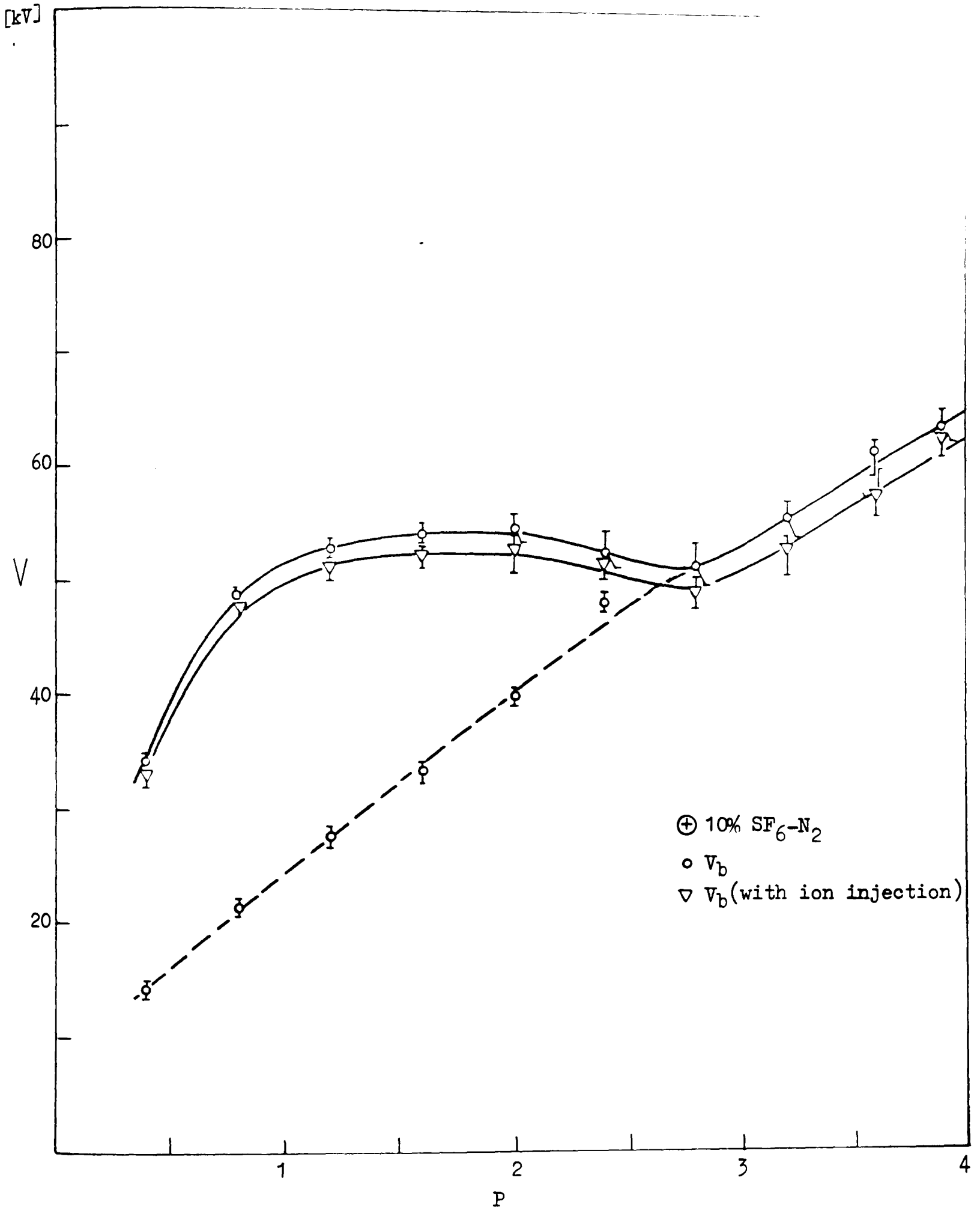


Figure 6.32(a) The variation of positive impulse-pressure characteristic of 10% SF<sub>6</sub>-N<sub>2</sub> mixture with ion injection ( $r_1/r_2 = 0.5/25$  mm)

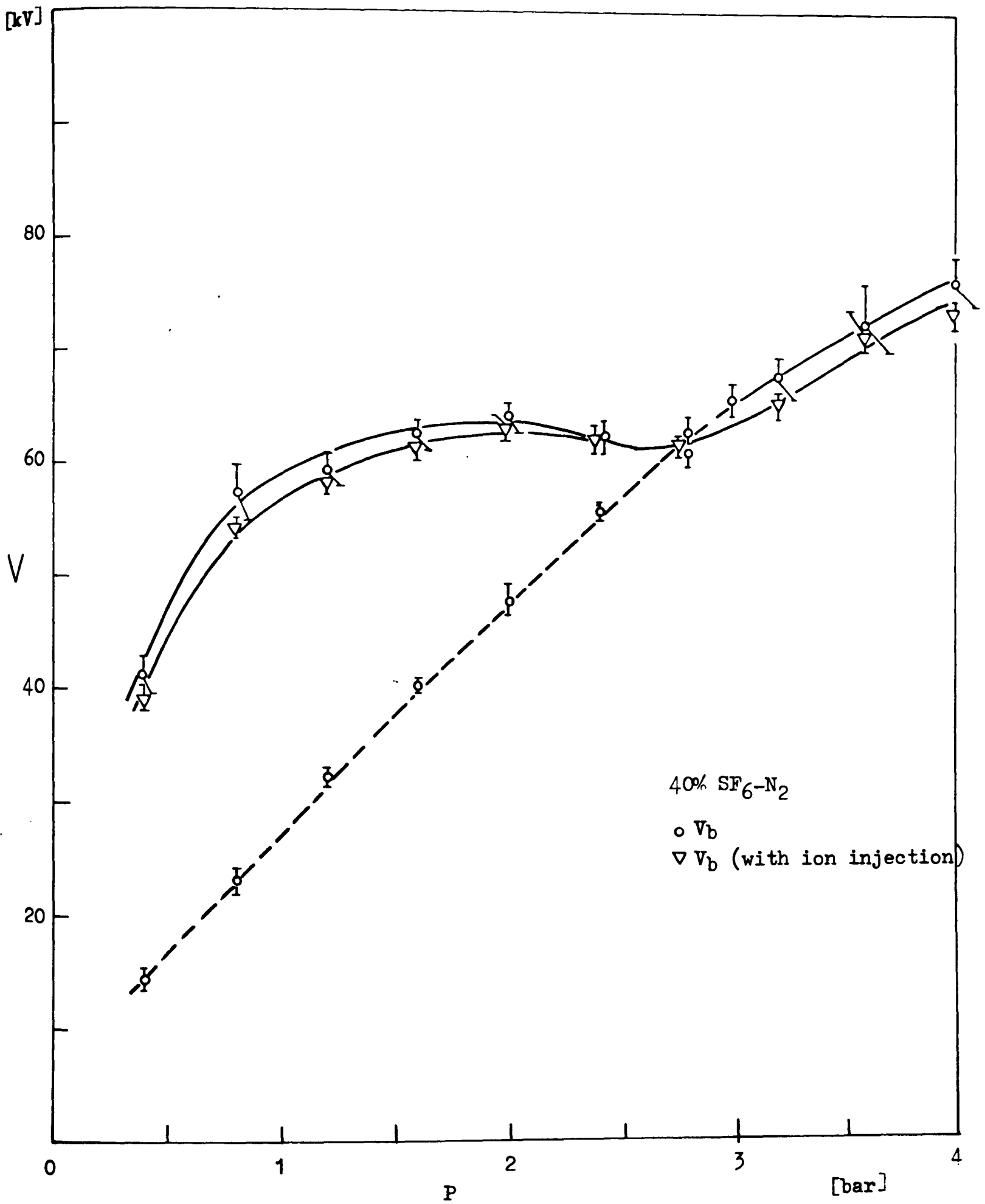


Figure 6.32(b) The variation of positive impulse-pressure characteristic of 40% SF<sub>6</sub>-N<sub>2</sub> with ion injection ( $r_1/r_2 = 0.5/25$  mm)

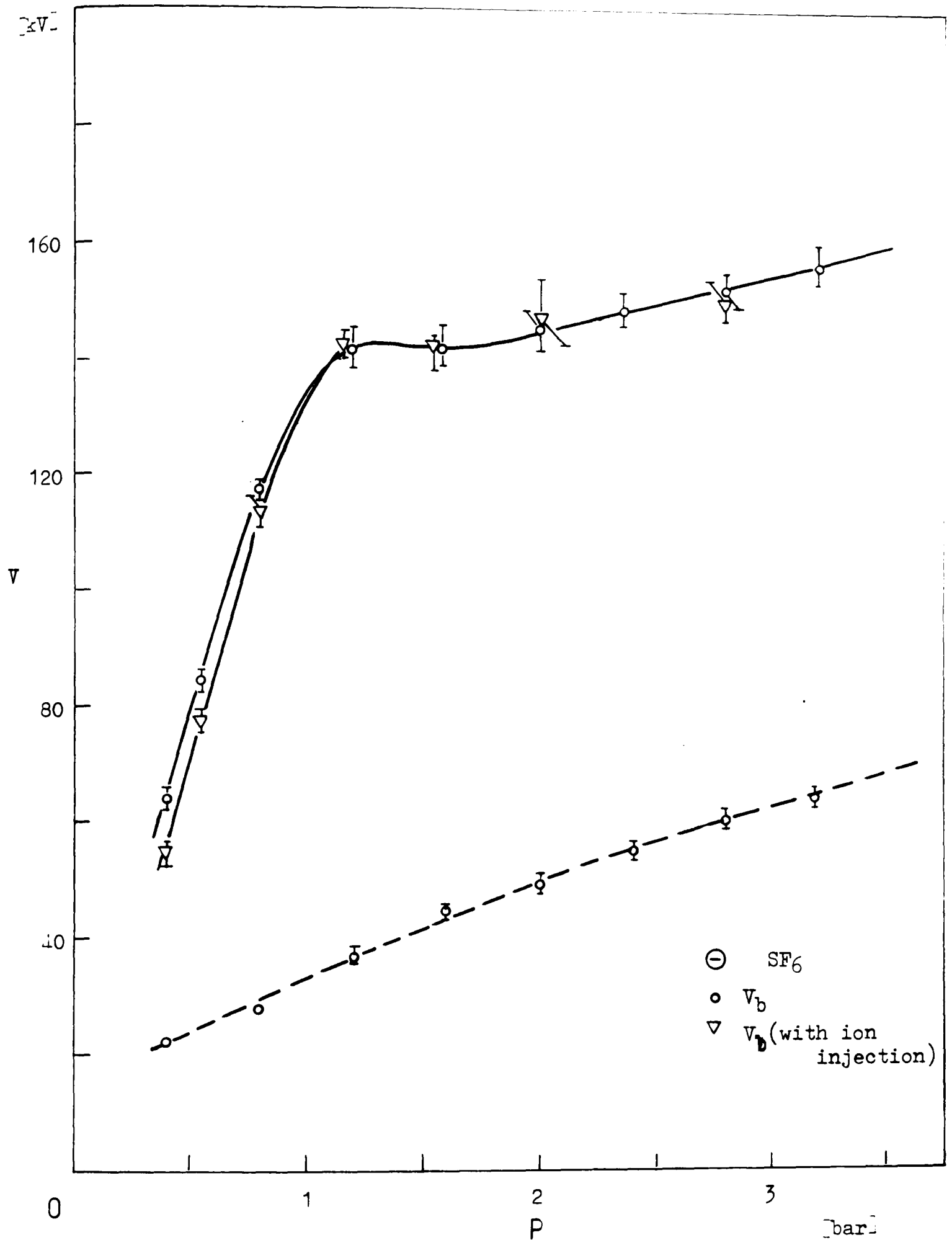


Figure 6.33 The variation of negative impulse voltage-pressure characteristic of SF<sub>6</sub> with ion injection ( $r_1/r_2 = 0.5/25$  mm)

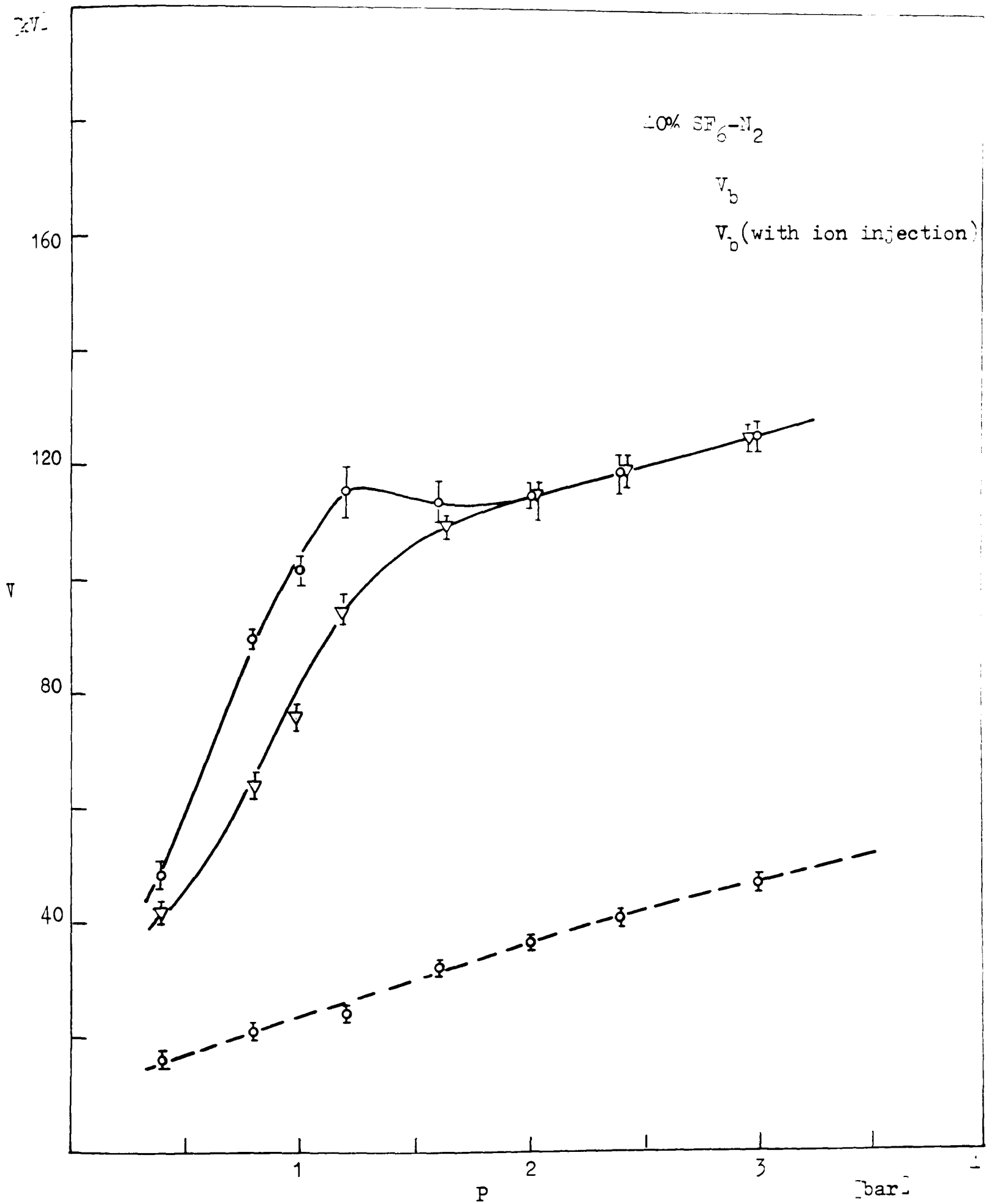


Figure 6.34 The variation of negative impulse voltage-pressure characteristic of 10% SF<sub>6</sub>-N<sub>2</sub> with ion injection ( $r_1/r_2 = 0.5/25$  mm)

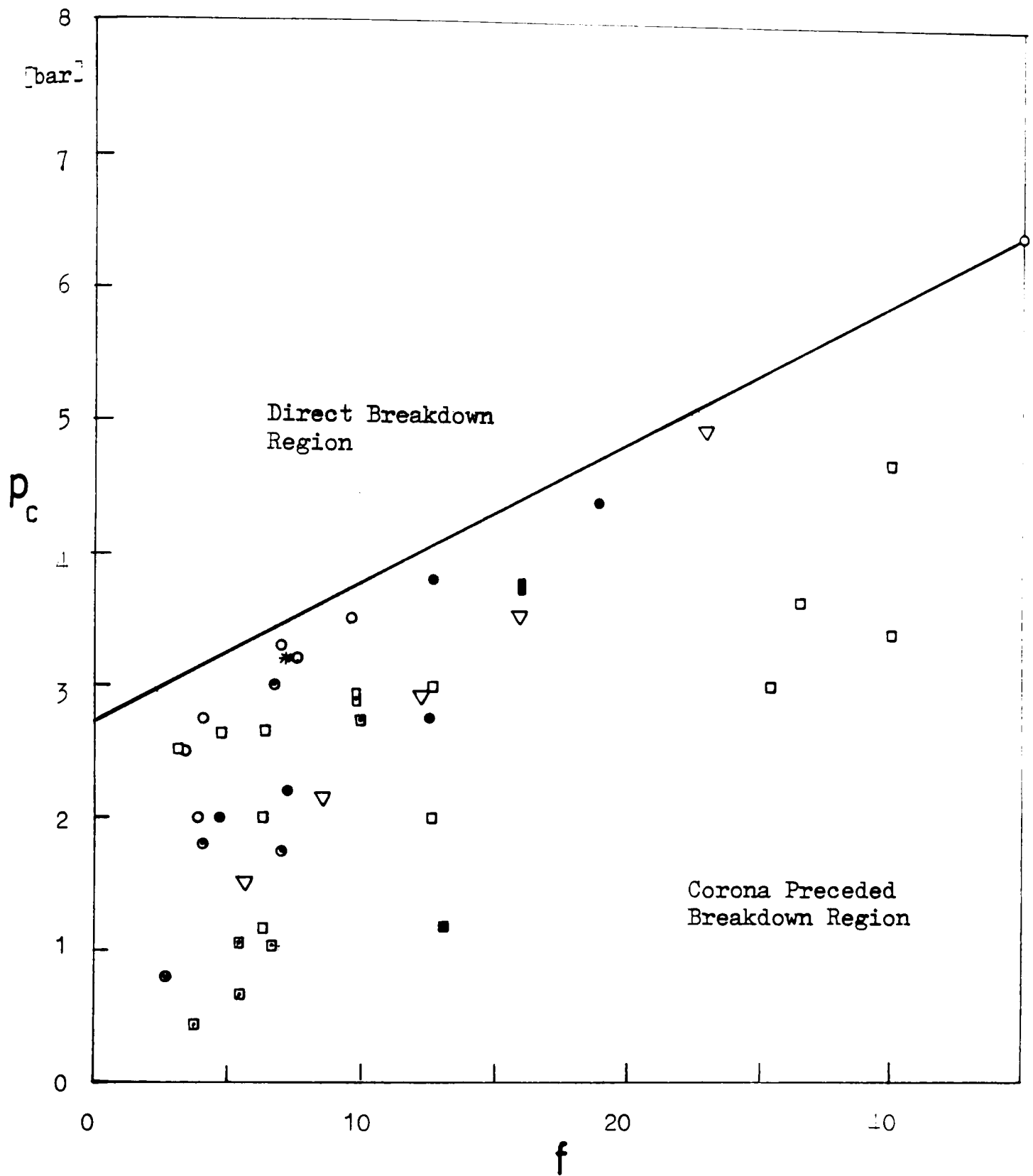


Figure 6.35(a) Variation of critical pressure with gap nonuniformity in SF<sub>6</sub> when the polarity of the stressed electrode is positive

- c-c Present
- " [223]
- Q-P [162]
- " [150]
- ▽ " [155]
- H-P [160]
- " [220]
- " [224]
- " [161]
- \* " [152]

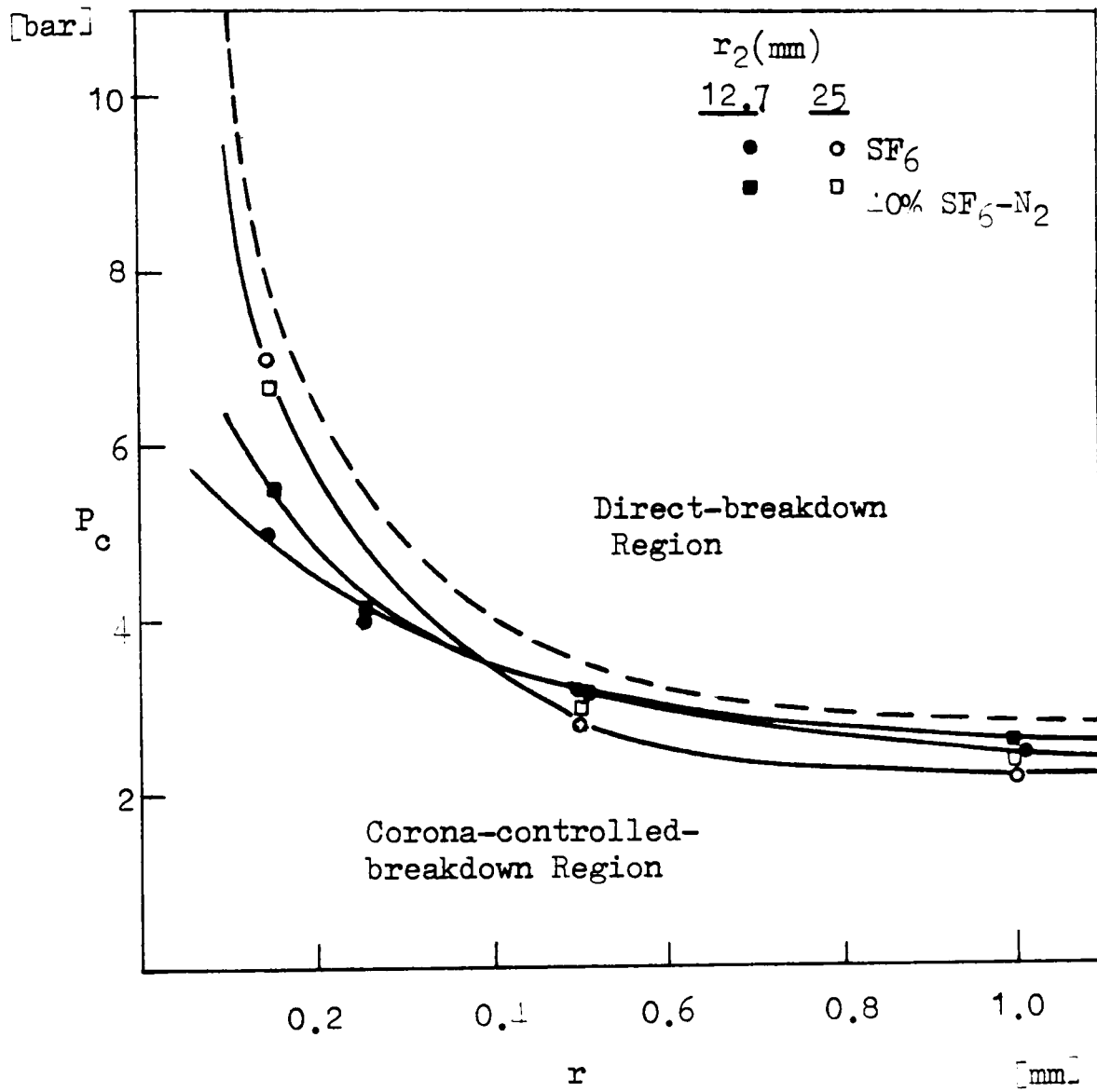


Figure 6.35(b) Variation of critical pressure as a function of inner electrode radius in  $\text{SF}_6$  and 10%  $\text{SF}_6\text{-N}_2$  mixture.

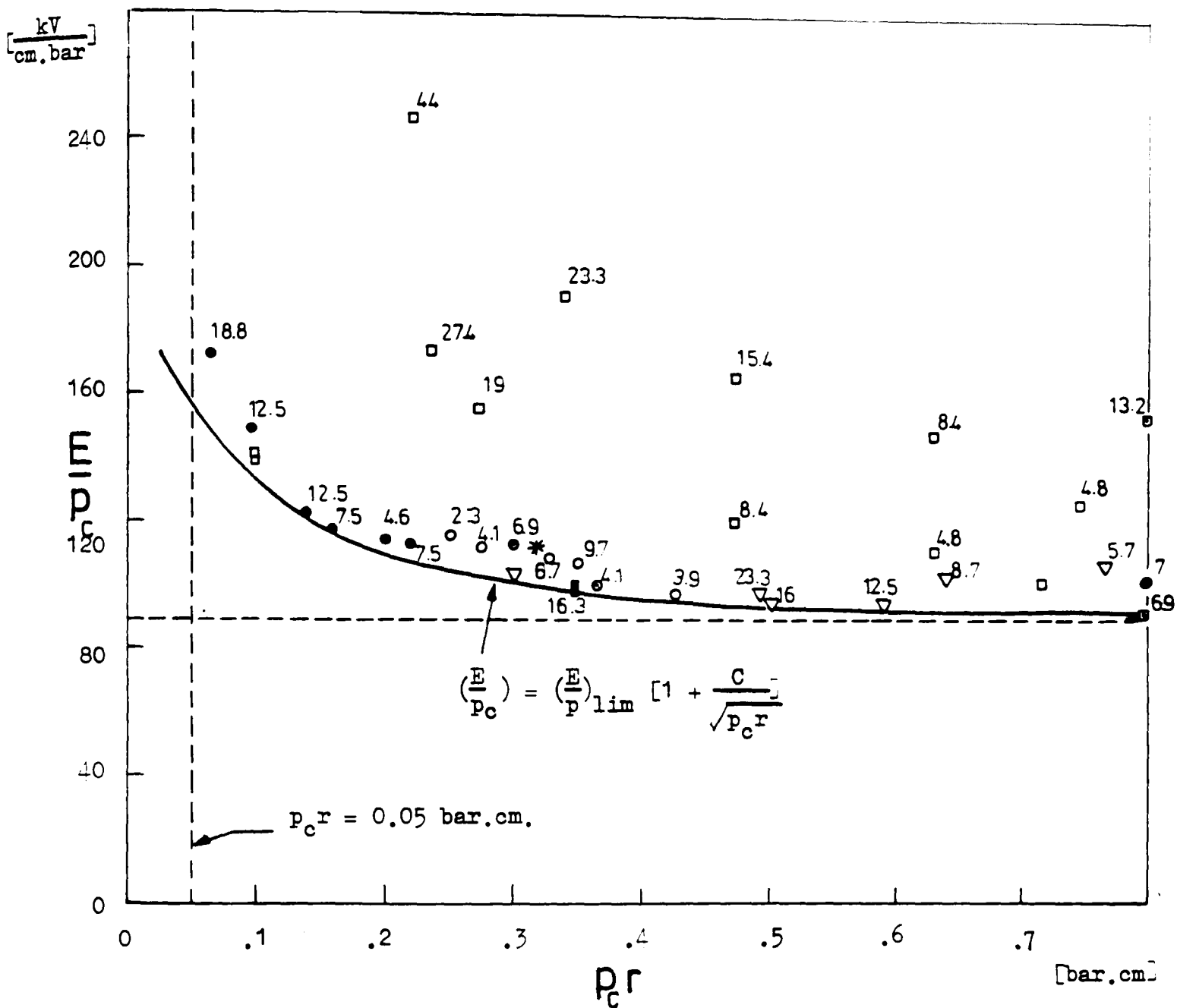


Figure 6.36 Positive  $E/p_c$  as a function of  $p_c \cdot r$  in  $SF_6$

| <u>Irradiated</u> |           | <u>Non-irradiated</u>         |       |
|-------------------|-----------|-------------------------------|-------|
| Coaxial cyl.      | ● Present | Point-plane                   | [161] |
| Point-plane       | ○ [220]   | "                             | [155] |
| "                 | ○ [160]   | Concentric                    |       |
| "                 | □ [162]   | sphere                        | [156] |
| "                 | ■ [150]   | Accompanying numbers indicate |       |
| Point-sphere      | * [223]   | gap nonuniformity factor      |       |

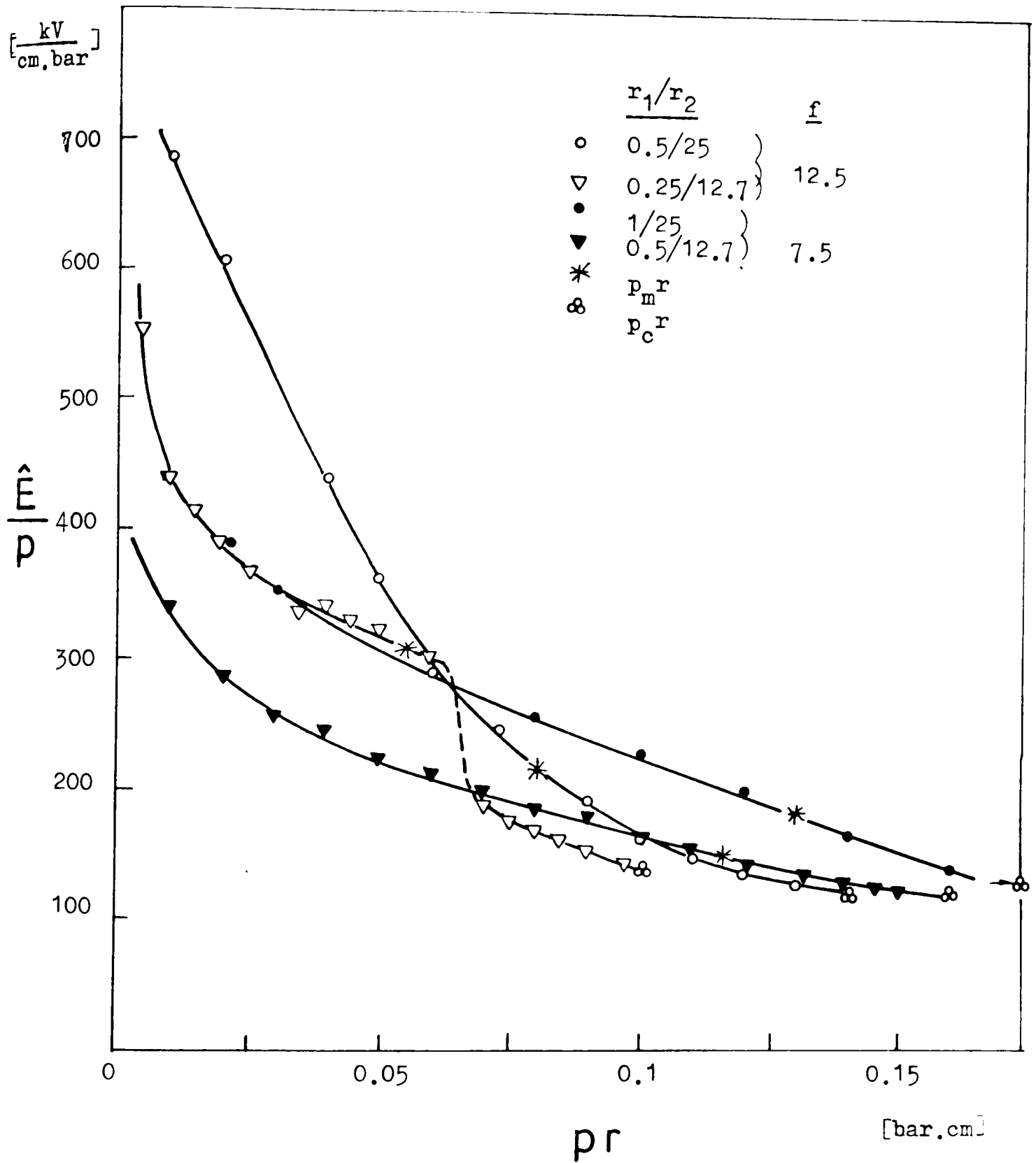


Figure 6.37 The variation of the parameter  $(\hat{E}/p)$  over the corona-stabilized breakdown-region as a function of  $pr$  in  $\text{SF}_6$  for several gaps (applied voltage is positive dc)

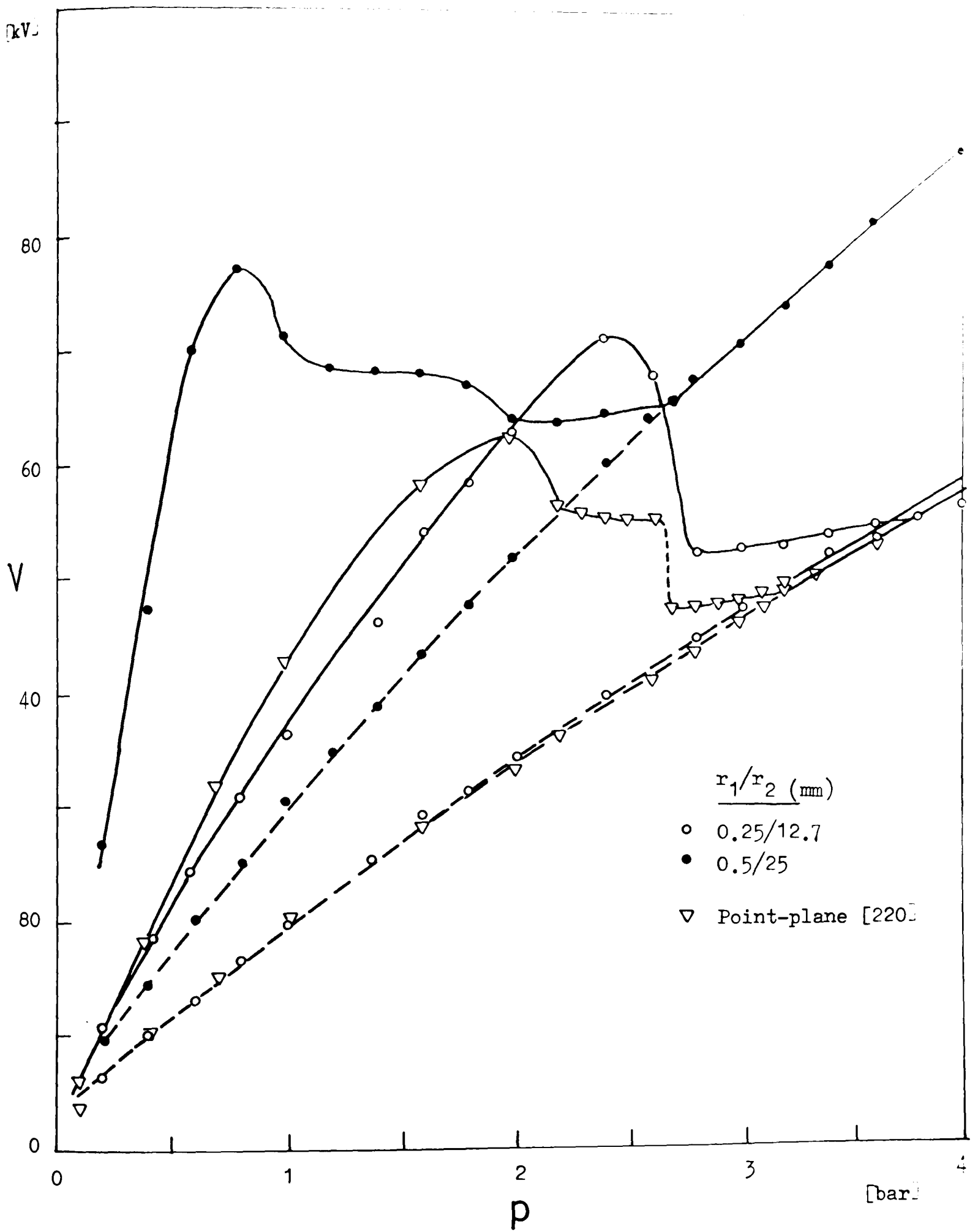


Figure 6.38 Comparison of positive voltage-pressure characteristics of point-plane and coaxial-electrode gaps in  $\text{SF}_6$  ( $\gamma = 7.5$ ). Point-plane gap; rod radius = 1.0 mm, gap length = 10 mm.

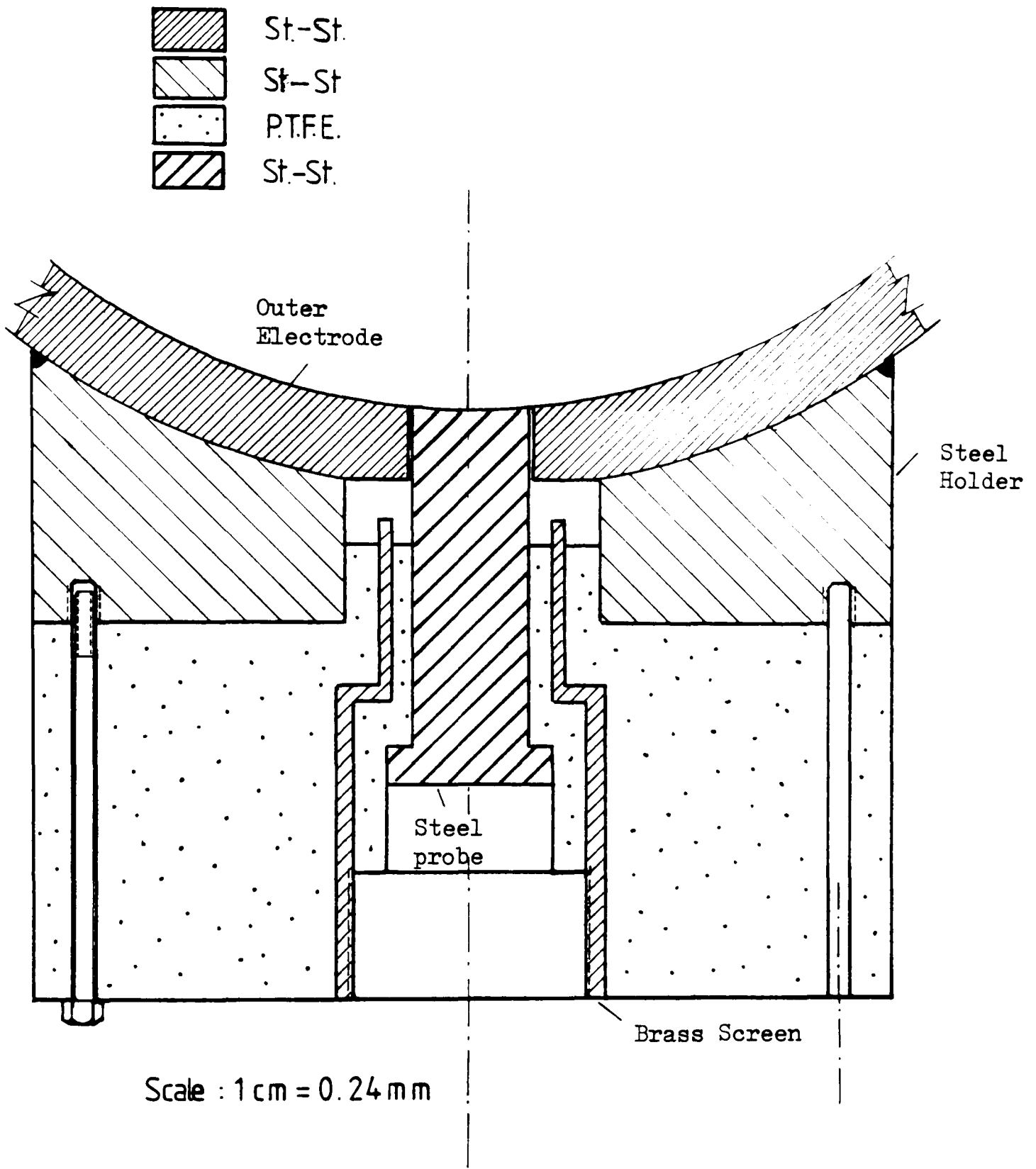


Figure 7.1(a) The details of the probe positioned on the outer conductor

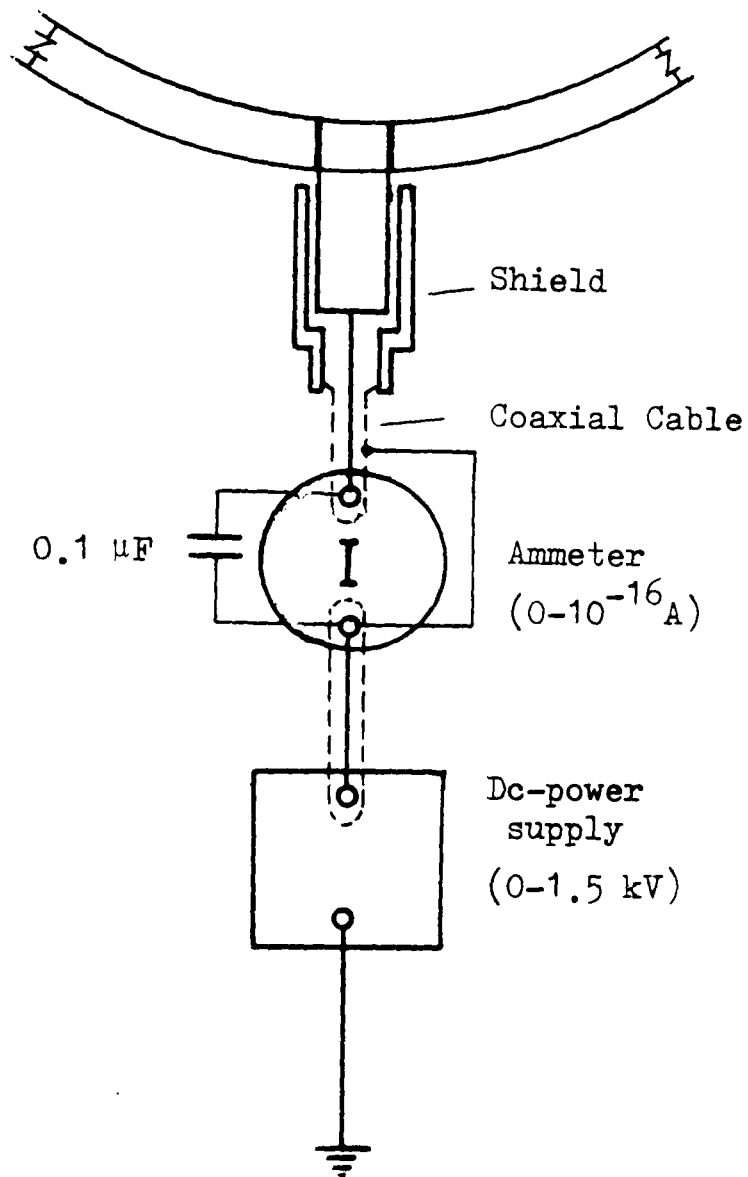


Figure 7.1(b) The connecting circuit of the field probe

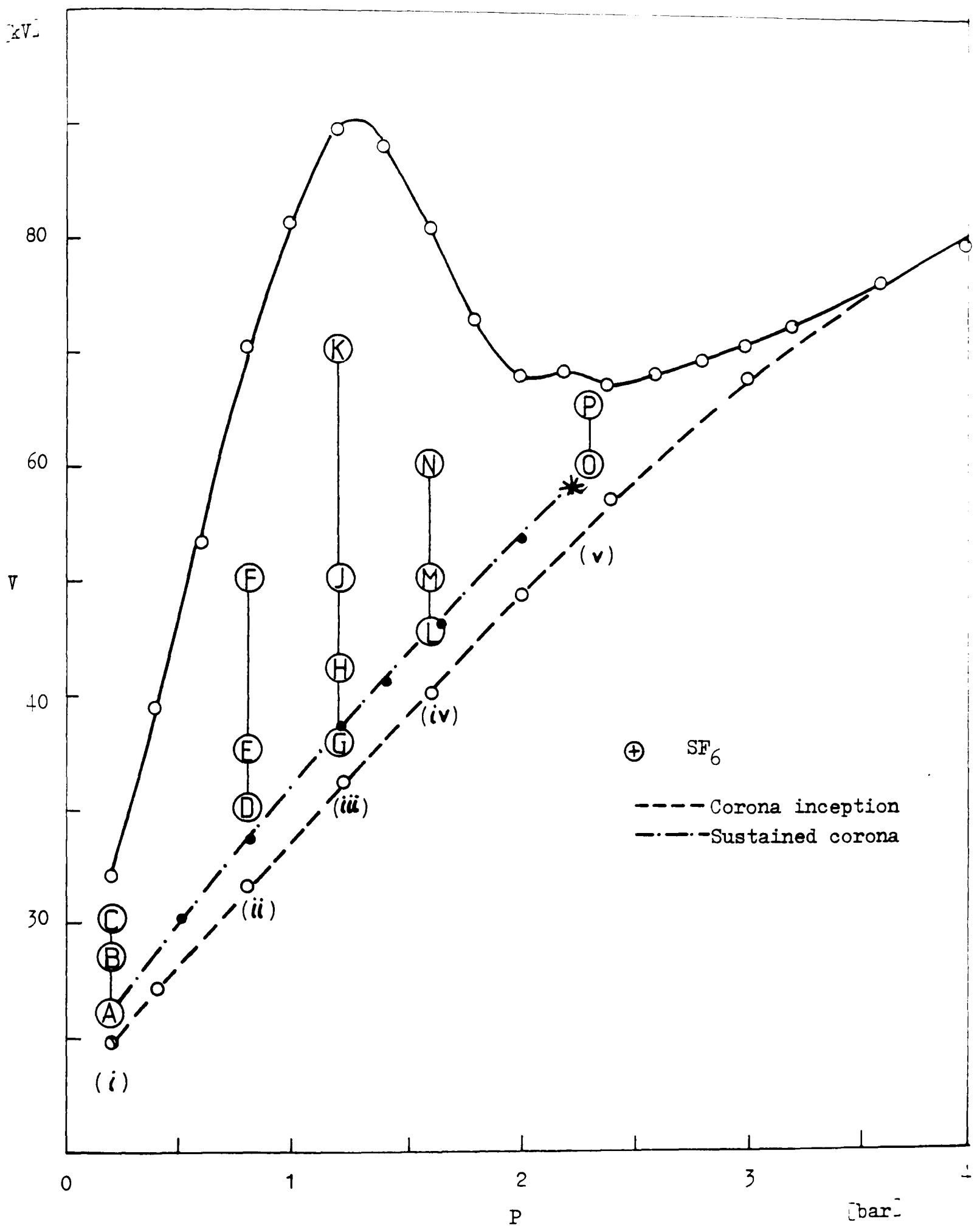


Figure 7.2 Positive voltage-pressure characteristic and discharge observation points of  $r_1/r_2 = 0.5/25$ -mm gap in SF<sub>6</sub>

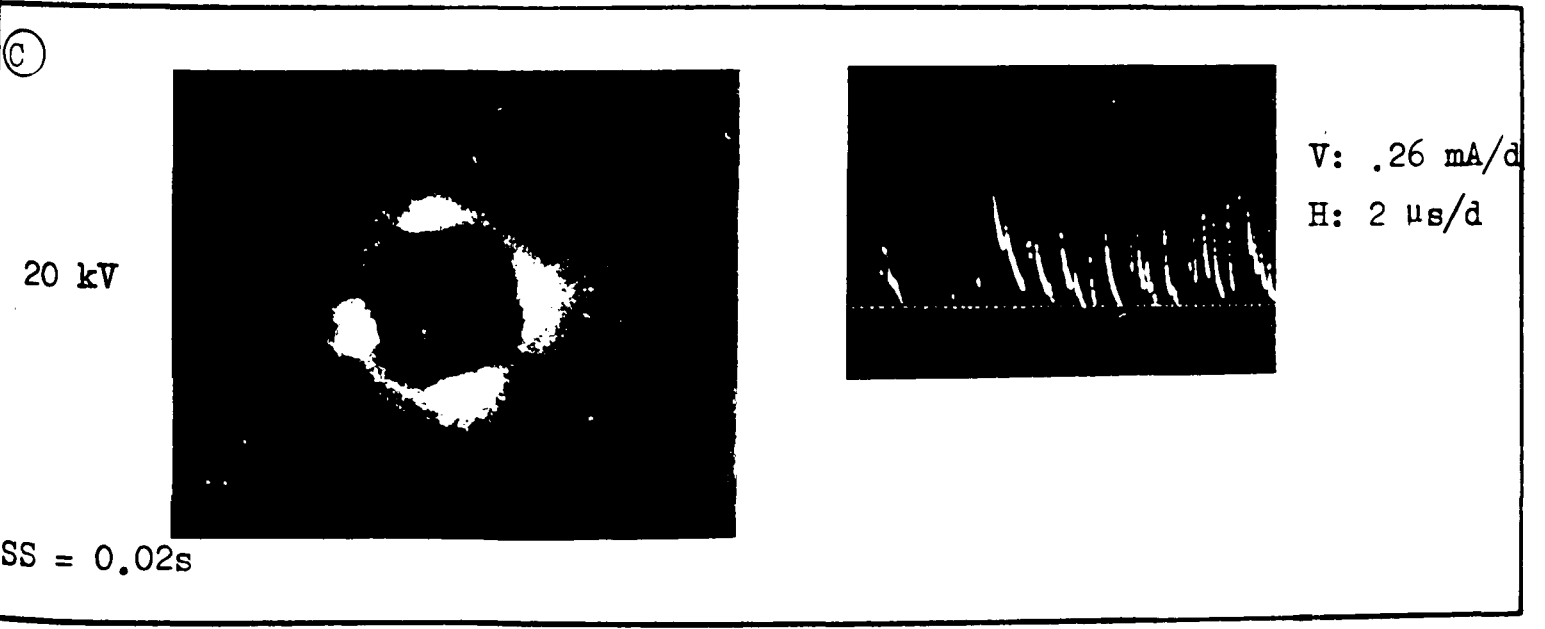
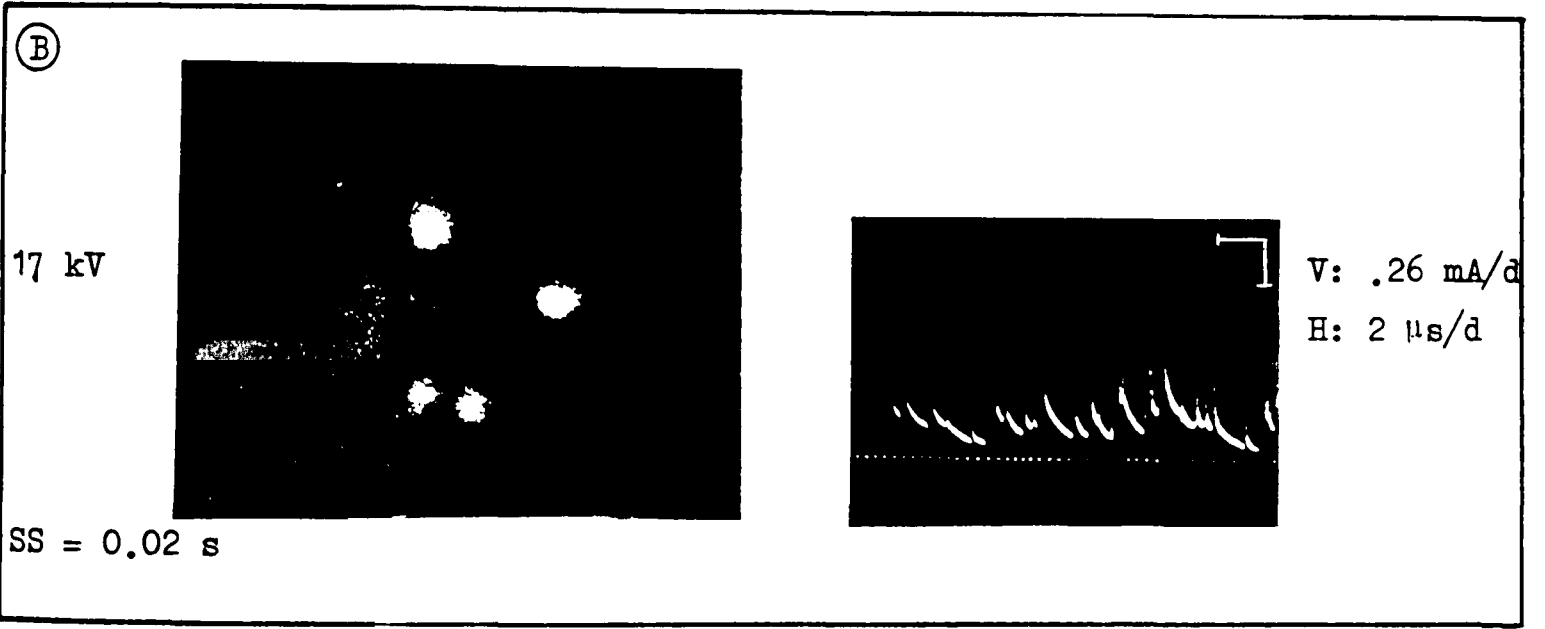
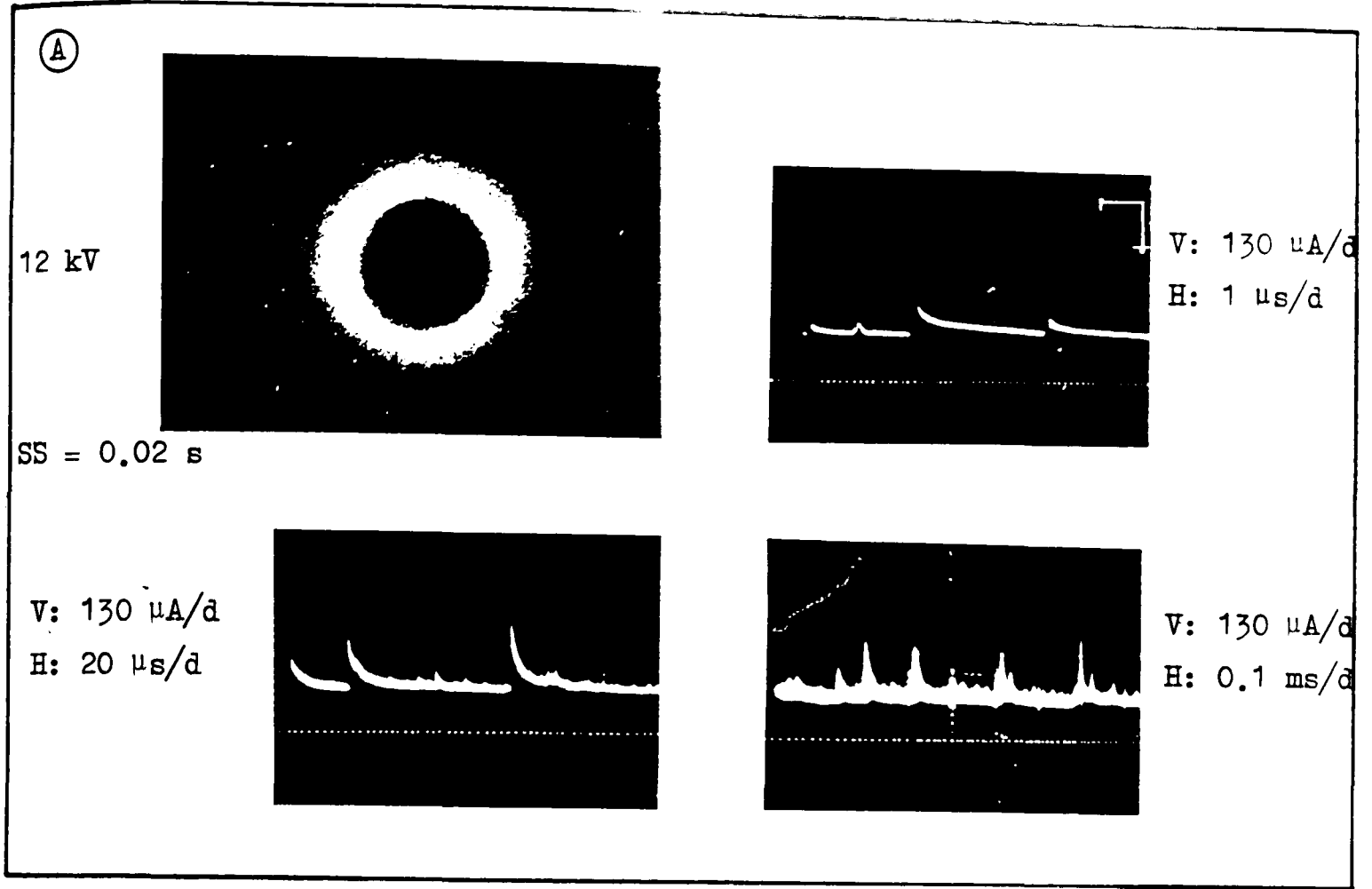


Figure 7.2(i) Positive corona discharge activity in SF<sub>6</sub> at  $p = 0.2$  bar  
( $r_1/r_2 = 0.5/25$  mm)

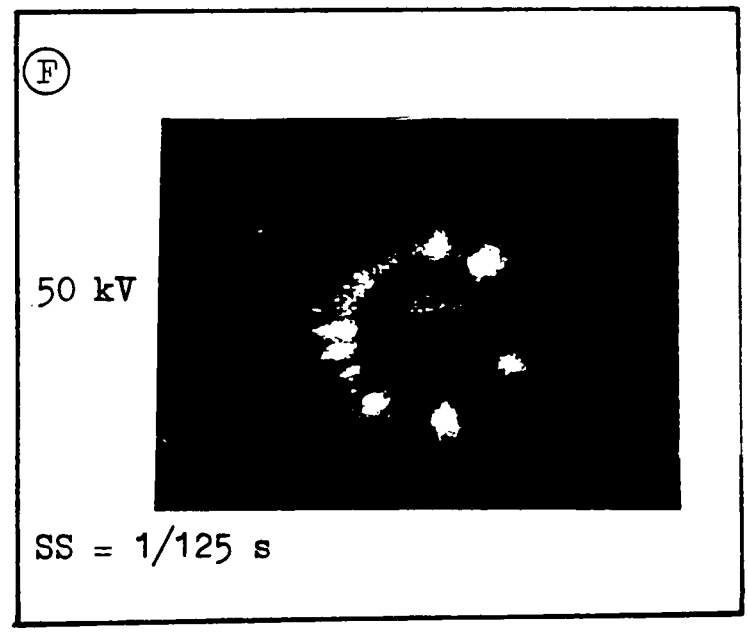
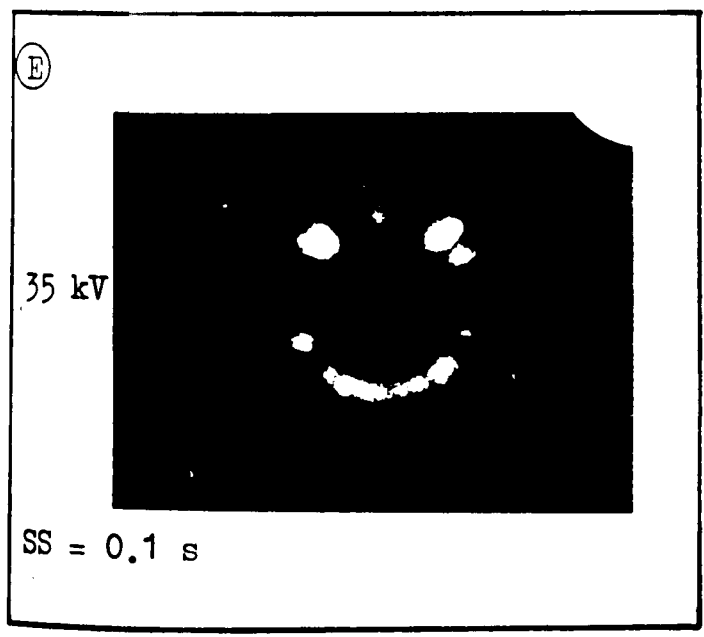
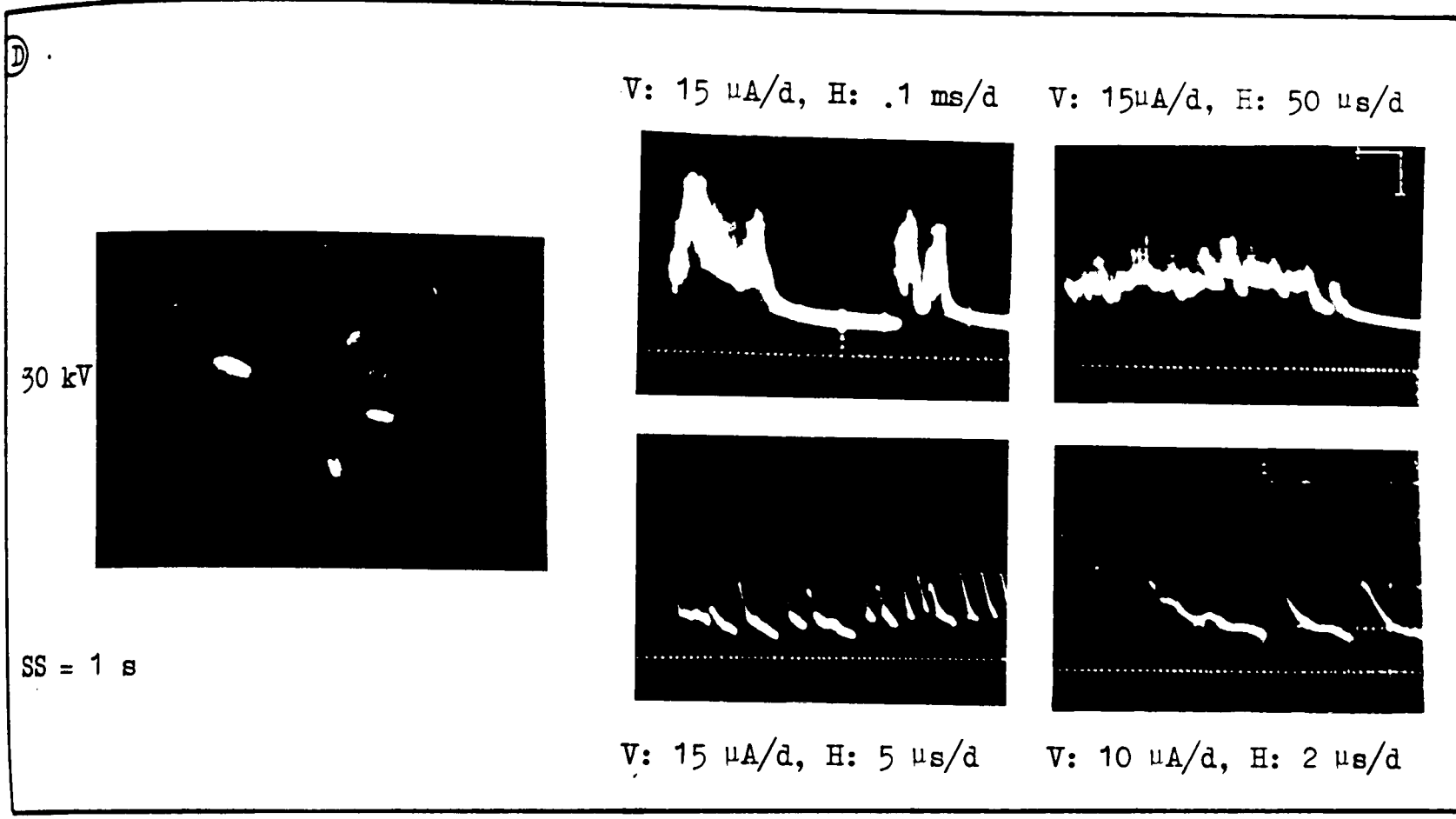


Figure 7.2 (ii) Positive corona discharge activity in SF<sub>6</sub> at p = 0.8 bar  
(r<sub>1</sub>/r<sub>2</sub> = 0.5/25 mm)

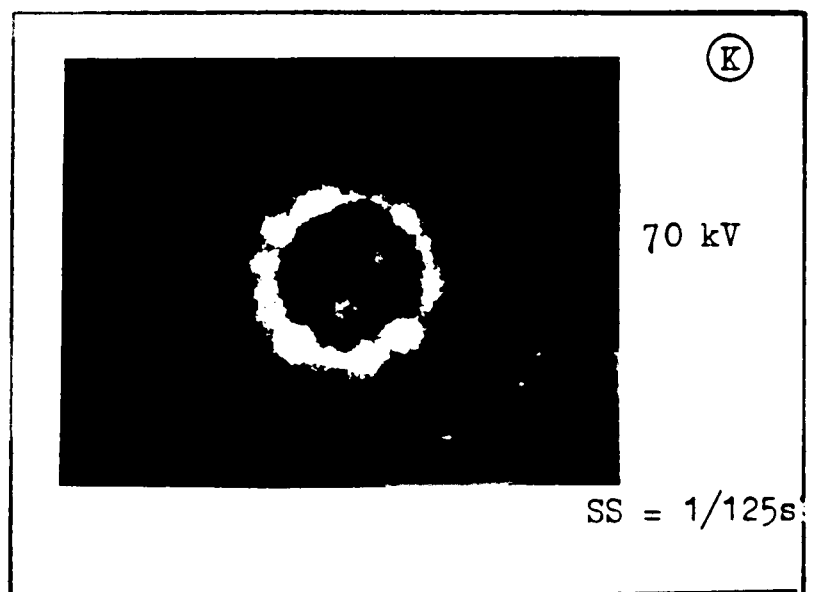
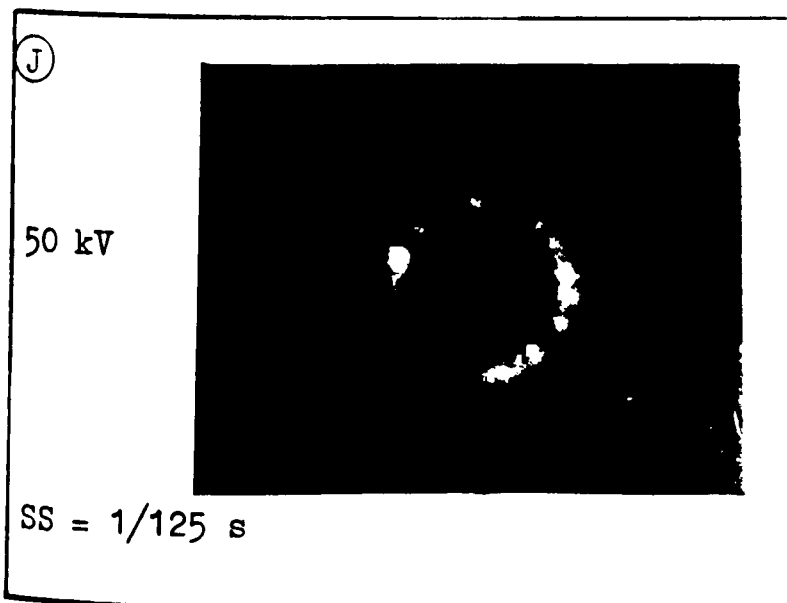
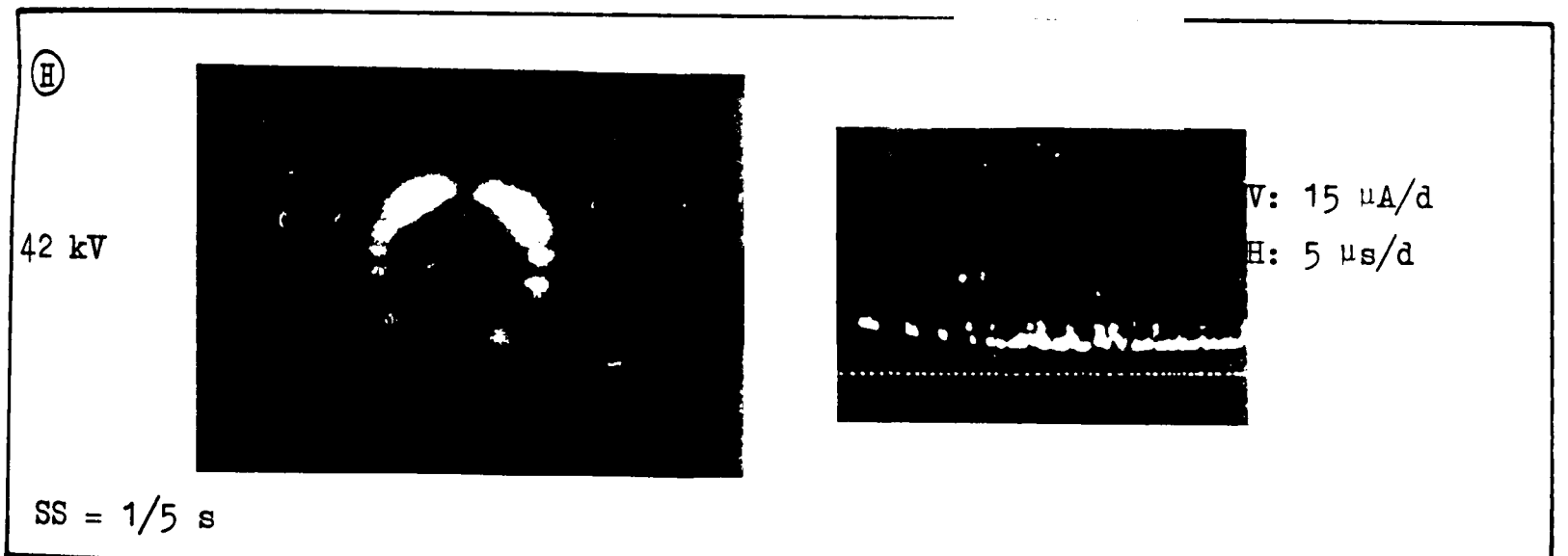
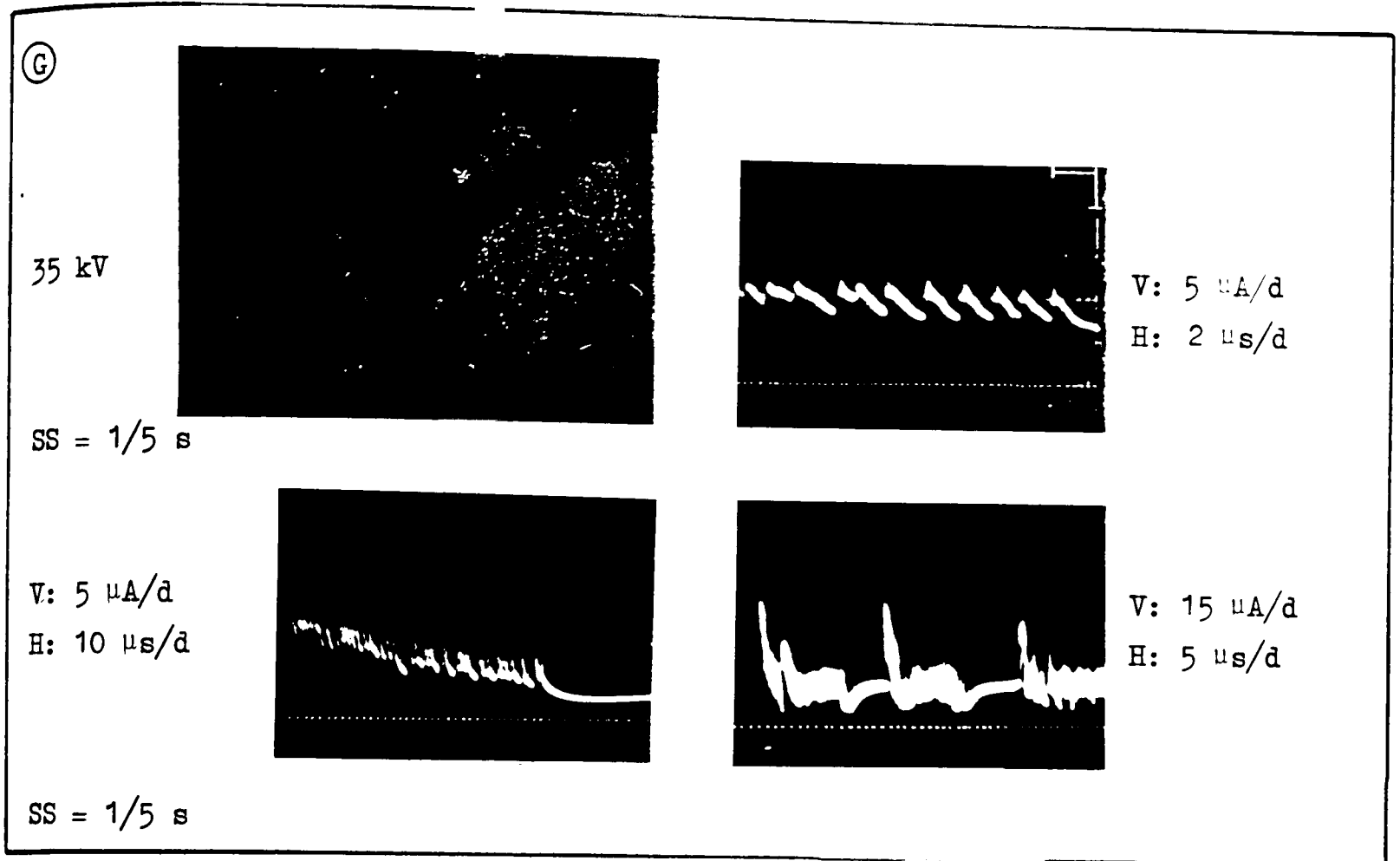
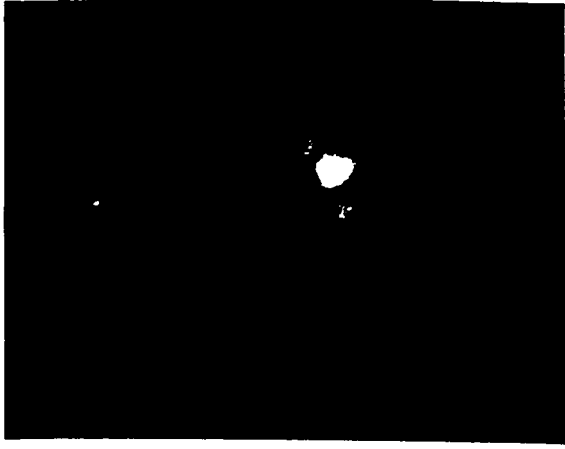


Figure 7.2(iii) Positive corona discharge activity in  $\text{SF}_6$  at  $p = 1.2 \text{ bar}$  ( $r_1/r_2 = 0.5/25 \text{ mm}$ )

(L)

45 kV

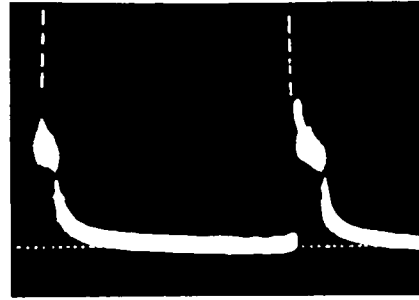
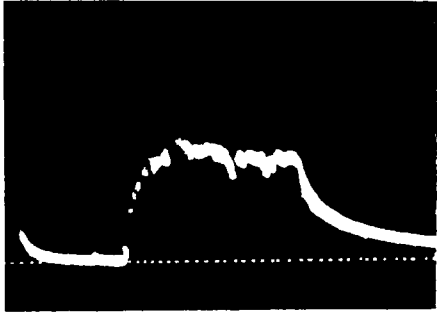


V: 10  $\mu$ A/d  
H: 5  $\mu$ s/d

SS = 1/125 s

V: 15  $\mu$ A/d

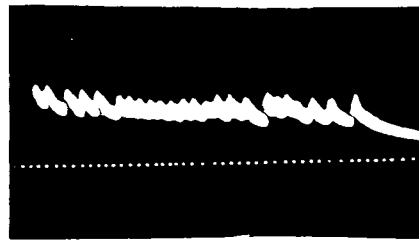
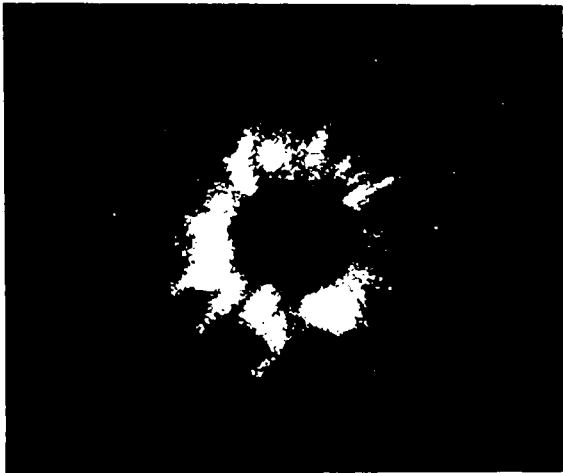
H: 50  $\mu$ s/d



V: 15  $\mu$ A/d  
H: .5 ms/d

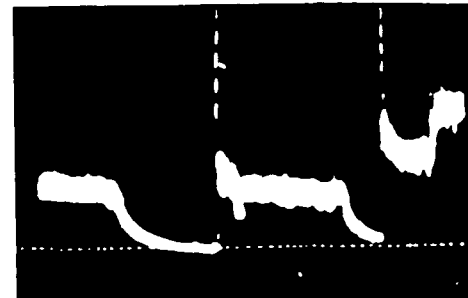
(M)

50 kV



V: 15  $\mu$ A/d  
H: 5  $\mu$ s/d

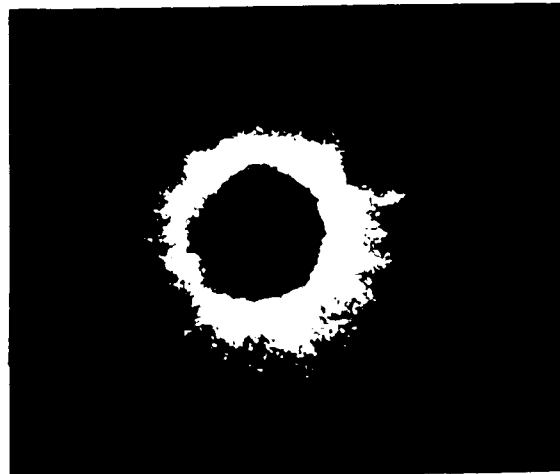
SS = 1/125 S



V: 15  $\mu$ A/d  
H: 50  $\mu$ s/d

(N)

60 kV



SS = 1/125 s

Figure 7.2(iv) Positive corona discharge activity in SF<sub>6</sub> at p = 1.6 bar (r<sub>1</sub>/r<sub>2</sub> = 0.5/25 mm)

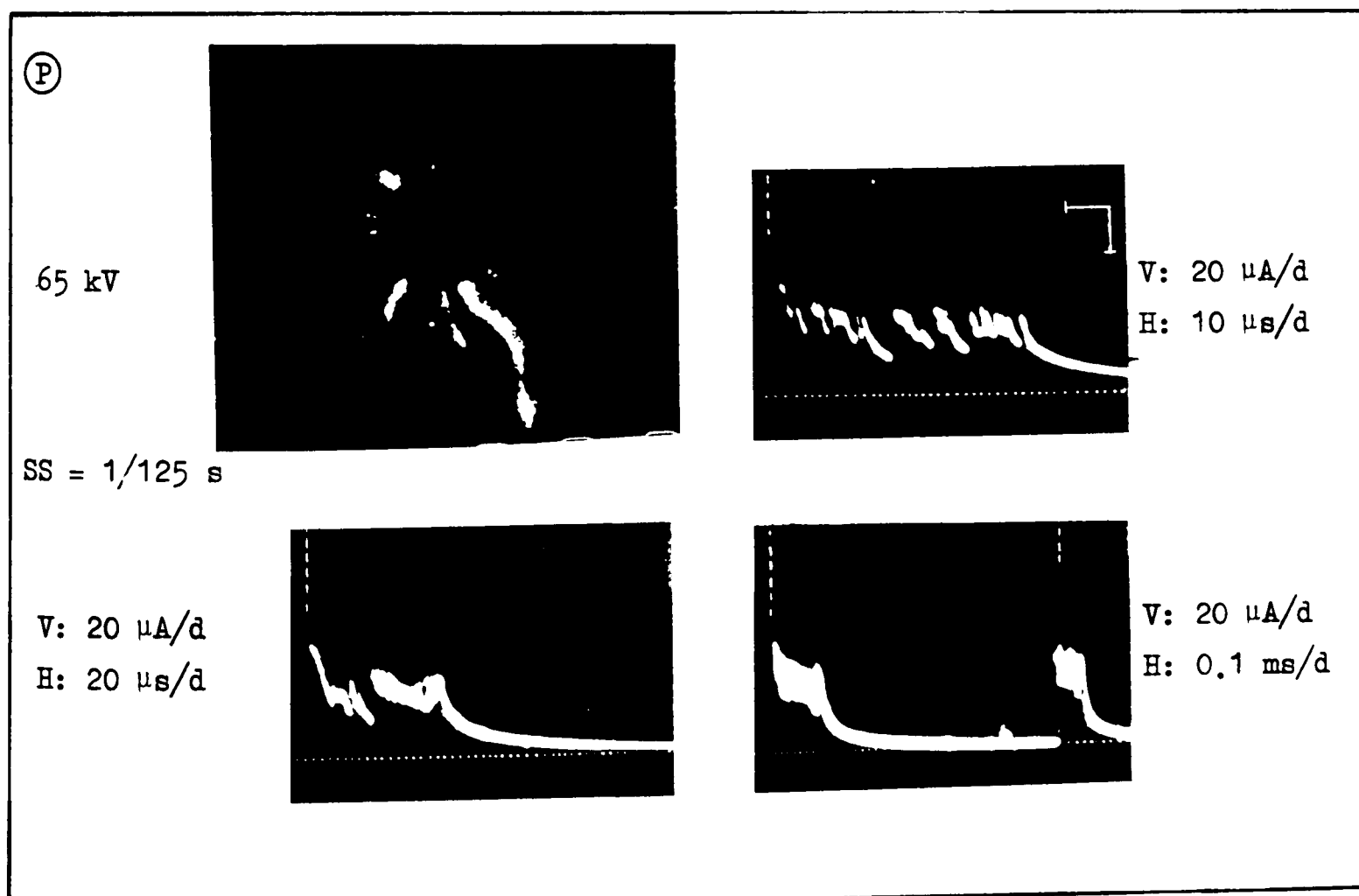
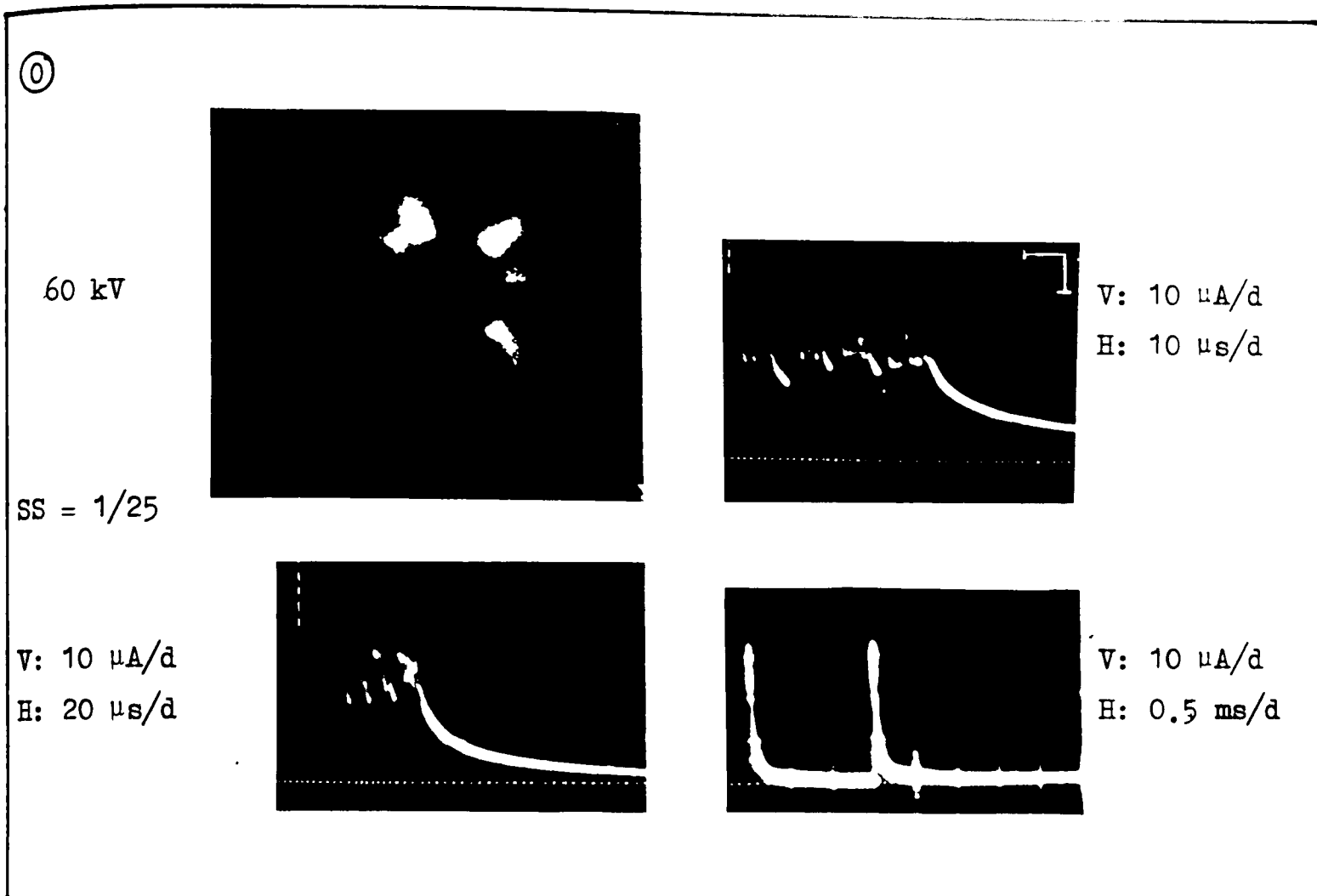


Figure 7.2(v) Positive corona discharge activity in SF<sub>6</sub> at  $p = 2.5$  bar

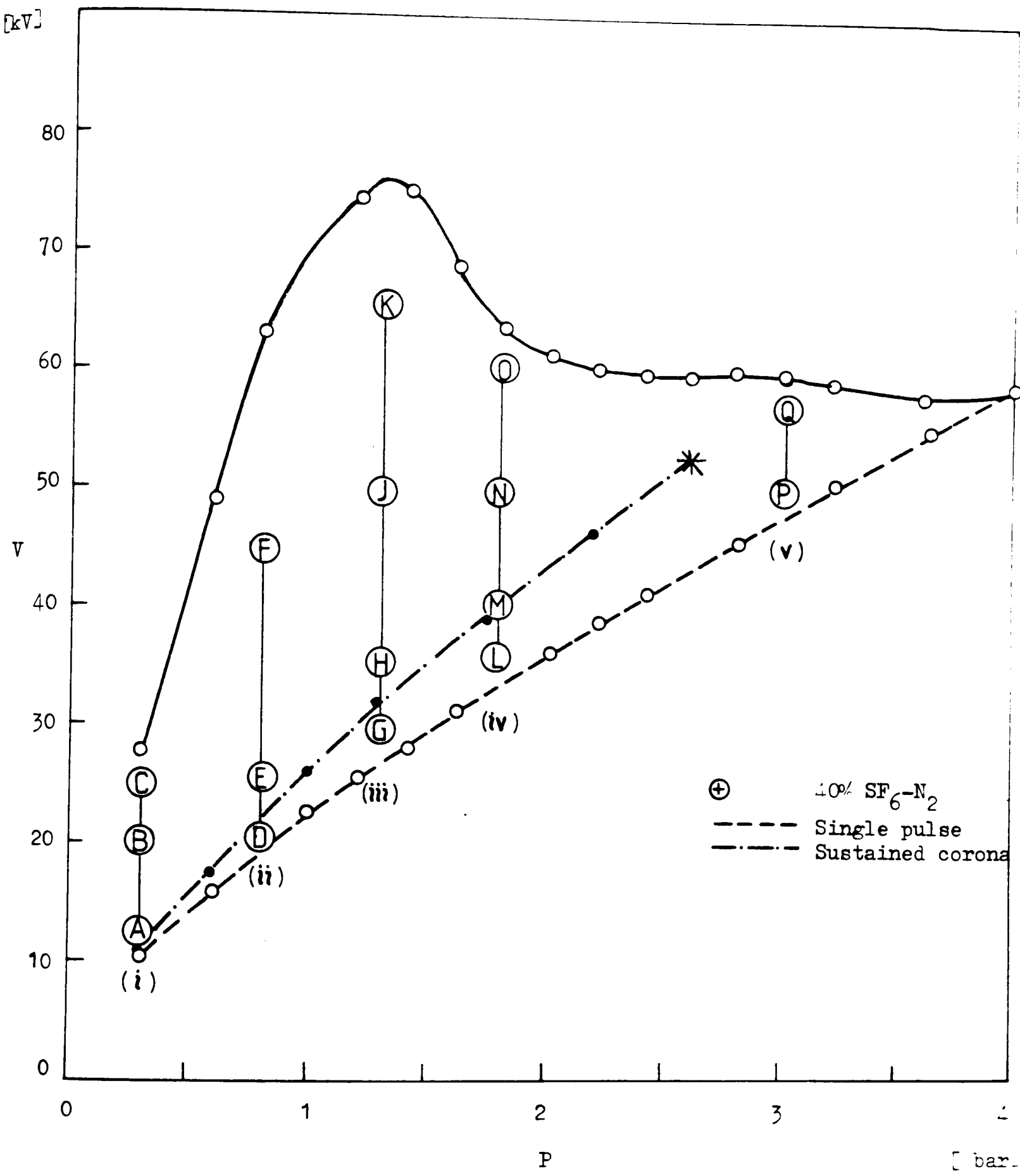


Figure 7.3 Positive voltage-pressure characteristic and discharge observation points of  $r_1/r_2 = 0.5/25$ -mm gap in  $40\% SF_6-N_2$  mixture

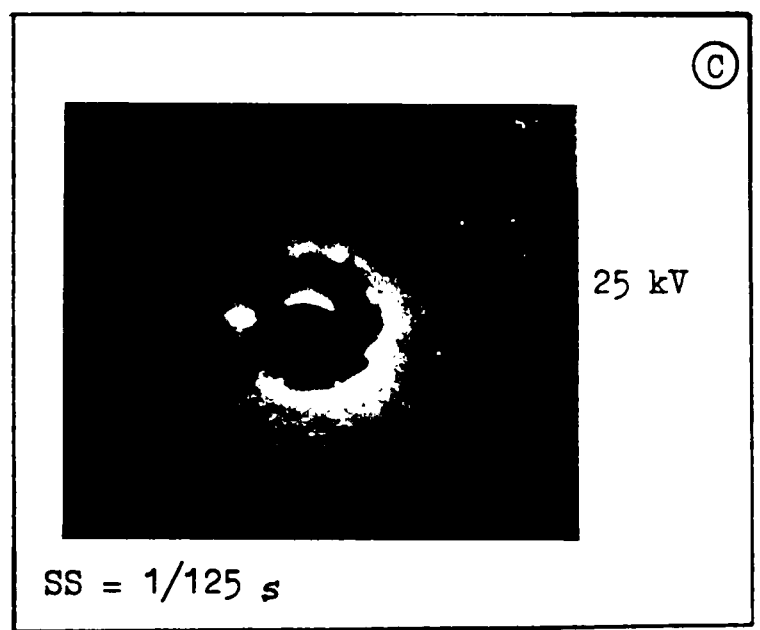
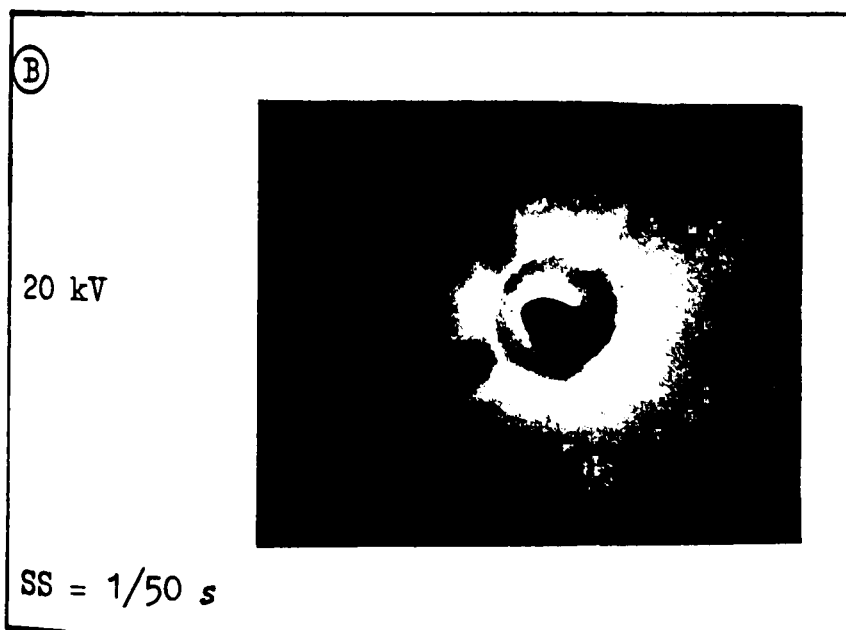
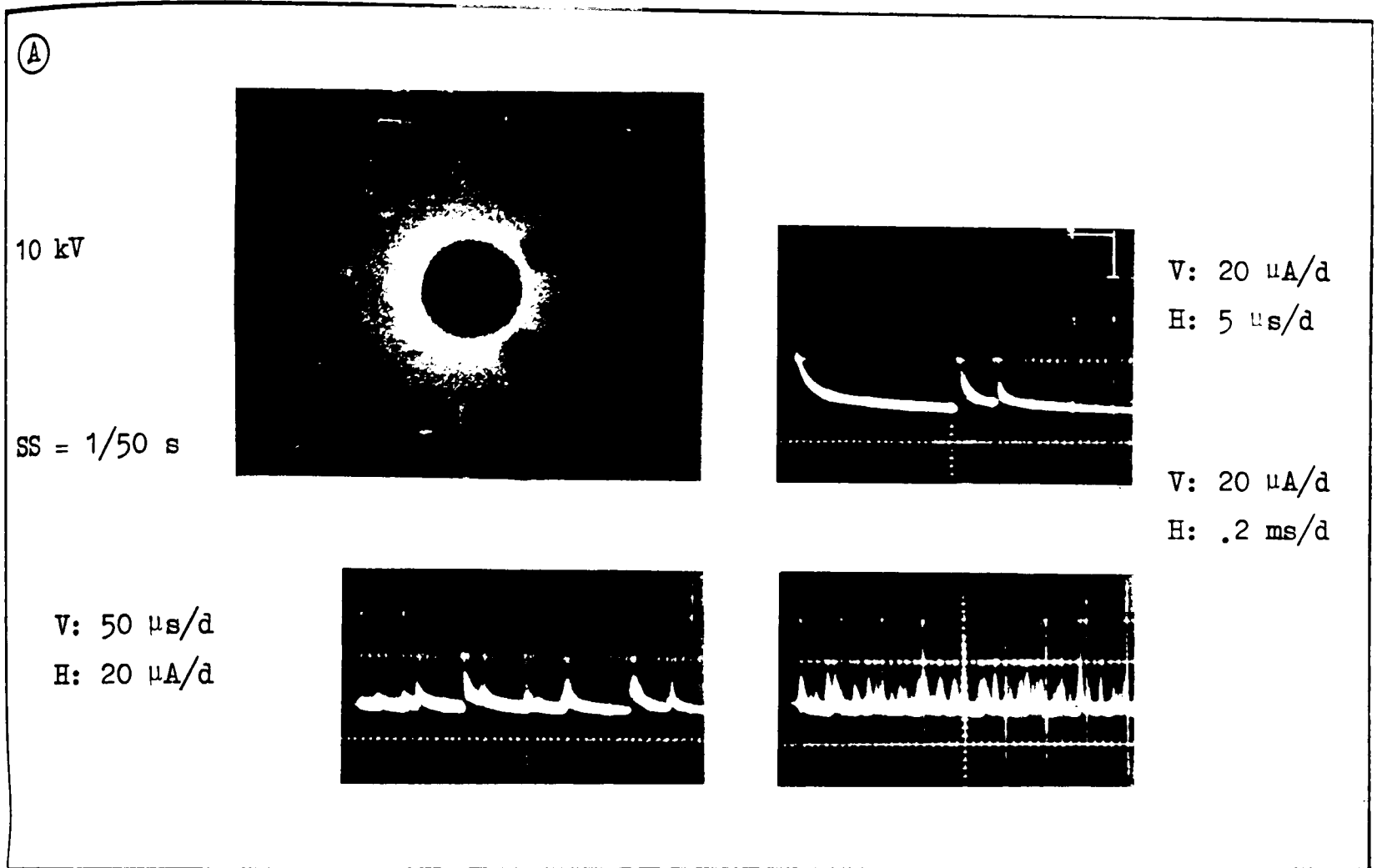


Figure 7.3(i) Positive corona discharge activity in 40% SF<sub>6</sub>-N<sub>2</sub> at p = 0.3 bar ( $r_1/r_2 = 0.5/25$  mm)

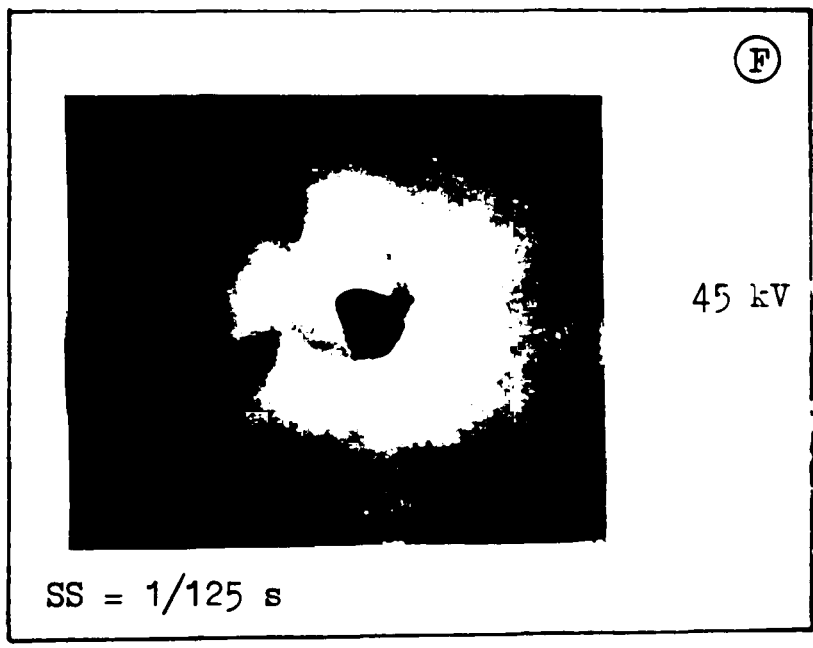
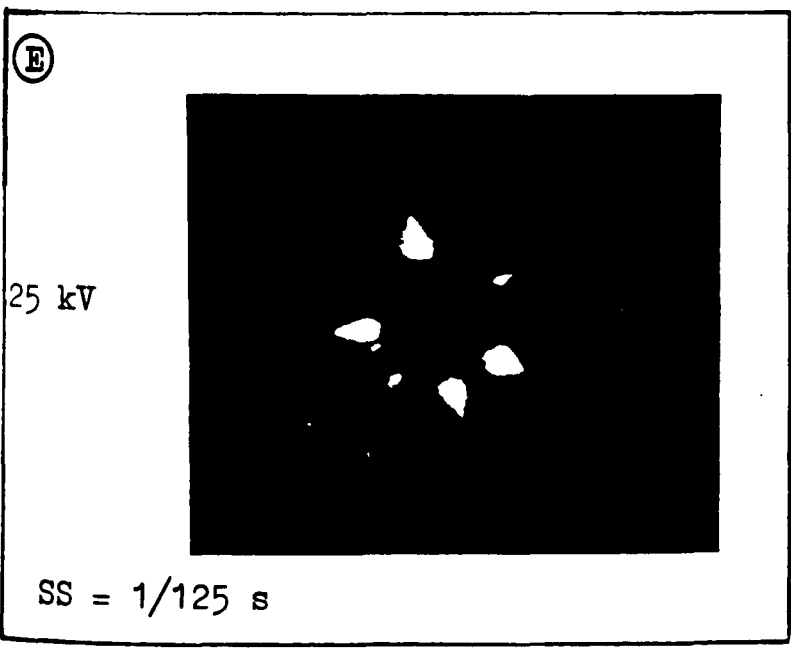
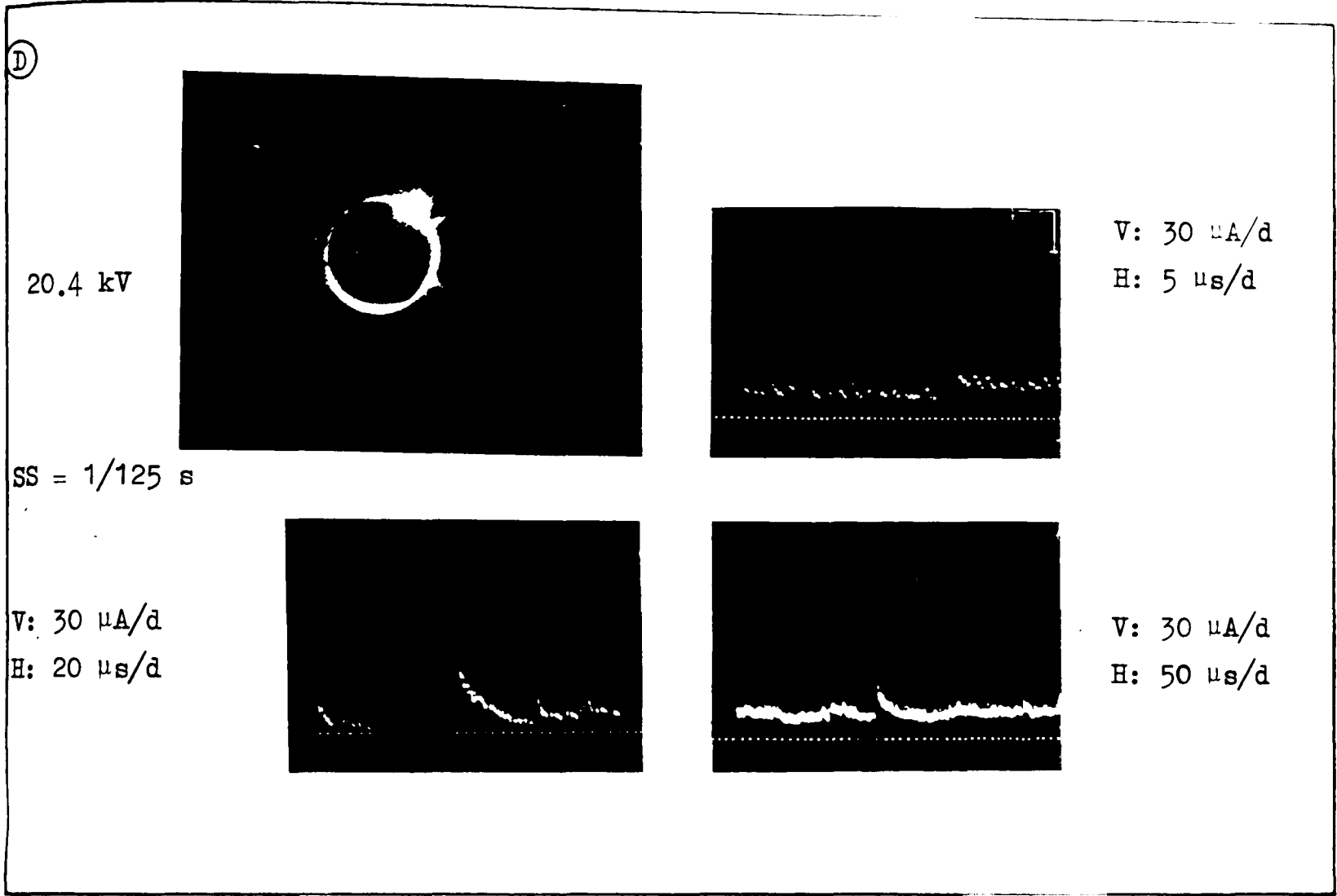


Figure 7.3(ii) Positive corona discharge activity in 40% SF<sub>6</sub>-N<sub>2</sub> at p = 0.8 bar ( $r_1/r_2 = 0.5/25$  mm)

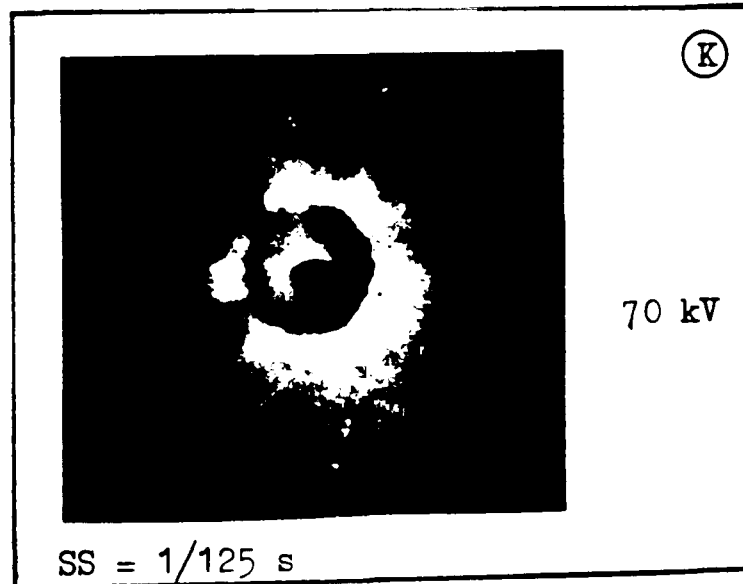
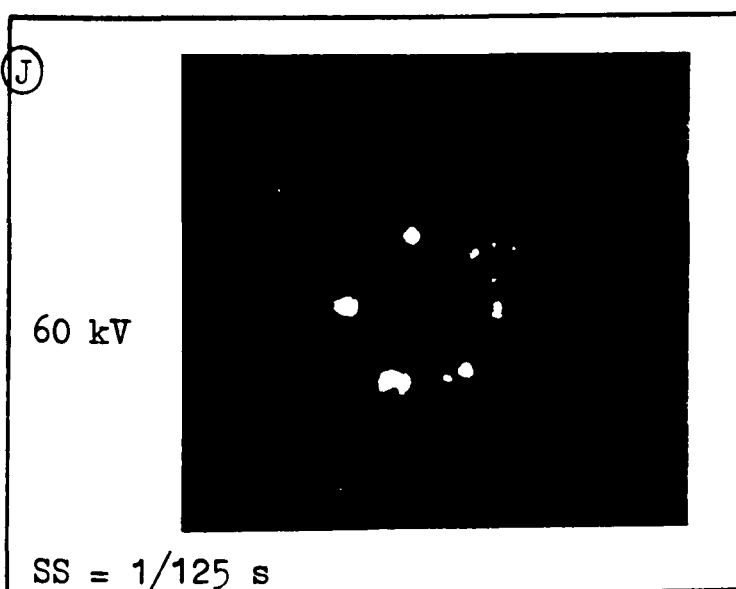
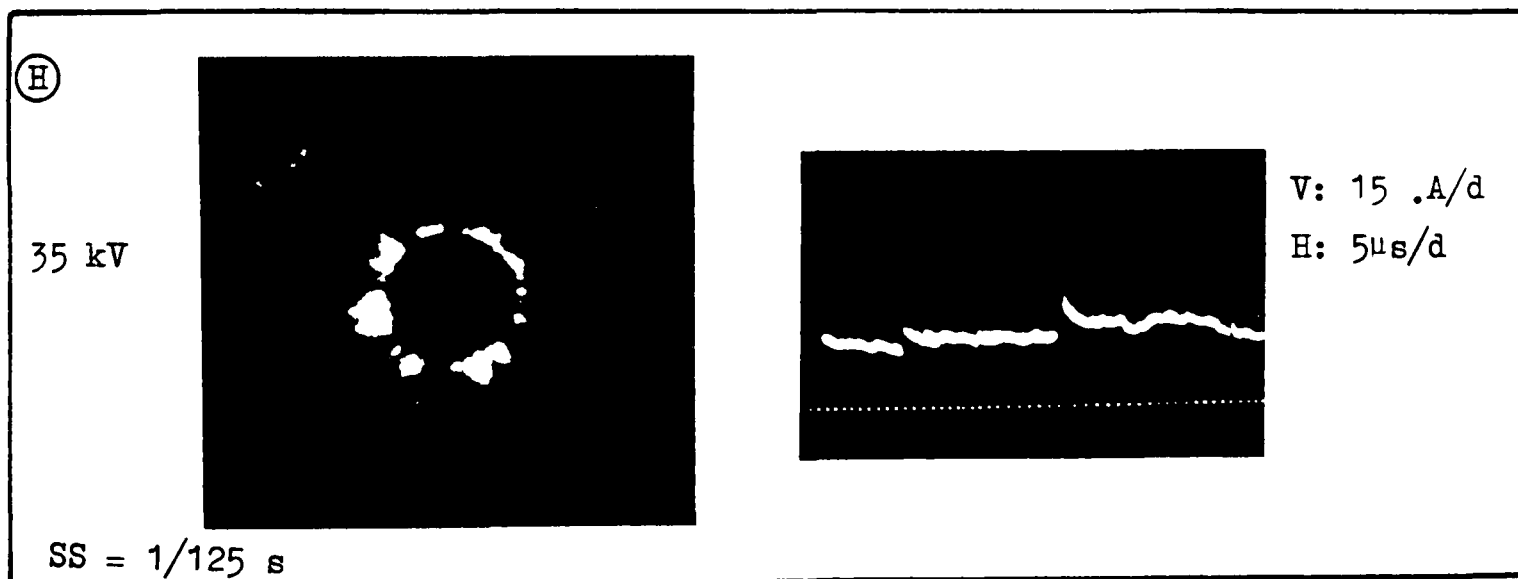
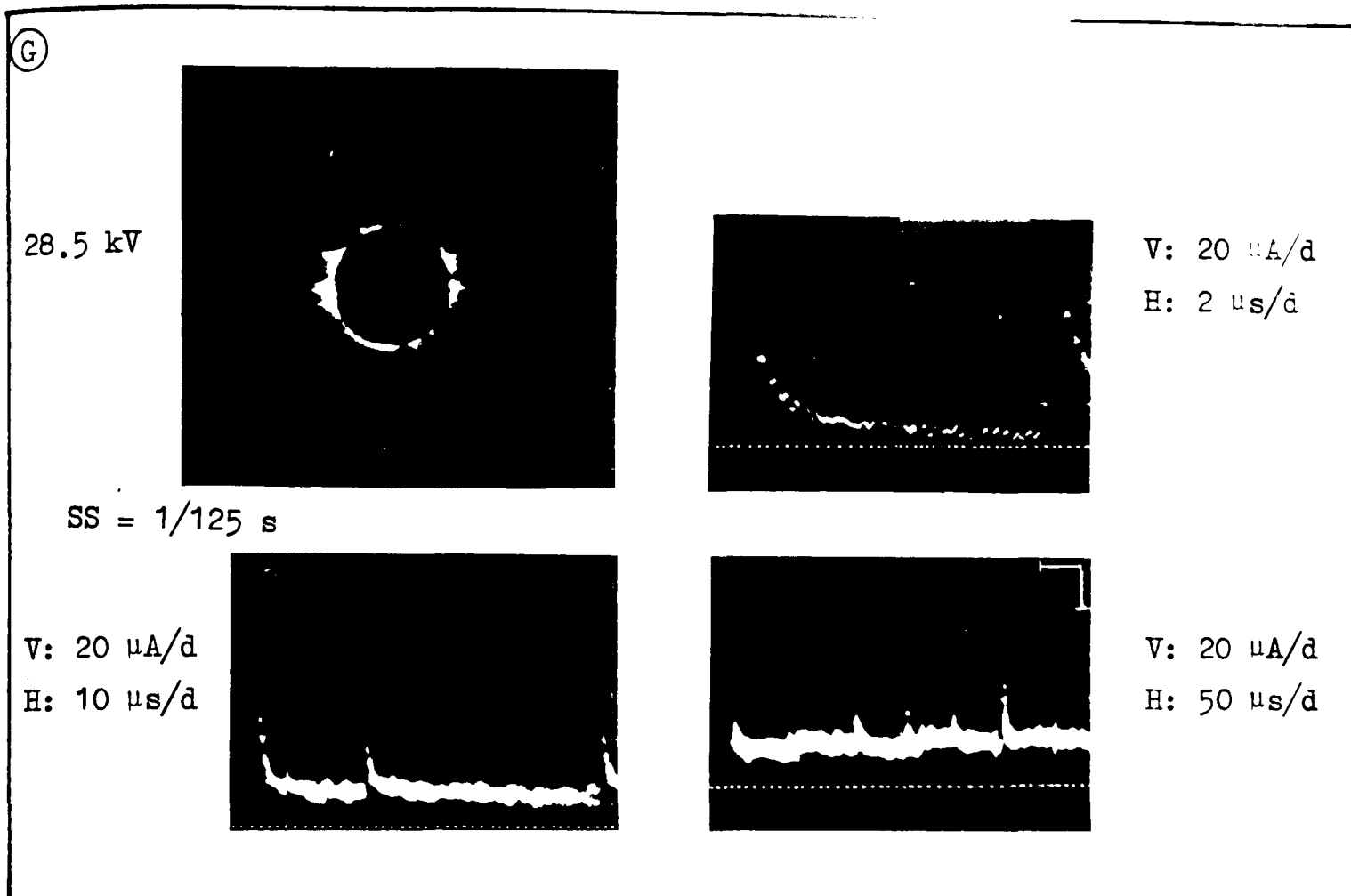


Figure 7.3(iii) Positive corona discharge activity in 40% SF<sub>6</sub>-N<sub>2</sub> at  
1.3 bar ( $r_1/r_2 = 0.5/25$  mm)

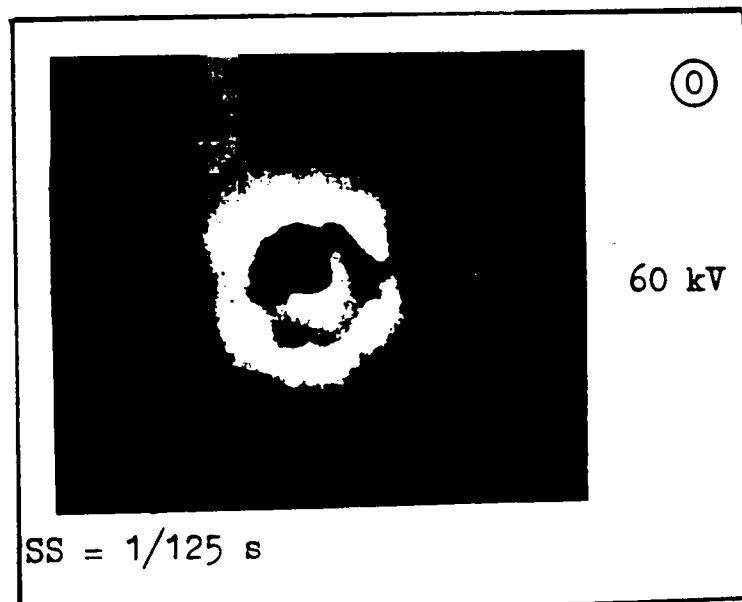
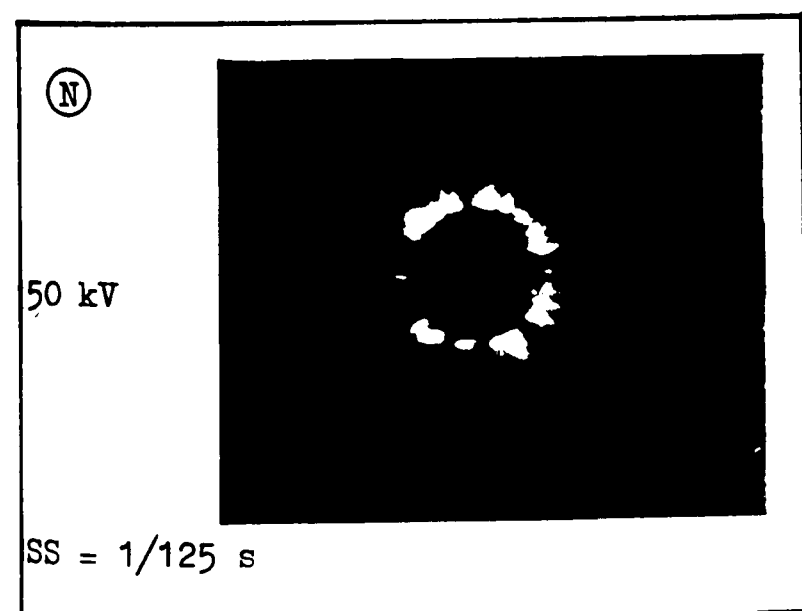
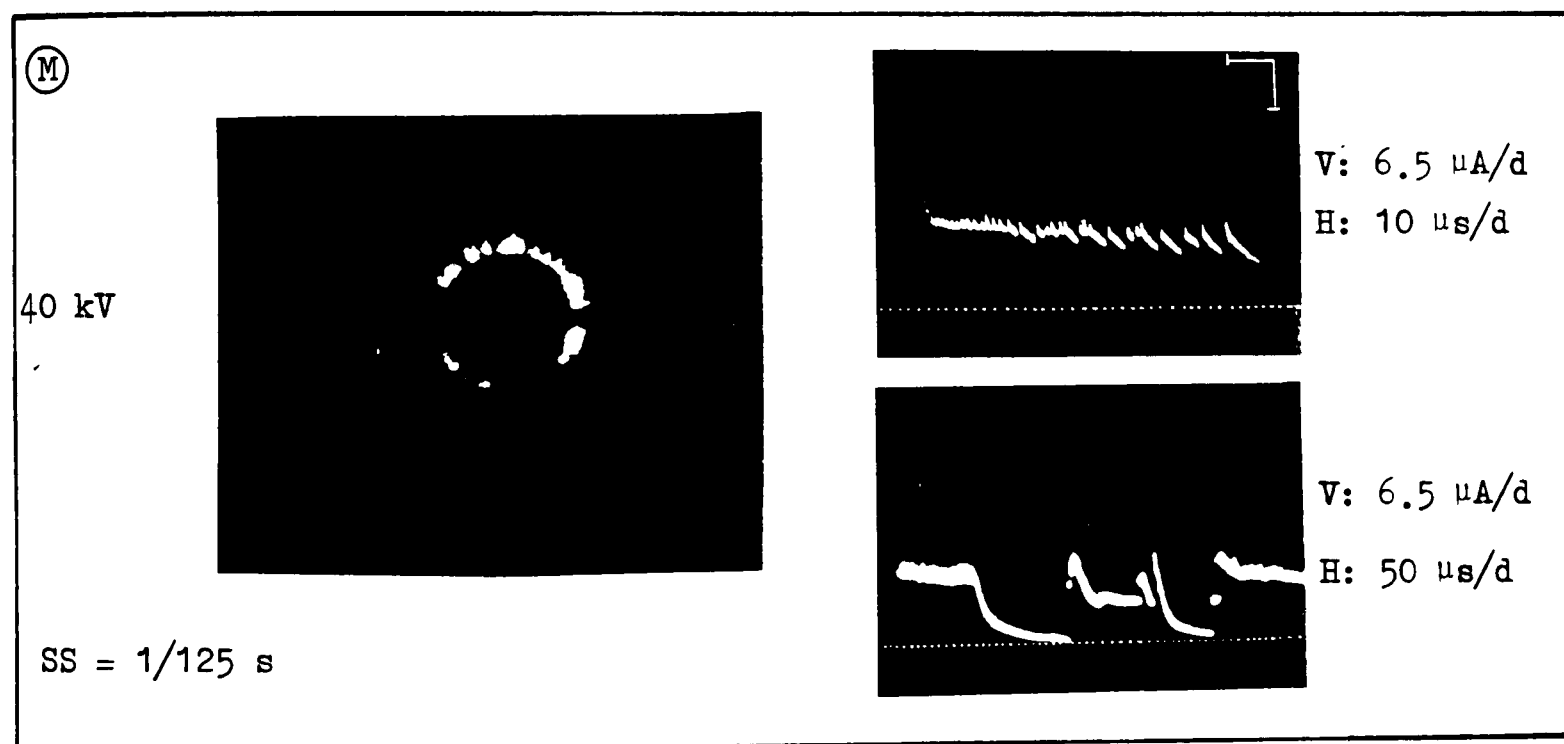
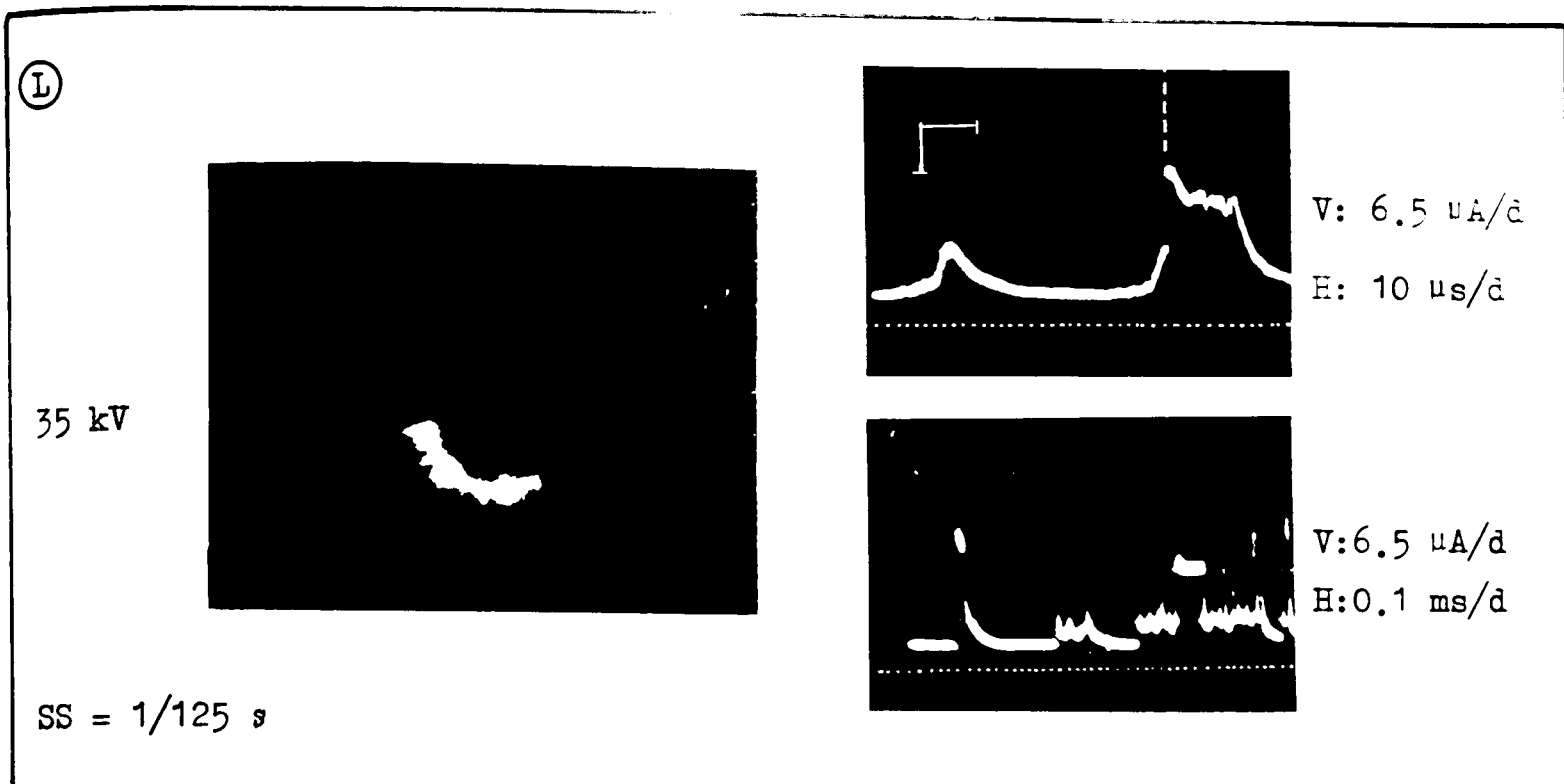
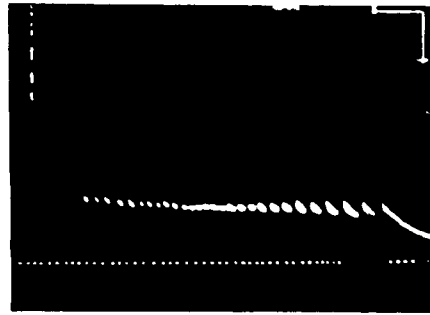


Figure 7.3(iv) Positive corona discharge activity in SF<sub>6</sub> at  $p = 1.8$  bar  
( $r_1/r_2 = 0.5/25$  mm)

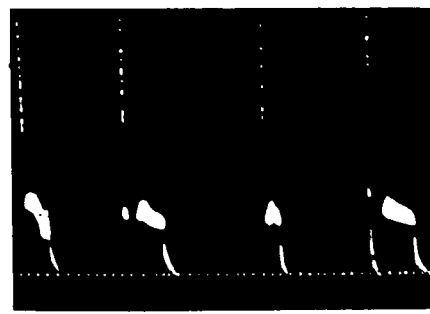
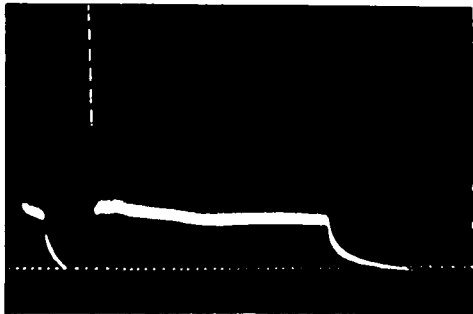
(P)

50 kV



V : 15  $\mu$ A/d  
H : 5  $\mu$ s/d

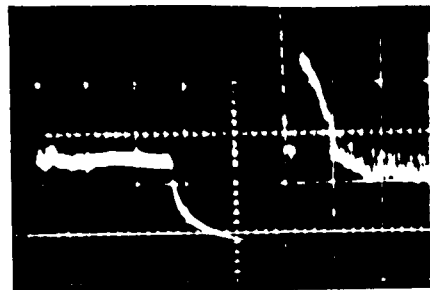
V : 5  $\mu$ A/d  
H : 50  $\mu$ s/d



V : 15  $\mu$ A/d  
H : .5 ms/d

(Q)

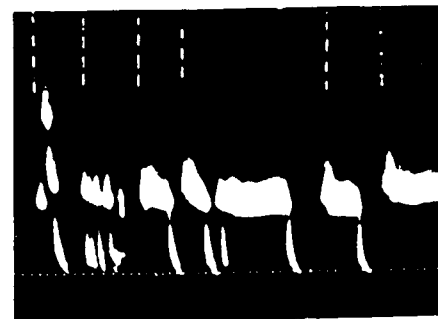
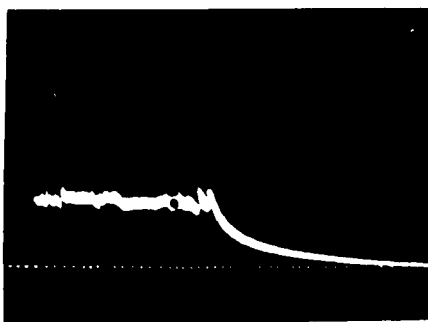
57 kV



V : 15  $\mu$ A/d  
H : 50  $\mu$ s/d

SS = 1/125

V : 15  $\mu$ A/d  
H : 10  $\mu$ s/d



V : 15  $\mu$ A/d  
H : 0.1 ms/d

Figure 7.3(v) Positive corona discharge activity in 40% SF<sub>6</sub>-N<sub>2</sub> at p = 3.0 bar

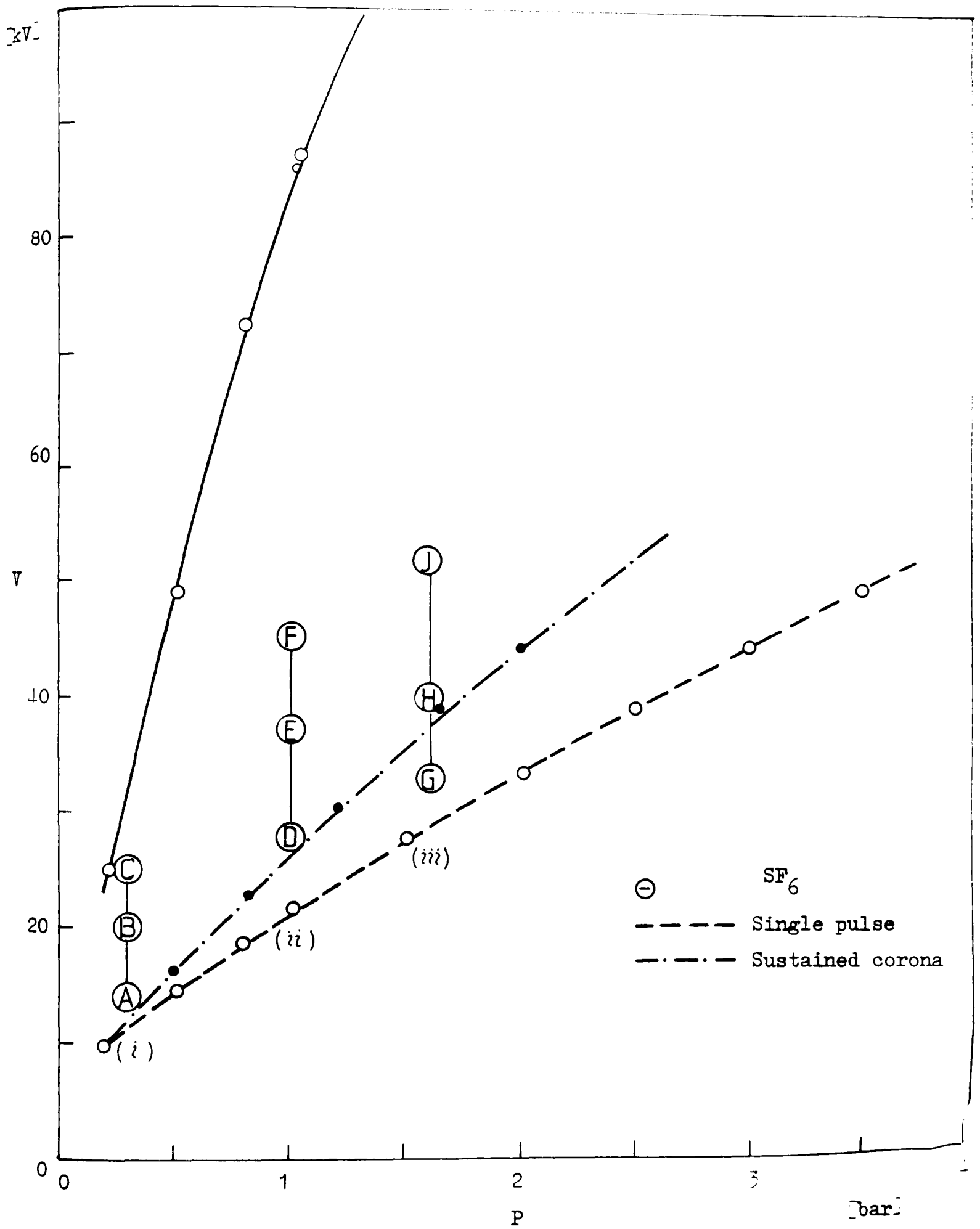


Figure 7.1 Negative voltage-pressure characteristic and discharge observation points of  $r_1/r_2 = 0.5/25$ -mm gap in  $SF_6$ .

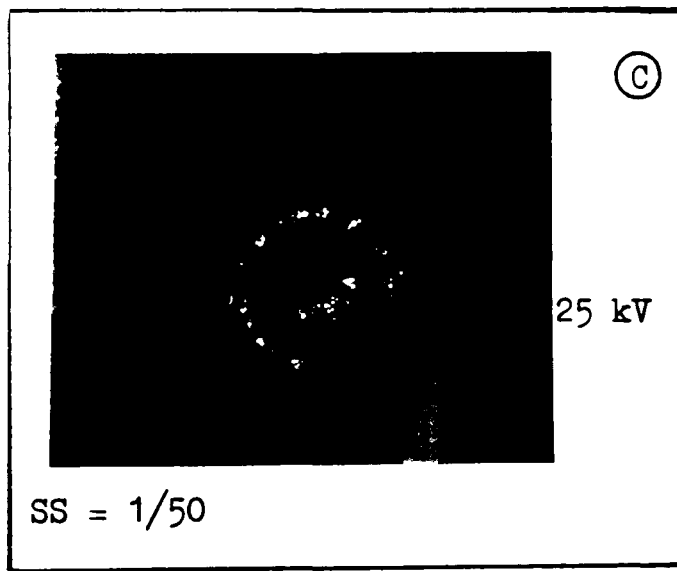
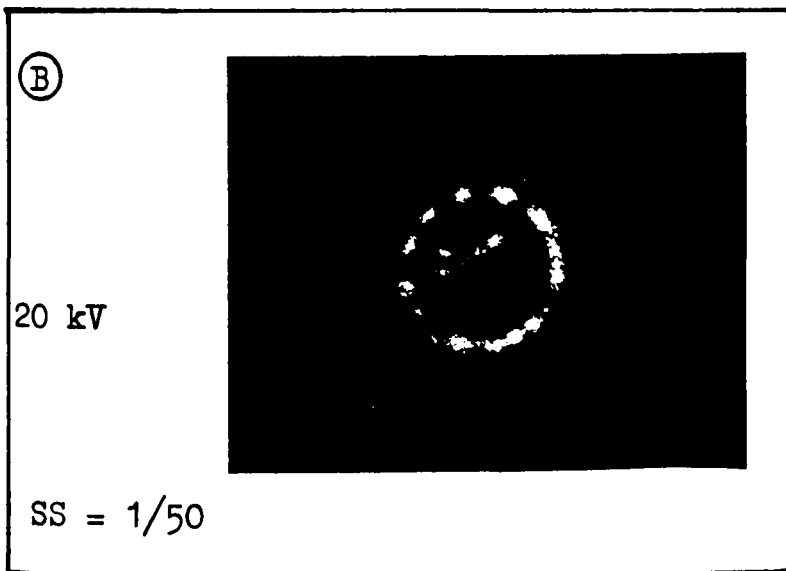
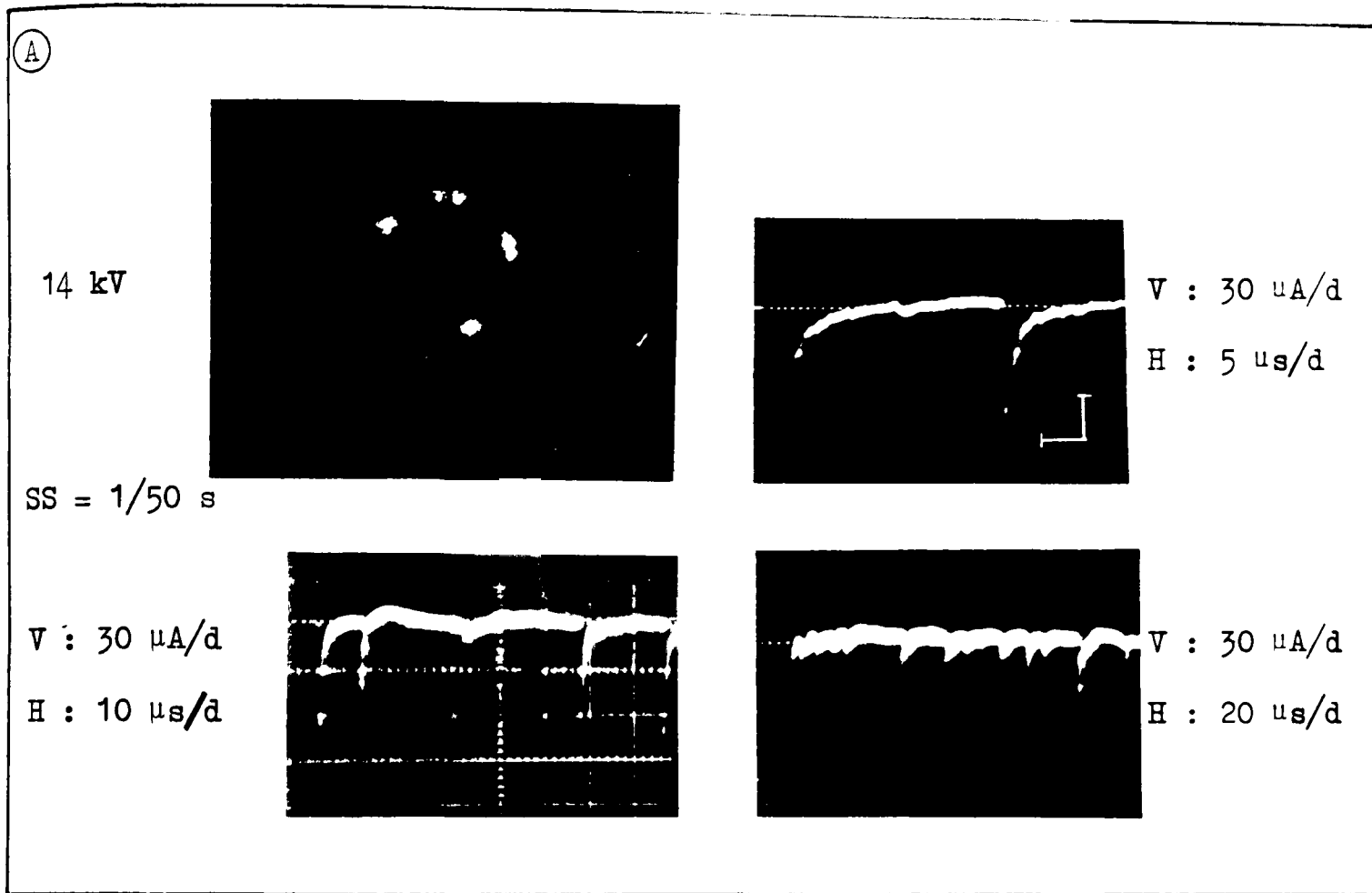


Figure 7.4(i) Negative corona discharge activity in SF<sub>6</sub> at p = 0.3 bar  
 (r<sub>1</sub>/r<sub>2</sub> = 0.5/25 mm)

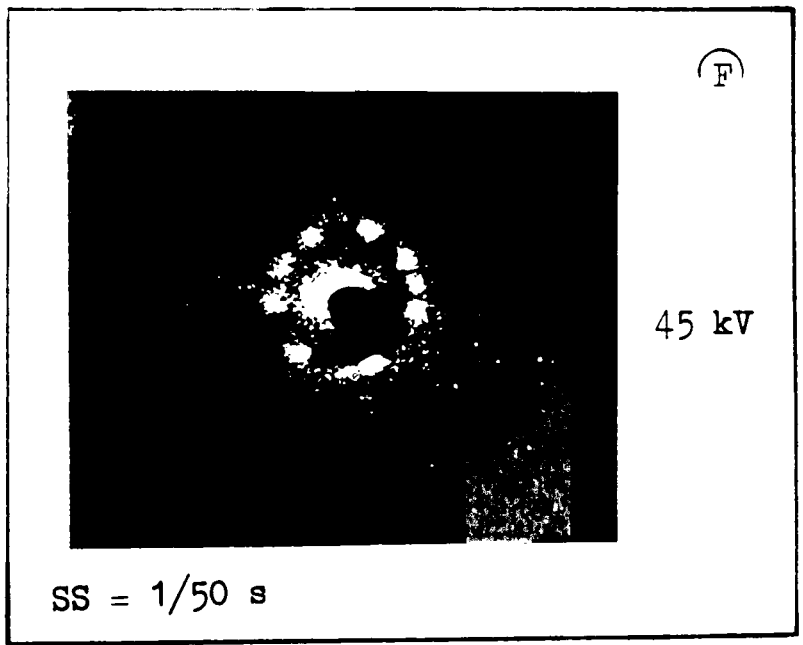
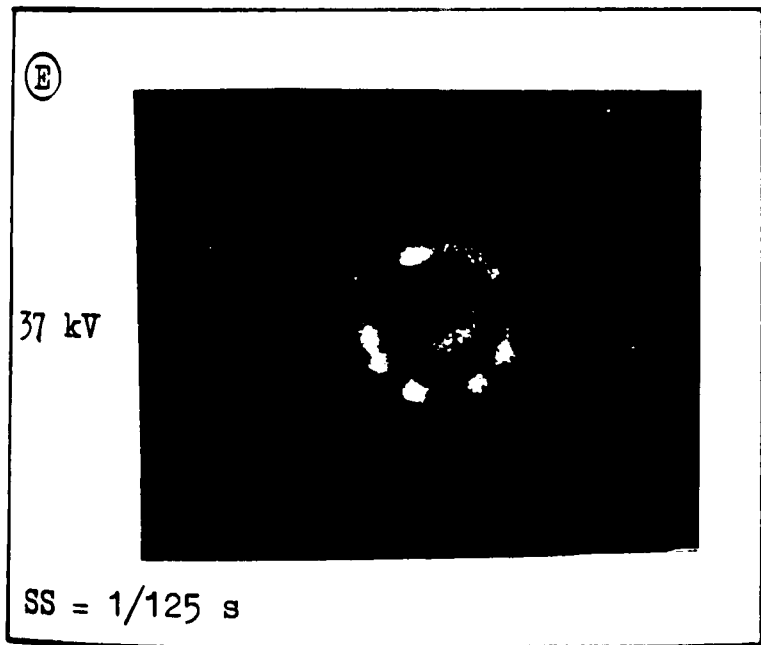
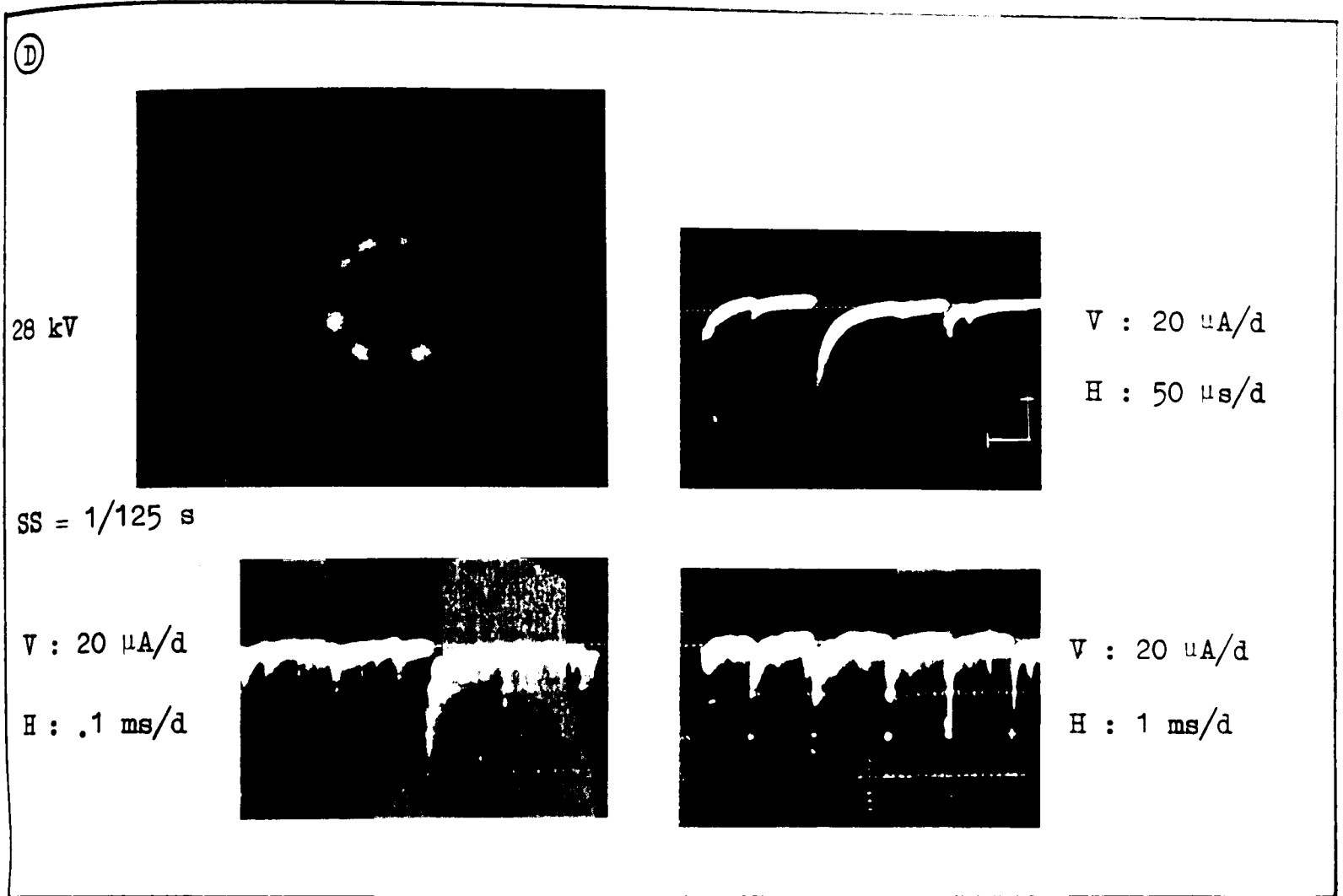
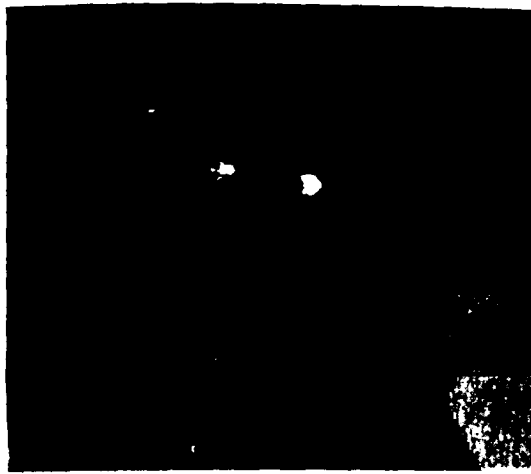
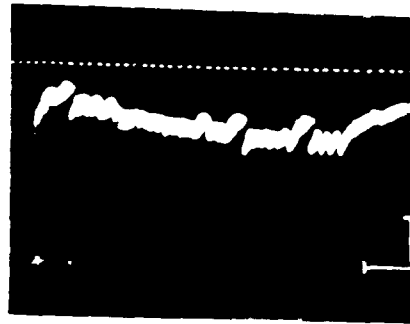


Figure 7.4(ii) Negative corona discharge activity in SF<sub>6</sub> at  $p = 1.0$  bar  
 ( $r_1/r_2 = 0.5/25$  mm)

33 kV



SS = 1/5



V: 5  $\mu$ A/d

H: 5  $\mu$ s/d



V: 5  $\mu$ A/d

H: .2 ms/d

(H)

40 kV

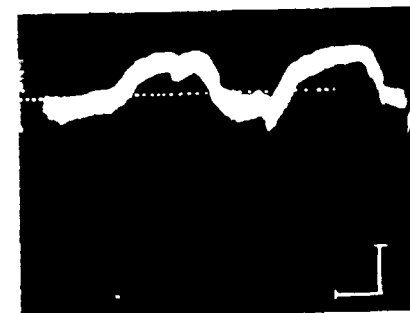


SS = 1/5



V: 5  $\mu$ A/d

H: 0.1 ms/d



V: 5  $\mu$ A/d

H: 20  $\mu$ s/d

(J)

52 kV



SS = 1/5 s

Figure 7.4(iii) Negative corona discharge activity in  $\text{SF}_6$  at  $p = 1.6$  bar

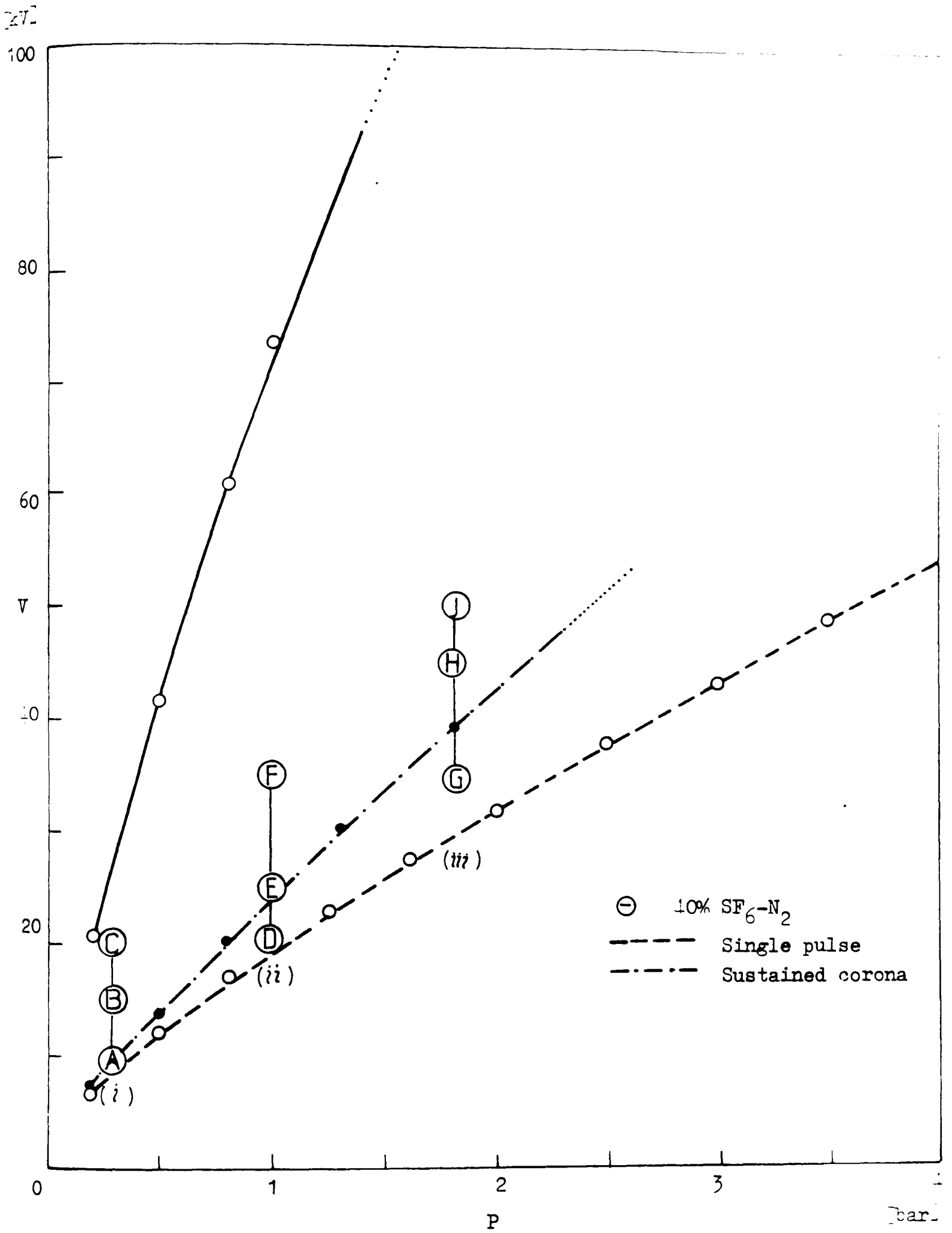


Figure 7.5 Negative voltage-pressure characteristic and discharge observation points of  $r_1/r_2 = 0.5/25$  mm.gap in 10% SF<sub>6</sub>-N<sub>2</sub> mixture

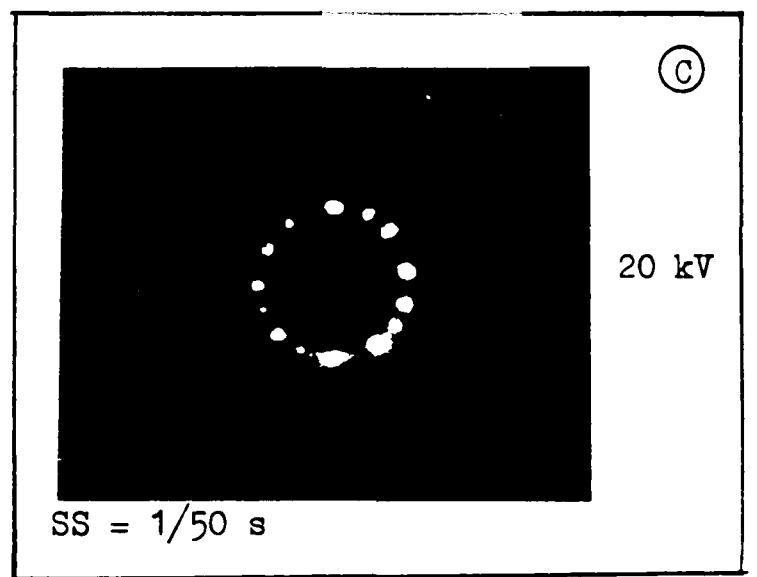
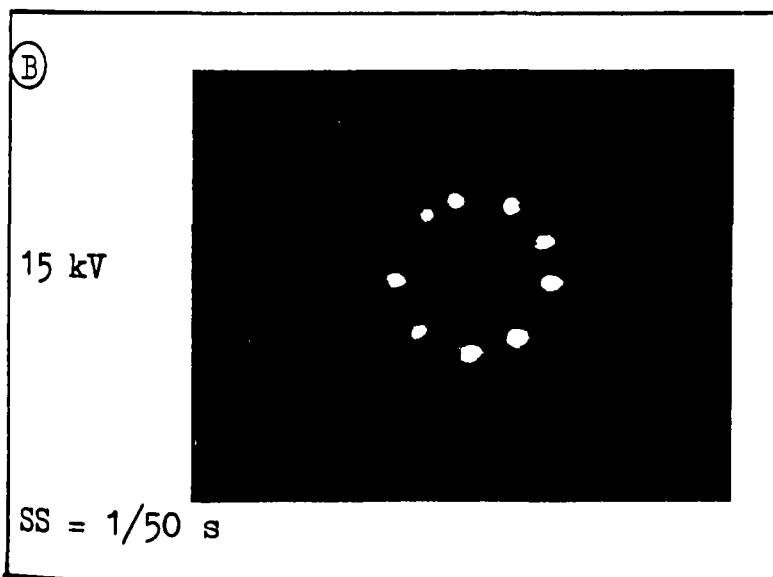
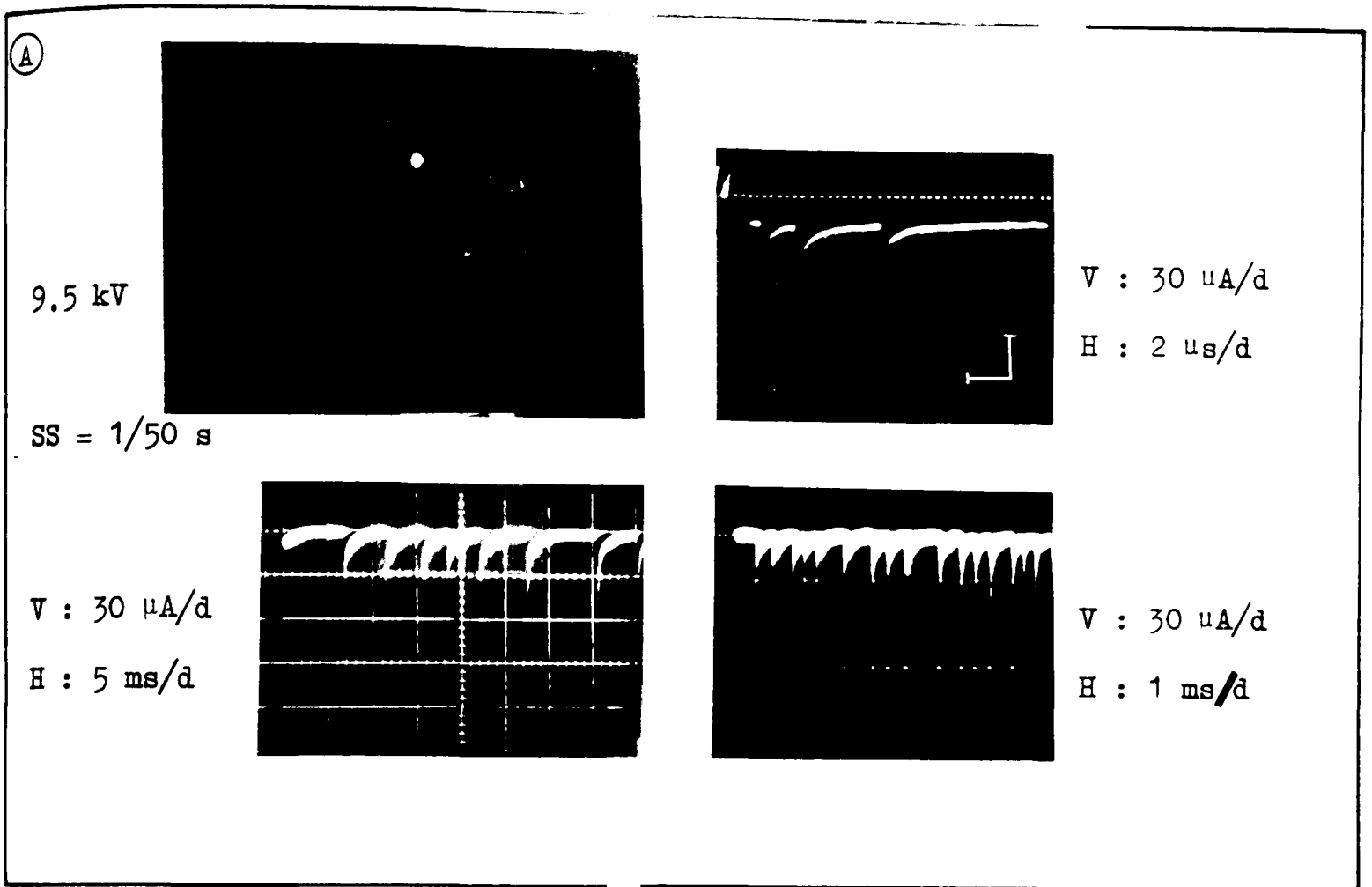


Figure 7.5(i) Negative corona discharge activity in 40% SF<sub>6</sub>-N<sub>2</sub> mixture at p = 0.3 bar ( $r_1/r_2 = 0.5/25$  mm)

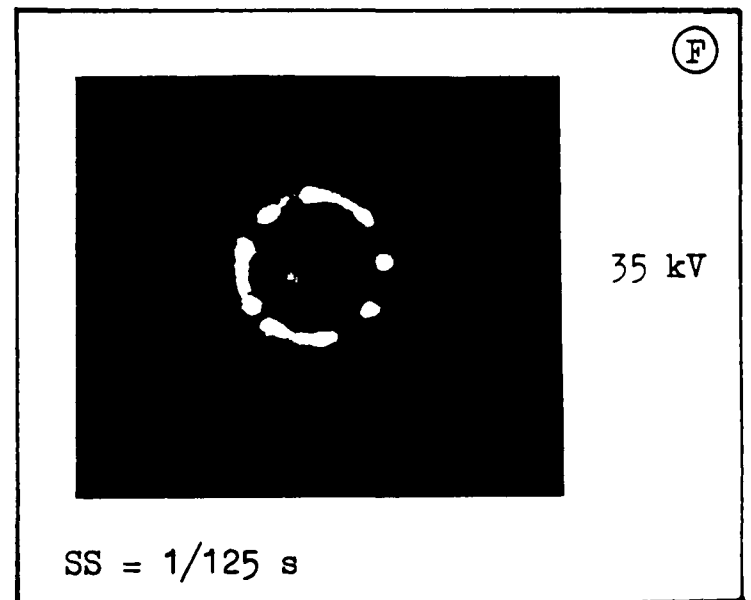
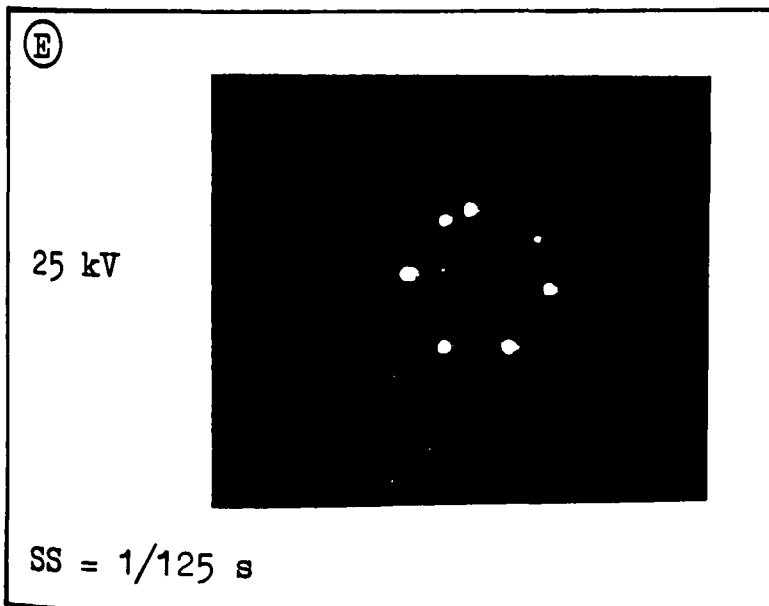
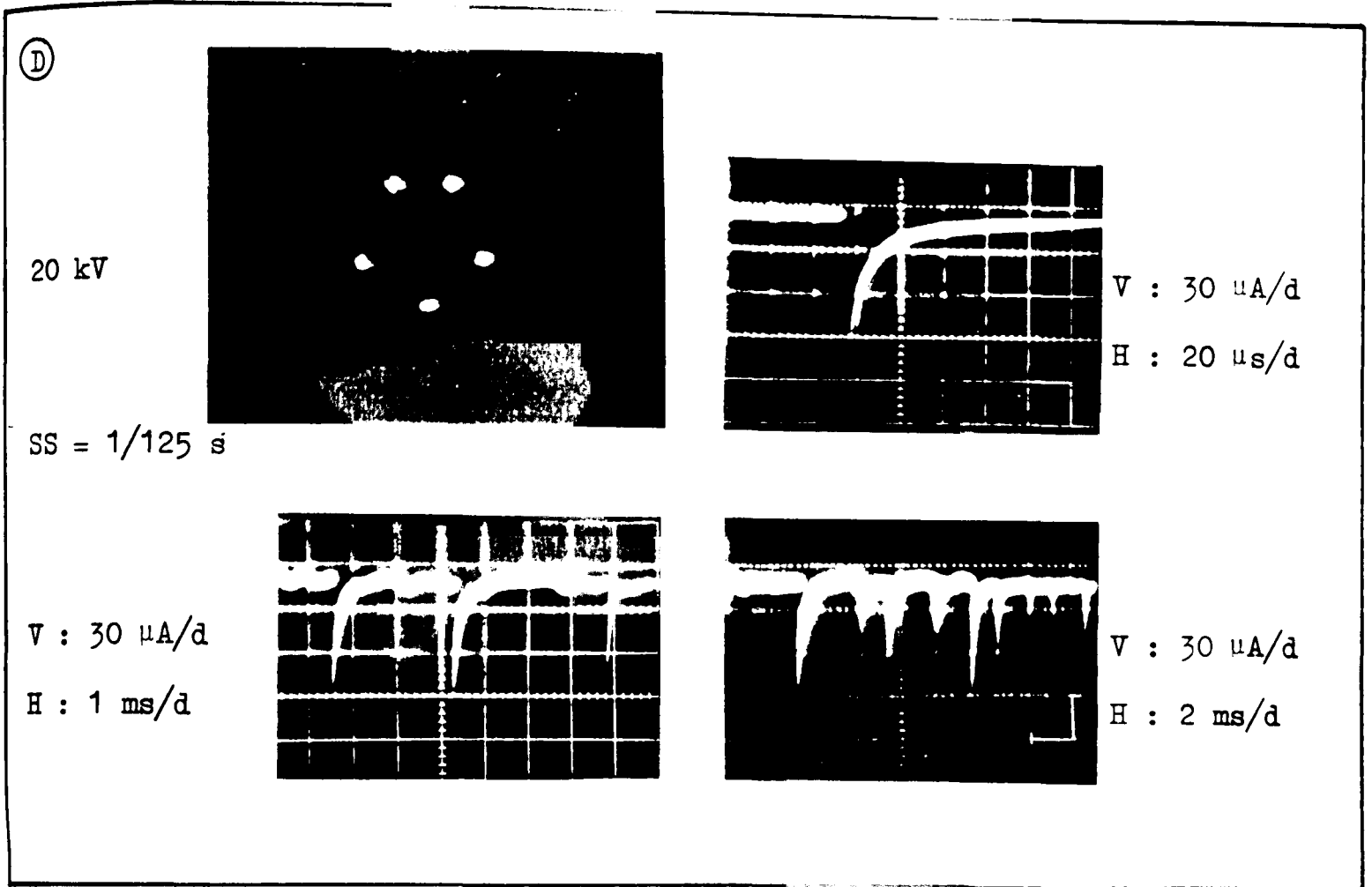


Figure 7.5 (ii) Negative corona discharge activity in a 40% SF<sub>6</sub>/N<sub>2</sub> mixture at p = 1.0 bar ( $r_1/r_2 = 0.5/25$  mm)

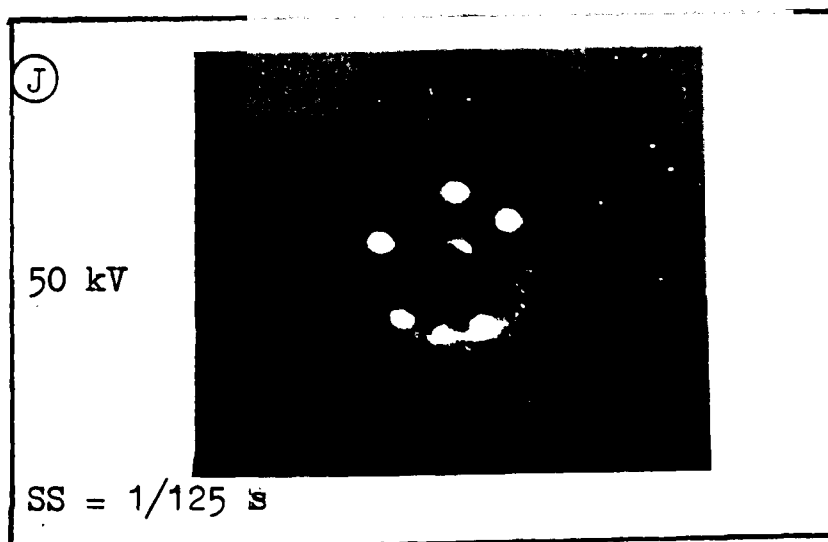
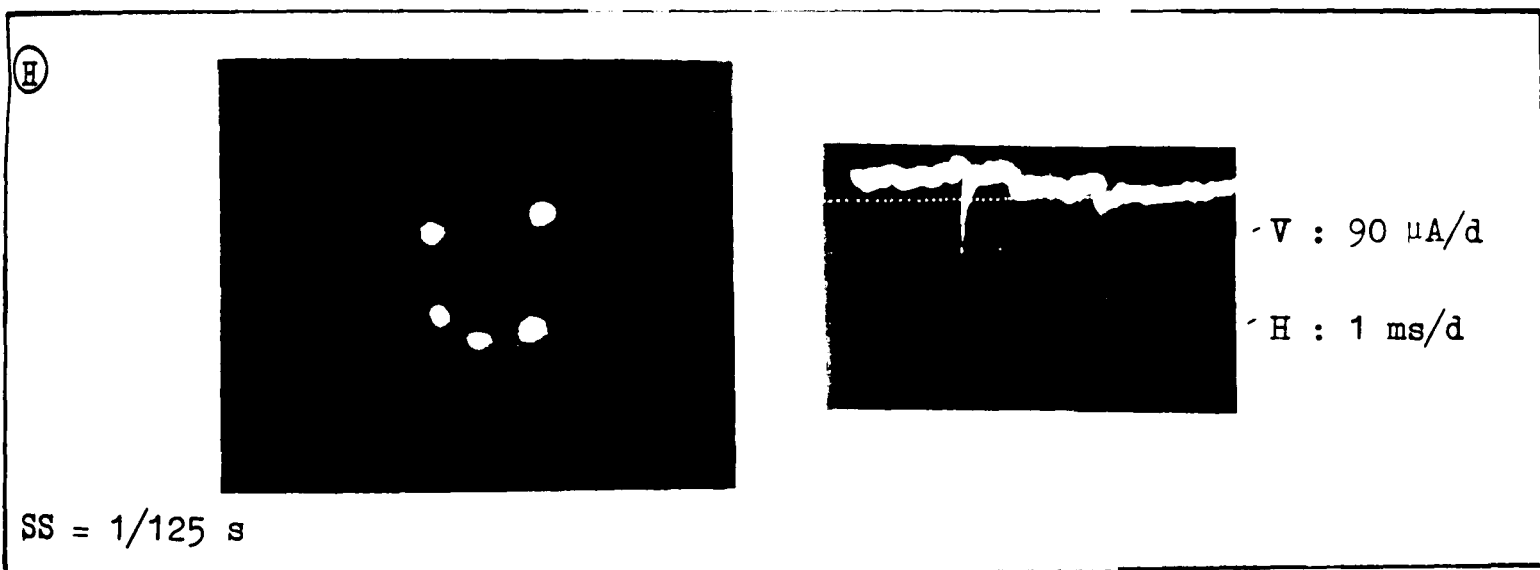
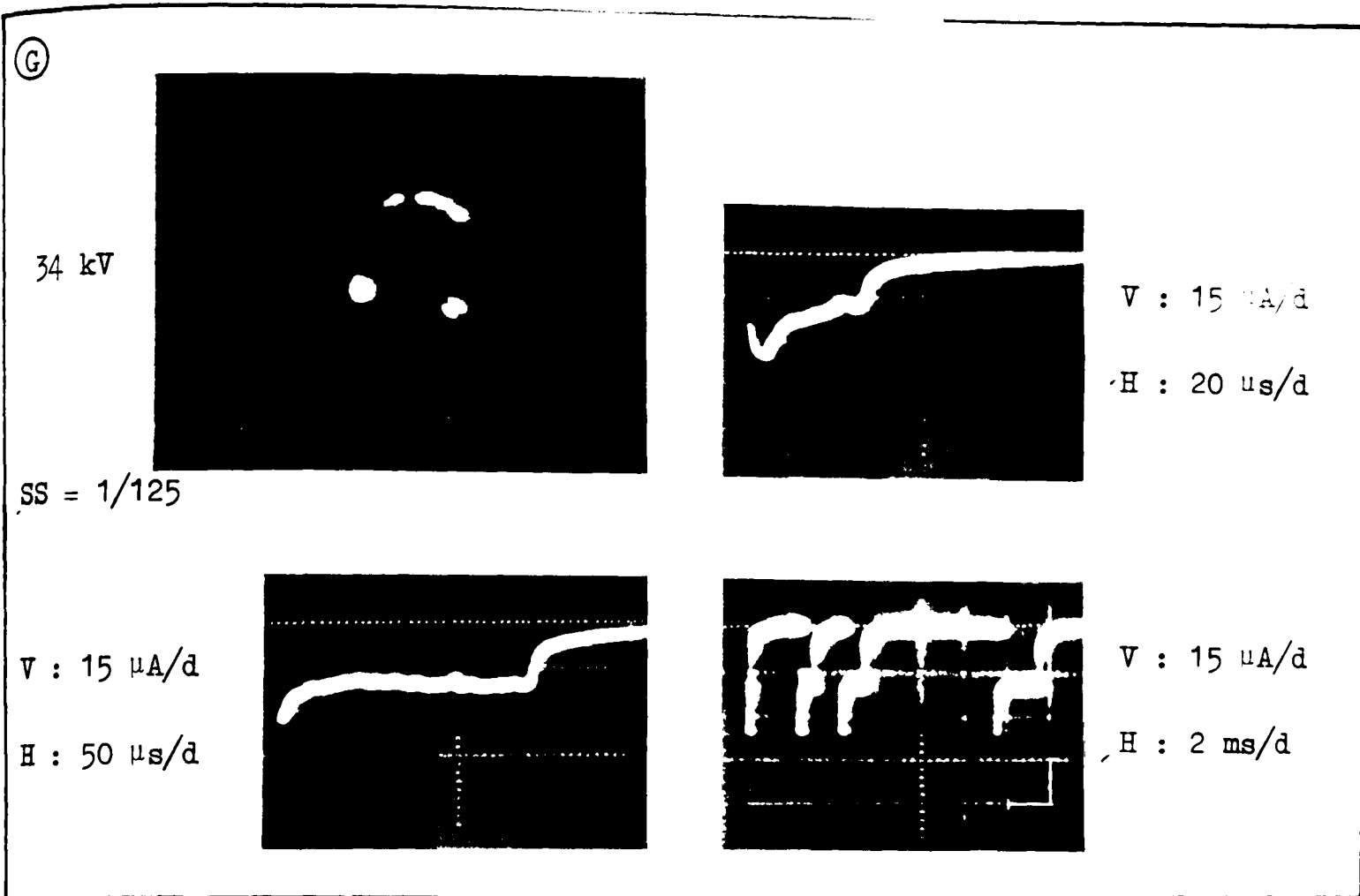


Figure 7.5(iii) Negative corona discharge activity in 40%  $\text{SF}_6\text{-N}_2$  mixture at  $p = 1.6$  bar ( $r_1/r_2 = 0.5/25$  mm)

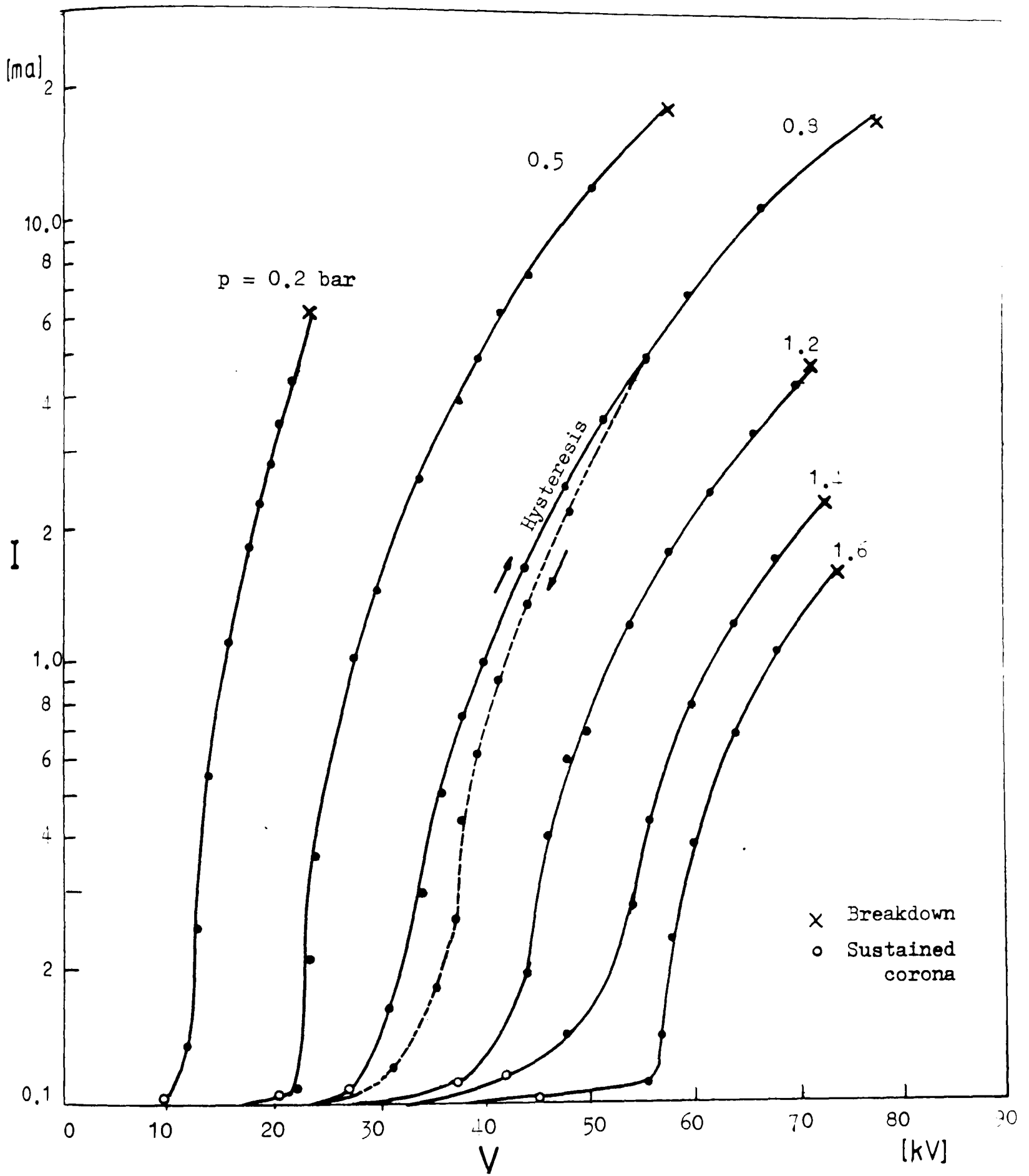


Figure 7.6 Positive current-voltage characteristics of  $\text{SF}_6$  at several pressures ( $r_1/r_2 = 0.5/25$  mm)

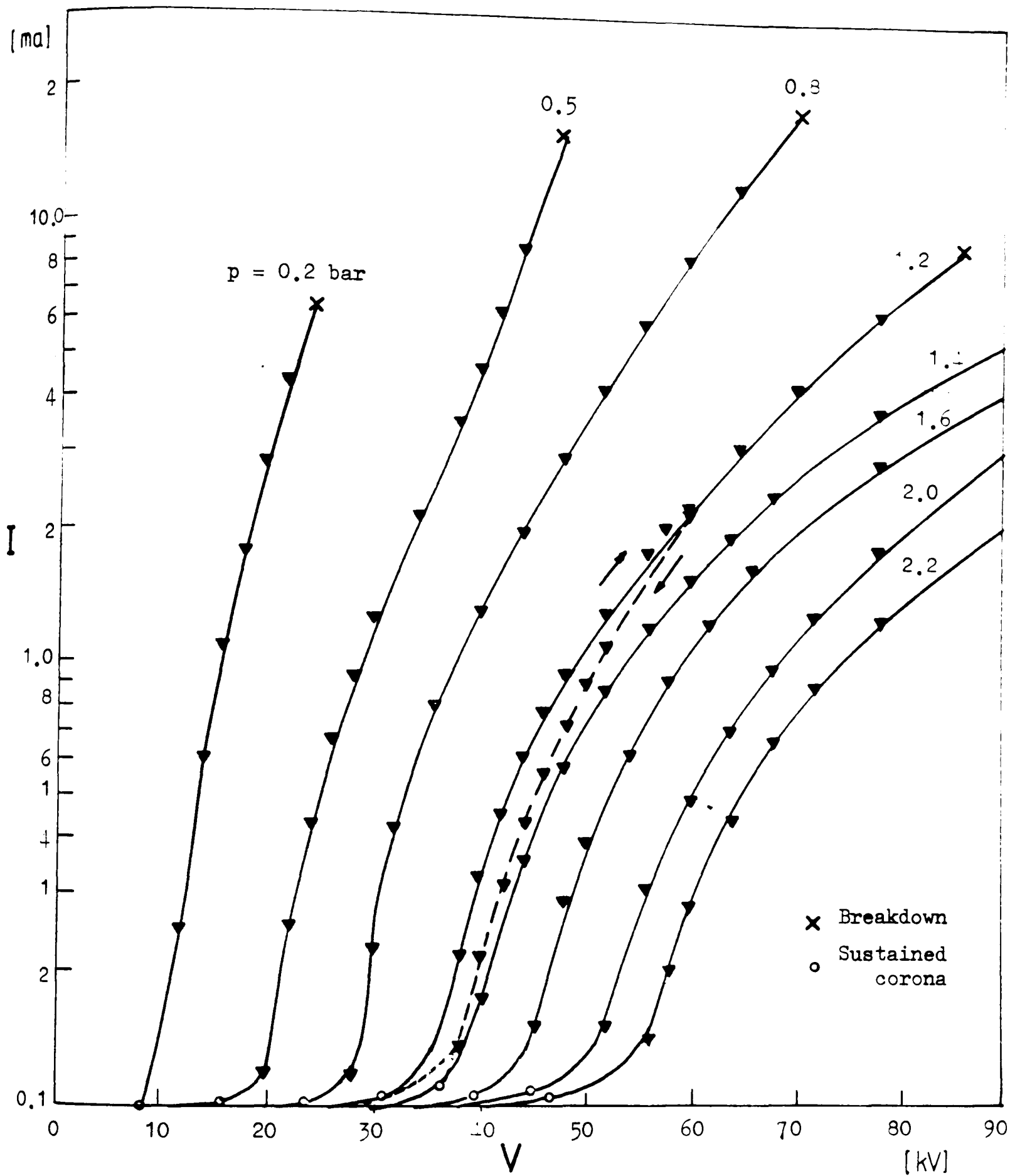


Figure 7.7 Negative current-voltage characteristics of  $\text{SF}_6$  at several pressures ( $r_1/r_2 = 0.5/25$  mm)

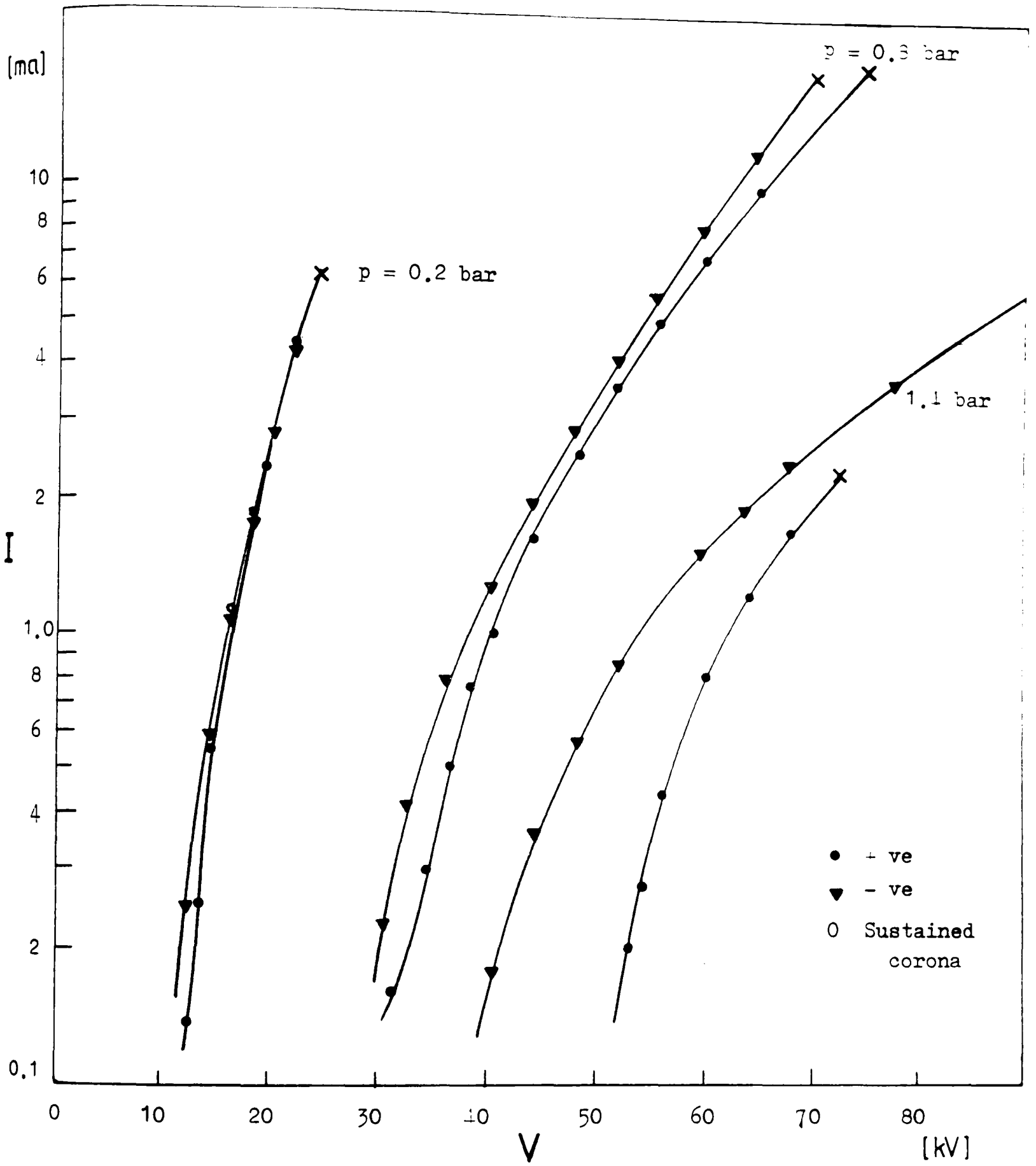


Figure 7.8 Comparison of I-V characteristics for polarity effect in SF<sub>6</sub> ( $r_1/r_2 = 0.5/25$  mm)

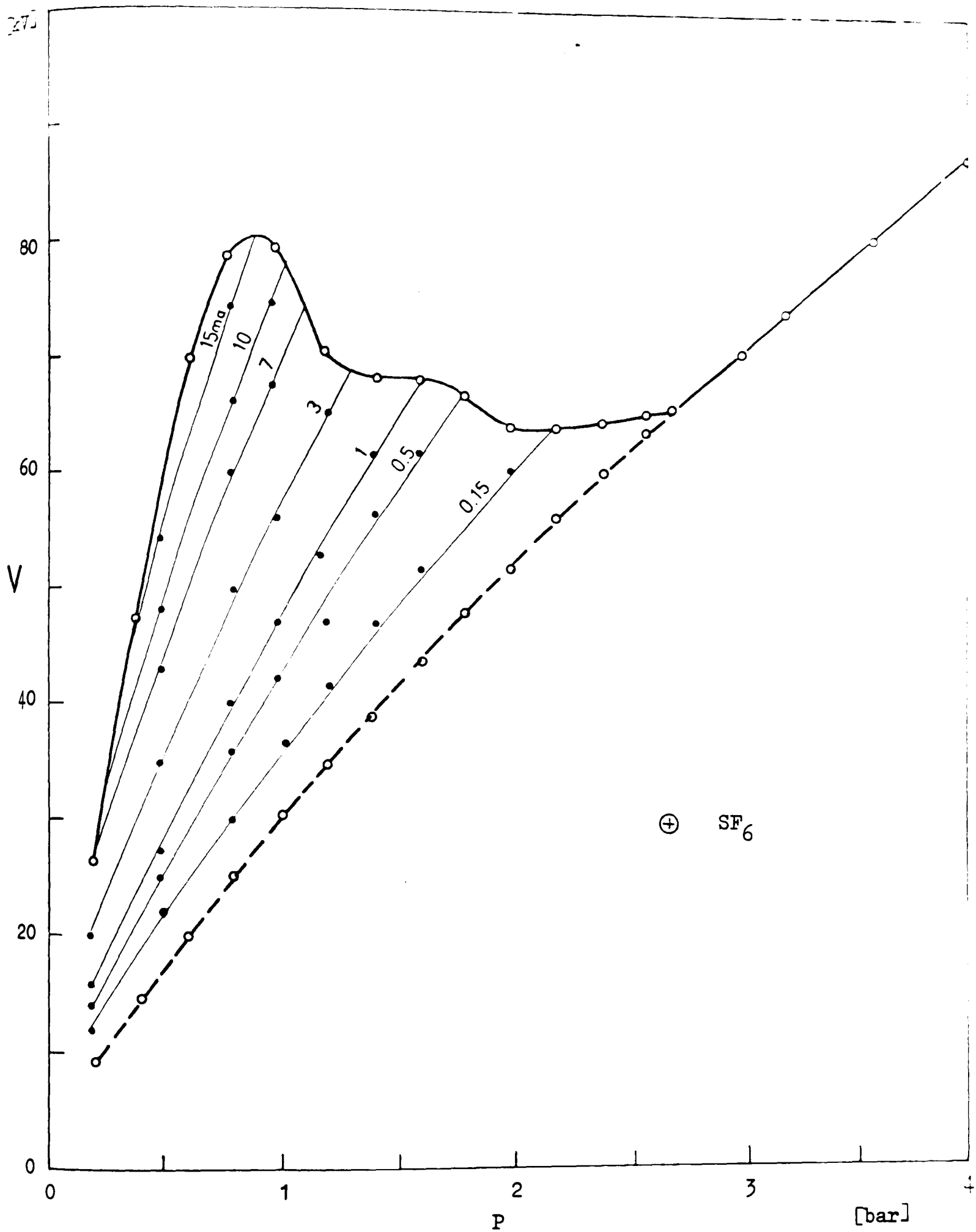


Figure 7.9 Relative corona current distribution of positive voltage-pressure characteristic of SF<sub>6</sub> ( $r_1/r_2 = 0.5/25$  mm)

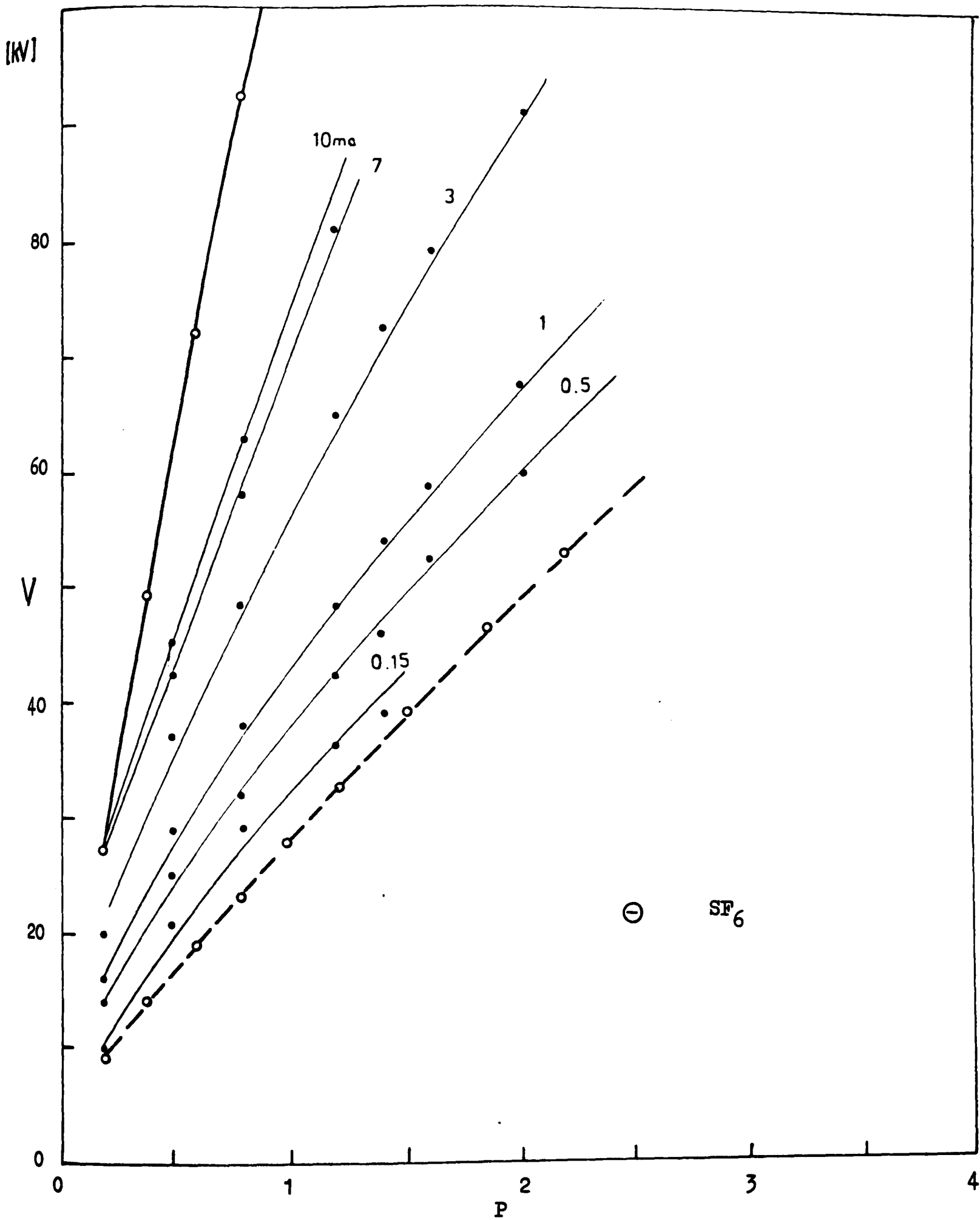


Figure 7.10 Relative corona current distribution of negative voltage-pressure characteristic of SF<sub>6</sub> ( $r_1/r_2 = 0.5/25$  mm)

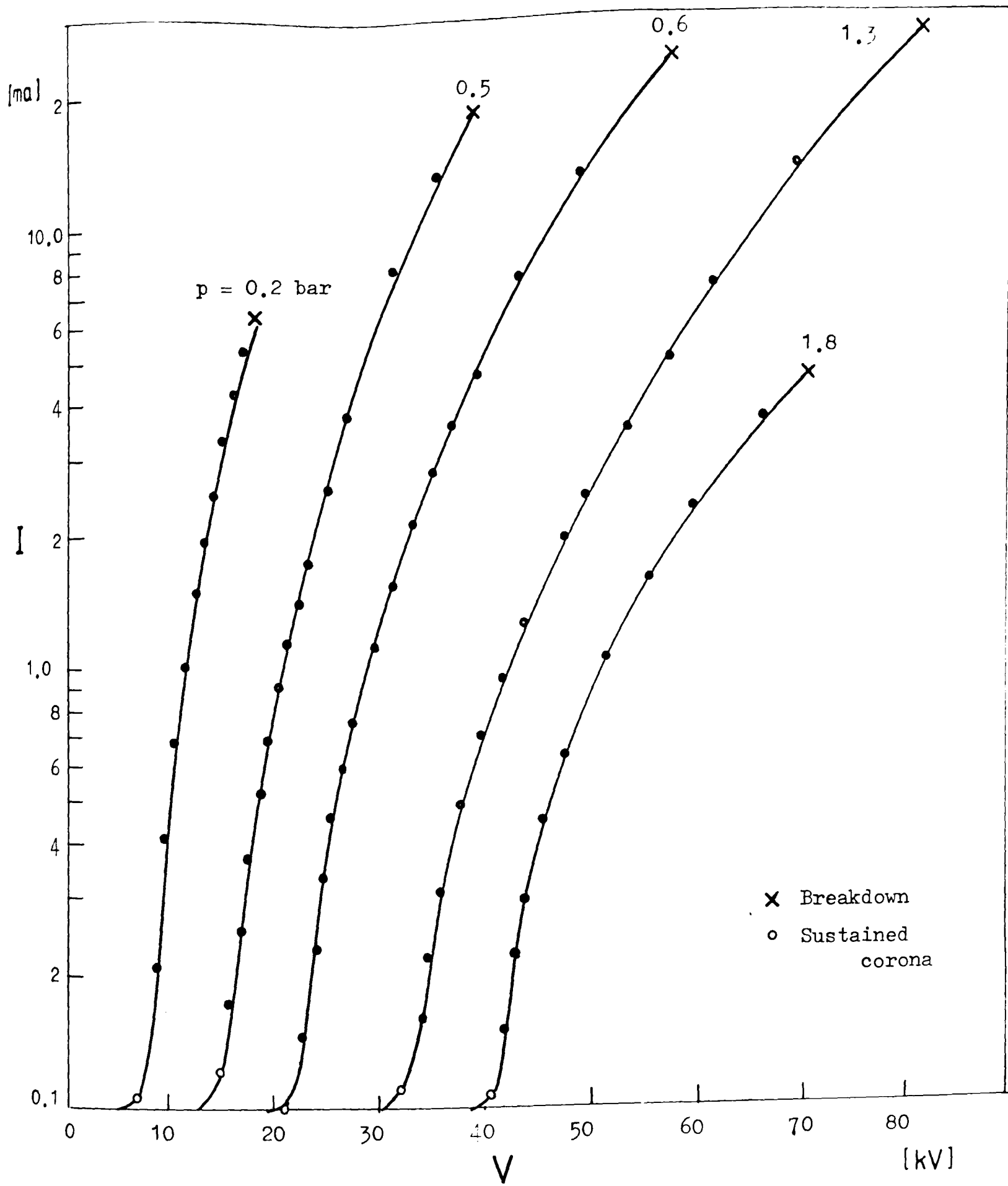


Figure 7.11 Positive current-voltage characteristics of 40% SF<sub>6</sub>-N<sub>2</sub> at several pressures ( $r_1/r_2 = 0.5/25$  mm)

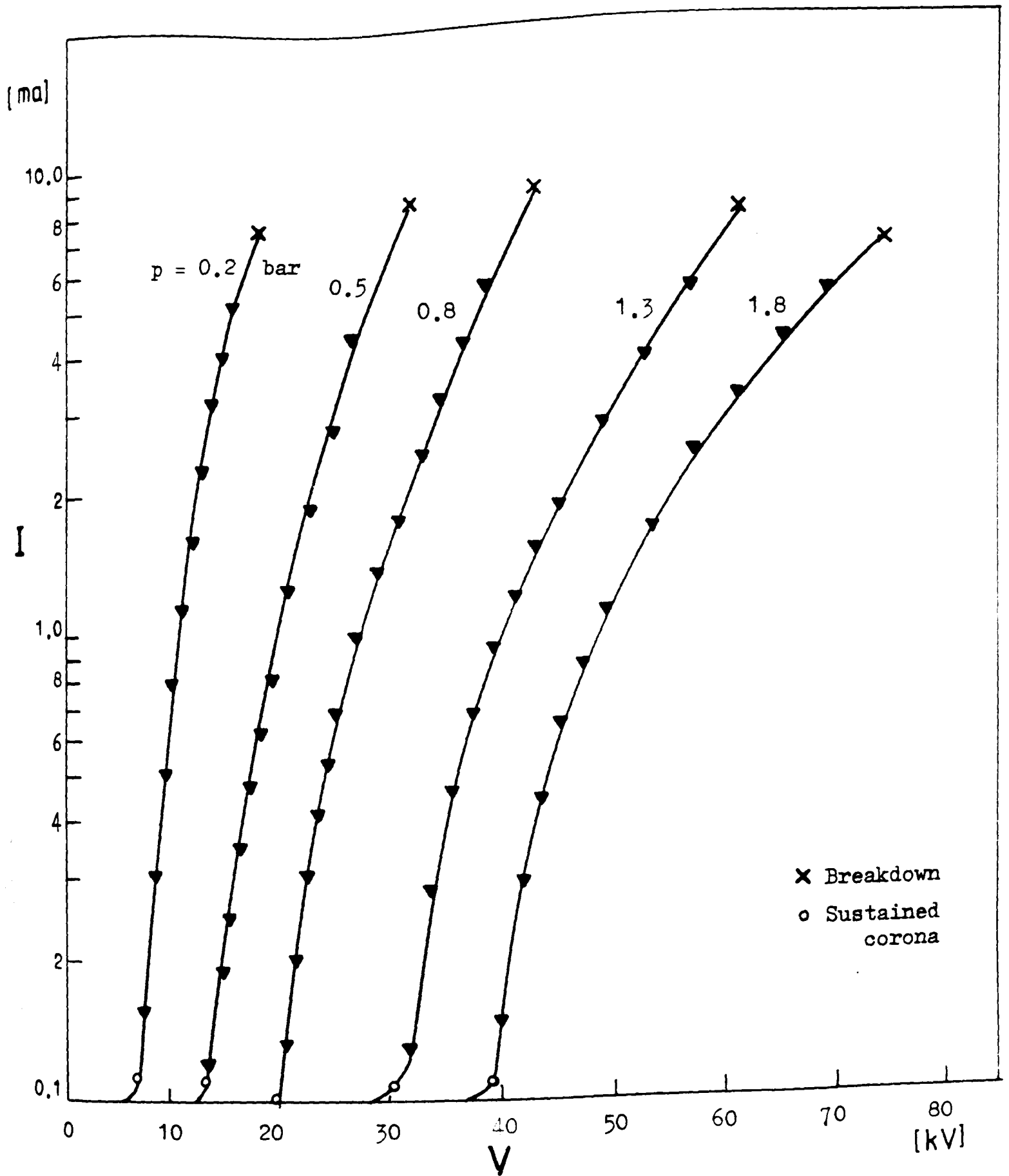


Figure 7.12 Negative current-voltage characteristics of 40% SF<sub>6</sub>/N<sub>2</sub> at several pressures ( $r_1/r_2 = 0.5/25$  mm)

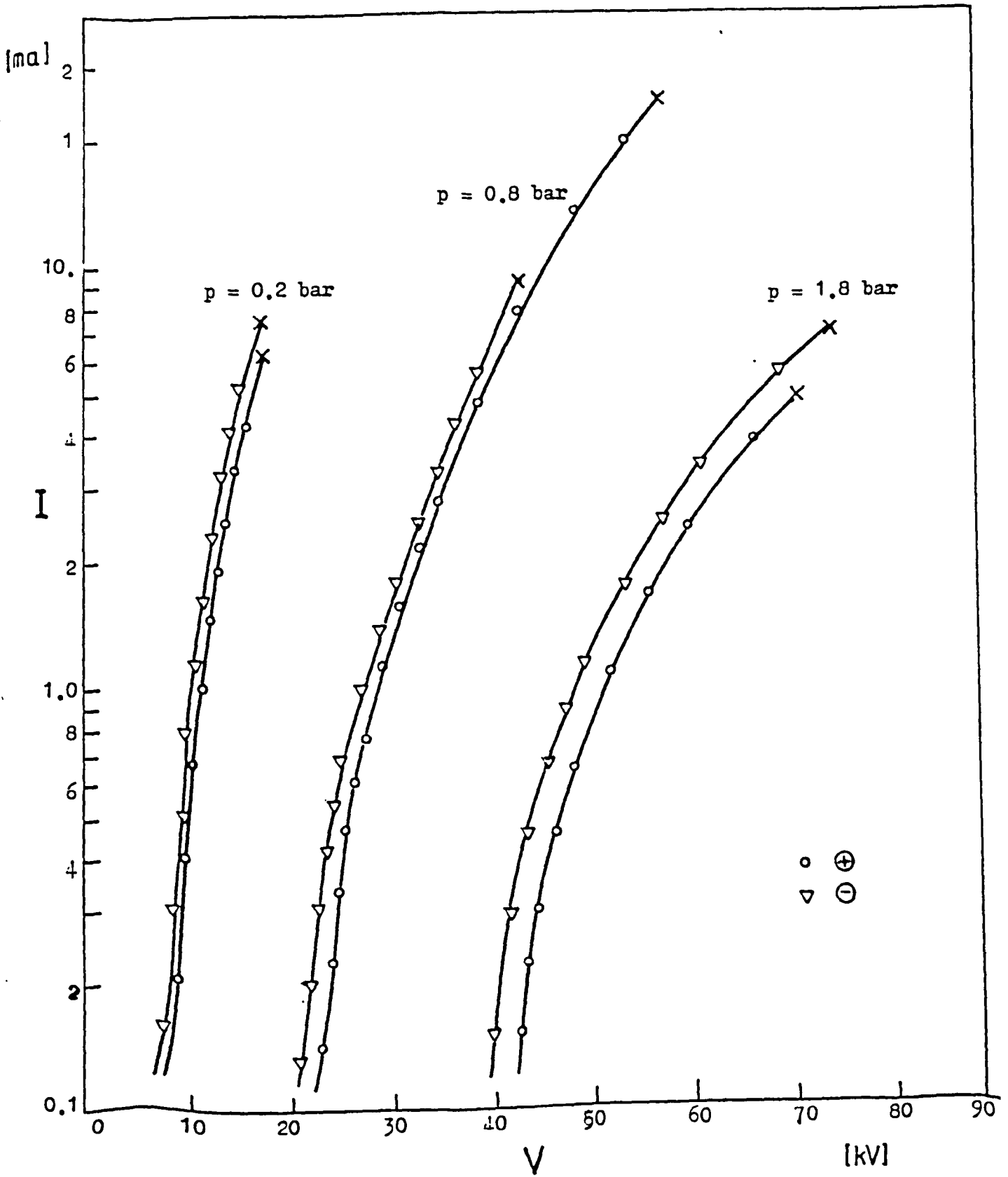


Figure 7.13 Comparisons of I-V characteristics for polarity effect in 40% SF<sub>6</sub>/N<sub>2</sub> (r<sub>1</sub>/r<sub>2</sub> = 0.5/25 mm)

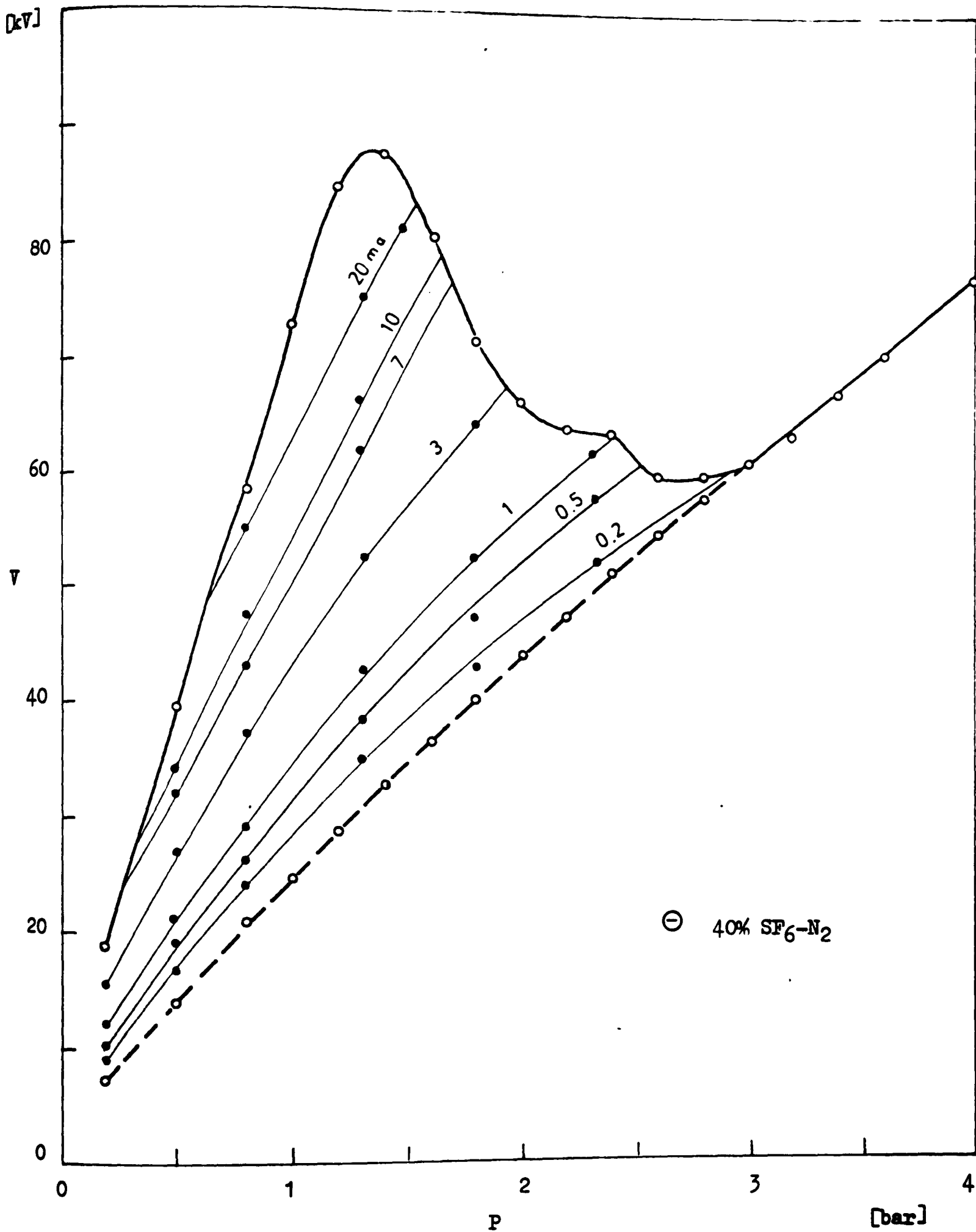


Figure 7.14 Relative corona current distribution of positive voltage-pressure characteristic of 40% SF<sub>6</sub>/N<sub>2</sub> mixture (r<sub>1</sub>/r<sub>2</sub> = 0.5/25 mm)

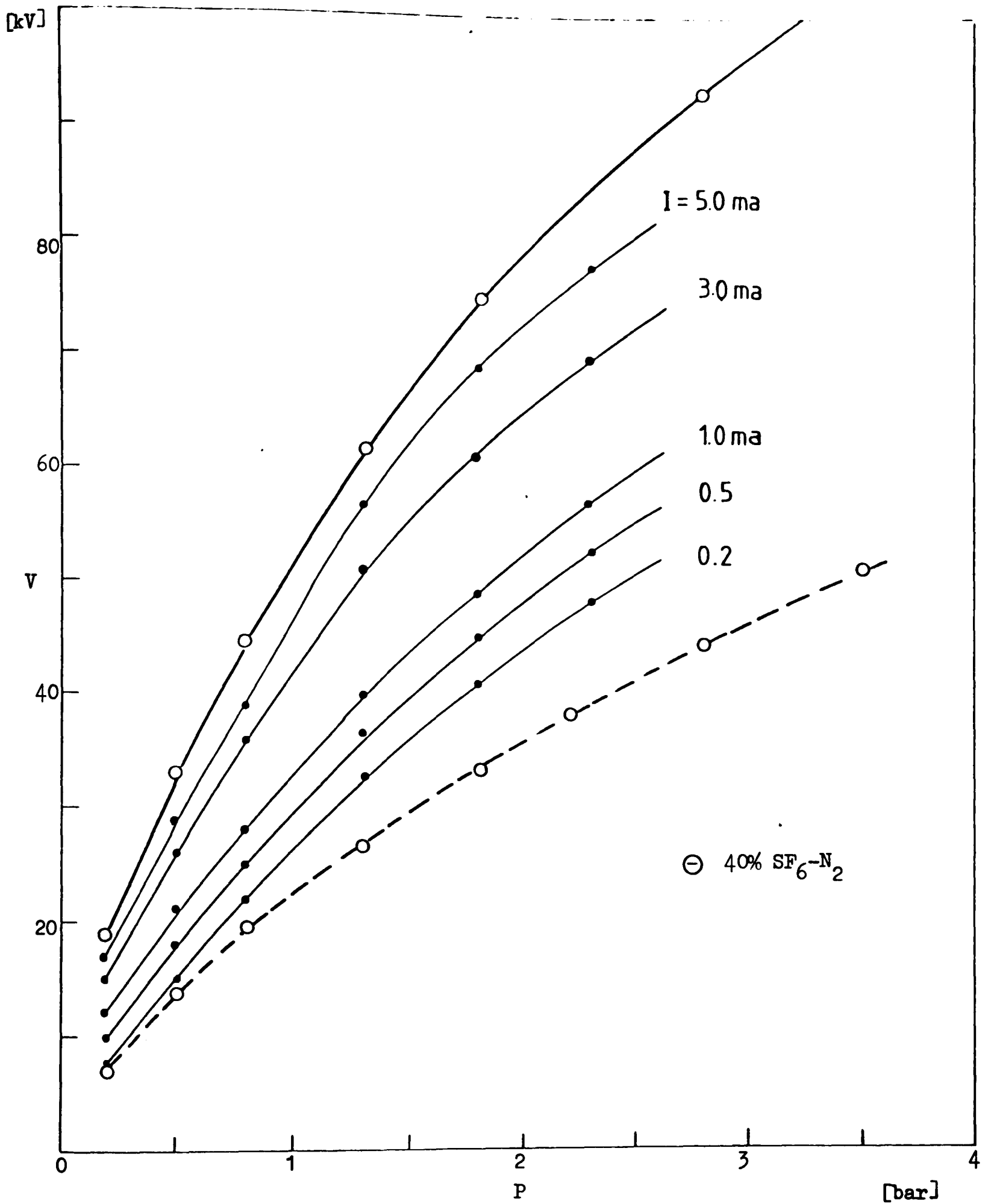


Figure 7.15 Relative corona current distribution of negative voltage-pressure characteristics of 40%  $\text{SF}_6\text{-N}_2$  mixture ( $r_1/r_2 = 0.5/25$  mm)

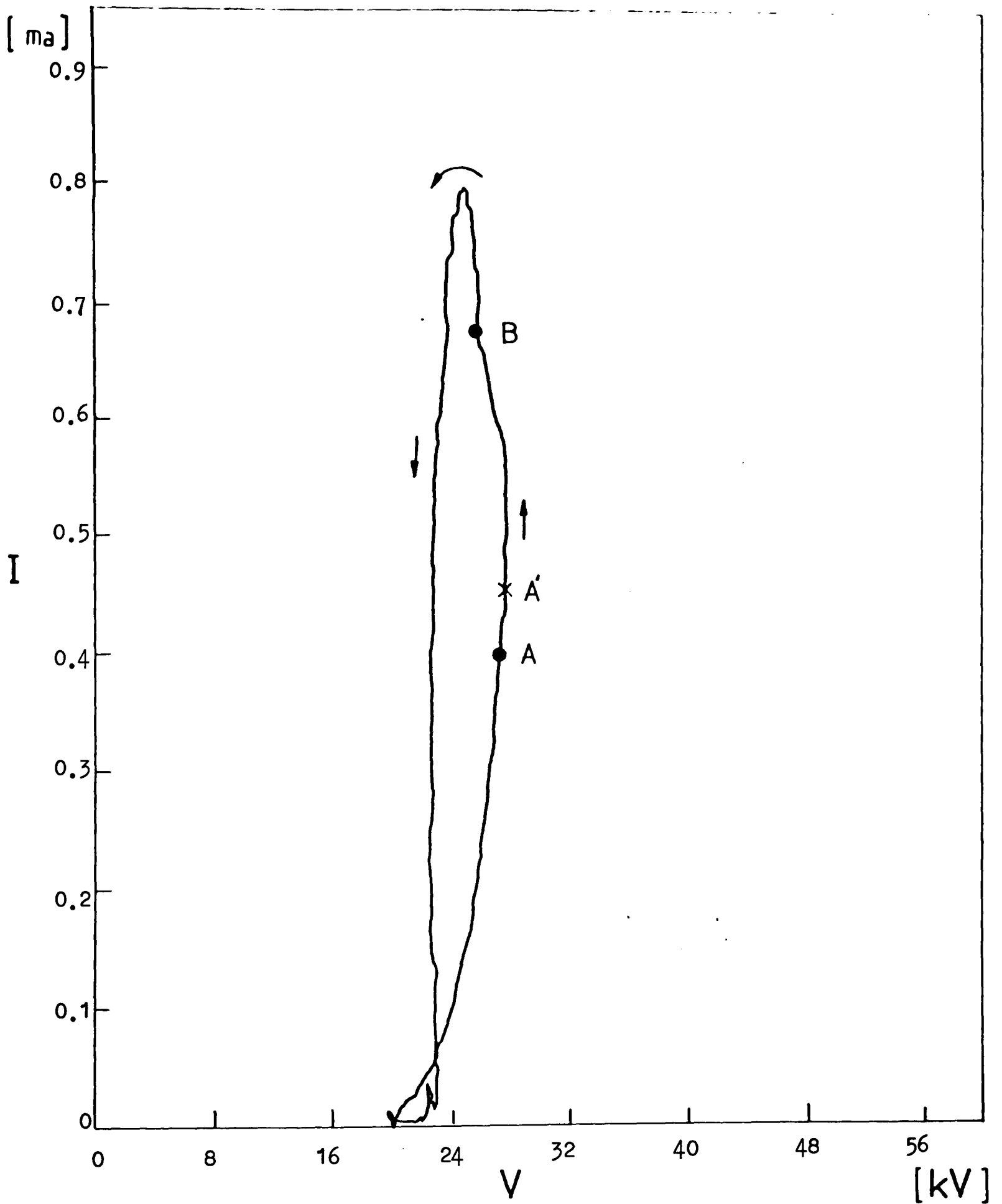


Figure 7.16 Typical positive current/voltage variation in coaxial electrode geometry showing hysteresis effect (in 40%  $\text{SF}_6\text{-N}_2$  at  $p = 1.0$  bar,  $r_1/r_2 = 0.5/12.7$  mm)

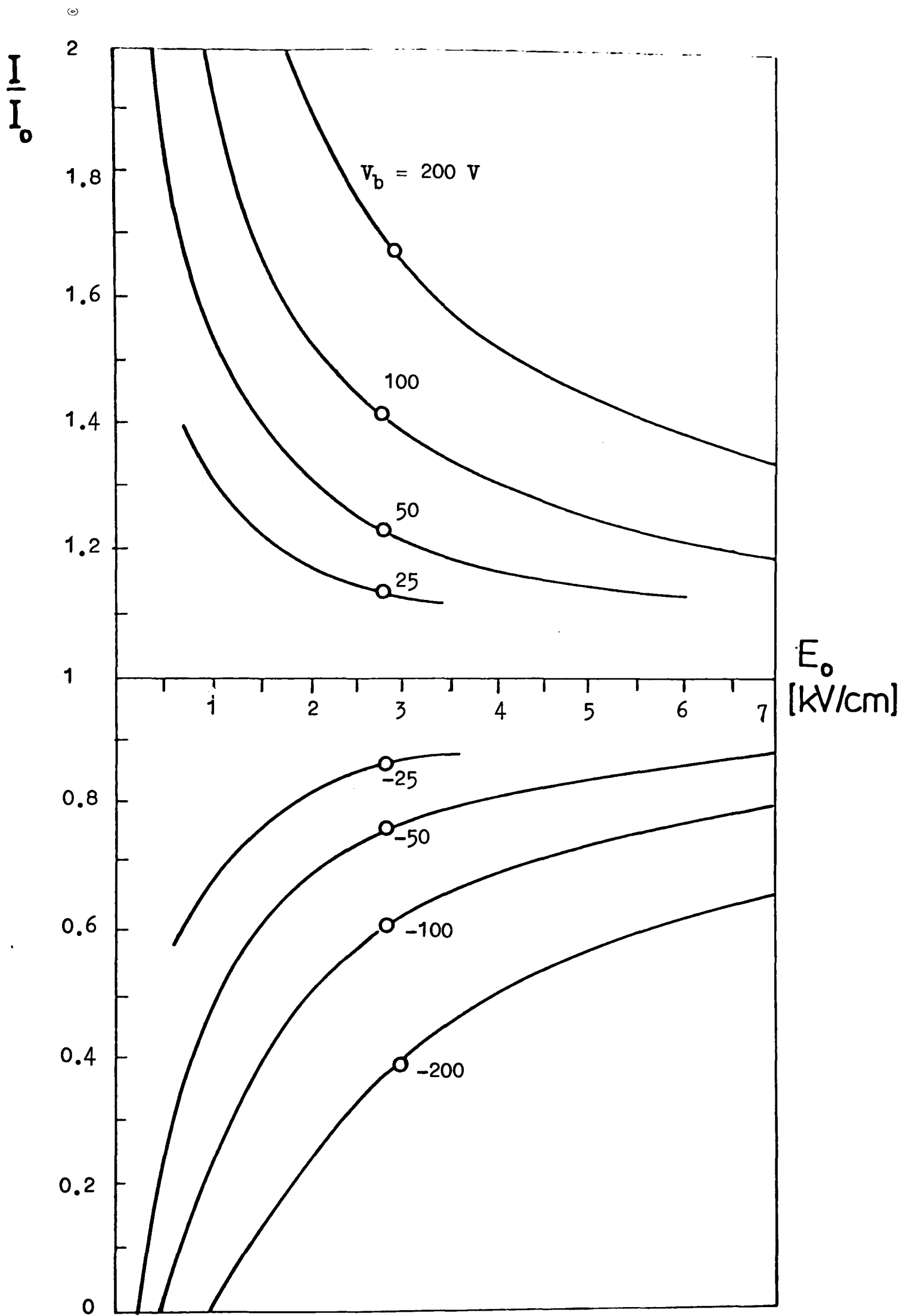


Figure 7.17 Computed  $I/I_0$  characteristics as a function of the boundary field  $E_0$  for several values of the parameter  $V_b$ . Experimental condition;  $r_1/r_2 = 0.5/25$  mm. Steady positive corona in air at  $V = 16$  kV.

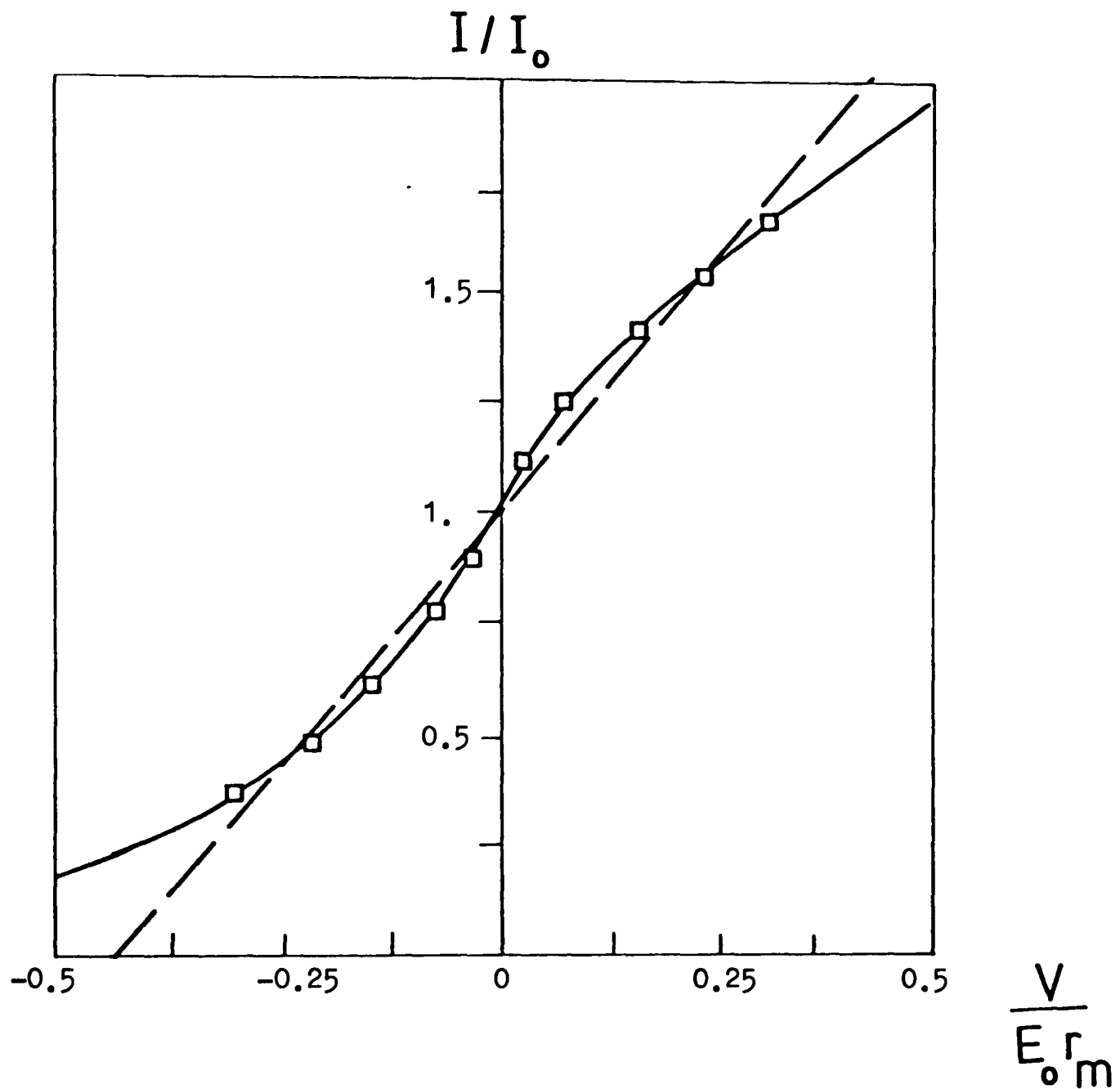


Figure 7.18 Normalized probe current variation with normalised bias voltage in air at atmospheric pressure

- Tassicker [231]
- Selim and Waters [221]
- Experiment  
 ( $r_1/r_2 = 0.5/25$  mm ;  $V = 16$  kV,  $E_0 = 2.8$  kV/cm)

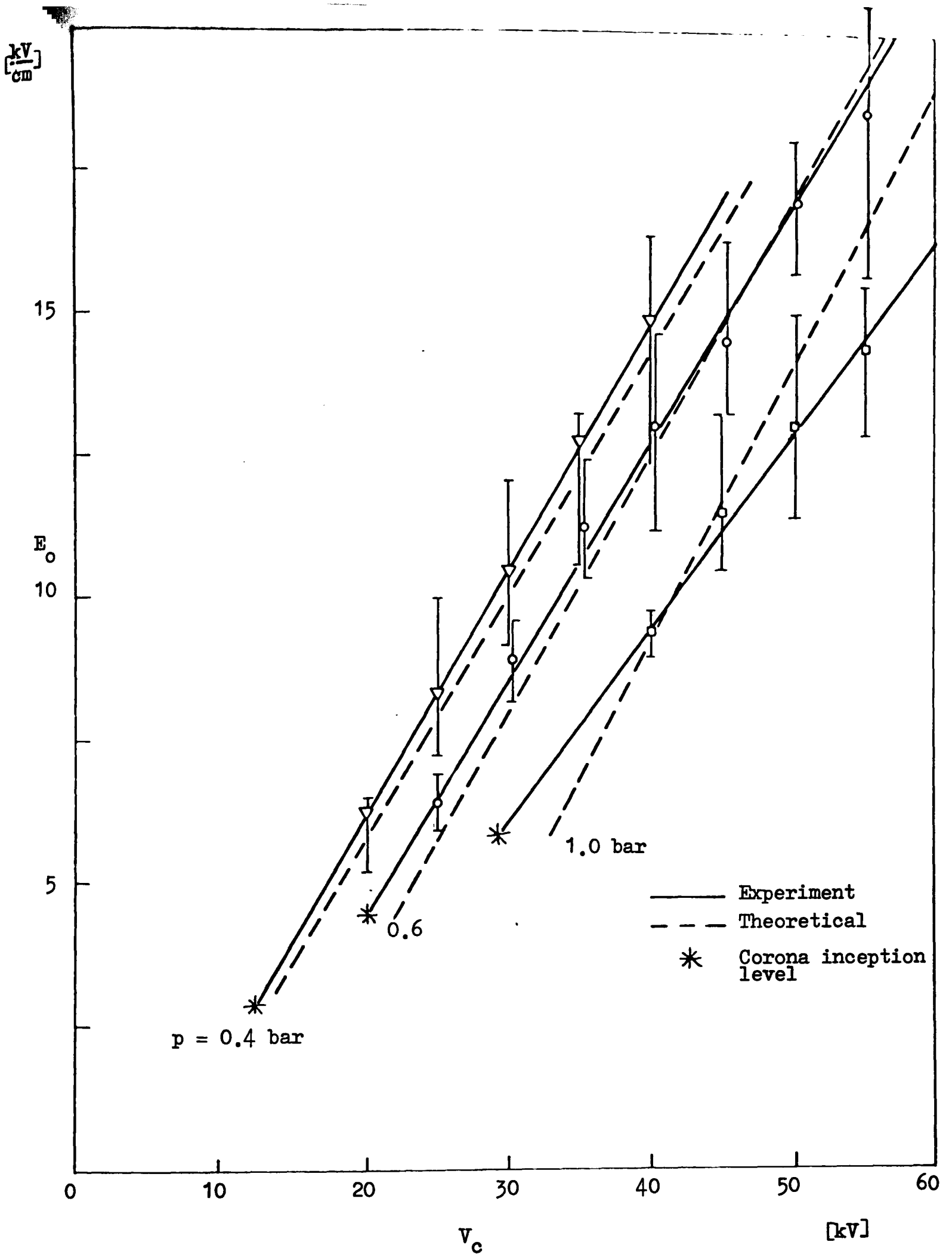


Figure 7.19 Electric field at the outer electrode as a function of the positive corona voltage applied to the inner electrode in  $SF_6$  for several pressures ( $r_1/r_2 = 0.5/25^6$  mm)

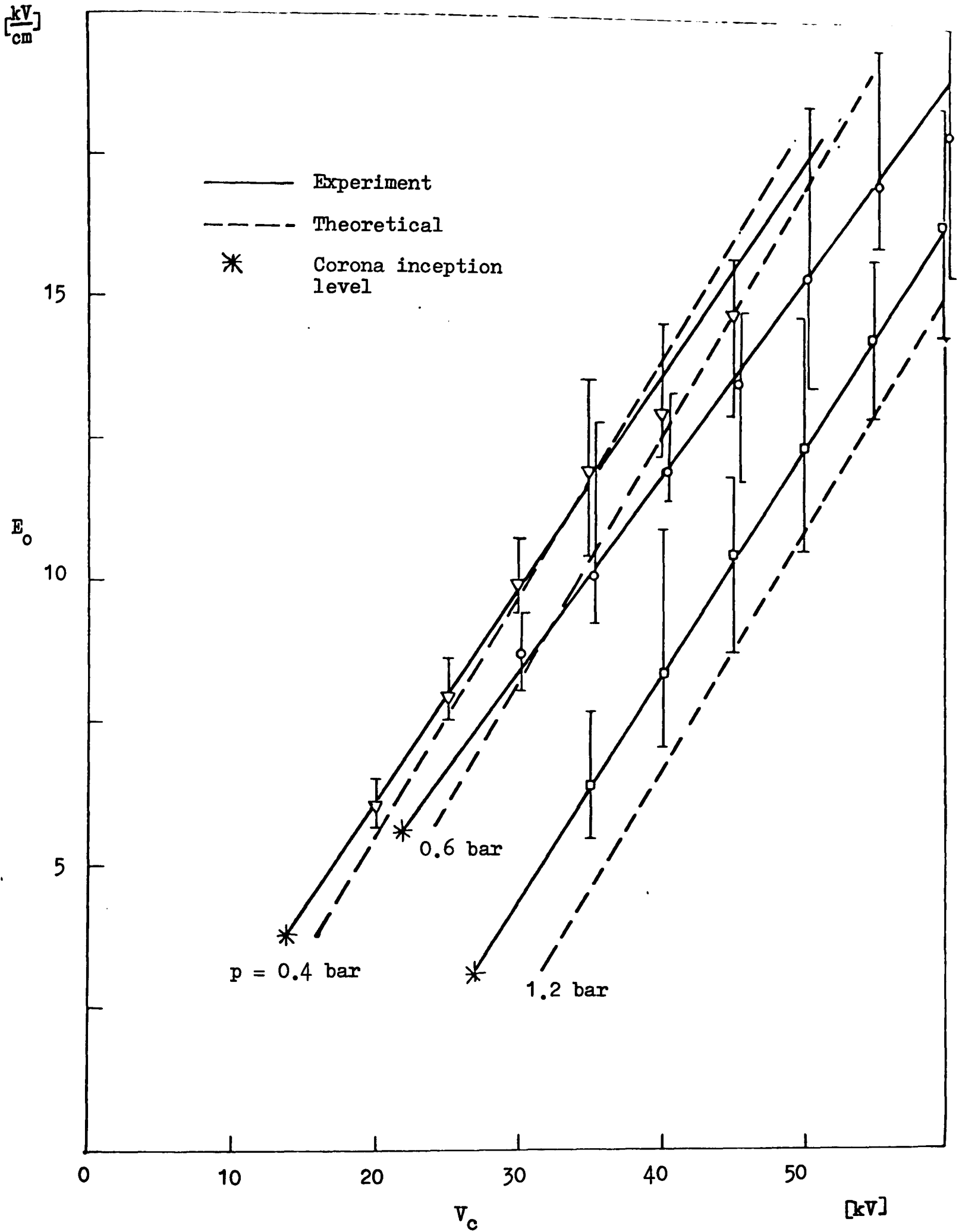


Figure 7.20 Electric field at the outer electrode as a function of the negative corona voltage applied to the inner electrode in  $SF_6$  at several pressures ( $r_1/r_2 = 0.5/25$  mm)

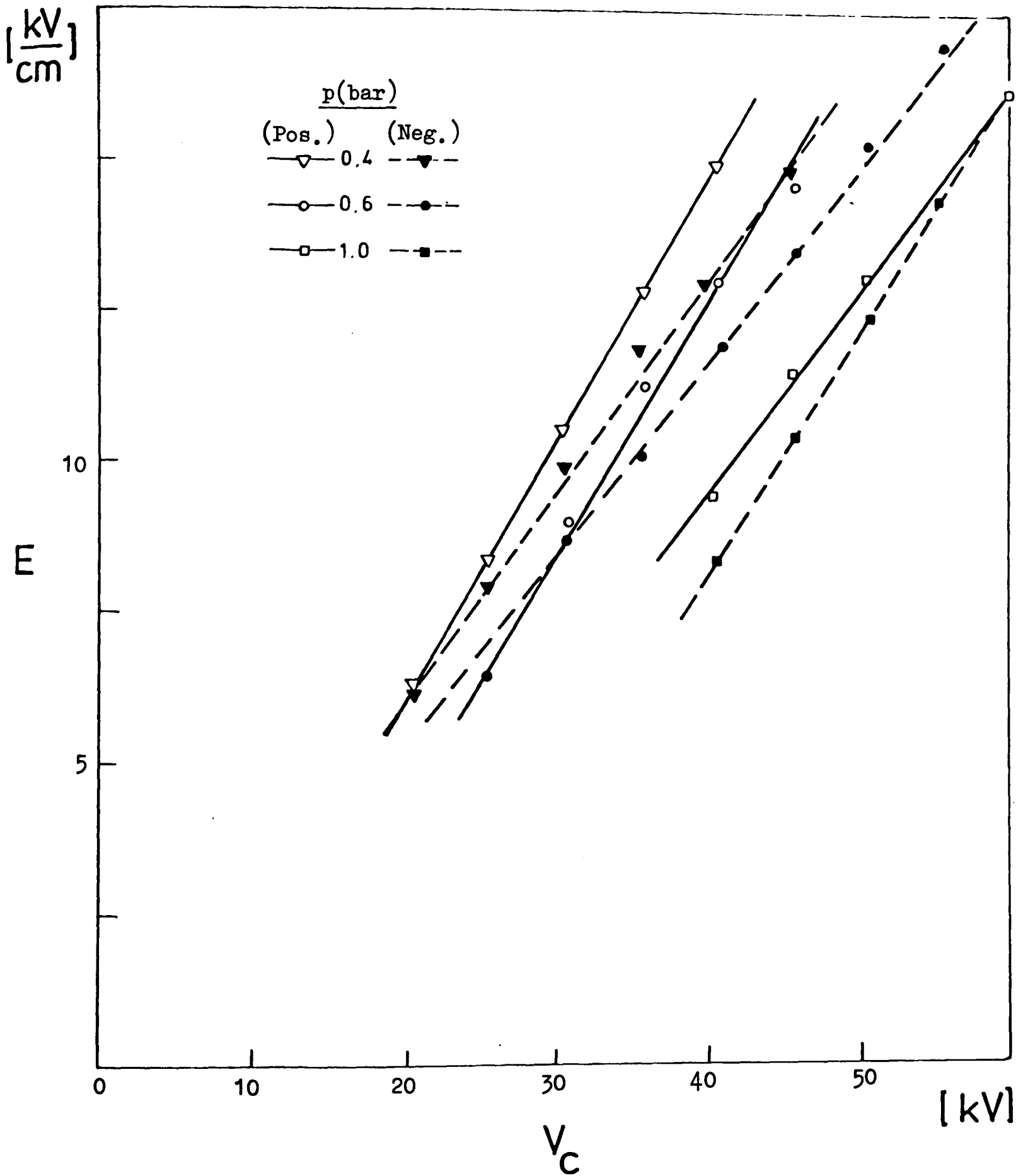


Figure 7.21 Comparison of measured positive and negative corona field strengths at the outer electrode in SF<sub>6</sub> ( $r_1/r_2 = 0.5/25$  mm)

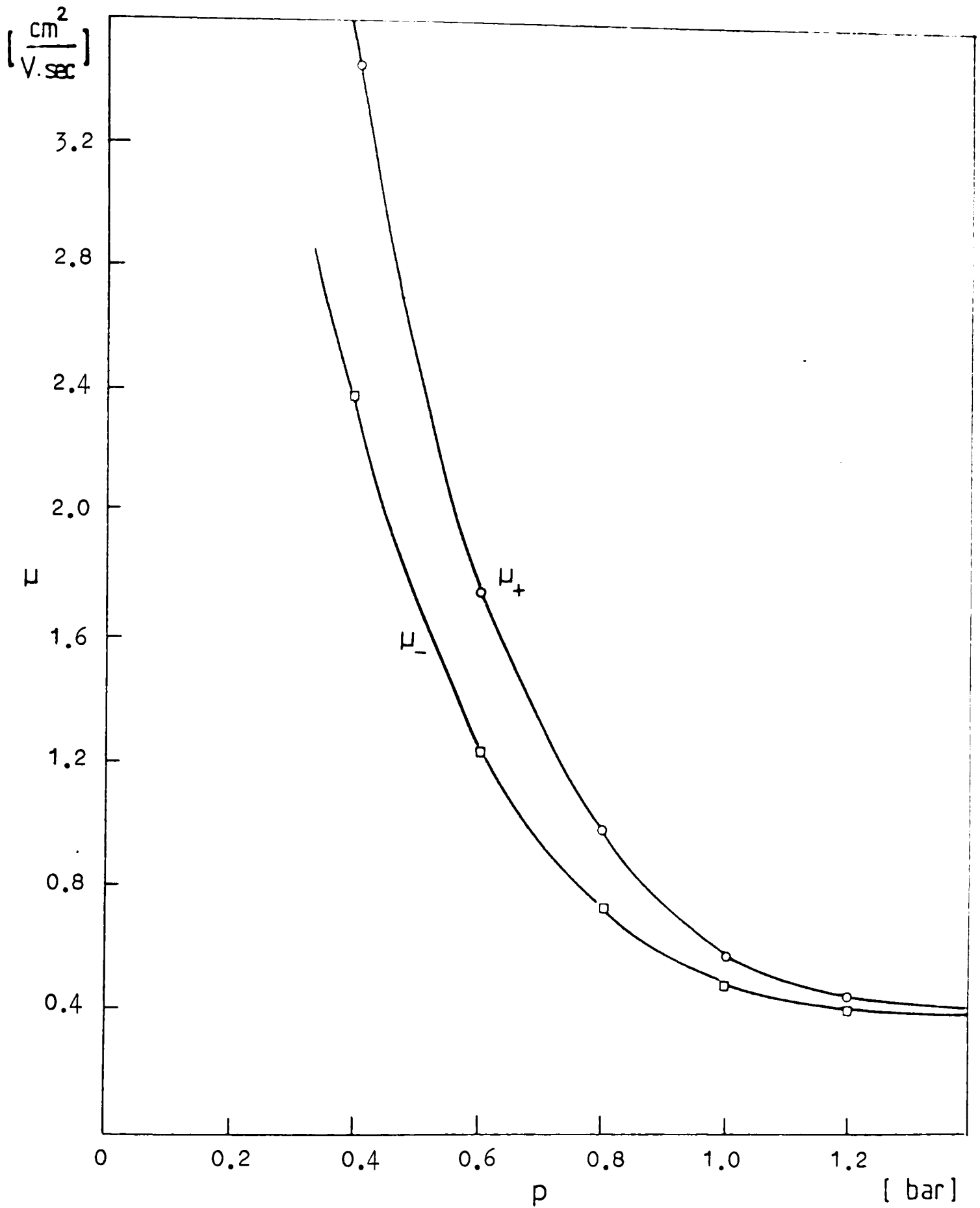


Figure 7.22 Ion mobilities in  $\text{SF}_6$  as a function of pressure ( $V_c = 40 \text{ kV}$ )

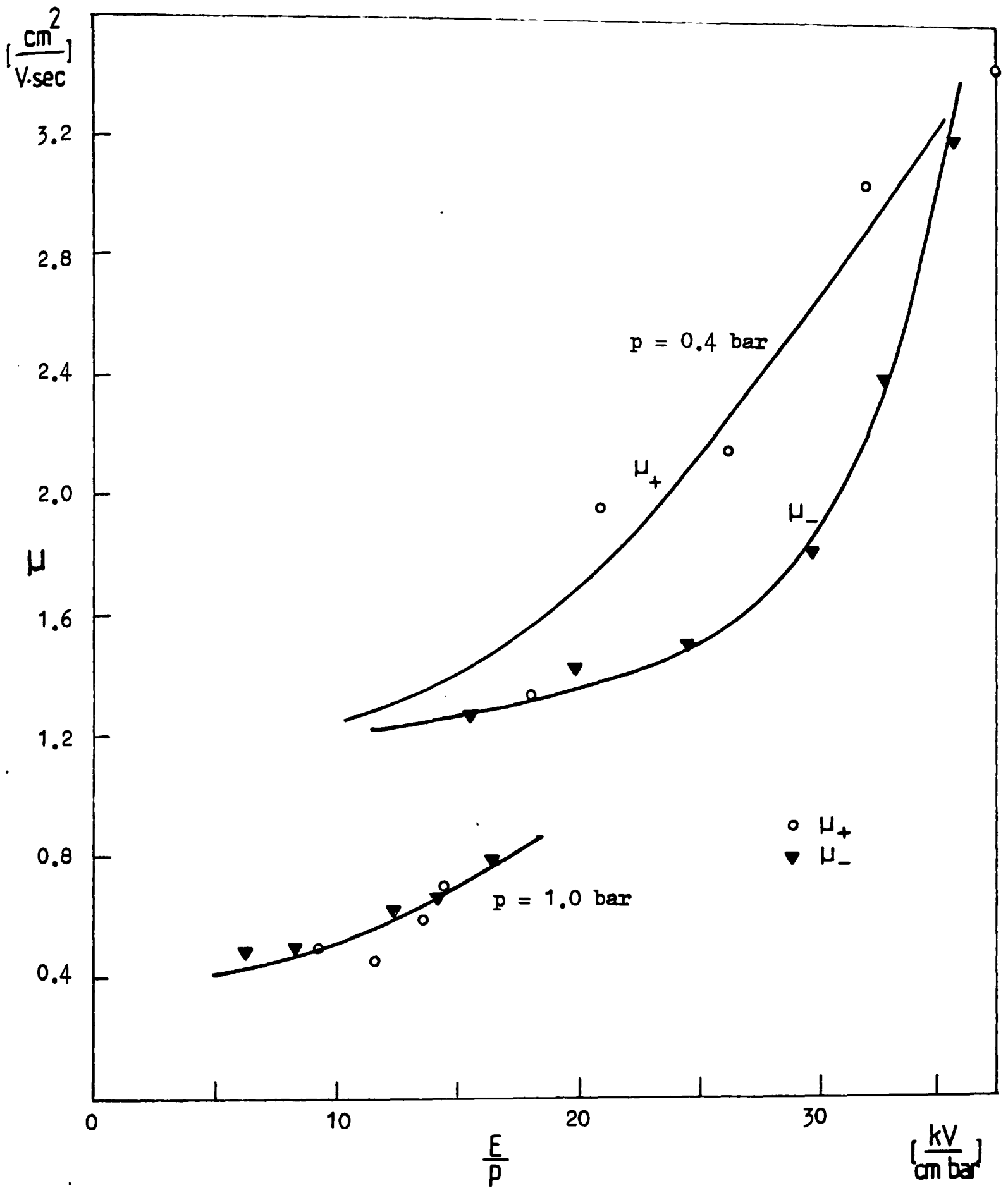


Figure 7.23 Ion mobilities in  $\text{SF}_6$  as a function of the field

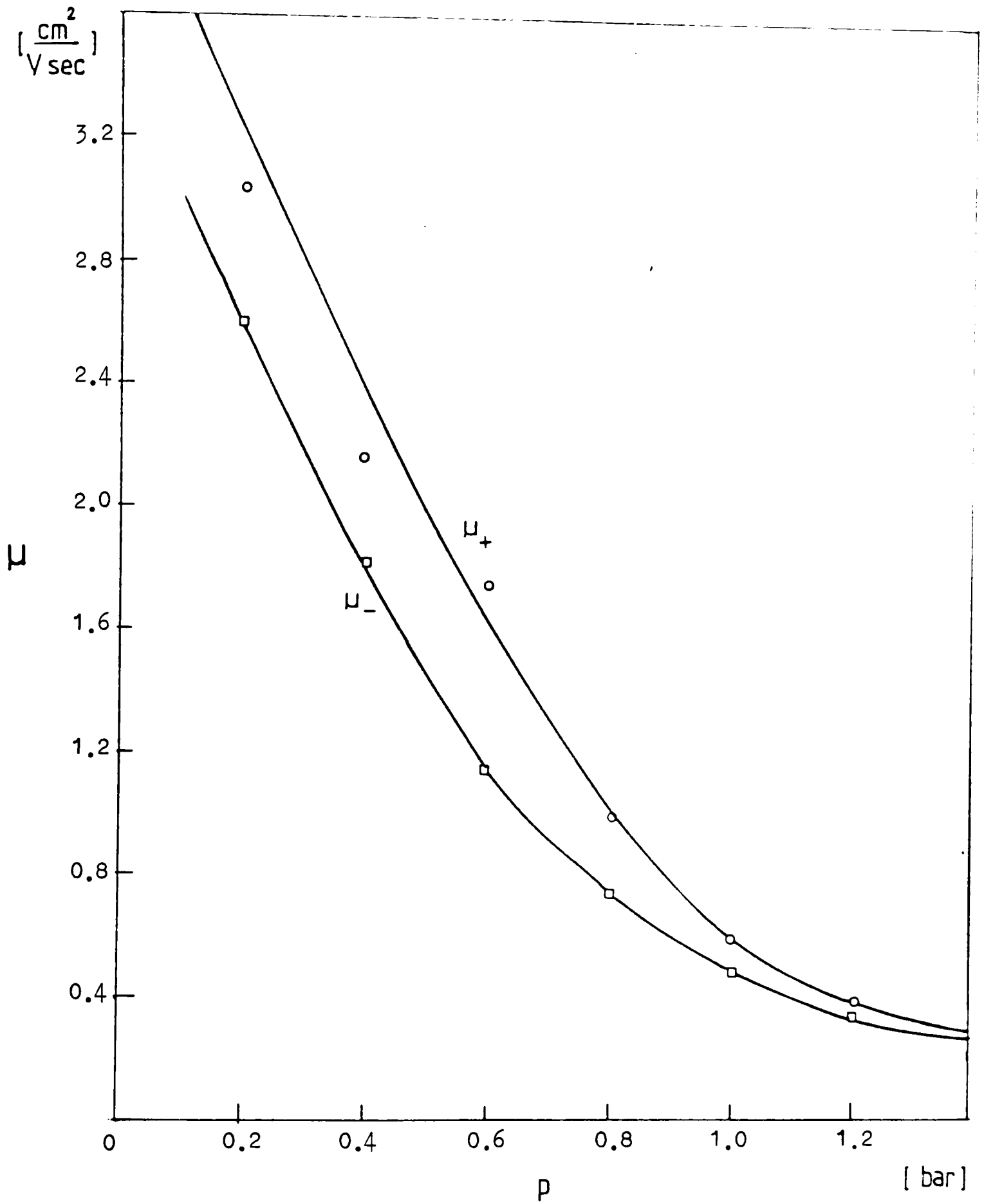


Figure 7.24 Ion mobilities in  $\text{SF}_6$  as a function of pressure ( $E = 8 - 12 \text{ kV/cm}$ )

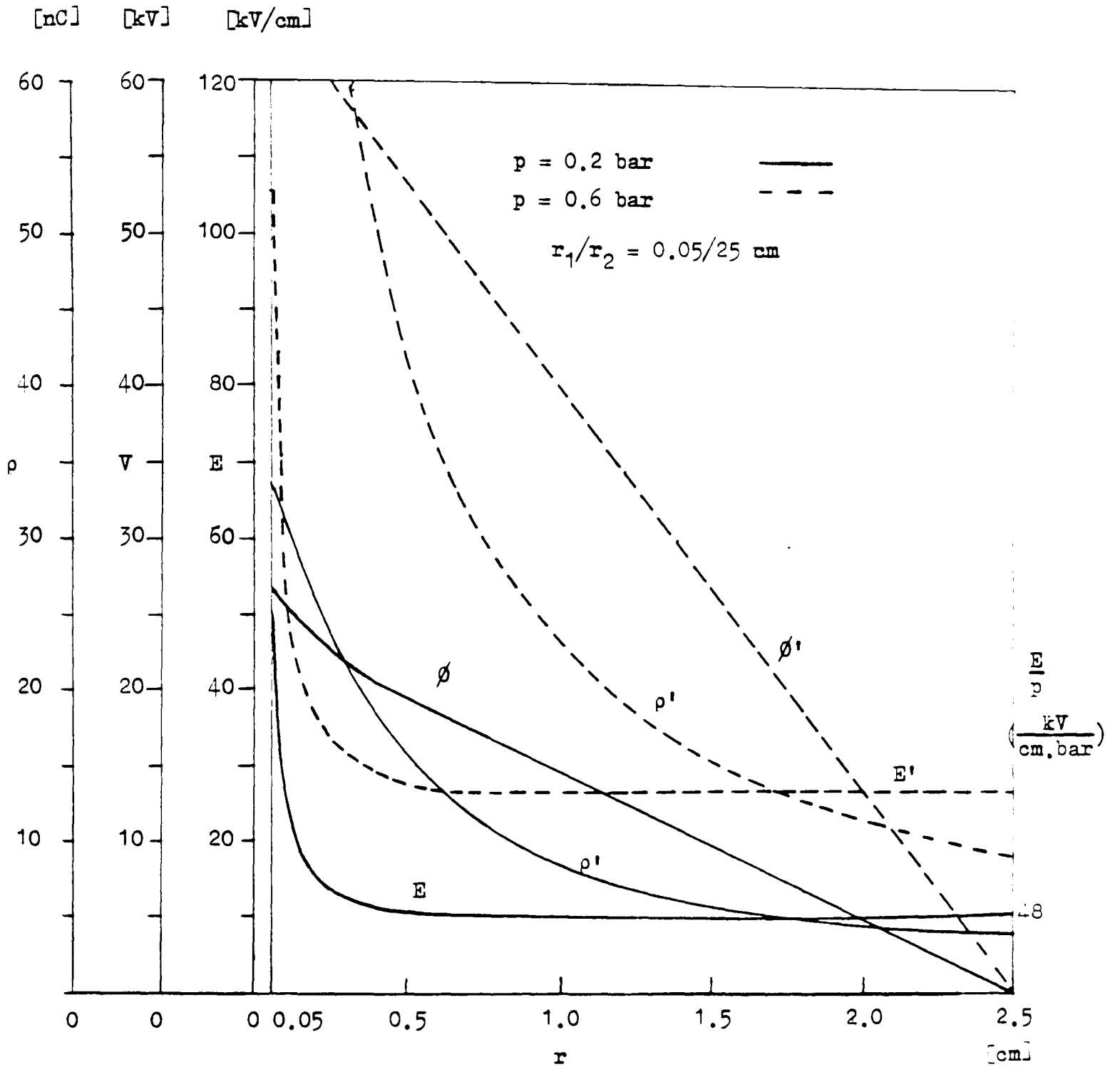


Figure 7.25 Theoretical distribution of  $\phi$ ,  $E$  and  $p$  at two pressures of  $\text{SF}_6$  ( $r_1/r_2 = 0.05/25 \text{ cm}$ , positive inner)

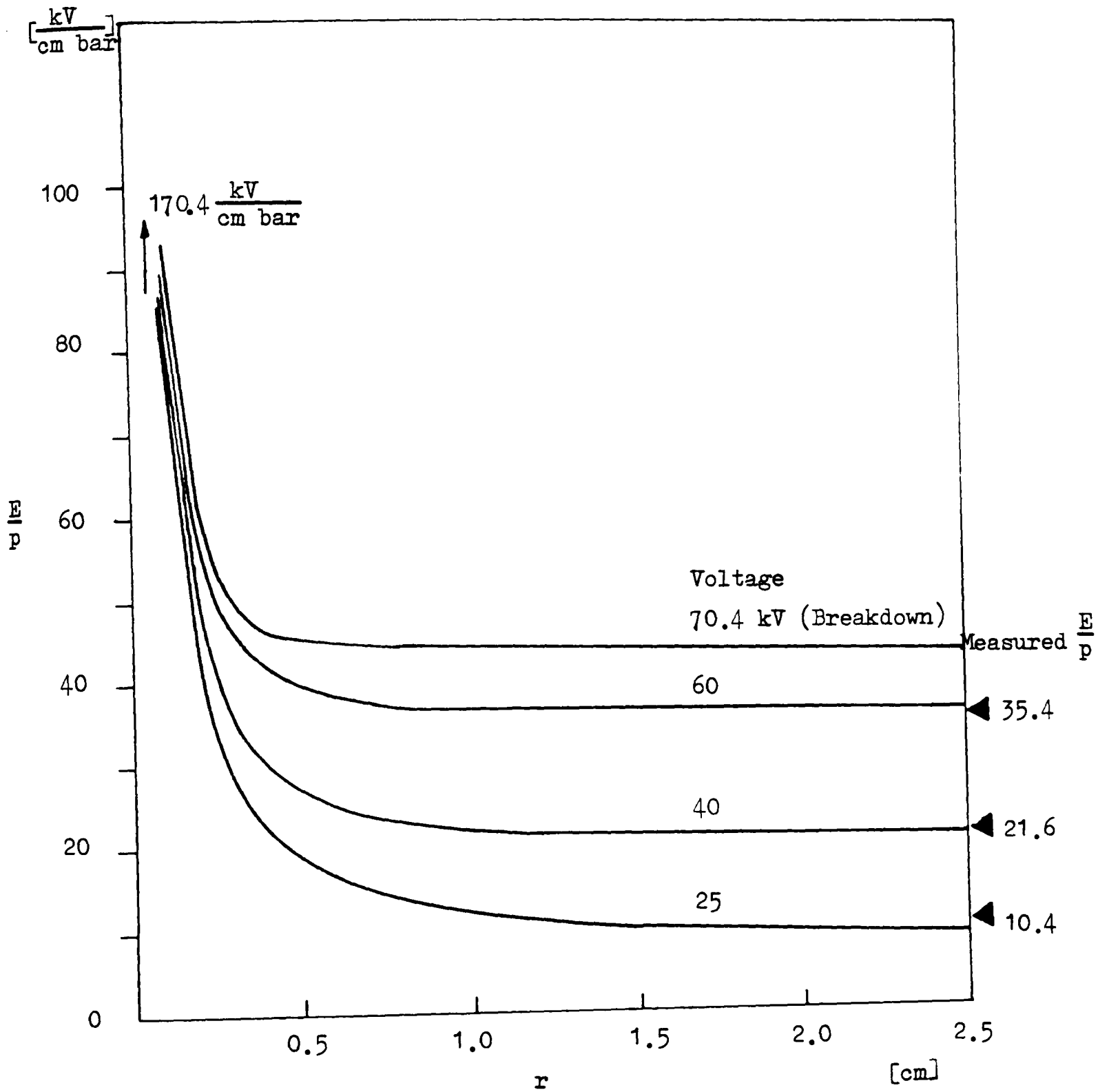


Figure 7.26 Estimated and measured values of the electric field at the outer electrode when the inner electrode is positive.

$$r_1/r_2 = 0.05/2.5 \text{ cm}, \quad p = 0.6 \text{ bar}, \quad V_0 = 20 \text{ kV}$$

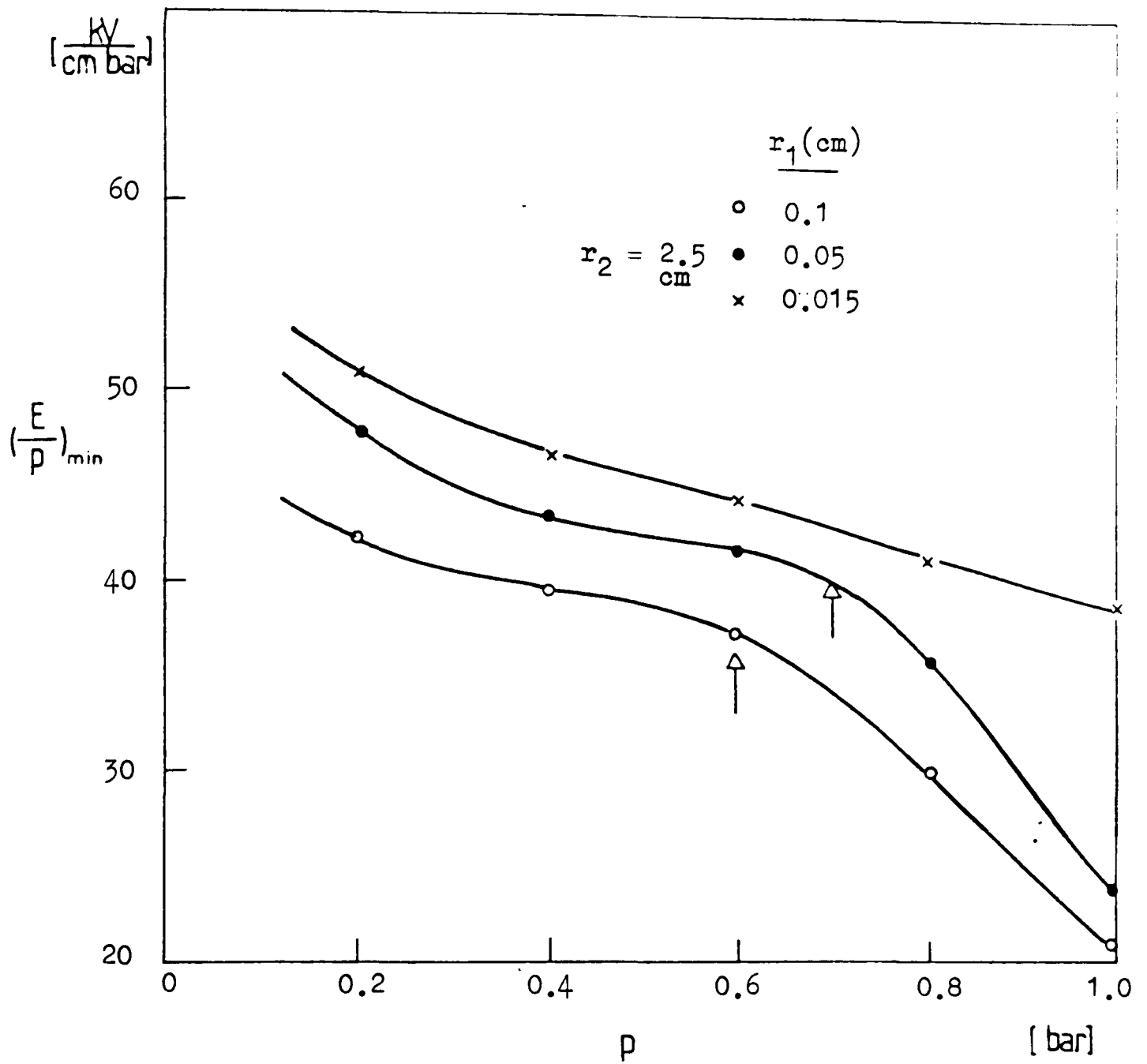


Figure 7.27 Variation of the calculated  $(\frac{E}{p})_{min}$  with gap pressure for several inner electrode radii ( $r_2 = 2.5 \text{ cm}$ ,  $\text{SF}_6$ )

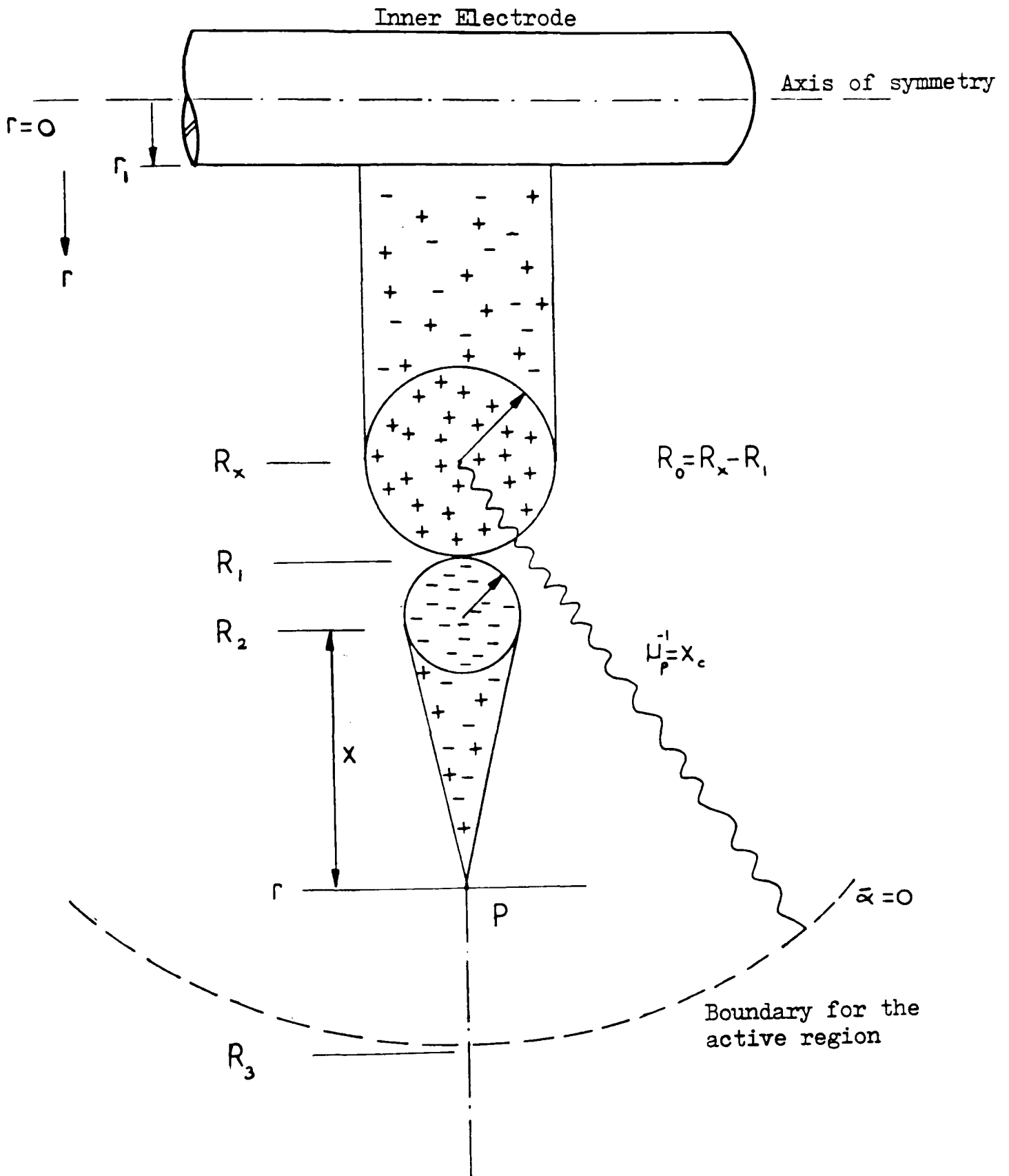


Figure 7.28 Simplified streamer propagation model with a single avalanche

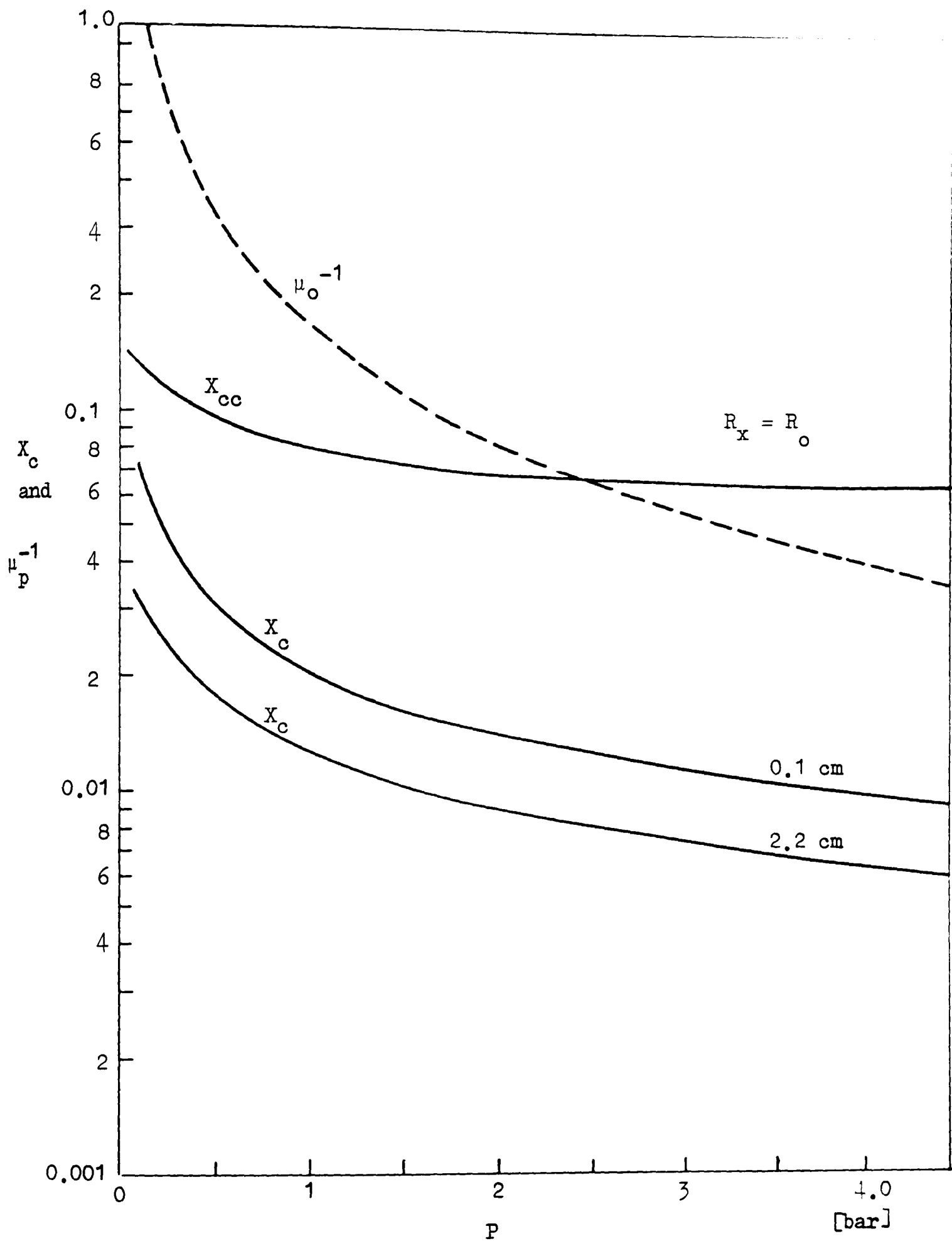


Figure 7.29 Relative variation of the critical avalanche length ( $X_{cc}$ ) and the mean photoionizing length ( $\mu_p^{-1}$ ) with pressure in  $SF_6$  ( $r_1/r_2 = 0.05/2.5$  cm)

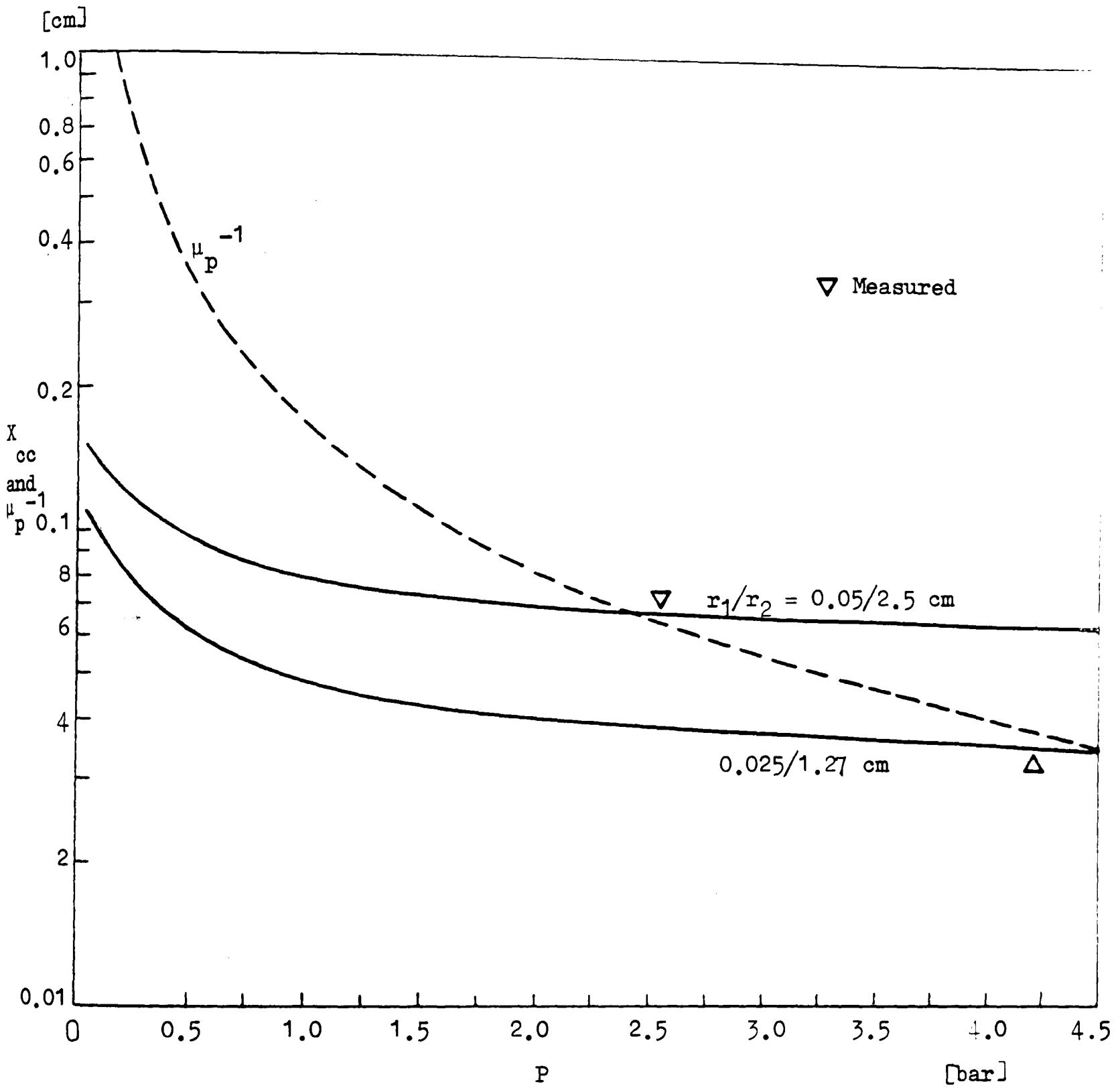


Figure 7.30 The variation of the critical avalanche length and the photoionizing mean length with pressure in  $SF_6$

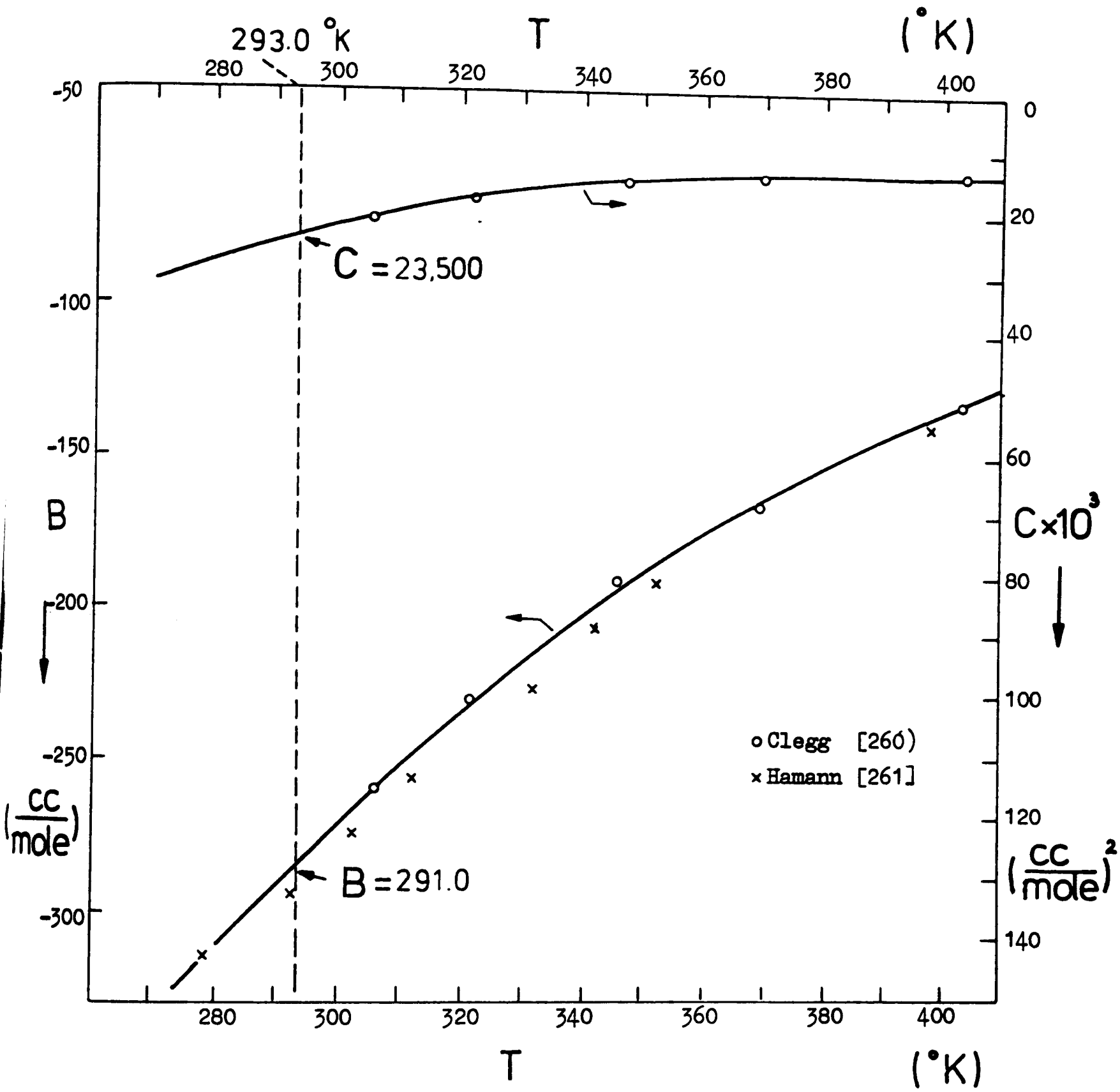


Figure A3.1 Variation of virial coefficients for SF<sub>6</sub> with temperature

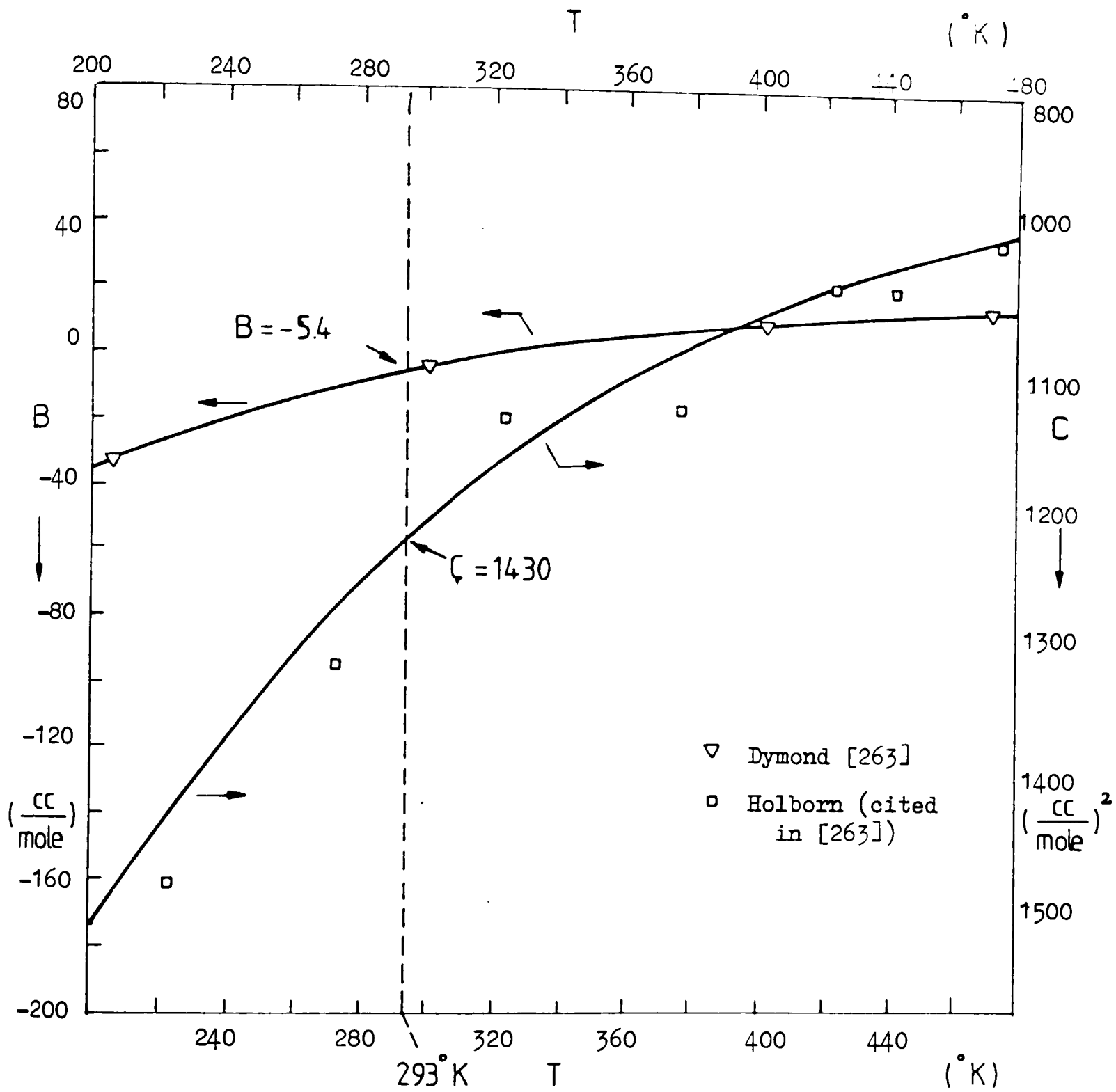


Figure A3.2 Variations of virial coefficients for  $N_2$  with temperature.

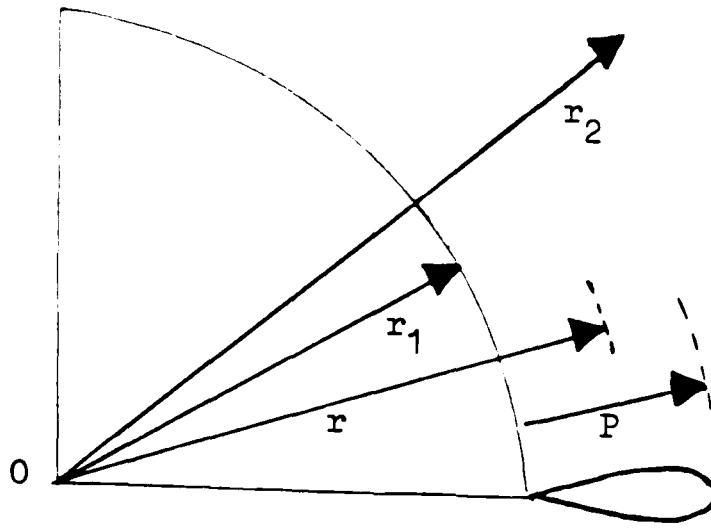


Figure A4.1 Simplified illustration for breakdown estimations in  $\text{SF}_6$  and  $\text{SF}_6/\text{N}_2$  mixtures

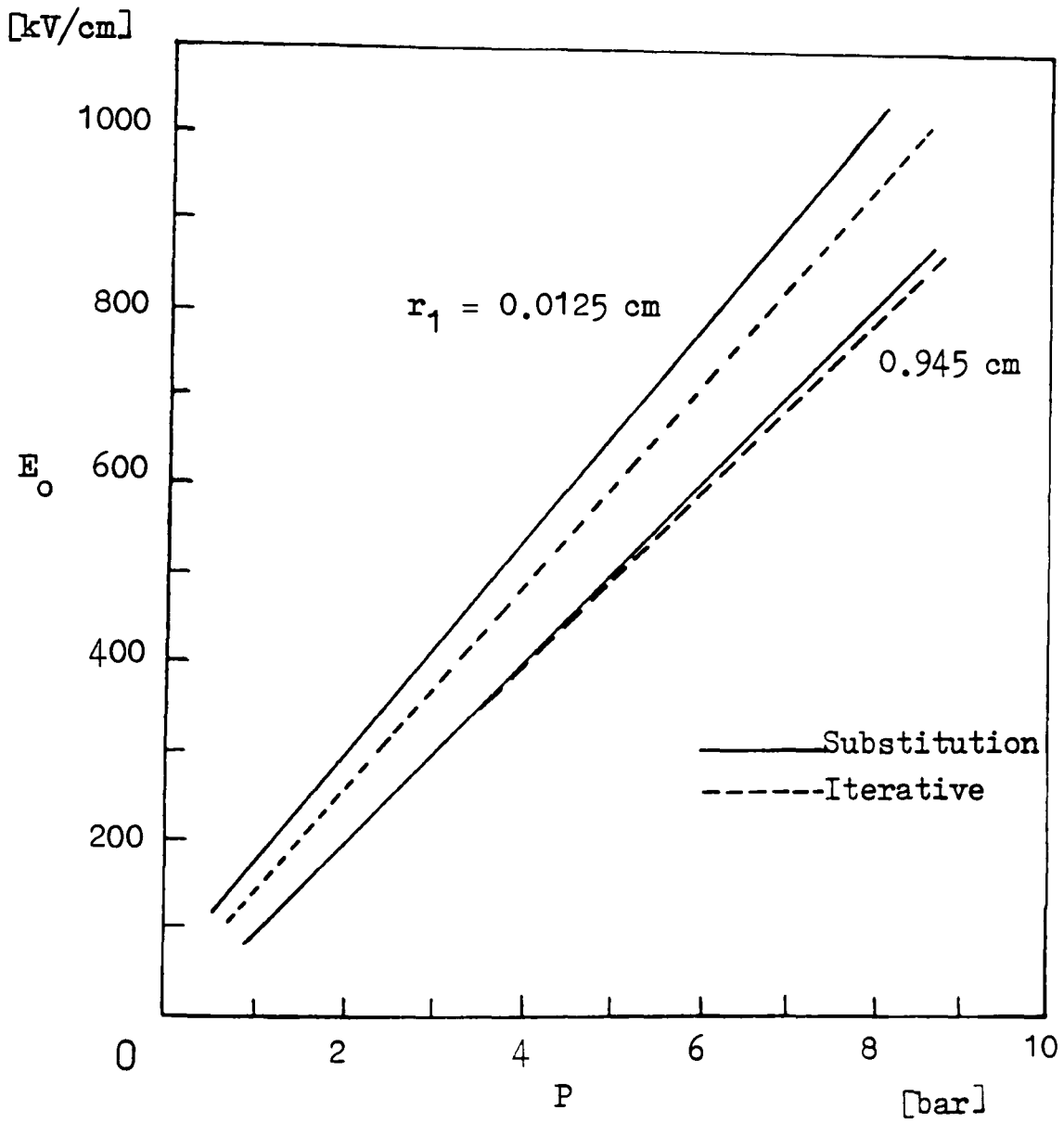


Figure A4.2 Comparison of results obtained by substitution and iterative solutions in  $\text{SF}_6$  ( $r_2 = 1.27$  cm)

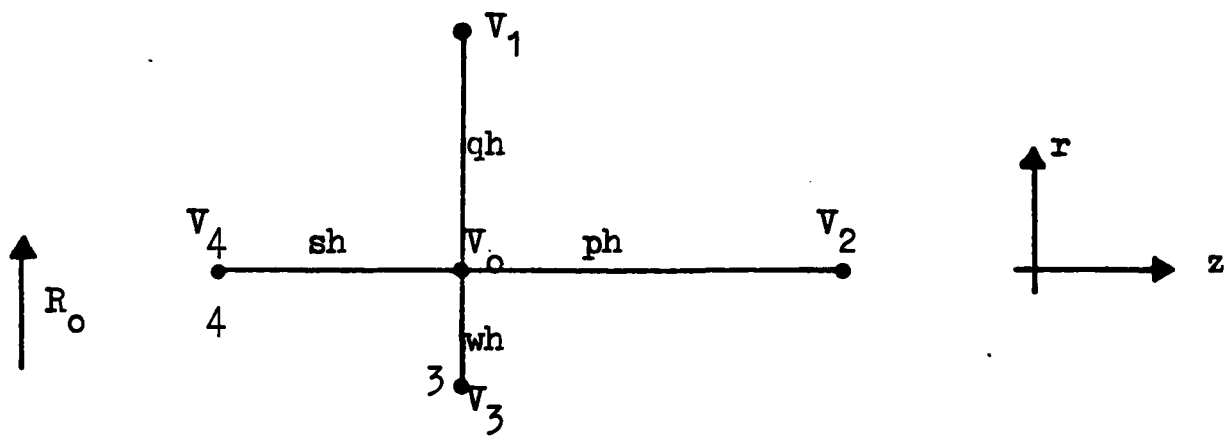


Figure A4.3 Illustration of irregular-star in cylindrical coordinate system